

Impact of Nanoparticles in the Stretched Flows



By

Maria Imtiaz

**Department of Mathematics
Quaid-I-Azam University
Islamabad, Pakistan
2016**

Impact of Nanoparticles in the Stretched Flows



By

Maria Imtiaz

Supervised By

Prof. Dr. Tasawar Hayat

**Department of Mathematics
Quaid-I-Azam University
Islamabad, Pakistan
2016**

Impact of Nanoparticles in the Stretched Flows



By

Maria Imtiaz

**A THESIS SUBMITTED IN THE PARTIAL FULFILLMENT OF THE REQUIREMENT FOR
THE DEGREE OF
DOCTOR OF PHILOSOPHY
IN
MATHEMATICS**

Supervised By

Prof. Dr. Tasawar Hayat

**Department of Mathematics
Quaid-I-Azam University
Islamabad, Pakistan**

2016

Impact of Nanoparticles in the Stretched Flows

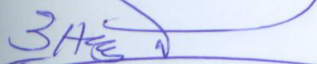
By

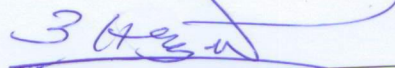
Maria Imtiaz

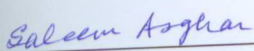
CERTIFICATE

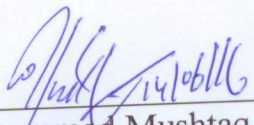
A THESIS SUBMITTED IN THE PARTIAL FULFILLMENT OF THE
REQUIREMENTS FOR THE DEGREE OF THE DOCTOR OF
PHILOSOPHY

We accept this thesis as conforming to the required standard

1. 
Prof. Dr. Tasawar Hayat
(Supervisor)

2. 
Prof. Dr. Tasawar Hayat
(Chairman)

3. 
Prof. Dr. Saleem Asghar
(External Examiner)

4. 
Dr. Muhammad Mushtaq
(External Examiner)

**Department of Mathematics
Quaid-I-Azam University
Islamabad, Pakistan
2016**

Preface

Fluid flow over stretching surface has gained wide interest among the researchers due to its various applications in industrial and engineering processes for example in manufacturing and extraction of polymer and rubber sheets, drawing of plastic films and wires, glass fiber and paper production, manufacture of foods, crystal growing, liquid films in condensation process etc. The convective heat transfer through nanoparticles over stretching sheet has been the current topic of extensive research. Nanofluids are formed by adding nanoparticles into conventional fluids like water, engine oil and ethylene glycol. The use of additive is a process which enhances the heat transfer performance of base fluids. Cooling is one of the technical challenges faced in many industries. Use of nanofluids as coolants allow for smaller size and better positioning of the radiators which eventually consumes less energy for overcoming resistance on the road. Nanoparticles in refrigerant/lubricant mixtures could enable a cost effective technology for improving the efficiency of chillers that cool buildings. Rate of heat cooling has key role in improving the desired characteristics of end product in such applications. The nanomaterials are more effective in micro-/nano-electro-mechanical devices, advanced cooling systems, large scale thermal management systems via evaporators, heat exchangers and industrial cooling applications. The MHD nanofluids are further important in hyperthermia, cancer therapy and safer surgery by cooling sink float separation, magnetic cell separation and contrast enhancement in magnetic resonance imaging. Motivated by all such facts we structure the present thesis as follows:

Literature review about nanofluid flow over stretched surface and description of solution procedure are given in chapter one. Chapter two addresses the effects of magnetohydrodynamics (MHD) in boundary layer flow of nanofluid over a permeable stretching sheet by using Buongiorno's model. Convective type boundary conditions are employed in modeling the heat and mass transfer process. Transformation method has been employed to reduce the nonlinear partial differential equations into the nonlinear ordinary differential equations. The resulting nonlinear system is solved for the series solutions. Convergence of derived series solution is shown explicitly. Physical interpretation of different parameters through graphs and numerical values of local skin friction coefficient and Nusselt number are discussed. The results of this chapter are published in "**Thermal Science (2014) DOI: 10.2298/TSCI140819139H**".

The purpose of chapter three is to investigate the flow of viscous nanofluid by a permeable exponentially stretching sheet in the presence of magnetic field. An incompressible fluid fills the porous space. A comparative study is made for the nanoparticles namely copper (Cu), silver (Ag), alumina (Al_2O_3) and titanium oxide (TiO_2). Heat transfer analysis is formulated through convective boundary condition. The ordinary differential equations are solved for the convergent series solutions of velocity and temperature. Skin friction coefficient and local Nusselt number are analyzed through numerical values. The results of this problem are published in **“Chinese Physics B 23 (5) (2014) 054701”**.

Chapter four deals with the effects of homogeneous-heterogeneous reactions in MHD boundary layer flow of nanofluid over a surface with velocity slip. Flow is caused by a stretching surface in a porous medium. Water is treated as base fluid and copper and silver as the nanoparticles. The relevant equations are first modeled and then solved by homotopy analysis method (HAM). The dimensionless expressions of velocity, concentration and wall shear stress are calculated and discussed. The contents of this chapter are published in **“Thermal Science (2015) DOI: 10.2298/TSCI140922067H”**.

Chapter five addresses the steady three-dimensional flow of viscous nanofluid induced by a permeable stretching sheet with homogeneous-heterogeneous reactions and second order velocity slip. Fluid is electrically conducting in the presence of an applied magnetic field. An incompressible fluid fills the porous space. Here copper is treated as nanoparticle with water as base fluid. The developed nonlinear problems have been solved for the series solutions. The convergence of the series solutions is carefully analyzed. The behaviors of various physical parameters are examined through graphical results of velocity and concentration distributions. The research presented in this chapter is published in **“Journal of Magnetism and Magnetic Materials 395 (2015) 294–302”**.

Chapter six is devoted to examine the boundary layer flow of ferrofluid due to a rotating disk. Homogeneous-heterogeneous reactions are also accounted. Magnetite- Fe_3O_4 in water are treated as ferrofluid. Fluid is electrically conducting in the presence of magnetic field. Energy equation in the presence of viscous dissipation is considered. Resulting nonlinear problem is formulated first and then solved for the convergent series solutions. The series solutions are constructed by homotopic procedure. Contributions of involved parameters on the flow, temperature and concentration are examined. Skin friction coefficient and Nusselt number are computed and

analyzed. The contents of this chapter are published in **“Journal of Molecular Liquids 216 (2016) 845-85”**.

Chapter seven considered the steady magnetohydrodynamic (MHD) two-dimensional flow of Cu-water nanofluid past a stretching sheet. Mathematical analysis is performed in the presence of viscous dissipation, Joule heating and non-uniform melting heat transfer. An incompressible fluid fills the porous space. The relevant boundary layer equations are reduced into ordinary differential equations by suitable transformations. The dimensionless mathematical problems are solved. Graphical results display the influence of interesting parameters. Numerical values of skin friction coefficient and local Nusselt number are computed and analyzed. This research is published in **“Advanced Powder Technology (2016) <http://dx.doi.org/10.1016/j.apt.2016.04.024>”**.

Two-dimensional unsteady flow of nanofluid by an inclined stretching sheet with thermal and solutal stratification is studied in chapter eight. In addition effects of magnetic field, thermal radiation and viscous dissipation are accounted. Unsteadiness in the flow is due to the time-dependence of the stretching velocity, stratified temperature and concentration. The developed nonlinear partial differential equations are reduced into the ordinary differential equations by suitable transformations. The governing equations are solved for the series solutions. The convergence of the series solutions for velocity, temperature and concentration fields is carefully analyzed. The effects of various physical parameters are analyzed through graphical and numerical results. These observations have been published in **“International Journal of Heat and Mass Transfer 92 (2016) 100-109”**.

Effects of heat and mass transfer in the stagnation point flow of Jeffrey nanofluid over a stretching sheet are discussed in chapter nine. Problems formulation and relevant analysis are given in the presence of Newtonian heating. The nonlinear partial differential equations are simplified using boundary layer approximations. The resultant nonlinear ordinary differential equations are solved for the series solutions. Effects of various physical parameters on the velocity, temperature and concentration fields are studied. Numerical values of local skin friction coefficient, Nusselt and Sherwood numbers are computed and analyzed. The contents of this chapter have been published in **“Journal of Aerospace Engineering 10.1061/(ASCE)AS.1943-5525.0000568 (2015) 04015063”**.

Chapter ten discloses the three-dimensional magnetohydrodynamic (MHD) flow of nanofluid induced by a permeable linear stretching sheet with velocity slip. Water is treated as base fluid and alumina as a nanoparticle. Entire different concept of nonlinear thermal radiation is utilized

in the heat transfer process. Appropriate transformations reduce the nonlinear partial differential system to ordinary differential system. Series solutions for the velocity and temperature fields are computed and examined by the graphical illustrations. The observations of conducted analysis are published in “**Journal of Magnetism and Magnetic Materials 396 (2015) 31-37**”.

Chapter eleven is concerned with the three-dimensional flow of copper-water nanofluid induced by a permeable shrinking surface in a porous medium. The present work addresses this concept in the presence of magnetic field, velocity and thermal slip effects. The relevant equations are first simplified under boundary layer assumptions and then transformed into ordinary differential equations by suitable transformations. The transformed ordinary differential equations are computed for the series solutions of velocity and temperature. Convergence analysis is shown explicitly. Velocity, temperature, wall shear stress and heat transfer rate at wall are discussed for different physical parameters through graphs and numerical values. These observations are published in “**Journal of Aerospace Engineering 10.106 / (ASCE) AS.1943-5525.0000533, (2015) 04015035**”.

Chapter twelve examines three-dimensional flow of nanofluid by a permeable shrinking sheet. Analysis is performed in the presence of applied uniform magnetic field. Copper is treated as nanoparticle with water as base fluid. An incompressible fluid fills the porous space. Convective boundary condition is used for the analysis of thermal boundary layer. Dimensionless mathematical equations are solved for the convergent series solution. Influences of embedded flow parameters on the velocity and temperature are displayed through graphs and discussed in detail. The main results of this chapter have been published in “**Journal of Molecular Liquids 212 (2015) 203-208**”.

Contents

1 Literature review and governing equations	6
1.1 Background	6
1.2 Fundamental laws for Buongiorno's model	12
1.2.1 Law of conservation of mass	12
1.2.2 Law of conservation of linear momentum	12
1.2.3 Law of conservation of energy	13
1.2.4 Law of conservation of concentration	13
1.3 Basic laws for two phase flow model	14
1.3.1 Law of conservation of linear momentum	14
1.3.2 Law of conservation of energy	14
1.4 Solution procedure	15
2 MHD flow of nanofluid over permeable stretching sheet with convective boundary conditions	16
2.1 Problem formulation	16
2.2 Homotopic solutions	19
2.2.1 Zeroth-order deformation problems	19
2.2.2 m^{th} order deformation problems	21
2.3 Analysis of series solutions	22
2.4 Results and discussion	24
2.5 Main points	37

3	MHD flow of nanofluids due to convectively exponential stretching sheet in a porous medium	38
3.1	Mathematical formulation	38
3.2	Homotopy analysis solutions	42
3.3	Convergence of the homotopy solutions	43
3.4	Discussion	44
3.5	Concluding remarks	54
4	MHD flow of nanofluid with homogeneous-heterogeneous reactions and velocity slip	56
4.1	Mathematical formulation	56
4.2	Solutions derivation	60
4.3	Convergence of the homotopy solutions	62
4.4	Results and discussion	64
4.4.1	Dimensionless velocity profiles	64
4.4.2	Dimensionless concentration profiles	67
4.4.3	Skin friction coefficient and surface concentration	69
4.5	Final remarks	72
5	Impact of magnetohydrodynamics in bidirectional flow of nanofluid subject to second order slip velocity and homogeneous-heterogeneous reactions	74
5.1	Model development	75
5.2	Homotopic solutions	79
5.3	Convergence analysis	81
5.4	Results and discussion	83
5.4.1	Dimensionless velocity profiles	83
5.4.2	Dimensionless concentration profiles	89
5.4.3	Surface concentration and skin friction coefficient	91
5.5	Conclusions	94

6	Effects of homogeneous-heterogeneous reactions in flow of magnetite-Fe_3O_4 nanoparticles by a rotating disk	96
6.1	Model development	97
6.2	Solutions procedure	100
6.3	Convergence of series solutions	104
6.4	Discussion	105
6.5	Main points	114
7	Melting heat transfer in the MHD flow of Cu-water nanofluid with viscous dissipation and Joule heating	116
7.1	Problem development	117
7.2	Homotopic solutions	120
7.3	Convergence of homotopic solutions	122
7.4	Results and discussion	125
7.4.1	Dimensionless velocity field	125
7.4.2	Dimensionless temperature field	125
7.4.3	Skin friction coefficient and Nusselt number	126
7.5	Concluding remarks	135
8	Unsteady flow of nanofluid with double stratification and magnetohydrodynamics	136
8.1	Flow equations	136
8.2	Homotopy analysis solutions	140
8.3	Convergence of the homotopy solutions	142
8.4	Interpretation of results	146
8.5	Concluding remarks	159
9	Magnetohydrodynamic stagnation point flow of Jeffrey nanofluid with Newtonian heating	161
9.1	Flow equations	161
9.2	Problem formulation	162

9.3	Series solutions	164
9.4	Convergence analysis	166
9.5	Results and discussion	168
9.6	Conclusions	183
10	MHD three-dimensional flow of nanofluid with velocity slip and nonlinear thermal radiation	185
10.1	Flow description	185
10.2	Heat transfer analysis	187
10.3	Analytical solutions	189
10.4	Convergence of the developed solutions	192
10.5	Discussion	194
10.5.1	Dimensionless velocity profiles	194
10.5.2	Dimensionless temperature profiles	194
10.5.3	Skin friction coefficient and Nusselt number	195
10.6	Concluding remarks	201
11	Magnetohydrodynamic three-dimensional flow of nanofluid over a porous shrinking surface	203
11.1	Problem formulation	204
11.2	Homotopy analysis solutions	207
11.3	Convergence analysis	209
11.4	Results and discussion	211
11.5	Concluding remarks	219
12	MHD three-dimensional flow of nanofluid in presence of convective conditions	221
12.1	Model development	221
12.2	Homotopy analysis solutions	224
12.3	Convergence of the series solutions	226
12.4	Discussion	227

12.5 Final remarks 235

Chapter 1

Literature review and governing equations

This chapter contains the literature review related to the nanofluid, magnetohydrodynamics, stretching surface, rotating disk, slip flows and homogeneous-heterogeneous reactions. Equations governing nanofluids flow for Buongiorno and two phase flow model are presented.

1.1 Background

Convective heat transfer through nanoparticles is a popular area of research at present. The nanoparticles (nanometer sized particles) are made up of metals, carbides, oxides or carbon nanotubes. The nanofluids are formed by adding nanoparticles into many conventional fluids like water, ethylene glycol and engine oil. The use of additive is a process which enhances the heat transfer performance of base fluids. Choi [1] experimentally found that addition of nanoparticles in conventional/base fluid appreciably enhances the thermal conductivity of the fluid. Eastman et al. [2] and Choi et al. [3] pointed out that a small amount ($< 1\%$ volume fraction) of Cu nanoparticles or carbon nanotubes dispersed in ethylene glycol or oil remarkably enhanced the thermal conductivity of a fluid by 40% and 50% respectively. Thus the nanomaterials are recognized more effective in micro/nano electromechanical devices, advanced cooling systems, large scale thermal management systems via evaporators, heat exchangers and industrial cooling applications. Use of nanofluids as coolants allow for smaller size and better

positioning of the radiators which eventually consumes less energy for overcoming resistance on the road. Nanoparticles in refrigerant/lubricant mixtures could enable a cost effective technology for improving the efficiency of chillers that cool buildings. Tiwari and Das [4] studied heat transfer augmentation in a two-sided lid-driven differentially heated square cavity utilizing nanofluids. At present, the literature on theoretical and experimental attempts about nanofluids is quite extensive. The comprehensive review on nanofluids can be found in the book [5] and refs. [6 – 11]. Detailed review on this topic up to 2012 has been made by Mohammed et al.[12] and Dalkilic et al. [13]. Besides these a comprehensive survey of convective transport in nanofluids is presented by Buongiorno [14]. He developed a non-homogeneous equilibrium model for convective transport to describe the heat transfer enhancement of nanofluids. He concluded that abnormal increase in thermal conductivity occurs due to the presence of two main velocity-slip effects, namely, the Brownian diffusion and the thermophoretic diffusion of the nanoparticles. Later Buongiorno et al. [15] conducted novel investigations which show no anomalous thermal conductivity enhancement in the considered fluids. Niu et al. [16] studied slip flow of a non-Newtonian nanofluid in a microtube. Effects of heat generation/absorption on stagnation point flow of nanofluid towards a surface with convective boundary conditions have been analyzed by Alsaedi et al. [17]. Xu et al. [18] examined unsteady flow in a nano-liquid film over a stretching surface. Imtiaz et al. [19] presented mixed convection flow of nanofluid with Newtonian heating. Khalili et al. [20] considered unsteady convective heat and mass transfer in flow of pseudoplastic nanofluid.

Magnetic nanofluids are more useful in the sense that their physical properties are tunable through the external magnetic field. Many equipments such as MHD generators, pumps, bearings and boundary layer control are affected by the interaction between the electrically conducting fluid and a magnetic field. The behavior of flow strongly depends on the orientation and intensity of the applied magnetic field. The exerted magnetic field manipulates the suspended particles and rearranges their concentration in the fluid which strongly changes heat transfer characteristics of the flow. A magnetic nanofluid has both the liquid and magnetic characteristics. Such materials have fascinating applications in optical modulators, magneto-optical wavelength filters, nonlinear optical materials, optical switches, optical gratings etc. Magnetic particles have pivotal role in the construction of loud speakers as sealing materials

and in sink float separation. Magneto nanofluids are useful to guide the particles up the blood stream to a tumor with magnets. This is due to the fact that the magnetic nanoparticles are regarded more adhesive to tumor cells than non-malignant cells. Such particles absorb more power than microparticles in alternating current magnetic fields tolerable in humans i.e. for cancer therapy. Numerous applications involving magnetic nanofluids include drug delivery, hyperthermia, contrast enhancement in magnetic resonance imaging and magnetic cell separation. Motivated by all the aforementioned facts, various scientists and engineers are engaged in the discussion of flows of nanofluids via different aspects. Rashidi et al. [21] analyzed entropy generation in MHD flow due to rotating porous disk in a nanofluid. Sheikholeslami et al. [22] investigated MHD nanofluid flow in a semi-porous channel. Khalili et al. [23] discussed unsteady MHD nanofluid flow over a stretching/shrinking sheet in porous medium filled with a nanofluid. Rashidi et al. [24] reported buoyancy effect on MHD stretched flow of nanofluid in presence of thermal radiation. Effect of thermal radiation on magnetohydrodynamic nanofluid flow and heat transfer by means of two phase model has been studied by Sheikholeslami et al. [25]. Numerical simulation of two phase unsteady nanofluid flow between parallel plates in presence of time dependent magnetic field has been investigated by Sheikholeslami et al. [26]. Lin et al. [27] analyzed MHD pseudoplastic nanofluid flow in a finite thin film over stretching surface. They also considered heat transfer analysis with internal heat generation. Melting heat transfer on MHD convective flow of a nanofluid with viscous dissipation and second order slip has been presented by Mabood and Mastroberardino [28]. Hayat et al. [29] explored 3D MHD flow of viscoelastic nanofluid with nonlinear thermal radiation. Hayat et al. [30] also examined interaction of magnetic field in flow of Maxwell nanofluid with convective effect.

The fluid flow over stretching surface has gained the attention of researchers due to its important applications in engineering processes namely polymer extrusion, drawing of plastic films and wires, glass fiber and paper production, manufacture of foods, crystal growing, liquid films in condensation process, etc. Crane [31] studied the flow caused by the stretching of a sheet. Most of the available literature dealt with the study of boundary layer flow over a stretching surface where the velocity of the stretching sheet is assumed linearly proportional to the distance from the fixed origin. However realistically stretching of plastic sheet may not necessarily be linear. Flow and heat transfer characteristics past an exponentially stretching

sheet has a wider applications in technology. For example, in case of annealing and thinning of copper wires, the final product depends on the rate of heat transfer at the surface with exponential variations of stretching velocity. During such processes, both the kinematics of stretching and the simultaneous heating or cooling have a decisive influence on the quality of the final product. Specific example in this direction can be mentioned through process in plastic industry. Gupta and Gupta [32] discussed heat and mass transfer on a stretching sheet with suction or blowing. Afzal et al. [33] studied momentum and heat transfer on a continuous flat surface moving in a parallel stream. Magyari and Keller [34] focused on heat and mass transfer in boundary layer flow due to an exponentially stretching sheet. Cortell [35] found the solutions for moving fluid over a flat surface. Zheng et al. [36] reported MHD flow and heat transfer over a porous shrinking surface with velocity slip and temperature jump. MHD stagnation point flow and heat transfer due to nanofluid towards a stretching sheet have been addressed by Ibrahim et al. [37]. Mukhopadhyay [38] investigated slip effects in MHD boundary layer flow by an exponentially stretching sheet with suction/blowing and thermal radiation. Exact solutions over stretching or shrinking sheet in an electrically conducting quiescent couple stress fluid have been computed by Turkyilmazoglu [39]. Malvandi et al. [40] presented slip effects on unsteady stagnation point flow of nanofluid over a stretching sheet. Casson fluid flow and heat transfer past an exponentially porous stretching surface in presence of thermal radiation been provided by Pramanik [41]. Three dimensional flow of viscoelastic fluid by an exponentially stretching surface with mass transfer has been obtained by Alhuthali et al. [42]. Rosca and Pop [43] studied Powell–Eyring fluid flow over a shrinking surface in a parallel free stream. Nandy and Pop [44] explored effects of magnetic field and thermal radiation on stagnation flow and heat transfer of nanofluid over a shrinking surface. Nandy [45] considered unsteady flow of Maxwell fluid in the presence of nanoparticles toward a permeable shrinking surface with Navier slip. Weidman and Ishak [46] computed multiple solutions of two-dimensional and three-dimensional flows induced by a stretching flat surface. Effects of viscous dissipation and heat source on unsteady MHD flow over a stretching sheet have been examined by Reddy et al. [47]. Chen et al. [48] discussed boundary layer flow of Maxwell fluid over an unsteady stretching surface. Mustafa et al. [49] analyzed radiation effects in flow by a bi-directional exponentially stretching sheet. Effects of convective heat and mass transfer in flow of Powell-Eyring fluid past

an exponentially stretching sheet have been examined by Hayat et al. [50].

Fluid flow by a rotating disk is important in engineering and geophysical applications such as flows in spin coating, manufacturing and use of computer disks, rotational viscometer, centrifugal machinery, pumping of liquid metals at high melting point, crystal growth from molten silicon, turbo-machinery etc. Karman [51] investigated the classical problem of a rotating disk. Erdogan [52] analyzed unsteady viscous fluid flow by non-coaxial rotations of disk and a fluid at infinity. A note on porous rotating disk is presented by Kelson and Desseaux [53]. Flow due to a rotating porous disk in presence of nanoparticles is analyzed by Bachok et al. [54]. Rashidi et al. [55] developed approximate solutions for steady flow due to a rotating disk. Here porous medium and heat transfer are also considered. Turkyilmazoglu [56] studied nanofluid flow and heat transfer due to a rotating disk. Hayat et al. [57] analyzed MHD flow of Cu-water nanofluid due to a rotating disk with partial slip.

The formation and use of micro devices have attracted the attention of recent scientists. The small size as well as high efficiency of micro-devices-such as microsensors, microvalves and micropumps are some of the advantages of using MEMS and NEMS (Micro and Nano Electro Mechanical Systems). Many attempts addressing the flow and heat transfer have been presented to guarantee the performance of such devices. The surface effects at micro scale level lead to change in the classical conditions. Thus no-slip condition is inadequate for the fluid flows in MEMS and NEMS. No slip conditions show unrealistic behavior for the cases like the extrusion of polymer melts from a capillary tube, corner flow and spreading of liquid on a solid substrate [58]. The flow analysis with heat transfer at micro-scale is encountered in micro-electro-mechanical systems (MEMS). Such systems have association with consideration of velocity slip and temperature jump. Khare et al. [59] presented relationship between velocity and thermal slip. Wu [60] derived a slip model for rarefied gas flows at arbitrary Knudsen number. Fang and Aziz [61] considered viscous flow with second-order slip velocity over a stretching sheet. Heat transfer enhancement using nanofluids in microchannels with slip and non-slip flow regimes has been investigated by Akbarinia et al. [62]. Mahmoud and Waheed [63] examined stretched flow of a micropolar fluid with heat generation (absorption) and slip velocity. Ibrahim and Shankar [64] presented MHD boundary layer flow and heat transfer of a nanofluid past a permeable stretching sheet with velocity, thermal and solutal slip boundary condition. Khan

et al. [65] analyzed hydrodynamic and thermal slip effect in double-diffusive free convective boundary layer flow of a nanofluid. Extension of a second order velocity slip/temperature jump boundary condition to simulate high speed micro/nanoflows has been given by Rooholghdos and Roohi [66]. Malvandi and Ganji [67] considered Brownian motion and thermophoresis - effects on slip flow of alumina/water nanofluid inside a circular microchannel. Second order slip flow of Cu-water nanofluid over a stretching sheet with heat transfer has been investigated by Sharma and Ishak [68]. Rashidi et al. [69] investigated entropy generation in MHD flow over a rotating porous disk with variable properties and slip condition. Karimipour et al. [70] analyzed the simulation of copper-water nanofluid in a microchannel with slip flow effect. Here the lattice Boltzman method is used for the simulation. Megahed [71] studied MHD Casson fluid flow and heat transfer with second-order slip velocity and thermal slip over a permeable stretching sheet. Hakeem et al. [72] presented magnetic field effect in second order slip flow of nanofluid over a radiative stretching/shrinking sheet.

Homogeneous-heterogeneous reactions occur in many chemically reacting systems such as in combustion, catalysis and biochemical systems. Some of the reactions have the ability to proceed very slowly or not at all, except in the presence of a catalyst. The interaction between the homogeneous and heterogeneous reactions is very complex. It is involved in the production and consumption of reactant species at different rates both within the fluid and on the catalytic surfaces. Especially chemical reaction effects are quite significant in food processing, hydrometallurgical industry, manufacturing of ceramics and polymer production, fog formation and dispersion, chemical processing equipment design, crops damage via freezing, cooling towers and temperature distribution and moisture over agricultural fields and groves of fruit trees. A model for isothermal homogeneous-heterogeneous reactions in boundary layer flow of viscous fluid past a flat plate is studied by Merkin [73]. He presented the homogeneous reaction by cubic autocatalysis and the heterogeneous reaction with a first order process. It is shown that the surface reaction is the dominant mechanism near the leading edge of the plate. Chaudhary and Merkin [74] studied the homogenous-heterogeneous reactions in boundary layer flow of viscous fluid. They found the numerical solution near the leading edge of a flat plate. Khan and Pop [75] studied two-dimensional stagnation-point flow with homogeneous-heterogeneous reaction. Bachok et al. [76] focused on the stagnation-point flow towards a stretching sheet with

homogeneous–heterogeneous reaction effects. Effects of homogeneous-heterogeneous reactions in the flow of viscoelastic fluid towards a stretching sheet are investigated by Khan and Pop [77]. Homogeneous-heterogeneous reactions in micropolar fluid flow from a permeable stretching or shrinking sheet in a porous medium have been studied by Shaw et al. [78]. Kameswaran et al. [79] extended the work of Khan and Pop [77] for nanofluid over a porous stretching sheet. Hayat et al. [80] analyzed homogeneous-heterogeneous reactions in the stagnation point flow of carbon nanotubes towards a stretching surface with Newtonian heating. Effect of homogeneous-heterogeneous reactions in flow of Powell-Eyring fluid is examined by Hayat et al. [81]. Abbasi et al. [82] investigated stagnation-point flow of viscous fluid towards stretching/shrinking sheet in the presence of homogeneous–heterogeneous reactions.

1.2 Fundamental laws for Buongiorno’s model

1.2.1 Law of conservation of mass

In absence of sources or sinks we can write equation of continuity as follows:

$$\frac{\partial \rho}{\partial t} + \nabla \cdot (\rho \mathbf{V}) = 0. \quad (1.1)$$

in which ρ is fluid density, t is time and \mathbf{V} is fluid velocity. The above equation for an incompressible fluid takes the form

$$\nabla \cdot \mathbf{V} = 0. \quad (1.2)$$

1.2.2 Law of conservation of linear momentum

Generalized equation of motion is

$$\rho \frac{d\mathbf{V}}{dt} = \nabla \cdot \boldsymbol{\tau} + \rho \mathbf{b}, \quad (1.3)$$

in which the left hand side represents an inertial force, the first term on right hand side is the surface force and the second term on right hand side is body force. For an incompressible viscous fluid $\boldsymbol{\tau} = -P\mathbf{I} + \mu\mathbf{A}_1$ is the Cauchy stress tensor, P the pressure, \mathbf{I} the identity tensor, $\mathbf{A}_1 = \nabla\mathbf{V} + (\nabla\mathbf{V})^t$ the first Rivlin-Erickson tensor, \mathbf{b} the body force and d/dt the material

time derivative.

1.2.3 Law of conservation of energy

The energy equation for a nanofluid can be written as

$$\rho c_p \frac{dT}{dt} = -\text{div } \tilde{\mathbf{q}} + h_p \nabla \cdot \vec{\mathbf{j}}_p, \quad (1.4)$$

where c_p is specific heat of nanofluid, T is the temperature, h_p is the specific enthalpy for nanoparticles, \vec{q} is the energy flux and $\vec{\mathbf{j}}_p$ is the nanoparticles diffusion mass flux. Energy flux \vec{q} and nanoparticles diffusion mass flux $\vec{\mathbf{j}}_p$ are given by

$$\tilde{\mathbf{q}} = -k \nabla T + h_p \vec{\mathbf{j}}_p, \quad (1.5)$$

$$\vec{\mathbf{j}}_p = -\rho_p D_B \nabla C - \rho_p D_T \frac{\nabla T}{T_\infty}, \quad (1.6)$$

in which k the thermal conductivity, ρ_p is the nanoparticle mass density, D_B the Brownian motion parameter, D_T the thermophoretic diffusion coefficient and C the nanoparticles volume fraction. Now Eq. (1.4) takes the form

$$\rho c_p \frac{dT}{dt} = k \nabla^2 T + \rho_p c_p \left[D_B \nabla C \cdot \nabla T + D_T \frac{\nabla T \cdot \nabla T}{T_\infty} \right], \quad (1.7)$$

which is the energy equation for nanofluids.

1.2.4 Law of conservation of concentration

The concentration equation for nanofluids is

$$\frac{\partial C}{\partial t} + \mathbf{V} \cdot \nabla C = -\frac{1}{\rho_p} \nabla \cdot \vec{\mathbf{j}}_p, \quad (1.8)$$

After utilizing Eq. (1.6), we get

$$\frac{\partial C}{\partial t} + \mathbf{V} \cdot \nabla C = D_B \nabla^2 C + D_T \frac{\nabla^2 T}{T_\infty}. \quad (1.9)$$

1.3 Basic laws for two phase flow model

1.3.1 Law of conservation of linear momentum

Generalized equation of motion is

$$\rho_{nf} \frac{d\mathbf{V}}{dt} = -\nabla \cdot \boldsymbol{\tau} + \rho_{nf} \mathbf{b}, \quad (1.10)$$

where the effective nanofluid density ρ_{nf} is taken as follows [4]:

$$\rho_{nf} = \rho_f(1 - \phi) + \rho_s\phi, \quad (1.11)$$

Here ϕ is the solid volume fraction, s in subscript is for nano-solid-particles and f in subscript is for base fluid.

1.3.2 Law of conservation of energy

The energy equation for a nanofluid in the presence of viscous dissipation and thermal radiation can be written as

$$(\rho c_p)_{nf} \frac{dT}{dt} = \boldsymbol{\tau} \cdot \mathbf{L} + k_{nf} \nabla^2 T - \nabla \cdot \mathbf{q}_r, \quad (1.12)$$

where $\boldsymbol{\tau} = -P\mathbf{I} + \mu_{nf}\mathbf{A}_1$ is the Cauchy stress tensor and \mathbf{q}_r is the radiative heat flux. The effective nanofluid heat capacity $(\rho c_p)_{nf}$ is [4]:

$$(\rho c_p)_{nf} = (\rho c_p)_f(1 - \phi) + (\rho c_p)_s\phi. \quad (1.13)$$

The dynamic viscosity of nanofluid μ_{nf} is [98]:

$$\mu_{nf} = \frac{\mu_f}{(1 - \phi)^{2.5}}, \quad (1.14)$$

and the effective thermal conductivity of nanofluid k_{nf} by Maxwell-Garnett model is given by [99]:

$$\frac{k_{nf}}{k_f} = \frac{k_s + 2k_f - 2\phi(k_f - k_s)}{k_s + 2k_f + \phi(k_f - k_s)}. \quad (1.15)$$

1.4 Solution procedure

Flow equations occurring in the field of science and engineering are highly nonlinear in general. Therefore it is very difficult to find the exact solution of such equations. Usually perturbation, Adomian decomposition and homotopy perturbation methods are used to find the solution of nonlinear equations. But these methods have some drawback through involvement of large/small parameters in the equations and convergence. Homotopy analysis method (HAM) [83 – 97] is one while is independent of small/large parameters. This method also gives us a way to adjust and control the convergence region (i.e. by plotting h-curve). It also provides exemption to choose different sets of base functions. We have used this technique in the subsequent chapters to get the convergent series solutions.

Chapter 2

MHD flow of nanofluid over permeable stretching sheet with convective boundary conditions

This chapter addresses the magnetohydrodynamic (MHD) boundary layer flow of nanofluid. Flow is induced by a permeable stretching sheet. Convective type boundary conditions are employed in modeling the heat and mass transfer process. Appropriate transformations reduce the nonlinear partial differential equations to ordinary differential equations. The convergent series solutions are constructed. Graphical results of different parameters are discussed. The behaviors of Brownian motion and thermophoretic diffusion of nanoparticles have been examined. The dimensionless expressions of local Nusselt and local Sherwood numbers have been evaluated and discussed.

2.1 Problem formulation

We consider the two-dimensional flow of nanofluid bounded by a permeable stretching sheet. The x -axis is taken along the stretching surface in the direction of motion and y -axis is perpendicular to it. A uniform magnetic field of strength B_0 is applied parallel to the y -axis. It is assumed that the effects of induced magnetic and electric fields are negligible. Salient features of Brownian motion and thermophoresis are present. The temperature T and the nanoparticle

fraction C at the surface have constant values T_w and C_w respectively. The ambient values of T and C attained as y tends to infinity are denoted by T_∞ and C_∞ respectively. The conservation of mass, momentum, energy and nanoparticles equations for nanofluids are:

$$\frac{\partial u}{\partial x} + \frac{\partial v}{\partial y} = 0, \quad (2.1)$$

$$u \frac{\partial u}{\partial x} + v \frac{\partial u}{\partial y} = \nu \frac{\partial^2 u}{\partial y^2} - \frac{\sigma B_0^2 u}{\rho}, \quad (2.2)$$

$$u \frac{\partial T}{\partial x} + v \frac{\partial T}{\partial y} = \alpha \frac{\partial^2 T}{\partial y^2} + \tau \left[D_B \frac{\partial C}{\partial y} \frac{\partial T}{\partial y} + \frac{D_T}{T_\infty} \left(\frac{\partial T}{\partial y} \right)^2 \right], \quad (2.3)$$

$$u \frac{\partial C}{\partial x} + v \frac{\partial C}{\partial y} = D_B \frac{\partial^2 C}{\partial y^2} + \frac{D_T}{T_\infty} \frac{\partial^2 T}{\partial y^2}, \quad (2.4)$$

where u and v are the velocity components along x and y - directions respectively, ν the kinematic viscosity, ρ the fluid density, σ the electrical conductivity of the base fluid, α the thermal diffusivity, $\tau = (\rho c)_p / (\rho c)_f$ is the ratio between the effective heat capacity of the nanoparticle material and heat capacity of the fluid, D_B is the Brownian diffusion coefficient and D_T is the thermophoretic diffusion coefficient.

The boundary conditions are prescribed as follows:

$$\begin{aligned} u = u_w(x) = cx, \quad v = V_w, \quad -k \frac{\partial T}{\partial y} = h(T_f - T), \quad -D_m \frac{\partial C}{\partial y} = k_m(C_f - C) \quad \text{at } y = 0, \\ u = 0, \quad T \rightarrow T_\infty, \quad C \rightarrow C_\infty \quad \text{as } y \rightarrow \infty, \end{aligned} \quad (2.5)$$

in which V_w is the wall mass transfer velocity, k is the thermal conductivity of fluid, h is the convective heat transfer coefficient, T_f is the heated fluid temperature, D_m is the molecular diffusivity of the species concentration, k_m is the wall mass transfer coefficient and C_f is the heated fluid concentration. Using the transformations

$$\eta = \sqrt{\frac{c}{\nu}} y, \quad u = cx f'(\eta), \quad v = -\sqrt{\nu c} f(\eta), \quad \theta(\eta) = \frac{T - T_\infty}{T_f - T_\infty}, \quad \Phi(\eta) = \frac{C - C_\infty}{C_f - C_\infty}, \quad (2.6)$$

equation (2.1) is satisfied automatically and Eqs. (2.2 – 2.5) take the following forms

$$f''' - f'^2 + f f'' - M f' = 0, \quad (2.7)$$

$$\frac{1}{\text{Pr}}\theta'' + f\theta' + N_b\Phi'\theta' + N_t\theta'^2 = 0, \quad (2.8)$$

$$\Phi'' + Scf\Phi' + \frac{N_t}{N_b}\theta'' = 0, \quad (2.9)$$

$$\begin{aligned} f(0) = S, \quad f'(0) = 1, \quad \theta'(0) = -\gamma_1[1 - \theta(0)], \quad \Phi'(0) = -\gamma_2[1 - \Phi(0)], \\ f'(\infty) = 0, \quad \theta(\infty) = 0, \quad \Phi(\infty) = 0, \end{aligned} \quad (2.10)$$

where prime indicates the differentiation with respect to η . Moreover the Hartman number M , the Prandtl number Pr , the Brownian motion parameter N_b , the thermophoresis parameter N_t , the Schmidt number Sc , the mass transfer parameter S with $S > 0$ for suction and $S < 0$ for injection, the thermal Biot number γ_1 and the concentration Biot number γ_2 are defined by the following definitions:

$$\begin{aligned} M &= \frac{\sigma B_0^2}{\rho c}, \quad \text{Pr} = \frac{\nu}{\alpha}, \quad N_b = \frac{(\rho c)_p D_B (C_f - C_\infty)}{(\rho c)_f \nu}, \quad N_t = \frac{(\rho c)_p D_T (T_f - T_\infty)}{(\rho c)_f T_\infty \nu}, \\ Sc &= \frac{\nu}{D_B}, \quad S = -\frac{V_w}{\sqrt{\nu c}}, \quad \gamma_1 = \frac{h}{k} \sqrt{\frac{\nu}{c}}, \quad \gamma_2 = \frac{k_m}{D_m} \sqrt{\frac{\nu}{c}}. \end{aligned} \quad (2.11)$$

The local Nusselt number Nu and Sherwood number Sh are

$$Nu = \frac{xq_w}{k(T_f - T_\infty)}; \quad q_w = -k \frac{\partial T}{\partial y} \Big|_{y=0}, \quad (2.12)$$

$$Sh = \frac{xq_m}{D_B(C_f - C_\infty)}; \quad q_m = -D \frac{\partial C}{\partial y} \Big|_{y=0}, \quad (2.13)$$

in which q_w and q_m denote the wall heat and mass fluxes respectively. In dimensionless form

$$Nu \text{Re}_x^{-1/2} = -\theta'(0), \quad Sh \text{Re}_x^{-1/2} = -\Phi'(0), \quad (2.14)$$

where $\text{Re}_x = u_w(x)x/\nu$ is the local Reynolds number.

2.2 Homotopic solutions

2.2.1 Zeroth-order deformation problems

We choose initial guesses $f_0(\eta)$, $\theta_0(\eta)$ and $\Phi_0(\eta)$ and linear operators \mathcal{L}_f , \mathcal{L}_θ and \mathcal{L}_Φ in the forms

$$f_0(\eta) = S + 1 - \exp(-\eta), \quad (2.15)$$

$$\theta_0(\eta) = \frac{\gamma_1}{1 + \gamma_1} \exp(-\eta), \quad (2.16)$$

$$\Phi_0(\eta) = \frac{\gamma_2}{1 + \gamma_2} \exp(-\eta), \quad (2.17)$$

$$\mathcal{L}_f(f) = f''' - f', \quad (2.18)$$

$$\mathcal{L}_\theta(\theta) = \theta'' - \theta, \quad (2.19)$$

$$\mathcal{L}_\Phi(\Phi) = \Phi'' - \Phi, \quad (2.20)$$

together with the properties

$$\mathcal{L}_f [c_1 + c_2 \exp(\eta) + c_3 \exp(-\eta)] = 0, \quad (2.21)$$

$$\mathcal{L}_\theta [c_4 \exp(\eta) + c_5 \exp(-\eta)] = 0, \quad (2.22)$$

$$\mathcal{L}_\Phi [c_6 \exp(\eta) + c_7 \exp(-\eta)] = 0, \quad (2.23)$$

where $c_1 - c_7$ are the constants. If $p \in [0, 1]$ denotes an embedding parameter and \hbar_f , \hbar_θ and \hbar_Φ represent the non-zero auxiliary parameters then the zeroth order deformation problems are defined as follows:

$$(1 - p)\mathcal{L}_f [\hat{f}(\eta; p) - f_0(\eta)] = p\hbar_f \mathcal{N}_f[\hat{f}(\eta; p)], \quad (2.24)$$

$$(1 - p)\mathcal{L}_\theta [\hat{\theta}(\eta; p) - \theta_0(\eta)] = p\hbar_\theta \mathcal{N}_\theta[\hat{\theta}(\eta; p), \hat{f}(\eta; p), \hat{\Phi}(\eta; p)], \quad (2.25)$$

$$(1 - p)\mathcal{L}_\Phi [\hat{\Phi}(\eta; p) - \Phi_0(\eta)] = p\hbar_\Phi \mathcal{N}_\Phi[\hat{\Phi}(\eta; p), \hat{f}(\eta; p), \hat{\theta}(\eta; p)], \quad (2.26)$$

$$\hat{f}(0; p) = S, \quad \hat{f}'(0; p) = 1, \quad \hat{f}'(\infty; p) = 0,$$

$$\hat{\theta}'(0; p) = -\gamma_1[1 - \hat{\theta}(0; p)], \quad \hat{\theta}(\infty; p) = 0,$$

$$\hat{\Phi}'(0; p) = -\gamma_2[1 - \hat{\Phi}(0; p)], \quad \hat{\Phi}(\infty; p) = 0, \quad (2.27)$$

where \mathcal{N}_f , \mathcal{N}_θ and \mathcal{N}_Φ are the nonlinear operators defined in the forms:

$$\mathcal{N}_f[\hat{f}(\eta; p)] = \frac{\partial^3 \hat{f}(\eta; p)}{\partial \eta^3} + \hat{f}(\eta; p) \frac{\partial^2 \hat{f}(\eta; p)}{\partial \eta^2} - \left(\frac{\partial \hat{f}(\eta; p)}{\partial \eta} \right)^2 - M \frac{\partial \hat{f}(\eta; p)}{\partial \eta}, \quad (2.28)$$

$$\begin{aligned} \mathcal{N}_\theta[\hat{\theta}(\eta; p), \hat{f}(\eta; p), \hat{\Phi}(\eta; p)] &= \frac{1}{\text{Pr}} \frac{\partial^2 \hat{\theta}(\eta; p)}{\partial \eta^2} + \hat{f}(\eta; p) \frac{\partial \hat{\theta}(\eta; p)}{\partial \eta} + N_t \left(\frac{\partial \hat{\theta}(\eta; p)}{\partial \eta} \right)^2 \\ &\quad + N_b \frac{\partial \hat{\Phi}(\eta; p)}{\partial \eta} \frac{\partial \hat{\theta}(\eta; p)}{\partial \eta}, \end{aligned} \quad (2.29)$$

$$\mathcal{N}_\Phi[\hat{\Phi}(\eta; p), \hat{f}(\eta; p), \hat{\theta}(\eta; p)] = \frac{\partial^2 \hat{\Phi}(\eta; p)}{\partial \eta^2} + Sc \hat{f}(\eta; p) \frac{\partial \hat{\Phi}(\eta; p)}{\partial \eta} + \frac{N_t}{N_b} \frac{\partial^2 \hat{\theta}(\eta; p)}{\partial \eta^2}. \quad (2.30)$$

For $p = 0$ and $p = 1$ we have

$$\begin{aligned} \hat{f}(\eta; 0) &= f_0(\eta), \quad \hat{f}(\eta; 1) = f(\eta), \\ \hat{\theta}(\eta; 0) &= \theta_0(\eta), \quad \hat{\theta}(\eta; 1) = \theta(\eta), \\ \hat{\Phi}(\eta; 0) &= \Phi_0(\eta), \quad \hat{\Phi}(\eta; 1) = \Phi(\eta). \end{aligned} \quad (2.31)$$

Note that $f_0(\eta)$, $\theta_0(\eta)$ and $\Phi_0(\eta)$ approach $f(\eta)$, $\theta(\eta)$ and $\Phi(\eta)$ respectively, when p has variation from 0 to 1. According to Taylor series we have

$$\begin{aligned} \hat{f}(\eta; p) &= f_0(\eta) + \sum_{m=1}^{\infty} f_m(\eta) p^m, \quad f_m(\eta) = \left. \frac{1}{m!} \frac{\partial^m \hat{f}(\eta; p)}{\partial p^m} \right|_{p=0}, \\ \hat{\theta}(\eta; p) &= \theta_0(\eta) + \sum_{m=1}^{\infty} \theta_m(\eta) p^m, \quad \theta_m(\eta) = \left. \frac{1}{m!} \frac{\partial^m \hat{\theta}(\eta; p)}{\partial p^m} \right|_{p=0}, \\ \hat{\Phi}(\eta; p) &= \Phi_0(\eta) + \sum_{m=1}^{\infty} \Phi_m(\eta) p^m, \quad \Phi_m(\eta) = \left. \frac{1}{m!} \frac{\partial^m \hat{\Phi}(\eta; p)}{\partial p^m} \right|_{p=0}, \end{aligned} \quad (2.32)$$

where the convergence depends upon \hbar_f , \hbar_θ and \hbar_Φ . By proper choice of \hbar_f , \hbar_θ and \hbar_Φ the series (2.32) converge for $p = 1$ and so

$$\begin{aligned} f(\eta) &= f_0(\eta) + \sum_{m=1}^{\infty} f_m(\eta), \\ \theta(\eta) &= \theta_0(\eta) + \sum_{m=1}^{\infty} \theta_m(\eta), \\ \Phi(\eta) &= \Phi_0(\eta) + \sum_{m=1}^{\infty} \Phi_m(\eta). \end{aligned} \quad (2.33)$$

2.2.2 m^{th} order deformation problems

The m^{th} order deformation problems are given by

$$\mathcal{L}_f [f_m(\eta) - \chi_m f_{m-1}(\eta)] = \hbar_f \mathcal{R}_{f,m}(\eta), \quad (2.34)$$

$$\mathcal{L}_\theta [\theta_m(\eta) - \chi_m \theta_{m-1}(\eta)] = \hbar_\theta \mathcal{R}_{\theta,m}(\eta), \quad (2.35)$$

$$\mathcal{L}_\Phi [\Phi_m(\eta) - \chi_m \Phi_{m-1}(\eta)] = \hbar_\Phi \mathcal{R}_{\Phi,m}(\eta), \quad (2.36)$$

$$f_m(0) = f'_m(0) = f'_m(\infty) = \theta'_m(0) - \gamma_1 \theta_m(0) = \theta_m(\infty) = \Phi'_m(0) - \gamma_2 \Phi_m(0) = \Phi_m(\infty) = 0, \quad (2.37)$$

$$\chi_m = \begin{cases} 0, & m \leq 1 \\ 1, & m > 1 \end{cases}, \quad (2.38)$$

$$\mathcal{R}_{f,m}(\eta) = f'''_{m-1} + \sum_{k=0}^{m-1} (f_{m-1-k} f''_k - f'_{m-1-k} f'_k) - M f'_{m-1}, \quad (2.39)$$

$$\mathcal{R}_{\theta,m}(\eta) = \frac{1}{\Gamma} \theta''_{m-1} + \sum_{k=0}^{m-1} (\theta'_{m-1-k} f_k + N_b \Phi_{m-1-k} \theta'_k + N_t \theta'_{m-1-k} \theta'_k), \quad (2.40)$$

$$\mathcal{R}_{\Phi,m}(\eta) = \Phi''_{m-1} + S_c \sum_{k=0}^{m-1} \Phi'_{m-1-k} f_k + \frac{N_t}{N_b} \theta''_{m-1}. \quad (2.41)$$

The general solutions can be expressed as follows:

$$f_m(\eta) = f_m^*(\eta) + c_1 + c_2 e^\eta + c_3 e^{-\eta}, \quad (2.42)$$

$$\theta_m(\eta) = \theta_m^*(\eta) + c_4 e^\eta + c_5 e^{-\eta}, \quad (2.43)$$

$$\Phi_m(\eta) = \Phi_m^*(\eta) + c_6 e^\eta + c_7 e^{-\eta}, \quad (2.44)$$

in which f_m^* , θ_m^* and Φ_m^* denote the particular solutions and the constants c_i ($i = 1 - 7$) can be determined by the boundary conditions (2.37). They are given by

$$\begin{aligned} c_3 &= \left. \frac{\partial f^*(\eta)}{\partial \eta} \right|_{\eta=0}, \quad c_1 = -c_3 - f^*(0), \quad c_5 = \frac{1}{1 + \gamma_1} \left[\left. \frac{\partial \theta^*(\eta)}{\partial \eta} \right|_{\eta=0} - \gamma_1 \theta^*(0) \right], \\ c_2 &= c_4 = c_6 = 0, \quad c_7 = \frac{1}{1 + \gamma_2} \left[\left. \frac{\partial \Phi^*(\eta)}{\partial \eta} \right|_{\eta=0} - \gamma_2 \Phi^*(0) \right]. \end{aligned} \quad (2.45)$$

2.3 Analysis of series solutions

The solution of problems consisting of Eqs. (2.7) – (2.10) is computed employing homotopy analysis method. The convergence region and rate of approximations for the functions f , θ and Φ can be controlled and adjusted through the auxiliary parameters \hbar_f , \hbar_θ and \hbar_Φ . The \hbar -curves are sketched at 14th-order of approximations to obtain valid ranges of these parameters (see Fig. 2.1). Permissible values of the auxiliary parameters are $-1.5 \leq \hbar_f \leq -0.4$, $-1.5 \leq \hbar_\theta \leq -0.5$ and $-1.4 \leq \hbar_\Phi \leq -0.7$. Further, the series solutions converge in the whole region of η ($0 < \eta < \infty$) when $\hbar_f = \hbar_\theta = \hbar_\Phi = -1.2$. Table 2.1 displays the convergence of homotopy solutions for different orders of approximations.

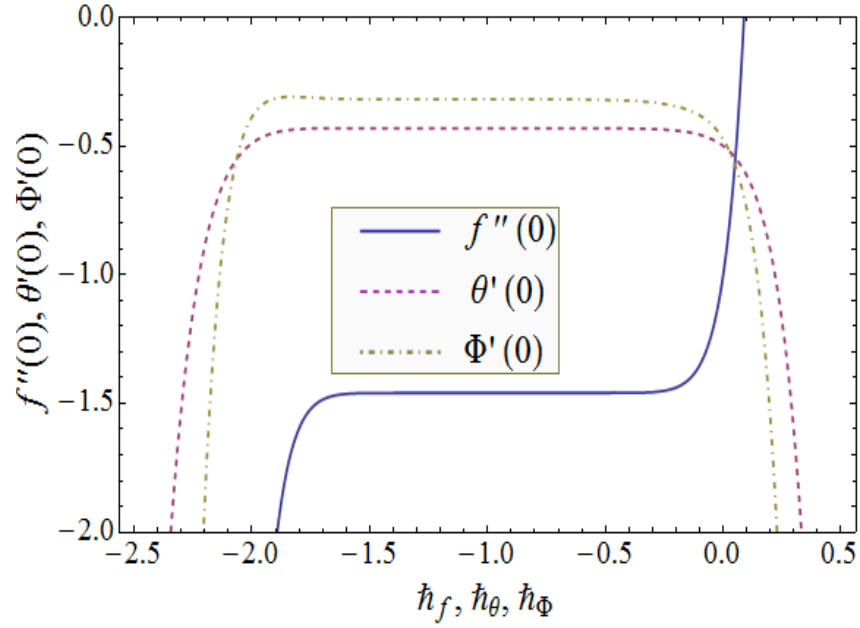


Fig. 2.1: \hbar -curves for velocity, temperature and concentration fields.

Table 2.1: Convergence of HAM solutions for different order of approximations when $M = N_b = 0.4$, $N_t = 0.3$, $Sc = Pr = \gamma_1 = 1$, $S = 0.5$ and $\gamma_2 = 0.9$.

Order of approximations	$-f''(0)$	$-\theta'(0)$	$-\Phi'(0)$
1	1.54000	0.441053	0.344668
5	1.45883	0.431349	0.319776
10	1.45934	0.430920	0.318765
15	1.45934	0.430912	0.318750
20	1.45934	0.430912	0.318750
25	1.45934	0.430912	0.318750
30	1.45934	0.430912	0.318750
35	1.45934	0.430912	0.318750
40	1.45934	0.430912	0.318750
50	1.45934	0.430912	0.318750
60	1.45934	0.430912	0.318750

2.4 Results and discussion

In this section, the effects of various involved parameters on the velocity, temperature and concentration profiles are discussed. Figs. (2.2–2.3) are plotted to show the effects of Hartman number M and mass transfer parameter S on the velocity profile f' . Fig. 2.2 shows the effects of M on f' . Application of magnetic field has the tendency to slow down the movement of the fluid particles and consequently the velocity decreases. Fig. 2.3 displays the effect of S on f' . In this Fig. the velocity field f' decreases when S increases. In fact applying suction leads to draw the amount of fluid particles into the wall and hence the velocity boundary layer decreases.

Effects of the Brownian motion parameter N_b , thermophoresis parameter N_t , Schmidt number Sc , Prandtl number Pr , Hartman number M , mass transfer parameter S , thermal Biot number γ_1 and concentration Biot number γ_2 on the temperature profile θ and the concentration profile ϕ are shown in the Figs. (2.4 – 2.18). It is noted that an increase in the Brownian motion parameter N_b , thermophoresis parameter N_t and Schmidt number Sc increase the temperature profile θ as shown in Figs. (2.4 – 2.6). The effects of Prandtl number Pr on the temperature profile are depicted in Fig. 2.7. This graph shows that the temperature profile θ decreases when Pr increases. In fact the thermal diffusivity decreases by increasing Pr and thus the heat diffused away slowly from the heated surface. Fig. 2.8 illustrates the effects of Hartman number M on temperature profile θ . The Lorentz force is a resistive force which opposes the fluid motion. As a sequence the heat is produced and thus thermal boundary layer thickness increases. Further, the temperature profile θ decreases when S is increased (see Fig. 2.9). Also the temperature profile θ increases when the thermal Biot number γ_1 increases (see Fig. 2.10). Fig. 2.11 illustrates the effects of N_b on Φ . The concentration profile Φ decreases by increasing the Brownian motion parameter N_b . Influence of N_t on Φ can be seen in Fig. 2.12. There is an increase in Φ when N_t is increased. Figs. (2.13 – 2.16) display the effects of Sc , Pr , M and S on the concentration profile Φ . It is observed that concentration profile Φ decreases by increasing these parameters. It is observed from Fig. 2.17 that the mass fraction field increases when thermal Biot number γ_1 is increased. Also the concentration profile increases by increasing concentration Biot number γ_2 as depicted in Fig. 2.18.

Numerical values of local Nusselt number and local Sherwood number for different emerging parameters are presented in Table 2. It is noticed that local Nusselt number $Nu(Re_x)^{-\frac{1}{2}}$

decreases for larger values of D_f , N_b and N_t . However it increases for larger values of S_r and Pr . The magnitude of local Sherwood number $Sh(Re_x)^{-\frac{1}{2}}$ decreases for larger values of S_r , Pr and N_t however it increases for larger values of D_f and N_b .

Figs. 2.19 and 2.20 describe the variations of the Nusselt number $Nu(Re_x)^{-1/2}$ for Brownian motion parameter N_b , thermophoresis parameter N_t and Schmidt number Sc . It is noticed that heat transfer rate decreases as N_b and N_t increase for Sc . Fig. 2.21 shows the effects of thermal Biot number γ_1 and mass transfer parameter S on the Nusselt number $Nu(Re_x)^{-1/2}$. In this figure, heat transfer rate increases as γ_1 enhances for S . Figs. 2.22 and 2.23 illustrate the variation in dimensionless mass transfer rate $Sh(Re_x)^{-1/2}$ vs Brownian motion parameter N_b and thermophoresis parameter N_t . Here the mass transfer rate increases for larger N_b and it decreases with an increase in N_t . Effects of concentration Biot number γ_2 and mass transfer parameter S on the Sherwood number $Sh(Re_x)^{-1/2}$ are displayed in Fig. 2.24. It is noted that mass transfer rate increases for higher γ_2 .

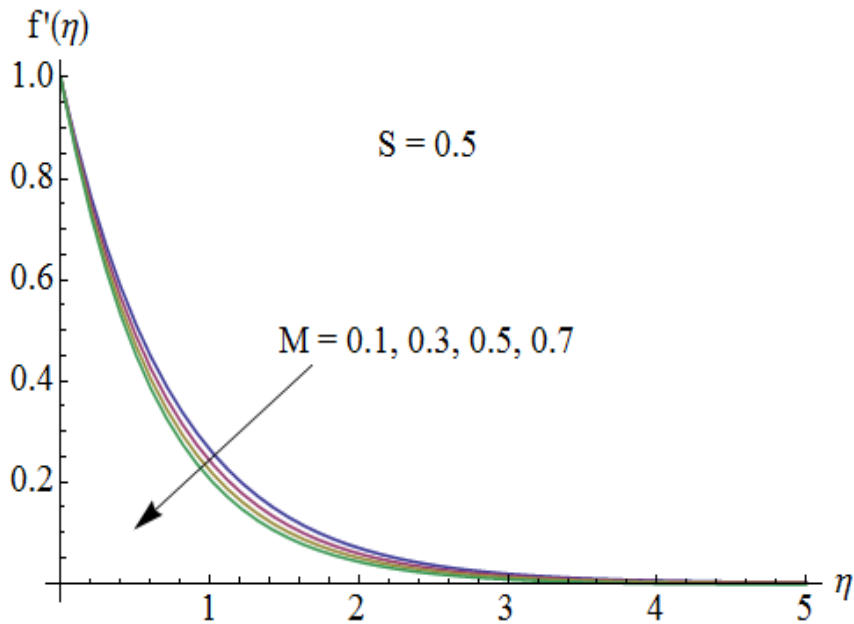


Fig. 2.2: Influence of M on $f'(\eta)$.

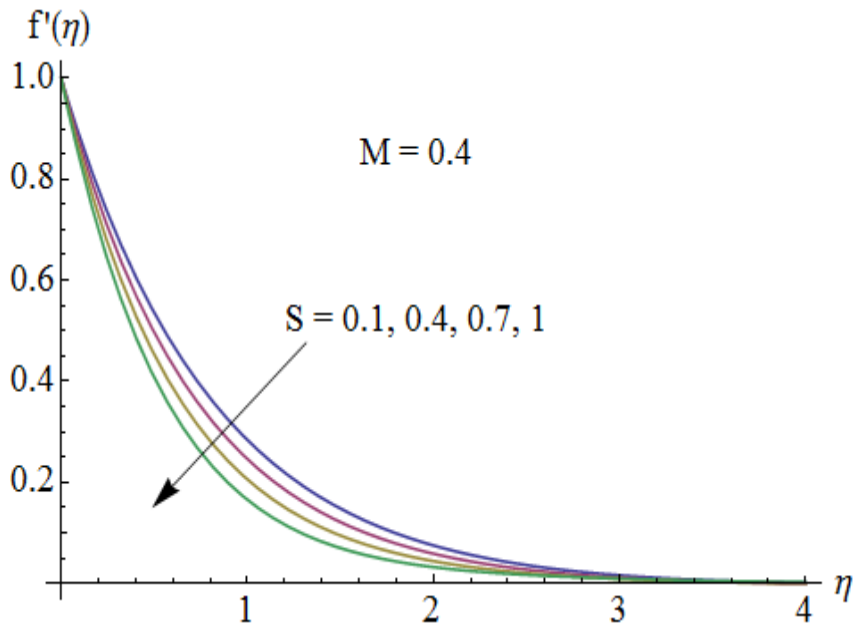


Fig. 2.3: Influence of S on $f'(\eta)$.

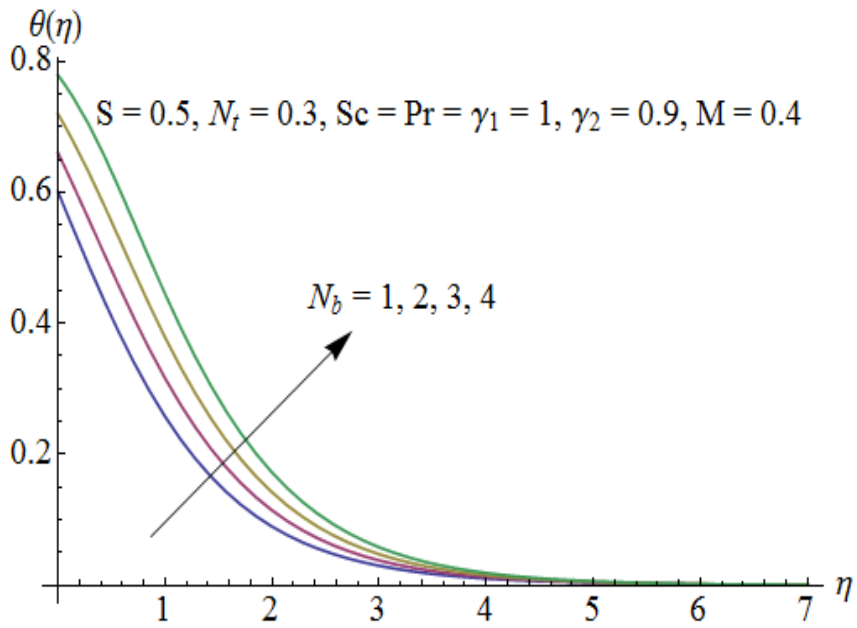


Fig. 2.4: Influence of N_b on $\theta(\eta)$.

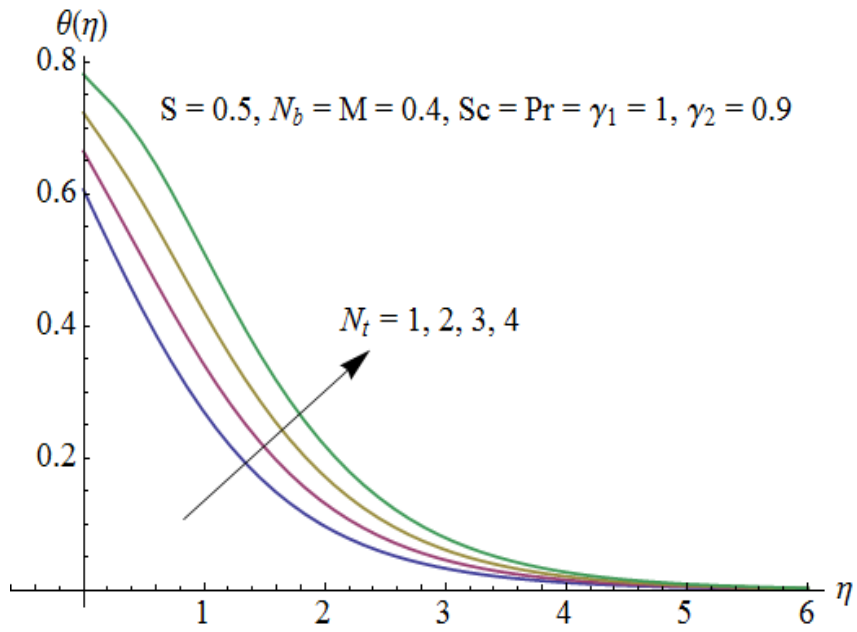


Fig. 2.5: Influence of N_t on $\theta(\eta)$.

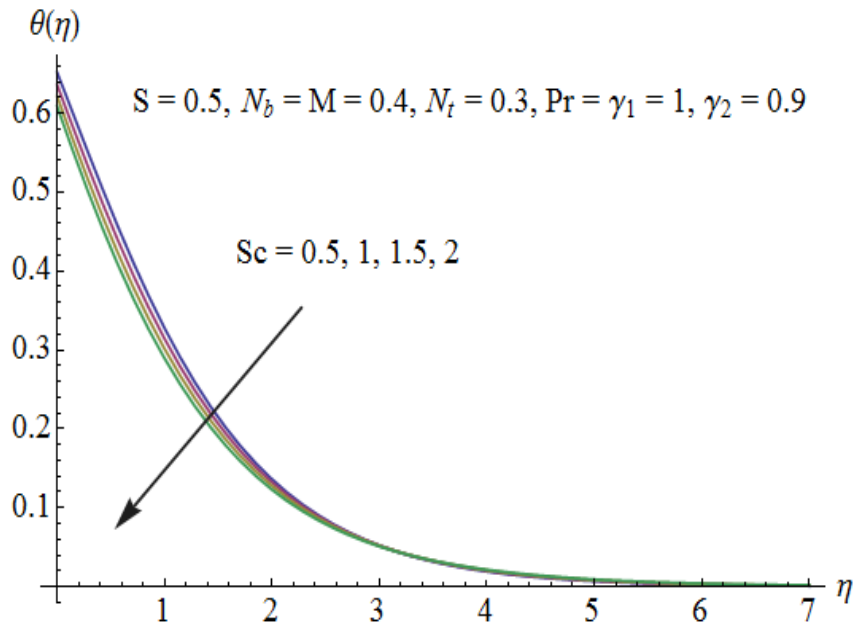


Fig. 2.6: Influence of Sc on $\theta(\eta)$.

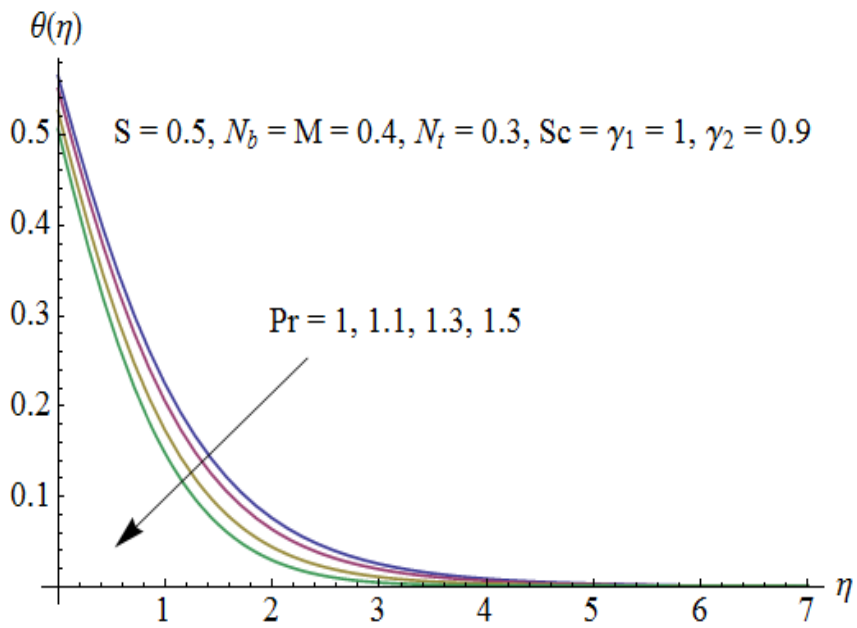


Fig. 2.7: Influence of Pr on $\theta(\eta)$.

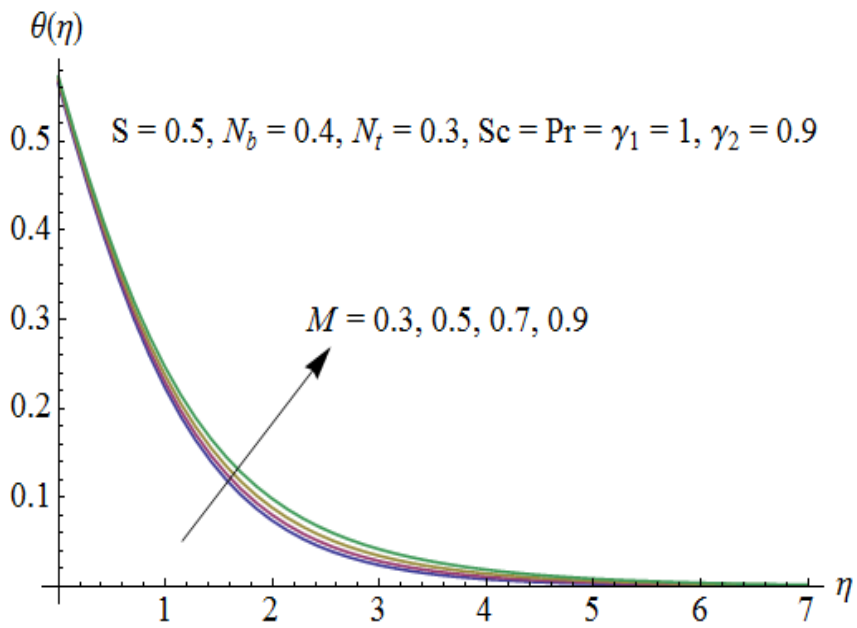


Fig. 2.8: Influence of M on $\theta(\eta)$.

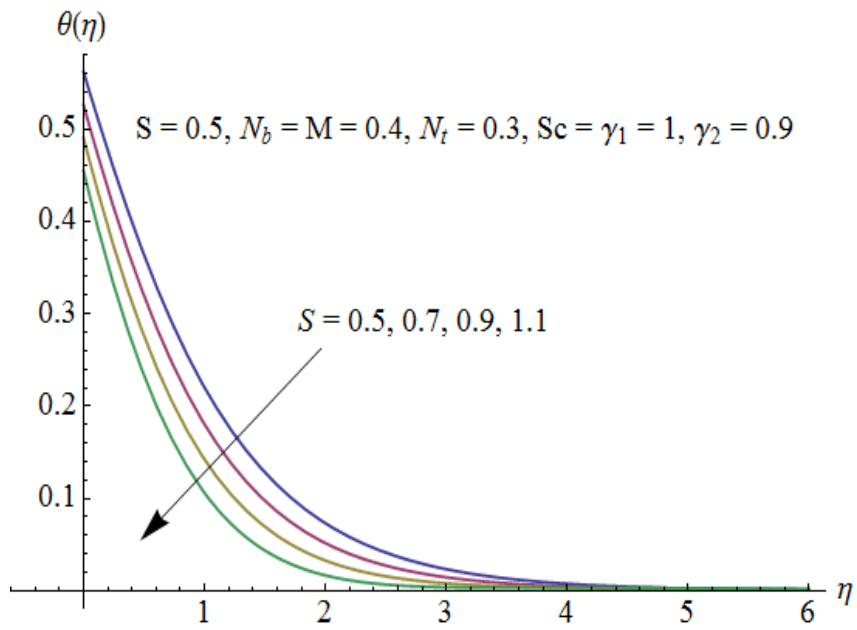


Fig. 2.9: Influence of S on $\theta(\eta)$.

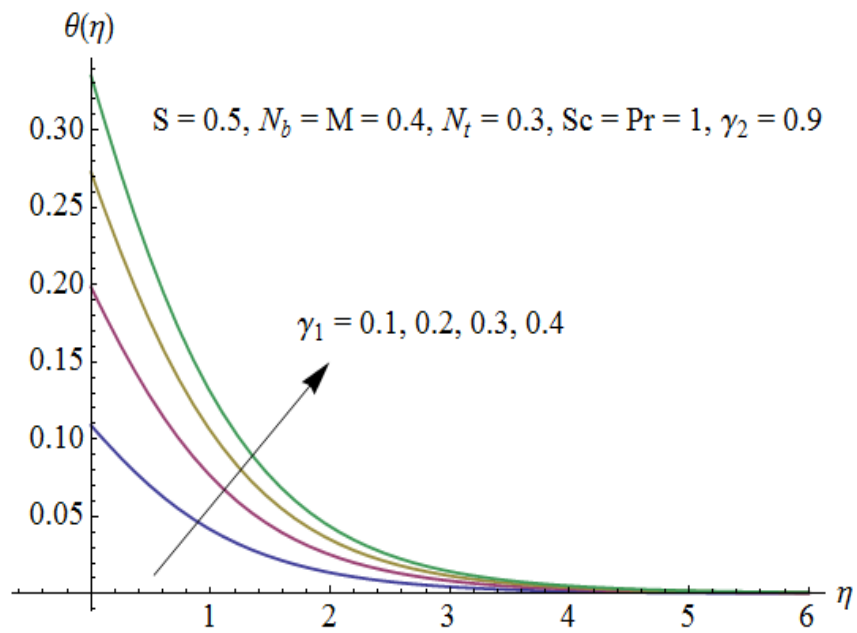


Fig. 2.10: Influence of γ_1 on $\theta(\eta)$.

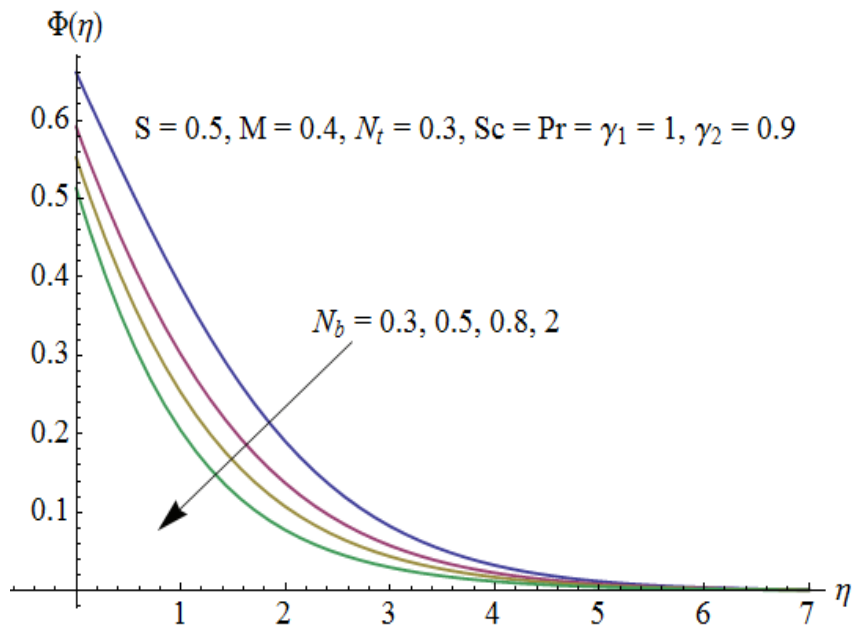


Fig. 2.11: Influence of N_b on $\Phi(\eta)$.

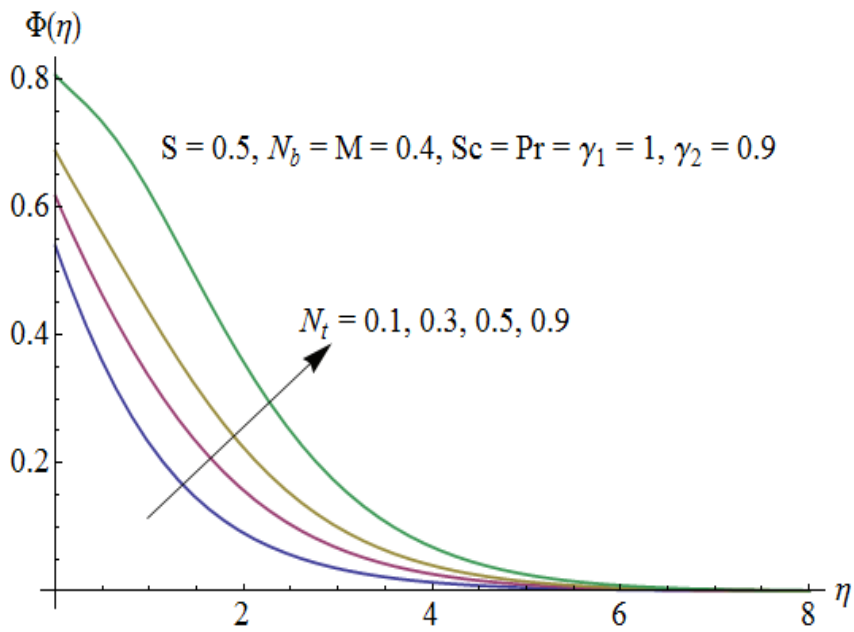


Fig. 2.12: Influence of N_t on $\Phi(\eta)$.

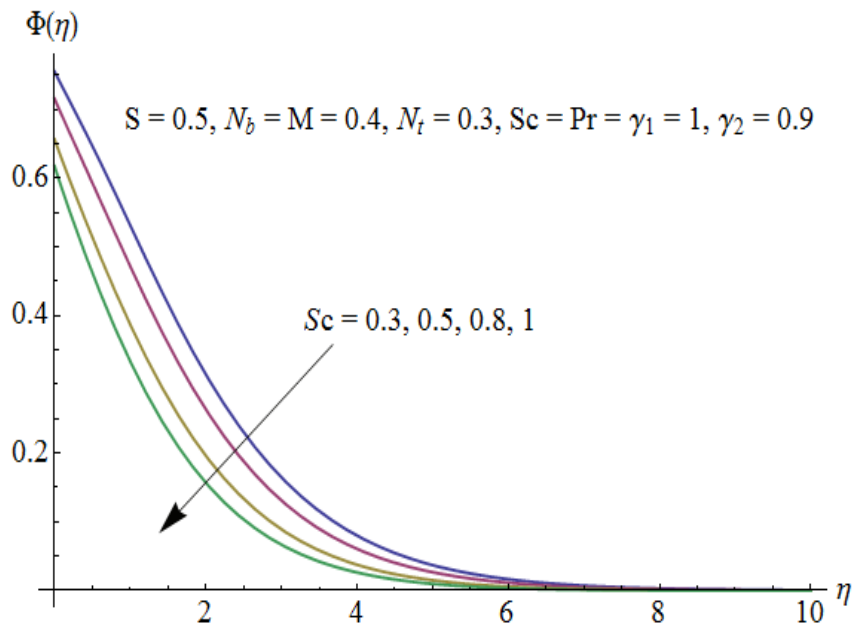


Fig. 2.13: Influence of Sc on $\Phi(\eta)$.

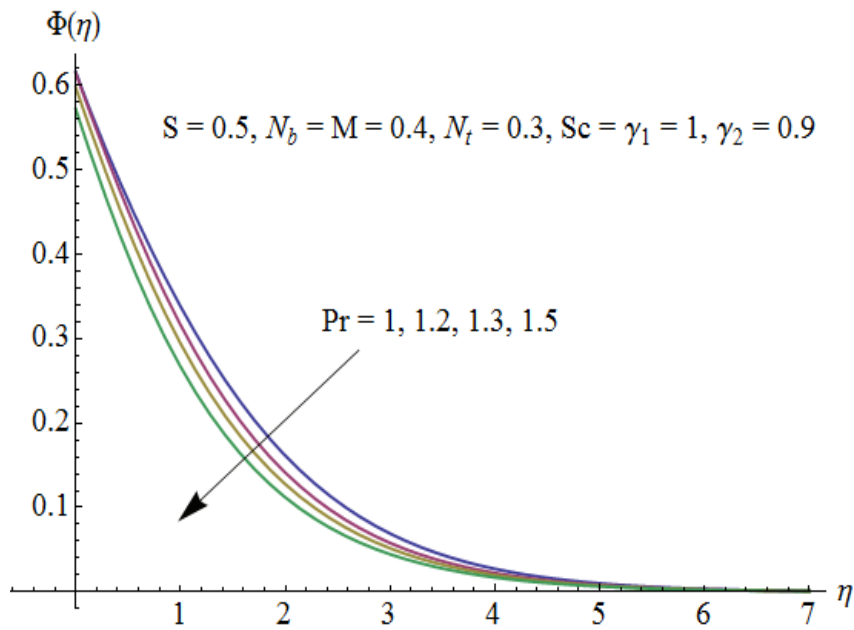


Fig. 2.14: Influence of Pr on $\Phi(\eta)$.

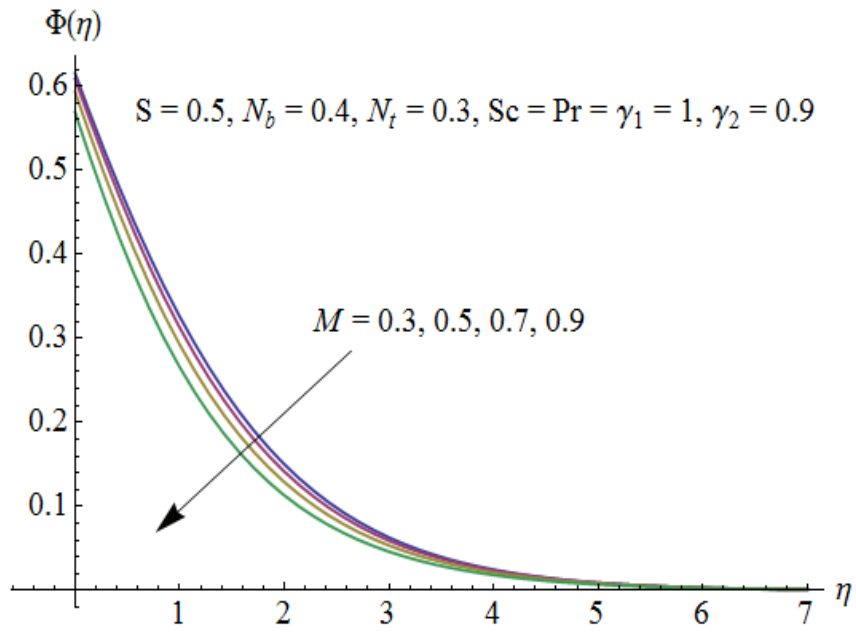


Fig. 2.15: Influence of M on $\Phi(\eta)$.

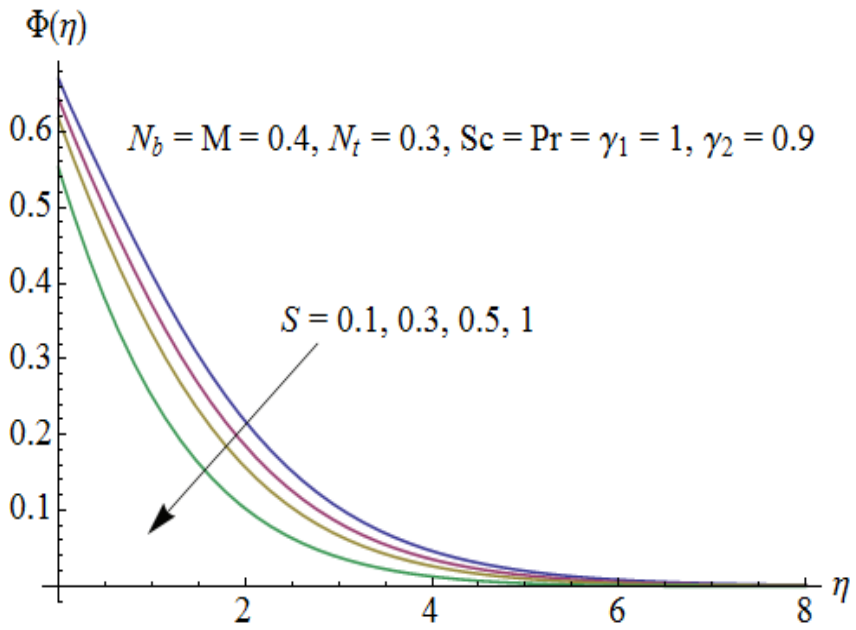


Fig. 2.16: Influence of S on $\Phi(\eta)$.

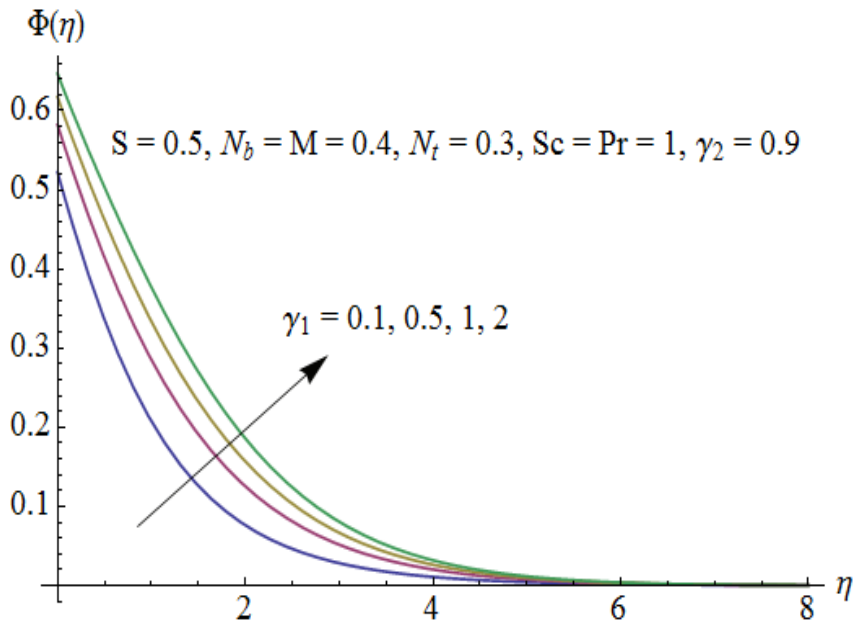


Fig. 2.17: Influence of γ_1 on $\Phi(\eta)$.

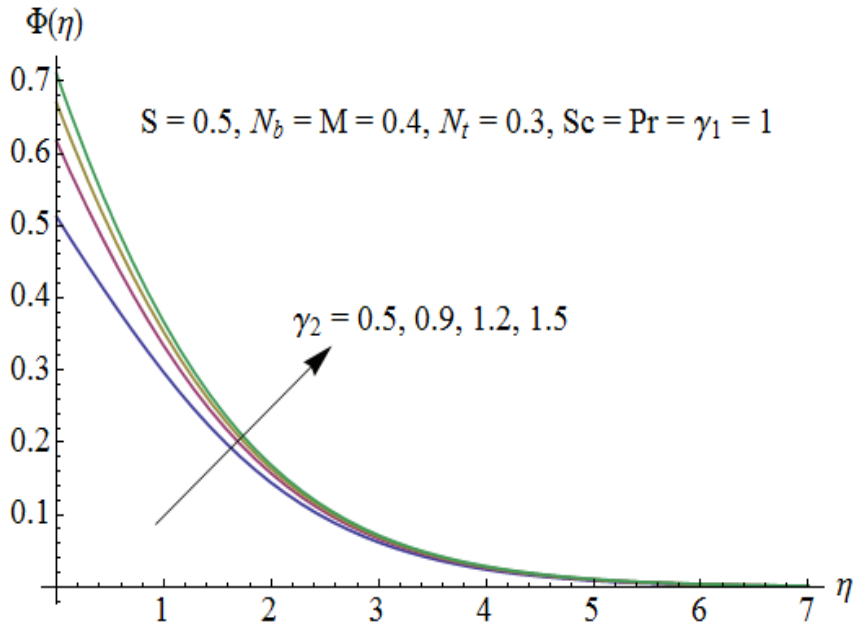


Fig. 2.18: Influence of γ_2 on $\Phi(\eta)$.

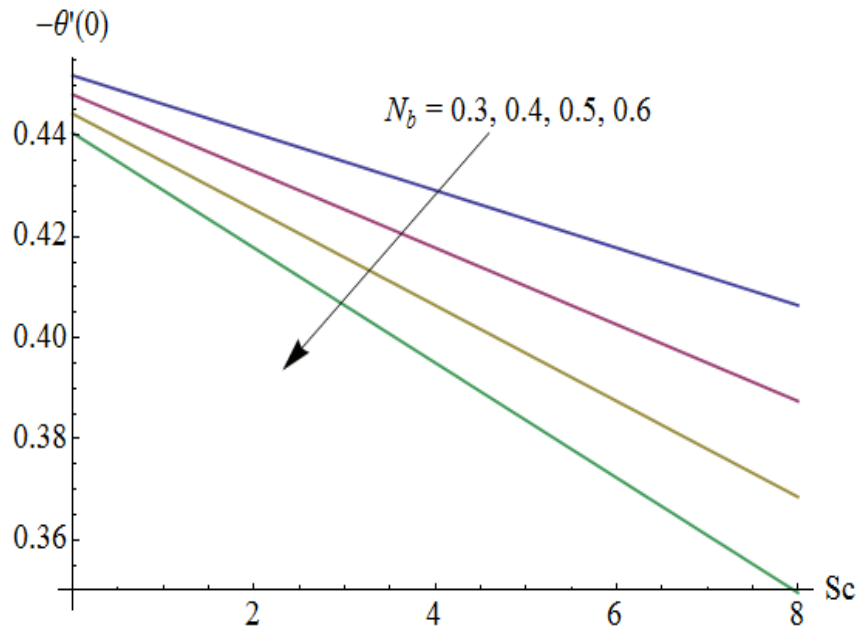


Fig. 2.19: Influences of N_b and Sc on $-\theta'(0)$.

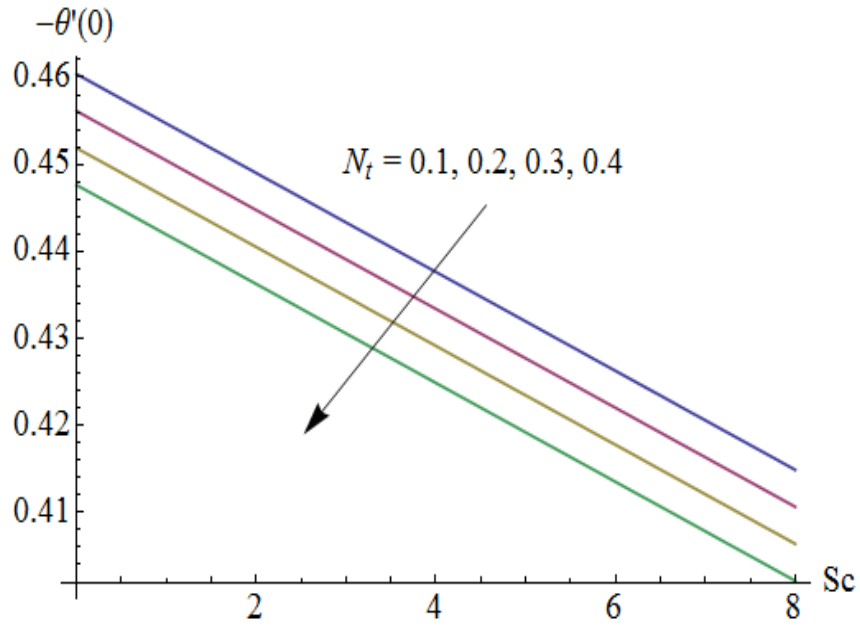


Fig. 2.20: Influences of N_t and Sc on $-\theta'(0)$.

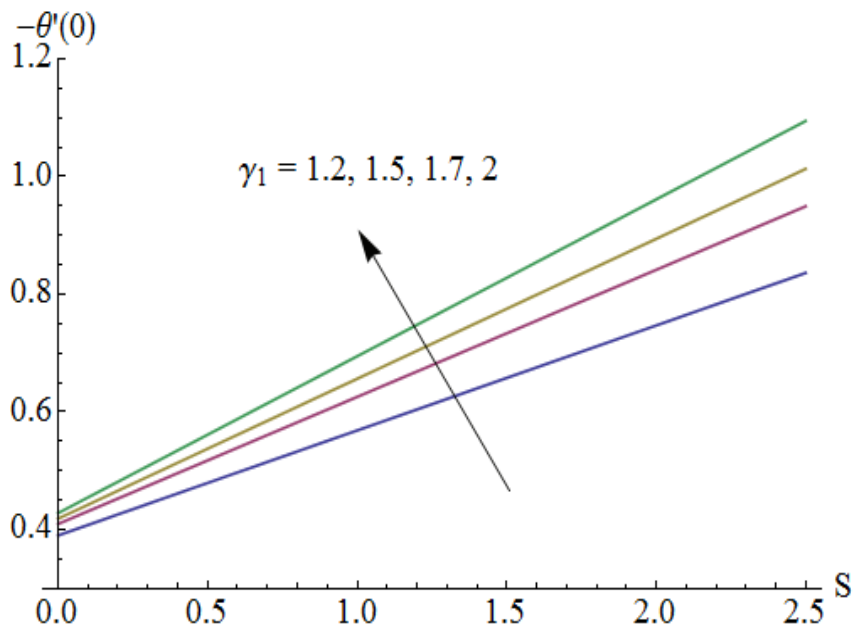


Fig. 2.21: Influences of γ_1 and S on $-\theta'(0)$.

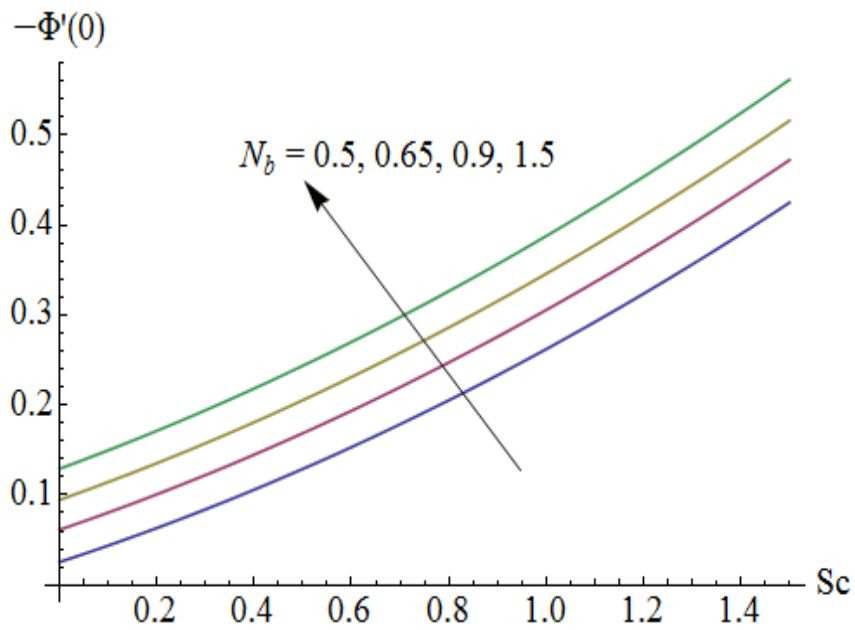


Fig. 2.22: Influences of N_b and Sc on $-\Phi'(0)$.

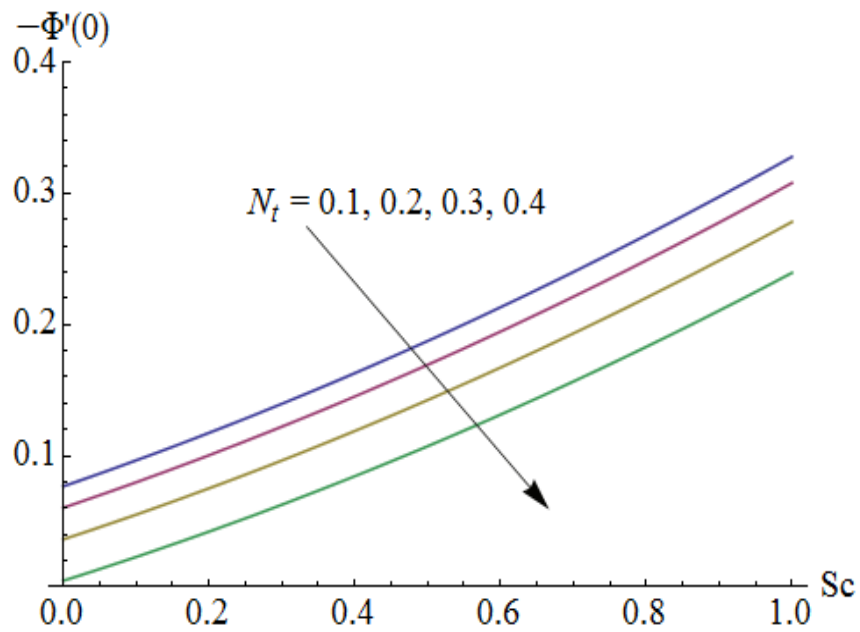


Fig. 2.23: Influences of N_t and Sc on $-\Phi'(0)$.

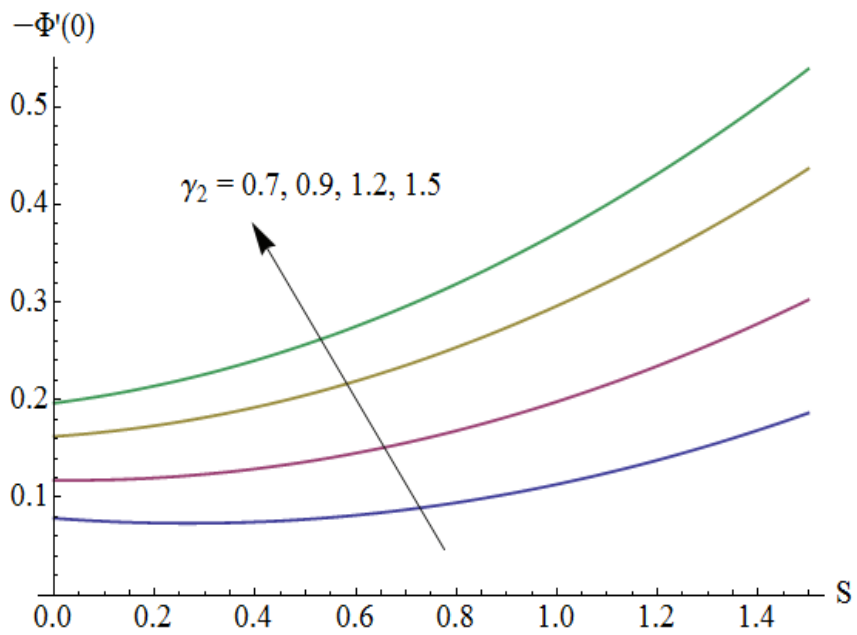


Fig. 2.24: Influences of γ_2 and S on $-\Phi'(0)$.

2.5 Main points

The flow of nanofluid generated by a permeable stretching sheet is studied. Effects of different parameters on the velocity, temperature and concentration distributions are explored. The following observations are worth mentioning.

- The effects of Hartman number and mass transfer parameter are similar on the velocity profile.
- Increase in Brownian motion parameter, thermophoresis parameter, Schmidt number, Hartman number and thermal Biot number enhances the temperature profile.
- There is enhancement of concentration for increasing thermophoresis parameter, thermal and concentration Biot numbers.
- Local Nusselt number increases by larger thermal Biot number.
- Local Sherwood number is an increasing function of Brownian motion parameter and concentration Biot number.

Chapter 3

MHD flow of nanofluids due to convectively exponential stretching sheet in a porous medium

This chapter concentrates on the steady magnetohydrodynamic (MHD) flow of viscous nanofluid. The flow is caused by a permeable exponentially stretching surface. An incompressible fluid fills the porous space. A comparative study is made for the nanoparticles namely copper (Cu), silver (Ag), alumina (Al_2O_3) and titanium oxide (TiO_2). Water is treated as a base fluid. Convective type boundary conditions are employed in modeling the heat transfer process. The non-linear partial differential equations governing the flow are reduced to the ordinary differential equation by similarity transformations. The obtained equations are then solved for the development of series solutions. Convergence of the obtained series solutions is explicitly discussed. Effects of different parameters on the velocity and temperature profiles are shown and analyzed through graphs.

3.1 Mathematical formulation

Here we investigate the steady two-dimensional flow of an incompressible nanofluid induced by an exponentially stretching surface in a porous medium with permeability K . The x -axis is

taken along the stretching surface in the direction of motion and y -axis is perpendicular to it.

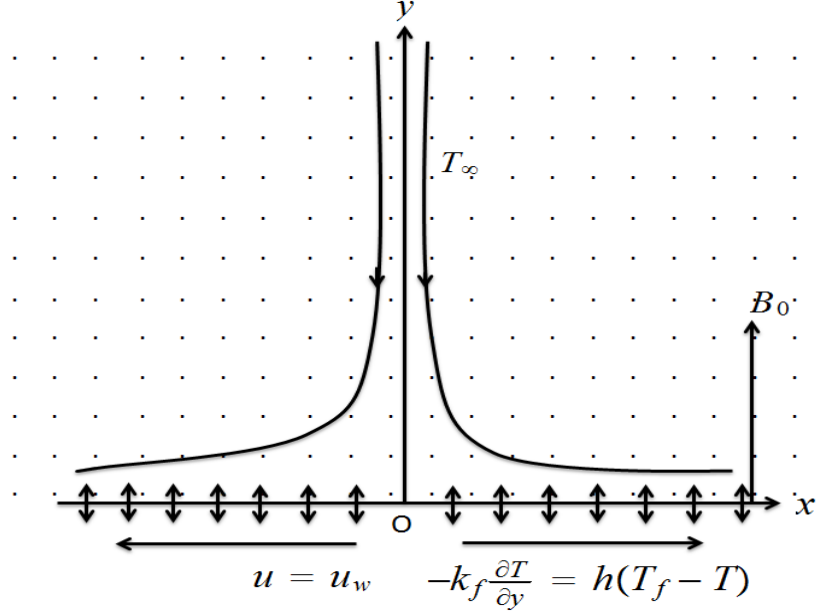


Fig. 3.1: Geometry of the problem.

A uniform transverse magnetic field of strength B_0 is applied parallel to the y -axis. It is assumed that the induced magnetic field and the electric field effects are negligible. Further, the surface exhibits convective type boundary conditions (see Fig. 3.1). The boundary layer flow in the present analysis is governed by the following equations:

$$\frac{\partial u}{\partial x} + \frac{\partial v}{\partial y} = 0, \quad (3.1)$$

$$\rho_{nf} \left(u \frac{\partial u}{\partial x} + v \frac{\partial u}{\partial y} \right) = \mu_{nf} \frac{\partial^2 u}{\partial y^2} - \frac{\mu_{nf}}{K} u - \sigma_{nf} B_0^2 u, \quad (3.2)$$

$$u \frac{\partial T}{\partial x} + v \frac{\partial T}{\partial y} = \frac{k_{nf}}{(\rho c_p)_{nf}} \frac{\partial^2 T}{\partial y^2}, \quad (3.3)$$

where u and v are the velocity components along the x - and y - directions respectively. The effective nanofluid density ρ_{nf} and heat capacity $(\rho c_p)_{nf}$ are taken as follows [4]:

$$\rho_{nf} = \rho_f(1 - \phi) + \rho_s \phi, \quad (3.4)$$

$$(\rho c_p)_{nf} = (\rho c_p)_f(1 - \phi) + (\rho c_p)_s\phi. \quad (3.5)$$

The dynamic viscosity of nanofluid μ_{nf} given by Brinkmann is [98]:

$$\mu_{nf} = \frac{\mu_f}{(1 - \phi)^{2.5}}, \quad (3.6)$$

The effective thermal conductivity of nanofluid k_{nf} by Maxwell-Garnett model is given by [99]:

$$\frac{k_{nf}}{k_f} = \frac{k_s + 2k_f - 2\phi(k_f - k_s)}{k_s + 2k_f + \phi(k_f - k_s)}. \quad (3.7)$$

and the electric conductivity σ_{nf} of nanofluid is [100]:

$$\frac{\sigma_{nf}}{\sigma_f} = 1 + \frac{3 \left(\frac{\sigma_s}{\sigma_f} - 1 \right) \phi}{\left(\frac{\sigma_s}{\sigma_f} + 2 \right) - \left(\frac{\sigma_s}{\sigma_f} - 1 \right) \phi}. \quad (3.8)$$

Here ϕ is the solid volume fraction, s in subscript is for nano-solid-particles and f in subscript is for base fluid. The subjected boundary conditions are

$$\begin{aligned} u &= u_w = U_0 e^{\frac{x}{L}}, \quad v = V_w, \quad -k_f \frac{\partial T}{\partial y} = h(T_f - T) \quad \text{at } y = 0, \\ u &\rightarrow 0, \quad T \rightarrow T_\infty, \quad \text{as } y \rightarrow \infty. \end{aligned} \quad (3.9)$$

Introducing

$$\eta = y \sqrt{\frac{U_0}{2\nu_f L}} e^{\frac{x}{2L}}, \quad u = U_0 e^{\frac{x}{L}} f'(\eta), \quad v = -\sqrt{\frac{\nu_f U_0}{2L}} e^{\frac{x}{2L}} [f(\eta) + \eta f'(\eta)], \quad \theta(\eta) = \frac{T - T_\infty}{T_f - T_\infty}. \quad (3.10)$$

Eq. (3.1) is satisfied automatically and Eqs. (3.2), (3.3) and (3.9) after using Eq. (3.10) can be reduced as follows:

$$\varepsilon_1 f''' + f f'' - 2f'^2 - \lambda \varepsilon_1 f' - (1 - \phi)^{2.5} M \varepsilon_1 \frac{\sigma_{nf}}{\sigma_f} f' = 0, \quad (3.11)$$

$$\frac{1}{\text{Pr}} \frac{k_{nf}}{k_f} \theta'' + \left((1 - \phi) + \frac{(\rho c_p)_s}{(\rho c_p)_f} \phi \right) f \theta' = 0, \quad (3.12)$$

$$\begin{aligned}
f'(0) &= 1, \quad f(0) = S, \quad \theta'(0) = -\gamma_1[1 - \theta(0)], \\
f'(\infty) &= 0, \quad \theta(\infty) = 0,
\end{aligned} \tag{3.13}$$

in which prime indicates the differentiation with respect to η and the value of ε_1 is

$$\varepsilon_1 = \frac{1}{\left((1 - \phi) + \frac{\rho_s}{\rho_f} \phi \right) (1 - \phi)^{2.5}}. \tag{3.14}$$

Moreover the porosity parameter λ , the Hartman number M , the Prandtl number Pr , the mass transfer parameter S with $S > 0$ for suction and $S < 0$ for injection and the thermal Biot number γ_1 are defined as follows:

$$\lambda = \frac{2\nu_f L}{KU_0} e^{-\frac{x}{L}}, \quad M = \frac{2\sigma_f B_0^2 L}{\rho_f U_0} e^{-\frac{x}{L}}, \quad \text{Pr} = \frac{\nu_f (\rho c_p)_f}{k_f}, \quad S = -\sqrt{\frac{2L}{\nu U_0}} e^{-\frac{x}{2L}} V_w, \quad \gamma_1 = \frac{h}{k_f} \sqrt{\frac{\nu_f}{a}}. \tag{3.15}$$

Local skin-friction coefficient C_{sf} and local Nusselt number Nu are given by

$$C_{sf} = \frac{\tau_w}{\frac{1}{2}\rho U_0^2 e^{\frac{2x}{L}}}, \quad Nu = \frac{xq_w}{k_f (T_w - T_\infty)}, \tag{3.16}$$

where the surface shear stress τ_w and wall heat flux q_w are

$$\tau_w = \mu_{nf} \left. \frac{\partial u}{\partial y} \right|_{y=0}, \quad q_w = -k_{nf} \left. \frac{\partial T}{\partial y} \right|_{y=0}. \tag{3.17}$$

Dimensionless forms of skin friction coefficient C_{sf} and local Nusselt number Nu can be represented by the relations

$$C_{sf} \sqrt{\frac{\text{Re}_x}{2}} = \frac{1}{(1 - \phi)^{2.5}} f''(0), \quad Nu \text{Re}_x^{-1/2} \sqrt{\frac{2L}{x}} = -\frac{k_{nf}}{k_f} \theta'(0), \tag{3.18}$$

in which $\text{Re}_x = U_0 e^{\frac{x}{L}} x / \nu$ denotes the local Reynolds number.

3.2 Homotopy analysis solutions

Employing the methodology of homotopy analysis solutions the initial approximations $f_0(\eta)$ and $\theta_0(\eta)$ and auxiliary linear operators \mathcal{L}_f and \mathcal{L}_θ are given by

$$f_0(\eta) = 1 + S - \exp(-\eta), \quad \theta_0(\eta) = \frac{\gamma_1}{1 + \gamma_1} \exp(-\eta), \quad (3.19)$$

$$\mathcal{L}_f(f) = f''' - f', \quad \mathcal{L}_\theta(\theta) = \theta'' - \theta, \quad (3.20)$$

together with the properties

$$\begin{aligned} \mathcal{L}_f [c_1 + c_2 \exp(\eta) + c_3 \exp(-\eta)] &= 0, \\ \mathcal{L}_\theta [c_4 \exp(\eta) + c_5 \exp(-\eta)] &= 0, \end{aligned} \quad (3.21)$$

where $c_1 - c_5$ are the constants. If $p \in [0, 1]$ indicates the embedding parameter then the zeroth order deformation problems are constructed as follows:

$$(1 - p)\mathcal{L}_f [\hat{f}(\eta; p) - f_0(\eta)] = p\hbar_f \mathcal{N}_f[\hat{f}(\eta; p)], \quad (3.22)$$

$$(1 - p)\mathcal{L}_\theta [\hat{\theta}(\eta; p) - \theta_0(\eta)] = p\hbar_\theta \mathcal{N}_\theta[\hat{\theta}(\eta; p), \hat{f}(\eta; p)], \quad (3.23)$$

$$\begin{aligned} \hat{f}'(0; p) &= 1, \quad \hat{f}(0; p) = S, \quad \hat{f}'(\infty; p) = 0, \\ \hat{\theta}'(0; p) &= -\gamma_1[1 - \hat{\theta}(0; p)], \quad \hat{\theta}(\infty; p) = 0, \end{aligned} \quad (3.24)$$

where \hbar_f and \hbar_θ are the nonzero auxiliary parameters. With Eqs. (3.11) and (3.12), the definitions of operators \mathcal{N}_f and \mathcal{N}_θ can be written as

$$\begin{aligned} \mathcal{N}_f [\hat{f}(\eta; p)] &= \varepsilon_1 \frac{\partial^3 \hat{f}(\eta; p)}{\partial \eta^3} + \hat{f}(\eta; p) \frac{\partial^2 \hat{f}(\eta; p)}{\partial \eta^2} - 2 \left(\frac{\partial \hat{f}(\eta; p)}{\partial \eta} \right)^2 \\ &\quad - \lambda \varepsilon_1 \frac{\partial \hat{f}(\eta; p)}{\partial \eta} - (1 - \phi)^{2.5} M \varepsilon_1 \frac{\sigma_{nf}}{\sigma_f} \frac{\partial \hat{f}(\eta; p)}{\partial \eta}, \end{aligned} \quad (3.25)$$

$$\mathcal{N}_\theta[\hat{\theta}(\eta; p), \hat{f}(\eta; p)] = \frac{1}{\text{Pr}} \frac{k_{nf}}{k_f} \frac{\partial^2 \hat{\theta}(\eta; p)}{\partial \eta^2} + \left((1 - \phi) + \frac{(\rho c_p)_s}{(\rho c_p)_f} \phi \right) \hat{f}(\eta; p) \frac{\partial \hat{\theta}(\eta; p)}{\partial \eta}. \quad (3.26)$$

The resulting problems at m^{th} order are given by

$$\mathcal{L}_f [f_m(\eta) - \chi_m f_{m-1}(\eta)] = \hbar_f \mathcal{R}_{f,m}(\eta), \quad (3.27)$$

$$\mathcal{L}_\theta [\theta_m(\eta) - \chi_m \theta_{m-1}(\eta)] = \hbar_\theta \mathcal{R}_{\theta,m}(\eta), \quad (3.28)$$

$$f_m(0) = f'_m(0) = f'_m(\infty) = \theta'_m(0) - \gamma_1 \theta_m(0) = \theta_m(\infty) = 0, \quad (3.29)$$

$$\chi_m = \begin{cases} 0, & m \leq 1 \\ 1, & m > 1 \end{cases}, \quad (3.30)$$

$$\mathcal{R}_{f,m}(\eta) = \varepsilon_1 f'''_{m-1} + \sum_{k=0}^{m-1} [f_{m-1-k} f''_k - 2f'_{m-1-k} f'_k] - \lambda \varepsilon_1 f'_{m-1} - (1 - \phi)^{2.5} M \varepsilon_1 \frac{\sigma_{nf}}{\sigma_f} f'_{m-1}, \quad (3.31)$$

$$\mathcal{R}_{\theta,m}(\eta) = \frac{1}{\text{Pr}} \frac{k_{nf}}{k_f} \theta''_{m-1} + \left((1 - \phi) + \frac{(\rho c_p)_s}{(\rho c_p)_f} \phi \right) \sum_{k=0}^{m-1} \theta'_{m-1-k} f_k, \quad (3.32)$$

where the general solutions are

$$\begin{aligned} f_m(\eta) &= f_m^*(\eta) + c_1 + c_2 e^\eta + c_3 e^{-\eta}, \\ \theta_m(\eta) &= \theta_m^*(\eta) + c_4 e^\eta + c_5 e^{-\eta}, \end{aligned} \quad (3.33)$$

in which f_m^* and θ_m^* denote the special solutions.

3.3 Convergence of the homotopy solutions

Now the solutions of Eqs. (3.11) and (3.12) subject to the boundary conditions (3.13) is computed by means of homotopy analysis method. We choose auxiliary parameters \hbar_f and \hbar_θ for the functions f and θ respectively. The convergence of obtained series and rate of the approximation for HAM strongly depend upon the values of the auxiliary parameters. For ranges of admissible values of \hbar_f and \hbar_θ , the \hbar -curves for 12^{th} -order of approximations are plotted in the Fig. 3.2. We can see that the permissible values for \hbar_f and \hbar_θ are $-0.7 \leq \hbar_f \leq -0.4$ and $-0.6 \leq \hbar_\theta \leq -0.45$. Further, the series solutions converge in the whole region of η

($0 < \eta < \infty$) when $\hbar_f = \hbar_\theta = -0.6$.

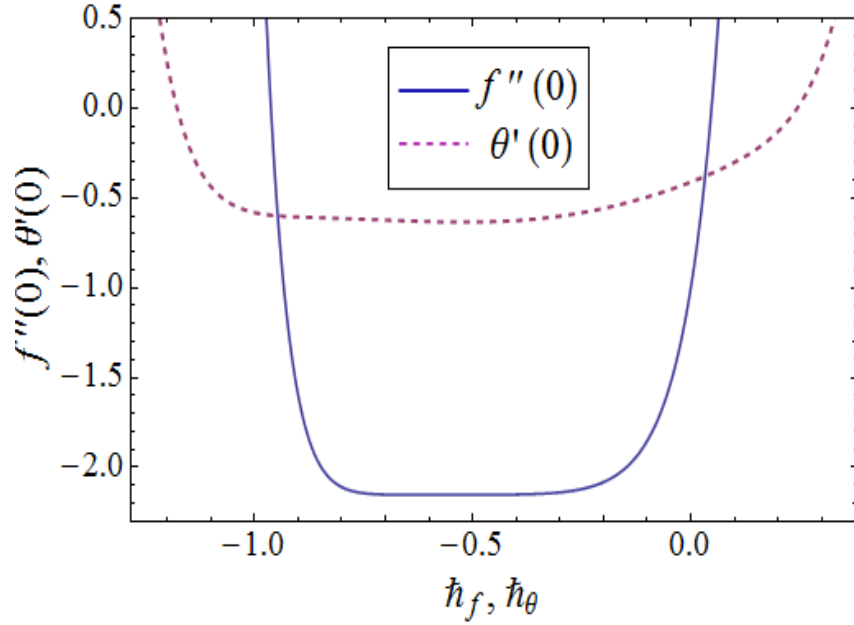


Fig. 3.2: \hbar -curves for velocity and temperature fields.

Table 3.1: Convergence of HAM solutions for different order of approximations when $\text{Pr} = 6.2$, $\phi = 0.03$, $\lambda = 0.5$, $\gamma_1 = 0.7$, $M = 0.1$ and $S = 0.9$.

Order of approximations	$-f''(0)$	$-\theta'(0)$
1	1.761	0.4432
5	2.144	0.5421
10	2.154	0.6139
16	2.154	0.6336
20	2.154	0.6271
30	2.154	0.6184
35	2.154	0.6241
40	2.154	0.6241

3.4 Discussion

In this section we discuss the influences of various parameters on the velocity $f'(\eta)$ and temperature fields $\theta(\eta)$. Figs. (3.3 – 3.6) are plotted to analyze the effects of volume fraction of

nanoparticles ϕ , mass transfer parameter S , Hartman number M and porosity parameter λ on the velocity field f' . Effects of volume fraction of nanoparticles ϕ on the velocity profile f' can be seen from Fig. 3.3. Here the values of f' and boundary layer thickness decrease when volume fraction for the nanoparticles increases. The effects of mass transfer parameter S on the velocity f' are depicted in Fig. 3.4. This graph shows that the value of velocity function f' and the boundary layer thickness decrease by increasing S . Because applying suction leads to draw the amount of fluid particles into the wall and consequently the velocity boundary layer decreases. Influence of Hartman number M and parameter λ on the velocity field f' is similar to that of S . As application of a magnetic field has the tendency to slow down the movement of the fluid, causing its velocity to decrease. Also by increasing porosity parameter λ , the resistance to the fluid motion also increases. This causes the fluid velocity to decrease.

Effects of volume fraction of nanoparticles ϕ , mass transfer parameter S , Hartman number M , porosity parameter λ and Biot number γ_1 on the temperature profile θ are shown in the Figs. (3.7 – 3.11). Effect of ϕ on the temperature is analyzed in Fig. 3.7. It is observed that increasing the volume fraction of nanoparticles ϕ , increases the thermal conductivity of nanofluid and consequently the thermal boundary layer thickness increases. The behavior of S on the temperature profile is similar to that of velocity profile (see Fig. 3.8). Fig. 3.9 illustrates the effects of M on temperature profile θ . As Lorentz force is a resistive force which opposes the fluid motion. So heat is produced and as a result thermal boundary layer thickness increases. Variations of λ on temperature profile θ can be seen in the Fig. 3.10. There is a decrease in temperature θ when porosity parameter λ is increased. Fig. 3.11 represents the effect of Biot number γ_1 on temperature profile θ . Temperature profile θ increases for larger γ_1 .

In Fig. 3.12 we observe that boundary layer thickness is maximum when Titanium oxide is chosen as nanoparticle. Fig. 3.13 shows the effects of nanoparticle volume fraction ϕ , mass transfer parameter S and porosity parameter λ on skin friction coefficient in case of Cu -water. It is noticed that magnitude of skin friction coefficient increases when we increase ϕ for both S and λ . Fig. 3.14 describes the variation of Nusselt number for nanoparticle volume fraction ϕ , mass transfer parameter S and porosity parameter λ . In this Fig. the heat transfer rates increase as ϕ increases for both S and λ .

Table 3.1 shows the convergence of the series solutions. In Table 3.2 some thermophysical

properties of water and nanoparticles are given. Table 3.3 shows the effects of nanoparticle volume fraction ϕ for different types of nanofluids on skin friction coefficient when $\lambda = 0.5$, $M = 0.1$ and $S = 0.9$. Table 3.4 shows the effects of nanoparticle volume fraction ϕ for different types of nanofluids on Nusselt number when $\lambda = 0.5$, $Pr = 6.2$, $\gamma_1 = 0.7$, $M = 0.1$ and $S = 0.9$. These tables show that the shear stress and heat transfer rate change when we use different types of nanoparticles.

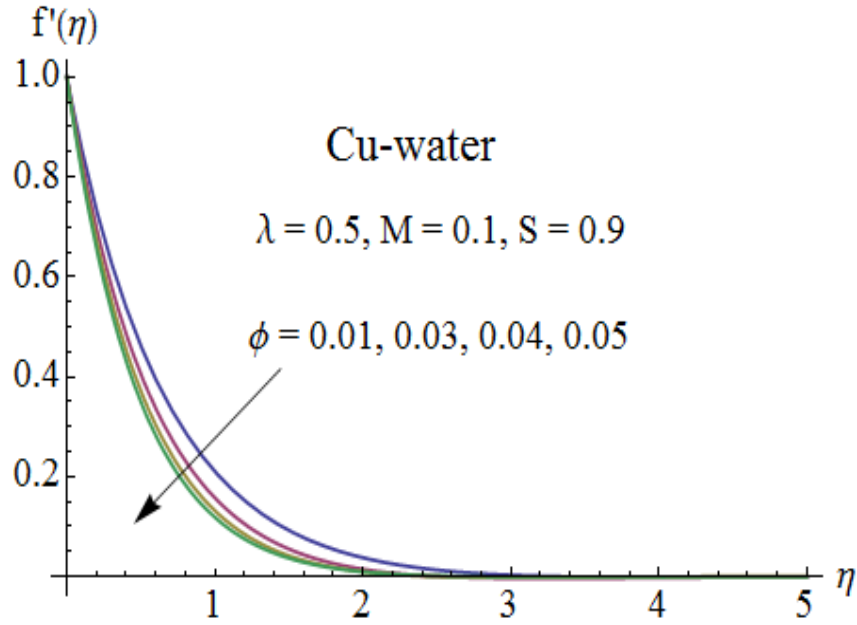


Fig. 3.3: Influence of ϕ on $f'(\eta)$.

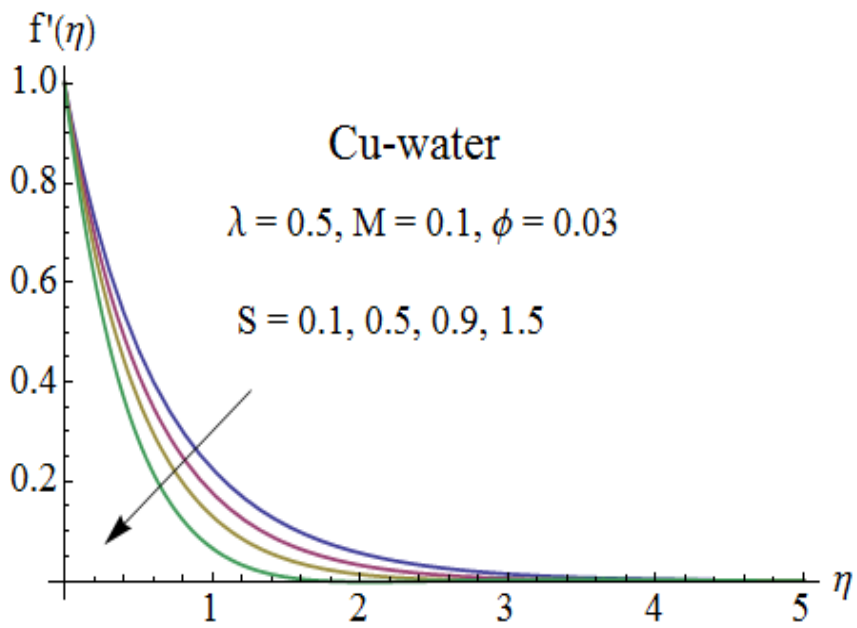


Fig. 3.4: Influence of S on $f'(\eta)$.

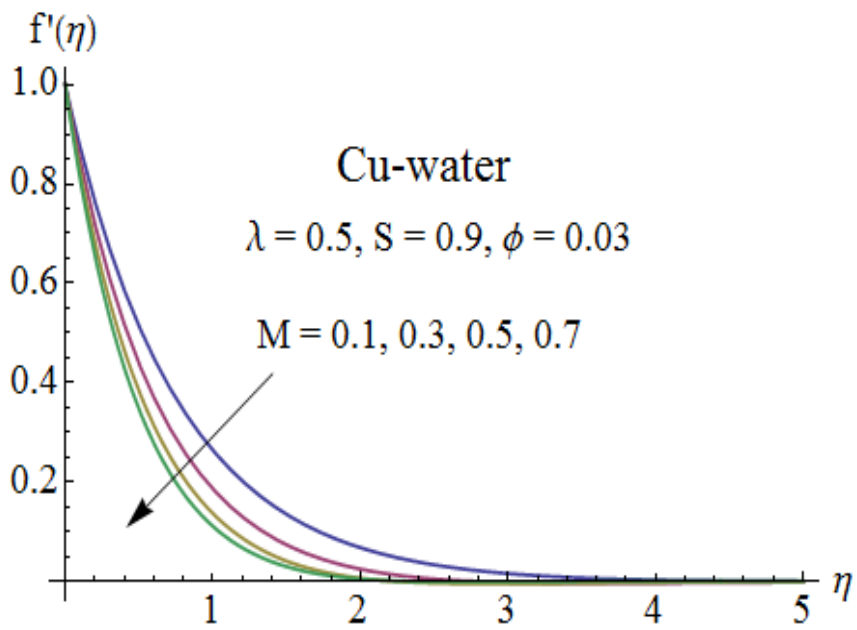


Fig. 3.5: Influence of M on $f'(\eta)$.

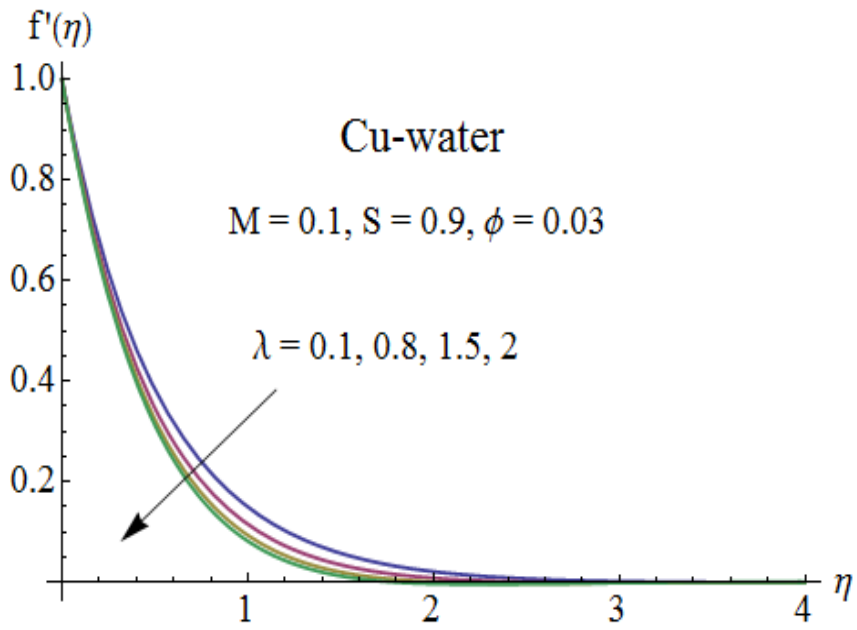


Fig. 3.6: Influence of λ on $f'(\eta)$.

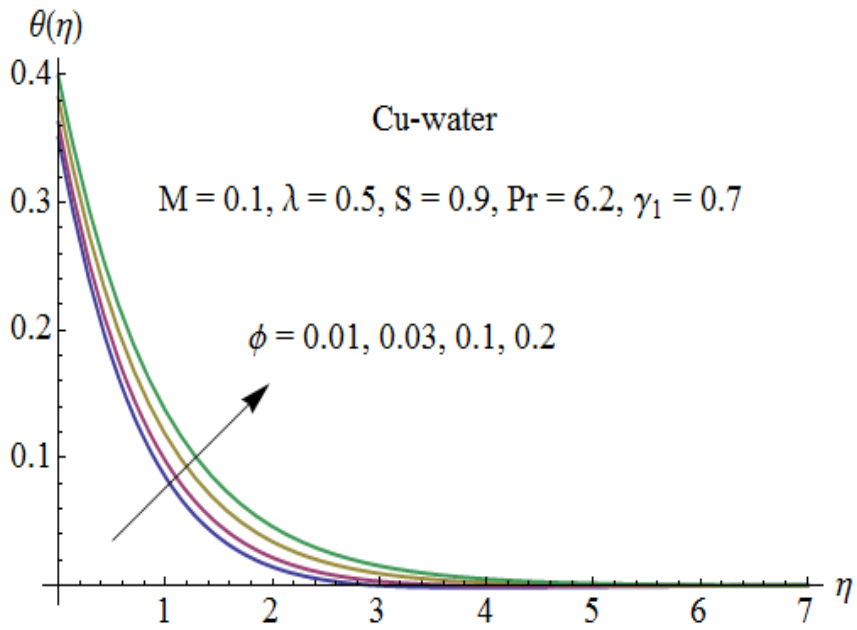


Fig. 3.7: Influence of ϕ on $\theta(\eta)$.

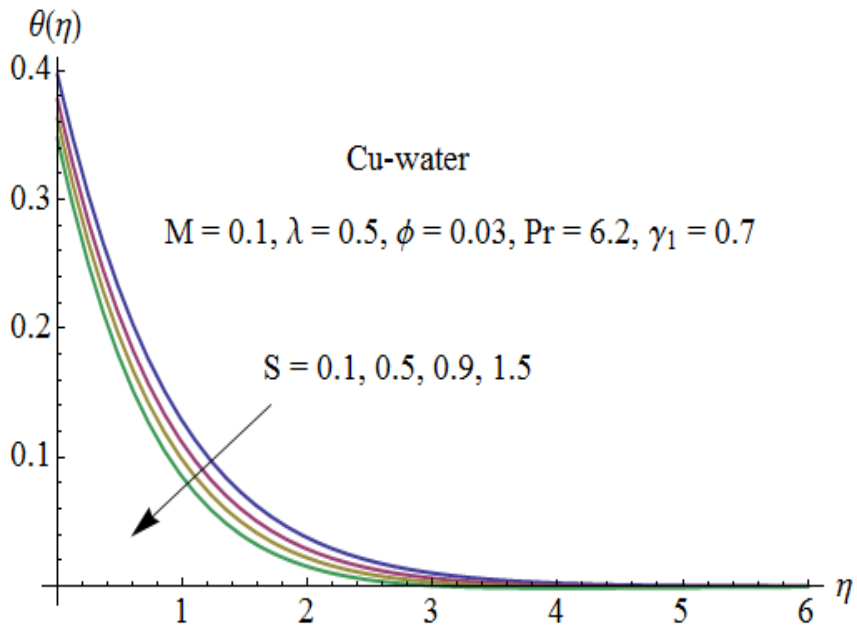


Fig. 3.8: Influence of S on $\theta(\eta)$.

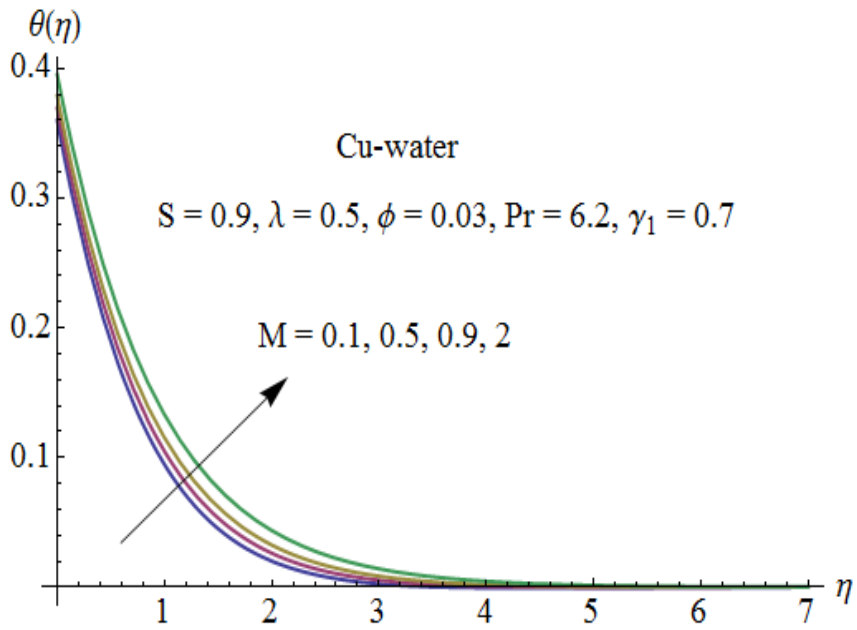


Fig. 3.9: Influence of M on $\theta(\eta)$.

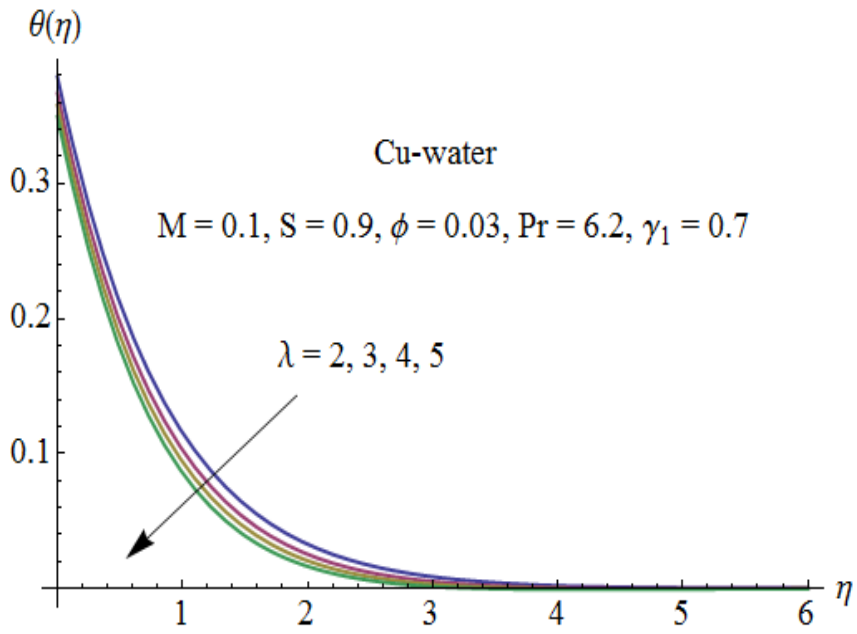


Fig. 3.10: Influence of λ on $\theta(\eta)$.

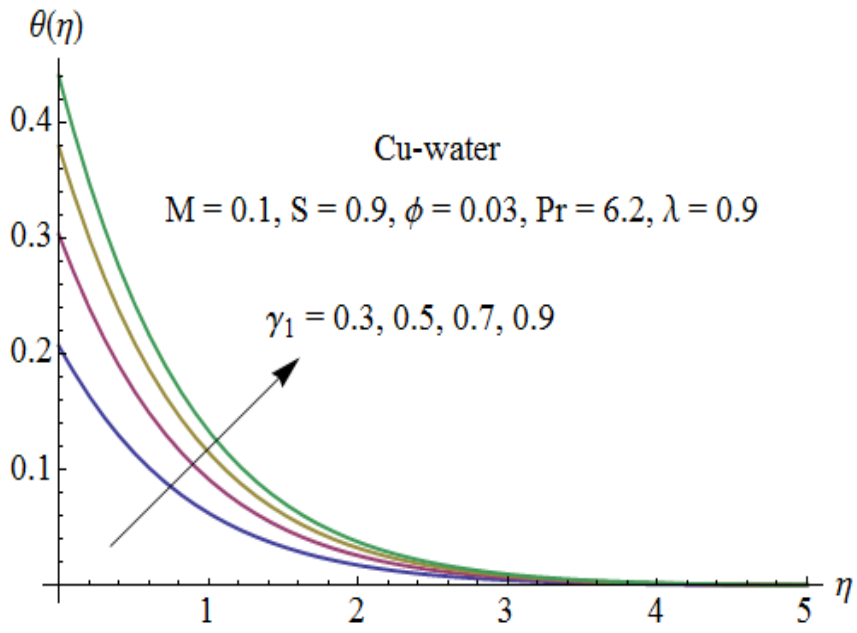
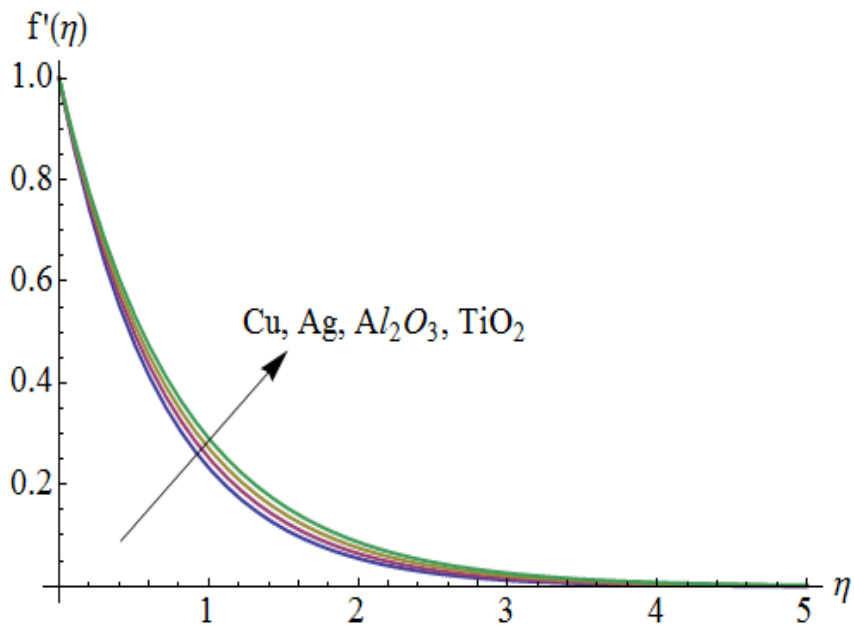
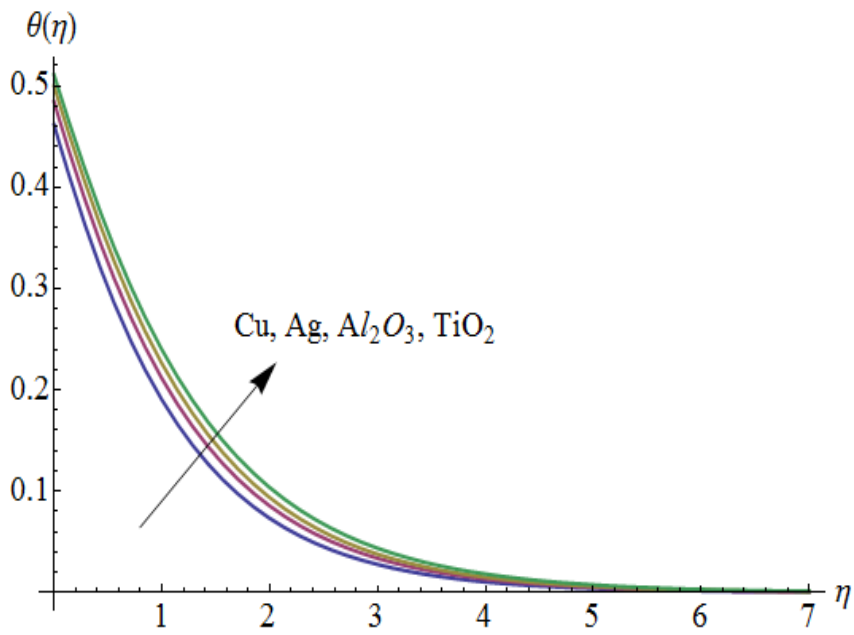


Fig. 3.11: Influence of γ_1 on $\theta(\eta)$.

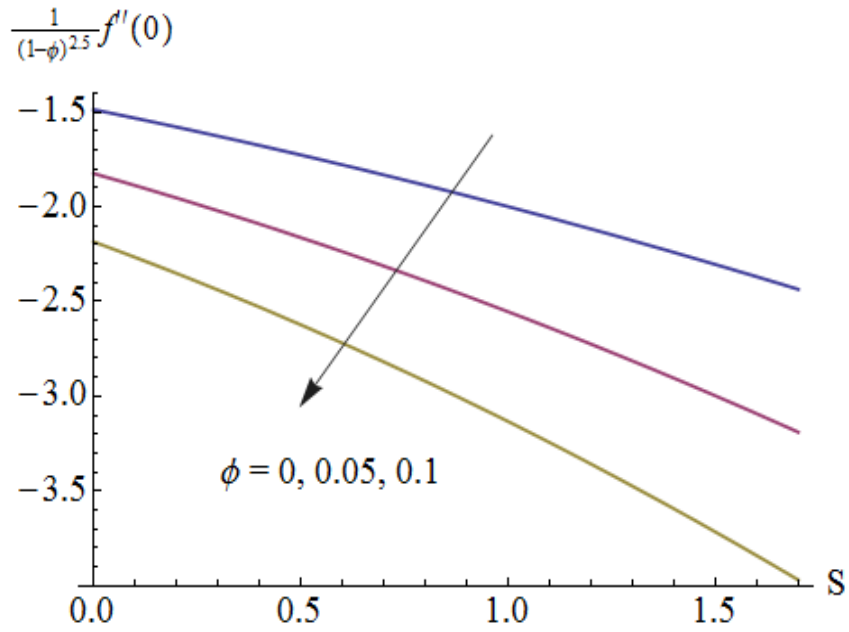


(a)

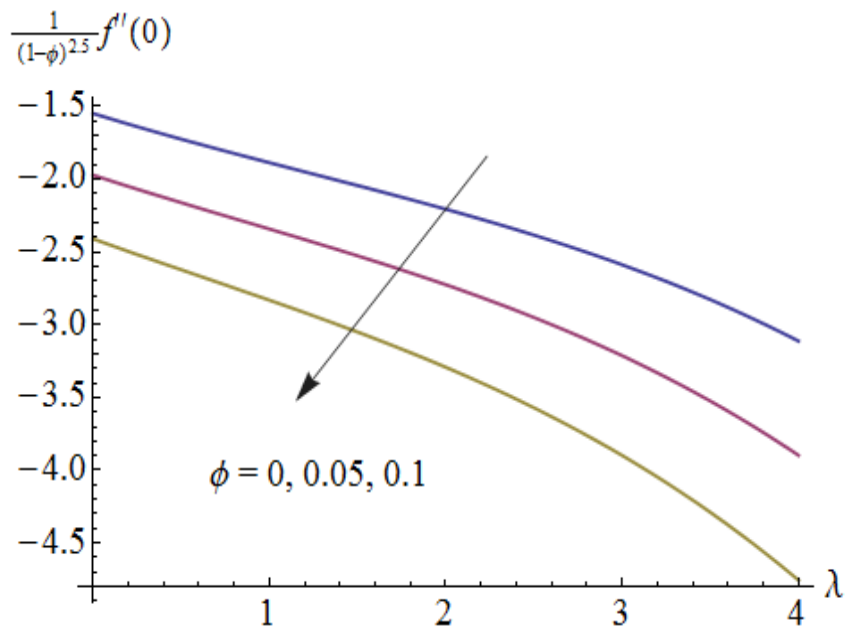


(b)

Fig. 3.12: (a) Velocity and (b) temperature profiles for different types of nanoparticles.



(a)



(b)

Fig. 3.13: Effects of nanoparticle volume fraction ϕ , (a) mass transfer parameter S and (b) porosity parameter λ on the skin friction coefficient when $M = 0.1$.

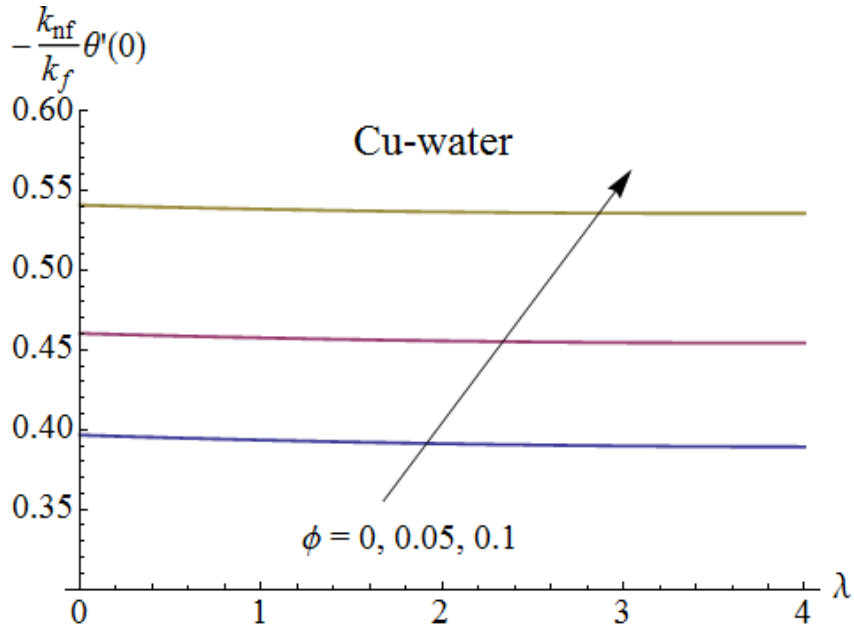
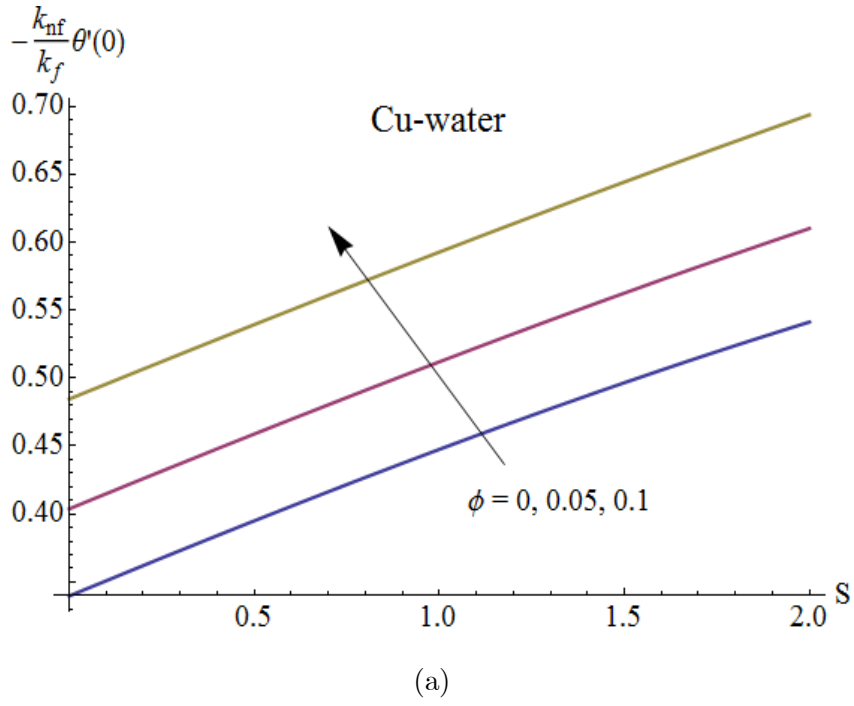


Fig. 3.14: Effects of nanoparticle volume fraction ϕ , (a) mass transfer parameter S and (b) porosity parameter λ on the Nusselt number when $M = 0.1$, $Pr = 6.2$ and $\gamma_1 = 0.7$.

Table 3.2: Thermophysical properties of water and nanoparticles [21].

	$\rho(kg/m^3)$	$c_p(j/kgk)$	$k(W/m.k)$	$\beta \times 10^5(K^{-1})$	$\sigma(\Omega m)^{-1}$
Pure water	997.1	4179	0.613	21	0.05
Copper(<i>Cu</i>)	8933	385	401	1.67	5.96×10^7
Silver(<i>Ag</i>)	10500	235	429	1.89	3.6×10^7
Alumina(<i>Al₂O₃</i>)	3970	765	40	0.85	1×10^{-10}
Titanium Oxide(<i>TiO₂</i>)	4250	686.2	8.9538	0.9	1×10^{-12}

Table 3.3: Effect of ϕ for different types of nanofluids on skin friction coefficient when $\lambda = 0.5$, $M = 0.1$ and $S = 0.9$.

ϕ	<i>Cu</i>	<i>Ag</i>	<i>Al₂O₃</i>	<i>TiO₂</i>
0.01	-2.05387	-2.07036	-2.00143	-2.00439
0.03	-2.15426	-2.20071	-2.00558	-2.01404
0.05	-2.23960	-2.31255	-2.00535	-2.01873

Table 3.4: Effect of ϕ for different types of nanofluids on Nusselt number when $\lambda = 0.5$, $Pr = 6.2$, $\gamma_1 = 0.7$, $M = 0.1$ and $S = 0.9$.

ϕ	<i>Cu</i>	<i>Ag</i>	<i>Al₂O₃</i>	<i>TiO₂</i>
0.01	0.436981	0.436452	0.437649	0.438380
0.03	0.423311	0.421702	0.425326	0.427566
0.05	0.409403	0.406691	0.412767	0.416582

3.5 Concluding remarks

Here MHD flow of nanofluid by an exponentially permeable stretching sheet is studied. Effects of different parameters on the velocity and temperature profiles are shown. Convergent approximate solution is constructed. The following observations are made

- An increase in the values of ϕ , S , M and λ have similar effects on the velocity profile in a qualitative sense.
- Temperature profile enhances by increasing ϕ , M and γ_1 while it decreases when S and λ are increased.

- Magnitude of skin friction coefficient is higher for increasing values of ϕ .
- Higher values of ϕ correspond to larger values of Nusselt number.

Chapter 4

MHD flow of nanofluid with homogeneous-heterogeneous reactions and velocity slip

Present chapter focuses on the steady magnetohydrodynamic (MHD) flow of viscous nanofluid. The flow is caused by a stretching surface with homogeneous-heterogeneous reactions. An incompressible fluid fills the porous space. Copper-water and silver-water nanofluids are investigated in this study. Transformation method reduces the nonlinear partial differential equations governing the flow into the ordinary differential equation by similarity transformations. The obtained equations are then solved for the development of series solutions. Convergence of the obtained series solutions is explicitly discussed. Effects of different parameters on the velocity, concentration and skin friction coefficient are shown and analyzed through graphs.

4.1 Mathematical formulation

We consider the steady two-dimensional flow of an incompressible nanofluid over a stretching surface in porous medium with permeability K . The x -axis is taken along the stretching surface in the direction of motion and y -axis is perpendicular to it. A uniform transverse magnetic field of strength B_0 is applied parallel to the y -axis. It is assumed that the induced magnetic and electric fields effects are negligible (see Fig. 4.1). Nanoparticles such as copper

(*Cu*) and silver (*Ag*) are considered. Water is treated as a base fluid.

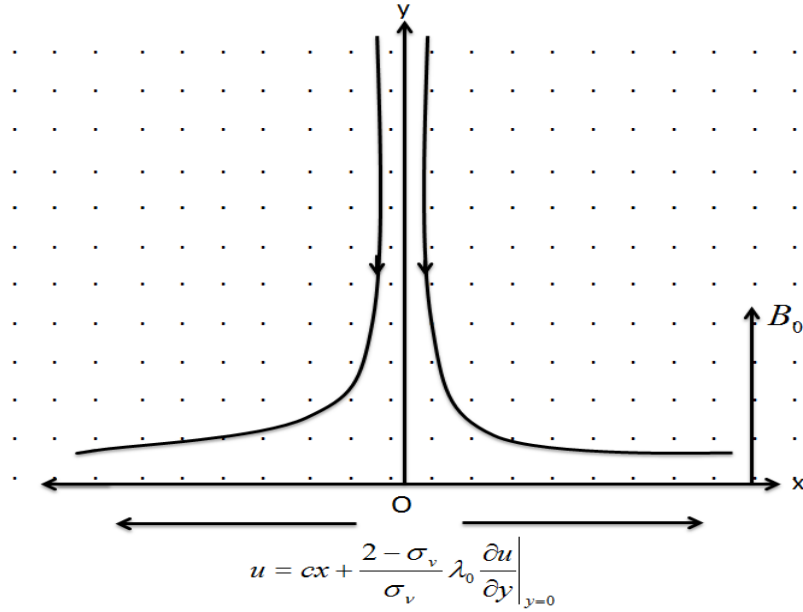
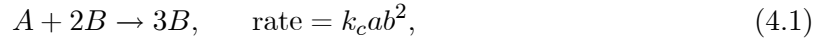


Fig. 4.1: Geometry of the problem.

We have taken a simple homogeneous-heterogeneous reaction model in the following form [73]:



while on the catalyst surface we have the single, isothermal, first order reaction



where a and b are the concentrations of the chemical species A and B and k_c and k_s denote the rate constants. We assume that both reaction processes are isothermal. Under these assumptions, the relevant boundary layer equations are

$$\frac{\partial u}{\partial x} + \frac{\partial v}{\partial y} = 0, \quad (4.3)$$

$$\rho_{nf} \left(u \frac{\partial u}{\partial x} + v \frac{\partial u}{\partial y} \right) = \mu_{nf} \frac{\partial^2 u}{\partial y^2} - \frac{\mu_{nf}}{K} u - \sigma_{nf} B_0^2 u, \quad (4.4)$$

$$u \frac{\partial a}{\partial x} + v \frac{\partial a}{\partial y} = D_A \frac{\partial^2 a}{\partial y^2} - k_c a b^2, \quad (4.5)$$

$$u \frac{\partial b}{\partial x} + v \frac{\partial b}{\partial y} = D_B \frac{\partial^2 b}{\partial y^2} + k_c a b^2. \quad (4.6)$$

The subjected boundary conditions are

$$\begin{aligned} u = cx + \frac{2 - \sigma_v}{\sigma_\nu} \lambda_0 \left. \frac{\partial u}{\partial y} \right|_{y=0}, \quad v = 0, \quad D_A \frac{\partial a}{\partial y} = k_s a, \quad D_B \frac{\partial b}{\partial y} = -k_s a \quad \text{at } y = 0, \\ u \rightarrow 0, \quad a \rightarrow a_0, \quad b \rightarrow 0 \quad \text{as } y \rightarrow \infty, \end{aligned} \quad (4.7)$$

where u and v are the velocity components along the x - and y - directions respectively, D_A and D_B are the respective diffusion species coefficients of A and B , σ_v the tangential momentum accommodation coefficient and λ_0 the molecular mean free path. The effective density ρ_{nf} , the dynamic viscosity μ_{nf} , the electrical conductivity σ_{nf} , the heat capacitance $(\rho C_p)_{nf}$ and the thermal conductivity k_{nf} of the nanofluid are given by

$$\rho_{nf} = \rho_f(1 - \phi) + \rho_s \phi, \quad (4.8)$$

$$\mu_{nf} = \frac{\mu_f}{(1 - \phi)^{2.5}}, \quad (4.9)$$

$$\frac{\sigma_{nf}}{\sigma_f} = 1 + \frac{3 \left(\frac{\sigma_s}{\sigma_f} - 1 \right) \phi}{\left(\frac{\sigma_s}{\sigma_f} + 2 \right) - \left(\frac{\sigma_s}{\sigma_f} - 1 \right) \phi}, \quad (4.10)$$

Here ϕ is the nanoparticle volume fraction, s in subscript is for nano-solid-particles and f in subscript is for base fluid. Denoting a_0 (a constant) and $\xi(\eta)$ and $h(\eta)$ the dimensionless concentration and defining

$$\eta = \sqrt{\frac{c}{\nu_f}} y, \quad u = cx f'(\eta), \quad v = -\sqrt{c \nu_f} f(\eta), \quad a = a_0 \xi(\eta), \quad b = a_0 h(\eta), \quad (4.11)$$

equation (4.3) is satisfied automatically and Eqs. (4.4 – 4.7) reduce to

$$\varepsilon_1 f'''' + f f'' - f'^2 - \lambda \varepsilon_1 f' - (1 - \phi)^{2.5} M \varepsilon_1 \frac{\sigma_{nf}}{\sigma_f} f' = 0, \quad (4.12)$$

$$\frac{1}{Sc} \xi'' + f \xi' - k_1 \xi h^2 = 0, \quad (4.13)$$

$$\frac{\delta}{Sc} h'' + f h' + k_1 \xi h^2 = 0, \quad (4.14)$$

$$f'(0) = 1 + \beta f''(0), \quad f(0) = 0, \quad f'(\infty) \rightarrow 0,$$

$$\xi'(0) = k_2 \xi(0), \quad \xi(\infty) \rightarrow 1,$$

$$\delta h'(0) = -k_2 \xi(0), \quad h(\infty) \rightarrow 0, \quad (4.15)$$

in which prime indicates the differentiation with respect to η . Moreover the non-dimensional constants in Eqs. (4.12 – 4.17) are the porosity parameter λ , the Hartman number M , the Schmidt number Sc , the measure of the strength of the homogeneous reaction k_1 , the measure of the strength of the heterogeneous reaction k_2 , the ratio of the diffusion coefficient δ and the velocity slip parameter β . These are defined as follows:

$$\lambda = \frac{\nu_f}{cK}, \quad M = \frac{\sigma_f B_0^2}{c\rho_f}, \quad Sc = \frac{\nu_f}{D_A}, \quad k_1 = \frac{k_c a_0^2}{c}, \quad k_2 = \frac{k_s}{D_A} \sqrt{\frac{\nu_f}{c}}, \quad \delta = \frac{D_B}{D_A}, \quad \beta = \frac{2 - \sigma_v}{\sigma_v} \lambda_0 \sqrt{\frac{c}{\nu_f}}, \quad (4.16)$$

where

$$\varepsilon_1 = \frac{1}{(1 - \phi)^{2.5} \left(1 - \phi + \phi \frac{\rho_s}{\rho_f}\right)}. \quad (4.17)$$

The diffusion coefficients of chemical species A and B are expected to be of a comparable size. This leads to make a further assumption that the diffusion coefficients D_A and D_B are equal, i.e. to take $\delta = 1$ [73]. In this case we have from Eqs. (4.15)

$$\xi(\eta) + h(\eta) = 1 \quad (4.18)$$

Thus Eqs. (4.13) and (4.14) become

$$\frac{1}{Sc} \xi'' + f \xi' - k_1 \xi (1 - \xi)^2 = 0, \quad (4.19)$$

subject to the boundary conditions

$$\xi'(0) = k_2 \xi(0), \quad \xi(\infty) \rightarrow 1. \quad (4.20)$$

The physical quantity of interest is the skin-friction coefficient C_{sf} . It characterizes the surface drag. The shearing stress at the surface of the wall τ_w is given by

$$\tau_w = -\mu_{nf} \left. \frac{\partial u}{\partial y} \right|_{y=0} = -\frac{1}{(1-\phi)^{2.5}} \sqrt{\mu_f \rho_f c^3} x f''(0). \quad (4.21)$$

The skin friction coefficient is defined as

$$C_{sf} = \frac{\tau_w}{\frac{1}{2} \rho_f u_w^2}, \quad (4.22)$$

$$C_{sf} \sqrt{\text{Re}_x} = -\frac{2}{(1-\phi)^{2.5}} f''(0), \quad (4.23)$$

in which $\text{Re}_x = u_w x / \nu_f$ denotes the local Reynolds number.

4.2 Solutions derivation

We choose the initial guesses $f_0(\eta)$ and $\xi_0(\eta)$ and the linear operators \mathcal{L}_f and \mathcal{L}_ξ in the forms

$$f_0(\eta) = \frac{1}{1+\beta} (1 - e^{-\eta}), \quad \xi_0(\eta) = 1 - \frac{1}{2} e^{-k_2 \eta}, \quad (4.24)$$

$$\mathcal{L}_f(f) = f''' - f', \quad \mathcal{L}_\xi(\xi) = \xi'' - \xi, \quad (4.25)$$

together with the properties

$$\begin{aligned} \mathcal{L}_f [c_1 + c_2 e^\eta + c_3 e^{-\eta}] &= 0, \\ \mathcal{L}_\xi [c_4 e^\eta + c_5 e^{-\eta}] &= 0, \end{aligned} \quad (4.26)$$

where $c_1 - c_5$ are the constants.

We construct the zeroth order problems as follows:

$$(1-p) \mathcal{L}_f [\hat{f}(\eta; p) - f_0(\eta)] = p \hbar_f \mathcal{N}_f[\hat{f}(\eta; p)], \quad (4.27)$$

$$(1-p) \mathcal{L}_\xi [\hat{\xi}(\eta; p) - \xi_0(\eta)] = p \hbar_\xi \mathcal{N}_\xi[\hat{\xi}(\eta; p), \hat{f}(\eta; p)], \quad (4.28)$$

$$\begin{aligned}
\hat{f}'(0; p) &= 1 + \beta \hat{f}''(0; p), \quad \hat{f}(0; p) = 0, \quad \hat{f}'(\infty; p) = 0, \\
\hat{\xi}'(0; p) &= k_2 \hat{\xi}(0; p), \quad \hat{\xi}(\infty; p) = 1,
\end{aligned} \tag{4.29}$$

where $p \in [0, 1]$ denotes an embedding parameter and \hbar_f and \hbar_ξ are the nonzero auxiliary parameters. With Eqs. (4.12) and (4.19), the definitions of operators \mathcal{N}_f and \mathcal{N}_ξ are

$$\begin{aligned}
\mathcal{N}_f [\hat{f}(\eta; p)] &= \varepsilon_1 \frac{\partial^3 \hat{f}(\eta; p)}{\partial \eta^3} + \hat{f}(\eta; p) \frac{\partial^2 \hat{f}(\eta; p)}{\partial \eta^2} - \left(\frac{\partial \hat{f}(\eta; p)}{\partial \eta} \right)^2 \\
&\quad - \lambda \varepsilon_1 \frac{\partial \hat{f}(\eta; p)}{\partial \eta} - (1 - \phi)^{2.5} M \varepsilon_1 \frac{\sigma_{nf}}{\sigma_f} \frac{\partial \hat{f}(\eta; p)}{\partial \eta},
\end{aligned} \tag{4.30}$$

$$\begin{aligned}
\mathcal{N}_\xi [\hat{\xi}(\eta; p), \hat{f}(\eta; p)] &= \frac{1}{S_c} \frac{\partial^2 \hat{\xi}(\eta; p)}{\partial \eta^2} + \hat{f}(\eta; p) \frac{\partial \hat{\xi}(\eta; p)}{\partial \eta} - k_1 (\hat{\xi}(\eta; p))^3 \\
&\quad - k_1 \hat{\xi}(\eta; p) + 2k_1 (\hat{\xi}(\eta; p))^2.
\end{aligned} \tag{4.31}$$

The resulting problems at m^{th} order are given by

$$\mathcal{L}_f [f_m(\eta) - \chi_m f_{m-1}(\eta)] = \hbar_f \mathcal{R}_{f,m}(\eta), \tag{4.32}$$

$$\mathcal{L}_\xi [\xi_m(\eta) - \chi_m \xi_{m-1}(\eta)] = \hbar_\xi \mathcal{R}_{\xi,m}(\eta), \tag{4.33}$$

$$f_m(0) = f'_m(0) - \beta f''_m(0) = f'_m(\infty) = \xi'_m(0) - k_2 \xi_m(0) = \xi_m(\infty) = 0, \tag{4.34}$$

$$\chi_m = \begin{cases} 0, & m \leq 1 \\ 1, & m > 1 \end{cases}, \tag{4.35}$$

$$\mathcal{R}_{f,m}(\eta) = \varepsilon_1 f'''_{m-1} + \sum_{l=0}^{m-1} [f_{m-1-l} f''_l - f'_{m-1-l} f'_l] - \lambda \varepsilon_1 f'_{m-1} - (1 - \phi)^{2.5} M \varepsilon_1 \frac{\sigma_{nf}}{\sigma_f} f'_{m-1}, \tag{4.36}$$

$$\mathcal{R}_{\xi,m}(\eta) = \frac{1}{S_c} \xi''_{m-1} + \sum_{l=0}^{m-1} \left[\xi'_{m-1-l} f_l - k_1 \xi_{m-1-l} \sum_{j=0}^l \xi_{l-j} \xi_j + 2k_1 \xi_{m-1-l} \xi_l \right] - k_1 \xi_{m-1}, \tag{4.37}$$

where the general solutions are

$$\begin{aligned} f_m(\eta) &= f_m^*(\eta) + c_1 + c_2 e^\eta + c_3 e^{-\eta}, \\ \xi_m(\eta) &= \xi_m^*(\eta) + c_4 e^\eta + c_5 e^{-\eta}, \end{aligned} \quad (4.38)$$

in which f_m^* and ξ_m^* denote the special solutions. constants c_i ($i = 1 - 5$) can be determined by the boundary conditions (4.34). They are given by

$$\begin{aligned} c_3 &= \frac{1}{1 + \beta} \left[\frac{\partial f^*(\eta)}{\partial \eta} - \beta \frac{\partial^2 f^*(\eta)}{\partial \eta^2} \right]_{\eta=0}, \quad c_1 = -c_3 - f^*(0), \\ c_2 &= c_4 = 0, \quad c_5 = \frac{1}{1 + k_2} \left[\frac{\partial \xi^*(\eta)}{\partial \eta} \Big|_{\eta=0} - k_2^* \xi(0) \right]. \end{aligned} \quad (4.39)$$

4.3 Convergence of the homotopy solutions

Now the solutions of Eqs. (4.12) and (4.19) subject to the boundary conditions (4.15) and (4.20) are computed by means of homotopy analysis method. We choose auxiliary parameters \hbar_f and \hbar_ξ for the functions f and ξ respectively. The convergence of obtained series and rate of the approximation for HAM strongly depend upon the values of the auxiliary parameters. For ranges of admissible values of \hbar_f and \hbar_ξ , the \hbar -curves for 13th-order of approximations are plotted in the Figs. (4.2 and 4.3). We can see that the permissible values of \hbar_f and \hbar_ξ for *Cu*-water are $-1.6 \leq \hbar_f \leq -0.5$ and $-1.2 \leq \hbar_\xi \leq -0.3$ and for *Ag*-water are $-1.6 \leq \hbar_f \leq -0.6$ and $-1 \leq \hbar_\xi \leq -0.1$. Further, the series solutions converge in the whole region of η ($0 < \eta < \infty$) when $\hbar_f = \hbar_\xi = -1$.

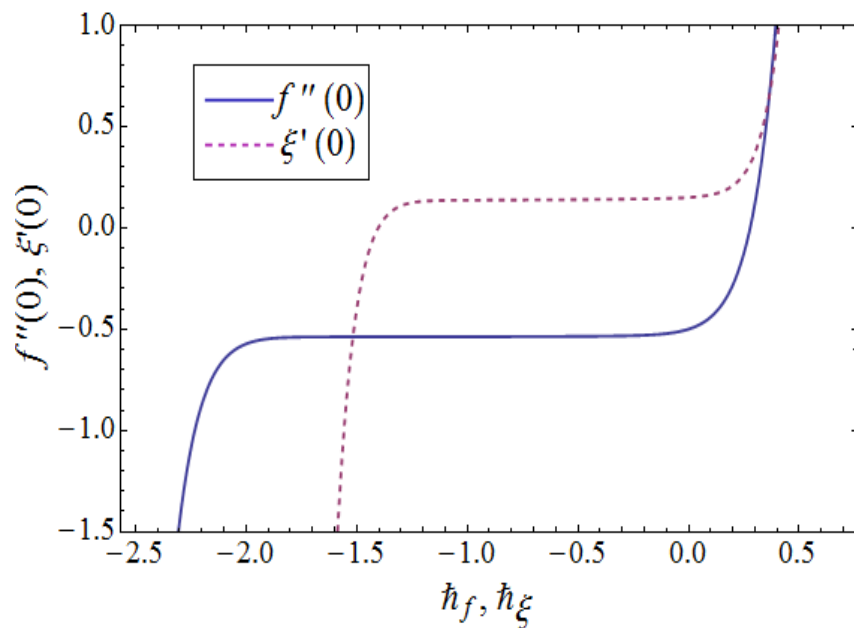


Fig. 4.2: \hbar -curves of $f''(0)$ and $\xi'(0)$ for Cu-water when $\phi = 0.2$, $\lambda = 0.4$, $k_1 = k_2 = 0.3$, $M = Sc = 0.5$ and $\beta = 1$.

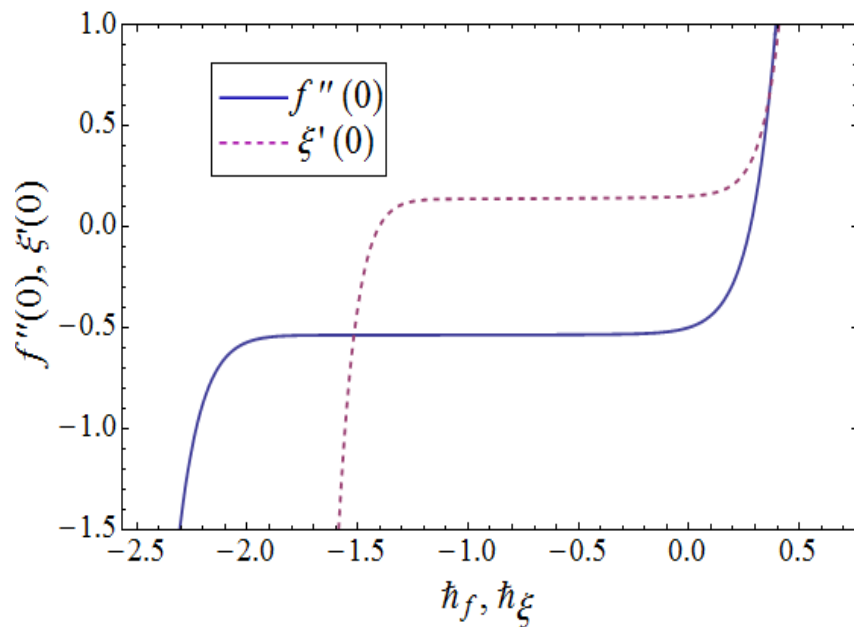


Fig. 4.3: \hbar -curves of $f''(0)$ and $\xi'(0)$ for Ag-water when $\phi = 0.2$, $\lambda = 0.4$, $k_1 = k_2 = 0.3$, $M = Sc = 0.5$ and $\beta = 1$.

Table 4.1: Convergence of HAM solutions for different order of approximations when $\phi = 0.2$, $\lambda = 0.4$, $k_1 = k_2 = 0.3$, $M = Sc = 0.5$ and $\beta = 1$.

Order of approximations	$-f''(0)$	$g'(0)$
1	0.5455	0.04916
5	0.5564	0.04835
10	0.5588	0.04788
15	0.5596	0.04755
17	0.5594	0.04736
20	0.5594	0.04736
25	0.5594	0.04736

4.4 Results and discussion

The effects of different parameters on the dimensionless flow and concentration profiles are investigated and presented graphically in this section.

4.4.1 Dimensionless velocity profiles

Figs. (4.4 – 4.7) exhibit the dimensionless velocity profiles for different values of nanoparticle volume fraction ϕ , Hartman number M , velocity slip parameter β and porosity parameter λ . Effects of volume fraction of nanoparticles (*Cu* and *Ag*) on the velocity profile f' can be seen from Fig. 4.4. Here the velocity profile and boundary layer thickness decrease when volume fraction for the nanoparticles increases. The effects of Hartman number M on the velocity f' are depicted in Fig. 4.5. We analyzed that the velocity is reduced when we increase the values of Hartman number. In fact applied magnetic field has the tendency to slow down the movement of the fluid which leads to a decrease in the velocity and momentum boundary layer thickness. Variations of velocity slip parameter β on velocity profile f' can be seen in the Fig. 4.6. There is a decrease in velocity when velocity slip parameter β is increased. From Fig. 4.7, we have seen that larger values of porosity parameter λ correspond to the less velocity. Porosity parameter depends on the permeability parameter K . Increase in porosity parameter leads to the lower permeability parameter. This lower permeability parameter causes a reduction in the fluid velocity.

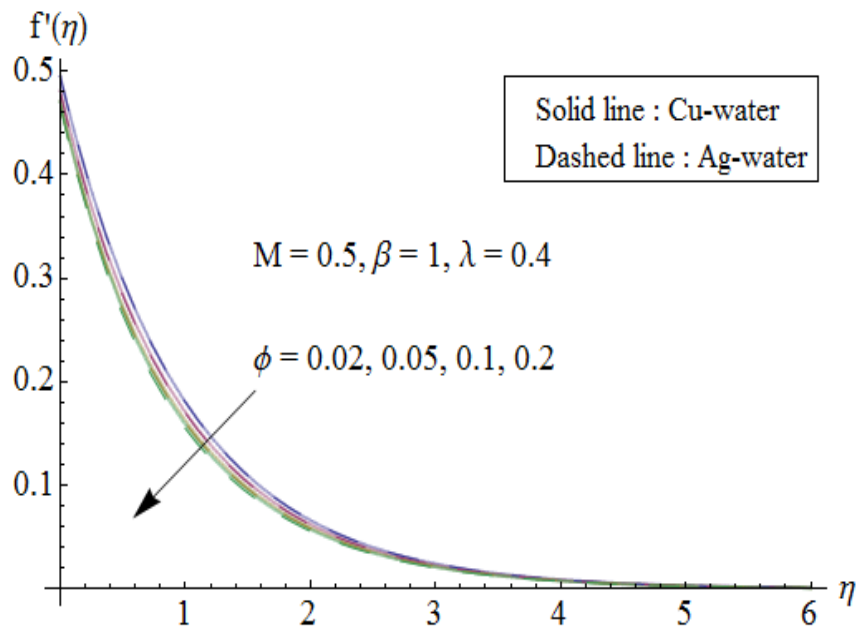


Fig. 4.4. Influence of ϕ on velocity field.

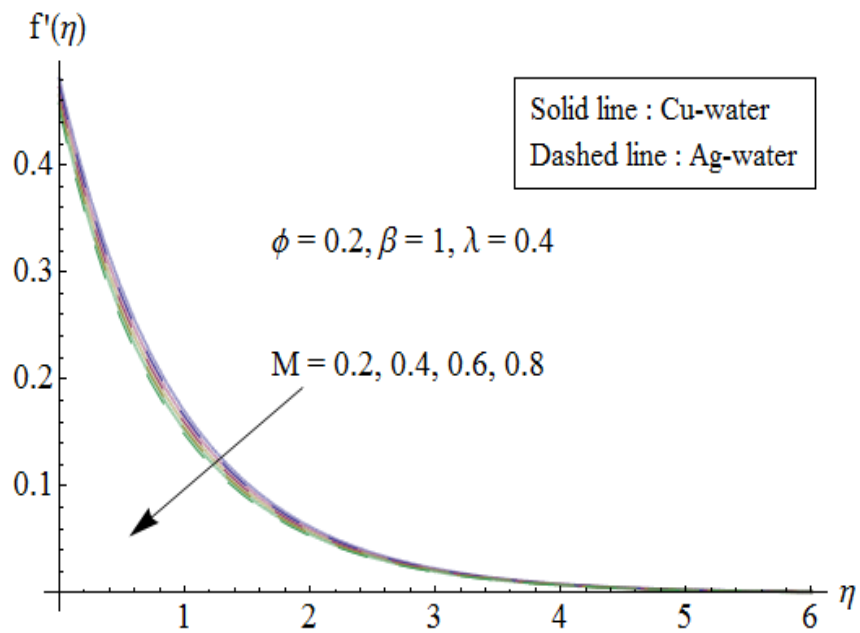


Fig. 4.5. Influence of M on velocity field.

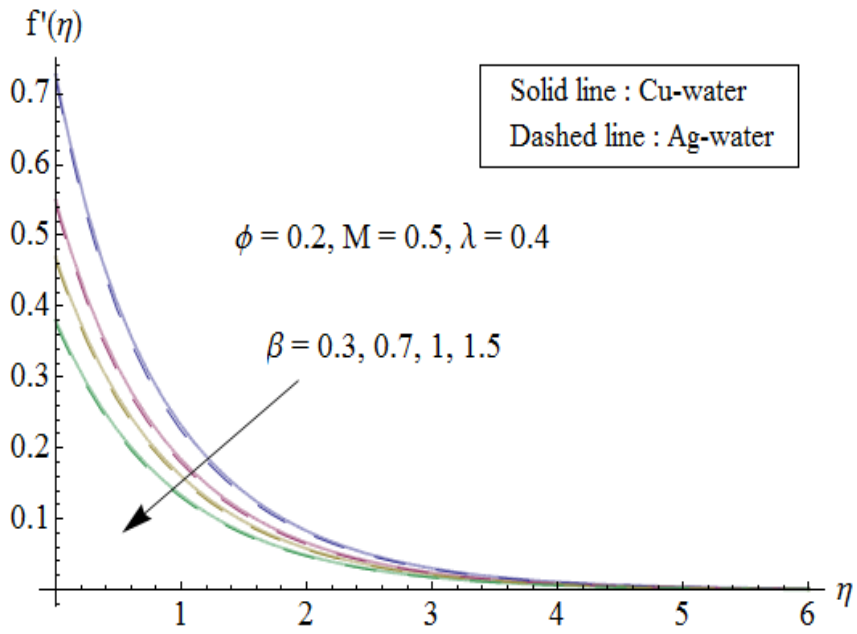


Fig. 4.6. Influence of β on velocity field.

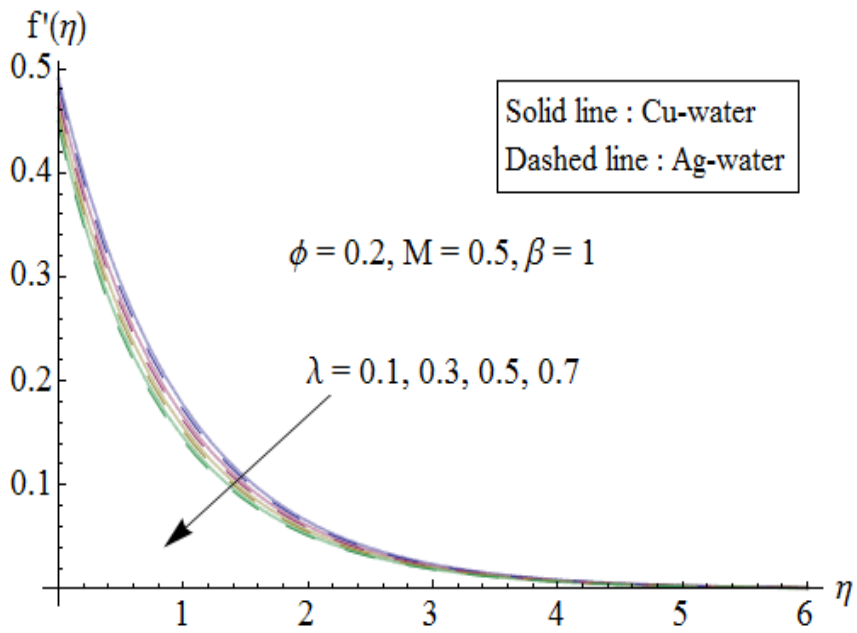


Fig. 4.7. Influence of λ on velocity field.

4.4.2 Dimensionless concentration profiles

Effects of the measure of strength of the homogeneous reaction k_1 , the measure of the strength of the heterogeneous reaction k_2 and the Schmidt number Sc on the concentration profile ξ are shown in the Figs. (4.8 – 4.10). Effect of k_1 on the concentration is analyzed in Fig. 4.8. It is observed that increasing the measure of the strength of the homogeneous reaction k_1 decreases the thermal boundary layer thickness. Fig. 4.9 illustrates the effects of k_2 on concentration profile ξ . There is an increase in concentration ξ when the measure of the strength of the heterogeneous reaction k_2 is increased. The behavior of Schmidt number Sc on the concentration profile is similar to that of k_2 (see Fig. 4.10).

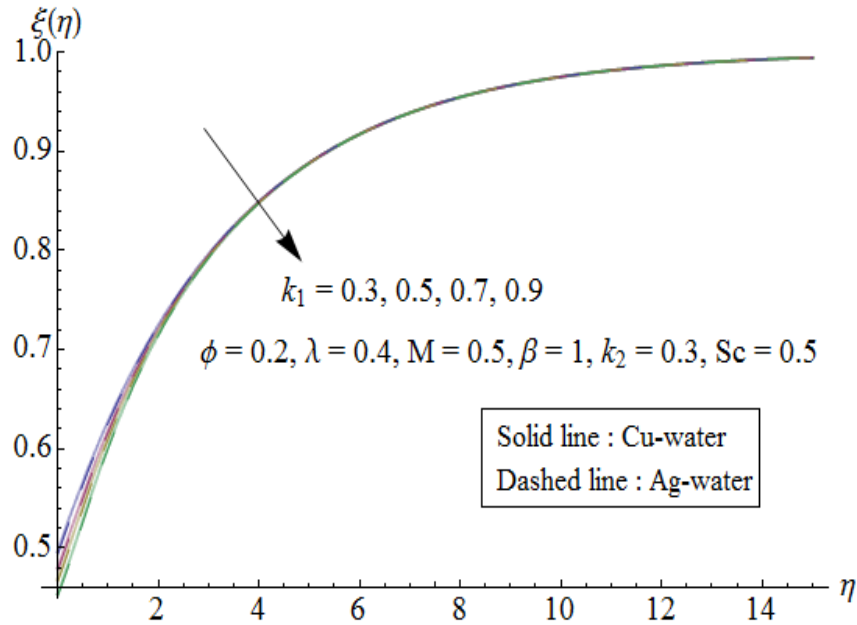


Fig. 4.8. Influence of k_1 on concentration field.

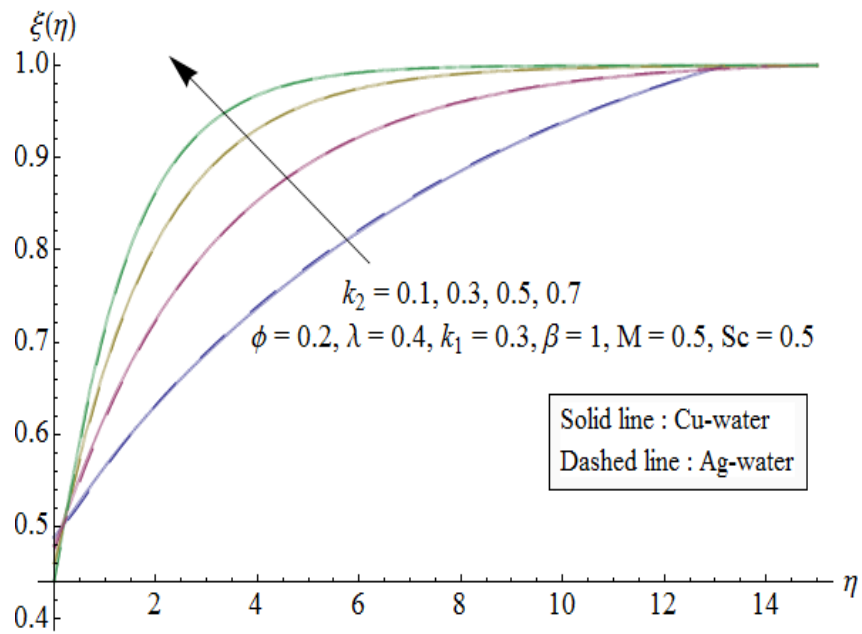


Fig. 4.9. Influence of k_2 on concentration field.

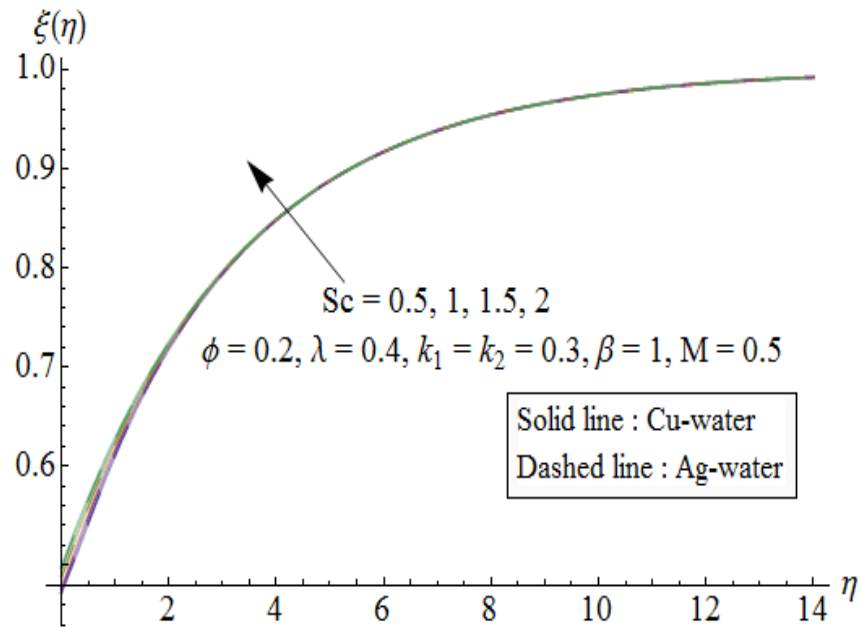


Fig. 4.10. Influence of Sc on concentration field.

4.4.3 Skin friction coefficient and surface concentration

Fig. 4.11 shows the skin friction coefficient $f''(0)$ as a function of nanoparticle volume fraction ϕ . The skin friction coefficient enhances with increasing values of ϕ . The results of the skin friction coefficient are examined for both types of nanofluids. We observe that the Ag -water nanofluid gives a higher drag force opposite to the flow when compared with the Cu -water nanofluid.

The variation of dimensionless concentration for different values of k_1 and k_2 are shown in Figs. 4.12 and 4.13 respectively. From Fig. 4.12 it is observed that concentration at the surface decreases as the strength of the heterogeneous reaction increases for different types of nanofluids. One can see from Fig. 4.13 that $\xi(0)$ decreases with the increase of homogeneous reaction strength k_1 . Influence of Sc on $\xi(0)$ for two different types of nanoparticles is shown in Fig. 4.14. It is clear that the concentration decreases with an increase of Schmidt number.

In Table 4.3 some numerical values of skin friction coefficient are given for copper and silver nanoparticles. Tabular values show that skin friction coefficient enhances by increasing ϕ and M while it decreases for larger β . Table 4.4 shows that surface concentration decreases by increasing k_1 , k_2 , Sc and β .

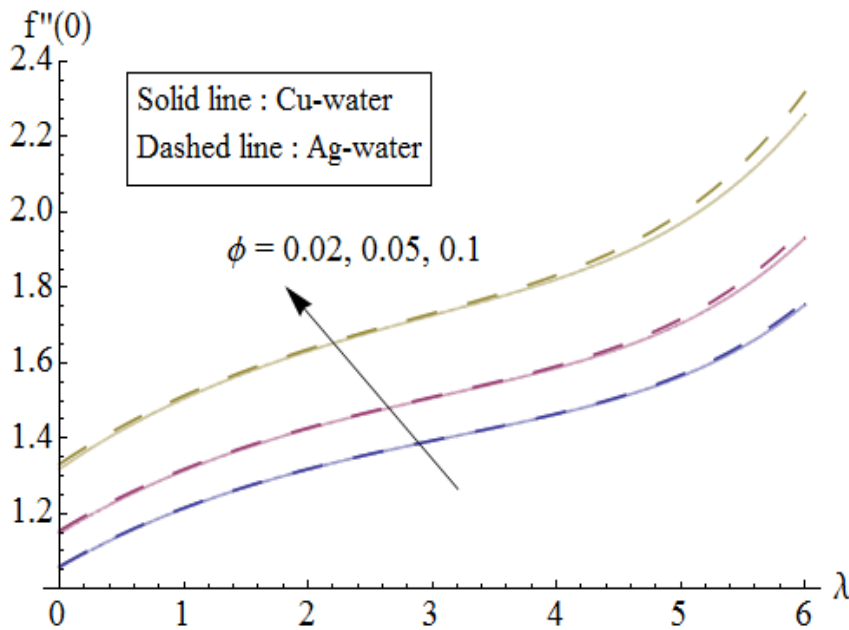


Fig. 4.11. Influence of ϕ on skin friction coefficient.

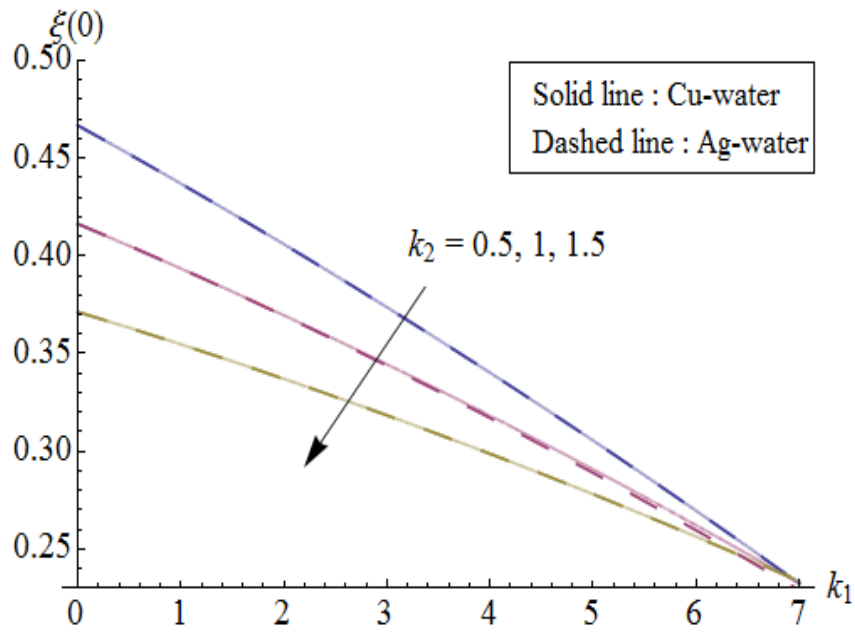


Fig. 4.12: Influence of k_2 on surface concentration.

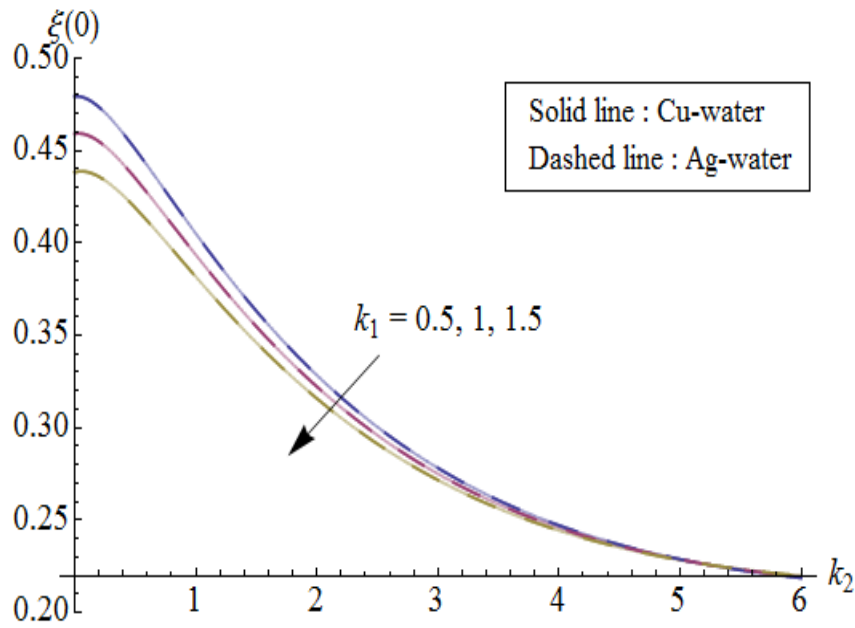


Fig. 4.13: Influence of k_1 on surface concentration.

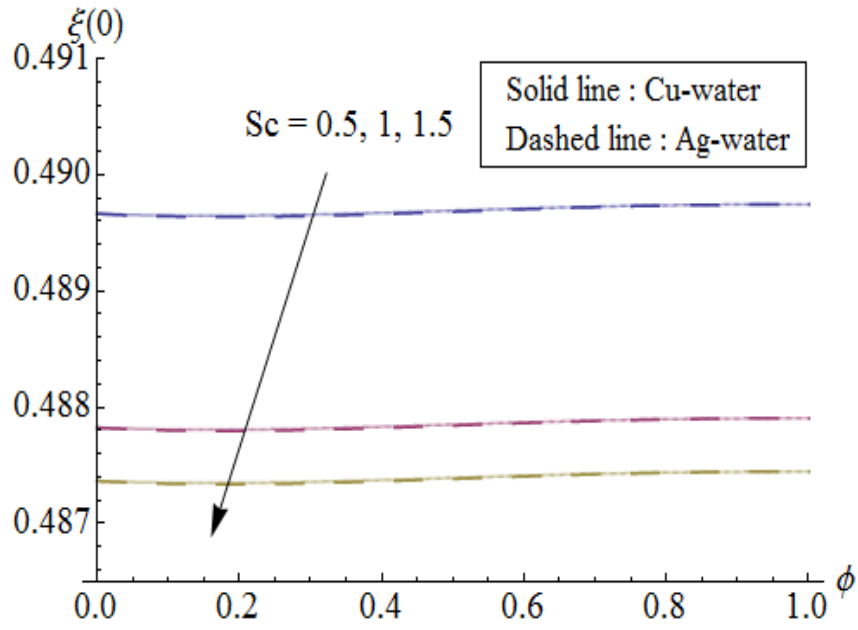


Fig. 4.14: Influence of Sc on surface concentration.

Table 4.2: Thermophysical properties of water and nanoparticles [21].

	$\rho(kg/m^3)$	$c_p(j/kgk)$	$k(W/m.k)$	$\beta \times 10^5(K^{-1})$	$\sigma(\Omega m)^{-1}$
Pure water	997.1	4179	0.613	21	0.05
Copper(Cu)	8933	385	401	1.67	5.96×10^7
Silver(Ag)	10500	235	429	1.89	3.6×10^7
Alumina(Al_2O_3)	3970	765	40	0.85	1×10^{-10}
Titanium Oxide(TiO_2)	4250	686.2	8.9538	0.9	1×10^{-12}

Table 4.3: Numerical values of skin friction coefficient for copper and silver when $\lambda = 0.4$.

ϕ	M	β	$C_{sf}\sqrt{\text{Re}_x}$ for <i>Cu</i>	$C_{sf}\sqrt{\text{Re}_x}$ for <i>Ag</i>
0.05	0.5		1.278	1.284
0.1			1.465	1.475
0.2			1.955	1.973
0.2	0.1		1.897	1.917
	0.3		1.928	1.945
	0.7		1.981	1.996
	0.5	0.1	4.542	4.672
		0.5	2.827	2.865
		0.9	2.079	2.098

Table 4.4: Numerical values of surface concentration for copper and silver when $\phi = 0.2$, $\lambda = 0.4$ and $M = 0.5$.

k_1	k_2	Sc	β	$\xi(0)$ for <i>Cu</i>	$\xi(0)$ for <i>Ag</i>
0.5				0.4407	0.4413
1				0.4087	0.3997
1.5				0.3645	0.3761
0.3	0.5			0.4169	0.4173
	1			0.3274	0.3321
	1.5			0.2856	0.2741
	0.5	0.4		0.4726	0.4675
		0.7		0.4703	0.4561
		1		0.4675	0.4532
		0.5	0.1	0.4618	0.4619
			0.5	0.4583	0.4537
			0.9	0.4565	0.4502

4.5 Final remarks

This chapter investigates the MHD flow of nanofluid by a stretching sheet with homogeneous-heterogeneous reactions. Convergent approximate solution is constructed. The following obser-

variations are made:

- An increase in the values of ϕ , M , β and λ has similar effects on the velocity in a qualitative sense.
- Concentration profile increases for larger k_2 and Sc while it decreases when k_1 is increased.
- The values of skin friction coefficient are higher for Ag -water when ϕ enhances.
- Higher values of k_1 , k_2 and Sc correspond to smaller values of dimensionless surface concentration.

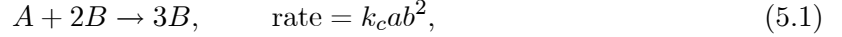
Chapter 5

Impact of magnetohydrodynamics in bidirectional flow of nanofluid subject to second order slip velocity and homogeneous-heterogeneous reactions

This chapter addresses the steady three-dimensional boundary layer flow of viscous nanofluid. The flow is caused by a permeable stretching surface with second order velocity slip and homogeneous-heterogeneous reactions. Water is treated as base fluid and copper as nanoparticle. An incompressible fluid fills the porous space. The fluid is electrically conducting in the presence of an applied magnetic field. A system of ordinary differential equations is obtained by using suitable transformations. Convergent series solutions are derived. Impact of various pertinent parameters on the velocity, concentration and skin friction coefficient is discussed. Analysis of the obtained results shows that the flow field is influenced appreciably by the presence of velocity slip parameters. Also concentration distribution decreases for larger values of strength of homogeneous reaction parameter while it increases for strength of heterogeneous reaction parameter.

5.1 Model development

We consider the steady three-dimensional incompressible flow of nanofluid saturating porous medium with permeability K . The porous medium features have been characterized by using Darcy's law. Material is water based nanofluid consisting of copper (Cu) as nanoparticle. Flow is induced by a permeable stretching sheet at $z = 0$. An incompressible fluid occupies $z > 0$. It is assumed that the sheet is stretched with velocities $u_w = cx$ and $v_w = dy$, where $c, d > 0$ are the stretching rates. A uniform magnetic field of strength B_0 is applied in the z -direction. Electric and induced magnetic fields are omitted. Flow analysis is carried out with homogeneous-heterogeneous reactions. The homogeneous reaction for cubic autocatalysis can be expressed as follows [73]:



while first-order isothermal reaction on the catalyst surface is presented in the form



where a and b are the concentrations of the chemical species A and B and k_c and k_s are the rate constants. We assume that both reaction processes are isothermal. Using the nanofluid model as proposed by Tiwari and Das [4], the boundary layer equations governing the flow can be written as follows:

$$\frac{\partial u}{\partial x} + \frac{\partial v}{\partial y} + \frac{\partial w}{\partial z} = 0, \quad (5.3)$$

$$\rho_{nf} \left(u \frac{\partial u}{\partial x} + v \frac{\partial u}{\partial y} + w \frac{\partial u}{\partial z} \right) = \mu_{nf} \frac{\partial^2 u}{\partial z^2} - \frac{\mu_{nf}}{K} u - \sigma_{nf} B_0^2 u, \quad (5.4)$$

$$\rho_{nf} \left(u \frac{\partial v}{\partial x} + v \frac{\partial v}{\partial y} + w \frac{\partial v}{\partial z} \right) = \mu_{nf} \frac{\partial^2 v}{\partial z^2} - \frac{\mu_{nf}}{K} v - \sigma_{nf} B_0^2 v, \quad (5.5)$$

$$u \frac{\partial a}{\partial x} + v \frac{\partial a}{\partial y} + w \frac{\partial a}{\partial z} = D_A \frac{\partial^2 a}{\partial z^2} - k_c ab^2, \quad (5.6)$$

$$u \frac{\partial b}{\partial x} + v \frac{\partial b}{\partial y} + w \frac{\partial b}{\partial z} = D_B \frac{\partial^2 b}{\partial z^2} + k_c ab^2. \quad (5.7)$$

The subjected boundary conditions are put into the form

$$u = u_w + u_{slip}, \quad v = v_w + v_{slip}, \quad w = w_0, \quad \text{at } z = 0,$$

$$D_A \frac{\partial a}{\partial z} = k_s a, \quad D_B \frac{\partial b}{\partial z} = -k_s a \quad \text{at } z = 0,$$

$$u \rightarrow 0, \quad v \rightarrow 0, \quad a \rightarrow a_0, \quad b \rightarrow 0 \quad \text{as } z \rightarrow \infty, \quad (5.8)$$

in which u , v and w are velocity components along x -, y - and z - directions respectively, w_0 is suction ($w_0 < 0$) or injection ($w_0 > 0$) velocity, D_A and D_B are diffusion species coefficients of A and B and a_0 is positive dimensional constant. Effective density ρ_{nf} , dynamic viscosity μ_{nf} and electrical conductivity σ_{nf} of nanofluid are given by

$$\rho_{nf} = \rho_f(1 - \phi) + \rho_s \phi, \quad (5.9)$$

$$\mu_{nf} = \frac{\mu_f}{(1 - \phi)^{2.5}}, \quad (5.10)$$

$$\frac{\sigma_{nf}}{\sigma_f} = 1 + \frac{3 \left(\frac{\sigma_s}{\sigma_f} - 1 \right) \phi}{\left(\frac{\sigma_s}{\sigma_f} + 2 \right) - \left(\frac{\sigma_s}{\sigma_f} - 1 \right) \phi}. \quad (5.11)$$

Here ϕ is the solid volume fraction, s in subscript is for nano-solid-particles and f in subscript is for base fluid. Also u_{slip} is the slip velocity at the wall. The Wu's slip velocity model (valid for arbitrary Knudsen number, Kn) is employed here as follows [60]:

$$\begin{aligned} u_{slip} &= \frac{2}{3} \left(\frac{3 - \kappa I^3}{\kappa} - \frac{3}{2} \frac{1 - I^2}{Kn} \right) \Lambda \frac{\partial u}{\partial z} - \frac{1}{4} \left(I^4 + \frac{2}{Kn^2} (1 - I^2) \right) \Lambda^2 \frac{\partial^2 u}{\partial z^2}, \\ &= N_1 \frac{\partial u}{\partial z} + N_2 \frac{\partial^2 u}{\partial z^2}, \\ v_{slip} &= \frac{2}{3} \left(\frac{3 - \kappa I^3}{\kappa} - \frac{3}{2} \frac{1 - I^2}{Kn} \right) \Lambda \frac{\partial v}{\partial z} - \frac{1}{4} \left(I^4 + \frac{2}{Kn^2} (1 - I^2) \right) \Lambda^2 \frac{\partial^2 v}{\partial z^2}, \\ &= N_3 \frac{\partial v}{\partial z} + N_4 \frac{\partial^2 v}{\partial z^2}, \end{aligned} \quad (5.12)$$

where $I = \min \left[\frac{1}{Kn}, 1 \right]$, κ is momentum accommodation coefficient with $0 \leq \kappa \leq 1$, Λ is molecular mean free path and Kn is Knudsen number defined as mean free path Λ divided by a characteristic length for the flow. Based on the definition of I , it is seen that for any given

value of Kn we have $0 \leq I \leq 1$. The molecular mean free path is always positive. Thus we know that $N_2, N_4 < 0$ and N_1, N_3 are positive numbers.

Making use of the following similarity transformations

$$\begin{aligned} u &= cx f'(\eta), \quad v = cy g'(\eta), \quad w = -\sqrt{c\nu} [f(\eta) + g(\eta)], \\ \eta &= \sqrt{\frac{c}{\nu}} z, \quad a = a_0 \xi(\eta), \quad b = a_0 h(\eta), \end{aligned} \quad (5.13)$$

the continuity equation is satisfied automatically and Eqs. (5.4 – 5.8) are reduced to

$$\varepsilon_1 f''' - f'^2 + (f + g)f'' - \lambda f' - \varepsilon_1(1 - \phi)^{2.5} M \frac{\sigma_{nf}}{\sigma_f} f' = 0, \quad (5.14)$$

$$\varepsilon_1 g''' - g'^2 + (f + g)g'' - \lambda g' - \varepsilon_1(1 - \phi)^{2.5} M \frac{\sigma_{ng}}{\sigma_g} g' = 0, \quad (5.15)$$

$$\frac{1}{Sc} \xi'' + (f + g)\xi' - k_1 \xi h^2 = 0, \quad (5.16)$$

$$\frac{\delta}{Sc} h'' + (f + g)h' + k_1 \xi h^2 = 0, \quad (5.17)$$

$$f'(0) = 1 + \beta_1 f''(0) + \beta_2 f'''(0), \quad g'(0) = \gamma + \beta_3 g''(0) + \beta_4 g'''(0),$$

$$f(0) + g(0) = S, \quad f'(\infty) \rightarrow 0, \quad g'(\infty) \rightarrow 0,$$

$$\xi'(0) = k_2 \xi(0), \quad \delta h'(0) = -k_2 \xi(0), \quad \xi(\infty) \rightarrow 1, \quad h(\infty) \rightarrow 0, \quad (5.18)$$

where λ is the porosity parameter, M is the Hartman number, γ is the ratio of the stretching rate along the y - direction to the stretching rate along the x - direction, β_1 and β_3 are the first order slip velocity parameters, β_2 and β_4 (< 0) are the second order slip velocity parameters, S is the suction/injection velocity parameter, Sc is the Schmidt number, k_1 is the measure of the strength of homogeneous reaction, δ is the ratio of diffusion coefficient and k_2 is the measure of

the strength of the heterogeneous reaction. These quantities are defined as follows:

$$\begin{aligned}
\varepsilon_1 &= \frac{1}{(1-\phi)^{2.5}(1-\phi+\frac{\rho_s}{\rho_f}\phi)}, \quad \lambda = \frac{\nu_f}{cK}, \quad M = \frac{\sigma_f B_0^2}{c\rho_f}, \quad \gamma = \frac{d}{c}, \\
\beta_1 &= N_1 \sqrt{\frac{c}{\nu_f}}, \quad \beta_2 = N_2 \sqrt{\frac{c}{\nu_f}}, \quad \beta_3 = N_3 \sqrt{\frac{c}{\nu_f}}, \quad \beta_4 = N_4 \sqrt{\frac{c}{\nu_f}}, \\
S &= -\frac{w_0}{\sqrt{c\nu_f}}, \quad Sc = \frac{\nu_f}{D_A}, \quad k_1 = \frac{k_c a_0^2}{c}, \quad \delta = \frac{D_B}{D_A}, \quad k_2 = \frac{k_s}{D_A} \sqrt{\frac{\nu_f}{c}}.
\end{aligned} \tag{5.19}$$

It is noticed that for $\beta = 0$ and $\beta = 1$ the two-dimensional and axisymmetric flows are respectively noticed. Here it is assumed that diffusion coefficients of chemical species A and B to be of a comparable size. This leads to make a further assumption that the diffusion coefficients D_A and D_B are equal, i.e. $\delta = 1$ [73] and thus

$$\xi(\eta) + h(\eta) = 1. \tag{5.20}$$

Now Eqs. (5.16) and (5.17) yield

$$\frac{1}{Sc} \xi'' + (f+g)\xi' - k_1 \xi(1-\xi)^2 = 0, \tag{5.21}$$

with the boundary conditions

$$\xi'(0) = k_2 \xi(0), \quad \xi(\infty) \rightarrow 1. \tag{5.22}$$

Skin friction coefficients along the x - and y - directions are defined as follows:

$$C_{fx} = \frac{\tau_{wx}}{\rho_f u_w^2}, \quad C_{fy} = \frac{\tau_{wy}}{\rho_f v_w^2}, \tag{5.23}$$

where the surface shear stresses τ_{wx} and τ_{wy} along the x - and y - directions are given by

$$\tau_{wx} = \mu_{nf} \left. \frac{\partial u}{\partial z} \right|_{z=0}, \quad \tau_{wy} = \mu_{nf} \left. \frac{\partial v}{\partial z} \right|_{z=0}. \tag{5.24}$$

Dimensionless skin friction coefficients are

$$C_{f_x}(\text{Re}_x)^{1/2} = \frac{1}{(1-\phi)^{2.5}} f''(0), \quad C_{f_y}(\text{Re}_y)^{1/2} = \frac{1}{\gamma^{3/2}(1-\phi)^{2.5}} g''(0), \quad (5.25)$$

where $(\text{Re}_x)^{1/2} = x\sqrt{c/\nu_f}$ and $(\text{Re}_y)^{1/2} = y\sqrt{c/\nu_f}$ denotes the local Reynolds number.

5.2 Homotopic solutions

The initial approximations $f_0(\eta)$, $g_0(\eta)$ and $\xi_0(\eta)$ and auxiliary linear operators \mathcal{L}_f , \mathcal{L}_g and \mathcal{L}_ξ are taken as follows:

$$f_0(\eta) = S + \frac{1}{1+\beta_1-\beta_2} (1-e^{-\eta}), \quad g_0(\eta) = \frac{\gamma}{1+\beta_3-\beta_4} (1-e^{-\eta}), \quad \xi_0(\eta) = 1 - \frac{1}{2} e^{-k_2\eta}, \quad (5.26)$$

$$\mathcal{L}_f = f''' - f', \quad \mathcal{L}_g = g''' - g', \quad \mathcal{L}_\xi = \xi'' - \xi, \quad (5.27)$$

$$\mathcal{L}_f [c_1 + c_2 e^\eta + c_3 e^{-\eta}] = 0,$$

$$\mathcal{L}_g [c_4 + c_5 e^\eta + c_6 e^{-\eta}] = 0,$$

$$\mathcal{L}_\xi [c_7 e^\eta + c_8 e^{-\eta}] = 0, \quad (5.28)$$

in which c_i ($i = 1 - 8$) are the constants.

If $p \in [0, 1]$ indicates the embedding parameter and \hbar_f , \hbar_g and \hbar_ξ the non-zero auxiliary parameters then the zeroth order deformation problems are constructed as follows:

$$(1-p)\mathcal{L}_f [\hat{f}(\eta; p) - f_0(\eta)] = p\hbar_f \mathcal{N}_f[\hat{f}(\eta; p), \hat{g}(\eta; p)], \quad (5.29)$$

$$(1-p)\mathcal{L}_g [\hat{g}(\eta; p) - g_0(\eta)] = p\hbar_g \mathcal{N}_g[\hat{g}(\eta; p), \hat{f}(\eta; p)], \quad (5.30)$$

$$(1-p)\mathcal{L}_\xi [\hat{\xi}(\eta; p) - \xi_0(\eta)] = p\hbar_\xi \mathcal{N}_\xi[\hat{\xi}(\eta; p), \hat{f}(\eta; p), \hat{g}(\eta; p)], \quad (5.31)$$

$$\hat{f}'(0; p) = 1 + \beta_1 \hat{f}''(0; p) + \beta_2 \hat{f}'''(0; p), \quad \hat{f}(0; p) = S, \quad \hat{f}'(\infty; p) = 0, \quad (5.32)$$

$$\hat{g}'(0; p) = \gamma + \beta_3 \hat{g}''(0; p) + \beta_4 \hat{g}'''(0; p), \quad \hat{g}(0; p) = 0, \quad \hat{g}'(\infty; p) = 0, \quad (5.33)$$

$$\hat{\xi}'(0; p) = k_2 \hat{\xi}(0; p), \quad \hat{\xi}(\infty; p) = 1, \quad (5.34)$$

where the nonlinear differential operators \mathcal{N}_f , \mathcal{N}_g and \mathcal{N}_ξ are given by

$$\begin{aligned} \mathcal{N}_f [\hat{f}(\eta; p), \hat{g}(\eta; p)] &= \varepsilon_1 \frac{\partial^3 \hat{f}(\eta; p)}{\partial \eta^3} - \left(\frac{\partial \hat{f}(\eta; p)}{\partial \eta} \right)^2 + \hat{f}(\eta; p) \frac{\partial^2 \hat{f}(\eta; p)}{\partial \eta^2} + \hat{g}(\eta; p) \frac{\partial^2 \hat{f}(\eta; p)}{\partial \eta^2} \\ &\quad - \left(\lambda + \varepsilon_1 (1 - \phi)^{2.5} M \frac{\sigma_{nf}}{\sigma_f} \right) \frac{\partial \hat{f}(\eta; p)}{\partial \eta}, \end{aligned} \quad (5.35)$$

$$\begin{aligned} \mathcal{N}_g [\hat{g}(\eta; p), \hat{f}(\eta; p)] &= \varepsilon_1 \frac{\partial^3 \hat{g}(\eta; p)}{\partial \eta^3} - \left(\frac{\partial \hat{g}(\eta; p)}{\partial \eta} \right)^2 + \hat{f}(\eta; p) \frac{\partial^2 \hat{g}(\eta; p)}{\partial \eta^2} + \hat{g}(\eta; p) \frac{\partial^2 \hat{g}(\eta; p)}{\partial \eta^2} \\ &\quad - \left(\lambda + \varepsilon_1 (1 - \phi)^{2.5} M \frac{\sigma_{nf}}{\sigma_f} \right) \frac{\partial \hat{g}(\eta; p)}{\partial \eta}, \end{aligned} \quad (5.36)$$

$$\begin{aligned} \mathcal{N}_\xi [\hat{\xi}(\eta; p), \hat{f}(\eta; p), \hat{g}(\eta; p)] &= \frac{1}{Sc} \frac{\partial^2 \hat{\xi}(\eta; p)}{\partial \eta^2} + \hat{f}(\eta; p) \frac{\partial \hat{\xi}(\eta; p)}{\partial \eta} + \hat{g}(\eta; p) \frac{\partial \hat{\xi}(\eta; p)}{\partial \eta} \\ &\quad - k_1 \left(\hat{\xi}(\eta; p) - 2 \left(\hat{\xi}(\eta; p) \right)^2 + \left(\hat{\xi}(\eta; p) \right)^3 \right). \end{aligned} \quad (5.37)$$

Here m^{th} order deformation equations can be written in the forms

$$\mathcal{L}_f [f_m(\eta) - \chi_m f_{m-1}(\eta)] = \hbar_f \mathcal{R}_{f,m}(\eta), \quad (5.38)$$

$$\mathcal{L}_g [g_m(\eta) - \chi_m g_{m-1}(\eta)] = \hbar_g \mathcal{R}_{g,m}(\eta), \quad (5.39)$$

$$\mathcal{L}_\xi [\xi_m(\eta) - \chi_m \xi_{m-1}(\eta)] = \hbar_\xi \mathcal{R}_{\xi,m}(\eta), \quad (5.40)$$

with

$$\begin{aligned} f'_m(0) - \beta_1 f''_m(0) - \beta_2 f'''_m(0) &= f_m(0) = f'_m(\infty) = 0 \\ g'_m(0) - \beta_3 g''_m(0) - \beta_4 g'''_m(0) &= g_m(0) = g'_m(\infty) = 0 \\ \xi'_m(0) - k_2 \xi_m(0) &= \xi_m(\infty) = 0, \end{aligned} \quad (5.41)$$

$$\mathcal{R}_{f,m}(\eta) = \varepsilon_1 f'''_{m-1} + \sum_{k=0}^{m-1} [f_{m-1-k} f''_k - f'_{m-1-k} f'_k + g_{m-1-k} f''_k] - \left(\lambda + \varepsilon_1 (1 - \phi)^{2.5} M \frac{\sigma_{nf}}{\sigma_f} \right) f'_{m-1}, \quad (5.42)$$

$$\mathcal{R}_{g,m}(\eta) = \varepsilon_1 g_{m-1}''' + \sum_{k=0}^{m-1} [f_{m-1-k} g_k'' - g'_{m-1-k} g'_k + g_{m-1-k} g_k''] - \left(\lambda + \varepsilon_1 (1 - \phi)^{2.5} M \frac{\sigma_{nf}}{\sigma_f} \right) g'_{m-1}, \quad (5.43)$$

$$\begin{aligned} \mathcal{R}_{\xi,m}(\eta) = & \frac{1}{Sc} \xi_{m-1}'' - k_1 \xi_{m-1} + \sum_{l=0}^{m-1} \left[\xi'_{m-1-l} f_l + \xi'_{m-1-l} g_l \right. \\ & \left. - k_1 \left(\xi_{m-1-l} \sum_{j=0}^l \xi_{l-j} \xi_j + 2 \xi_{m-1-l} \xi_l \right) \right], \end{aligned} \quad (5.44)$$

$$\chi_m = \begin{cases} 0, & m \leq 1 \\ 1, & m > 1 \end{cases}. \quad (5.45)$$

The general solutions (f_m, g_m, ξ_m) comprising the special solutions (f_m^*, g_m^*, ξ_m^*) are

$$\begin{aligned} f_m(\eta) &= f_m^*(\eta) + c_1 + c_2 e^\eta + c_3 e^{-\eta}, \\ g_m(\eta) &= g_m^*(\eta) + c_4 + c_5 e^\eta + c_6 e^{-\eta}, \\ \xi_m(\eta) &= \xi_m^*(\eta) + c_7 e^\eta + c_8 e^{-\eta}, \end{aligned} \quad (5.46)$$

where the constants c_i ($i = 1, 2, \dots, 8$) through the boundary conditions (5.41) have the values

$$\begin{aligned} c_2 &= c_5 = c_7 = 0, \quad c_1 = -c_3 - f_m^*(0), \quad c_4 = -c_6 - g_m^*(0), \\ c_3 &= \frac{1}{1 + \beta_1 - \beta_2} \left(\frac{\partial f_m^*(\eta)}{\partial \eta} - \beta_1 \frac{\partial^2 f_m^*(\eta)}{\partial \eta^2} - \beta_2 \frac{\partial^3 f_m^*(\eta)}{\partial \eta^3} \right) \Big|_{\eta=0}, \\ c_6 &= \frac{1}{1 + \beta_3 - \beta_4} \left(\frac{\partial g_m^*(\eta)}{\partial \eta} - \beta_3 \frac{\partial^2 g_m^*(\eta)}{\partial \eta^2} - \beta_4 \frac{\partial^3 g_m^*(\eta)}{\partial \eta^3} \right) \Big|_{\eta=0}, \\ c_8 &= \frac{1}{1 + k_2} \left(\frac{\partial \xi_m^*(\eta)}{\partial \eta} \Big|_{\eta=0} - k_2 \xi_m^*(0) \right). \end{aligned} \quad (5.47)$$

5.3 Convergence analysis

Homotopy analysis technique provides us great freedom and an easy way to adjust and control the convergence region of the series solutions. The auxiliary parameters \hbar_f , \hbar_g and \hbar_ξ play an important role for the convergence of the series solutions. Therefore, we have sketched the \hbar -curves at 10th-order of approximations (see Fig. 5.1). The admissible ranges of the auxiliary parameters are $-1.4 \leq \hbar_f \leq -0.2$, $-1.5 \leq \hbar_g \leq -0.2$ and $-1.9 \leq \hbar_\xi \leq -0.8$. Also the HAM

solutions converge in the whole region of η ($0 < \eta < \infty$) when $\hbar_f = \hbar_g = -1$ and $\hbar_\xi = -1.2$. Table 5.1 shows the convergence of series solutions of momentum and concentration equations. It is noted that 14th order of approximations are sufficient for the convergence of functions $f''(0)$, $g''(0)$ and $\theta'(0)$.

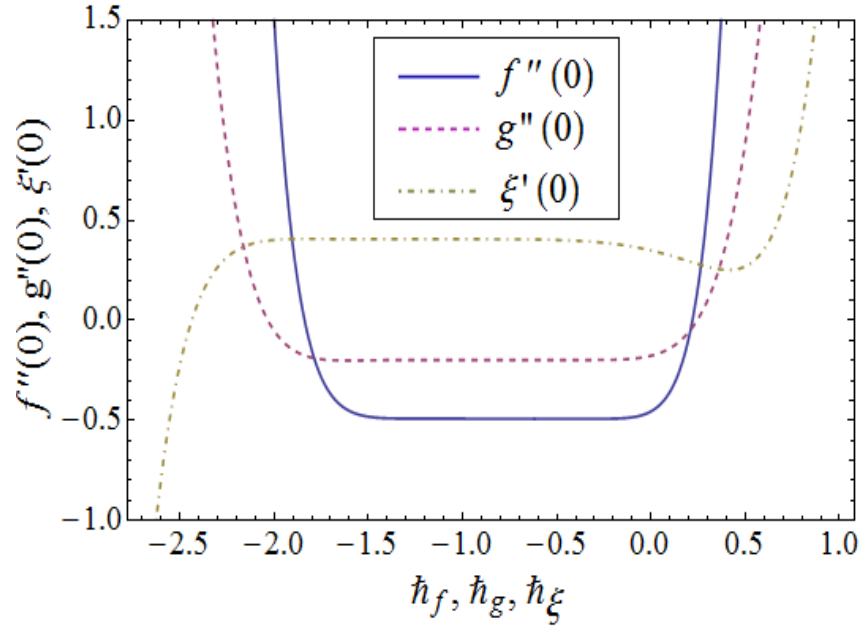


Fig. 5.1: \hbar -curves for $f''(0)$, $g''(0)$ and $\theta'(0)$ when $\phi = M = 0.5$, $\lambda = \beta_2 = \gamma = 0.3$, $S = \beta_1 = Sc = 0.9$, $k_1 = k_2 = 0.7$, $\beta_3 = -0.3$ and $\beta_4 = -0.2$.

Table 5.1: Convergence of HAM solutions for different order of approximations when $\phi = M = 0.5$, $\lambda = \beta_2 = \gamma = 0.3$, $S = \beta_1 = Sc = 0.9$, $k_1 = k_2 = 0.7$, $\beta_3 = -0.3$ and $\beta_4 = -0.2$.

Order of approximations	$-f''(0)$	$-g''(0)$	$\xi'(0)$
1	0.507202	0.200061	0.364126
5	0.491527	0.198039	0.395551
10	0.491387	0.197965	0.396517
14	0.491389	0.197965	0.396476
20	0.491389	0.197965	0.396476
26	0.491389	0.197965	0.396476
30	0.491389	0.197965	0.396476
35	0.491389	0.197965	0.396476
40	0.491389	0.197965	0.396476
45	0.491389	0.197965	0.396476

5.4 Results and discussion

This section presents the behavior of various involved parameters on the velocities along x - and y - directions and concentration in the form of graphical and tabulated results (see Figs. (5.2 – 5.15) and Tables (5.2 – 5.5)).

5.4.1 Dimensionless velocity profiles

The effects of nanoparticle volume fraction ϕ on both the x - and y - components of velocity f' and g' are depicted in Fig. 5.2. It is observed that velocity profiles decrease when ϕ is increased. Behaviors of porosity parameter λ on velocity profiles f' and g' are displayed in Fig. 5.3. An increase in the porosity parameter leads to the lower permeability parameter which decreases the fluid motion. Hence velocity profiles decreases. Fig. 5.4 displays the velocity profiles for different values of M . The applied magnetic field has the tendency to slow down the movement of the fluid which decreases the velocities and momentum boundary layer thickness. Influence of suction/injection velocity parameter S on f' and g' can be visualized in the Fig. 5.5. It is obvious that an increase in S reduces the velocity fields. Here applying suction leads to draw the amount of the fluid particles into the wall and consequently the velocity fields decrease.

From Figs. (5.6 – 5.9), we have seen that larger values of first order slip velocity parameters and magnitude of second order slip velocity parameters correspond to lower velocity. With an increase in slip velocity parameter, stretching velocity is partially transferred to the fluid so velocity profile decreases. Fig. 5.10 illustrates the impact of stretching rates ratio γ on the velocity fields. Increasing values of γ indicates higher rate of stretching along the y - direction in comparison to x - direction. Therefore the velocity along x - direction f' decreases and velocity along y - direction g' increases when stretching rates ratio is increased.

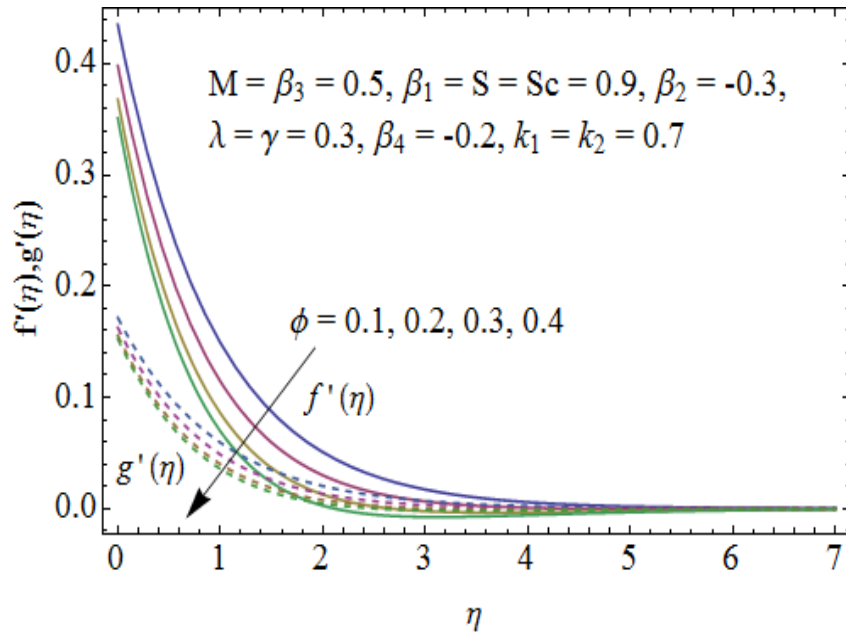


Fig. 5.2: Variation of ϕ on $f'(\eta)$ and $g'(\eta)$.

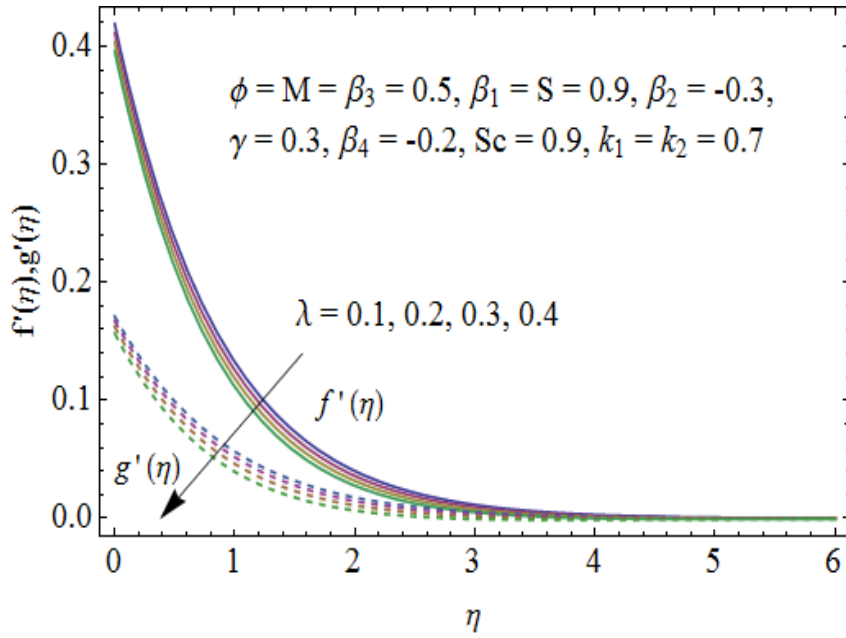


Fig. 5.3: Variation of λ on $f'(\eta)$ and $g'(\eta)$.

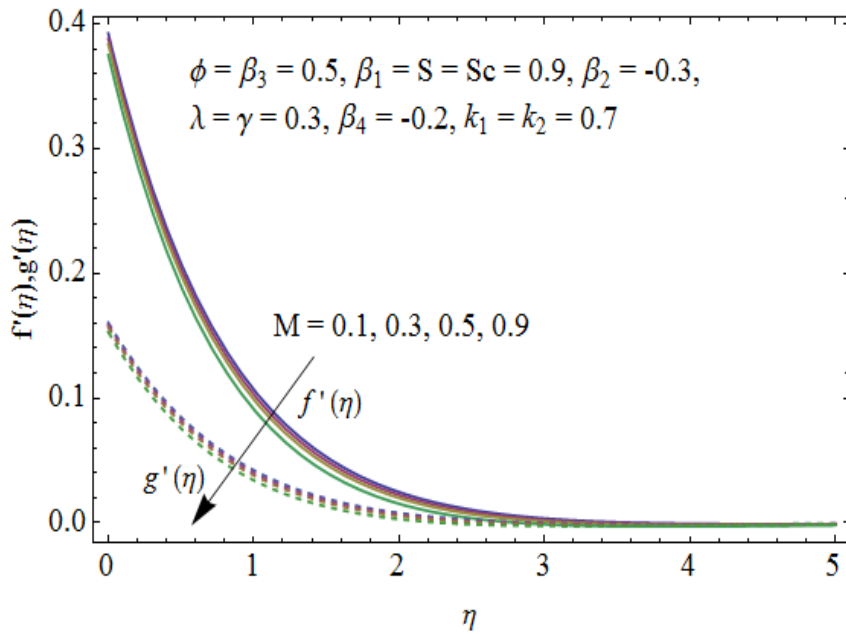


Fig. 5.4: Variation of M on $f'(\eta)$ and $g'(\eta)$.

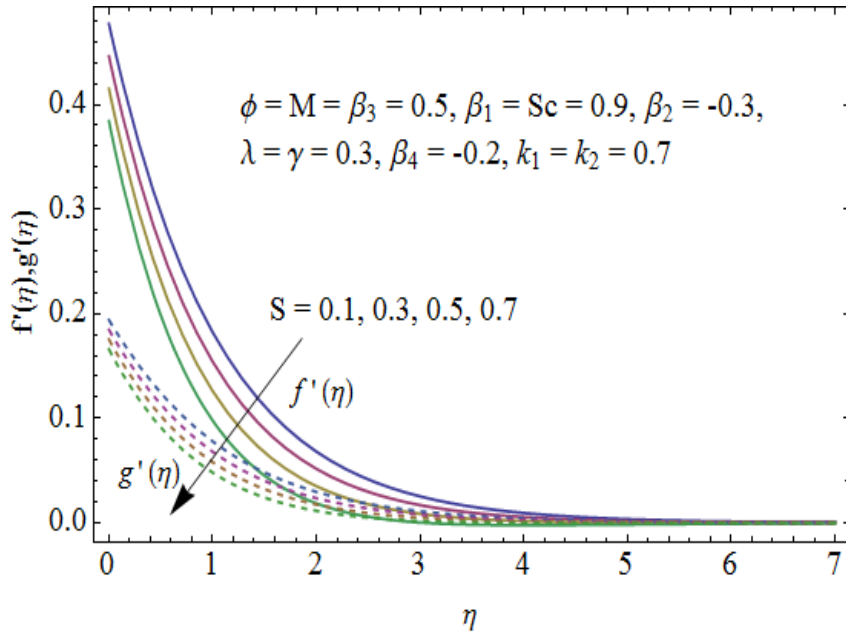


Fig. 5.5: Variation of S on $f'(\eta)$ and $g'(\eta)$.

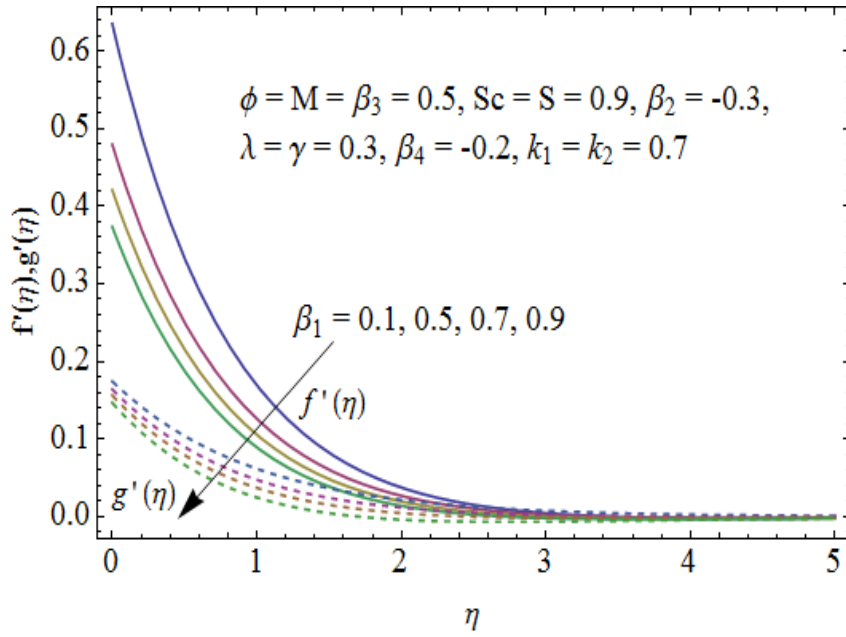


Fig. 5.6: Variation of β_1 on $f'(\eta)$ and $g'(\eta)$.

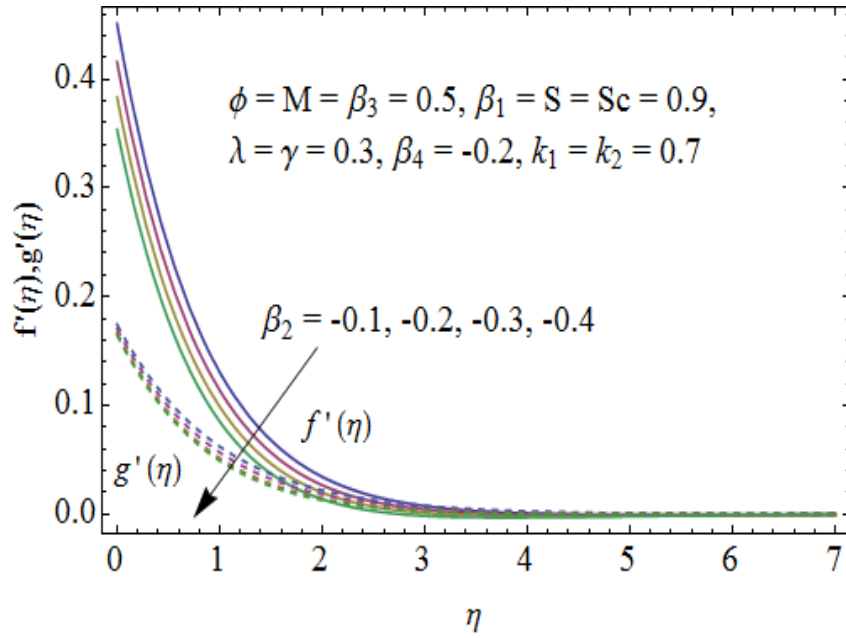


Fig. 5.7: Variation of β_2 on $f'(\eta)$ and $g'(\eta)$.

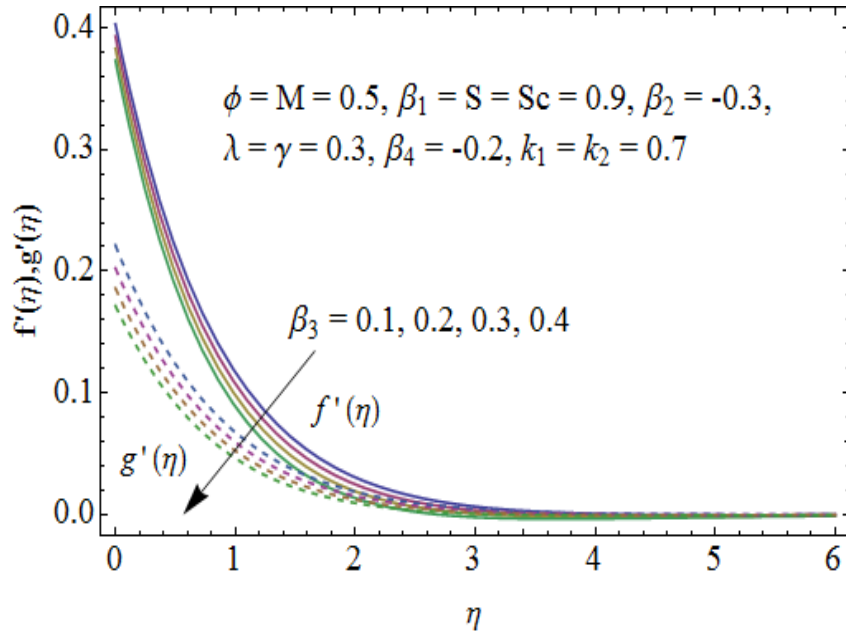


Fig. 5.8: Variation of β_3 on $f'(\eta)$ and $g'(\eta)$.

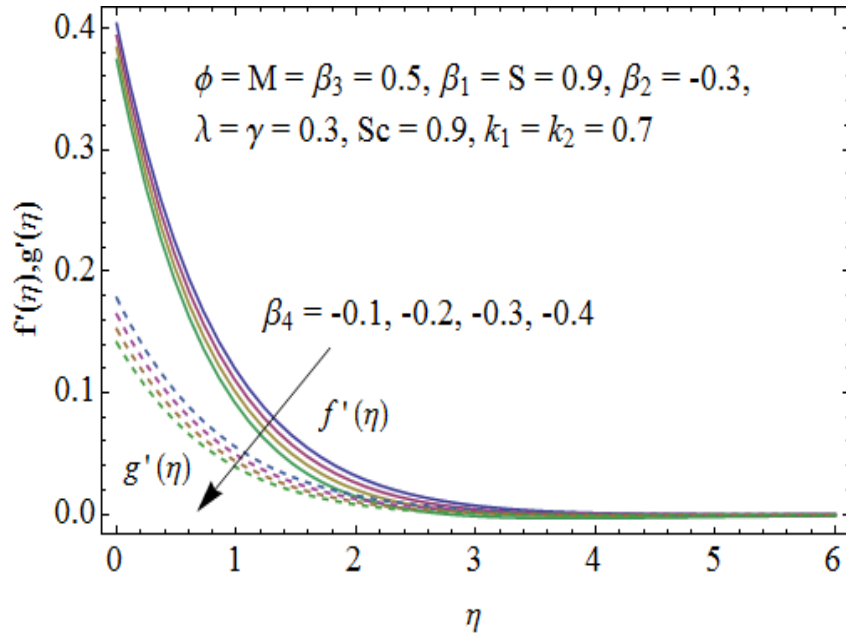


Fig. 5.9: Variation of β_4 on $f'(\eta)$ and $g'(\eta)$.

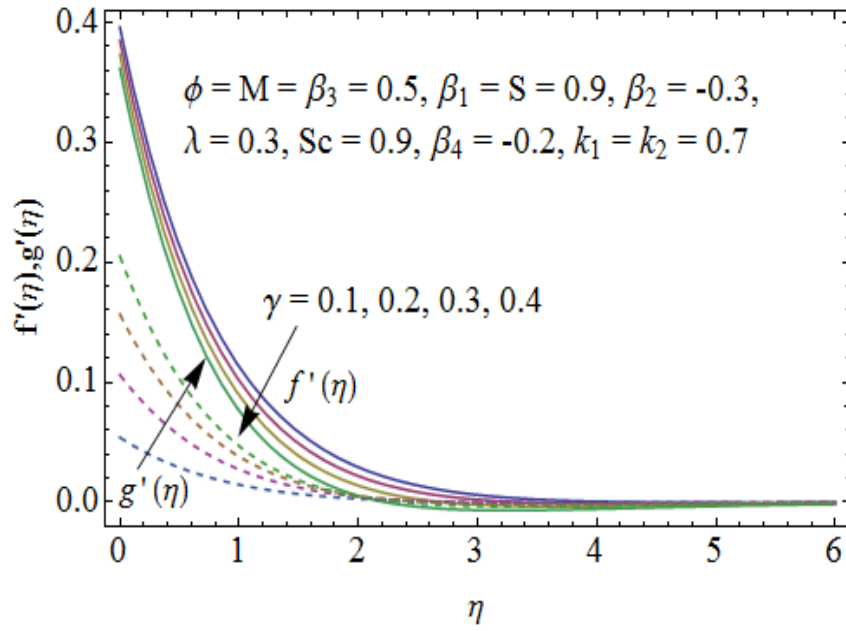


Fig. 5.10: Variation of γ on $f'(\eta)$ and $g'(\eta)$.

5.4.2 Dimensionless concentration profiles

Figs. (5.11 – 5.13) exhibit the dimensionless concentration profile for different values of measure of the strength of homogeneous reaction k_1 , measure of the strength of heterogeneous reaction k_2 and Schmidt number Sc . Effect of the strength of the homogeneous reaction k_1 on the concentration is analyzed in Fig. 5.11. There is a decrease in concentration when k_1 is increased. Fig. 5.12 illustrates the variation of measure of the strength of heterogeneous reaction k_2 on concentration field ξ . Here concentration profile enhances with an increase in k_2 . Effect of Schmidt number Sc on concentration profile is shown in Fig. 5.13. Increasing behavior of concentration profile is noted for larger Schmidt number. In fact Schmidt number is the ratio of momentum diffusivity to mass diffusivity, so higher values of Schmidt number correspond to small mass diffusivity. Therefore concentration profile increases.

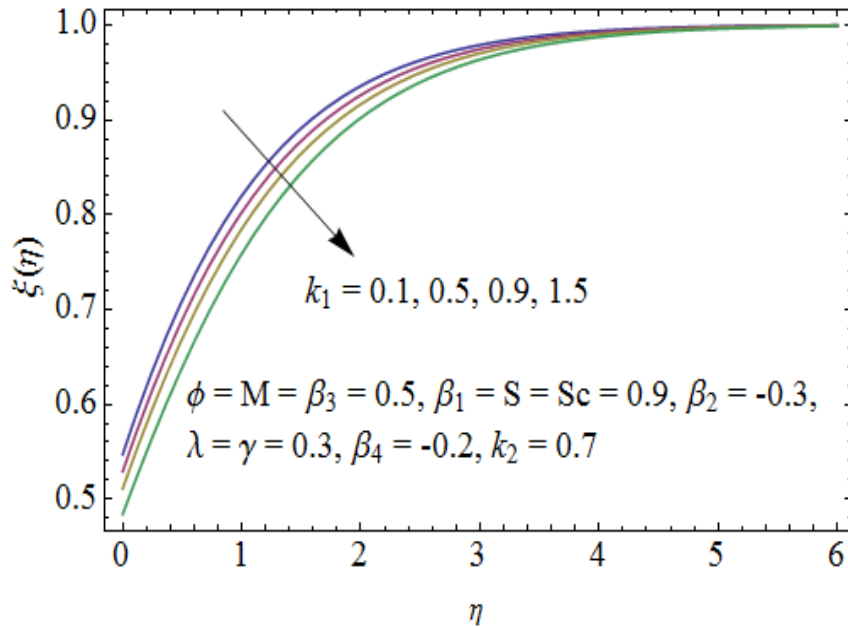


Fig. 5.11: Variation of k_1 on $\xi(\eta)$.

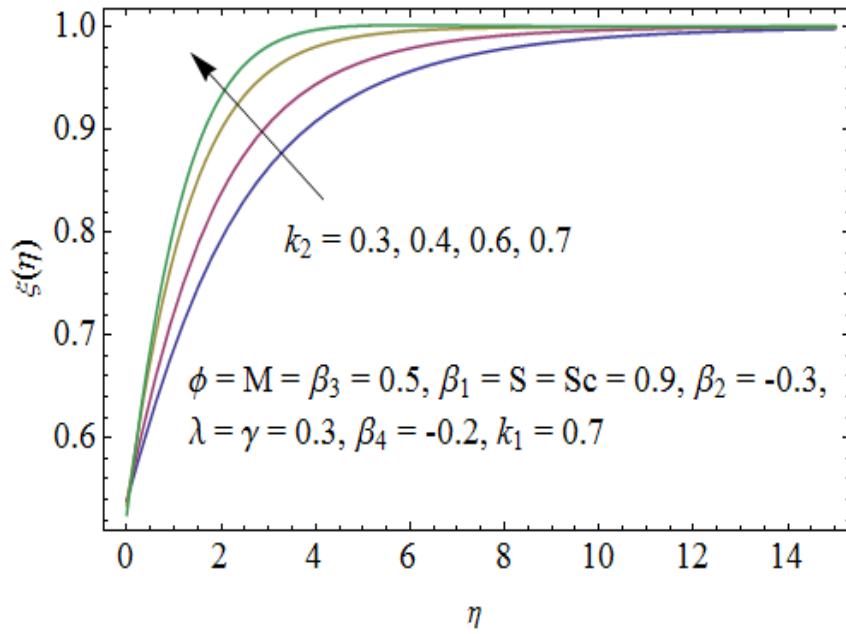


Fig. 5.12: Variation of k_2 on $\xi(\eta)$.

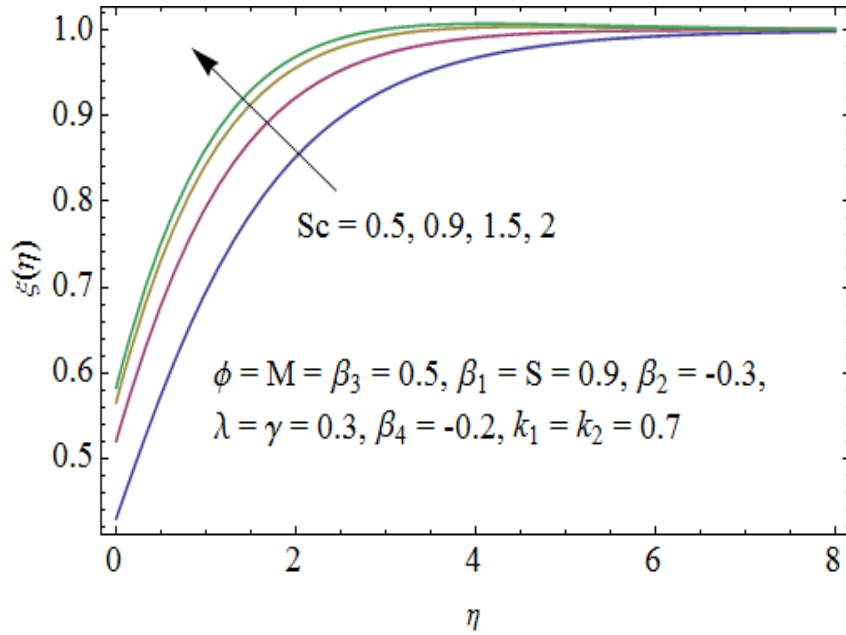


Fig. 5.13: Variation of Sc on $\xi(\eta)$.

5.4.3 Surface concentration and skin friction coefficient

The variation of dimensionless wall concentration $\xi(0)$ for different values of the strength of heterogeneous reaction parameter k_2 , strength of homogeneous reaction parameter k_1 and Schmidt number Sc are shown in Figs. 5.14 and 5.15 respectively. One can see from these Figs. that $\xi(0)$ decreases with the increase of the parameters k_1 and k_2 . Some thermophysical properties of water and nanoparticles are given in Table 5.2. Effects of nanoparticle volume fraction for different types of nanofluids on skin friction coefficient along x - and y - directions are presented in Tables 5.3 and 5.4. Here we see that magnitude of skin friction coefficient increases with the increase in ϕ . Numerical values of skin friction coefficient for different values of first and second order slip velocity parameters, porosity parameter, Hartman number and suction/injection parameter are presented in Table 5.5. It is noted that the skin friction coefficients decrease for increasing values of first order slip velocity parameters and magnitude of second order slip velocity parameters while it increases for larger porosity parameter, Hartman number and suction/injection parameter.

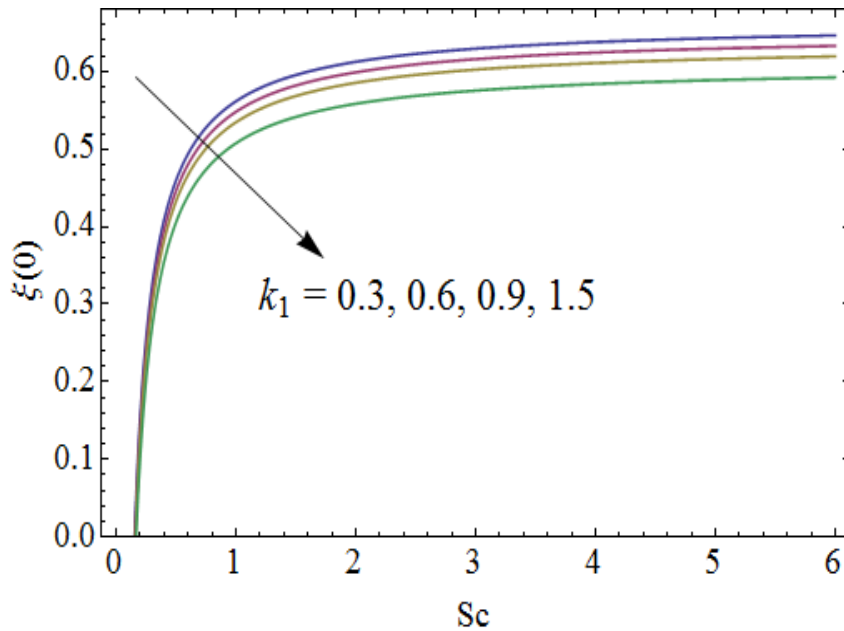


Fig. 5.14: Variations of k_1 and Sc on $\xi(0)$.

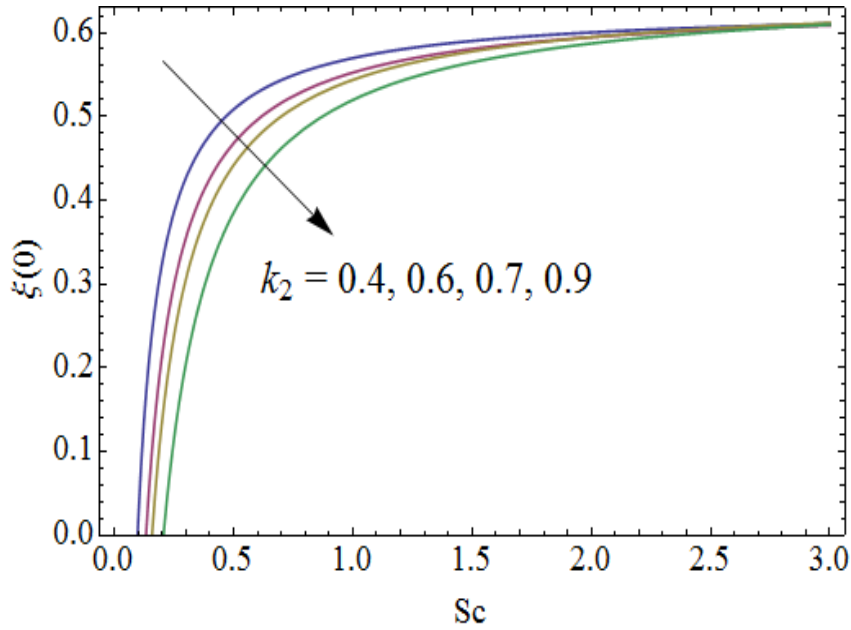


Fig. 5.15: Variations of k_2 and Sc on $\xi(0)$.

Table 5.2: Thermophysical properties of water and nanoparticles [21].

	$\rho(kg/m^3)$	$c_p(j/kgk)$	$k(W/m.k)$	$\beta \times 10^5(K^{-1})$	$\sigma(\Omega m)^{-1}$
Pure water	997.1	4179	0.613	21	0.05
Copper(<i>Cu</i>)	8933	385	401	1.67	5.96×10^7
Silver(<i>Ag</i>)	10500	235	429	1.89	3.6×10^7
Alumina(Al_2O_3)	3970	765	40	0.85	1×10^{-10}
Titanium Oxide(TiO_2)	4250	686.2	8.9538	0.9	1×10^{-12}

Table 5.3: Effects of the nanoparticle volume fraction for different types of nanofluids on skin friction coefficient along x -direction when $M = \beta_3 = 0.5$, $\lambda = \gamma = 0.3$, $S = \beta_1 = Sc = 0.9$, $k_1 = k_2 = 0.7$, $\beta_2 = -0.3$ and $\beta_4 = -0.2$.

ϕ	<i>Cu</i>	<i>Ag</i>	Al_2O_3	TiO_2
0.1	-0.6555	-0.6543	-0.6516	-0.6521
0.2	-0.8795	-0.8757	-0.8684	-0.8703
0.3	-1.229	-1.226	-1.191	-1.195

Table 5.4: Effects of the nanoparticle volume fraction for different types of nanofluids on skin friction coefficient along y -direction when $M = \beta_3 = 0.5$, $\lambda = \gamma = 0.3$, $S = \beta_1 = Sc = 0.9$, $k_1 = k_2 = 0.7$, $\beta_2 = -0.3$ and $\beta_4 = -0.2$.

ϕ	<i>Cu</i>	<i>Ag</i>	<i>Al₂O₃</i>	<i>TiO₂</i>
0.1	-1.704	-1.714	-1.645	-1.650
0.2	-2.296	-2.310	-2.164	-2.176
0.3	-3.184	-3.215	-2.906	-2.931

Table 5.5: Numerical values of skin friction coefficient for different values of $\beta_1, \beta_2, \beta_3, \beta_4, \lambda, M$ and S .

β_1	β_2	β_3	β_4	λ	M	S	$-C_{fx}(\text{Re}_x)^{1/2}$	$-C_{fy}(\text{Re}_y)^{1/2}$
0.3	-0.3	0.5	-0.2	0.3	0.5	0.9	3.979	6.896
							3.477	6.863
							3.089	6.837
	-0.1						3.203	6.844
	-0.2						2.974	6.829
	-0.3						2.779	6.815
	-0.3	0.1					2.789	9.314
		0.4					2.781	7.306
		0.7					2.776	6.008
		0.5	-0.1				2.781	7.403
			-0.3				2.777	6.19
			-0.5				2.774	5.526
			-0.2	0.1			2.748	6.641
				0.4			2.791	6.887
				0.5			2.802	6.949
				0.3	0.3		2.774	6.784
					0.7		2.784	6.845
					0.9		2.789	6.871
					0.5	0.2	2.592	5.906
						0.4	2.656	6.199
						0.7	2.737	6.691

5.5 Conclusions

Here flow of Cu-water nanofluid induced by bidirectional stretching surface is investigated. The effects of homogeneous-heterogeneous reactions and second order velocity slip are also taken into account. The key points are summarized as follows:

- Velocity profiles f' and g' are decreasing functions of velocity slip parameters and nanoparticle volume fraction.
- The velocity component f' decreases while g' increases for larger stretching rates ratio.
- Concentration of the reactants decreases for higher values of strength of homogeneous reaction parameter.
- Strength of heterogeneous reaction parameter results in the enhancement of concentration profile.
- There is an enhancement in concentration profile when Schmidt number increases.
- Concentration at the surface decreases for increasing values of the strengths of homogeneous and heterogeneous reaction parameters.
- Skin friction coefficients decrease for increasing values of first and second order velocity slip parameters.

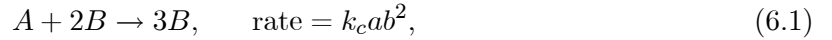
Chapter 6

Effects of homogeneous-heterogeneous reactions in flow of magnetite- Fe_3O_4 nanoparticles by a rotating disk

This chapter investigates the flow of ferrofluid due to a rotating disk in the presence of homogeneous-heterogeneous reactions. Water is used as base fluid while magnetite- Fe_3O_4 as nanoparticle. Fluid is electrically conducting in the presence of applied magnetic field. Effects of viscous dissipation are also considered. Appropriate transformations reduce the nonlinear partial differential system to ordinary differential system. Convergent series solutions are computed for the resulting nonlinear problems. Effects of different parameters on the velocity, temperature and concentration profiles are shown and analyzed. Computations for skin friction coefficient and Nusselt number are presented and examined for the influences of pertinent parameters. It is noted that concentration distribution decreases for larger values of strength of homogeneous reaction parameter while it increases for strength of heterogeneous reaction parameter. Skin friction coefficient and rate of heat transfer are enhanced when the strength of magnetic field is increased.

6.1 Model development

Here we consider an incompressible flow of ferrofluid induced by a rotating disk at $z = 0$. Magnetite– Fe_3O_4 nanoparticles in water are known as ferrofluid. The disk rotates with constant angular velocity Ω about the z -axis. Components of flow velocity are (u, v, w) in the direction of increasing (r, Θ, z) , respectively. A uniform magnetic field of strength B_0 is applied parallel to the z -axis. It is assumed that the induced magnetic field and the electric field effects are negligible. Effects of viscous dissipation are taken into account. The disk is kept at uniform temperature T_w while temperature far away from the disk is T_∞ . In view of the rotational symmetry, the derivatives in the azimuthal direction are neglected. Flow analysis is carried out with homogeneous-heterogeneous reactions of two chemical species A and B . The homogeneous reaction for cubic autocatalysis can be expressed as follows [73]:



while first-order isothermal reaction on the catalyst surface is presented in the form



where a and b are the concentrations of the chemical species A and B and k_c and k_s are the rate constants. We assume that both reaction processes are isothermal. Under these assumptions the relevant mass, momentum, energy and concentration equations are

$$\frac{\partial u}{\partial r} + \frac{u}{r} + \frac{\partial w}{\partial z} = 0, \quad (6.3)$$

$$\rho_{nf} \left(u \frac{\partial u}{\partial r} - \frac{v^2}{r} + w \frac{\partial u}{\partial z} \right) = -\frac{\partial P}{\partial r} + \mu_{nf} \left(\frac{\partial^2 u}{\partial r^2} + \frac{1}{r} \frac{\partial u}{\partial r} - \frac{u}{r^2} + \frac{\partial^2 u}{\partial z^2} \right) - \sigma_{nf} B_0^2 u, \quad (6.4)$$

$$\rho_{nf} \left(u \frac{\partial v}{\partial r} + \frac{uv}{r} + w \frac{\partial v}{\partial z} \right) = \mu_{nf} \left(\frac{\partial^2 v}{\partial r^2} + \frac{1}{r} \frac{\partial v}{\partial r} - \frac{v}{r^2} + \frac{\partial^2 v}{\partial z^2} \right) - \sigma_{nf} B_0^2 v, \quad (6.5)$$

$$\rho_{nf} \left(u \frac{\partial w}{\partial r} + w \frac{\partial w}{\partial z} \right) = -\frac{\partial P}{\partial z} + \mu_{nf} \left(\frac{\partial^2 w}{\partial r^2} + \frac{1}{r} \frac{\partial w}{\partial r} + \frac{\partial^2 w}{\partial z^2} \right), \quad (6.6)$$

$$\begin{aligned}
u \frac{\partial T}{\partial r} + w \frac{\partial T}{\partial z} &= \alpha_{nf} \left(\frac{\partial^2 T}{\partial r^2} + \frac{1}{r} \frac{\partial T}{\partial r} + \frac{\partial^2 T}{\partial z^2} \right) + \frac{\mu_{nf}}{(\rho c_p)_{nf}} \left[2 \left\{ \left(\frac{\partial u}{\partial r} \right)^2 + \left(\frac{u}{r} \right)^2 + \left(\frac{\partial w}{\partial z} \right)^2 \right\} \right. \\
&\quad \left. + \left(r \frac{\partial}{\partial r} \left(\frac{v}{r} \right) \right)^2 + \left(\frac{\partial v}{\partial z} \right)^2 + \left(\frac{\partial u}{\partial z} + \frac{\partial w}{\partial r} \right)^2 \right], \tag{6.7}
\end{aligned}$$

$$u \frac{\partial a}{\partial r} + w \frac{\partial a}{\partial z} = D_A \left(\frac{\partial^2 a}{\partial r^2} + \frac{1}{r} \frac{\partial a}{\partial r} + \frac{\partial^2 a}{\partial z^2} \right) - k_c a b^2, \tag{6.8}$$

$$u \frac{\partial b}{\partial r} + w \frac{\partial b}{\partial z} = D_B \left(\frac{\partial^2 b}{\partial r^2} + \frac{1}{r} \frac{\partial b}{\partial r} + \frac{\partial^2 b}{\partial z^2} \right) + k_c a b^2, \tag{6.9}$$

with boundary conditions

$$\begin{aligned}
u = 0, \quad v = r\Omega, \quad w = 0, \quad T = T_w, \quad D_A \frac{\partial a}{\partial z} = k_s a, \quad D_B \frac{\partial b}{\partial z} = -k_s a \quad \text{at } z = 0, \\
u \rightarrow 0, \quad v \rightarrow 0, \quad T \rightarrow T_\infty, \quad a \rightarrow a_0, \quad b \rightarrow 0 \quad \text{as } z \rightarrow \infty, \tag{6.10}
\end{aligned}$$

where P is the pressure, T is the temperature, $\alpha_{nf} = k_{nf}/(\rho c)_{nf}$ is the thermal diffusivity and a_0 is the positive dimensional constant. The effective nanofluid dynamic viscosity μ_{nf} , density ρ_{nf} , heat capacity $(\rho c_p)_{nf}$, thermal conductivity k_{nf} and electric conductivity σ_{nf} are taken as follows:

$$\mu_{nf} = \frac{\mu_f}{(1 - \phi)^{2.5}}, \tag{6.11}$$

$$\rho_{nf} = (1 - \phi)\rho_f + \phi\rho_s, \tag{6.12}$$

$$(\rho c_p)_{nf} = (1 - \phi)(\rho c_p)_f + \phi(\rho c_p)_s, \tag{6.13}$$

$$\frac{k_{nf}}{k_f} = \frac{(k_s + 2k_f) - 2\phi(k_f - k_s)}{(k_s + 2k_f) + \phi(k_f - k_s)}, \tag{6.14}$$

$$\frac{\sigma_{nf}}{\sigma_f} = 1 + \frac{3 \left(\frac{\sigma_s}{\sigma_f} - 1 \right) \phi}{\left(\frac{\sigma_s}{\sigma_f} + 2 \right) - \left(\frac{\sigma_s}{\sigma_f} - 1 \right) \phi}, \tag{6.15}$$

where ϕ denotes the solid volume fraction of nanoparticles, s in subscript is for nano-solid-particles and f in subscript is for base fluid. We now consider transformations

$$\begin{aligned} u &= r\Omega f(\eta), \quad v = r\Omega g(\eta), \quad w = \sqrt{\nu_f \Omega} H(\eta), \quad \eta = \sqrt{\frac{\Omega}{\nu_f}} z, \quad P - P_\infty = \rho_f \nu_f \Omega \tilde{P}(\eta), \\ \theta(\eta) &= \frac{T - T_\infty}{T_w - T_\infty}, \quad a = a_0 \xi(\eta), \quad b = a_0 h(\eta). \end{aligned} \quad (6.16)$$

Equations (6.3) – (6.10) after using Eq. (6.16) can be reduced as follows:

$$H' + 2f = 0, \quad (6.17)$$

$$\frac{1}{(1-\phi)^{2.5} \left(1 - \phi + \phi \frac{\rho_s}{\rho_f}\right)} f'' - Hf' - f^2 + g^2 - \left(\frac{\frac{\sigma_{nf}}{\sigma_f}}{1 - \phi + \phi \frac{\rho_s}{\rho_f}}\right) Mf = 0, \quad (6.18)$$

$$\frac{1}{(1-\phi)^{2.5} \left(1 - \phi + \phi \frac{\rho_s}{\rho_f}\right)} g'' - Hg' - 2fg - \left(\frac{\frac{\sigma_{nf}}{\sigma_f}}{1 - \phi + \phi \frac{\rho_s}{\rho_f}}\right) Mg = 0, \quad (6.19)$$

$$\frac{1}{\text{Pr}} \frac{k_{nf}}{k_f} \theta'' - \left(1 - \phi + \phi \frac{(\rho c_p)_s}{(\rho c_p)_f}\right) H\theta' + \frac{Ec}{(1-\phi)^{2.5}} \left(f'^2 + g'^2 + \frac{1}{\text{Re}_r} (4f^2 + 2H'^2)\right) = 0, \quad (6.20)$$

$$\frac{1}{Sc} \xi'' - H\xi' - k_1 \xi h^2 = 0, \quad (6.21)$$

$$\frac{\delta}{Sc} h'' - Hh' + k_1 \xi h^2 = 0, \quad (6.22)$$

$$\begin{aligned} H(0) &= 0, \quad f(0) = 0, \quad g(0) = 1, \quad \theta(0) = 1, \quad \xi'(0) = k_2 \xi(0), \quad \delta h'(0) = -k_2 h(0), \\ f(\infty) &\rightarrow 0, \quad g(\infty) \rightarrow 0, \quad \theta(\infty) \rightarrow 0, \quad \xi(\infty) \rightarrow 1, \quad h(\infty) \rightarrow 0, \end{aligned} \quad (6.23)$$

where $M = \sigma_f B_0^2 / \rho_f \Omega$ is the Hartman number, $\text{Pr} = \nu_f / \alpha_f$ is the Prandtl number, $Ec = (r\Omega)^2 / (T_w - T_\infty) (c_p)_f$ is the local Eckert number, $\text{Re}_r = r^2 \Omega / \nu_f$ is the local Reynolds number, $Sc = \nu_f / D_A$ is the Schmidt number, $k_1 = a_0^2 k_c / \Omega$ is the measure of strength of homogeneous reaction, $\delta = D_B / D_A$ is the ratio of diffusion coefficient and $k_2 = k_s \sqrt{\nu_f} / D_A \sqrt{\Omega}$ is the measure of strength of the heterogeneous reaction.

Here it is assumed that diffusion coefficients of chemical species A and B to be of a comparable size. This leads to make a further assumption that the diffusion coefficients D_A and D_B

are equal, i.e. $\delta = 1$ and thus

$$\xi(\eta) + h(\eta) = 1. \quad (6.24)$$

Now Eqs. (6.21) and (6.22) yield

$$\frac{1}{Sc} \xi'' - H\xi' - k_1\xi(1 - \xi)^2 = 0, \quad (6.25)$$

with the boundary conditions

$$\xi'(0) = k_2\xi(0), \quad \xi(\infty) \rightarrow 1. \quad (6.26)$$

The important physical quantities of interest in this problem are the local skin-friction coefficient C_{sf} and Nusselt number Nu which are given by

$$C_{sf} = \frac{\sqrt{\tau_r^2 + \tau_\theta^2}}{\rho(r\Omega)^2}, \quad Nu = \frac{rq_w}{k_f(T_w - T_\infty)}, \quad (6.27)$$

where the surface radial stress τ_r , tangential stress τ_θ and heat flux q_w are given by

$$\tau_r = \mu_{nf} \left. \frac{\partial u}{\partial z} \right|_{z=0}, \quad \tau_\theta = \mu_{nf} \left. \frac{\partial v}{\partial z} \right|_{z=0}, \quad q_w = -k_{nf} \left. \frac{\partial T}{\partial z} \right|_{z=0}. \quad (6.28)$$

In dimensionless form the local skin friction coefficient C_{sf} and Nusselt number Nu can be written as follows:

$$C_{sf}(\text{Re}_r)^{1/2} = \frac{1}{(1 - \phi)^{2.5}} \sqrt{[f'(0)]^2 + [g'(0)]^2}, \quad Nu(\text{Re}_r)^{-1/2} = -\frac{k_{nf}}{k_f} \theta'(0). \quad (6.29)$$

6.2 Solutions procedure

Initial approximations $H_0(\eta)$, $f_0(\eta)$, $g_0(\eta)$, $\theta_0(\eta)$ and $\xi_0(\eta)$ and auxiliary linear operators \mathcal{L}_H , \mathcal{L}_f , \mathcal{L}_g , \mathcal{L}_θ and \mathcal{L}_ξ are taken in the forms

$$H_0(\eta) = 0, \quad f_0(\eta) = \eta e^{-\eta}, \quad g_0(\eta) = e^{-\eta}, \quad \theta_0(\eta) = e^{-\eta}, \quad \xi_0(\eta) = 1 - \frac{1}{2} e^{-k_2\eta}, \quad (6.30)$$

$$\mathcal{L}_H = H', \quad \mathcal{L}_f = f'' - f, \quad \mathcal{L}_g = g'' - g, \quad \mathcal{L}_\theta = \theta'' - \theta, \quad \mathcal{L}_\xi = \xi'' - \xi, \quad (6.31)$$

subject to the properties

$$\begin{aligned}
\mathcal{L}_H[c_1] &= 0 \\
\mathcal{L}_f[c_2e^\eta + c_3e^{-\eta}] &= 0, \\
\mathcal{L}_g[c_4e^\eta + c_5e^{-\eta}] &= 0, \\
\mathcal{L}_\theta[c_6e^\eta + c_7e^{-\eta}] &= 0, \\
\mathcal{L}_\xi[c_8e^\eta + c_9e^{-\eta}] &= 0,
\end{aligned} \tag{6.32}$$

in which c_i ($i = 1 - 9$) are the constants.

If $p \in [0, 1]$ indicates the embedding parameter then the zeroth order deformation problems are constructed as follows:

$$(1 - p)\mathcal{L}_H[\hat{H}(\eta, p) - H_0(\eta)] = p\hbar_H\mathcal{N}_H[\hat{H}(\eta, p), \hat{f}(\eta, p), \hat{g}(\eta, p)], \tag{6.33}$$

$$(1 - p)\mathcal{L}_f[\hat{f}(\eta, p) - f_0(\eta)] = p\hbar_f\mathcal{N}_f[\hat{f}(\eta, p), \hat{H}(\eta, p), \hat{g}(\eta, p)], \tag{6.34}$$

$$(1 - p)\mathcal{L}_g[\hat{g}(\eta, p) - g_0(\eta)] = p\hbar_g\mathcal{N}_g[\hat{g}(\eta, p), \hat{f}(\eta, p), \hat{H}(\eta, p)], \tag{6.35}$$

$$(1 - p)\mathcal{L}_\theta[\hat{\theta}(\eta, p) - \theta_0(\eta)] = p\hbar_\theta\mathcal{N}_\theta[\hat{\theta}(\eta, p), \hat{H}(\eta, p), \hat{f}(\eta, p), \hat{g}(\eta, p)], \tag{6.36}$$

$$(1 - p)\mathcal{L}_\xi[\hat{\xi}(\eta, p) - \xi_0(\eta)] = p\hbar_\xi\mathcal{N}_\xi[\hat{\xi}(\eta, p), \hat{H}(\eta, p), \hat{f}(\eta, p), \hat{g}(\eta, p)], \tag{6.37}$$

$$\begin{aligned}
\hat{H}(0, p) &= 0, \quad \hat{f}(0, p) = 0, \quad \hat{g}(0, p) = 1, \quad \hat{\theta}(0, p) = 1, \quad \hat{\xi}'(0, p) = k_2\hat{\xi}(0, p), \\
\hat{f}(\infty, p) &= 0, \quad \hat{g}(\infty, p) = 0, \quad \hat{\theta}(\infty, p) = 0, \quad \hat{\xi}(\infty, p) = 1,
\end{aligned} \tag{6.38}$$

where $\hbar_H, \hbar_f, \hbar_g, \hbar_\theta$ and \hbar_ξ are the nonzero auxiliary parameters and the nonlinear operators $\mathcal{N}_H, \mathcal{N}_f, \mathcal{N}_g, \mathcal{N}_\theta$ and \mathcal{N}_ξ are given by

$$\mathcal{N}_H = \frac{\partial \hat{H}(\eta, p)}{\partial \eta} + 2\hat{f}(\eta, p), \tag{6.39}$$

$$\begin{aligned}\mathcal{N}_f &= \frac{1}{(1-\phi)^{2.5} \left(1-\phi+\phi\frac{\rho_s}{\rho_f}\right)} \frac{\partial^2 \hat{f}(\eta, p)}{\partial \eta^2} - \hat{H}(\eta, p) \frac{\partial \hat{f}(\eta, p)}{\partial \eta} - \left(\hat{f}(\eta, p)\right)^2 \\ &\quad + (\hat{g}(\eta, p))^2 - \left(\frac{\frac{\sigma_{nf}}{\sigma_f}}{1-\phi+\phi\frac{\rho_s}{\rho_f}}\right) M \hat{f}(\eta, p),\end{aligned}\quad (6.40)$$

$$\begin{aligned}\mathcal{N}_g &= \frac{1}{(1-\phi)^{2.5} \left(1-\phi+\phi\frac{\rho_s}{\rho_f}\right)} \frac{\partial^2 \hat{g}(\eta, p)}{\partial \eta^2} - \hat{H}(\eta, p) \frac{\partial \hat{g}(\eta, p)}{\partial \eta} - 2\hat{f}(\eta, p)\hat{g}(\eta, p) \\ &\quad - \left(\frac{\frac{\sigma_{nf}}{\sigma_f}}{1-\phi+\phi\frac{\rho_s}{\rho_f}}\right) M \hat{g}(\eta, p),\end{aligned}\quad (6.41)$$

$$\begin{aligned}\mathcal{N}_\theta &= \frac{1}{\text{Pr}} \frac{k_{nf}}{k_f} \frac{\partial^2 \hat{\theta}(\eta, p)}{\partial \eta^2} - \left(1-\phi+\phi\frac{(\rho c_p)_s}{(\rho c_p)_f}\right) \hat{H}(\eta, p) \frac{\partial \hat{\theta}(\eta, p)}{\partial \eta} + \frac{Ec}{(1-\phi)^{2.5}} \left[\left(\frac{\partial \hat{f}(\eta, p)}{\partial \eta}\right)^2 \right. \\ &\quad \left. + \left(\frac{\partial \hat{g}(\eta, p)}{\partial \eta}\right)^2 + \frac{1}{\text{Re}} \left(4\left(\hat{f}(\eta, p)\right)^2 + 2\left(\frac{\partial \hat{H}(\eta, p)}{\partial \eta}\right)^2\right) \right],\end{aligned}\quad (6.42)$$

$$\mathcal{N}_\xi = \frac{1}{Sc} \frac{\partial^2 \hat{\xi}(\eta, p)}{\partial \eta^2} - \hat{H}(\eta, p) \frac{\partial \hat{\xi}(\eta, p)}{\partial \eta} - k_1 \hat{\xi}(\eta, p) \left(1 - \hat{\xi}(\eta, p)\right)^2. \quad (6.43)$$

The resulting problems at m^{th} order can be presented in the following forms

$$\mathcal{L}_H [H_m(\eta) - \chi_m H_{m-1}(\eta)] = \hbar_H \mathcal{R}_{H,m}(\eta), \quad (6.44)$$

$$\mathcal{L}_f [f_m(\eta) - \chi_m f_{m-1}(\eta)] = \hbar_f \mathcal{R}_{f,m}(\eta), \quad (6.45)$$

$$\mathcal{L}_g [g_m(\eta) - \chi_m g_{m-1}(\eta)] = \hbar_g \mathcal{R}_{g,m}(\eta), \quad (6.46)$$

$$\mathcal{L}_\theta [\theta_m(\eta) - \chi_m \theta_{m-1}(\eta)] = \hbar_\theta \mathcal{R}_{\theta,m}(\eta), \quad (6.47)$$

$$\mathcal{L}_\xi [\xi_m(\eta) - \chi_m \xi_{m-1}(\eta)] = \hbar_\xi \mathcal{R}_{\xi,m}(\eta), \quad (6.48)$$

$$H_m(0) = f_m(0) = f_m(\infty) = g_m(0) = g_m(\infty) = \theta_m(0) = \theta_m(\infty) = \xi'_m(0) - k_2 \xi_m(0) = \xi_m(\infty) = 0, \quad (6.49)$$

$$\mathcal{R}_{H,m}(\eta) = H'_{m-1} + 2f_{m-1}, \quad (6.50)$$

$$\begin{aligned}\mathcal{R}_{f,m}(\eta) &= \frac{1}{(1-\phi)^{2.5} \left(1-\phi+\phi\frac{\rho_s}{\rho_f}\right)} f''_{m-1} - \sum_{k=0}^{m-1} [H_{m-1-k} f'_k + f_{m-1-k} f_k - g_{m-1-k} g_k] \\ &\quad - \left(\frac{\frac{\sigma_{nf}}{\sigma_f}}{1-\phi+\phi\frac{\rho_s}{\rho_f}} \right) M f_{m-1},\end{aligned}\tag{6.51}$$

$$\begin{aligned}\mathcal{R}_{g,m}(\eta) &= \frac{1}{(1-\phi)^{2.5} \left(1-\phi+\phi\frac{\rho_s}{\rho_f}\right)} g''_{m-1} - \sum_{k=0}^{m-1} [H_{m-1-k} g'_k + 2f_{m-1-k} g_k] \\ &\quad - \left(\frac{\frac{\sigma_{nf}}{\sigma_f}}{1-\phi+\phi\frac{\rho_s}{\rho_f}} \right) M g_{m-1},\end{aligned}\tag{6.52}$$

$$\begin{aligned}\mathcal{R}_{\theta,m}(\eta) &= \frac{1}{\text{Pr}} \frac{k_{nf}}{k_f} \theta''_{m-1} - \left(1-\phi+\phi\frac{(\rho c_p)_s}{(\rho c_p)_f}\right) \sum_{k=0}^{m-1} H_{m-1-k} \theta'_k + \frac{Ec}{(1-\phi)^{2.5}} \sum_{k=0}^{m-1} [f'_{m-1-k} f'_k \\ &\quad + g'_{m-1-k} g'_k + \frac{1}{\text{Re}} (4f_{m-1-k} f_k + 2H'_{m-1-k} H'_k)],\end{aligned}\tag{6.53}$$

$$\mathcal{R}_{\xi,m}(\eta) = \frac{1}{Sc} \xi''_{m-1} - \sum_{k=0}^{m-1} \left[H'_{m-1-k} \xi_k - k_1 \left(\xi_{m-1-l} \sum_{j=0}^l \xi_{l-j} \xi_j - 2\xi_{m-1-l} \xi_l \right) \right] - k_1 \xi_{m-1},\tag{6.54}$$

$$\chi_m = \begin{cases} 0, & m \leq 1 \\ 1, & m > 1 \end{cases}.\tag{6.55}$$

The general solutions $(H_m, f_m, g_m, \theta_m, \xi_m)$ comprising the special solutions $(H_m^*, f_m^*, g_m^*, \theta_m^*, \xi_m^*)$ are

$$\begin{aligned}H_m(\eta) &= H_m^*(\eta) + c_1, \\ f_m(\eta) &= f_m^*(\eta) + c_2 e^\eta + c_3 e^{-\eta}, \\ g_m(\eta) &= g_m^*(\eta) + c_4 e^\eta + c_5 e^{-\eta}, \\ \theta_m(\eta) &= \theta_m^*(\eta) + c_6 e^\eta + c_7 e^{-\eta}, \\ \xi_m(\eta) &= \xi_m^*(\eta) + c_8 e^\eta + c_9 e^{-\eta},\end{aligned}\tag{6.56}$$

where the constants c_i ($i = 1 - 9$) through the boundary conditions (6.49) have the values

$$\begin{aligned} c_1 &= -H_m^*(0), \quad c_2 = c_4 = c_6 = c_8 = 0, \quad c_3 = -f_m^*(0), \quad c_5 = -g_m^*(0), \\ c_7 &= \theta_m^*(0), \quad c_9 = \frac{1}{1+k_2} \left[\frac{\partial \xi_m^*(\eta)}{\partial \eta} \Big|_{\eta=0} - k_2 \xi_m^*(0) \right]. \end{aligned} \quad (6.57)$$

6.3 Convergence of series solutions

The auxiliary parameters \hbar_H , \hbar_f , \hbar_g , \hbar_θ and \hbar_ξ play an important role for convergence of series solutions. The \hbar -curves are sketched at 10^{th} -order of approximations to obtain valid ranges of these parameters (see Fig. 6.1). Permissible values of the auxiliary parameters are $-1.1 \leq \hbar_H \leq -0.7$, $-1.1 \leq \hbar_f \leq -0.6$, $-1.2 \leq \hbar_g \leq -0.6$, $-1.1 \leq \hbar_\theta \leq -1$ and $-1.5 \leq \hbar_\xi \leq -0.5$. Further the series solutions converge in the whole region of η ($0 < \eta < \infty$) when $\hbar_H = \hbar_g = -0.7$ and $\hbar_f = \hbar_\theta = \hbar_\xi = -1$. Also Table 6.1 ensures that the series solutions are convergent up to four decimal places.

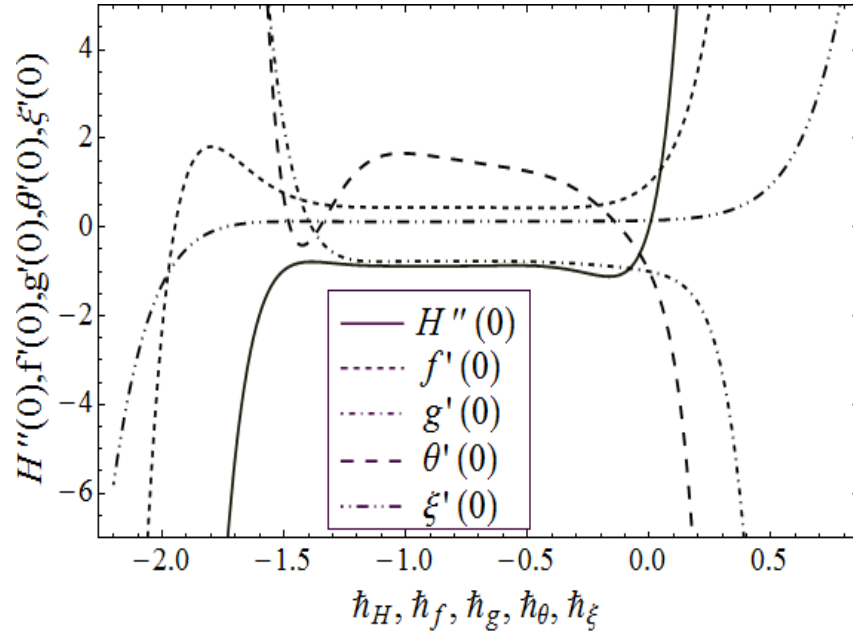


Fig. 6.1: The \hbar -curves for $H''(0)$, $f'(0)$, $g'(0)$, $\theta'(0)$ and $\xi'(0)$ when $M = k_1 = k_2 = 0.3$, $\phi = 0.2$, $\text{Pr} = 6.2$, $Ec = 0.7$ and $\text{Re}_r = \text{Sc} = 0.9$.

Table 6.1: Convergence of HAM solutions for different order of approximations when $M = k_1 = k_2 = 0.3$, $\phi = 0.2$, $Pr = 6.2$, $Ec = 0.7$ and $Re_r = Sc = 0.9$.

Order of approximations	$-H''(0)$	$f'(0)$	$-g'(0)$	$\theta'(0)$	$\xi'(0)$
1	1.400	0.4754	0.9230	0.1656	0.1349
5	0.8466	0.4276	0.7790	1.343	0.1260
10	0.8832	0.4420	0.7672	1.660	0.1208
15	0.8863	0.4434	0.7680	1.797	0.1194
20	0.8858	0.4429	0.7683	1.830	0.1190
26	0.8858	0.4429	0.7683	1.839	0.1193
30	0.8858	0.4429	0.7683	1.839	0.1193
35	0.8858	0.4429	0.7683	1.839	0.1193

6.4 Discussion

The effects of different parameters on the dimensionless velocity, temperature and concentration are examined graphically in this section. Effects of Hartman number M on the axial velocity profile $H(\eta)$ can be seen from Fig. 6.2. Here negative values of $H(\eta)$ indicate downward flow in the vertical direction. As the magnetic field has the tendency to slow down the movement of the fluid which leads to a decrease in the velocity and momentum boundary layer thickness. Fig. 6.3 illustrates the behavior of M on the radial component of velocity $f(\eta)$. There is a decrease in velocity and associated boundary layer thickness when M is increased. Also flow distribution is parabolic and positive values of $f(\eta)$ indicate radially outward flow. Fig. 6.4 depicts the distribution of azimuthal velocity $g(\eta)$ at various values of M . It is observed that $g(\eta)$ is decreasing function of Hartman number M .

Influence of Hartman number M on the temperature profile $\theta(\eta)$ is analyzed in Fig. 6.5. Since Lorentz force is a resistive force which opposes the fluid motion therefore heat is produced and consequently thermal boundary layer thickness increases. Fig. 6.6 shows that temperature is an increasing function of nanoparticle volume fraction ϕ . It is because of the fact that when the volume fraction of nanoparticles increases, the thermal conductivity enhances and consequently thermal boundary layer thickness increases. Variations of Eckert number Ec on temperature profile $\theta(\eta)$ can be seen in Fig. 6.7. When Ec is increased the temperature profile

first rises to a maximum value and then it asymptotically approaches to zero. It reveals that "Sparrow-Gregg type Hill" phenomenon exists in the presence of viscous dissipation. Fig. 6.8 represents the effect of rotational Reynolds number Re_r on temperature profile $\theta(\eta)$. Here the temperature profile and thermal boundary layer thickness decrease when Re_r is increased.

Fig. 6.9 shows the impact of strength of homogeneous reaction parameter k_1 on the concentration profile $\xi(\eta)$. Concentration decreases since the reactants are consumed during homogeneous reaction. Influence of strength of heterogeneous reaction parameter k_2 on the concentration distribution is analyzed in Fig. 6.10. It is noted that for higher values of k_2 the diffusion reduces and less diffused particles enhance the concentration. Influence of Schmidt number Sc on concentration profile $\xi(\eta)$ is shown in Fig. 6.11. Increasing behavior of concentration profile is noted for larger Schmidt number. In fact Schmidt number is the ratio of viscous diffusion rate to molecular diffusion rate. Therefore higher values of Schmidt number correspond to higher viscous diffusion rate which in turn increases the fluid concentration.

Fig. 6.12 presents the skin friction coefficient $C_{sf}(Re_r)^{1/2}$ as a function of nanoparticles volume fraction ϕ for different values of Hartman number M . When ϕ increases the magnitude of $C_{sf}(Re_r)^{1/2}$ grows in nonlinear way. Also magnitude of $C_{sf}(Re_r)^{1/2}$ is directly proportional to M . Fig. 6.13 shows local Nusselt number $Nu(Re_r)^{-1/2}$ as a function of ϕ at different values of Re_r . There is an increase in the magnitude of $Nu(Re_r)^{-1/2}$ when ϕ is increased. While magnitude of $Nu(Re_r)^{-1/2}$ has inverse relationship with Re_r .

Variations of surface concentration $\xi(0)$ via nanoparticles volume fraction ϕ for different values of the strength of homogeneous reaction parameter k_1 and strength of heterogeneous reaction parameter k_2 are shown in the Figs. 6.14 and 6.15. One can see from these Figs. that $\xi(0)$ decreases with the increase of k_1 and k_2 . It is in view of the fact that surface concentration reduces due to the consumption of reactants during homogeneous-heterogeneous reactions.

Some thermophysical properties of water and magnetite Fe_3O_4 are given in Table 6.2. In Table 6.3 we compared the results of $f'(0)$, $g'(0)$, $H(\infty)$ and $\theta'(0)$ with existing literature in limiting sense. Obtained results are in good agreement. Table 6.4 includes the values of local Nusselt number $Nu(Re_r)^{-1/2}$ for different values of ϕ , M and Ec . It is noted that heat transfer rate enhances by increasing $Nu(Re_r)^{-1/2}$ for different values of ϕ , M and Ec .

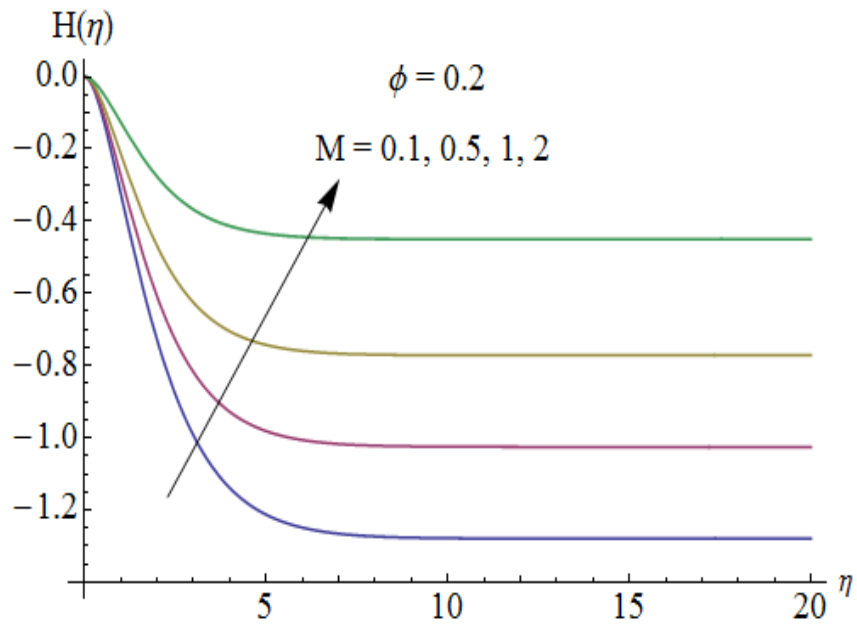


Fig. 6.2: Influence of M on $H(\eta)$.

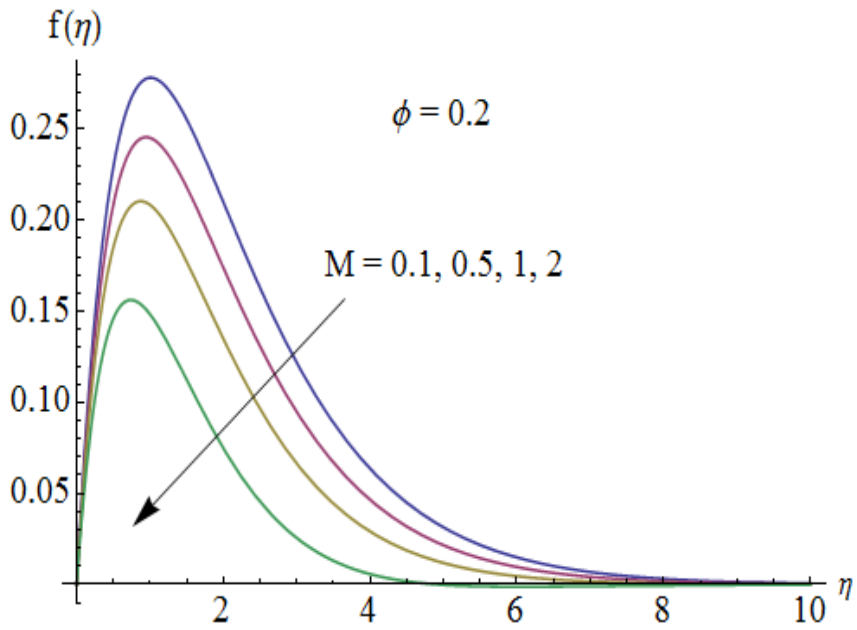


Fig. 6.3: Influence of M on $f(\eta)$.

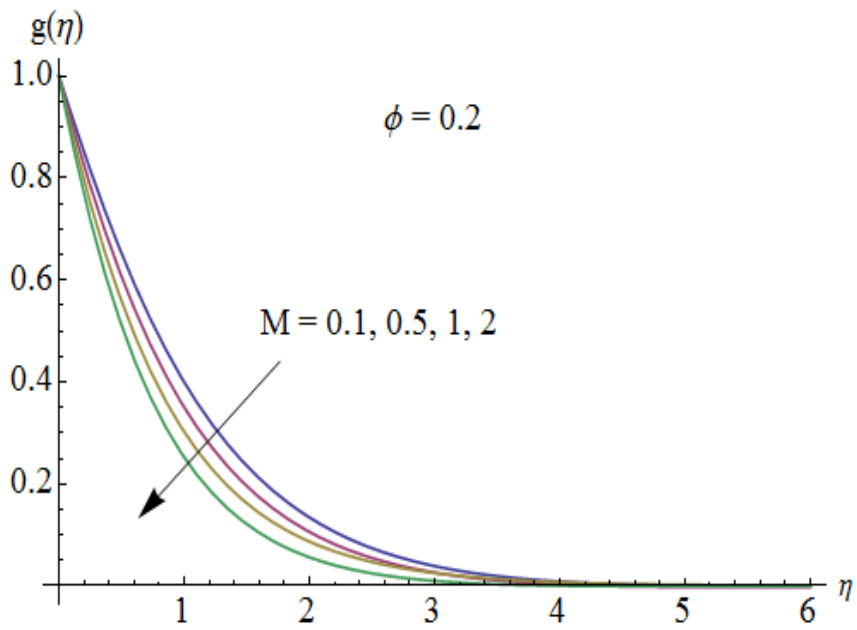


Fig. 6.4: Influence of M on $g(\eta)$.

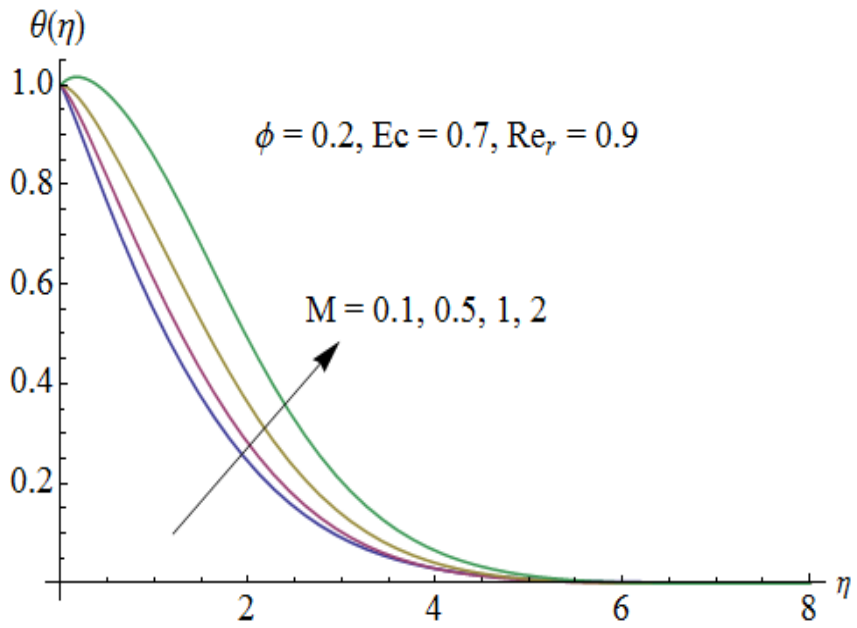


Fig. 6.5: Influence of M on $\theta(\eta)$.

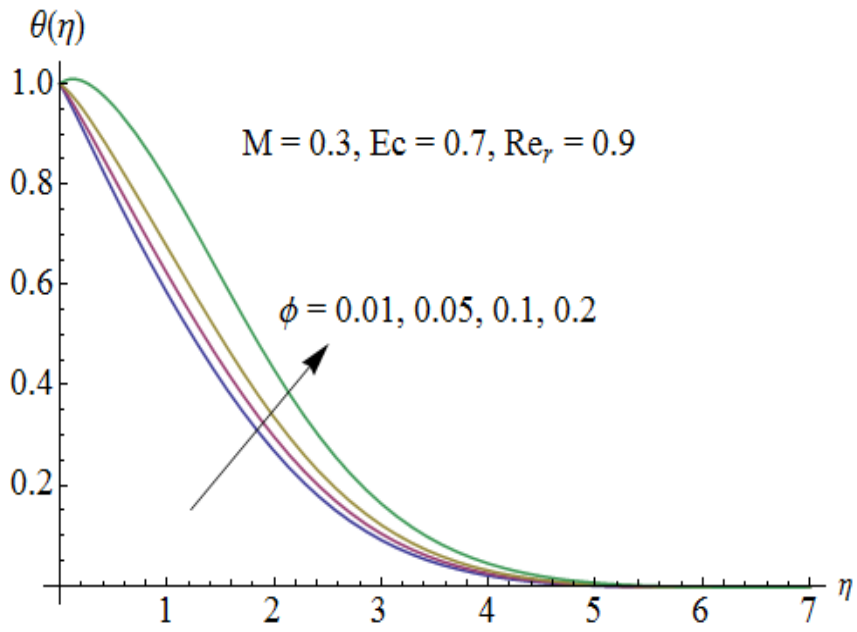


Fig. 6.6: Influence of ϕ on $\theta(\eta)$.

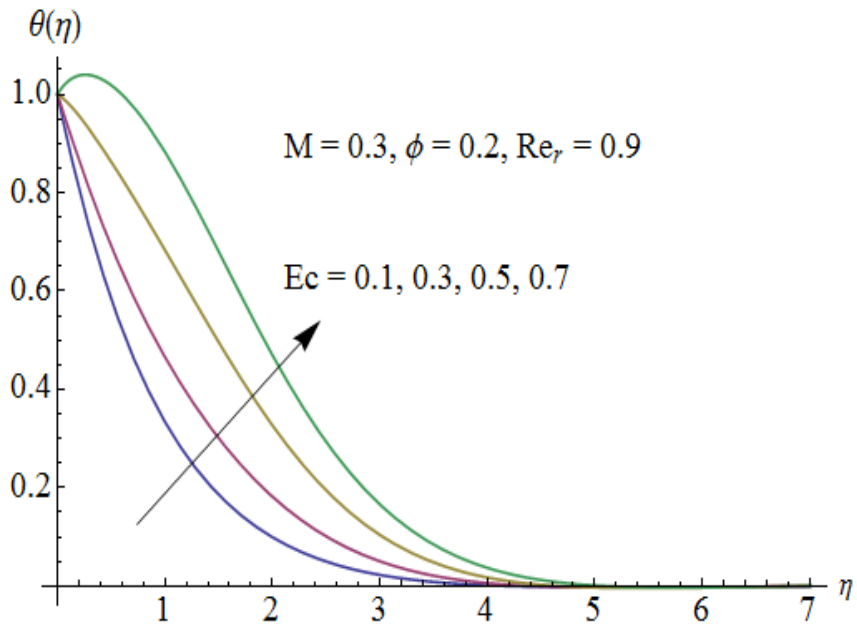


Fig. 6.7: Influence of Ec on $\theta(\eta)$.

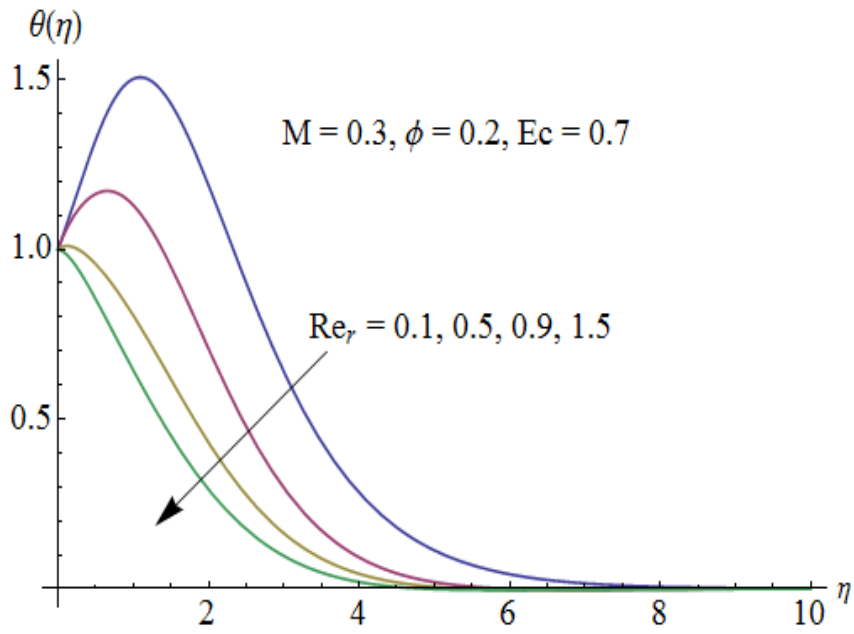


Fig. 6.8: Influence of Re_r on $\theta(\eta)$.

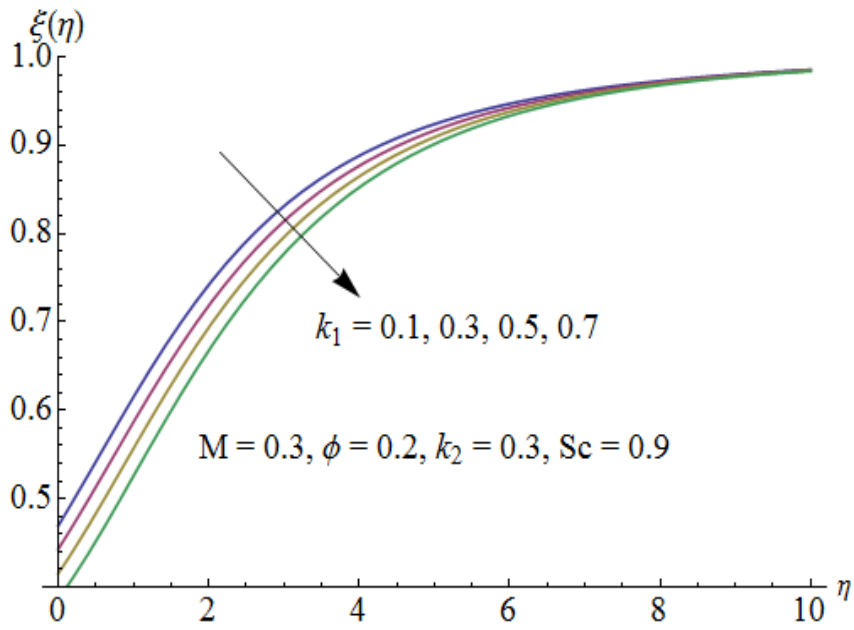


Fig. 6.9: Influence of k_1 on $\xi(\eta)$.

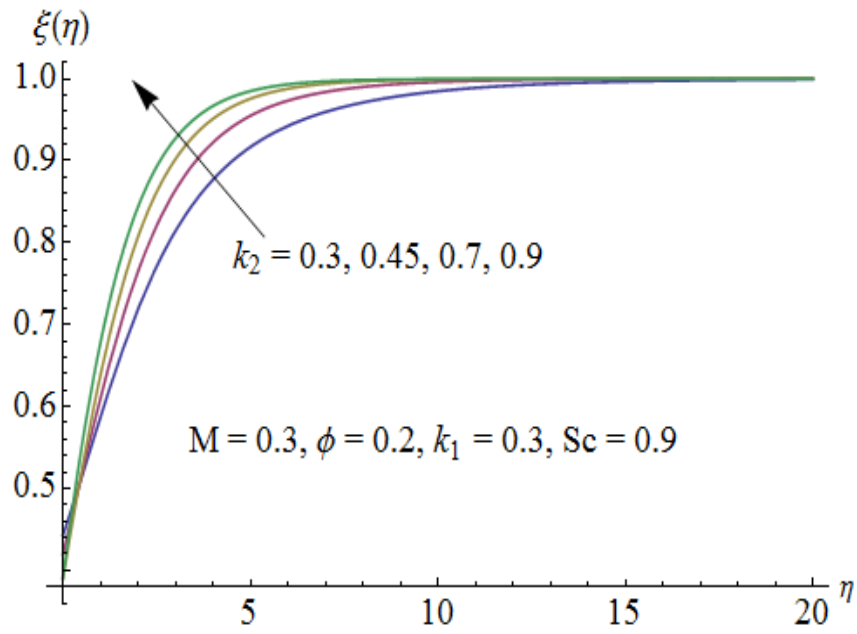


Fig. 6.10: Influence of k_2 on $\xi(\eta)$.

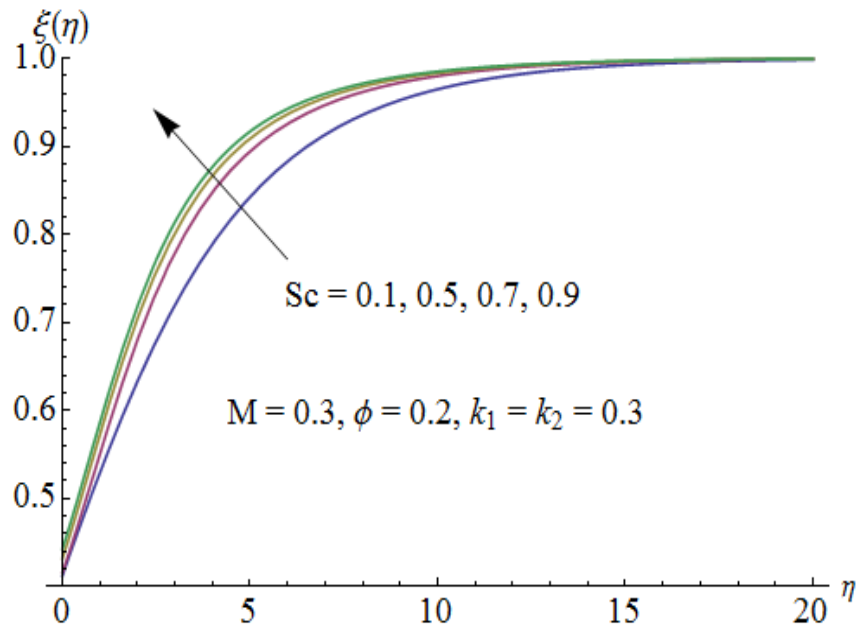


Fig. 6.11: Influence of Sc on $\xi(\eta)$.

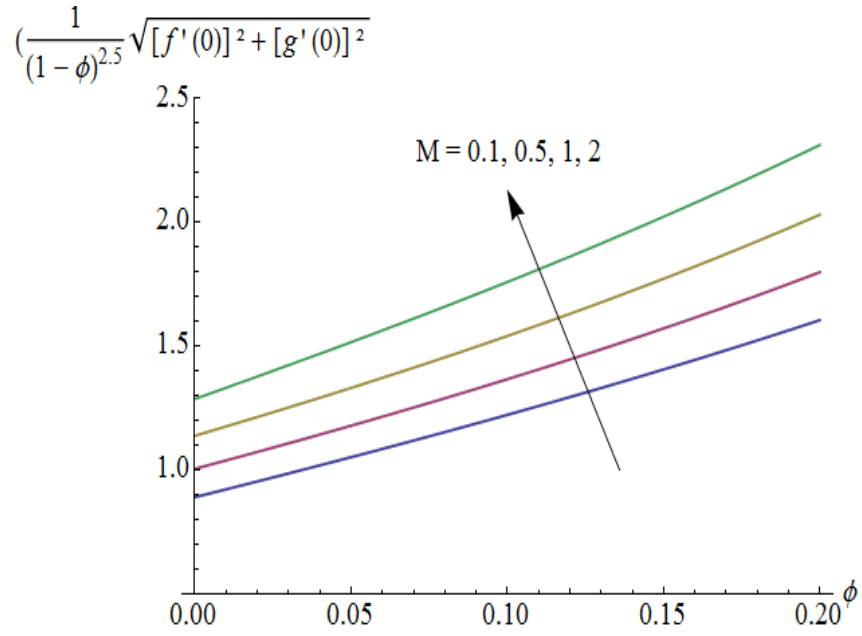


Fig. 6.12. Influence of M on $C_{sf}(\text{Re}_r)^{1/2}$.

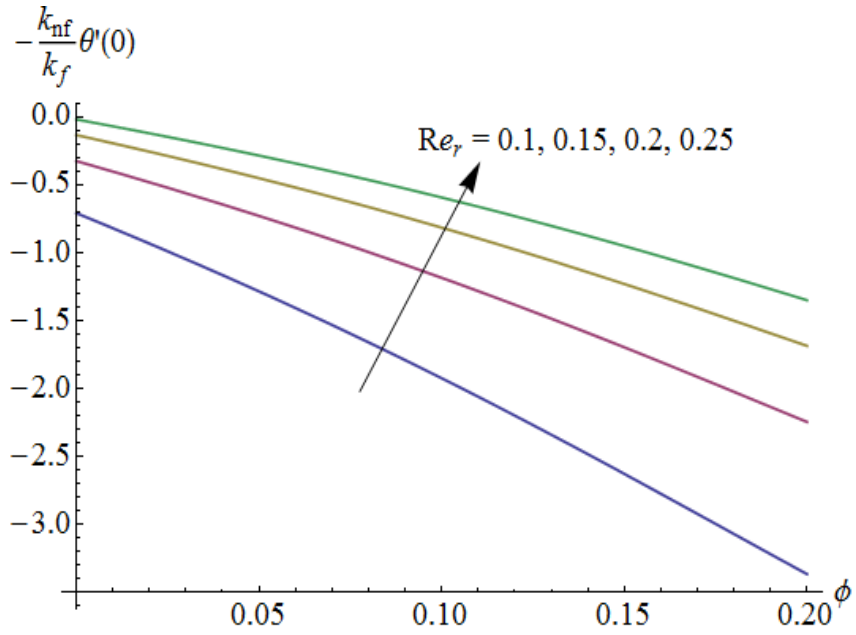


Fig. 6.13: Influence of Re_r on $Nu(\text{Re}_r)^{-1/2}$

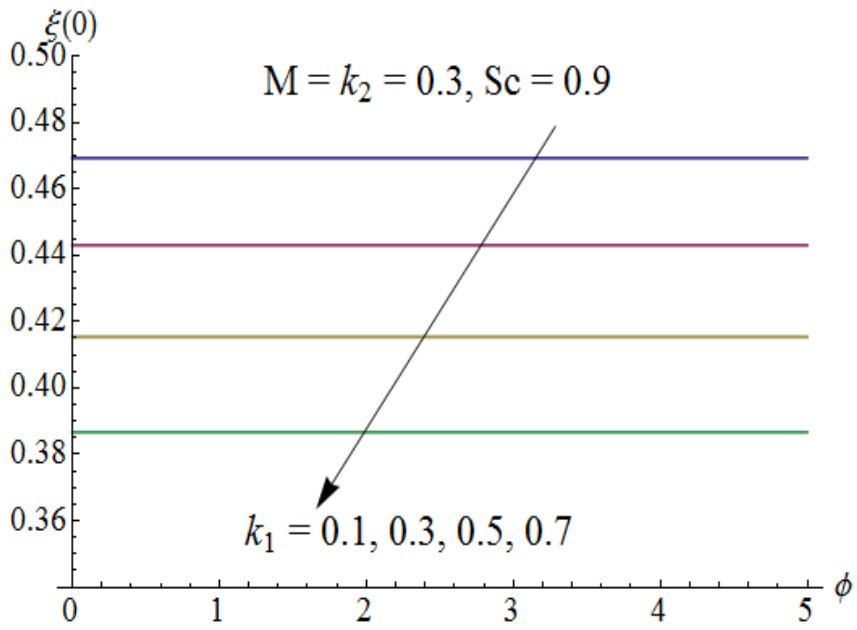


Fig. 6.14: Influence of k_1 on $\xi(0)$.

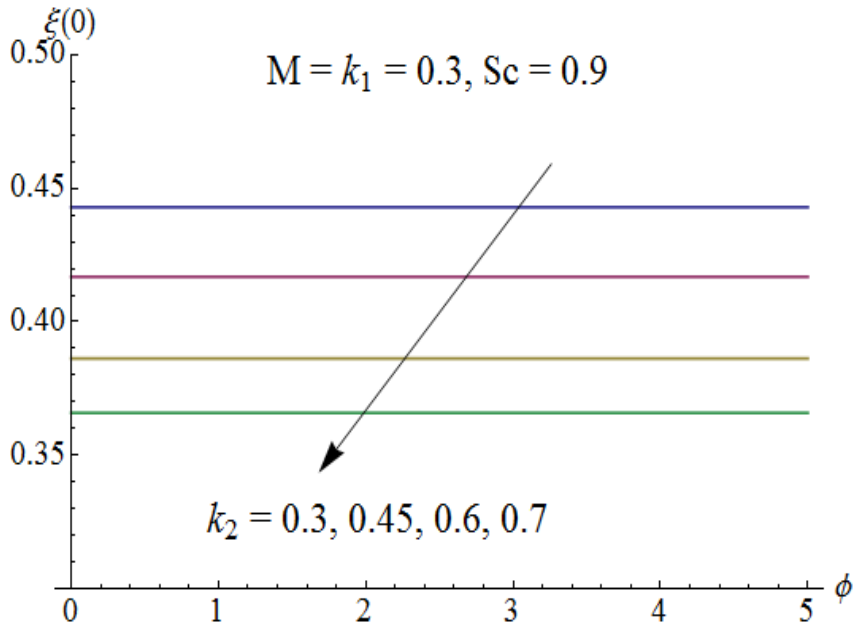


Fig. 6.15: Influence of k_2 on $\xi(0)$.

Table 6.2: Thermophysical properties of water and magnetite Fe_3O_4 .

	$\rho(\text{kg}/\text{m}^3)$	$c_p(\text{J}/\text{kgK})$	$k(\text{W}/\text{mK})$	$\sigma(\Omega\text{m})^{-1}$
Water	997.1	4179	0.613	0.05
Fe_3O_4	5180	670	9.7	25000

Table 6.3: Comparison of present results with previously published works when $M = \phi = Ec = 0$.

	Kelson and Desseaux [53]	Bachok et al. [54]	Turkyilmazoglu [56]	Present
$f'(0)$	0.510233	0.5101	0.51023262	0.5102
$-g'(0)$	0.615922	0.6158	0.61592201	0.6160
$-H(\infty)$	0.884474	—	0.88447411	0.8843
$-\theta'(0)$	—	0.9337	0.93387794	0.9335

Table 6.4: Numerical values of Nusselt number $Nu(\text{Re}_r)^{-1/2}$ for different values of ϕ , M and Ec when $\text{Pr} = 6.2$ and $\text{Re}_r = 0.9$.

ϕ	M	Ec	$-\frac{k_{nf}}{k_f}\theta'(0)$
0	0.3	0.7	-1.189
0.05			-1.532
0.1			-1.847
0.2	0.5		-2.853
	0.7		-3.065
	1		-3.391
	0.3	0.4	-1.229
		0.6	-2.327
		0.8	-3.549

6.5 Main points

Here flow of ferrofluid induced by a rotating disk is investigated. Effects of homogeneous–heterogeneous reactions and viscous dissipation are also taken into account. The following observations are made.

- The axial, radial and azimuthal velocity profiles are decreasing functions of Hartman number.
- Opposite behavior of homogeneous and heterogeneous reaction parameters are seen on the concentration profiles.
- Surface drag force has direct relationship with the strength of magnetic field.
- Heat transfer rate rises for increasing values of nanoparticles volume fraction, Hartman number and Eckert number.
- Surface concentration decreases for both the strength of homogeneous reaction and heterogeneous reaction parameters.
- There is an excellent agreement between present and previously published results in limiting case when $M = \phi = Ec = 0$.

Chapter 7

Melting heat transfer in the MHD flow of Cu-water nanofluid with viscous dissipation and Joule heating

An analysis has been carried out in this chapter for the characteristics of non-uniform melting heat transfer in the boundary layer flow of nanofluid past a stretching sheet. Water is treated as a base fluid and copper as nanoparticle. An incompressible fluid saturates the porous space. Effects of viscous dissipation and Joule heating are also examined. Fluid is electrically conducting in the presence of applied magnetic field. Appropriate transformations reduce the nonlinear partial differential system to ordinary differential system. Convergent series solutions are computed for the velocity and temperature. Effects of different parameters on the velocity and temperature profiles are shown and analyzed. It is revealed that an increase in the melting parameter increases the velocity and decreases the temperature. Impact of different parameters on skin friction coefficient and Nusselt number are computed through numerical values. It is concluded that temperature gradient at the surface increases for higher Hartman number and nanoparticle volume fraction.

7.1 Problem development

We consider the steady two-dimensional incompressible flow of nanofluid past a stretching sheet situated at $y = 0$. We have taken x - and y - axes along and perpendicular to the sheet respectively. Flow is confined to $y \geq 0$. It is assumed that the velocity of the stretching sheet is $u_w(x) = cx$, where c is a positive constant. We have chosen $T_\infty > T_m$ where $T_m = T_\infty - \tilde{a}x^2$ is the non-uniform temperature of the melting surface and T_∞ is the ambient temperature. Also a uniform magnetic field of intensity B_0 acts in the y -direction. The magnetic Reynolds number is assumed to be small so that the induced magnetic field is negligible in comparison with the applied magnetic field. We incorporate the Joule heating and viscous dissipation effects in the energy equation. The continuity, momentum and energy equations which govern such type of flow are written as:

$$\frac{\partial u}{\partial x} + \frac{\partial v}{\partial y} = 0, \quad (7.1)$$

$$u \frac{\partial u}{\partial x} + v \frac{\partial u}{\partial y} = \nu_{nf} \frac{\partial^2 u}{\partial y^2} - \frac{\nu_{nf}}{K} u - \frac{\sigma_{nf} B_0^2}{\rho_{nf}} u, \quad (7.2)$$

$$u \frac{\partial T}{\partial x} + v \frac{\partial T}{\partial y} = \alpha_{nf} \frac{\partial^2 T}{\partial y^2} + \frac{\mu_{nf}}{(\rho c_p)_{nf}} \left(\frac{\partial u}{\partial y} \right)^2 + \frac{\sigma_{nf} B_0^2}{(\rho c_p)_{nf}} u^2. \quad (7.3)$$

The subjected boundary conditions are

$$\begin{aligned} u &= u_w = cx, \quad v = 0, \quad T = T_m \quad \text{at } y = 0, \\ u &\rightarrow 0, \quad T \rightarrow T_\infty \quad \text{as } y \rightarrow \infty, \end{aligned} \quad (7.4)$$

and

$$k_{nf} \left(\frac{\partial T}{\partial y} \right)_{y=0} = \rho_{nf} [\Gamma + c_s(T_m - T_0)v(x, 0)], \quad (7.5)$$

where u and v are the velocity components along the x - and y - directions respectively, K is the permeability of porous medium, c is the stretching constant, $\Gamma = \Gamma_0 x^2$ is the non-uniform latent heat of the fluid and c_s is the heat capacity of the solid surface. The boundary condition (7.5) shows that the heat conducted to the melting surface is equal to the heat of melting plus the sensible heat required to raise the solid temperature $T_0 = T_m - \tilde{b}x^2$ to its melting temperature T_m .

The effective nanofluid dynamic viscosity μ_{nf} , density ρ_{nf} , thermal diffusivity α_{nf} , heat capacitance $(\rho c_p)_{nf}$, thermal conductivity k_{nf} and electrical conductivity σ_{nf} are

$$\mu_{nf} = \frac{\mu_f}{(1 - \phi)^{2.5}}, \quad (7.6)$$

$$\rho_{nf} = \rho_f(1 - \phi) + \rho_s\phi, \quad (7.7)$$

$$\alpha_{nf} = \frac{k_{nf}}{(\rho c_p)_{nf}}, \quad (7.8)$$

$$(\rho c_p)_{nf} = (\rho c_p)_f(1 - \phi) + (\rho c_p)_s\phi, \quad (7.9)$$

$$\frac{k_{nf}}{k_f} = \frac{k_s + 2k_f - 2\phi(k_f - k_s)}{k_s + 2k_f + 2\phi(k_f - k_s)}, \quad (7.10)$$

$$\frac{\sigma_{nf}}{\sigma_f} = 1 + \frac{3 \left(\frac{\sigma_s}{\sigma_f} - 1 \right) \phi}{\left(\frac{\sigma_s}{\sigma_f} + 2 \right) - \left(\frac{\sigma_s}{\sigma_f} - 1 \right) \phi}, \quad (7.11)$$

where ϕ denotes the solid volume fraction of nanoparticles. Here the subscripts nf represents the thermophysical properties of the nanofluid, f explains base fluid and s is defined as nano solid particles. We now introduce the following similarity transformations

$$u = cx f'(\eta), \quad v = -\sqrt{\nu_f c} f(\eta), \quad \eta = \sqrt{\frac{c}{\nu_f}} y, \quad \theta(\eta) = \frac{T - T_m}{T_\infty - T_m}, \quad (7.12)$$

Now Eq. (7.1) is satisfied automatically and substituting Eq. (7.12) into Eqs. (7.2) and (7.3), we get the following ordinary differential equations:

$$\varepsilon_1 (f''' - \lambda f') - f'^2 + f f'' - M \varepsilon_1 (1 - \phi)^{2.5} \frac{\sigma_{nf}}{\sigma_f} f' = 0, \quad (7.13)$$

$$\frac{1}{\text{Pr}} \frac{k_{nf}}{k_f} \varepsilon_2 (1 - \phi)^{2.5} \theta'' + f \theta' - 2 f' \theta + 2 f'' + \varepsilon_2 Ec M (1 - \phi)^{2.5} \frac{\sigma_{nf}}{\sigma_f} f'^2 + \varepsilon_2 Ec f''^2 = 0, \quad (7.14)$$

where prime indicates the differentiation with respect to η , λ is the porosity parameter, M is the Hartman number, Pr is the Prandtl number and Ec is the Eckert number. These quantities are defined as

$$\lambda = \frac{\nu_f}{cK}, \quad M = \frac{\sigma_f B_0^2}{c\rho_f}, \quad \text{Pr} = \frac{\nu_f}{\alpha_f}, \quad Ec = \frac{\rho_f u_w^2}{(\rho c_p)_f (T_\infty - T_m)} = \frac{\rho_f c^2}{(\rho c_p)_f \tilde{a}}, \quad (7.15)$$

The boundary conditions (7.4) and (7.5) become

$$\begin{aligned} f'(0) &= 1, \quad \varepsilon_3 \text{Pr} f(0) + \frac{k_{nf}}{k_f} \epsilon \theta'(0) = 0, \quad \theta(0) = 0, \\ f'(\infty) &\rightarrow 0, \quad \theta(\infty) \rightarrow 1, \end{aligned} \quad (7.16)$$

where ϵ is the dimensionless melting parameter

$$\epsilon = \frac{c_f(T_\infty - T_m)}{\Gamma + c_s(T_m - T_0)} = \frac{c_f \tilde{a}}{\Gamma_0 + c_s \tilde{b}}, \quad (7.17)$$

which is a combination of the Stefan numbers $c_f(T_\infty - T_m)/\Gamma$ and $c_s(T_m - T_0)/\Gamma$ for the liquid and solid phases, respectively. When $\phi = 0$ we obtain the governing equations for a viscous fluid. Also

$$\varepsilon_1 = \frac{1}{(1 - \phi)^{2.5} \left(1 - \phi + \frac{\rho_s}{\rho_f} \phi\right)}, \quad \varepsilon_2 = \frac{1}{(1 - \phi)^{2.5} \left(1 - \phi + \frac{(\rho c_p)_s}{(\rho c_p)_f} \phi\right)}, \quad \varepsilon_3 = 1 - \phi + \frac{\rho_s}{\rho_f} \phi. \quad (7.18)$$

Local skin friction coefficient C_{sf} and Nusselt number Nu are given by

$$C_{sf} = \frac{\tau_w}{\rho u_w^2}, \quad Nu = \frac{x q_w}{k_{nf} (T_\infty - T_m)}, \quad (7.19)$$

where the surface shear stress τ_w and wall heat flux q_w are given by

$$\tau_w = \mu_{nf} \left. \frac{\partial u}{\partial y} \right|_{y=0}, \quad q_w = -k_{nf} \left. \frac{\partial T}{\partial y} \right|_{y=0}. \quad (7.20)$$

By using the above equations we get

$$C_{sf}(\text{Re}_x)^{1/2} = \frac{1}{(1 - \phi)^{2.5}} f''(0), \quad Nu(\text{Re}_x)^{-1/2} = -\frac{k_{nf}}{k_f} \theta'(0), \quad (7.21)$$

where $\text{Re}_x = x\sqrt{a/\nu_f}$ is the local Reynolds number.

7.2 Homotopic solutions

The initial approximations $f_0(\eta)$ and $\theta_0(\eta)$ and auxiliary linear operators \mathcal{L}_f and \mathcal{L}_θ are taken as follows:

$$f_0(\eta) = 1 - e^{-\eta} - \frac{k_{nf}\delta}{k_f \varepsilon_3 \text{Pr}}, \quad \theta_0(\eta) = 1 - e^{-\eta}, \quad (7.22)$$

$$\mathcal{L}_f = f''' - f', \quad \mathcal{L}_\theta = \theta'' - \theta, \quad (7.23)$$

with

$$\begin{aligned} \mathcal{L}_f [c_1 + c_2 e^\eta + c_3 e^{-\eta}] &= 0, \\ \mathcal{L}_\theta [c_4 e^\eta + c_5 e^{-\eta}] &= 0, \end{aligned} \quad (7.24)$$

in which c_i ($i = 1 - 5$) are the constants.

If $p \in [0, 1]$ indicates the embedding parameter then the zeroth order deformation problems are established as follows:

$$(1 - p)\mathcal{L}_f [\hat{f}(\eta; p) - f_0(\eta)] = p\hbar_f \mathcal{N}_f[\hat{f}(\eta; p)], \quad (7.25)$$

$$(1 - p)\mathcal{L}_\theta [\hat{\theta}(\eta; p) - \theta_0(\eta)] = p\hbar_\theta \mathcal{N}_\theta[\hat{\theta}(\eta; p), \hat{f}(\eta; p)], \quad (7.26)$$

$$\hat{f}'(0; p) = 1, \quad \varepsilon_3 \text{Pr} \hat{f}(0; p) + \frac{k_{nf}}{k_f} \varepsilon \hat{\theta}'(0; p) = 0, \quad \hat{f}'(\infty; p) = 0, \quad (7.27)$$

$$\hat{\theta}(0; p) = 0, \quad \hat{\theta}(\infty; p) = 1, \quad (7.28)$$

where nonzero auxiliary parameters are represented as \hbar_f and \hbar_θ and the nonlinear operators \mathcal{N}_f and \mathcal{N}_θ are

$$\begin{aligned} \mathcal{N}_f [\hat{f}(\eta; p)] &= \varepsilon_1 \left(\frac{\partial^3 \hat{f}(\eta; p)}{\partial \eta^3} - \lambda \frac{\partial \hat{f}(\eta; p)}{\partial \eta} \right) - \left(\frac{\partial \hat{f}(\eta; p)}{\partial \eta} \right)^2 + \hat{f}(\eta; p) \frac{\partial^2 \hat{f}(\eta; p)}{\partial \eta^2} \\ &\quad - M \varepsilon_1 (1 - \phi)^{2.5} \frac{\sigma_{nf}}{\sigma_f} \frac{\partial \hat{f}(\eta; p)}{\partial \eta}, \end{aligned} \quad (7.29)$$

$$\begin{aligned}
\mathcal{N}_\theta [\hat{\theta}(\eta; p), \hat{f}(\eta; p)] &= \frac{1}{\text{Pr}} \frac{k_{nf}}{k_f} \varepsilon_2 (1 - \phi)^{2.5} \frac{\partial^2 \hat{\theta}(\eta; p)}{\partial \eta^2} + \hat{f}(\eta; p) \frac{\partial \hat{\theta}(\eta; p)}{\partial \eta} \\
&+ \varepsilon_2 Ec \left(\frac{\partial^2 \hat{f}(\eta; p)}{\partial \eta^2} \right)^2 - 2 \frac{\partial \hat{f}(\eta; p)}{\partial \eta} \hat{\theta}(\eta; p) + 2 \frac{\partial \hat{f}(\eta; p)}{\partial \eta} \\
&+ \varepsilon_2 EcM (1 - \phi)^{2.5} \frac{\sigma_{nf}}{\sigma_f} \left(\frac{\partial \hat{f}(\eta; p)}{\partial \eta} \right)^2.
\end{aligned} \tag{7.30}$$

The m^{th} order deformation problems can be written as follows

$$\mathcal{L}_f [f_m(\eta) - \chi_m f_{m-1}(\eta)] = \hbar_f \mathcal{R}_{f,m}(\eta), \tag{7.31}$$

$$\mathcal{L}_\theta [\theta_m(\eta) - \chi_m \theta_{m-1}(\eta)] = \hbar_\theta \mathcal{R}_{\theta,m}(\eta), \tag{7.32}$$

$$f'_m(0) = \varepsilon_3 \text{Pr} f_m(0) + \frac{k_{nf}}{k_f} \varepsilon \theta'_m(0) = f'_m(\infty) = \theta_m(0) = \theta_m(\infty) = 0, \tag{7.33}$$

$$\begin{aligned}
\mathcal{R}_{f,m}(\eta) &= \varepsilon_1 (f'''_{m-1} - \lambda f'_{m-1}) + \sum_{k=0}^{m-1} [f_{m-1-k} f''_k - f'_{m-1-k} f'_k] - M \varepsilon_1 (1 - \phi)^{2.5} \frac{\sigma_{nf}}{\sigma_f} f'_{m-1},
\end{aligned} \tag{7.34}$$

$$\begin{aligned}
\mathcal{R}_{\theta,m}(\eta) &= \frac{1}{\text{Pr}} \frac{k_{nf}}{k_f} \varepsilon_2 (1 - \phi)^{2.5} \theta''_{m-1} + \sum_{k=0}^{m-1} f_{m-1-k} \theta'_k + \varepsilon_2 Ec \sum_{k=0}^{m-1} f''_{m-1-k} f''_k \\
&+ \varepsilon_2 EcM (1 - \phi)^{2.5} \frac{\sigma_{nf}}{\sigma_f} \sum_{k=0}^{m-1} f'_{m-1-k} f'_k,
\end{aligned} \tag{7.35}$$

$$\chi_m = \begin{cases} 0, & m \leq 1 \\ 1, & m > 1 \end{cases}. \tag{7.36}$$

The general solutions (f_m, θ_m) comprising the special solutions (f_m^*, θ_m^*) are

$$\begin{aligned}
f_m(\eta) &= f_m^*(\eta) + c_1 + c_2 e^\eta + c_3 e^{-\eta}, \\
\theta_m(\eta) &= \theta_m^*(\eta) + c_4 e^\eta + c_5 e^{-\eta}.
\end{aligned} \tag{7.37}$$

7.3 Convergence of homotopic solutions

Homotopy analysis method is employed to obtain the solutions of Eqs. (7.13) and (7.14) along with the boundary conditions (7.16). The auxiliary parameters \hbar_f and \hbar_θ play an important role for the convergence of the series solutions. Here \hbar -curves are sketched at 14th-order of approximations to get valid ranges of these parameters (see Fig. 7.1). The permissible values of auxiliary parameters are $-1.5 \leq \hbar_f \leq -0.85$ and $-1.2 \leq \hbar_\theta \leq -1$. The residual errors are calculated for momentum and energy equations by the expressions

$$\begin{aligned}\Delta_m^f &= \int_0^1 \left[R_m^f(\eta, \hbar_f) \right]^2 d\eta, \\ \Delta_m^\theta &= \int_0^1 \left[R_m^\theta(\eta, \hbar_\theta) \right]^2 d\eta.\end{aligned}\tag{7.38}$$

In Figs. (7.2 – 7.3), the \hbar -curves for residual error of f and θ are sketched in order to get the admissible range for \hbar . It is noted that correct result up to 4th decimal place is obtained by choosing the values of \hbar from this range. Also, the HAM solutions converge in the whole region of η ($0 < \eta < \infty$) when $\hbar_f = -1.5$ and $\hbar_\theta = -1$. Table 7.1 is prepared to check the convergence of obtained HAM solutions. Tablular values show that convergence is attained for the functions $f''(0)$ and $\theta'(0)$ at 24th and 40th order of approximations respectively.

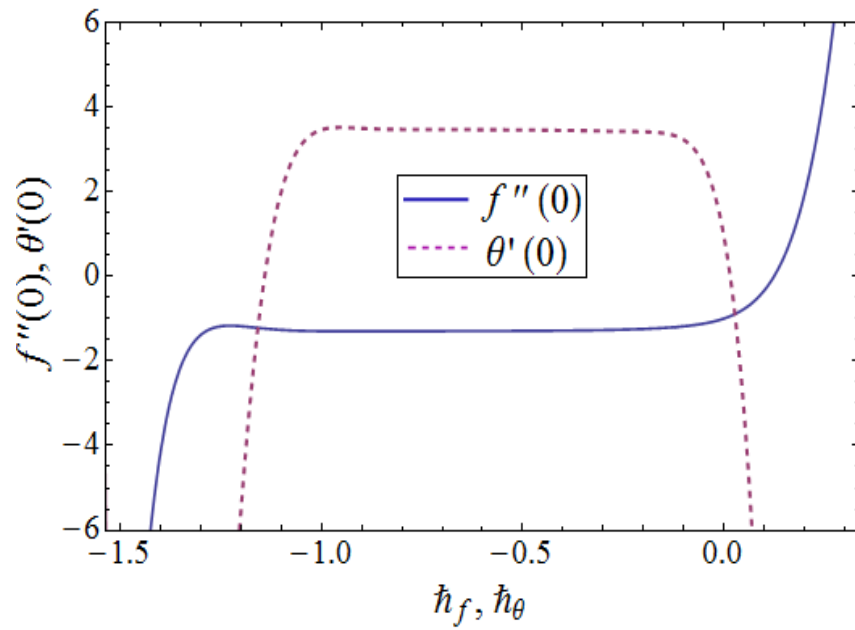


Fig. 7.1: Combined \hbar -curves for velocity and temperature when $M = 0.7$, $\lambda = 0.3$, $Ec = \epsilon = 0.5$ and $\phi = 0.1$.

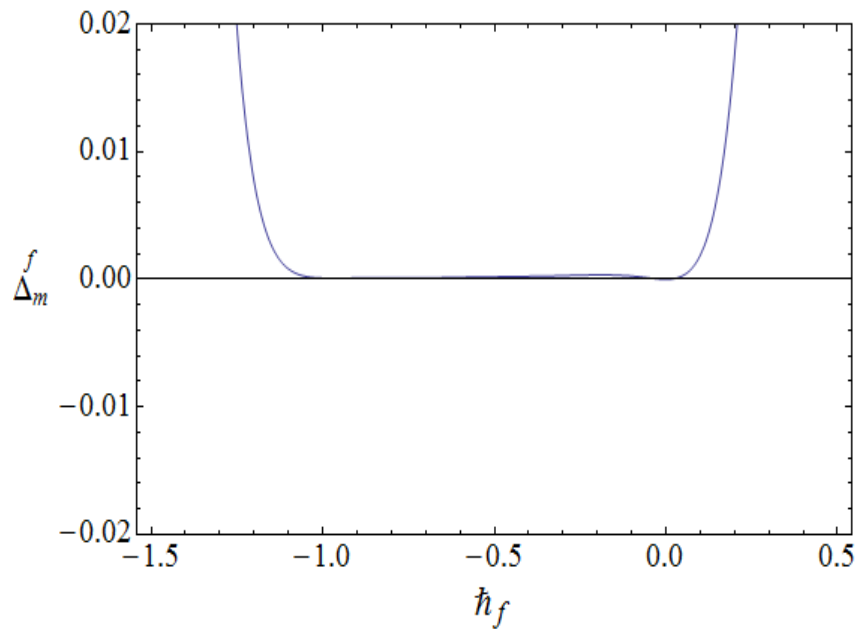


Fig. 7.2: \hbar_f -curve for the residual error Δ_m^f .

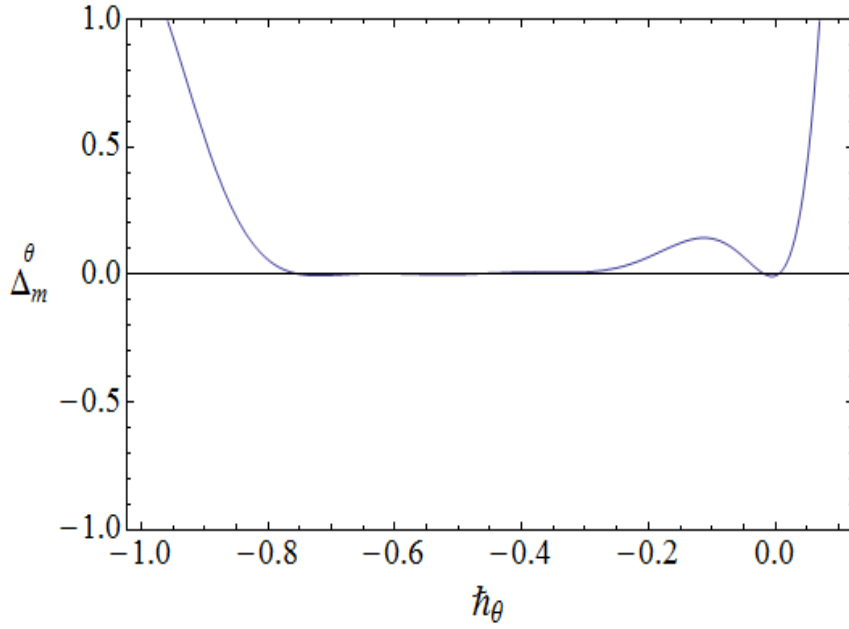


Fig. 7.3: \hbar_θ -curve for the residual error Δ_m^θ .

Table 7.1: Convergence of HAM solutions for different order of approximations when $M = 0.7$, $\lambda = 0.3$, $Ec = \epsilon = 0.5$ and $\phi = 0.1$.

Order of approximations	$-f''(0)$	$\theta'(0)$
1	1.225	3.215
5	1.286	3.433
10	1.296	3.467
15	1.300	3.475
20	1.302	3.479
25	1.303	3.481
32	1.304	3.483
40	1.309	3.484
50	1.309	3.484

7.4 Results and discussion

This section presents the effects of various parameters on the velocity, temperature, skin friction coefficient and Nusselt number in the form of graphical and tabulated results (see Figs. (7.4 – 7.17) and Table 7.2).

7.4.1 Dimensionless velocity field

Fig. (7.4 – 7.7) exhibit the dimensionless velocity profiles for different values of porosity parameter λ , Hartman number M , nanoparticle volume fraction ϕ and melting parameter ϵ . Fig. 7.4 displays the velocity profiles for different values of porosity parameter λ . The porosity parameter depends on the permeability parameter K . An increase in the porosity parameter leads to the lower permeability parameter. This lower permeability parameter causes a reduction in the fluid velocity. Fig. 7.5 illustrates the influence of Hartman number M on the velocity $f'(\eta)$. As the applied magnetic field is a resistive force which reduces the fluid motion, so the velocity field decreases. The effects of nanoparticle volume fraction ϕ on the velocity field $f'(\eta)$ are depicted in the Fig. 7.6. It is evident that an increase in the values of nanoparticle volume fraction corresponds to a decrease in the velocity profile $f'(\eta)$. The effect of melting parameter ϵ is seen in Fig. 7.7. It is quite obvious from the Fig. that larger values of ϵ increase the velocity profile. It is because of the fact that an increase in melting causes an increase in the molecular motion which enhances the flow.

7.4.2 Dimensionless temperature field

Effects of Eckert number Ec , Hartman number M , nanoparticle volume fraction ϕ and melting parameter ϵ on the temperature profile θ are shown in the Figs. (7.8 – 7.11). Fig. 7.8 depicts that temperature is an increasing function of the Eckert number Ec . Eckert number is defined as the ratio of kinetic energy to enthalpy. With the increase in Ec , kinetic energy increases which consequently enhances temperature. Effect of Hartman number M on the temperature is analyzed in Fig. 7.9. As the Lorentz force opposes the fluid motion, so heat is produced and as a result the thermal boundary layer thickness increases. Fig. 7.10 illustrates the variation of nanoparticle volume fraction ϕ on temperature field θ . Here temperature profile θ increases for

an increase in ϕ . Since there is enhancement in thermal conductivity by increasing the volume fraction of nanoparticles so thermal boundary layer thickness enhances. Fig. 7.11 shows the variations of melting parameter ϵ on temperature profile. It is noted that temperature profile decreases for larger values of melting parameter due to the fact that temperature difference increases between ambient and melting surface which reduces the temperature of the fluid. Further the thermal boundary layer thickness increases when melting parameter is increased.

7.4.3 Skin friction coefficient and Nusselt number

Figs. (7.12 – 7.14) represent variation of skin friction coefficient for larger values of porosity parameter, nanoparticles volume fraction and melting parameter. It is observed that λ and ϕ are increasing functions of $f''(0)$ whereas with the increase of ϵ it decreases. The variation of heat transfer rate for Ec , ϵ and ϕ is shown in Figs. (7.15 – 7.17). It is found that the Nusselt number decreases with the increase of ϵ while it increases by increasing Ec and ϕ .

Some thermophysical properties of water and copper are given in Table 7.2. CPU time in seconds is given for different order of approximations in Table 7.3. Table 7.4 presents some numerical values of $-C_{sf}(\text{Re}_x)^{1/2}$ and $-Nu(\text{Re}_x)^{-1/2}$ for different parameters. It is noted here that magnitude of skin friction coefficient increases for higher Cu –nanoparticles volume fraction ϕ , Hartman number M and porosity parameter λ . However it decreases when Eckert number Ec and melting parameter ϵ are increased. The increase in the values of Cu –nanoparticles volume fraction ϕ , Hartman number M , porosity parameter λ and Eckert number Ec enhances the magnitude of local Nusselt number. Furthermore rate of heat transfer decreases when melting parameter ϵ is increased.

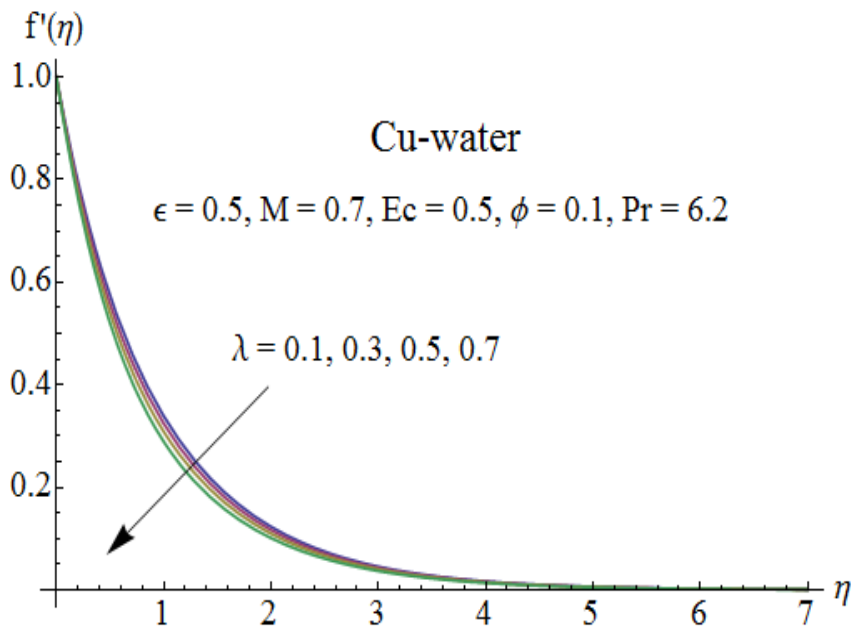


Fig. 7.4: Influence of λ on velocity field.

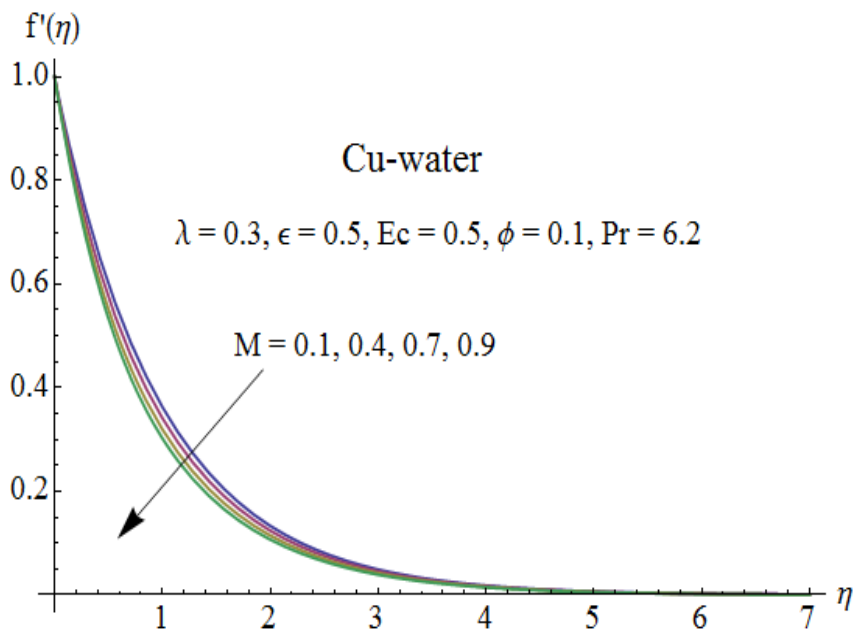


Fig. 7.5: Influence of M on velocity field.

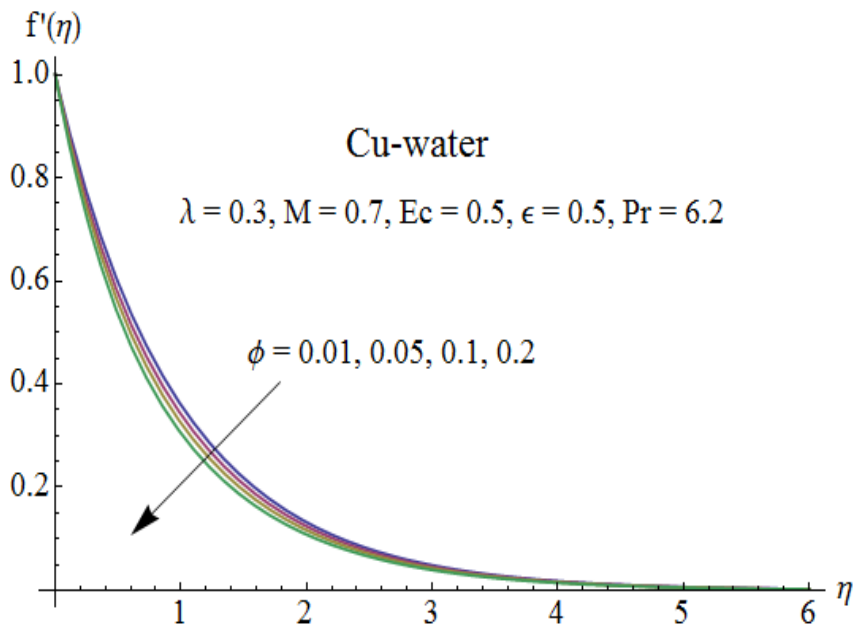


Fig. 7.6: Influence of ϕ on velocity field.

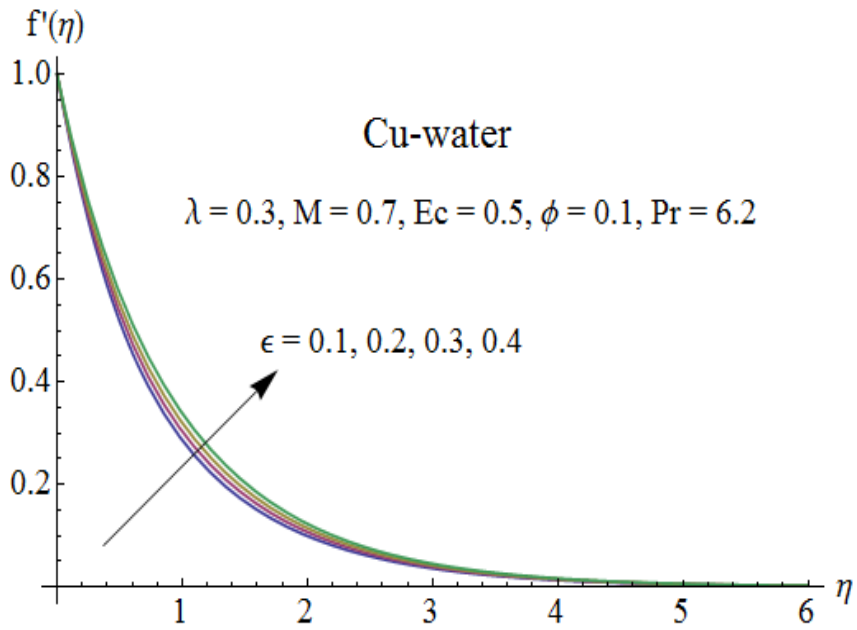


Fig. 7.7: Influence of ϵ on velocity field.

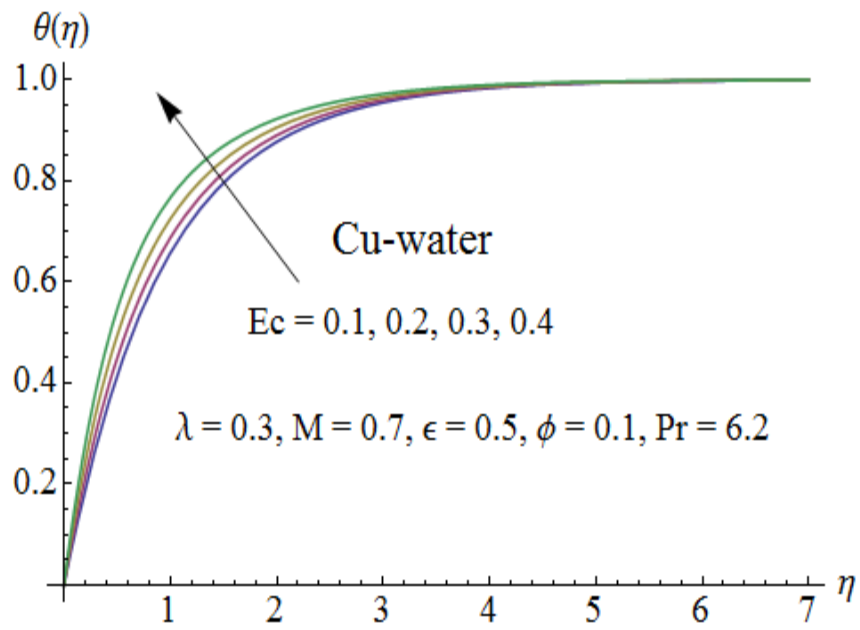


Fig. 7.8: Influence of Ec on temperature field.

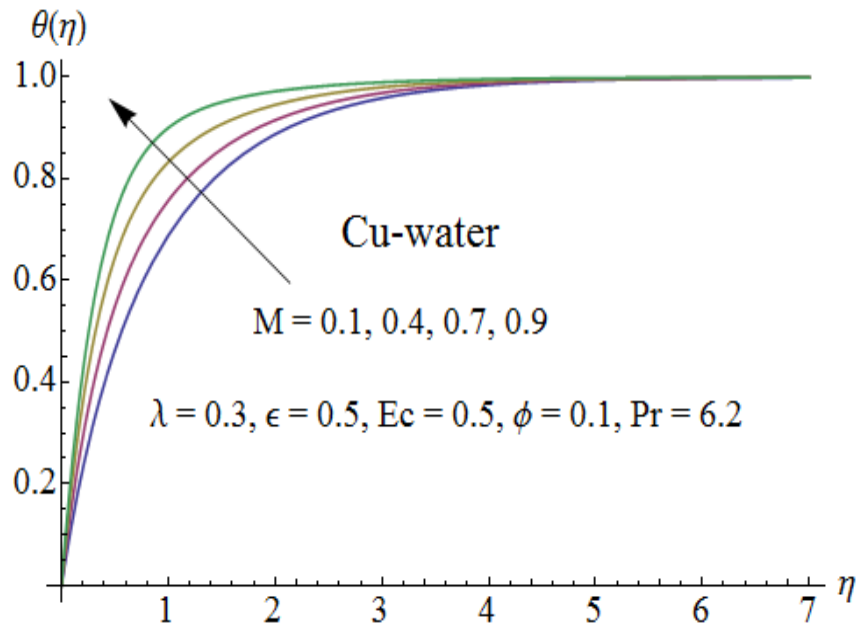


Fig. 7.9: Influence of M on temperature field.

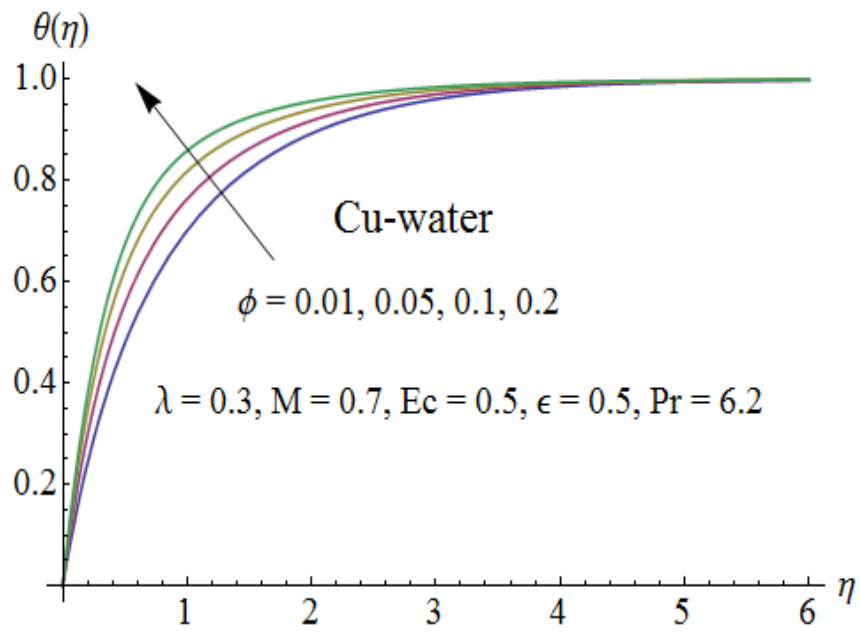


Fig. 7.10: Influence of ϕ on temperature field.

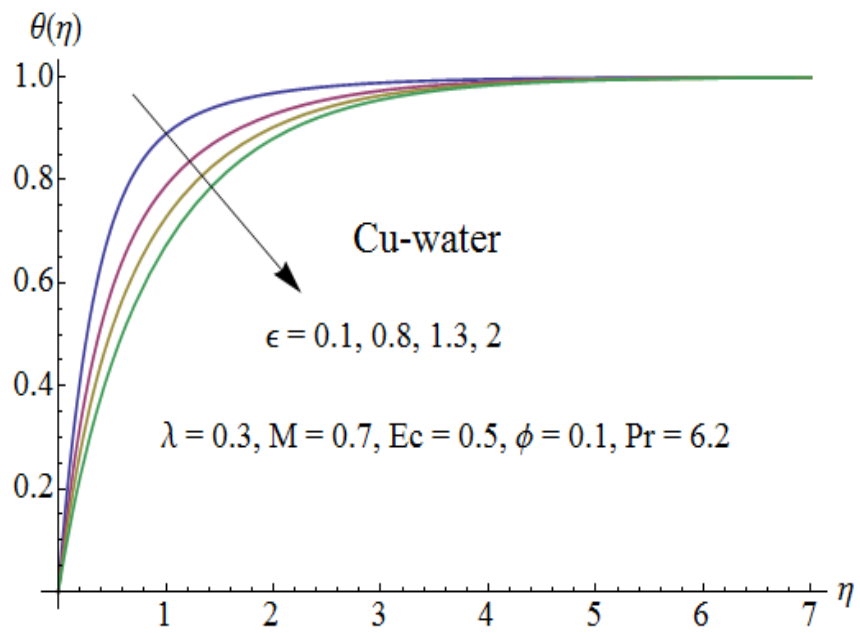


Fig. 7.11: Influence of ϵ on temperature field.

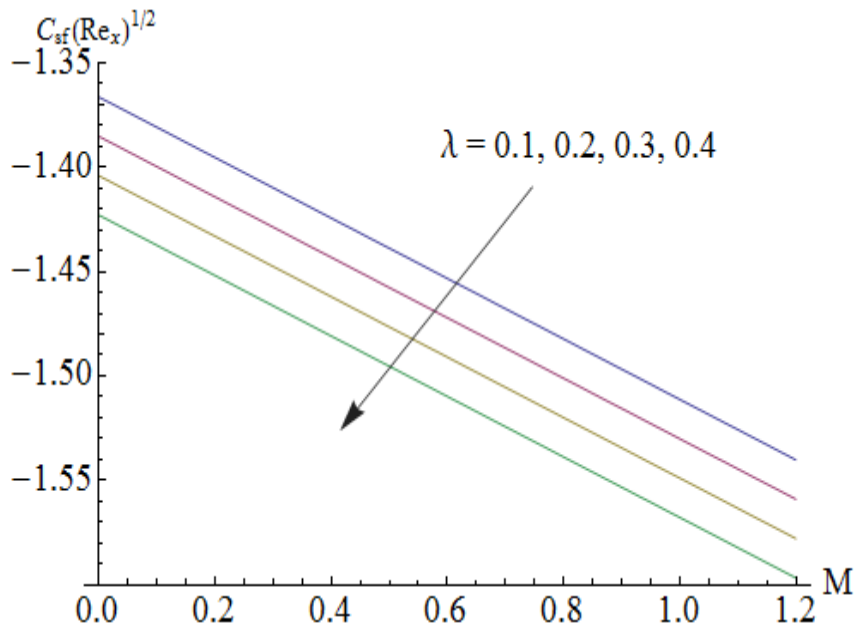


Fig. 7.12: Influences of λ and M on skin friction coefficient.

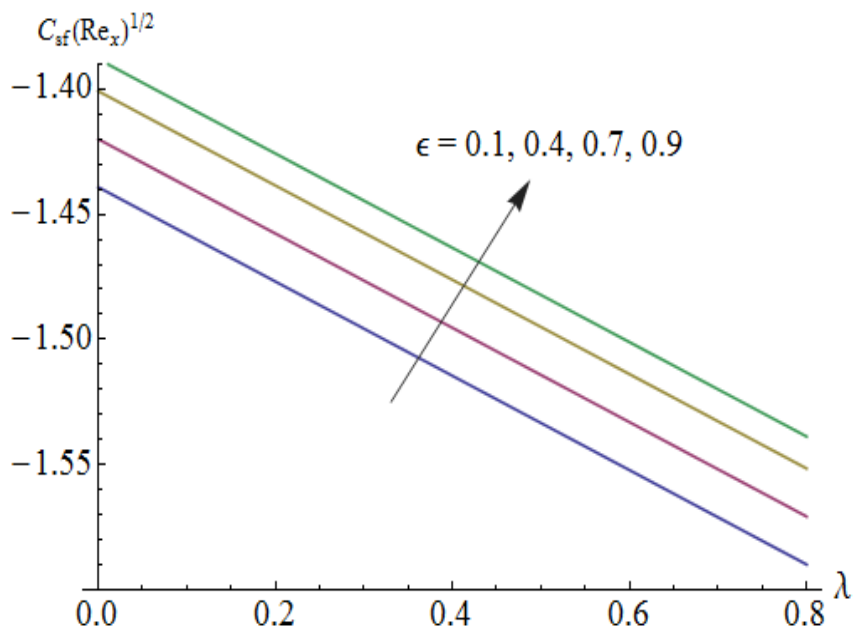


Fig. 7.13: Influences of ϵ and λ on skin friction coefficient.

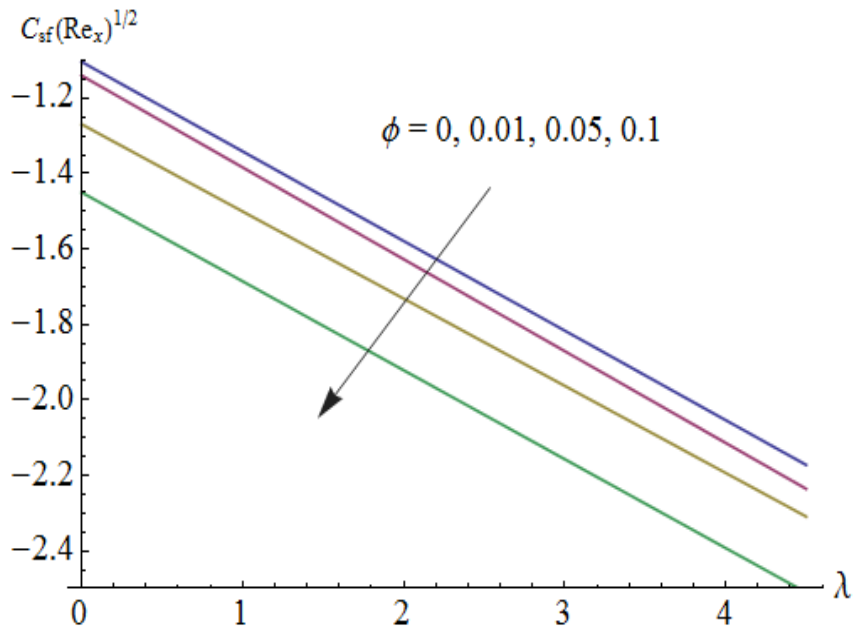


Fig. 7.14: Influences of ϕ and λ on skin friction coefficient.

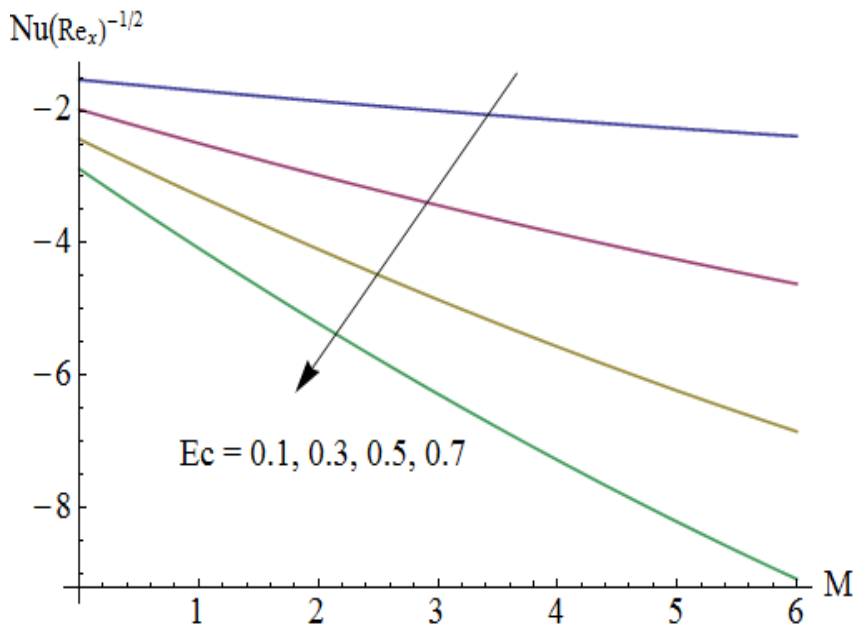


Fig. 7.15: Influences of Ec and M on Nusselt number.

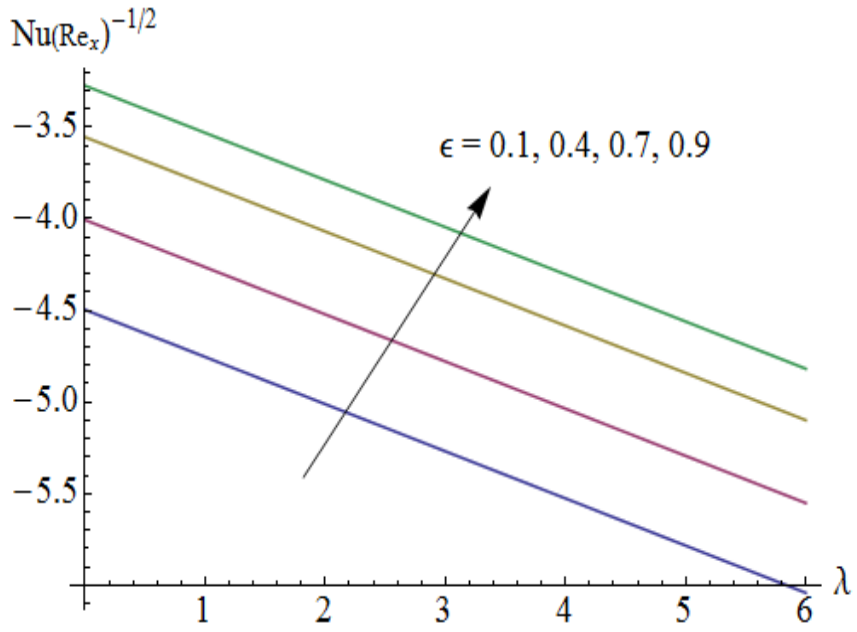


Fig. 7.16: Influences of ϵ and λ on Nusselt number.

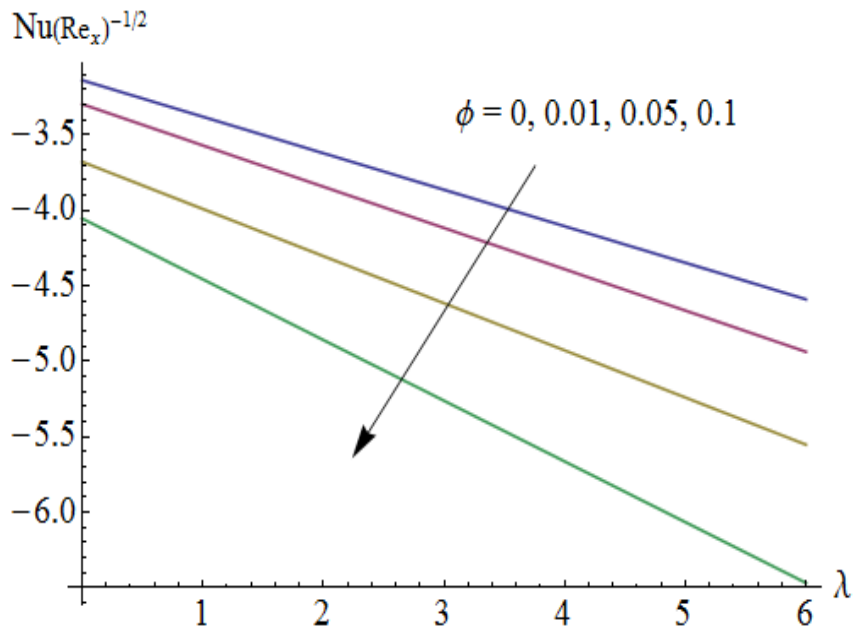


Fig. 7.17: Influences of ϕ and λ on Nusselt number.

Table 7.2: Thermophysical properties of water and copper [21].

	$\rho(kg/m^3)$	$c_p(j/kgk)$	$k(W/m.k)$	$\beta \times 10^5(K^{-1})$	$\sigma(\Omega m)^{-1}$
Pure water	997.1	4179	0.613	21	0.05
Copper(<i>Cu</i>)	8933	385	401	1.67	5.96×10^7

Table 7.3: CPU time (seconds) used by HAM for different order of approximations.

Order of approximations	CPU time (sec)
2	0.387022
4	0.932053
6	1.99511
8	3.84522
10	6.46637
12	10.3336
14	15.6849
16	20.6332
18	27.0535
20	35.221

Table 7.4: Numerical values of skin friction coefficient and Nusselt number for different parameters.

ϕ	M	λ	Ec	ϵ	$-C_{sf}(\text{Re}_x)^{1/2}$	$-Nu(\text{Re}_x)^{-1/2}$
0.01	0.7	0.3	0.5	0.5	1.3065	3.9187
0.05					1.4749	4.2285
0.1					1.6971	4.6398
0.1	0.1				1.4543	4.1486
	0.4				1.5798	4.4009
	0.9				1.7713	4.7915
	0.7	0.1			1.6151	4.5939
		0.2			1.6565	4.6167
		0.4			1.7369	4.6615
		0.3	0.1		1.7645	3.5463
			0.2		1.7459	3.8347
			0.3		1.7292	4.1119
			0.5	0.1	1.9215	5.8563
				0.4	1.7420	4.8745
				0.7	1.6204	4.2512

7.5 Concluding remarks

Influence of MHD flow of Cu -water nanofluid over a stretching sheet is presented in this article. Melting heat transfer and effects of viscous dissipation are also considered. HAM is used to obtain semi-analytic solutions. It is observed that velocity profile is decreasing function of Eckert number, Hartman number and nanoparticle volume fraction. Melting parameter enhances the velocity and reduces the temperature field. Temperature profile increases when volume fraction of copper nanoparticles is increased. Higher values of Cu -nanoparticles volume fraction, Hartman number and porosity parameter correspond to larger values of skin friction coefficient and local Nusselt number. Temperature gradient at the surface decreases for larger values of melting parameter.

Chapter 8

Unsteady flow of nanofluid with double stratification and magnetohydrodynamics

This chapter aims to examine the unsteady flow of viscous nanofluid caused by an inclined stretching sheet. Effects of thermal radiation, viscous dissipation and stratification process due to temperature and concentration are analyzed. Fluid is electrically conducting in the presence of applied magnetic field. The flow consideration is subjected to small magnetic Reynolds number. Induced magnetic field is absent. Appropriate transformations reduce the nonlinear partial differential system to ordinary differential system. Convergent solutions are computed. Interval of convergence is determined. Effects of different parameters on the velocity, temperature and concentration profiles are shown and analyzed. It is concluded that thermal and solutal stratification parameters reduce the velocity distribution. It is also observed that velocity is decreasing function of Hartman number.

8.1 Flow equations

Consider an unsteady two-dimensional incompressible flow of nanofluid past a stretching sheet. The sheet makes an angle Ψ with the horizontal direction. The x - and y -axes are perpendicular to each other. Thermal and concentration buoyancy forces are applied to the fluid with

double stratified phenomena due to temperature and concentration. The sheet is maintained at temperature $T_w = T_0 + A^*x/(1 - a^*t)$ and concentration $C_w = C_0 + D^*x/(1 - a^*t)$. The temperature and mass concentration of the ambient fluid are assumed to be stratified in the form $T_\infty = T_0 + B^*x/(1 - a^*t)$ and $C_\infty = C_0 + E^*x/(1 - a^*t)$ respectively (see Fig. 8.1).

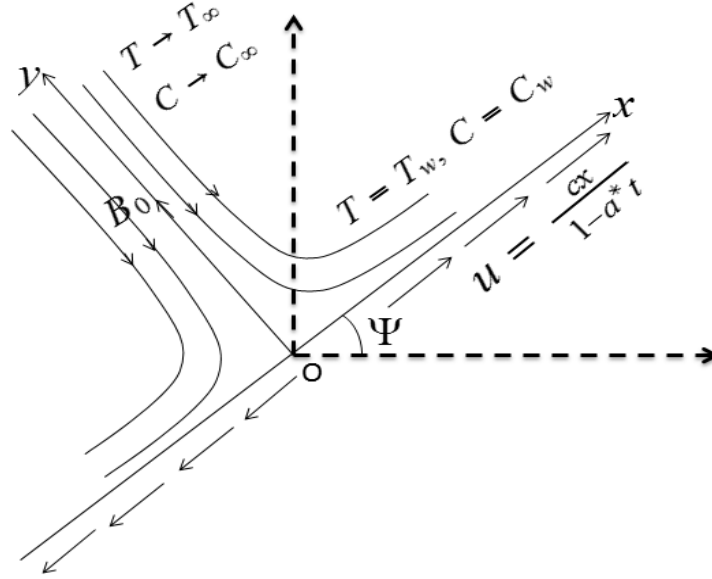


Fig. 8.1: Geometry of the problem.

It is assumed that a uniform magnetic field of intensity B_0 acts in the y -direction. The magnetic Reynolds number is assumed small and the induced magnetic field is negligible in comparison with the applied magnetic field. In addition the effects of thermal radiation and viscous dissipation are considered. The continuity, momentum, energy and concentration equations yield

$$\frac{\partial u}{\partial x} + \frac{\partial v}{\partial y} = 0, \quad (8.1)$$

$$\begin{aligned} \frac{\partial u}{\partial t} + u \frac{\partial u}{\partial x} + v \frac{\partial u}{\partial y} &= \nu \frac{\partial^2 u}{\partial y^2} + g \sin \Psi \left[\beta_T (T - T_\infty)(1 - C_\infty) + \frac{(\rho^* - \rho)}{\rho} (C - C_\infty) \right] \\ &\quad - \frac{\sigma B_0^2 u}{\rho}, \end{aligned} \quad (8.2)$$

$$\begin{aligned} \frac{\partial T}{\partial t} + u \frac{\partial T}{\partial x} + v \frac{\partial T}{\partial y} &= \alpha \frac{\partial^2 T}{\partial y^2} + \tau \left[D_B \frac{\partial T}{\partial y} \frac{\partial C}{\partial y} + \frac{D_T}{T_\infty} \left(\frac{\partial T}{\partial y} \right)^2 \right] + \frac{\mu}{(\rho c_p)_f} \left(\frac{\partial u}{\partial y} \right)^2 \\ &+ \frac{16\sigma^* T_\infty^3}{3k^*(\rho c_p)_f} \frac{\partial^2 T}{\partial y^2}, \end{aligned} \quad (8.3)$$

$$\frac{\partial C}{\partial t} + u \frac{\partial C}{\partial x} + v \frac{\partial C}{\partial y} = D_B \frac{\partial^2 C}{\partial y^2} + \frac{D_T}{T_\infty} \frac{\partial^2 T}{\partial y^2}. \quad (8.4)$$

The boundary conditions are

$$\begin{aligned} u &= U = \frac{cx}{1-a^*t}, \quad v = 0, \quad T = T_w = T_0 + \frac{A^*x}{1-a^*t}, \quad C = C_w = C_0 + \frac{D^*x}{1-a^*t} \quad \text{at } y = 0, \\ u &\rightarrow 0, \quad T \rightarrow T_\infty = T_0 + \frac{B^*x}{1-a^*t}, \quad C \rightarrow C_\infty = C_0 + \frac{E^*x}{1-a^*t} \quad \text{as } y \rightarrow \infty, \end{aligned} \quad (8.5)$$

where u and v are the velocity components along the x - and y - directions respectively, ν , ρ and σ are the kinematic viscosity, density and electrical conductivity of the fluid, g is the gravitational acceleration, β_T is the coefficient of thermal expansion, T , T_∞ , C and C_∞ are the fluid temperature, ambient fluid temperature, fluid concentration and ambient fluid concentration, $\alpha = k/(\rho c_p)_f$ is the thermal diffusivity, $\tau = (\rho c)_p/(\rho c)_f$ is the ratio between the effective heat capacity of the nanoparticle material and heat capacity of the fluid, D_B is the Brownian diffusion coefficient, D_T is the thermophoretic diffusion coefficient, k^* is the mean absorption coefficient, σ^* is the Stefan-Boltzmann constant, k is the thermal conductivity, c and a^* are positive constants having dimension T^{-1} , A^* , B^* , D^* and E^* are the dimensional constants having dimension L^{-1} and T_0 and C_0 are the reference temperature and concentration.

We now introduce the following similarity transformations

$$\begin{aligned} u &= \frac{cx}{1-a^*t} f'(\eta), \quad v = -\sqrt{\frac{\nu c}{1-a^*t}} f(\eta), \quad \eta = \sqrt{\frac{c}{\nu(1-a^*t)}} y, \\ \theta(\eta) &= \frac{T - T_\infty}{T_w - T_0}, \quad \Phi(\eta) = \frac{C - C_\infty}{C_w - C_0}. \end{aligned} \quad (8.6)$$

Now Eq. (8.1) is satisfied automatically and Eqs. (8.2) – (8.5) after using Eq. (8.6) can be reduced as follows:

$$f''' - f'^2 + f f'' - \delta^* \left(f' + \frac{1}{2} \eta f'' \right) + N_c \sin \Psi[\theta + N_r \Phi] - M f' = 0, \quad (8.7)$$

$$\frac{1}{\text{Pr}} \left(1 + \frac{4}{3}R_d\right) \theta'' + f\theta' - f'\theta - S_t f' - \delta^* \left(S_t + \theta + \frac{1}{2}\eta\theta'\right) + N_b\theta'\Phi' + N_t\theta'^2 + Ec f''^2 = 0, \quad (8.8)$$

$$\Phi'' + Sc(f\Phi' - f'\Phi) - S_m Sc f' - \delta^* Sc \left(S_m + \Phi + \frac{1}{2}\eta\Phi'\right) + \frac{N_t}{N_b}\theta'' = 0, \quad (8.9)$$

$$\begin{aligned} f'(0) &= 1, \quad f(0) = 0, \quad \theta(0) = 1 - S_t, \quad \Phi(0) = 1 - S_m, \\ f'(\infty) &= 0, \quad \theta(\infty) = 0, \quad \Phi(\infty) = 0, \end{aligned} \quad (8.10)$$

where prime indicates the differentiation with respect to η . Moreover the unsteady parameter δ^* , mixed convection parameter N_c , Buoyancy ratio N_r , Hartman number M , Prandtl number Pr , radiation parameter R_d , thermal stratification parameter S_t , Brownian motion parameter N_b , thermophoresis parameter N_t , Eckert number Ec , Schmidt number Sc and solutal stratification parameter S_m are defined by the following definitions:

$$\begin{aligned} \delta^* &= \frac{a^*}{c}, \quad N_c = \frac{g(1-a^*t)^2\beta_T}{c^2x}(1-C_\infty)(T_w - T_0), \quad N_r = \frac{(\rho^* - \rho)(C_w - C_0)}{\rho\beta_T(T_w - T_0)(1-C_\infty)}, \\ M &= \frac{\sigma B_0^2(1-a^*t)}{\rho c}, \quad \text{Pr} = \frac{\nu}{\alpha}, \quad R_d = \frac{4\sigma^*T_\infty^3}{3kk^*}, \quad S_t = \frac{B^*}{A^*}, \quad N_b = \frac{\tau D_B(C_w - C_0)}{\nu}, \\ N_t &= \frac{\tau D_T(T_w - T_0)}{\nu T_\infty}, \quad Ec = \frac{\rho U^2}{(\rho c_p)_f(T_w - T_0)}, \quad Sc = \frac{\nu}{D_B}, \quad S_m = \frac{E^*}{D^*}. \end{aligned} \quad (8.11)$$

The important physical quantities of interest in this problem are the local skin friction coefficient C_{sf} , Nusselt number Nu and Sherwood number Sh . These are given by

$$C_{sf} = \frac{\tau_w}{\frac{1}{2}\rho U^2}, \quad Nu = \frac{xq_w}{k(T_w - T_\infty)}, \quad Sh = \frac{xq_m}{D_B(C_w - C_\infty)}, \quad (8.12)$$

where the surface shear stress τ_w , wall heat flux q_w and wall mass flux q_m are given by

$$\tau_w = \mu \frac{\partial u}{\partial y} \Big|_{y=0}, \quad q_w = - \left(k + \frac{16\sigma^*T_\infty^3}{3k^*} \right) \frac{\partial T}{\partial y} \Big|_{y=0}, \quad q_m = - D_B \frac{\partial C}{\partial y} \Big|_{y=0}. \quad (8.13)$$

By using the above equations we get

$$\begin{aligned} C_{sf} \left(\frac{\text{Re}_x}{2} \right)^{1/2} &= f''(0), \quad Nu(\text{Re}_x)^{-1/2} = - \left(1 + \frac{4}{3} R_d \right) \left(\frac{1}{1 - S_t} \right) \theta'(0), \\ Sh(\text{Re}_x)^{-1/2} &= - \left(\frac{1}{1 - S_m} \right) \Phi'(0), \end{aligned} \quad (8.14)$$

where $\text{Re}_x = Ux/\nu$ is the local Reynolds number.

8.2 Homotopy analysis solutions

Initial approximations $f_0(\eta)$, $\theta_0(\eta)$ and $\Phi_0(\eta)$, auxiliary linear operators \mathcal{L}_f , \mathcal{L}_θ and \mathcal{L}_Φ and auxiliary functions \mathcal{H}_f , \mathcal{H}_θ and \mathcal{H}_Φ are taken in the forms

$$f_0(\eta) = 1 - e^{-\eta}, \quad \theta_0(\eta) = (1 - S_t)e^{-\eta}, \quad \Phi_0(\eta) = (1 - S_m)e^{-\eta}, \quad (8.15)$$

$$\mathcal{L}_f = f''' - f', \quad \mathcal{L}_\theta = \theta'' - \theta, \quad \mathcal{L}_\Phi = \Phi'' - \Phi, \quad (8.16)$$

$$\mathcal{H}_f = e^{-\eta}, \quad \mathcal{H}_\theta = e^{-\eta}, \quad \mathcal{H}_\Phi = e^{-\eta}, \quad (8.17)$$

with

$$\begin{aligned} \mathcal{L}_f [c_1 + c_2 e^\eta + c_3 e^{-\eta}] &= 0, \\ \mathcal{L}_\theta [c_4 e^\eta + c_5 e^{-\eta}] &= 0, \\ \mathcal{L}_\Phi [c_6 e^\eta + c_7 e^{-\eta}] &= 0, \end{aligned} \quad (8.18)$$

in which c_i ($i = 1 - 7$) are the constants.

If $p \in [0, 1]$ indicates the embedding parameter then the zeroth order deformation problems are constructed as follows:

$$(1 - p)\mathcal{L}_f \left[\hat{f}(\eta; p) - f_0(\eta) \right] = p\hbar_f \mathcal{H}_f \mathcal{N}_f [\hat{f}(\eta; p), \hat{\theta}(\eta; p), \hat{\Phi}(\eta; p)], \quad (8.19)$$

$$(1 - p)\mathcal{L}_\theta \left[\hat{\theta}(\eta; p) - \theta_0(\eta) \right] = p\hbar_\theta \mathcal{H}_\theta \mathcal{N}_\theta [\hat{\theta}(\eta; p), \hat{f}(\eta; p), \hat{\Phi}(\eta; p)], \quad (8.20)$$

$$(1 - p)\mathcal{L}_\Phi \left[\hat{\Phi}(\eta; p) - \Phi_0(\eta) \right] = p\hbar_\Phi \mathcal{H}_\Phi \mathcal{N}_\Phi [\hat{\Phi}(\eta; p), \hat{f}(\eta; p), \hat{\theta}(\eta; p)], \quad (8.21)$$

$$\begin{aligned}
\hat{f}'(0;p) &= 1, \quad \hat{f}(0;p) = 0, \quad \hat{f}'(\infty;p) = 0, \\
\hat{\theta}(0;p) &= 1 - S_t, \quad \hat{\theta}(\infty;p) = 0, \\
\hat{\Phi}(0;p) &= 1 - S_m, \quad \hat{\Phi}(\infty;p) = 0,
\end{aligned} \tag{8.22}$$

where \hbar_f , \hbar_θ and \hbar_ϕ are the nonzero auxiliary parameters and the nonlinear operators \mathcal{N}_f , \mathcal{N}_θ and \mathcal{N}_ϕ are given by

$$\begin{aligned}
\mathcal{N}_f \left[\hat{f}(\eta;p), \hat{\theta}(\eta;p), \hat{\Phi}(\eta;p) \right] &= \frac{\partial^3 \hat{f}(\eta;p)}{\partial \eta^3} - \left(\frac{\partial \hat{f}(\eta;p)}{\partial \eta} \right)^2 + \hat{f}(\eta;p) \frac{\partial^2 \hat{f}(\eta;p)}{\partial \eta^2} \\
&\quad - \delta^* \left(\frac{\partial \hat{f}(\eta;p)}{\partial \eta} + \frac{1}{2} \eta \frac{\partial^2 \hat{f}(\eta;p)}{\partial \eta^2} \right) + N_c \sin \Psi[\hat{\theta}(\eta;p) \\
&\quad + N_r \hat{\Phi}(\eta;p)] - M \frac{\partial \hat{f}(\eta;p)}{\partial \eta},
\end{aligned} \tag{8.23}$$

$$\begin{aligned}
\mathcal{N}_\theta \left[\hat{\theta}(\eta;p), \hat{f}(\eta;p), \hat{\Phi}(\eta;p) \right] &= \frac{1}{\text{Pr}} \left(1 + \frac{4}{3} R_d \right) \frac{\partial^2 \hat{\theta}(\eta;p)}{\partial \eta^2} + \hat{f}(\eta;p) \frac{\partial \hat{\theta}(\eta;p)}{\partial \eta} - \hat{\theta}(\eta;p) \frac{\partial \hat{f}(\eta;p)}{\partial \eta} \\
&\quad - S_t \frac{\partial \hat{f}(\eta;p)}{\partial \eta} - \delta^* \left(S_t + \hat{\theta}(\eta;p) + \frac{1}{2} \eta \frac{\partial \hat{\theta}(\eta;p)}{\partial \eta} \right) + N_t \left(\frac{\partial \hat{\theta}(\eta;p)}{\partial \eta} \right)^2 \\
&\quad + N_b \frac{\partial \hat{\theta}(\eta;p)}{\partial \eta} \frac{\partial \hat{\Phi}(\eta;p)}{\partial \eta} + E_c \left(\frac{\partial^2 \hat{\theta}(\eta;p)}{\partial \eta^2} \right)^2,
\end{aligned} \tag{8.24}$$

$$\begin{aligned}
\mathcal{N}_\phi \left[\hat{\Phi}(\eta;p), \hat{f}(\eta;p), \hat{\theta}(\eta;p) \right] &= \frac{\partial^2 \hat{\Phi}(\eta;p)}{\partial \eta^2} + S_c \left(\hat{f}(\eta;p) \frac{\partial \hat{\Phi}(\eta;p)}{\partial \eta} - \hat{\Phi}(\eta;p) \frac{\partial \hat{f}(\eta;p)}{\partial \eta} \right) \\
&\quad - S_m S_c \frac{\partial \hat{f}(\eta;p)}{\partial \eta} - \delta^* S_c \left(S_m + \hat{\Phi}(\eta;p) + \frac{1}{2} \eta \frac{\partial \hat{\Phi}(\eta;p)}{\partial \eta} \right) \\
&\quad + \frac{N_t}{N_b} \frac{\partial^2 \hat{\theta}(\eta;p)}{\partial \eta^2}.
\end{aligned} \tag{8.25}$$

The resulting problems at m^{th} order can be presented in the following forms

$$\mathcal{L}_f [f_m(\eta) - \chi_m f_{m-1}(\eta)] = \hbar_f \mathcal{R}_{f,m}(\eta), \tag{8.26}$$

$$\mathcal{L}_\theta [\theta_m(\eta) - \chi_m \theta_{m-1}(\eta)] = \hbar_\theta \mathcal{R}_{\theta,m}(\eta), \quad (8.27)$$

$$\mathcal{L}_\Phi [\Phi_m(\eta) - \chi_m \Phi_{m-1}(\eta)] = \hbar_\Phi \mathcal{R}_{\Phi,m}(\eta), \quad (8.28)$$

$$f'_m(0) = f_m(0) = f'_m(\infty) = \theta_m(0) = \theta_m(\infty) = \Phi_m(0) = \Phi_m(\infty) = 0, \quad (8.29)$$

$$\mathcal{R}_{f,m}(\eta) = f'''_{m-1} + \sum_{k=0}^{m-1} [f_{m-1-k} f''_k - f'_{m-1-k} f'_k] - \delta^* \left(f'_{m-1} + \frac{1}{2} \eta f''_{m-1} \right) + N_c \sin \Psi [\theta_{m-1} + N_r \Phi_{m-1}] - M f'_{m-1}, \quad (8.30)$$

$$\begin{aligned} \mathcal{R}_{\theta,m}(\eta) &= \frac{1}{\text{Pr}} \left(1 + \frac{4}{3} R_d \right) \theta''_{m-1} + \sum_{k=0}^{m-1} (f_{m-1-k} \theta'_k - \theta_{m-1-k} f'_k) - S_t f'_{m-1} - \delta^* \left(S_t + \theta_{m-1} + \frac{1}{2} \eta \theta'_{m-1} \right) \\ &+ \sum_{k=0}^{m-1} (N_b \theta'_{m-1-k} \Phi'_k + N_t \theta'_{m-1-k} \theta'_k + E c f''_{m-1-k} f''_k), \end{aligned} \quad (8.31)$$

$$\mathcal{R}_{\Phi,m}(\eta) = \Phi''_{m-1} + S c \sum_{k=0}^{m-1} (f_{m-1-k} \Phi'_k - \Phi_{m-1-k} f'_k) - S_m S c f'_{m-1} - \delta^* S c \left(S_m + \Phi_{m-1} + \frac{1}{2} \eta \Phi'_{m-1} \right) + \frac{N_t}{N_b} \theta''_{m-1}, \quad (8.32)$$

$$\chi_m = \begin{cases} 0, & m \leq 1 \\ 1, & m > 1 \end{cases}. \quad (8.33)$$

The general solutions (f_m, θ_m, Φ_m) subject to the special solutions $(f_m^*, \theta_m^*, \Phi_m^*)$ are

$$\begin{aligned} f_m(\eta) &= f_m^*(\eta) + c_1 + c_2 e^\eta + c_3 e^{-\eta}, \\ \theta_m(\eta) &= \theta_m^*(\eta) + c_4 e^\eta + c_5 e^{-\eta}, \\ \Phi_m(\eta) &= \Phi_m^*(\eta) + c_6 e^\eta + c_7 e^{-\eta}, \end{aligned} \quad (8.34)$$

where the constants c_i ($i = 1, 2, \dots, 7$) through the boundary conditions (8.29) have the values

$$\begin{aligned} c_2 &= c_4 = c_6 = 0, \quad c_1 = -c_3 - f_m^*(0), \quad c_3 = \left. \frac{\partial f_m^*(\eta)}{\partial \eta} \right|_{\eta=0}, \\ c_5 &= -\theta_m^*(0), \quad c_7 = -\Phi_m^*(0). \end{aligned} \quad (8.35)$$

8.3 Convergence of the homotopy solutions

Now the solutions of Eqs. (8.7 – 8.9) subject to the boundary conditions (8.10) are computed by means of homotopy analysis method. The convergence of the series solutions is highly

dependent upon the auxiliary parameters \hbar_f , \hbar_θ and \hbar_Φ . For valid ranges of these parameters, we have sketched the \hbar -curves at 15th-order of approximations (see Fig. 8.2). We can see that the admissible values of \hbar_f , \hbar_θ and \hbar_Φ are $-1.5 \leq \hbar_f \leq -0.7$, $-1.3 \leq \hbar_\theta \leq -0.4$ and $-1.2 \leq \hbar_\Phi \leq -0.4$. The residual errors are calculated for momentum, energy and concentration equations by the expressions

$$\begin{aligned}\Delta_m^f &= \int_0^1 [R_m^f(\eta, \hbar_f)]^2 d\eta, \\ \Delta_m^\theta &= \int_0^1 [R_m^\theta(\eta, \hbar_\theta)]^2 d\eta, \\ \Delta_m^\Phi &= \int_0^1 [R_m^\Phi(\eta, \hbar_\Phi)]^2 d\eta.\end{aligned}\tag{8.36}$$

In Figs. (8.3 – 8.5), the \hbar -curves for residual error of f , θ and Φ are sketched in order to get the admissible range for \hbar . It is noted that correct result up to 4th decimal place is obtained by choosing the values of \hbar from this range. Further the series solutions converge in the whole region of η ($0 < \eta < \infty$) when $\hbar_f = -1.2$, $\hbar_\theta = -1.1$ and $\hbar_\Phi = -0.9$.

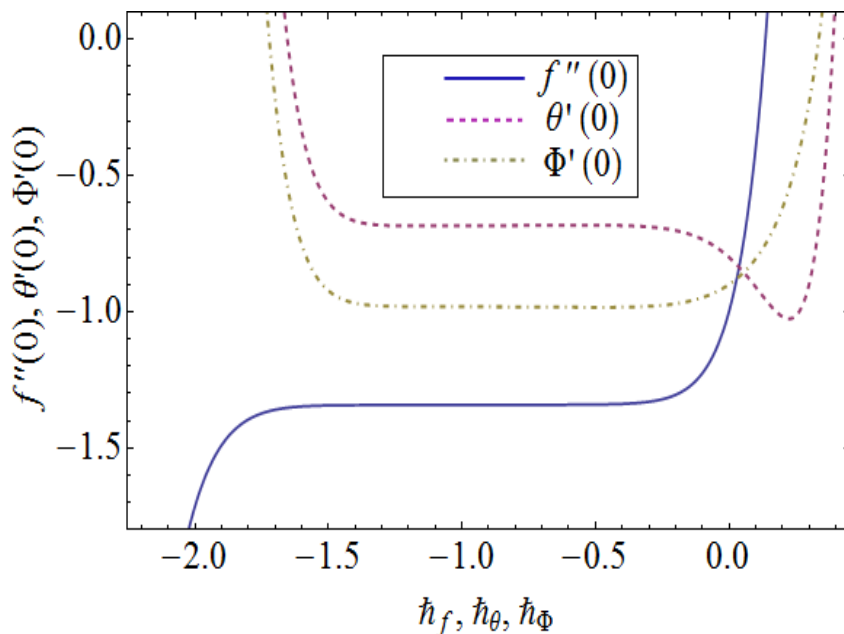


Fig. 8.2. \hbar - curves for $f''(0)$, $\theta'(0)$ and $\Phi'(0)$.

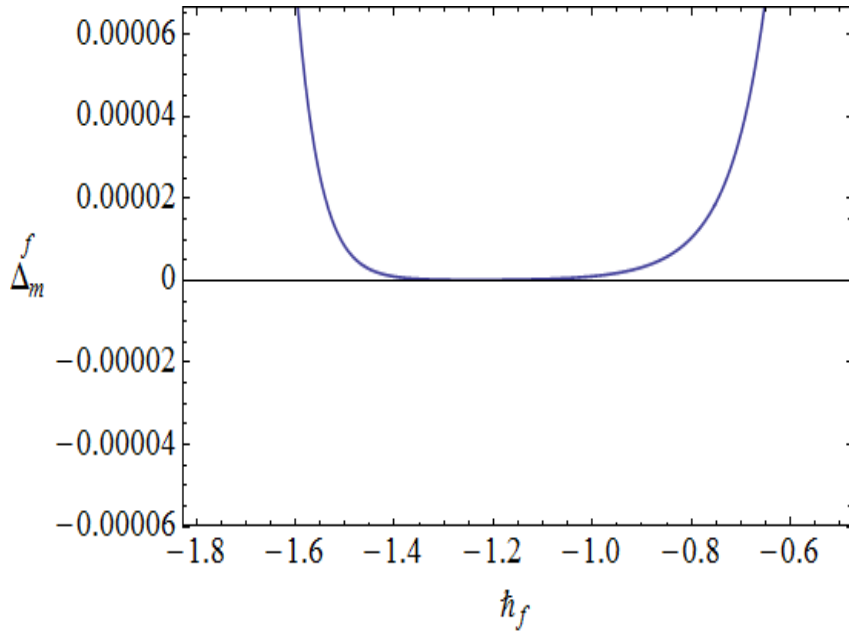


Fig. 8.3: h_f -curve for the residual error Δ_m^f .

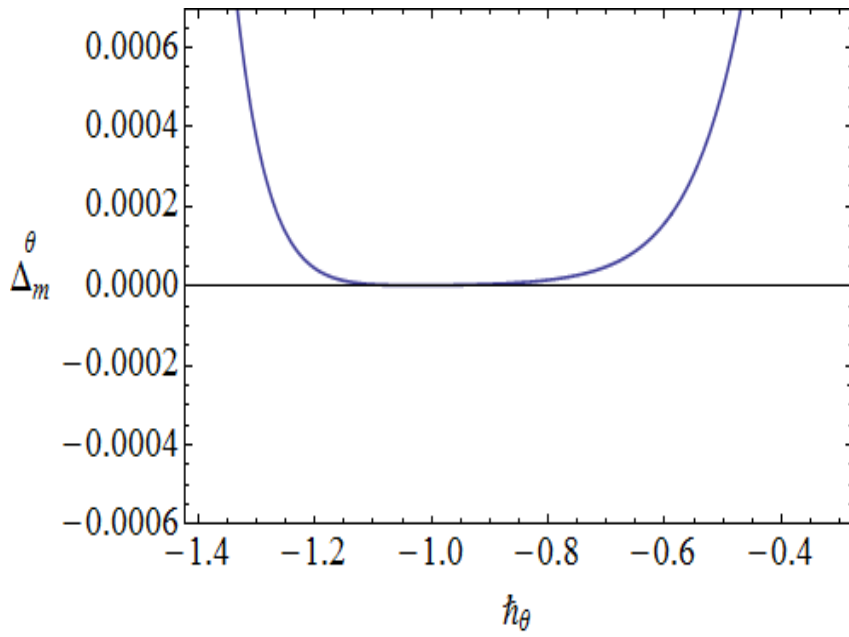


Fig. 8.4: h_θ -curve for the residual error Δ_m^θ .

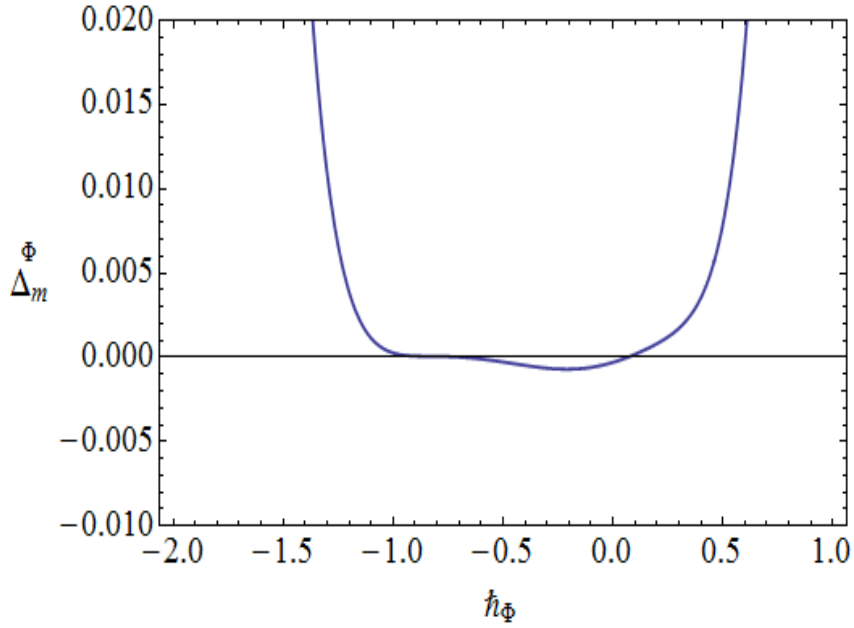


Fig. 8.5: h_Φ -curve for the residual error Δ_m^Φ .

Table 8.1: Convergence of HAM solutions for different order of approximations when $M = 0.7$, $N_c = R_d = 0.4$, $N_r = 0.3$, $\Psi = \pi/4$, $\text{Pr} = 1.2$, $S_t = 0.2$, $\delta^* = N_b = 0.5$, $N_t = 0.1$, $Sc = 0.9$, $Ec = 0.6$ and $S_m = 0.1$.

Order of approximations	$-f''(0)$	$-\theta'(0)$	$-\phi'(0)$
1	1.358	0.7193	0.9608
5	1.341	0.6832	0.9856
10	1.342	0.6839	0.9815
14	1.343	0.6855	0.9810
20	1.343	0.6868	0.9808
25	1.343	0.6876	0.9809
29	1.343	0.6880	0.9810
35	1.343	0.6887	0.9810
40	1.343	0.6887	0.9810
45	1.343	0.6887	0.9810

8.4 Interpretation of results

The effects of different parameters on the velocity, temperature and concentration fields are investigated through plots in this section. Figs. (8.6 – 8.12) exhibit the dimensionless velocity profiles for different values of inclination angle Ψ , unsteady parameter δ^* , Hartman number M , mixed convection parameter N_c , buoyancy ratio N_r , thermal stratification parameter S_t and solutal stratification parameter S_m . Variation in velocity with an increase in angle of inclination Ψ can be seen from Fig. 8.6. It is noticed that with an increase in Ψ i.e. when the sheet moves from horizontal to vertical direction, the strength of buoyancy force increases and consequently the velocity and boundary layer thickness increase. Influence of unsteady parameter δ^* on the velocity profile f' can be seen in Fig. 8.7. Increasing values of δ^* indicate smaller stretching rate in the x - direction which eventually decrease the velocity and boundary layer thickness. The effects of Hartman number M are displayed in Fig. 8.8, which shows that an increase in M reduces the velocity profile. It is because of the reason that Lorentz force acts as a retarding force. Such retarding force enhances the frictional resistance opposing the fluid motion in the momentum boundary layer thickness. Fig. 8.9 elucidates the behavior of mixed convection parameter N_c on the velocity profile. This Fig. shows that the values of velocity function f' and the boundary layer thickness increase by increasing N_c . This is because a larger value of N_c accompanies a stronger buoyancy force which leads to an increase in velocity. The effects of buoyancy ratio N_r on the velocity profile are depicted in Fig. 8.10. This Fig. shows that velocity profile enhances when N_r increases. N_r is the ratio of concentration to thermal buoyancy forces. With an increase in buoyancy ratio parameter, concentration buoyancy force increases which results in higher velocity profile. Fig. 8.11 is plotted to show the influence of thermal stratification parameter S_t on the velocity profile $f'(\eta)$. With an increase in thermal stratification parameter the density of fluid in the lower region is high than the upper region. So thermal stratification reduces the convective flow between the sheet and ambient fluid. Therefore velocity profile decreases. Behavior of solutal stratification parameter S_m on velocity profile is sketched in Fig. 8.12. It is depicted that velocity and boundary layer thickness decrease with an increase in solutal stratification parameter.

Effects of Prandtl number Pr , unsteady parameter δ^* , Brownian motion parameter N_b , thermophoresis parameter N_t , thermal stratification parameter S_t , radiation parameter R_d and

Eckert number Ec on the temperature profile θ are shown in the Figs. (8.13 – 8.19). Fig. 8.13 indicates that temperature profile θ is a decreasing function of Pr . In fact thermal diffusivity decreases by increasing Pr and thus heat diffuses away slowly from the heated surface. Effect of unsteady parameter δ^* on the temperature is analyzed in Fig. 8.14. It is observed that the temperature and thermal boundary layer thickness are decreasing function of δ^* . Fig. 8.15 illustrates the effects of Brownian motion parameter N_b on temperature profile θ . When N_b increases, random motion of nanoparticles increases. Therefore collision of particles increases and kinetic energy converted to heat energy. Hence temperature profile θ increases for an increase in N_b . The behavior of N_t on the temperature profile is similar to that of N_b (see Fig. 8.16). Also the temperature profile θ and thermal boundary layer thickness decrease when the thermal stratification parameter S_t increases (see Fig. 8.17). Because temperature difference gradually decreases between the sheet and ambient fluid which causes a reduction in the temperature profile. Radiation effects on the temperature profile are displayed in Fig. 8.18. An increase in R_d enhances the heat flux from the sheet which gives rise to the fluid's temperature. Therefore the temperature profile and thermal boundary layer increase with an increase in R_d . Fig. 8.19 depicts that temperature is an increasing function of the Eckert number Ec . Eckert number is defined as the ratio of kinetic energy to enthalpy. With the increase in Ec , kinetic energy increases which consequently enhances temperature.

Figs. (8.20 – 8.24) illustrate the effects of Schmidt number Sc , unsteady parameter δ^* , Brownian motion parameter N_b , thermophoresis parameter N_t and concentration stratification number S_m on the dimensionless nanoparticle volume fraction profile Φ . It is observed that the mass fraction Φ and the associated boundary layer decrease for an increase in Schmidt number Sc (see Fig. 8.20). It is due to the fact that an increase in Sc reduces the molecular diffusivity. Fig. 8.21 indicates that an increase in the unsteady parameter δ^* decreases the concentration profile. The effects of Brownian motion parameter N_b on the concentration profile are depicted in Fig. 8.22. This Fig. shows that Φ decreases when N_b increases. Also the concentration profile Φ increases when thermophoresis parameter N_t is increased (see Fig. 8.23). Variations of solutal stratification parameter S_m on the dimensionless nanoparticle volume fraction profile Φ can be seen in Fig. 8.24. It is noted that there is a decrease in concentration profile when S_m is increased. Infact an increase in S_m decreases the concentration difference between the sheet

and ambient fluid.

Table 8.1 shows the convergence of the series solutions. It is observed that convergence for velocity, temperature and concentration is achieved at 14th, 35th and 29th order of approximations respectively. Table 8.2 shows the comparison of the present results with the numerical solution of Ibrahim and Shankar [64] in limiting case. It is found that our solution has good agreement with the limiting numerical solution. In Table 8.3 some numerical values of skin friction coefficient are given. Tabular values show that skin friction coefficient decreases by increasing Ψ , N_c and N_r while it increases for larger values of M , δ^* , S_t and S_m . Numerical values of local Nusselt and Sherwood numbers for different emerging parameters are presented in Table 8.4. It is noted that local Nusselt number increases for larger values of S_t , S_m and Pr . However it decreases for larger values of N_b , N_t and Sc . It is noted that local Sherwood number decreases by increasing N_t , S_t and Pr and it increases for larger values of N_b , S_m and Sc .

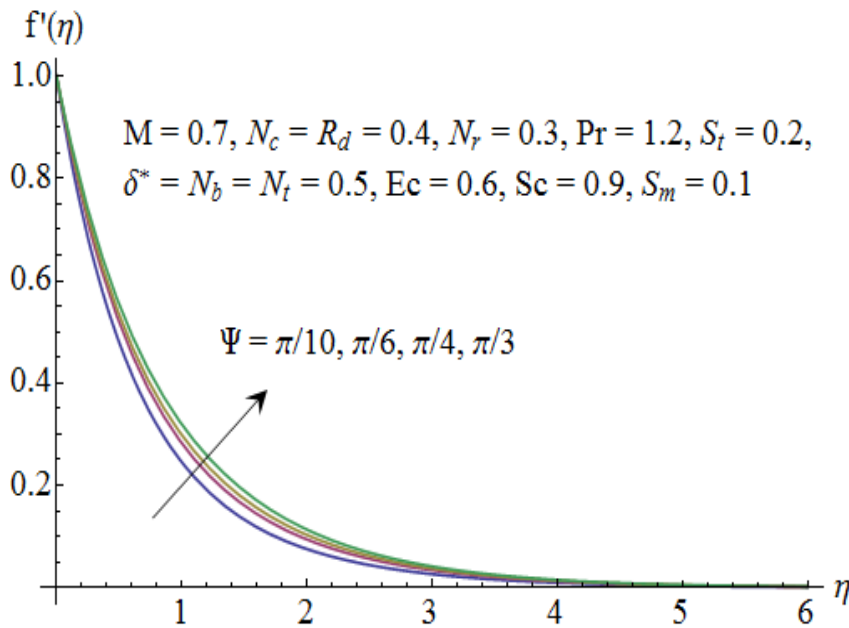


Fig. 8.6: Influence of Ψ on $f'(\eta)$.

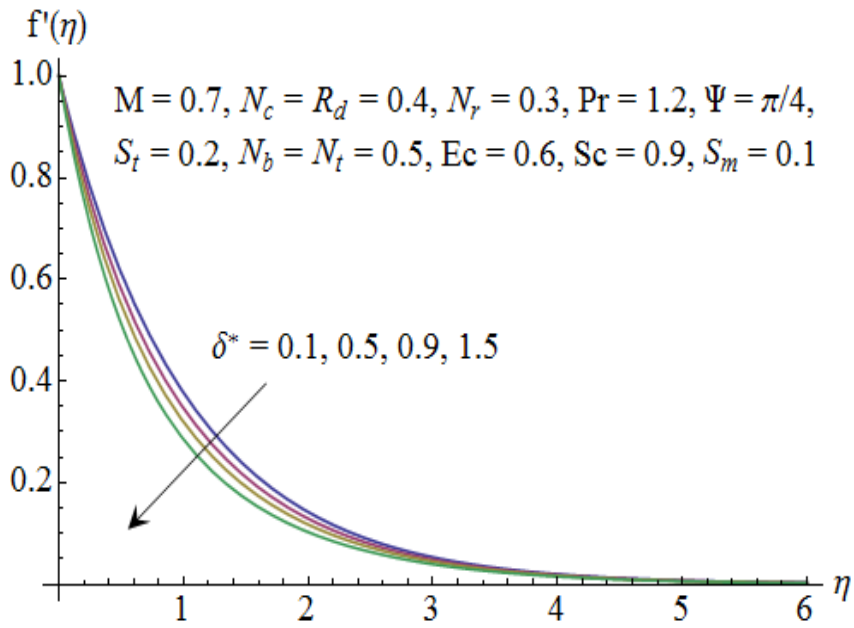


Fig. 8.7: Influence of δ^* on $f'(\eta)$.

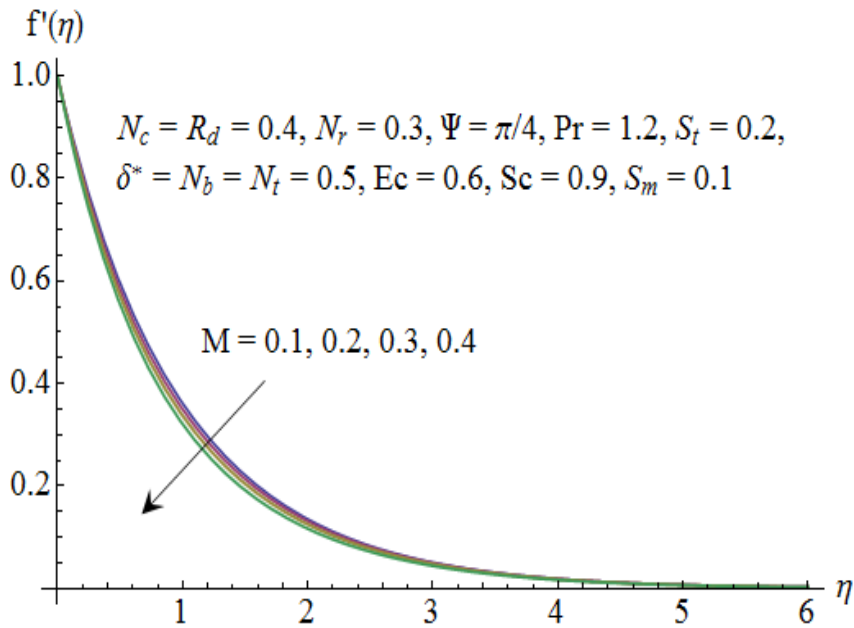


Fig. 8.8: Influence of M on $f'(\eta)$.

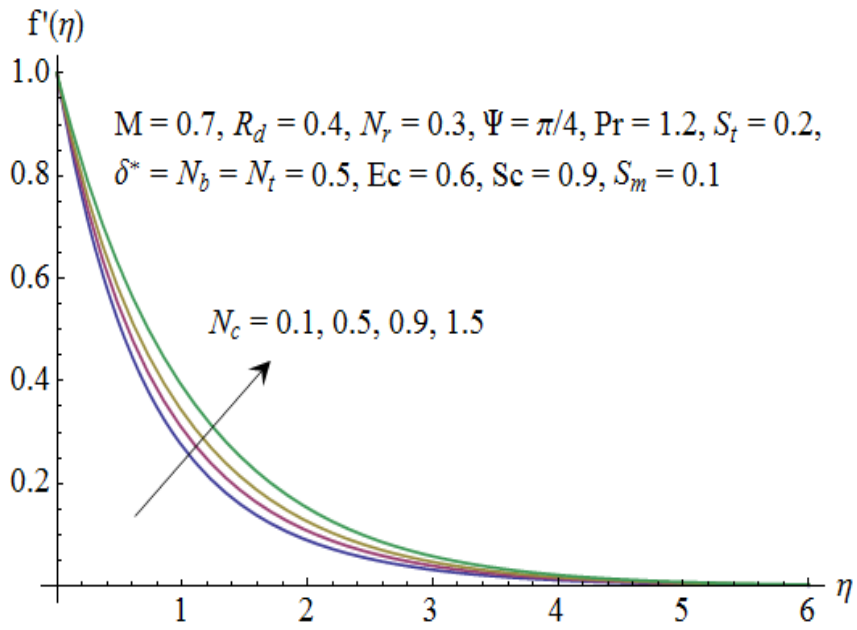


Fig. 8.9: Influence of N_c on $f'(\eta)$.

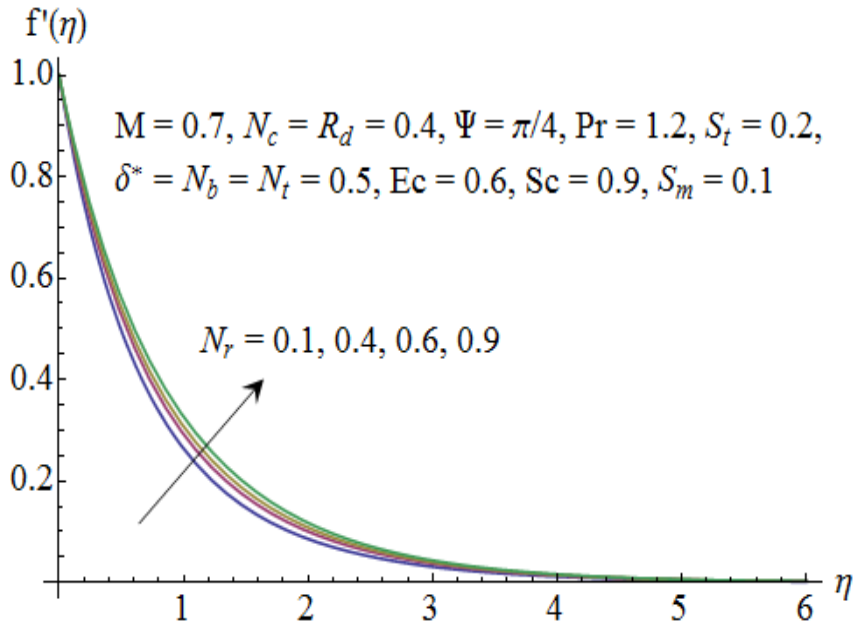


Fig. 8.10: Influence of N_r on $f'(\eta)$.

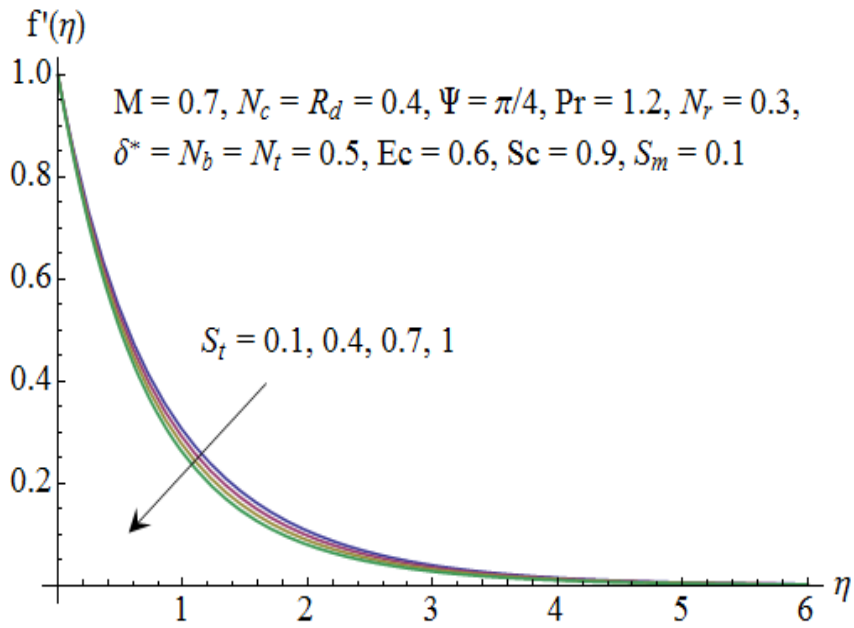


Fig. 8.11: Influence of S_t on $f'(\eta)$.

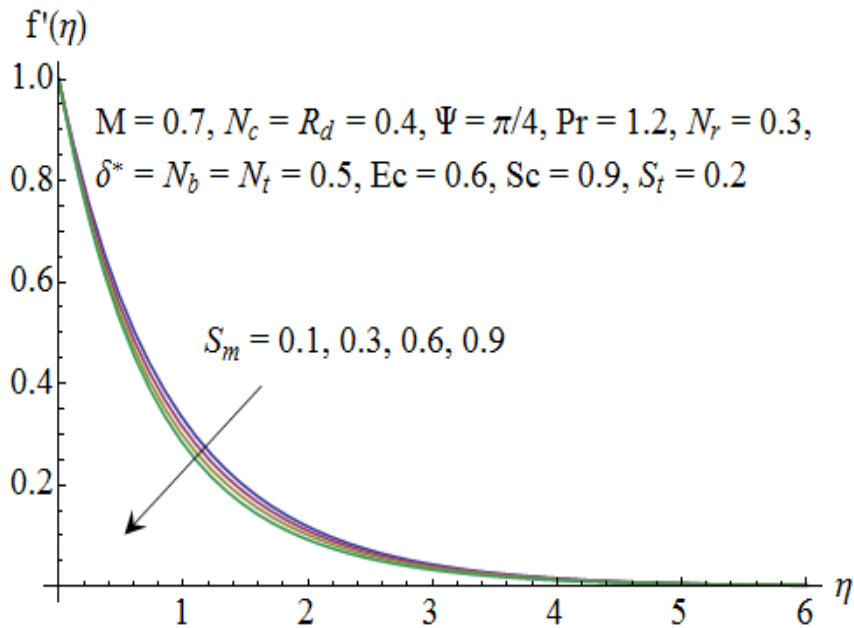


Fig. 8.12: Influence of S_m on $f'(\eta)$.

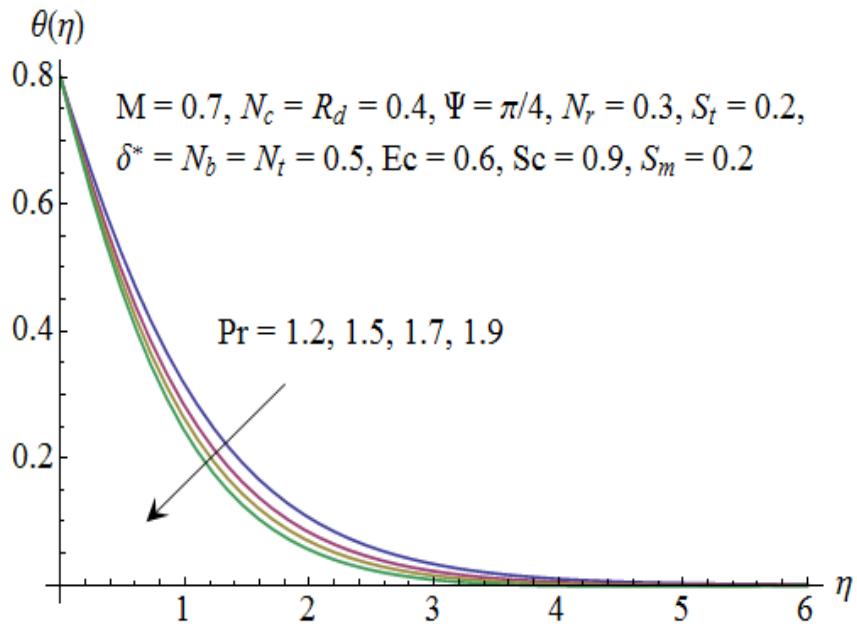


Fig. 8.13: Influence of Pr on $\theta(\eta)$.

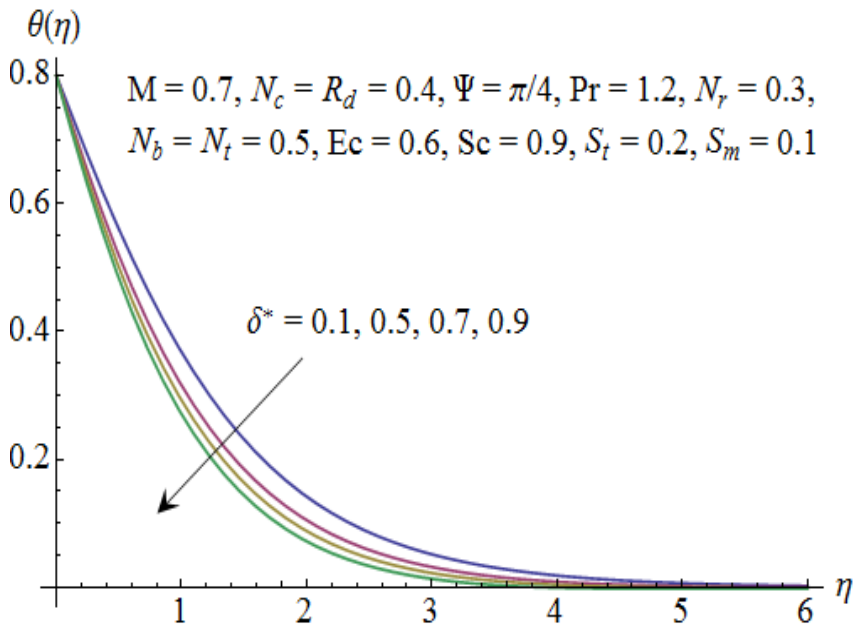


Fig. 8.14: Influence of δ^* on $\theta(\eta)$.

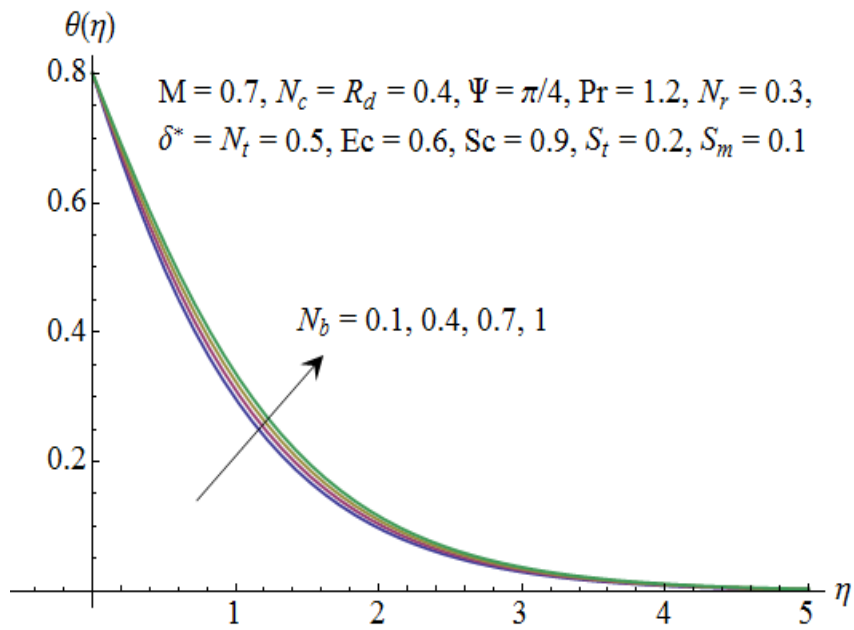


Fig. 8.15: Influence of N_b on $\theta(\eta)$.

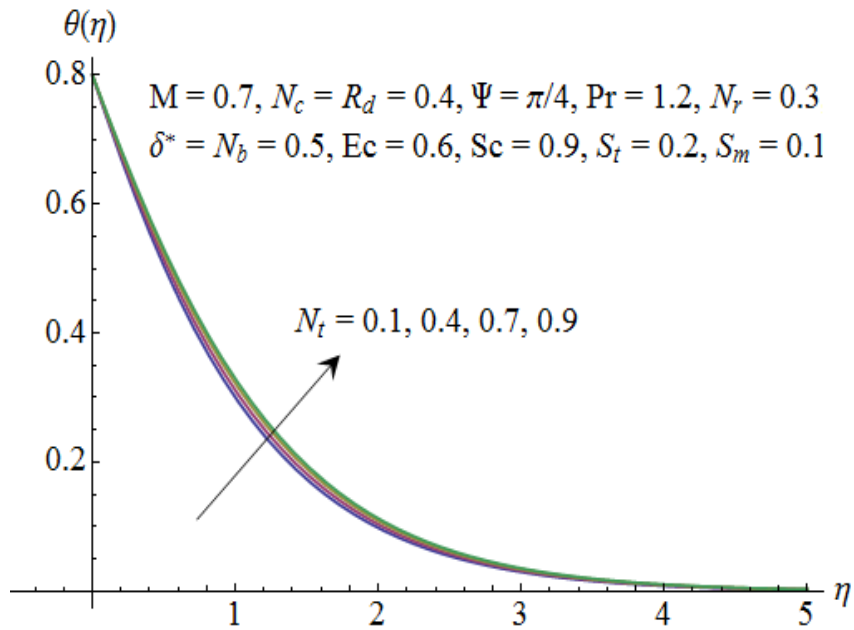


Fig. 8.16: Influence of N_t on $\theta(\eta)$.

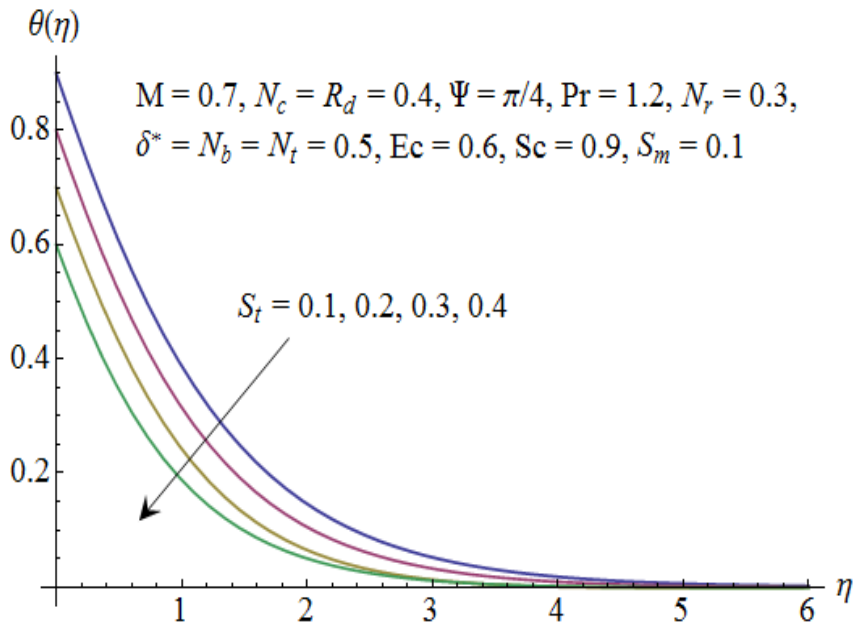


Fig. 8.17: Influence of S_t on $\theta(\eta)$.

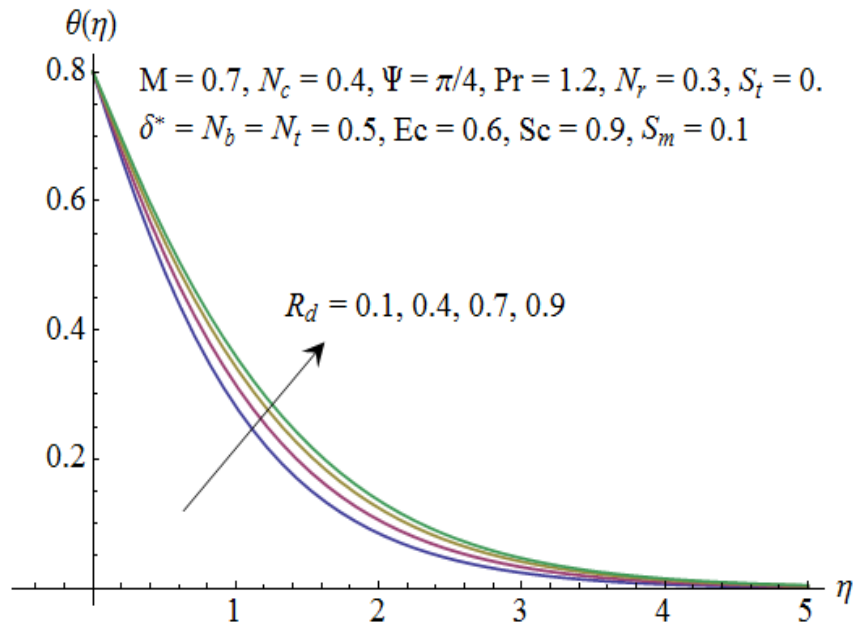


Fig. 8.18: Influence of R_d on $\theta(\eta)$.

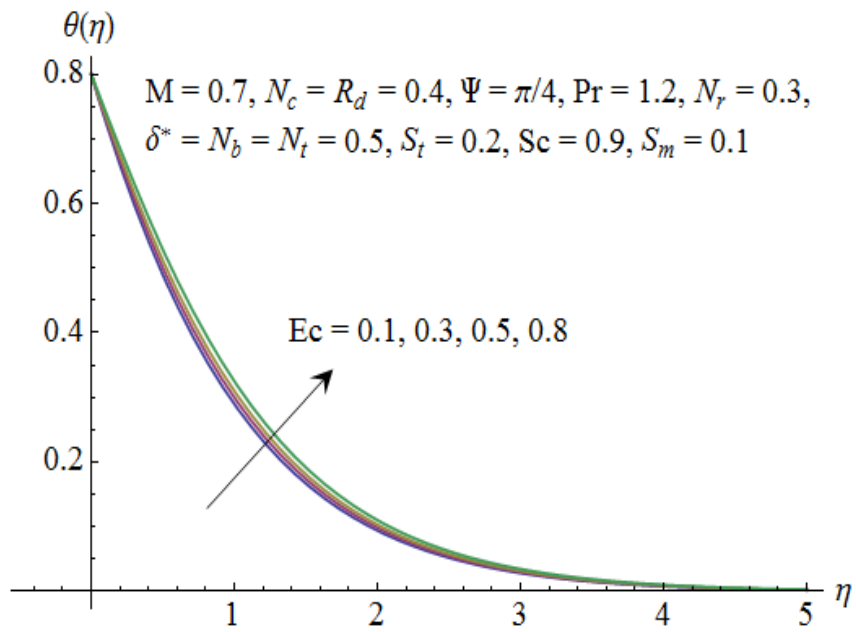


Fig. 8.19: Influence of Ec on $\theta(\eta)$.

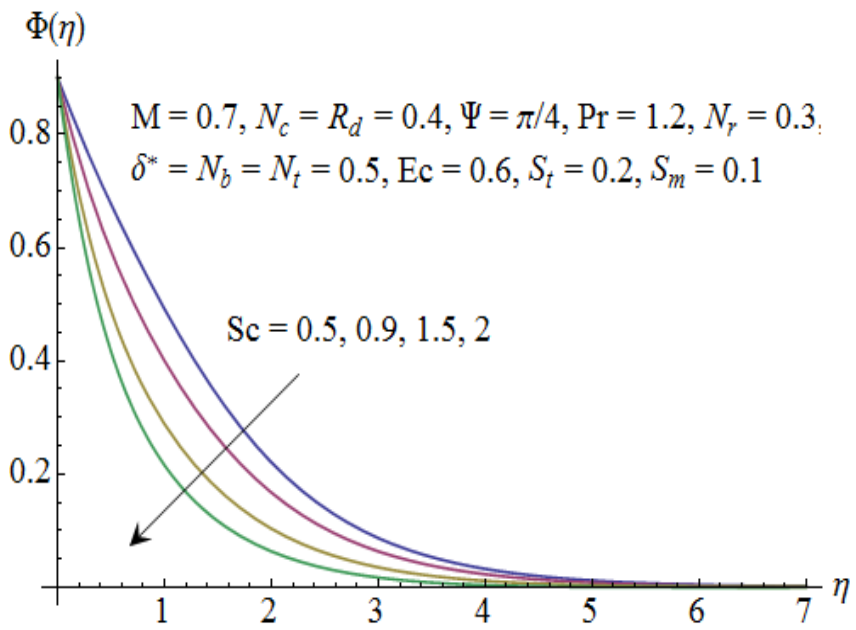


Fig. 8.20: Influence of Sc on $\Phi(\eta)$.

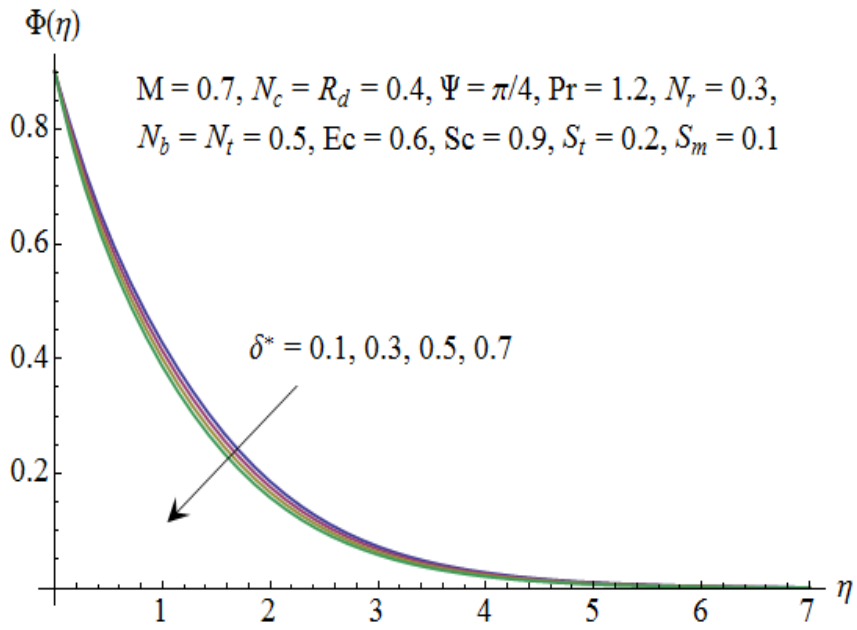


Fig. 8.21: Influence of δ^* on $\Phi(\eta)$.

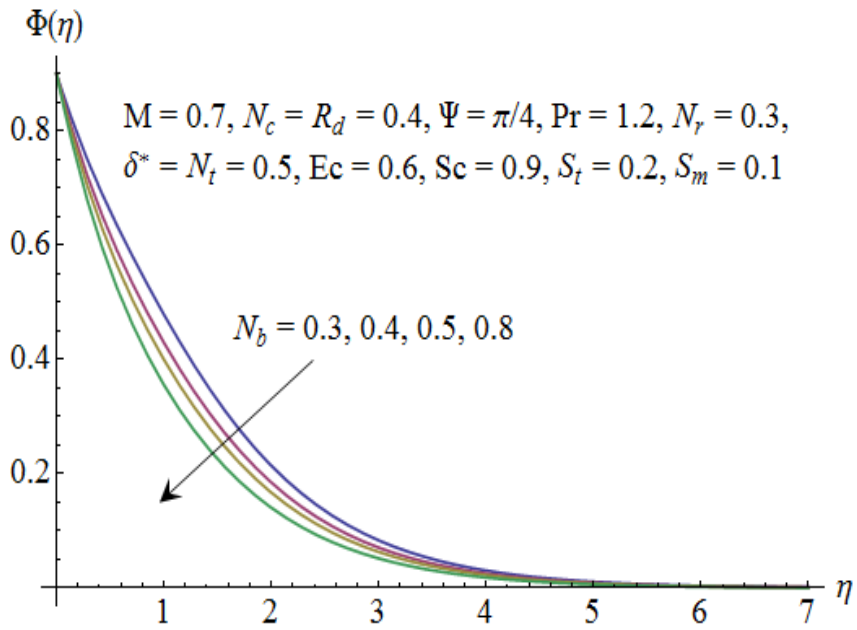


Fig. 8.22: Influence of N_b on $\Phi(\eta)$.

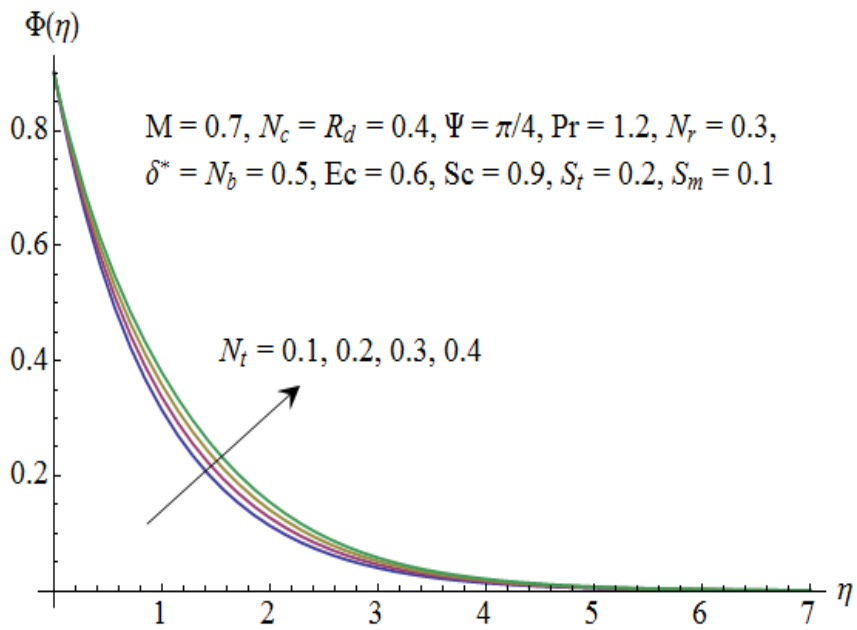


Fig. 8.23: Influence of N_t on $\Phi(\eta)$.

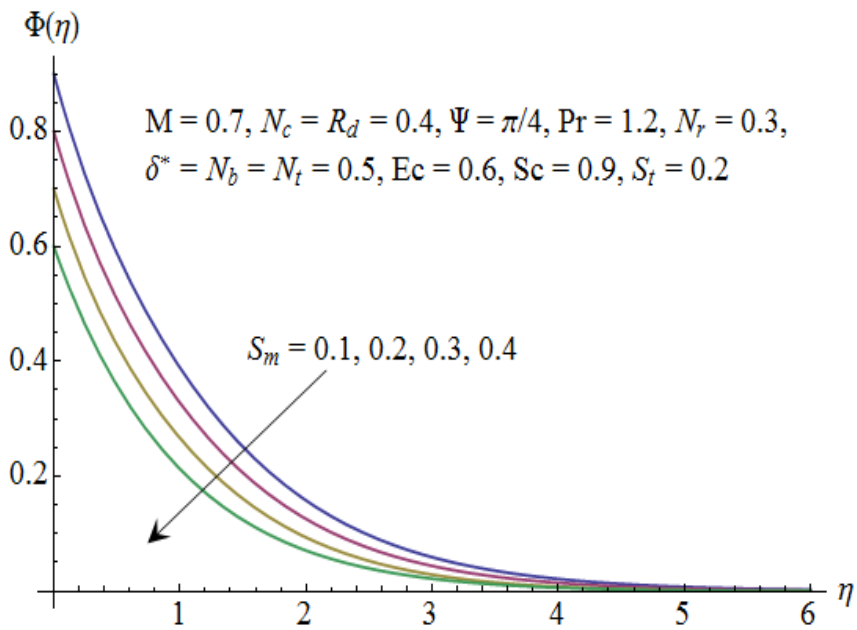


Fig. 8.24: Influence of S_m on $\Phi(\eta)$.

Table 8.2: Comparison of skin friction coefficient with Ibrahim and Shankar [64] when $N_c = R_d = N_r = \Psi = \text{Pr} = S_t = \delta^* = N_b = N_t = Sc = Ec = S_m = 0$.

M	Ibrahim and Shankar [64]	Present results
0	1.2808	1.2808
1	1.4142	1.4142
5	2.4494	2.4494

Table 8.3: Numerical values of skin friction coefficient for different parameters when $N_b = 0.9$, $N_t = 0.2$, $\text{Pr} = 1.2$, $Sc = 0.9$, $R_d = 0.4$ and $Ec = 0.6$.

Ψ	M	λ	N_r	δ	S_t	S_m	$-f''(0)$
$\pi/6$	0.7	0.4	0.3	0.6	0.1	0.1	1.365
$\pi/3$							1.294
$\pi/2$							1.269
$\pi/4$	0.5						1.252
	0.6						1.289
	0.8						1.360
	0.7	0.1					1.428
		0.3					1.359
		0.5					1.291
		0.4	0.5				1.306
			0.6				1.297
			0.7				1.287
			0.3	0.1			1.169
				0.2			1.203
				0.3			1.235
				0.6	0.1		1.325
					0.2		1.342
					0.3		1.359
					0.1	0.2	1.330
						0.3	1.336
						0.4	1.341

Table 8.4: Numerical values of Nusselt and Sherwood numbers for different parameters when $M = 0.7$, $N_c = 0.4$, $N_r = 0.3$, $\Psi = \pi/4$, $R_d = 0.4$, $\delta^* = 0.6$ and $Ec = 0.6$.

S_t	S_m	N_b	N_t	Pr	Sc	$-\left(1 + \frac{4}{3}R_d\right)\left(\frac{1}{1-S_t}\right)\theta'(0)$	$-\left(\frac{1}{1-S_m}\right)\phi'(0)$
0.1	0.1	0.9	0.2	1.2	0.9	1.078	1.197
0.2						1.190	1.193
0.3						1.334	1.189
0.1	0.2					1.080	1.333
	0.3					1.082	1.511
	0.4					1.083	1.746
	0.1	0.5				1.209	1.157
		0.7				1.142	1.183
		1.0				1.047	1.201
		0.9	0.1			1.078	1.197
			0.3			1.047	1.142
			0.5			1.017	1.093
			0.2	1.5		1.215	1.187
				1.7		1.294	1.183
				2.0		1.398	1.177
				1.2	0.5	1.141	0.8375
					0.7	1.105	1.028
					1.0	1.066	1.275

8.5 Concluding remarks

MHD unsteady flow of viscous nanofluid due to an inclined stretching sheet has been studied. Effects of different parameters on the velocity, temperature and concentration profiles are analyzed. The following observations are worth mentioning.

- Angle of inclination enhances the velocity.
- Velocity profile decreases with an increase in thermal and solutal stratification parameters.

- Increase in the mixed convection parameter enhances the velocity profile.
- Thermal stratification parameter reduces the temperature field.
- Concentration profile decreases with the increase in solutal stratification parameter.
- Impact of thermophoresis parameter and Schmidt number on the concentration profile is opposite.
- Higher values of solutal stratification parameter correspond to larger values of local Nusselt and Sherwood numbers.

Chapter 9

Magnetohydrodynamic stagnation point flow of Jeffrey nanofluid with Newtonian heating

The purpose of present chapter is to explore the stagnation point flow of Jeffrey nanofluid towards a stretching surface with Newtonian heating. Fluid is electrically conducting in the presence of applied magnetic field. Governing nonlinear ordinary differential system is computed for the convergent solutions. Results of velocity, temperature and concentration fields are calculated in series forms. Effects of different parameters on the velocity, temperature and concentration profiles are shown and analyzed. Skin friction coefficient, Nusselt and Sherwood numbers are also computed and examined.

9.1 Flow equations

The extra stress tensor for Jeffrey fluid is

$$\mathbf{S} = \frac{\mu}{1 + \lambda_1} \left[\mathbf{A}_1 + \lambda_2 \frac{d\mathbf{A}_1}{dt} \right]. \quad (9.1)$$

In above expressions μ is the dynamic viscosity, λ_1 is the ratio of relaxation to retardation times, λ_2 is the retardation time, \mathbf{A}_1 is the first Rivlin-Erickson tensor, d/dt is the material

derivative defined as

$$\frac{d}{dt} = \frac{\partial}{\partial t} + (\mathbf{V} \cdot \nabla). \quad (9.2)$$

Eq. (9.1) reduces to a Newtonian fluid when $\lambda_1 = \lambda_2 = 0$.

9.2 Problem formulation

Let us consider the steady two-dimensional stagnation point flow of Jeffrey nanofluid towards a stretching surface-. The x -axis is taken along the stretching surface in the direction of motion and y -axis is perpendicular to it. A uniform transverse magnetic field of strength B_0 is applied parallel to the y -axis. It is assumed that the induced magnetic field and the electric field effects are negligible. Effects of Brownian motion and thermophoresis are presented. Further, the surface exhibits Newtonian heating boundary condition. The boundary layer flow problems are

$$\frac{\partial u}{\partial x} + \frac{\partial v}{\partial y} = 0, \quad (9.3)$$

$$\begin{aligned} u \frac{\partial u}{\partial x} + v \frac{\partial u}{\partial y} &= \frac{\mu}{1 + \lambda_1} \left[\frac{\partial^2 u}{\partial y^2} + \lambda_2 \left(\frac{\partial u}{\partial y} \frac{\partial^2 u}{\partial x \partial y} + u \frac{\partial^3 u}{\partial x \partial y^2} - \frac{\partial u}{\partial x} \frac{\partial^2 u}{\partial y^2} + v \frac{\partial^3 u}{\partial y^3} \right) \right] \\ &+ U_\infty \frac{\partial U_\infty}{\partial x} + \frac{\sigma B_0^2}{\rho} (U_\infty - u), \end{aligned} \quad (9.4)$$

$$u \frac{\partial T}{\partial x} + v \frac{\partial T}{\partial y} = \alpha \frac{\partial^2 T}{\partial y^2} + \tau \left[D_B \frac{\partial T}{\partial y} \frac{\partial C}{\partial y} + \frac{D_T}{T_\infty} \left(\frac{\partial T}{\partial y} \right)^2 \right], \quad (9.5)$$

$$u \frac{\partial C}{\partial x} + v \frac{\partial C}{\partial y} = D_B \frac{\partial^2 C}{\partial y^2} + \frac{D_T}{T_\infty} \frac{\partial^2 T}{\partial y^2}, \quad (9.6)$$

$$\begin{aligned} u &= u_w(x) = cx, \quad v = 0, \quad \frac{\partial T}{\partial y} = -h_s T, \quad C = C_w \text{ at } y = 0, \\ u &\rightarrow dx, \quad T \rightarrow T_\infty, \quad C \rightarrow C_\infty \text{ as } y \rightarrow \infty. \end{aligned} \quad (9.7)$$

where u and v are the velocity components along the x - and y - directions respectively, μ , ρ and σ are the dynamic viscosity, density and electrical conductivity of the fluid, λ_1 is the ratio of relaxation to retardation times, λ_2 is the retardation time, U_∞ is the free stream

velocity, T , T_∞ , C_w and C_∞ are the fluid temperature, ambient fluid temperature, constant wall concentration and ambient fluid concentration, $\tau = (\rho c)_p/(\rho c)_f$ is the ratio between the effective heat capacity of the nanoparticle material and heat capacity of the fluid, D_B is the Brownian diffusion coefficient, D_T is the thermophoretic diffusion coefficient, $\alpha = k/(\rho c)_f$ is the thermal diffusivity and h_s is the heat transfer parameter.

We now use the following similarity transformations

$$u = cx f'(\eta), \quad v = -\sqrt{\nu c} f(\eta), \quad \eta = \sqrt{\frac{c}{\nu}} y, \quad \theta(\eta) = \frac{T - T_\infty}{T_\infty}, \quad \Phi(\eta) = \frac{C - C_\infty}{C_w - C_\infty}. \quad (9.8)$$

Eq. (9.3) is satisfied automatically and Eqs. (9.4 – 9.7) after using Eq. (9.8) can be reduced as follows:

$$f''' + (1 + \lambda_1)(f f'' - f'^2) + \beta^*(f''^2 - f f^{iv}) + (1 + \lambda_1)(\gamma^2 + M(\gamma - f')) = 0, \quad (9.9)$$

$$\frac{1}{\text{Pr}} \theta'' + f \theta' + N_b \theta' \Phi' + N_t \theta'^2 = 0, \quad (9.10)$$

$$\Phi'' + Sc f \Phi' + \frac{N_t}{N_b} \theta'' = 0, \quad (9.11)$$

$$\begin{aligned} f'(0) &= 1, \quad f(0) = 0, \quad \theta'(0) = -\gamma^*[1 + \theta(0)], \quad \Phi(0) = 1 \\ f'(\infty) &\rightarrow \frac{d}{c} = \gamma, \quad \theta(\infty) \rightarrow 0, \quad \Phi(\infty) \rightarrow 0, \end{aligned} \quad (9.12)$$

where $\beta^* = c\lambda_2$ is the Deborah number, $M = \sigma B_0^2/\rho c$ is the Hartman number, $\text{Pr} = \nu/\alpha$ is the Prandtl number, $N_b = \tau D_B(C_w - C_\infty)/\nu$ is the Brownian motion parameter, $N_t = \tau D_T/\nu$ is the thermophoresis parameter, $\gamma^* = h_s \sqrt{\nu/c}$ is the conjugate parameter for Newtonian heating, γ is the ratio of rates and $Sc = \nu/D_B$ is the Schmidt number.

The important physical quantities of interest in this problem are the local skin-friction coefficient C_{sf} , local Nusselt number Nu and the local Sherwood number Sh which are given by

$$C_{sf} = \frac{\tau_w}{\frac{1}{2}\rho u_w^2}, \quad Nu = \frac{xq_w}{k(T - T_\infty)}, \quad Sh = \frac{xq_m}{D_B(C_w - C_\infty)}, \quad (9.13)$$

where the surface shear stress τ_w , wall heat flux q_w and wall mass flux q_m are given by

$$\tau_w = \mu \frac{\partial u}{\partial y} \Big|_{y=0}, \quad q_w = -k \frac{\partial T}{\partial y} \Big|_{y=0}, \quad q_m = -D_B \frac{\partial C}{\partial y} \Big|_{y=0}. \quad (9.14)$$

By using the above equations, we get

$$C_{sf}(\text{Re}_x)^{1/2} = f''(0), \quad Nu(\text{Re}_x)^{-1/2} = \gamma^* \left[1 + \frac{1}{\theta(0)} \right], \quad Sh(\text{Re}_x)^{-1/2} = -\Phi'(0), \quad (9.15)$$

where $\text{Re}_x = cx^2/\nu$ is the local Reynolds number.

9.3 Series solutions

Initial approximations $f_0(\eta)$, $\theta_0(\eta)$ and $\Phi_0(\eta)$ and auxiliary linear operators \mathcal{L}_f , \mathcal{L}_θ and \mathcal{L}_Φ are taken in the forms

$$f_0(\eta) = \gamma\eta + (1-\gamma)(1-e^{-\eta}), \quad \theta_0(\eta) = \frac{\gamma^*}{1-\gamma^*}e^{-\eta}, \quad \Phi_0(\eta) = e^{-\eta}, \quad (9.16)$$

$$\mathcal{L}_f = f''' + f'', \quad \mathcal{L}_\theta = \theta'' - \theta, \quad \mathcal{L}_\Phi = \Phi'' - \Phi, \quad (9.17)$$

subject to the properties

$$\begin{aligned} \mathcal{L}_f[c_1 + c_2\eta + c_3e^{-\eta}] &= 0, \\ \mathcal{L}_\theta[c_4e^\eta + c_5e^{-\eta}] &= 0, \\ \mathcal{L}_\Phi[c_6e^\eta + c_7e^{-\eta}] &= 0, \end{aligned} \quad (9.18)$$

in which c_i ($i = 1 - 7$) are the constants.

If $p \in [0, 1]$ indicates the embedding parameter then the zeroth order deformation problems are constructed as follows:

$$(1-p)\mathcal{L}_f[\hat{f}(\eta; p) - f_0(\eta)] = p\hbar_f \mathcal{N}_f[\hat{f}(\eta; p)], \quad (9.19)$$

$$(1-p)\mathcal{L}_\theta[\hat{\theta}(\eta; p) - \theta_0(\eta)] = p\hbar_\theta \mathcal{N}_\theta[\hat{\theta}(\eta; p), \hat{f}(\eta; p), \hat{\Phi}(\eta; p)], \quad (9.20)$$

$$(1-p)\mathcal{L}_\Phi[\hat{\Phi}(\eta;p) - \Phi_0(\eta)] = p\hbar_\Phi\mathcal{N}_\Phi[\hat{\Phi}(\eta;p), \hat{f}(\eta;p), \hat{\theta}(\eta;p)], \quad (9.21)$$

$$\begin{aligned} \hat{f}'(0;p) &= 1, \quad \hat{f}(0;p) = 0, \quad \hat{f}'(\infty;p) = \gamma, \\ \hat{\theta}'(0;p) &= -\gamma^*[1 + \hat{\theta}(0;p)], \quad \hat{\theta}(\infty;p) = 0, \\ \hat{\Phi}(0;p) &= 1, \quad \hat{\Phi}(\infty;p) = 0, \end{aligned} \quad (9.22)$$

where \hbar_f , \hbar_θ and \hbar_Φ are the nonzero auxiliary parameters and the nonlinear operators \mathcal{N}_f , \mathcal{N}_θ and \mathcal{N}_Φ are given by

$$\begin{aligned} \mathcal{N}_f[\hat{f}(\eta;p)] &= \frac{\partial^3 \hat{f}(\eta;p)}{\partial \eta^3} + (1 + \lambda_1) \left[\hat{f}(\eta;p) \frac{\partial^2 \hat{f}(\eta;p)}{\partial \eta^2} - \left(\frac{\partial \hat{f}(\eta;p)}{\partial \eta} \right)^2 \right] \\ &+ \beta^* \left[\left(\frac{\partial^2 \hat{f}(\eta;p)}{\partial \eta^2} \right)^2 - \hat{f}(\eta;p) \frac{\partial^4 \hat{f}(\eta;p)}{\partial \eta^4} \right] + (1 + \lambda_1) [\gamma^2 \\ &+ M \left(\gamma - \frac{\partial \hat{f}(\eta;p)}{\partial \eta} \right)], \end{aligned} \quad (9.23)$$

$$\begin{aligned} \mathcal{N}_\theta[\hat{\theta}(\eta;p), \hat{f}(\eta;p), \hat{\Phi}(\eta;p)] &= \frac{1}{\text{Pr}} \frac{\partial^2 \hat{\theta}(\eta;p)}{\partial \eta^2} + \hat{f}(\eta;p) \frac{\partial \hat{\theta}(\eta;p)}{\partial \eta} + N_b \frac{\partial \hat{\theta}(\eta;p)}{\partial \eta} \frac{\partial \hat{\Phi}(\eta;p)}{\partial \eta} \\ &+ N_t \left(\frac{\partial \hat{\theta}(\eta;p)}{\partial \eta} \right)^2, \end{aligned} \quad (9.24)$$

$$\mathcal{N}_\Phi[\hat{\Phi}(\eta;p), \hat{f}(\eta;p), \hat{\theta}(\eta;p)] = \frac{\partial^2 \hat{\Phi}(\eta;p)}{\partial \eta^2} + S_c \hat{f}(\eta;p) \frac{\partial \hat{\Phi}(\eta;p)}{\partial \eta} + \frac{N_t}{N_b} \frac{\partial^2 \hat{\theta}(\eta;p)}{\partial \eta^2}. \quad (9.25)$$

The m^{th} order deformation equations can be presented in the following forms

$$\mathcal{L}_f [f_m(\eta) - \chi_m f_{m-1}(\eta)] = \hbar_f \mathcal{R}_{f,m}(\eta), \quad (9.26)$$

$$\mathcal{L}_\theta [\theta_m(\eta) - \chi_m \theta_{m-1}(\eta)] = \hbar_\theta \mathcal{R}_{\theta,m}(\eta), \quad (9.27)$$

$$\mathcal{L}_\Phi [\Phi_m(\eta) - \chi_m \Phi_{m-1}(\eta)] = \hbar_\Phi \mathcal{R}_{\Phi,m}(\eta), \quad (9.28)$$

$$f_m(0) = f'_m(0) = f'_m(\infty) = \theta'_m(0) + \gamma^* \theta_m(0) = \theta_m(\infty) = \Phi_m(0) = \Phi_m(\infty) = 0, \quad (9.29)$$

$$\begin{aligned} \mathcal{R}_{f,m}(\eta) &= f'''_{m-1} + (1 + \lambda_1) \sum_{k=0}^{m-1} [f_{m-1-k} f''_k - f'_{m-1-k} f'_k] + \beta^* [f''_{m-1-k} f''_k - f_{m-1-k} f_k^{iv}] \\ &\quad + (1 + \lambda_1) [\gamma^2 + M(\gamma - f'_{m-1})], \end{aligned} \quad (9.30)$$

$$\mathcal{R}_{\theta,m}(\eta) = \frac{1}{\text{Pr}} \theta''_{m-1} + \sum_{k=0}^{m-1} [f_{m-1-k} \theta'_k + N_b \theta'_{m-1-k} \Phi'_k + N_t \theta'_{m-1-k} \theta'_k], \quad (9.31)$$

$$\mathcal{R}_{\Phi,m}(\eta) = \Phi''_{m-1} + Sc \sum_{k=0}^{m-1} f_{m-1-k} \Phi'_k + \frac{N_t}{N_b} \theta''_{m-1}, \quad (9.32)$$

$$\chi_m = \begin{cases} 0, & m \leq 1 \\ 1, & m > 1 \end{cases}. \quad (9.33)$$

The general solutions (f_m, θ_m, Φ_m) comprising the special solutions $(f_m^*, \theta_m^*, \Phi_m^*)$ are

$$\begin{aligned} f_m(\eta) &= f_m^*(\eta) + c_1 + c_2 \eta + c_3 e^{-\eta}, \\ \theta_m(\eta) &= \theta_m^*(\eta) + c_4 e^\eta + c_5 e^{-\eta}, \\ \Phi_m(\eta) &= \Phi_m^*(\eta) + c_6 e^\eta + c_7 e^{-\eta}. \end{aligned} \quad (9.34)$$

9.4 Convergence analysis

Now the solutions of Eqs. (9.9 – 9.11) subject to the boundary conditions (9.12) is computed by means of homotopy analysis method. The convergence of the series solutions is highly dependent upon the auxiliary parameters \hbar_f , \hbar_θ and \hbar_Φ . For valid ranges of these parameters, we have sketched the \hbar -curves at 15th-order of approximations (see Figs. 9.1 – 9.3). We can see that the admissible values of \hbar_f , \hbar_θ and \hbar_Φ are $-1.3 \leq \hbar_f \leq -0.2$, $-1.3 \leq \hbar_\theta \leq -0.2$ and $-1.5 \leq \hbar_\Phi \leq -0.7$. Further, the series solutions converge in the whole region of η ($0 < \eta < \infty$) when $\hbar_f = -1$, $\hbar_\theta = -1.1$ and $\hbar_\Phi = -1.3$.

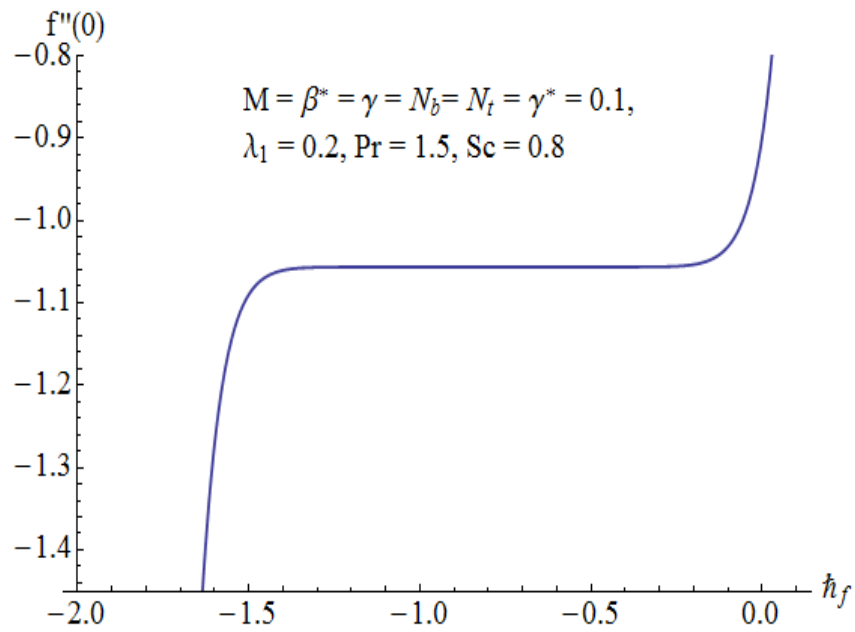


Fig. 9.1: \hbar - curve for the velocity field.

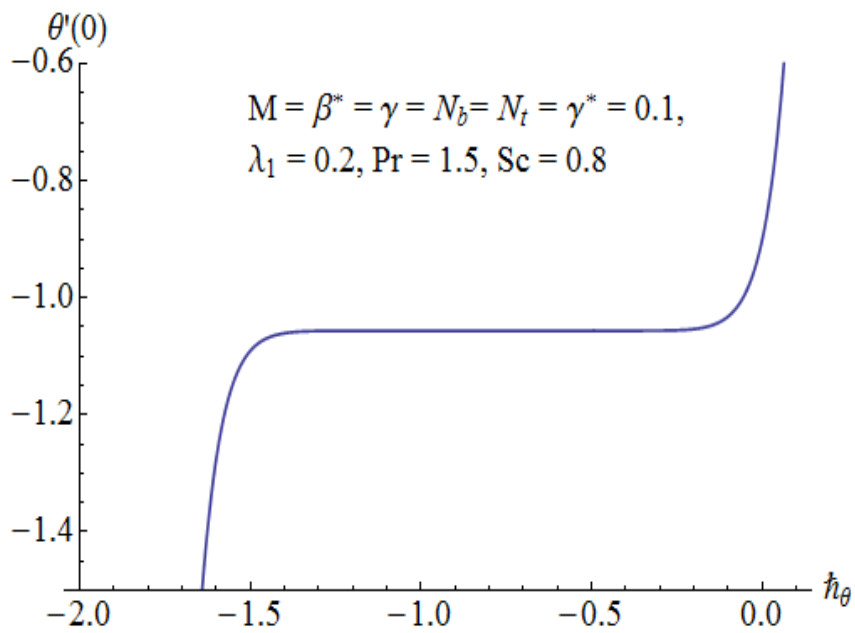


Fig. 9.2: \hbar - curve for the temperature field.

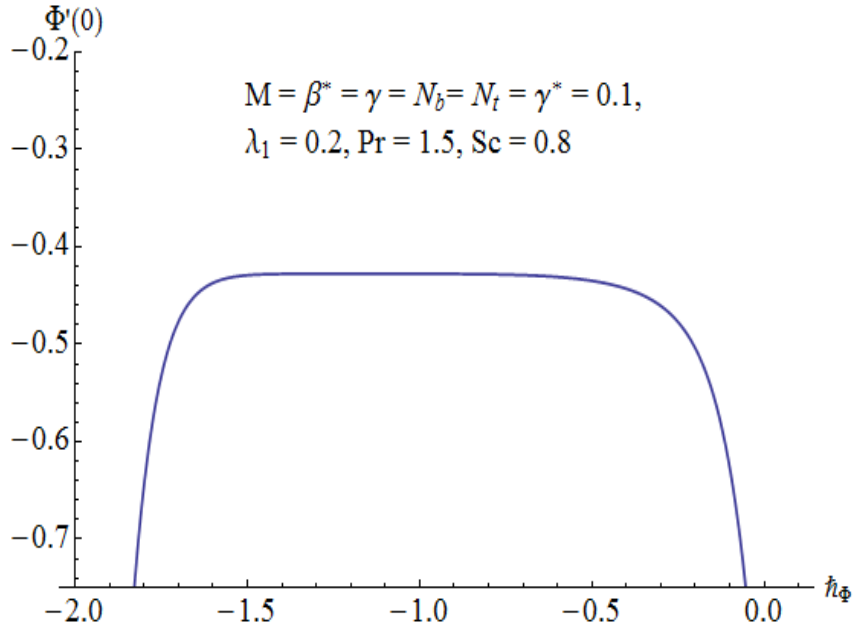


Fig. 9.3: \tilde{h} - curve for the concentration field.

Table 9.1: Convergence of HAM solutions for different order of approximations when $\lambda_1 = 0.2$, $\text{Pr} = 1.5$, $\beta^* = \gamma = M = N_b = N_t = \gamma^* = 0.1$ and $\text{Sc} = 0.8$.

Order of approximations	$-f''(0)$	$-\theta'(0)$	$-\Phi'(0)$
1	1.08225	0.113764	0.459778
5	1.05658	0.116260	0.433609
8	1.05648	0.116289	0.428189
15	1.05648	0.116273	0.427542
18	1.05648	0.116273	0.427544
20	1.05648	0.116273	0.427544
25	1.05648	0.116273	0.427544
30	1.05648	0.116273	0.427544
35	1.05648	0.116273	0.427544

9.5 Results and discussion

The effects of different parameters on the dimensionless flow and heat and mass transfer rates are investigated and presented graphically in this section. Figs. (9.4 – 9.7) exhibit the di-

dimensionless velocity profiles for different values of ratio of relaxation to retardation times λ_1 , Hartman number M , Deborah number β^* and ratio parameter γ . Effects of λ_1 on the velocity profile f' can be seen from Fig. 9.4. Here the values of f' and boundary layer thickness decrease when λ_1 increases. Effects of Hartman number M on the velocity f' are depicted in Fig. 9.5. The graph shows that the values of velocity f' and the boundary layer thickness decrease by increasing M . As the magnetic field has the tendency to slow down the movement of the fluid which leads to a decrease in the velocity and momentum boundary layer thickness. Fig. 9.6 shows that larger values of Deborah number β^* correspond to higher velocity. Fig. 9.7 illustrates the influence of ratio parameter γ on the velocity profile f' . There is an increase in velocity field f' and boundary layer thickness when the velocity of the stretching sheet exceeds the free stream velocity ($\gamma < 1$).

Effects of ratio of relaxation to retardation times λ_1 , Hartman number M , Deborah number β^* , ratio parameter γ , Prandtl number Pr , Brownian motion parameter N_b , thermophoresis parameter N_t , Schmidt number Sc and Newtonian heating parameter γ^* on the temperature profile θ are shown in the Figs. (9.8 – 9.16). Effect of λ_1 on the temperature is analyzed in Fig. 9.8. It is observed that the temperature and the thermal boundary layer thickness are increasing function of λ_1 . Fig. 9.9 illustrates the effects of M on temperature profile θ . As Lorentz force is a resistive force that opposes the fluid motion. So heat is produced and as a result thermal boundary layer thickness increases. Variations of β^* , γ and Pr on temperature profile θ can be seen in the Figs. (9.10 – 9.12). There is a decrease in temperature θ when Deborah number β^* , ratio parameter γ and Prandtl number Pr are increased. In fact the thermal diffusivity decreases by increasing Pr and thus the heat diffused away slowly from the heated surface. Fig. 9.13 represents the effect of Brownian motion parameter N_b on temperature profile θ . Temperature profile θ increases for an increase in N_b . The behavior of N_t on the temperature profile is similar to that of N_b (see Fig. 9.14). Also the temperature profile θ and thermal boundary layer thickness decrease when the Schmidt number Sc increases. This is due to the fact that an increase in Sc reduces the molecular diffusivity. Fig. 9.16 displays the effect of Newtonian heating parameter γ on temperature field θ . The temperature field θ is found to increase when γ increases.

Figs. (9.17 – 9.25) illustrate the effects of ratio of relaxation to retardation times λ_1 ,

Hartman number M , Deborah number β^* , ratio parameter γ , Brownian motion parameter N_b , Schmidt number Sc , Prandtl number Pr , thermophoresis parameter N_t and Newtonian heating parameter γ^* on the dimensionless nanoparticle volume fraction profile Φ . It is observed that the mass fraction Φ and the associated boundary layer decrease when the values of λ_1 , M , β^* , γ , N_b and Sc are increased and these quantities increase for higher Pr , N_t and γ^* .

Table 9.1 shows the convergence of the series solutions. It is observed that convergence is achieved at 18th order of approximations. In Table 9.2 some numerical values of skin friction coefficient are given. Tabulated values depict that skin friction coefficient decreases by increasing λ_1 and M while it increases for larger values of β^* and γ . Table 9.3 includes the values of local Nusselt and Sherwood numbers. It is noted that Nusselt number decreases by increasing N_b , N_t , M and γ^* while Sherwood number increases for higher N_b and it decreases for larger vales of N_t , M and γ^* .

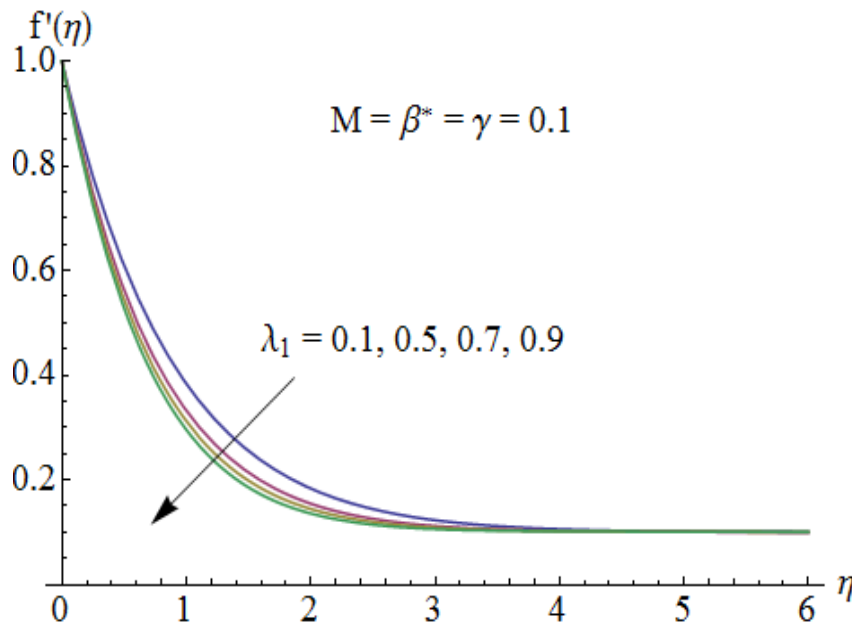


Fig. 9.4: Influence of λ_1 on $f'(\eta)$.

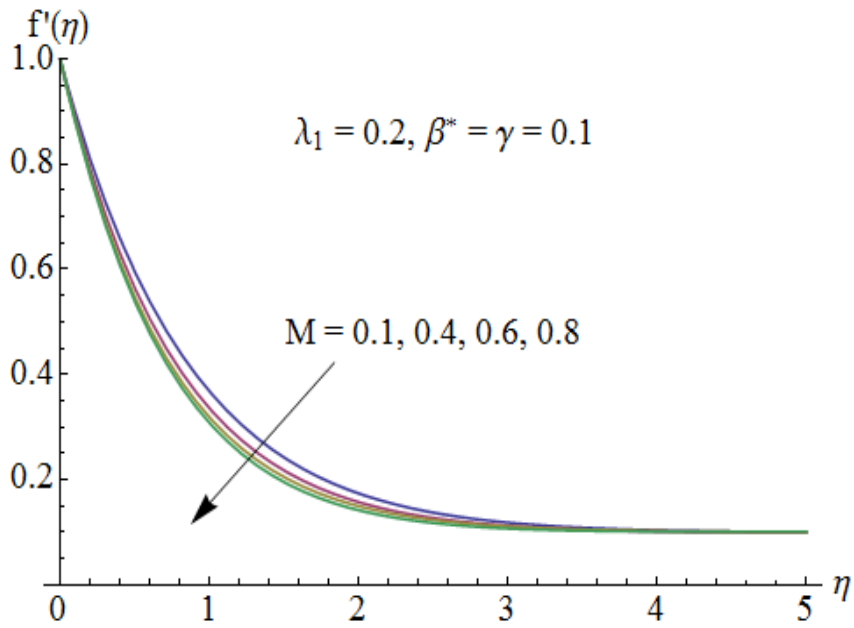


Fig. 9.5: Influence of M on $f'(\eta)$.

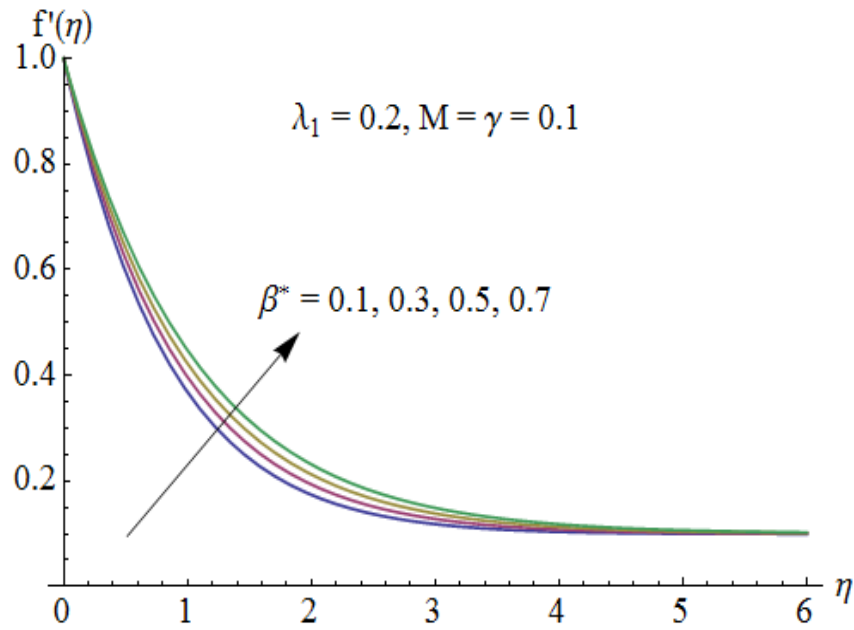


Fig. 9.6: Influence of β^* on $f'(\eta)$.

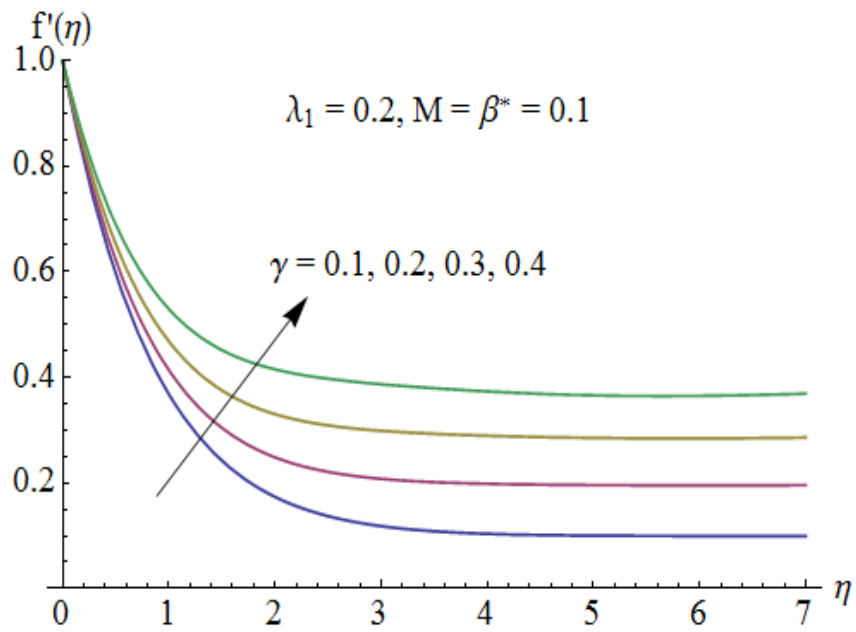


Fig. 9.7: Influence of γ on $f'(\eta)$.

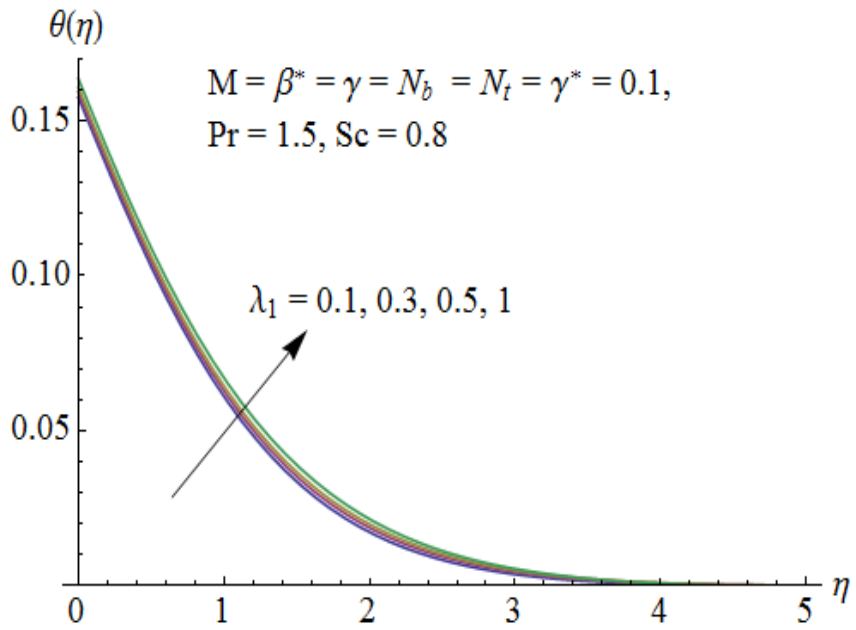


Fig. 9.8: Influence of λ_1 on $\theta(\eta)$.

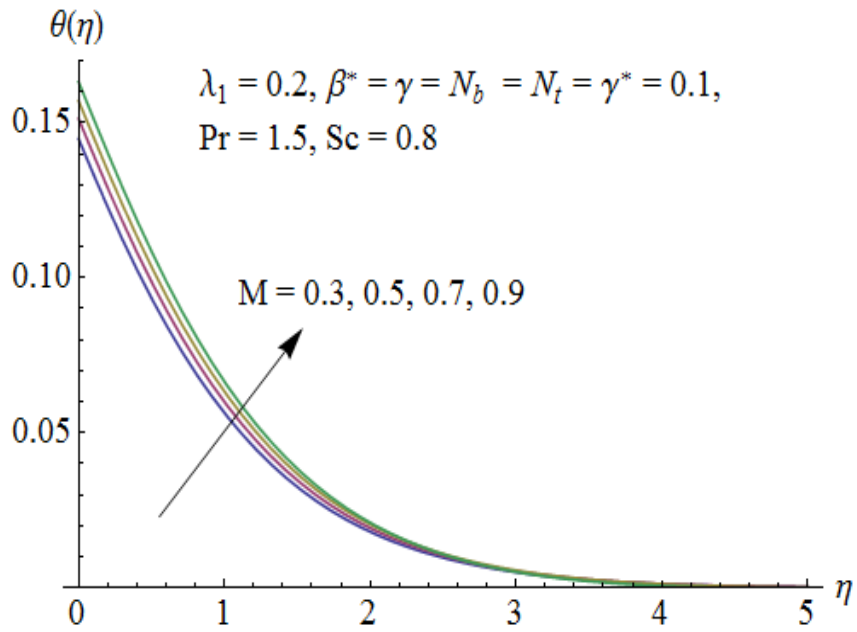


Fig. 9.9: Influence of M on $\theta(\eta)$.

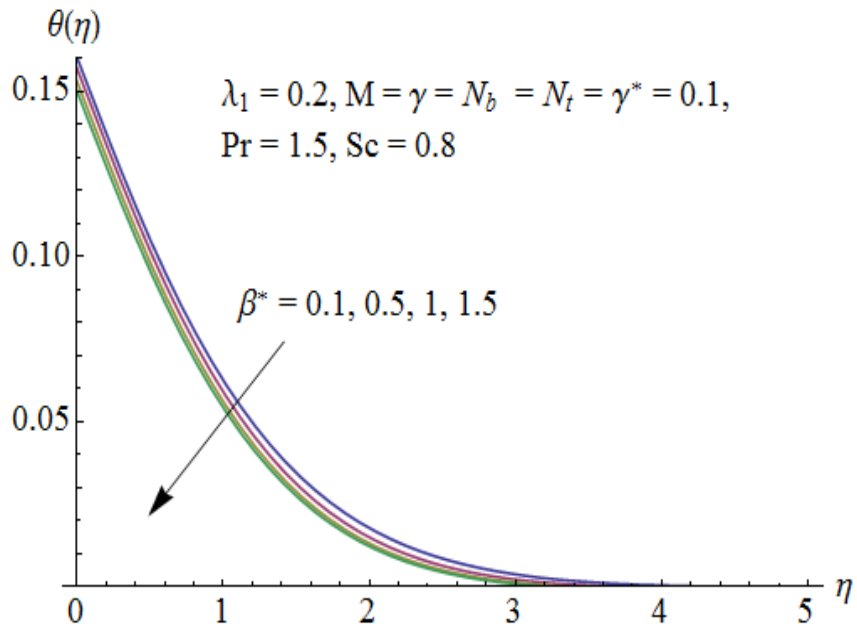


Fig. 9.10: Influence of β^* on $\theta(\eta)$.

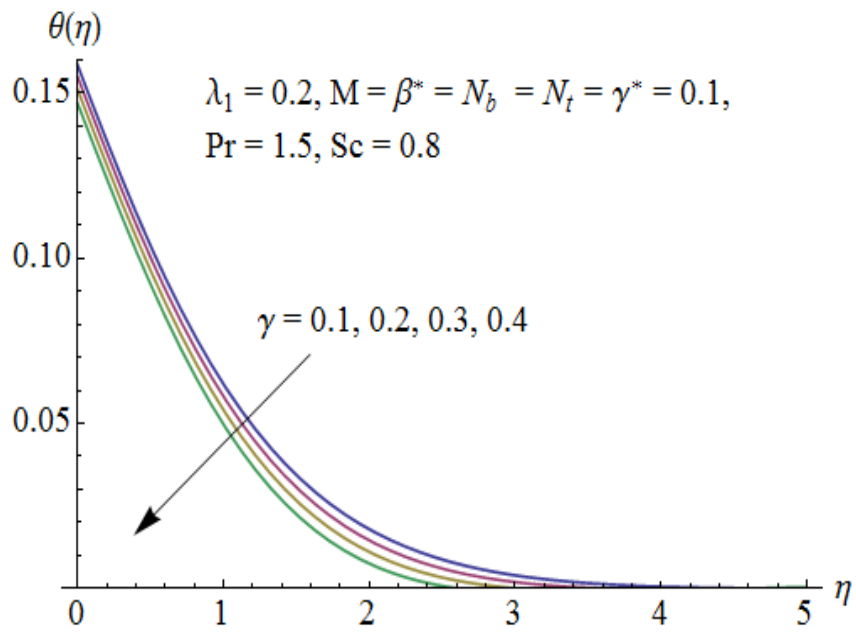


Fig. 9.11: Influence of γ on $\theta(\eta)$.

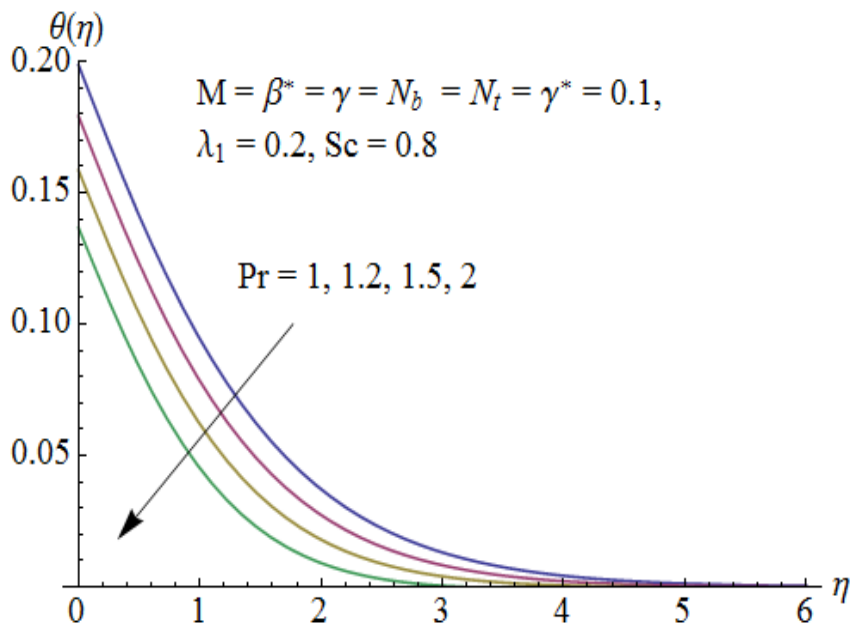


Fig. 9.12: Influence of Pr on $\theta(\eta)$.

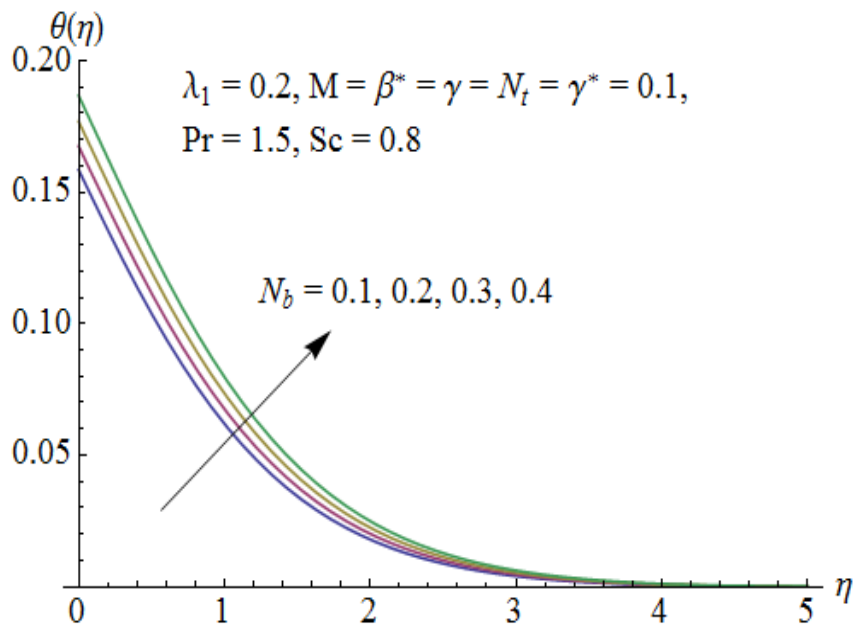


Fig. 9.13: Influence of N_b on $\theta(\eta)$.

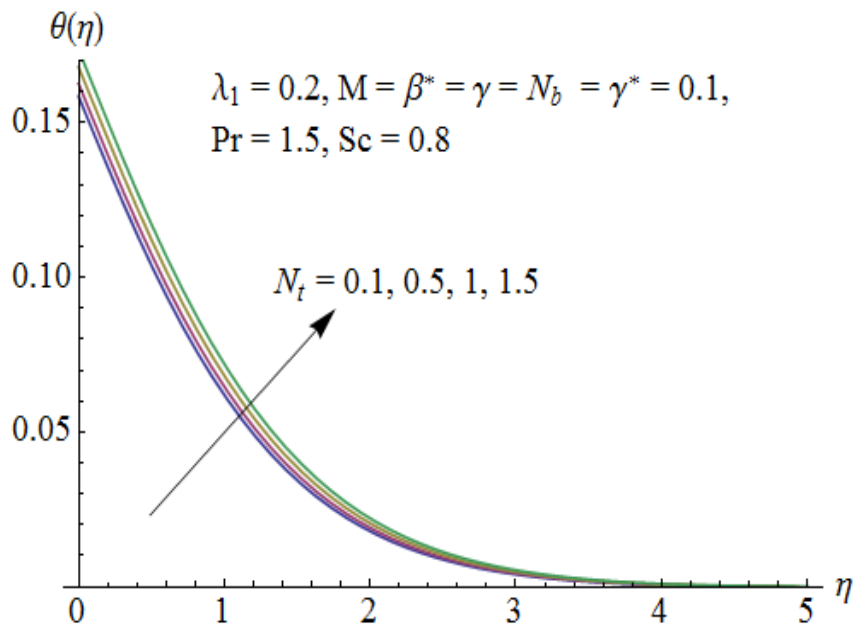


Fig. 9.14: Influence of N_t on $\theta(\eta)$.

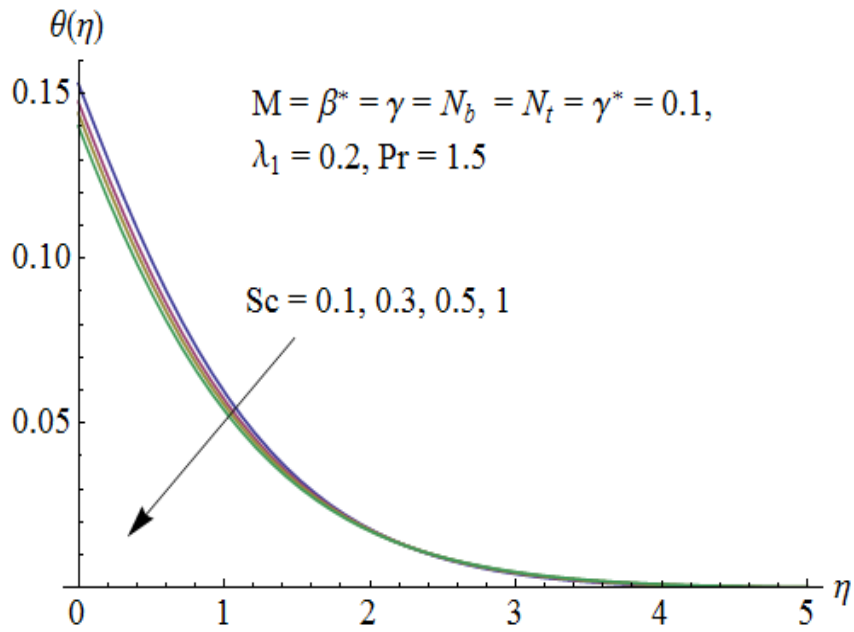


Fig. 9.15: Influence of Sc on $\theta(\eta)$.

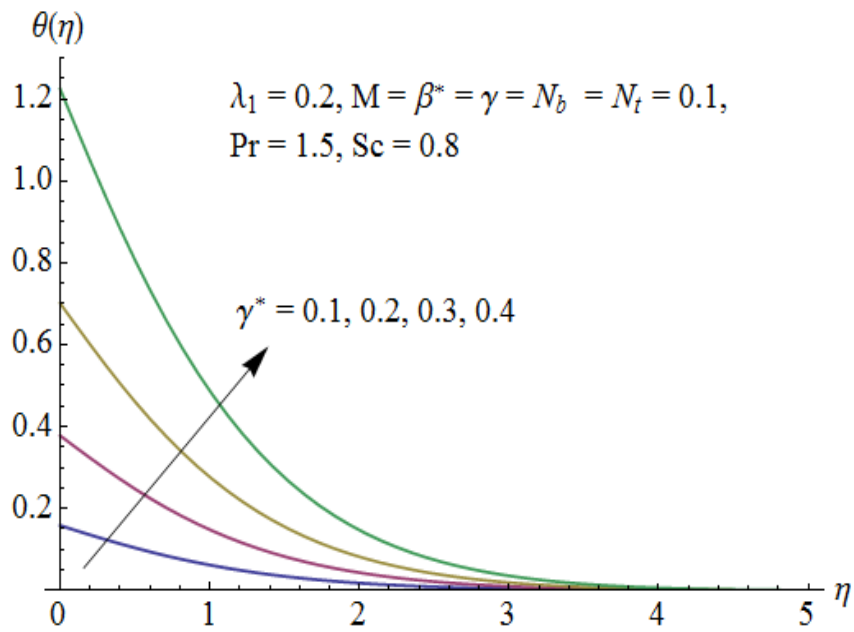


Fig. 9.16: Influence of γ^* on $\theta(\eta)$.

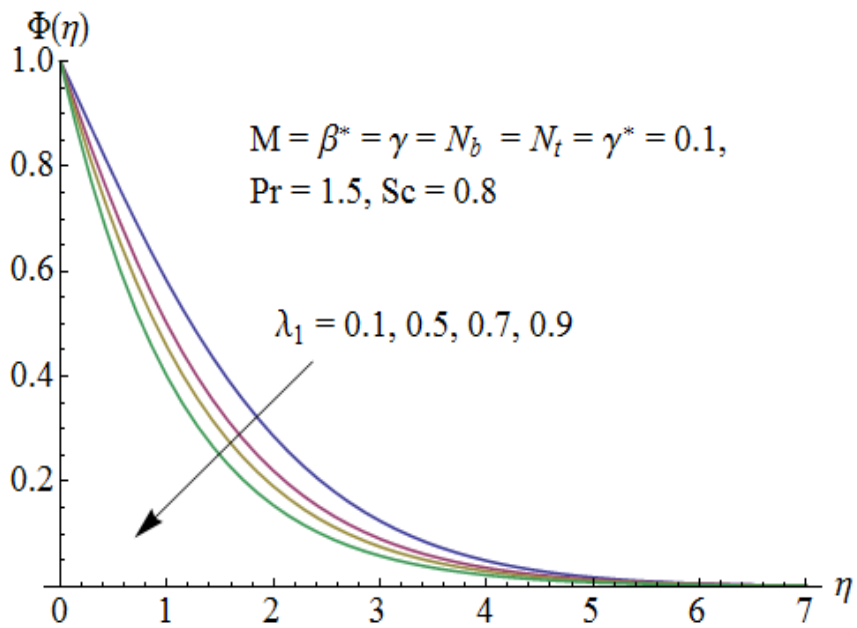


Fig. 9.17: Influence of λ_1 on $\Phi(\eta)$.

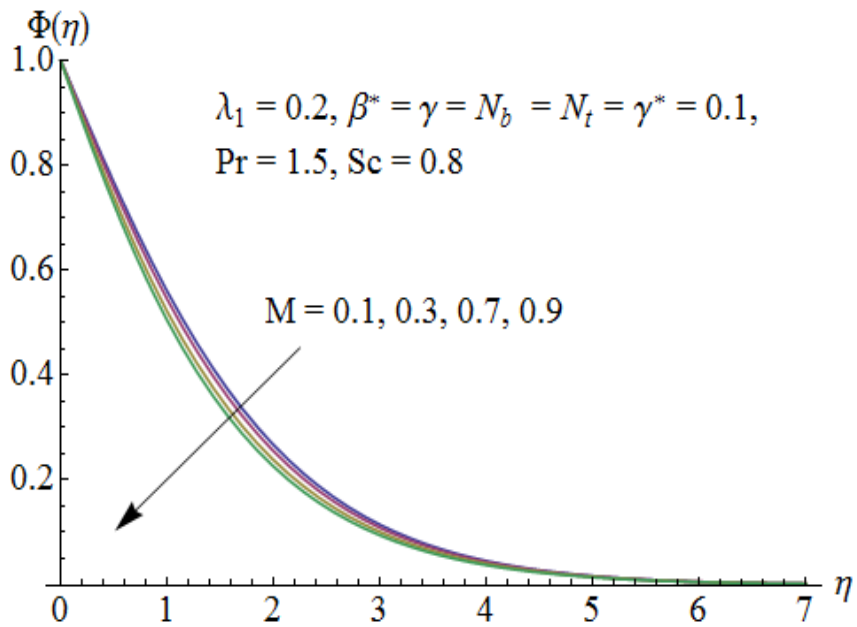


Fig. 9.18: Influence of M on $\Phi(\eta)$.

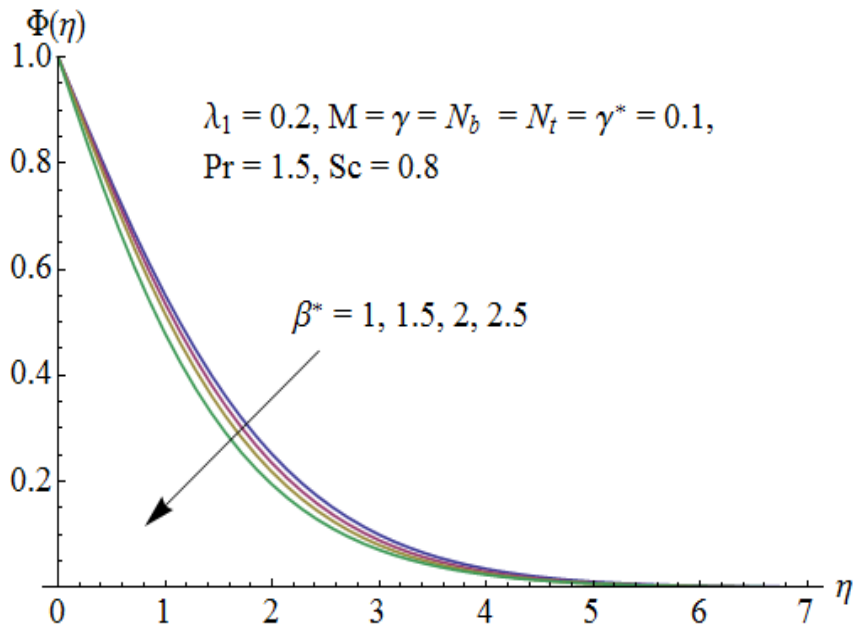


Fig. 9.19: Influence of β^* on $\Phi(\eta)$.

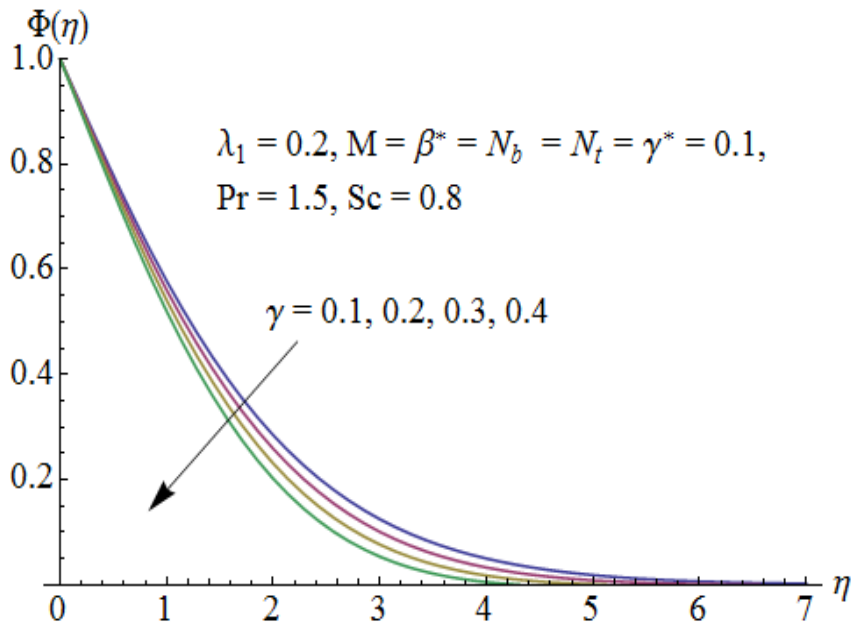


Fig. 9.20: Influence of γ on $\Phi(\eta)$.

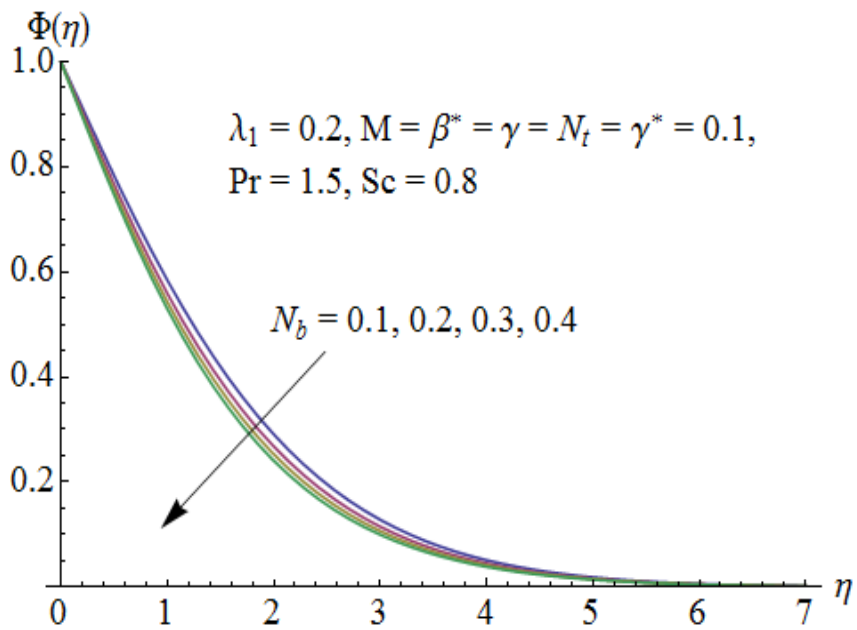


Fig. 9.21: Influence of N_b on $\Phi(\eta)$.

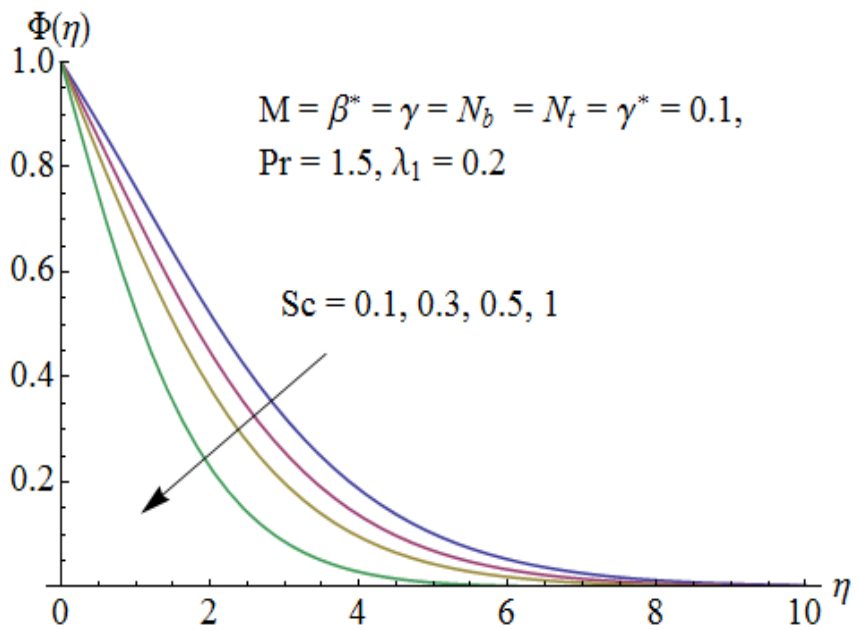


Fig. 9.22: Influence of Sc on $\Phi(\eta)$.

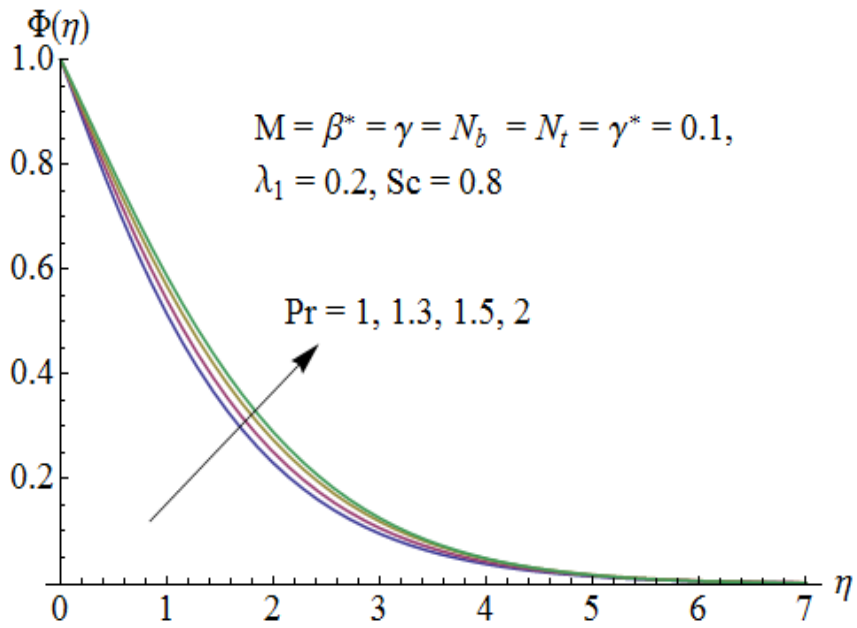


Fig. 9.23: Influence of Pr on $\Phi(\eta)$.

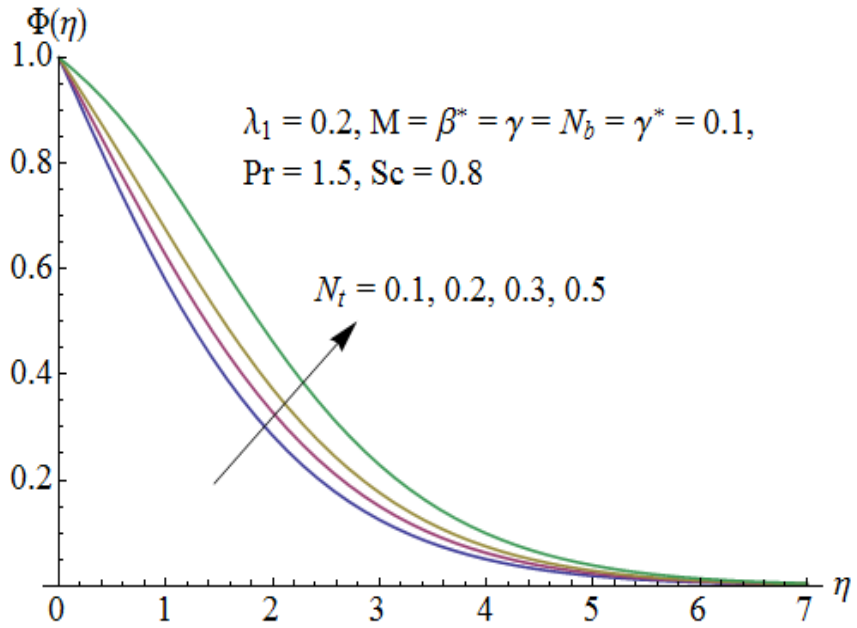


Fig. 9.24: Influence of N_t on $\Phi(\eta)$.

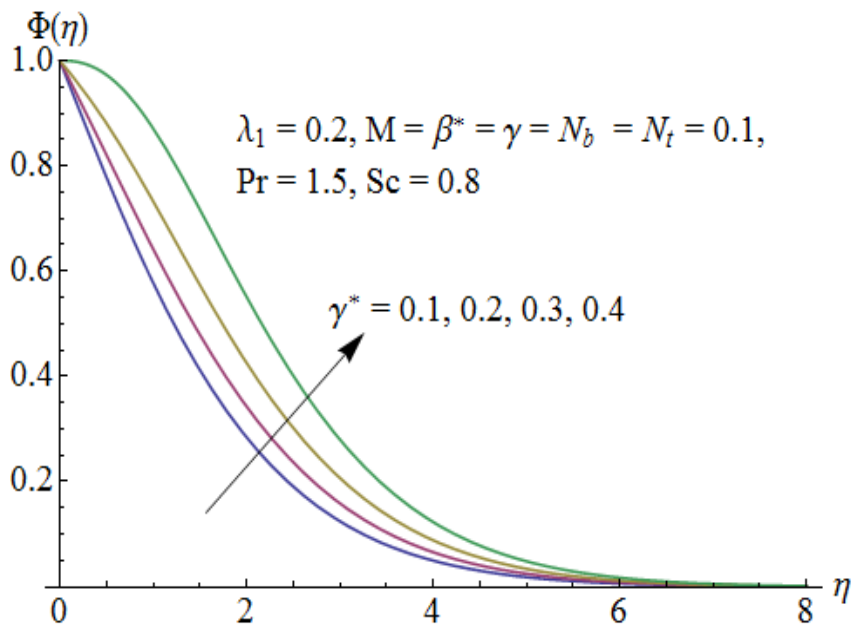


Fig. 9.25: Influence of γ^* on $\Phi(\eta)$.

Table 9.2: Numerical values of skin friction coefficient for different values of λ_1 , M , β^* and γ .

λ_1	M	β^*	γ	$C_{sf}(\text{Re}_x)^{1/2}$
0.1	0.1	0.1	0.1	-1.05648
			0.3	-1.09962
			0.4	-1.14114
			0.5	-1.18116
0.2	0.15			-1.03400
			0.2	-1.09737
			0.3	-1.13684
			0.4	-1.17502
	0.1	0.15		-1.03399
			0.2	-1.01290
			0.25	-0.993061
			0.3	-0.974349
		0.1	0.01	-1.09255
			0.03	-1.08605
			0.05	-1.07866
			0.07	-1.07040

Table 9.3: Numerical values of local Nusselt and Sherwood numbers when $\lambda_1 = 0.2$, $\beta^* = \gamma = 0.1$, $Pr = 1.5$ and $Sc = 0.8$.

N_b	N_t	M	γ^*	$\gamma^* \left(1 + \frac{1}{\theta(0)}\right)$	$-\Phi'(0)$
0.1	0.1	0.1	0.1	0.714516	0.427544
				0.673145	0.468469
				0.633230	0.482122
				0.557819	0.493069
0.1	0.2			0.710164	0.346337
				0.705776	0.265221
				0.701351	0.184186
				0.696886	0.103238
	0.1	0.2		0.708029	0.421407
		0.25		0.704905	0.418477
		0.3		0.701856	0.415635
		0.4		0.695969	0.410193
		0.1	0.15	0.711763	0.376091
			0.2	0.708442	0.314421
			0.25	0.704340	0.238845
			0.3	0.699108	0.143430

9.6 Conclusions

Here MHD stagnation point flow of Jeffrey nanofluid towards a stretching sheet is studied. Effects of different parameters on the velocity, temperature and concentration profiles are analyzed. The following observations are made.

- Velocity profile decreases by increasing λ_1 and M while it increases when β^* and γ are increased.
- An increase in the values of λ_1 , M , N_b , N_t and γ^* have similar effects on the temperature $\theta(\eta)$ in a qualitative sense.

- Temperature profile decreases by increasing β^* , γ and Sc .
- An increase in Prandtl number Pr reduces the temperature and thermal boundary layer thickness.
- Concentration profile $\Phi(\eta)$ decreases by increasing λ_1 , M , β^* , γ , N_b and Sc .
- The values of skin friction coefficient are higher for increasing values of β^* and γ .
- Higher values of N_t , M and γ^* correspond to smaller values of local Nusselt and Sherwood numbers.

Chapter 10

MHD three-dimensional flow of nanofluid with velocity slip and nonlinear thermal radiation

An analysis has been carried out in this chapter to investigate three-dimensional flow of viscous nanofluid in the presence of partial slip and thermal radiation effects. The flow is induced by a permeable stretching surface. Water is treated as a base fluid and alumina as a nanoparticle. Fluid is electrically conducting in the presence of applied magnetic field. Entire different concept of nonlinear thermal radiation is utilized in the heat transfer process. Different from the previous literature, the nonlinear system for temperature distribution is solved and analyzed. Appropriate transformations reduce the nonlinear partial differential system to ordinary differential system. Convergent series solutions are computed for the velocity and temperature. Effects of different parameters on the velocity, temperature, skin friction coefficient and Nusselt number are computed and examined. It is concluded that heat transfer rate increases when temperature and radiation parameters are increased.

10.1 Flow description

Consider the steady three-dimensional nanofluid flow over a stretching sheet situated at $z = 0$. Let (u, v, w) be the velocity components along the (x, y, z) directions, respectively. A constant

magnetic field of strength B_0 is applied in the z -direction. The governing boundary layer equations can be written as

$$\frac{\partial u}{\partial x} + \frac{\partial v}{\partial y} = 0, \quad (10.1)$$

$$u \frac{\partial u}{\partial x} + v \frac{\partial u}{\partial y} + w \frac{\partial u}{\partial z} = \nu_{nf} \frac{\partial^2 u}{\partial z^2} - \frac{\sigma_{nf} B_0^2 u}{\rho_{nf}}, \quad (10.2)$$

$$u \frac{\partial v}{\partial x} + v \frac{\partial v}{\partial y} + w \frac{\partial v}{\partial z} = \nu_{nf} \frac{\partial^2 v}{\partial z^2} - \frac{\sigma_{nf} B_0^2 v}{\rho_{nf}}, \quad (10.3)$$

with the boundary conditions given by

$$\begin{aligned} u &= cx + \frac{2 - \sigma_\nu}{\sigma_\nu} \lambda_0 \frac{\partial u}{\partial z}, \quad v = dy + \frac{2 - \sigma_\nu}{\sigma_\nu} \lambda_0 \frac{\partial v}{\partial z}, \quad w = -W \quad \text{at } z = 0, \\ u &\rightarrow 0, \quad v \rightarrow 0 \quad \text{as } z \rightarrow \infty, \end{aligned} \quad (10.4)$$

where c and d are stretching rate constants, $W (> 0)$ is the suction velocity, σ_ν is the tangential momentum accommodation coefficient and λ_0 is the molecular mean free path. The effective nanofluid dynamic viscosity μ_{nf} , density ρ_{nf} , thermal diffusivity α_{nf} , heat capacitance $(\rho c_p)_{nf}$, thermal conductivity k_{nf} and electrical conductivity σ_{nf} are given by

$$\rho_{nf} = \rho_f(1 - \phi) + \rho_s \phi, \quad (10.5)$$

$$\mu_{nf} = \frac{\mu_f}{(1 - \phi)^{2.5}}, \quad (10.6)$$

$$(\rho c_p)_{nf} = (\rho c_p)_f(1 - \phi) + (\rho c_p)_s \phi, \quad (10.7)$$

$$\frac{k_{nf}}{k_f} = \frac{k_s + 2k_f - 2\phi(k_f - k_s)}{k_s + 2k_f + 2\phi(k_f - k_s)}, \quad (10.8)$$

$$\frac{\sigma_{nf}}{\sigma_f} = 1 + \frac{3 \left(\frac{\sigma_s}{\sigma_f} - 1 \right) \phi}{\left(\frac{\sigma_s}{\sigma_f} + 2 \right) - \left(\frac{\sigma_s}{\sigma_f} - 1 \right) \phi}. \quad (10.9)$$

Here ϕ is the nanoparticle volume fraction, ρ_f and ρ_s are the densities of the fluid and of the solid fractions, respectively, k_f and k_s are the thermal conductivities of the fluid and of the solid fractions, respectively, and σ_f and σ_s are the electrical conductivity of the fluid and of the solid fractions, respectively.

Making use of the following transformations

$$u = cx f'(\eta), \quad v = cy g'(\eta), \quad w = -\sqrt{\nu_f c}(f + g), \quad \eta = \sqrt{\frac{c}{\nu_f}} z, \quad (10.10)$$

equation (10.1) is identically satisfied and Eqs. (10.2 – 10.4) become

$$\frac{1}{(1 - \phi)^{2.5} [1 - \phi + \frac{\rho_s}{\rho_f} \phi]} f''' - f'^2 + (f + g) f'' - \frac{M}{1 - \phi + \frac{\rho_s}{\rho_f} \phi} \frac{\sigma_{nf}}{\sigma_f} f' = 0, \quad (10.11)$$

$$\frac{1}{(1 - \phi)^{2.5} [1 - \phi + \frac{\rho_s}{\rho_f} \phi]} g''' - g'^2 + (f + g) g'' - \frac{M}{1 - \phi + \frac{\rho_s}{\rho_f} \phi} \frac{\sigma_{ng}}{\sigma_g} g' = 0, \quad (10.12)$$

$$\begin{aligned} f'(0) &= 1 + \beta f''(0), \quad g'(0) = \gamma + \beta g''(0), \quad f(0) + g(0) = S, \\ f'(\infty) &\rightarrow 0, \quad g'(\infty) \rightarrow 0, \end{aligned} \quad (10.13)$$

where prime denotes the differentiation with respect to η , M is the Hartman number, β is the velocity slip parameter, γ is the ratio of stretching rates and S is the suction/injection parameter. These quantities are defined by

$$M = \frac{\sigma_f B_0^2}{\rho_f c}, \quad \beta = \frac{2 - \sigma_\nu}{\sigma_\nu} \sqrt{\frac{c}{\nu_f}} \lambda_0, \quad \gamma = \frac{d}{c}, \quad S = \frac{W}{\sqrt{\nu_f c}}. \quad (10.14)$$

10.2 Heat transfer analysis

The boundary layer energy equation in the presence of thermal radiation effects is given by

$$u \frac{\partial T}{\partial x} + v \frac{\partial T}{\partial y} + w \frac{\partial T}{\partial z} = \alpha_{nf} \frac{\partial^2 T}{\partial z^2} - \frac{1}{(\rho c_p)_{nf}} \frac{\partial q_r}{\partial z}, \quad (10.15)$$

where T is the temperature, α_{nf} is the nanofluid thermal diffusivity, c_p is the specific heat at constant pressure and q_r is the radiative heat flux. Using Rosseland approximation for thermal radiation, the radiative heat flux is simplified as follows:

$$q_r = -\frac{4\sigma^*}{3k^*} \frac{\partial T^4}{\partial z} = -\frac{16\sigma^*}{3k^*} T^3 \frac{\partial T}{\partial z}, \quad (10.16)$$

in which σ^* and k^* are the Stefan-Boltzmann constant and the mean absorption coefficient, respectively. Now Eq. (10.15) can be written in the form

$$u \frac{\partial T}{\partial x} + v \frac{\partial T}{\partial y} + w \frac{\partial T}{\partial z} = \alpha_{nf} \frac{\partial^2 T}{\partial z^2} + \frac{16\sigma^*}{3k^*(\rho c_p)_{nf}} \frac{\partial}{\partial z} \left(T^3 \frac{\partial T}{\partial z} \right). \quad (10.17)$$

It is worth mentioning to note that for thermal radiation effect in the existing literature, T^4 in Eq. (10.16) was expanded about the ambient temperature T_∞ . However in the present case this has been avoided to get more meaningful results. Therefore in present analysis the energy equation is nonlinear.

The boundary conditions are

$$T = T_w \text{ at } z = 0, \quad T \rightarrow T_\infty \text{ as } z \rightarrow \infty, \quad (10.18)$$

where T_w and T_∞ are the sheet and ambient fluid temperatures respectively. We define the non-dimensional temperature by

$$\theta(\eta) = \frac{T - T_\infty}{T_w - T_\infty}, \quad (10.19)$$

or

$$T = T_\infty(1 + (\theta_w - 1)\theta), \quad (10.20)$$

where $\theta_w = T_w/T_\infty$ is the temperature parameter. Using Eq. (10.20), Eq. (10.17) takes the form

$$\begin{aligned} \frac{1}{\text{Pr}} \left(\frac{k_{nf}}{k_f} + R_d \right) \theta'' + \frac{R_d}{\text{Pr}} \left[(\theta_w - 1)^3 (3\theta^2 \theta'^2 + \theta^3 \theta'') + 3(\theta_w - 1)^2 (2\theta \theta'^2 + \theta^2 \theta'') \right. \\ \left. + 3(\theta_w - 1)(\theta'^2 + \theta \theta'') \right] + \left(1 - \phi + \frac{(\rho c_p)_s}{(\rho c_p)_f} \phi \right) \theta'(f + g) = 0 \end{aligned} \quad (10.21)$$

where Prandtl number Pr and radiation parameter R_d are defined by

$$\text{Pr} = \frac{\nu_f (\rho c_p)_f}{k_f}, \quad R_d = \frac{16\sigma^* T_\infty^3}{3kk^*}, \quad (10.22)$$

with the boundary conditions

$$\theta(0) = 1, \quad \theta(\infty) \rightarrow 0. \quad (10.23)$$

Surface shear stresses τ_{wx} and τ_{wy} along the x and y directions are given by

$$\tau_{wx} = \mu_{nf} \left. \frac{\partial u}{\partial z} \right|_{z=0}, \quad \tau_{wy} = \mu_{nf} \left. \frac{\partial v}{\partial z} \right|_{z=0}, \quad (10.24)$$

The heat transfer rate at the sheet is defined as follows:

$$q_w = -k_{nf} \left(\frac{\partial T}{\partial z} \right)_{z=0} + (q_r)_w = -(T_w - T_\infty) \sqrt{\frac{c}{\nu_f}} (1 + R_d \theta_w^3) \theta'(0). \quad (10.25)$$

Local skin friction coefficients along the x and y directions and Nusselt number for the problem are given by

$$\begin{aligned} (\text{Re}_x)^{\frac{1}{2}} C_{fx} &= \frac{1}{(1-\phi)^{2.5}} f''(0), \quad (\text{Re}_y)^{\frac{1}{2}} C_{fy} = \frac{1}{\gamma^{\frac{3}{2}} (1-\phi)^{2.5}} g''(0), \\ \frac{Nu}{\sqrt{\text{Re}_x}} &= -(1 + R_d \theta_w^3) \theta'(0), \end{aligned} \quad (10.26)$$

in which $(\text{Re}_x)^{\frac{1}{2}} = x \sqrt{c/\nu_f}$ and $(\text{Re}_y)^{\frac{1}{2}} = y \sqrt{c/\nu_f}$ denote the local Reynolds number.

10.3 Analytical solutions

Employing the homotopy analysis method the initial approximations and auxiliary linear operators are given by

$$f_0(\eta) = S + \frac{1}{1+\beta}(1 - e^{-\eta}), \quad g_0(\eta) = \frac{\gamma}{1+\beta}(1 - e^{-\eta}), \quad \theta_0(\eta) = e^{-\eta}, \quad (10.27)$$

$$\mathcal{L}_f(f) = \frac{d^3 f}{d\eta^3} - \frac{df}{d\eta}, \quad \mathcal{L}_g(g) = \frac{d^3 g}{d\eta^3} - \frac{dg}{d\eta}, \quad \mathcal{L}_\theta(\theta) = \frac{d^2 \theta}{d\eta^2} - \theta, \quad (10.28)$$

with

$$\mathcal{L}_f [c_1 + c_2 \exp(\eta) + c_3 \exp(-\eta)] = 0, \quad (10.29)$$

$$\mathcal{L}_g [c_4 + c_5 \exp(\eta) + c_6 \exp(-\eta)] = 0, \quad (10.30)$$

$$\mathcal{L}_\theta [c_7 \exp(\eta) + c_8 \exp(-\eta)] = 0, \quad (10.31)$$

in which c_i ($i = 1 - 8$) are the arbitrary constants. If $p \in [0, 1]$ indicates the embedding parameter then the zeroth order deformation problems are constructed as follows:

$$(1 - p) \mathcal{L}_f \left[\hat{f}(\eta; p) - f_0(\eta) \right] = p \hbar_f \mathcal{N}_f \left[\hat{f}(\eta; p), \hat{g}(\eta; p) \right], \quad (10.32)$$

$$(1 - p) \mathcal{L}_g \left[\hat{g}(\eta; p) - g_0(\eta) \right] = p \hbar_g \mathcal{N}_g \left[\hat{g}(\eta; p), \hat{f}(\eta; p) \right], \quad (10.33)$$

$$(1 - p) \mathcal{L}_\theta \left[\hat{\theta}(\eta; p) - \theta_0(\eta) \right] = p \hbar_\theta \mathcal{N}_\theta \left[\hat{\theta}(\eta; p), \hat{f}(\eta; p), \hat{g}(\eta; p) \right], \quad (10.34)$$

$$\hat{f}(0; p) = S, \quad \hat{f}'(0; p) = 1 + \beta \hat{f}''(0; p), \quad \hat{f}'(\infty; p) = 0, \quad (10.35)$$

$$\hat{g}(0; p) = 0, \quad \hat{g}'(0; p) = \gamma + \beta \hat{g}''(0; p), \quad \hat{g}'(\infty; p) = 0, \quad (10.36)$$

$$\hat{\theta}(0; p) = 1, \quad \hat{\theta}(\infty; p) = 0, \quad (10.37)$$

where \hbar_f , \hbar_g and \hbar_θ are the nonzero auxiliary parameters and the nonlinear operators \mathcal{N}_f , \mathcal{N}_g and \mathcal{N}_θ are given by

$$\begin{aligned} \mathcal{N}_f \left[\hat{f}(\eta; p), \hat{g}(\eta; p) \right] &= \frac{1}{(1 - \phi)^{2.5} [1 - \phi + \frac{\rho_s}{\rho_f} \phi]} \frac{\partial^3 \hat{f}(\eta; p)}{\partial \eta^3} - \left(\frac{\partial \hat{f}(\eta; p)}{\partial \eta} \right)^2 \\ &+ \hat{f}(\eta; p) \frac{\partial^2 \hat{f}(\eta; p)}{\partial \eta^2} + \hat{g}(\eta; p) \frac{\partial^2 \hat{f}(\eta; p)}{\partial \eta^2} \\ &- \frac{M}{1 - \phi + \frac{\rho_s}{\rho_f} \phi} \frac{\sigma_{nf}}{\sigma_f} \frac{\partial \hat{f}(\eta; p)}{\partial \eta}, \end{aligned} \quad (10.38)$$

$$\begin{aligned} \mathcal{N}_g \left[\hat{g}(\eta; p), \hat{f}(\eta; p) \right] &= \frac{1}{(1 - \phi)^{2.5} [1 - \phi + \frac{\rho_s}{\rho_f} \phi]} \frac{\partial^3 \hat{g}(\eta; p)}{\partial \eta^3} - \left(\frac{\partial \hat{g}(\eta; p)}{\partial \eta} \right)^2 \\ &+ \hat{f}(\eta; p) \frac{\partial^2 \hat{g}(\eta; p)}{\partial \eta^2} + \hat{g}(\eta; p) \frac{\partial^2 \hat{g}(\eta; p)}{\partial \eta^2} \\ &- \frac{M}{1 - \phi + \frac{\rho_s}{\rho_f} \phi} \frac{\sigma_{ng}}{\sigma_g} \frac{\partial \hat{g}(\eta; p)}{\partial \eta}, \end{aligned} \quad (10.39)$$

$$\begin{aligned}
\mathcal{N}_\theta \left[\hat{\theta}(\eta; p), \hat{f}(\eta; p), \hat{g}(\eta; p) \right] &= \frac{1}{\text{Pr}} \left(\frac{k_{nf}}{k_f} + R_d \right) \frac{\partial^2 \hat{\theta}(\eta; p)}{\partial \eta^2} + \frac{R_d}{\text{Pr}} \left[(\theta_w - 1)^3 \right. \\
&\quad \left. \left(3 \left(\hat{\theta}(\eta; p) \right)^2 \left(\frac{\partial \hat{\theta}(\eta; p)}{\partial \eta} \right)^2 + \left(\hat{\theta}(\eta; p) \right)^3 \frac{\partial^2 \hat{\theta}(\eta; p)}{\partial \eta^2} \right) \right. \\
&\quad \left. + 3(\theta_w - 1)^2 \left(2\hat{\theta}(\eta; p) \left(\frac{\partial \hat{\theta}(\eta; p)}{\partial \eta} \right)^2 + \left(\hat{\theta}(\eta; p) \right)^2 \frac{\partial^2 \hat{\theta}(\eta; p)}{\partial \eta^2} \right) \right. \\
&\quad \left. + 3(\theta_w - 1) \left(\left(\frac{\partial \hat{\theta}(\eta; p)}{\partial \eta} \right)^2 + \hat{\theta}(\eta; p) \frac{\partial^2 \hat{\theta}(\eta; p)}{\partial \eta^2} \right) \right] \\
&\quad + \left(1 - \phi + \frac{(\rho c_p)_s}{(\rho c_p)_f} \phi \right) \left(\hat{f}(\eta; p) + \hat{g}(\eta; p) \right) \frac{\partial \hat{\theta}(\eta; p)}{\partial \eta}. \quad (10.40)
\end{aligned}$$

The m^{th} order deformation problems are

$$\mathcal{L}_f [f_m(\eta) - \chi_m f_{m-1}(\eta)] = \hbar_f \mathcal{R}_{f,m}(\eta), \quad (10.41)$$

$$\mathcal{L}_g [g_m(\eta) - \chi_m g_{m-1}(\eta)] = \hbar_g \mathcal{R}_{g,m}(\eta), \quad (10.42)$$

$$\mathcal{L}_\theta [\theta_m(\eta) - \chi_m \theta_{m-1}(\eta)] = \hbar_\theta \mathcal{R}_{\theta,m}(\eta), \quad (10.43)$$

$$f_m(0) = f'_m(0) - \beta f''_m(0) = f'_m(\infty) = 0, \quad (10.44)$$

$$g_m(0) = g'_m(0) - \beta g''_m(0) = g'_m(\infty) = 0, \quad (10.45)$$

$$\theta_m(0) = \theta_m(\infty) = 0, \quad (10.46)$$

$$\begin{aligned}
\mathcal{R}_{f,m}(\eta) &= \frac{1}{(1-\phi)^{2.5} \left[1 - \phi + \frac{\rho_s}{\rho_f} \phi \right]} f'''_{m-1}(\eta) + \sum_{k=0}^{m-1} (f_{m-1-k} f''_k + g_{m-1-k} f''_k - f'_{m-1-k} f'_k) \\
&\quad - \frac{\sigma_{nf}}{\sigma_f} \frac{M}{1 - \phi + \frac{\rho_s}{\rho_f} \phi} f'_{m-1}, \quad (10.47)
\end{aligned}$$

$$\begin{aligned}
\mathcal{R}_{g,m}(\eta) &= \frac{1}{(1-\phi)^{2.5} \left[1 - \phi + \frac{\rho_s}{\rho_f} \phi \right]} g'''_{m-1}(\eta) + \sum_{k=0}^{m-1} (f_{m-1-k} g''_k + g_{m-1-k} g''_k - g'_{m-1-k} g'_k) \\
&\quad - \frac{\sigma_{ng}}{\sigma_f} \frac{M}{1 - \phi + \frac{\rho_s}{\rho_f} \phi} g'_{m-1}, \quad (10.48)
\end{aligned}$$

$$\begin{aligned}
\mathcal{R}_{\theta,m}(\eta) &= \frac{1}{\text{Pr}} \left(\frac{k_{nf}}{k_f} + R_d \right) \theta''_{m-1} + \frac{R_d}{\text{Pr}} \sum_{k=0}^{m-1} \left[(\theta_w - 1)^3 \theta_{m-1-k} \sum_{l=0}^k \theta_{k-l} \sum_{s=0}^l (3\theta'_{l-s} \theta'_s + \theta_{l-s} \theta''_s) \right. \\
&\quad \left. + 3(\theta_w - 1)^2 \theta_{m-1-k} \sum_{l=0}^k (2\theta'_{k-l} \theta'_l + \theta_{k-l} \theta''_l) + 3(\theta_w - 1)(\theta'_{m-1-k} \theta'_k + \theta_{m-1-k} \theta''_k) \right] \\
&\quad + \left(1 - \phi + \frac{(\rho c_p)_s}{(\rho c_p)_f} \phi \right) \sum_{k=0}^{m-1} (\theta'_{m-1-k} f_k + \theta'_{m-1-k} g_k), \tag{10.49}
\end{aligned}$$

$$\chi_m = \begin{cases} 0, & m \leq 1 \\ 1, & m > 1 \end{cases}. \tag{10.50}$$

The general solutions in terms of particular solutions f_m^* , g_m^* and θ_m^* are

$$f_m(\eta) = f_m^*(\eta) + c_1 + c_2 e^\eta + c_3 e^{-\eta}, \tag{10.51}$$

$$g_m(\eta) = g_m^*(\eta) + c_4 + c_5 e^\eta + c_6 e^{-\eta}, \tag{10.52}$$

$$\theta_m(\eta) = \theta_m^*(\eta) + c_7 e^\eta + c_8 e^{-\eta}, \tag{10.53}$$

10.4 Convergence of the developed solutions

The convergence of the series solutions is highly dependent upon auxiliary parameters \hbar_f , \hbar_g and \hbar_θ . For valid ranges of these parameters, we have sketched the \hbar -curves at 10th-order of approximations (see Fig. 10.1). This Fig. shows that the admissible values of \hbar_f , \hbar_g and \hbar_θ are $-2 \leq \hbar_f \leq -0.2$, $-2 \leq \hbar_g \leq -0.2$ and $-1.6 \leq \hbar_\theta \leq -1.3$. Further Table 10.1 ensures that when $\hbar_f = \hbar_g = -1.1$ and $\hbar_\theta = -1.3$ the series solutions are convergent up to six decimal places.

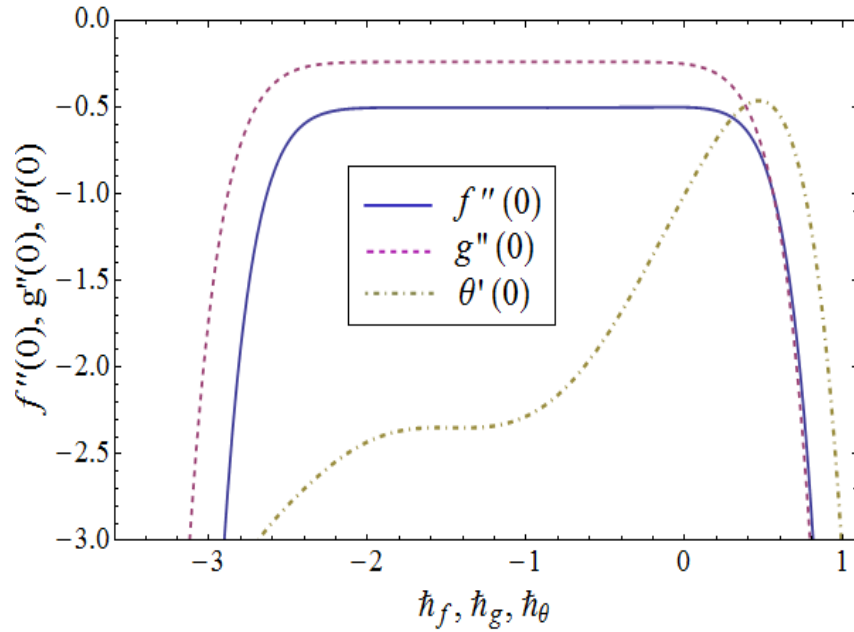


Fig. 10.1: Combined h -curves for $f''(0)$, $g''(0)$ and $\theta'(0)$ when $\text{Pr} = 6.2$, $\gamma = 0.5$, $\phi = 0.03$, $\beta = 1$, $R_d = M = 0.1$, $\theta_w = 1.1$ and $S = 0.3$.

Table 10.1: Convergence of HAM solutions for different order of approximations when $\text{Pr} = 6.2$, $\gamma = 0.5$, $\phi = 0.03$, $\beta = 1$, $R_d = M = 0.1$, $\theta_w = 1.1$ and $S = 0.3$ and $h_f = h_g = -1.1$ and $h_\theta = -1.3$.

Order of approximation	$-f''(0)$	$-g''(0)$	$-\theta'(0)$
5	0.501136	0.238561	2.18655
9	0.501129	0.238543	2.34913
15	0.501129	0.238543	2.41402
20	0.501129	0.238543	2.40545
25	0.501129	0.238543	2.39321
30	0.501129	0.238543	2.39321
35	0.501129	0.238543	2.39321
40	0.501129	0.238543	2.39321

10.5 Discussion

This section presents the effects of various parameters on the velocity, temperature, skin friction coefficient and Nusselt number in the form of graphical and tabulated results.

10.5.1 Dimensionless velocity profiles

Figs. (10.2 – 10.6) display the dimensionless velocity profiles for different values of Hartman number M , velocity slip parameter β , nanoparticle volume fraction ϕ , suction/injection velocity parameter S and stretching parameter γ . Fig. 10.2 plots the velocity profiles f' and g' for various values of Hartman number M . It is observed that velocity fields f' and g' decrease when M increases. The application of an applied magnetic field has the tendency to slow down the movement of the fluid, which leads to a decrease in the velocity and momentum boundary layer thickness. Fig. 10.3 shows the effects of velocity slip parameter β . This Fig. shows that by increasing the values of velocity slip parameter β , there is a gradual decrease in the velocity profiles. The effects of nanoparticle volume fraction ϕ on velocity profile are presented in the Fig. 10.4. It is noted that an increase in the values of ϕ decreases the velocity profiles f' and g' . Effect of suction/injection velocity parameter S on f' and g' can be visualized in the Fig. 10.5. It is obvious that an increase in S reduces the velocity fields f' and g' . Because applying suction leads to draw the amount of fluid particles into the wall and consequently the velocity boundary layer decreases. Also suction is an agent which causes a reduction in the fluid velocity. Influence of stretching parameter γ on the velocity profiles is displayed in the Fig. 10.6. It is observed that velocity field f' decreases with an increase in γ while g' increases when γ is enhanced.

10.5.2 Dimensionless temperature profiles

Effects of Hartman number M , nanoparticle volume fraction ϕ , temperature parameter θ_w and radiation parameter R_d on the temperature profile θ are shown in the Figs. (10.7 – 10.10). To capture the effects of Hartman number M on the temperature θ , Fig. 10.7 is displayed. It is depicted that temperature is an increasing function of M . As the Lorentz force is a resistive force which opposes the fluid motion so heat is produced and as a result the thermal boundary

layer thickness increases. Fig. 10.8 portrays the influence of ϕ on θ . It is found that temperature increases when values of nanoparticle volume fraction ϕ are increased. It is because of the fact that by increasing the volume fraction of nanoparticles, the thermal conductivity and thermal boundary layer are increased. Figs. 10.9 and 10.10 indicate that temperature increases by increasing values of temperature parameter θ_w and radiation parameter R_d . Physically this is due to the fact that with the increase in radiation parameter, the mean absorption coefficient decreases. Hence the rate of radiative heat transfer to the fluid increases.

10.5.3 Skin friction coefficient and Nusselt number

In Table 10.2 the thermophysical properties of water and nanoparticles are given. Tables 10.3 and 10.4 show the effects of nanoparticle volume fraction ϕ on skin friction coefficient for different types of nanofluids in the x and y -directions. Effects of the nanoparticle volume fraction ϕ on Nusselt number are presented in Table 10.5. These values of skin friction coefficient and Nusselt number change for different nanofluids. It means that by using different types of nanofluid, the shear stress and rate of heat transfer alter. Numerical values of local Nusselt number for different emerging parameters are presented in Table 10.6. It is noticed that local Nusselt number $Nu(Re_x)^{-\frac{1}{2}}$ increases for larger values of θ_w and R_d . However it decreases by increasing M .

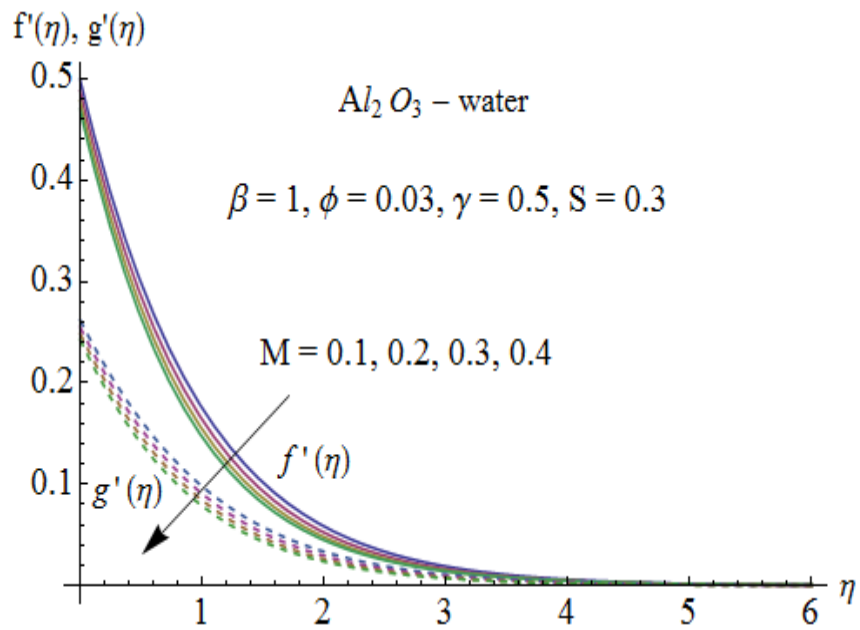


Fig. 10.2: Effect of M on f' and g' .

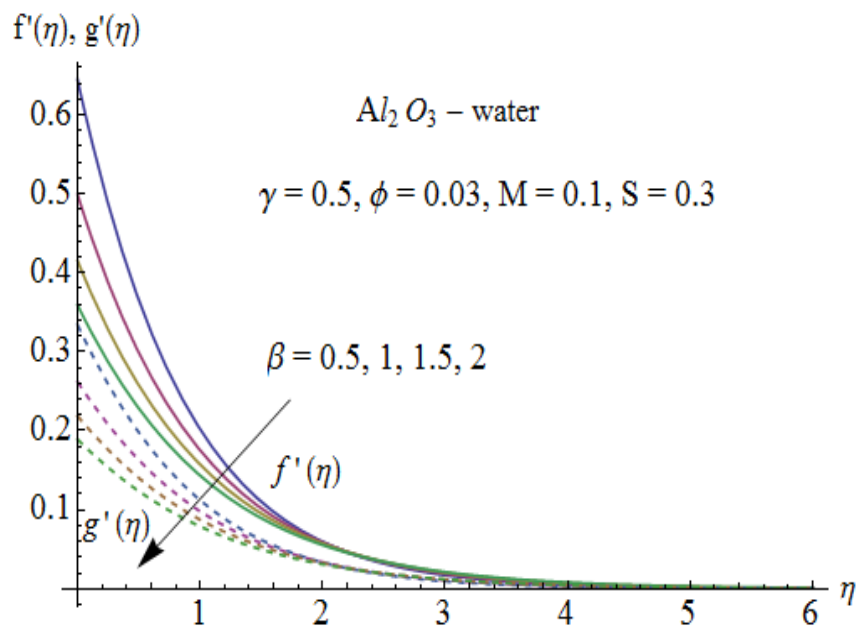


Fig. 10.3: Effect of β on f' and g' .

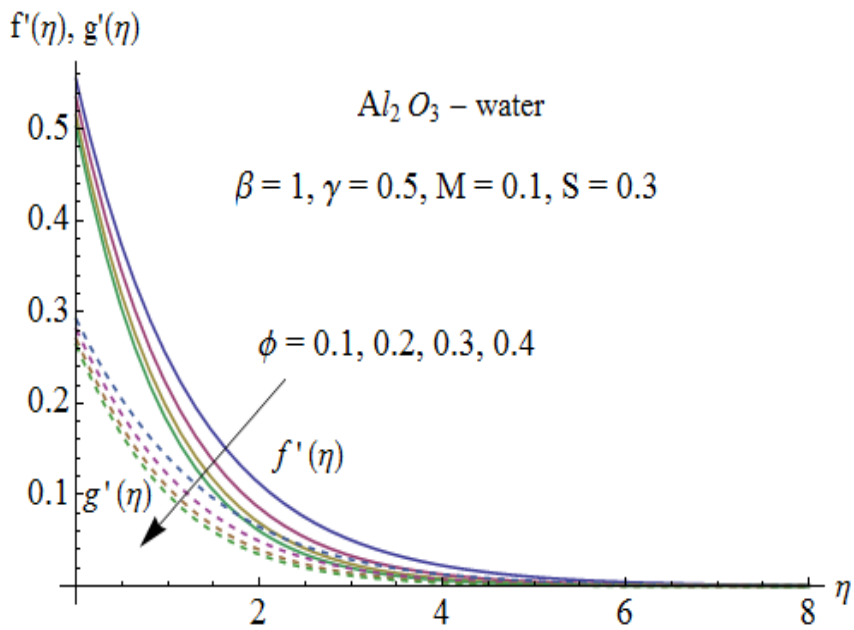


Fig. 10.4: Effect of ϕ on f' and g' .

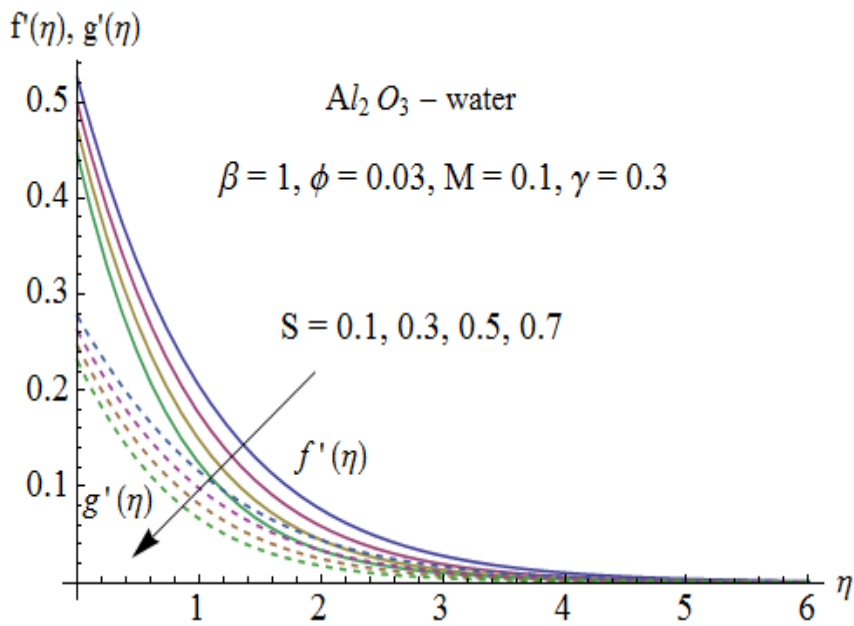


Fig. 10.5: Effect of S on f' and g' .

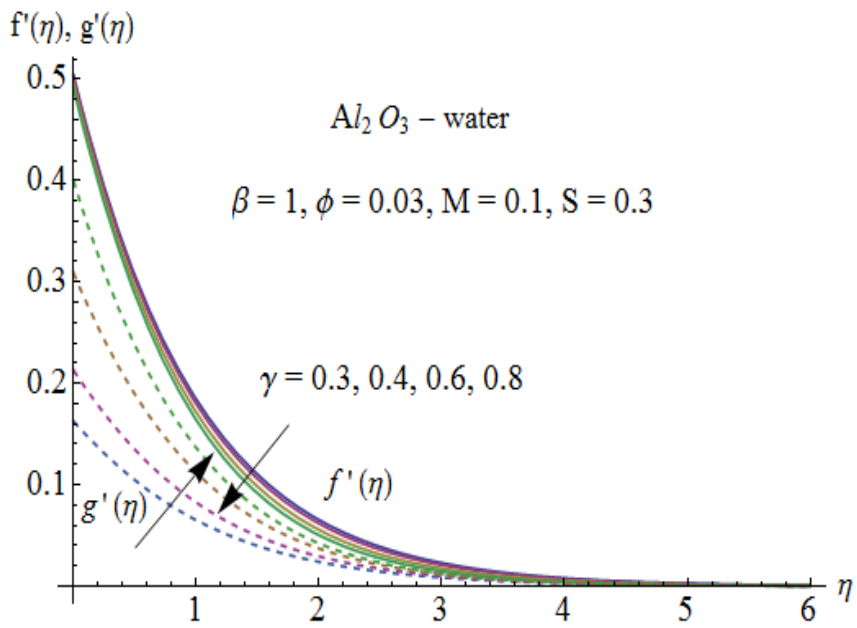


Fig. 10.6: Effect of γ on f' and g' .

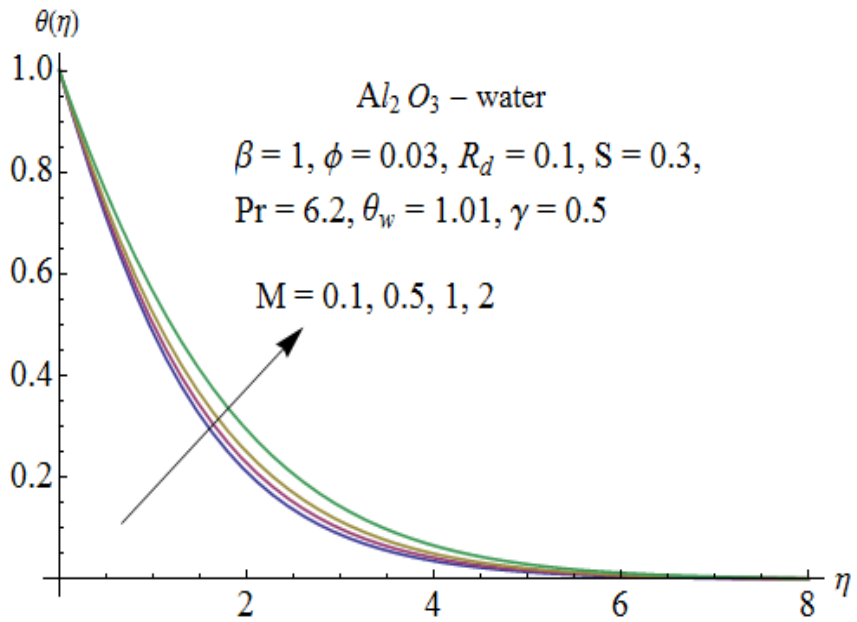


Fig. 10.7: Effect of M on $\theta(\eta)$.

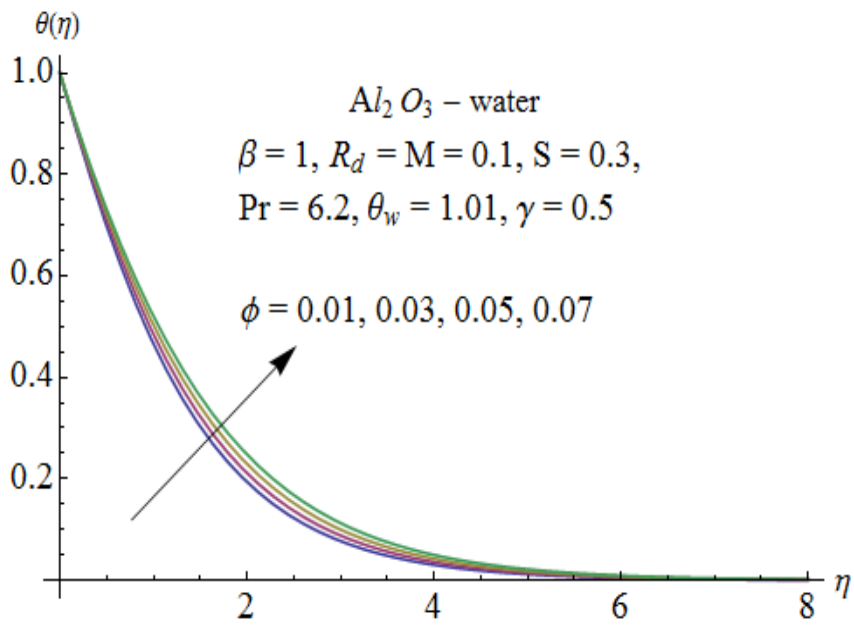


Fig. 10.8: Effect of ϕ on $\theta(\eta)$.

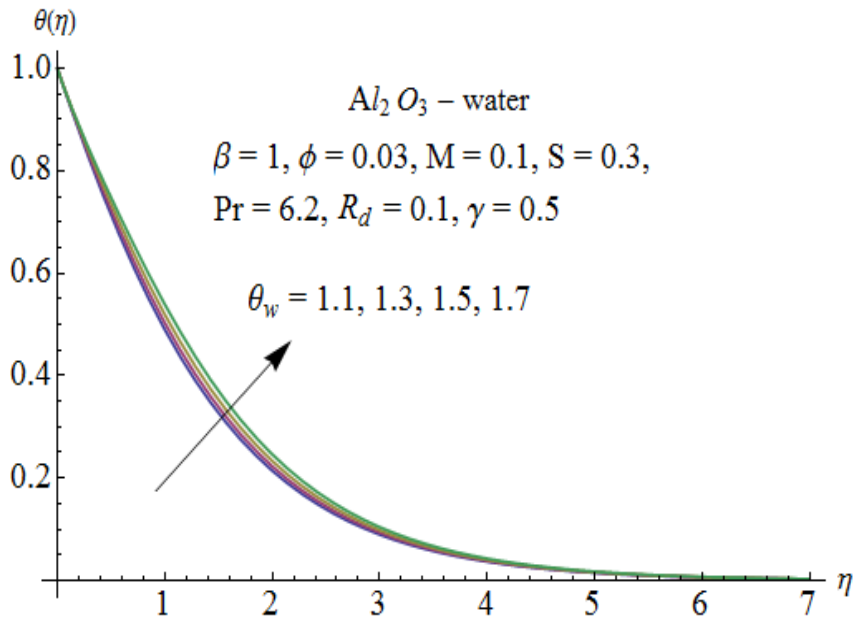


Fig. 10.9: Effect of θ_w on $\theta(\eta)$.

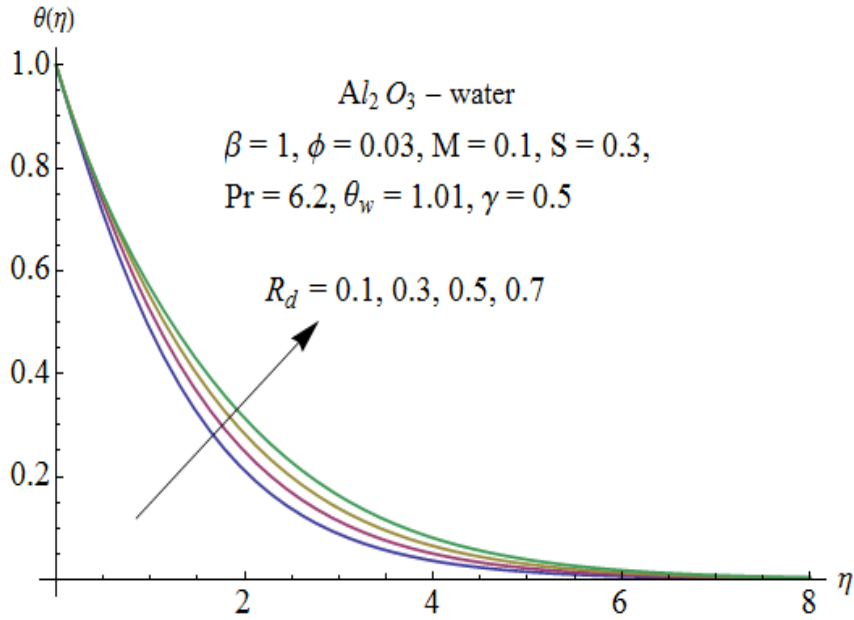


Fig. 10.10: Effect of R_d on $\theta(\eta)$.

Table 10.2: Thermophysical properties of water and nanoparticles [21].

	$\rho(kg/m^3)$	$c_p(j/kgk)$	$k(W/m.k)$	$\beta \times 10^5(K^{-1})$	$\sigma(\Omega m)^{-1}$
Pure water	997.1	4179	0.613	21	0.05
Copper(<i>Cu</i>)	8933	385	401	1.67	5.96×10^7
Silver(<i>Ag</i>)	10500	235	429	1.89	3.6×10^7
Alumina(Al_2O_3)	3970	765	40	0.85	1×10^{-10}
Titanium Oxide(TiO_2)	4250	686.2	8.9538	0.9	1×10^{-12}

Table 10.3: Effects of the nanoparticle volume fraction for different types of nanofluids on skin friction coefficient along x -direction when $M = 0.1$, $\beta = 1$, $Pr = 6.2$, $S = 0.3$, $\gamma = 0.5$, $R_d = 0.1$ and $\theta_w = 1.1$.

ϕ	<i>Cu</i>	<i>Ag</i>	Al_2O_3	TiO_2
0.01	-0.519383	-0.521081	-0.513864	-0.514181
0.03	-0.556763	-0.561468	-0.540779	-0.541729
0.05	-0.595136	-0.602496	-0.569204	-0.570789

Table 10.4: Effects of the nanoparticle volume fraction for different types of nanofluids on skin friction coefficient along y -direction when $M = 0.1$, $\beta = 1$, $Pr = 6.2$, $S = 0.3$, $\gamma = 0.5$, $R_d = 0.1$ and $\theta_w = 1.1$.

ϕ	Cu	Ag	Al_2O_3	TiO_2
0.01	-0.699999	-0.702450	-0.692049	-0.692506
0.03	-0.751194	-0.758029	-0.728085	-0.729453
0.05	-0.803691	-0.814440	-0.766089	-0.768375

Table 10.5: Effects of the nanoparticle volume fraction for different types of nanofluids on Nusselt number when $M = 0.1$, $\beta = 1$, $Pr = 6.2$, $S = 0.3$, $\gamma = 0.5$, $R_d = 0.1$ and $\theta_w = 1.1$.

ϕ	Cu	Ag	Al_2O_3	TiO_2
0.01	-0.726911	-0.723181	-0.733826	-0.732487
0.03	-0.720997	-0.710335	-0.740837	-0.736838
0.05	-0.716675	-0.699623	-0.748444	-0.741798

Table 10.6: Values of $Nu(Re_x)^{-\frac{1}{2}}$ when $\phi = 0.03$, $\beta = 1$, $S = 0.3$ and $\gamma = 0.5$.

M	θ_w	R_d	$-(1 + R_d\theta_w^3)\theta'(0)$
0.1	1.1	0.1	0.74084
0.3			0.70977
0.5			0.68279
0.1	1.2		0.74410
	1.3		0.74775
	1.4		0.75180
	1.1	0.05	0.73328
		0.15	0.74802
		0.2	0.75482

10.6 Concluding remarks

Three-dimensional flow of Al_2O_3 nanofluid over a permeable stretching surface with partial slip and nonlinear thermal radiation is studied. The outcomes are mentioned below.

- Increasing values of Hartman number, velocity slip parameter and suction/injection velocity parameter decrease the velocity profiles.
- The velocity profiles f' and g' decrease by Increasing nanoparticle volume fraction.
- Effects of stretching parameter on the velocity profiles and momentum boundary layers are opposite.
- The temperature and thermal boundary layer thickness increase via larger nanoparticle volume fraction.
- Increasing values of temperature and radiation parameters show enhancement in the temperature and thermal boundary layer thickness.
- Temperature gradient at the surface increases for higher temperature and radiation parameters.
- The governing equations for viscous fluid are obtained when $\phi = 0$.

Chapter 11

Magnetohydrodynamic three-dimensional flow of nanofluid over a porous shrinking surface

This chapter investigates the steady three-dimensional flow of viscous nanofluid past a permeable shrinking surface with velocity slip and temperature jump. An incompressible fluid fills the porous space. The fluid is electrically conducting in the presence of an applied magnetic field. The governing nonlinear partial differential equations are reduced to ordinary differential equations by similarity transformations. The series solutions are presented by the homotopy analysis method. Convergence of the obtained series solutions is explicitly discussed. The velocity and temperature profiles are shown and analyzed for different emerging parameters of interest. It is observed that by increasing the volume of copper nanoparticles, the thermal conductivity increases and the boundary layer thickness decreases. The velocity profile increases and temperature profile decreases for the larger velocity slip parameter. Temperature is a decreasing function of the thermal slip parameter. Hence less heat is transferred to the fluid from the sheet

11.1 Problem formulation

Let us consider steady three-dimensional flow of viscous nanofluid over a shrinking surface. A Cartesian coordinate system is used with (u, v, w) as the velocity components in the (x, y, z) directions. An incompressible nanofluid occupies $z > 0$, where z is the coordinate measured normal to the shrinking surface (see Fig. 11.1). The fluid is water based nanofluid consisting of nanoparticles like copper (Cu), silver (Ag), alumina (Al_2O_3), titanium oxide (TiO_2) and copper oxide (CuO).

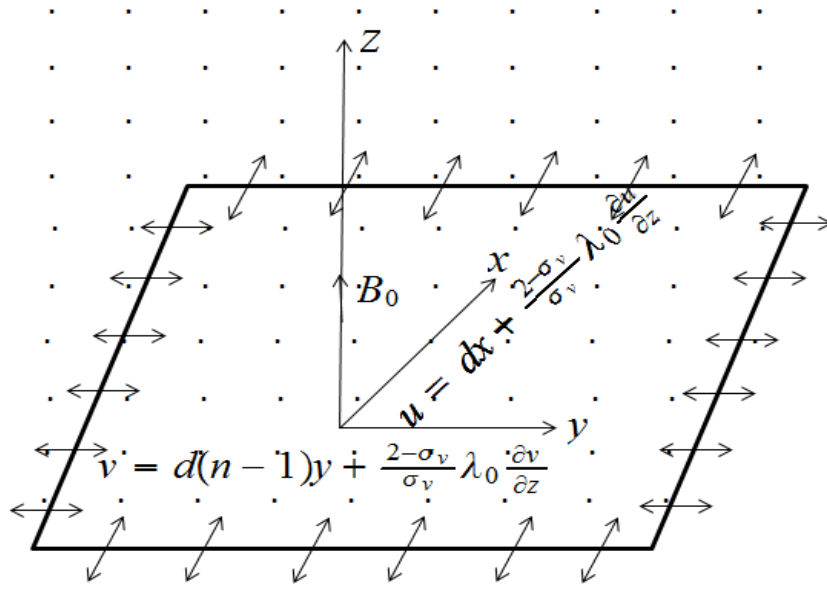


Fig. 11.1: Physical model of the problem.

Further the fluid is subjected to a uniform magnetic field with strength B_0 in the transverse direction to flow. Here induced magnetic field is taken small in comparison to the applied magnetic field and thus neglected. Under the aforementioned assumptions the equations of continuity, momentum and thermal energy can be expressed in the forms

$$\frac{\partial u}{\partial x} + \frac{\partial v}{\partial y} + \frac{\partial w}{\partial z} = 0, \quad (11.1)$$

$$u \frac{\partial u}{\partial x} + v \frac{\partial u}{\partial y} + w \frac{\partial u}{\partial z} = \nu_{nf} \left(\frac{\partial^2 u}{\partial x^2} + \frac{\partial^2 u}{\partial y^2} + \frac{\partial^2 u}{\partial z^2} \right) - \frac{1}{\rho_{nf}} \frac{\partial P}{\partial x} - \frac{\sigma_{nf} B_0^2 u}{\rho_{nf}} - \frac{\nu_{nf} u}{K}, \quad (11.2)$$

$$u \frac{\partial v}{\partial x} + v \frac{\partial v}{\partial y} + w \frac{\partial v}{\partial z} = \nu_{nf} \left(\frac{\partial^2 v}{\partial x^2} + \frac{\partial^2 v}{\partial y^2} + \frac{\partial^2 v}{\partial z^2} \right) - \frac{1}{\rho_{nf}} \frac{\partial P}{\partial y} - \frac{\sigma_{nf} B_0^2 v}{\rho_{nf}} - \frac{\nu_{nf} v}{K}, \quad (11.3)$$

$$u \frac{\partial w}{\partial x} + v \frac{\partial w}{\partial y} + w \frac{\partial w}{\partial z} = \nu_{nf} \left(\frac{\partial^2 w}{\partial x^2} + \frac{\partial^2 w}{\partial y^2} + \frac{\partial^2 w}{\partial z^2} \right) - \frac{1}{\rho_{nf}} \frac{\partial P}{\partial z}, \quad (11.4)$$

$$u \frac{\partial T}{\partial x} + v \frac{\partial T}{\partial y} + w \frac{\partial T}{\partial z} = \alpha_{nf} \left(\frac{\partial^2 T}{\partial x^2} + \frac{\partial^2 T}{\partial y^2} + \frac{\partial^2 T}{\partial z^2} \right), \quad (11.5)$$

with

$$u = dx + \frac{2 - \sigma_v}{\sigma_v} \lambda_0 \frac{\partial u}{\partial z}, \quad v = d(n-1)y + \frac{2 - \sigma_v}{\sigma_v} \lambda_0 \frac{\partial v}{\partial z}, \quad w = -W,$$

$$T = T_w + \frac{2 - \sigma_T}{\sigma_T} \left(\frac{2\tilde{r}}{\tilde{r} + 1} \right) \frac{\lambda_0}{\text{Pr}} \frac{\partial T}{\partial z} \quad \text{at } z = 0,$$

$$u \rightarrow 0, \quad v \rightarrow 0, \quad T \rightarrow T_\infty, \quad \text{as } z \rightarrow \infty. \quad (11.6)$$

In the above equations ρ_{nf} denotes the effective density of the nanofluid, ν_{nf} the effective kinematic viscosity of the nanofluid, μ_{nf} the effective dynamic viscosity, σ_{nf} the effective electrical conductivity, P the pressure, K the permeability of porous medium, $W > 0$ the suction velocity, $d < 0$ the shrinking rate, T the temperature of nanofluid, σ_ν the tangential momentum accommodation coefficient, σ_T the thermal accommodation coefficient, λ_0 the molecular mean free path, \tilde{r} the specific heat ratio and sheet shrinks only in the x -direction when $n = 1$. The sheet shrinks asymmetrically for $n = 2$.

The effective dynamic viscosity of the nanofluid is

$$\mu_{nf} = \frac{\mu_f}{(1 - \phi)^{2.5}}, \quad (11.7)$$

where ϕ is the solid volume fraction of nanoparticles and the effective density of nanofluids is given by

$$\rho_{nf} = (1 - \phi)\rho_f + \phi\rho_s. \quad (11.8)$$

The thermal diffusivity of the nanofluid is

$$\alpha_{nf} = \frac{k_{nf}}{(\rho c_p)_{nf}}, \quad (11.9)$$

where the heat capacitance of nanofluid is given by

$$(\rho c_p)_{nf} = (1 - \phi)(\rho c_p) + \phi(\rho c_p). \quad (11.10)$$

For spherical nanoparticles, the thermal conductivity of the nanofluid is

$$\frac{k_{nf}}{k_f} = \frac{k_s + 2k_f - 2\phi(k_f - k_s)}{k_s + 2k_f + 2\phi(k_f - k_s)}. \quad (11.11)$$

The effective electrical conductivity is

$$\frac{\sigma_{nf}}{\sigma_f} = 1 + \frac{3 \left(\frac{\sigma_s}{\sigma_f} - 1 \right) \phi}{\left(\frac{\sigma_s}{\sigma_f} + 2 \right) - \left(\frac{\sigma_s}{\sigma_f} - 1 \right) \phi}. \quad (11.12)$$

Here the subscripts nf represents the thermophysical properties of the nanofluid, f explains base fluid and s is defined as nano solid particles.

In order to attain similarity solution, the following transformations can be posited:

$$u = cx f'(\eta), \quad v = c(n-1)y f'(\eta), \quad w = -\sqrt{cv_f} n f'(\eta), \quad \eta = \sqrt{\frac{c}{v_f}} z, \quad \theta(\eta) = \frac{T - T_\infty}{T_w - T_\infty}. \quad (11.13)$$

Continuity equation (11.1) is automatically satisfied and the other equations and conditions give

$$\varepsilon_1 f''' - \varepsilon_1 \left[M^2 (1 - \phi)^{2.5} \frac{\sigma_{nf}}{\sigma_f} + \lambda \right] f' - f'^2 + n f'' f = 0, \quad (11.14)$$

$$\frac{k_{nf}}{k_f} \frac{1}{\text{Pr}} \theta'' + \left(1 - \phi + \phi \frac{(\rho c)_s}{(\rho c)_f} \right) n f \theta' = 0, \quad (11.15)$$

$$\begin{aligned} f'(0) &= \gamma + \beta f''(0), \quad f(0) = S, \quad \theta(0) = 1 + \tilde{\beta} \theta'(0), \\ f'(\infty) &\rightarrow 0, \quad \theta(\infty) \rightarrow 0, \end{aligned} \quad (11.16)$$

where M^2 is the Hartman number, Pr the Prandtl number, S the mass suction parameter, $\gamma < 0$ the shrinking parameter, β the velocity slip parameter, λ the porosity parameter and $\tilde{\beta}$

the temperature jump parameter. These parameters are defined by

$$\begin{aligned} M^2 &= \frac{B_0^2 \sigma_f}{\rho_f c}, \quad \text{Pr} = \frac{\nu_f}{\alpha}, \quad S = \frac{W}{\sqrt{c\nu_f n}}, \quad \gamma = \frac{d}{c}, \quad \beta = \frac{2 - \sigma_v}{\sigma_v} \lambda_0 \sqrt{\frac{c}{\nu_f}}, \\ \lambda &= \frac{\nu_f}{cK}, \quad \tilde{\beta} = \frac{2 - \sigma_T}{\sigma_T} \left(\frac{2\tilde{r}}{\tilde{r} + 1} \right) \frac{\lambda_0}{\text{Pr}} \sqrt{\frac{c}{\nu_f}}, \end{aligned} \quad (11.17)$$

where ε_1 is defined by

$$\varepsilon_1 = \frac{1}{(1 - \phi)^{2.5} \left[1 - \phi + \phi \left(\frac{\rho_s}{\rho_f} \right) \right]}, \quad (11.18)$$

with ρ_s as nano-solid particle density and ρ_f as base fluid density.

The important physical quantities of interest are local skin friction coefficient C_{sf} and Nusselt number Nu which are given by

$$C_{sf} = \frac{\tau_w|_{z=0}}{\frac{1}{2}\rho u_w^2}, \quad Nu = \frac{xq_w}{k_f(T_f - T_\infty)}, \quad (11.19)$$

where the surface shear stress τ_w and surface heat flux q_w satisfy

$$\tau_w = -\mu_{nf} \left. \frac{\partial u}{\partial z} \right|_{z=0}, \quad q_w = -k_{nf} \left. \frac{\partial T}{\partial z} \right|_{z=0}. \quad (11.20)$$

Dimensionless forms of local skin friction coefficient and Nusselt number are

$$C_{sf} \sqrt{\frac{\text{Re}_x}{2}} = \frac{1}{(1 - \phi)^{2.5}} f''(0), \quad Nu \text{Re}_x^{-\frac{1}{2}} = -\frac{k_{nf}}{k_f} \theta'(0), \quad (11.21)$$

in which $\text{Re}_x = u_w x / \nu_f$ denotes the local Reynolds number.

11.2 Homotopy analysis solutions

The initial guesses $f_0(\eta)$ and $\theta_0(\eta)$ and the linear operators \mathcal{L}_f and \mathcal{L}_θ are selected in the following forms

$$f_0(\xi) = S + \frac{\gamma}{1 + \beta} - \frac{\gamma}{1 + \beta} \exp(-\eta), \quad \theta_0(\eta) = \frac{1}{1 + \tilde{\beta}} \exp(-\eta), \quad (11.22)$$

$$\mathcal{L}_f(f) = \frac{\partial^3 f}{\partial \eta^3} - \frac{\partial f}{\partial \eta}, \quad \mathcal{L}_\theta(\theta) = \frac{\partial^2 \theta}{\partial \eta^2} - \theta, \quad (11.23)$$

with the properties mentioned below

$$\begin{aligned} \mathcal{L}_f [c_1 + c_2 \eta + c_3 e^{-\eta}] &= 0, \\ \mathcal{L}_\theta [c_4 + c_5 e^{-\eta}] &= 0, \end{aligned} \quad (11.24)$$

and $c_1 - c_5$ are the constants. With Eqs. (11.14) and (11.15), the definitions of operators \mathcal{N}_f and \mathcal{N}_θ can be introduced as follows:

$$\begin{aligned} \mathcal{N}_f [\hat{f}(\eta; p)] &= \varepsilon_1 \frac{\partial^3 \hat{f}(\eta; p)}{\partial \eta^3} - \varepsilon_1 \left[M^2 (1 - \phi)^{2.5} \frac{\sigma_{nf}}{\sigma_f} + \lambda \right] \frac{\partial \hat{f}(\eta; p)}{\partial \eta} \\ &\quad - \left(\frac{\partial \hat{f}(\eta; p)}{\partial \eta} \right)^2 + n \frac{\partial \hat{f}(\eta; p)}{\partial \eta} \frac{\partial^2 \hat{f}(\eta; p)}{\partial \eta^2}, \end{aligned} \quad (11.25)$$

$$\mathcal{N}_\theta [\hat{\theta}(\eta; p), \hat{f}(\eta; p)] = \frac{k_{nf}}{k_f} \frac{1}{\text{Pr}} \frac{\partial^2 \hat{\theta}(\eta; p)}{\partial \eta^2} + \left(1 - \phi + \phi \frac{(\rho c)_s}{(\rho c)_f} \right) n \hat{f}(\eta; p) \frac{\partial \hat{\theta}(\eta; p)}{\partial \eta}. \quad (11.26)$$

The problems subjected to zeroth order deformation can be written as follows:

$$(1 - p) \mathcal{L}_f [\hat{f}(\eta; p) - f_0(\eta)] = p \hbar_f \mathcal{N}_f [\hat{f}(\eta; p)], \quad (11.27)$$

$$(1 - p) \mathcal{L}_\theta [\hat{\theta}(\eta; p) - \theta_0(\eta)] = p \hbar_\theta \mathcal{N}_\theta [\hat{\theta}(\eta; p), \hat{f}(\eta; p)], \quad (11.28)$$

$$\begin{aligned} \hat{f}(0; p) &= S, \quad \frac{\partial \hat{f}(0; p)}{\partial \eta} = \gamma + \beta \frac{\partial^2 \hat{f}(0; p)}{\partial \eta^2}, \quad \frac{\partial \hat{f}(\infty; p)}{\partial \eta} = 0, \\ \hat{\theta}(0; p) &= 1 + \tilde{\beta} \frac{\partial \hat{\theta}(0; p)}{\partial \eta}, \quad \hat{\theta}(\infty; p) = 0, \end{aligned} \quad (11.29)$$

in which \hbar_f and \hbar_θ are the nonzero auxiliary parameters.

The corresponding problems at m^{th} order satisfy the following expressions

$$\mathcal{L}_f [f_m(\eta) - \chi_m f_{m-1}(\eta)] = \hbar_f \mathcal{R}_{f,m}(\eta), \quad (11.30)$$

$$\mathcal{L}_\theta [\theta_m(\eta) - \chi_m \theta_{m-1}(\eta)] = \hbar_\theta \mathcal{R}_{\theta,m}(\eta), \quad (11.31)$$

$$f_m(0) = f'_m(0) - \beta f''_m(0) = f'_m(\infty) = \theta_m(0) - \hat{\beta}\theta'_m(0) = \theta_m(\infty) = 0, \quad (11.32)$$

$$\mathcal{R}_{f,m}(\eta) = \varepsilon_1 f'''_{m-1}(\eta) - \varepsilon_1 \left[M^2(1-\phi)^{2.5} \frac{\sigma_{nf}}{\sigma_f} + \lambda \right] f'_{m-1}(\eta) + \sum_{k=0}^{m-1} [n f_{m-1-k} f''_k - f'_{m-1-k} f'_k], \quad (11.33)$$

$$\mathcal{R}_{\theta,m}(\eta) = \frac{k_{nf}}{k_f} \frac{1}{\text{Pr}} \theta''_{m-1}(\eta) + \left(1 - \phi + \phi \frac{(\rho c)_s}{(\rho c)_f} \right) n \sum_{k=0}^{m-1} f_{m-1-k} \theta'_k, \quad (11.34)$$

and

$$\chi_m = \begin{cases} 0, & m \leq 1 \\ 1, & m > 1 \end{cases}. \quad (11.35)$$

If f_m^* and θ_m^* denote the special solutions then the general solutions are

$$f_m(\eta) = f_m^*(\eta) + c_1 + c_2\eta + c_3e^{-\eta},$$

$$\theta_m(\eta) = \theta_m^*(\eta) + c_4 + c_5e^{-\eta}. \quad (11.36)$$

11.3 Convergence analysis

We note that the computed series solutions depend upon the auxiliary parameters. The convergence region and rate of approximations for the functions f and θ can be controlled and adjusted through the auxiliary parameters \hbar_f and \hbar_θ . For admissible values of \hbar_f and \hbar_θ , the \hbar -curves of $f''(0)$ and $\theta'(0)$ for 17th-order of approximations are displayed. Figs. 11.1 and 11.2 depict that the range of admissible values of \hbar_f and \hbar_θ are $-1.5 \leq \hbar_f \leq -0.1$ and $-1.4 \leq \hbar_\theta \leq -0.6$. It is found that the series solutions converge in the whole region of η ($0 < \eta < \infty$) when $\hbar_f = -0.7$ and $\hbar_\theta = -0.9$.

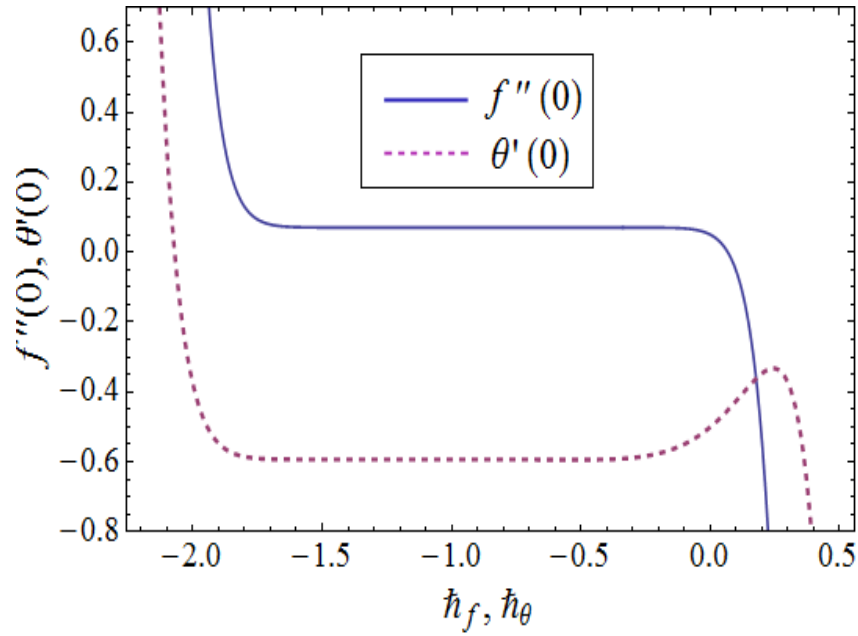


Fig. 11.2: \hbar -curves of $f''(0)$ and $\theta'(0)$.

Table 11.1: Convergence of HAM solutions for different order of approximations when $\gamma = -0.1$, $\tilde{\beta} = \beta = M = 1$, $n = 2$, $\lambda = \phi = 0.3$ and $S = 0.5$.

Order of approximations	$f''(0)$	$-\theta'(0)$
1	0.0661678	0.532809
5	0.0700218	0.589974
10	0.0700198	0.594100
15	0.0700198	0.593038
20	0.0700198	0.593149
25	0.0700198	0.593162
28	0.0700198	0.593155
35	0.0700198	0.593155
40	0.0700198	0.593155
45	0.0700198	0.593155

11.4 Results and discussion

This section is prepared to examine the impact of pertinent parameters on the velocity and temperature. This objective has been achieved by plots of Figs. (11.3 – 11.14). Here Figs (11.3 – 11.8) have been plotted for the effects of M (Hartman number), λ (porosity parameter), S (mass suction parameter), β (velocity slip parameter), ϕ (nanoparticles volume fraction) on the velocity f' and γ (shrinking parameter). The behavior of Hartman number M for the boundary layer is shown in Fig. 11.3. There is decrease in thickness of boundary layer due to an increase in M . This is because of the reason that Lorentz force acts as a retarding force. Such retarding force enhances the frictional resistance opposing the fluid motion in the momentum boundary layer. Fig. 11.4 depicts that the velocity is increased when porosity parameter λ increases. As noted in Fig. 11.5 the associated boundary layer thickness decays when mass suction parameter S increases. Because applying suction leads to draw the amount of fluid particles into the wall and consequently the velocity boundary layer decreases. Also suction is an agent which causes a reduction in the fluid velocity. Fig. 11.6 shows that velocity rises when values of velocity slip parameter β are enhanced. However velocity is a decreasing function of ϕ (see Fig. 11.7). This is because of the fact that by increasing the volume of copper nanoparticles, the thermal conductivity increases and the boundary layer thickness decreases. Fig. 11.8 portrays the influence of γ on f' . It is found that velocity increases when values of γ are increased. Figs. 11.9 – 11.14 depict the effects of Hartman number M , porosity parameter λ , mass suction parameter S , velocity slip parameter β , temperature jump parameter $\tilde{\beta}$ and shrinking parameter γ on temperature profile θ . Effect of M on the temperature is analyzed in Fig. 11.9. As Lorentz force is a resistive force which opposes the fluid motion. So heat is produced and as a result thermal boundary layer thickness increases. It is observed that increasing the porosity parameter λ decreases the thermal boundary layer thickness. Variations of S and β on temperature profile θ can be seen in the Figs. (11.11 – 11.12). There is a decrease in temperature when mass suction parameter S and velocity slip parameter β are increased. Fig. 11.13 indicates that the surface temperature and thermal boundary layer decrease by increasing value of temperature jump $\tilde{\beta}$. With the increase of thermal slip parameter, less heat is transferred to the fluid from the sheet and so temperature is found to decrease. Fig. 11.14 represents the effect of shrinking parameter γ on temperature profile. It is observed that

temperature profile decreases for an increase in γ .

Table 11.1 is prepared for the convergence of series solutions. It is observed that convergence for velocity is achieved at 10^{th} order of approximation and for temperature convergence is achieved at 28^{th} order of approximation. The values of shear stress at the surface are compared with previous published results in Table 11.2. Here it is seen that the obtained solutions agree well with results of Zheng et al. [36]. Numerical values of the local Nusselt number for different emerging parameters are presented in Table 11.3. It is noted that the local Nusselt number increases for larger values of ϕ , γ , S and β . However it decreases for larger values of $\tilde{\beta}$.

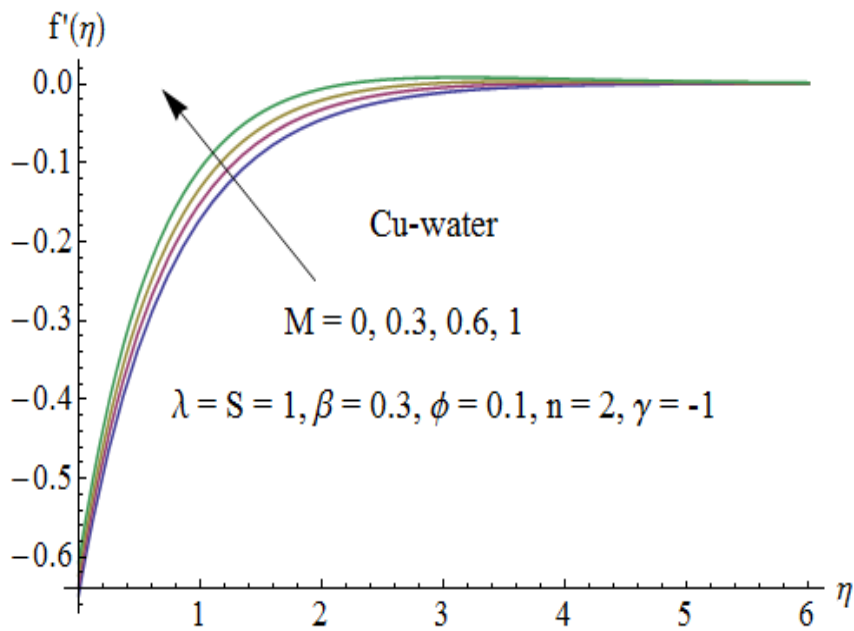


Fig. 11.3: Influence of M on $f'(\eta)$.

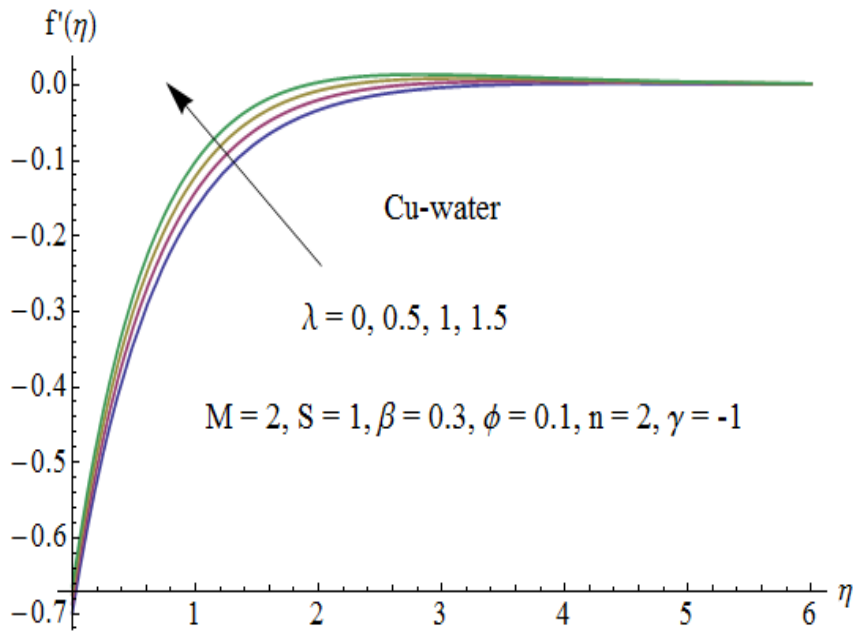


Fig. 11.4: Influence of λ on $f'(\eta)$.

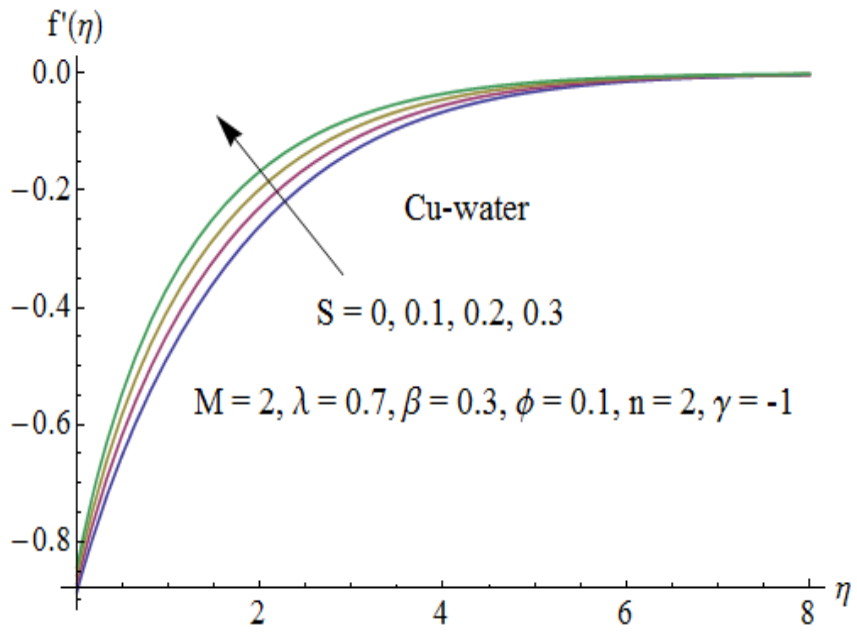


Fig. 11.5: Influence of S on $f'(\eta)$.

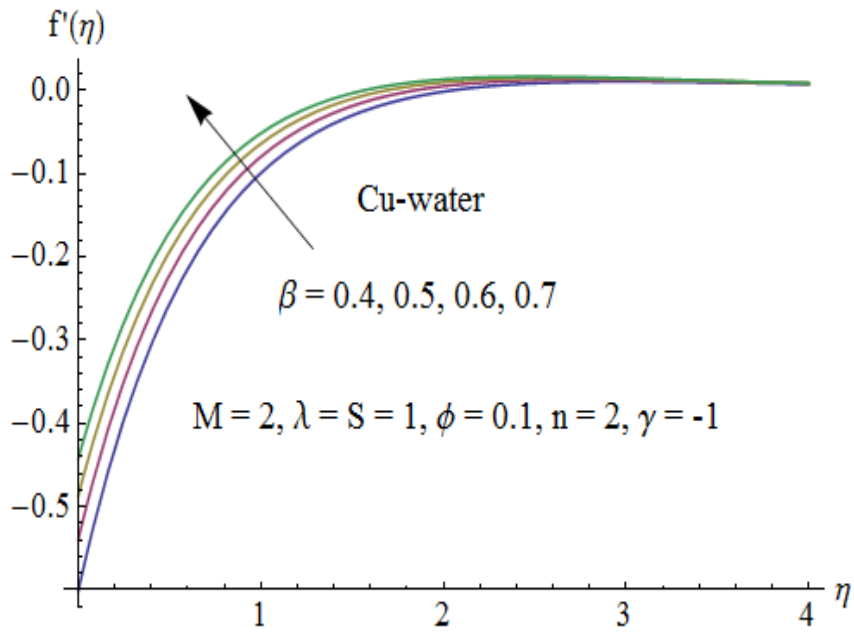


Fig. 11.6: Influence of β on $f'(\eta)$.

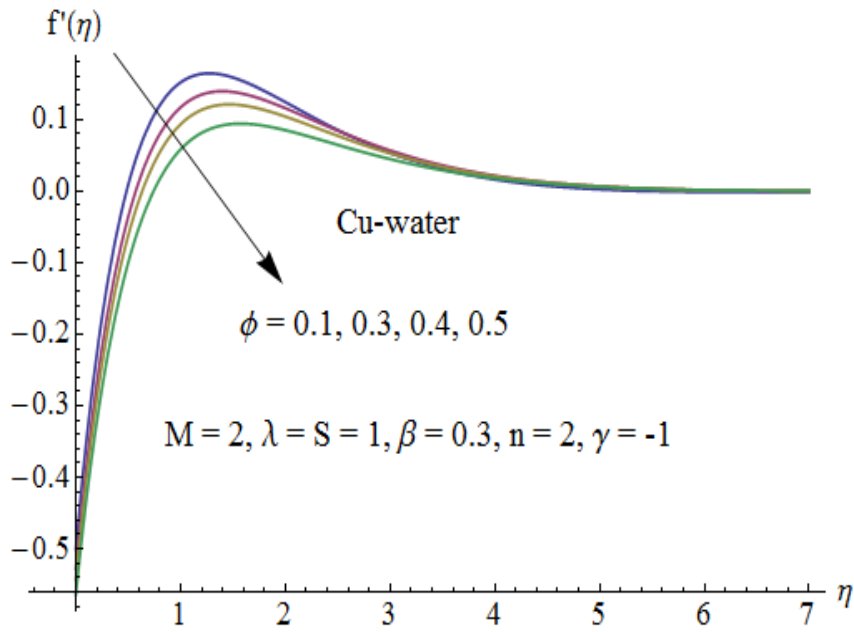


Fig. 11.7: Influence of ϕ on $f'(\eta)$.

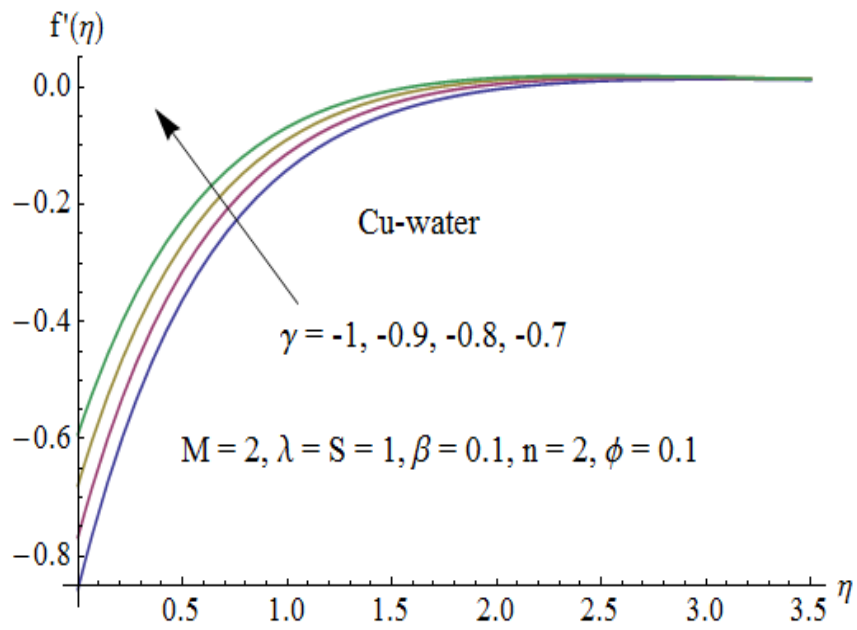


Fig. 11.8: Influence of γ on $f'(\eta)$.

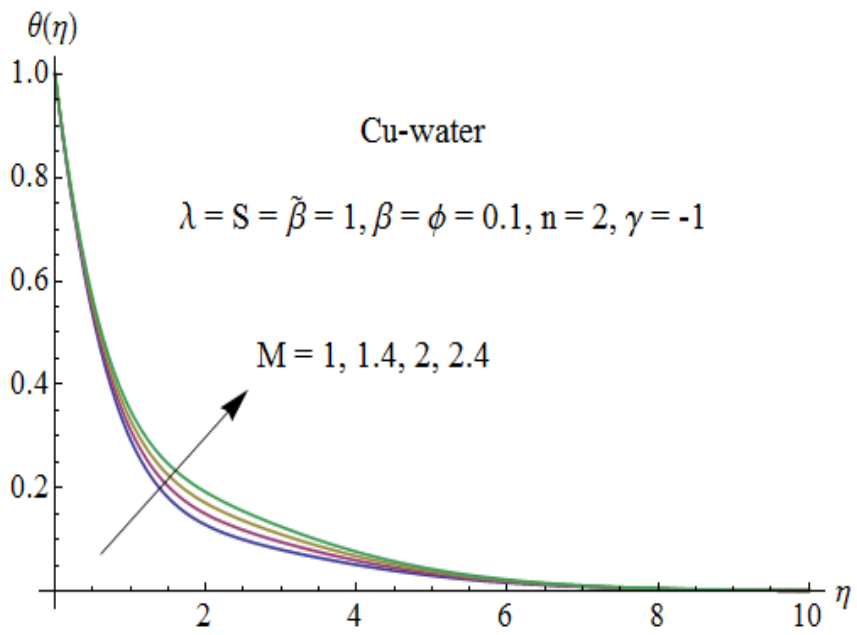


Fig. 11.9: Influence of M on $\theta(\eta)$.

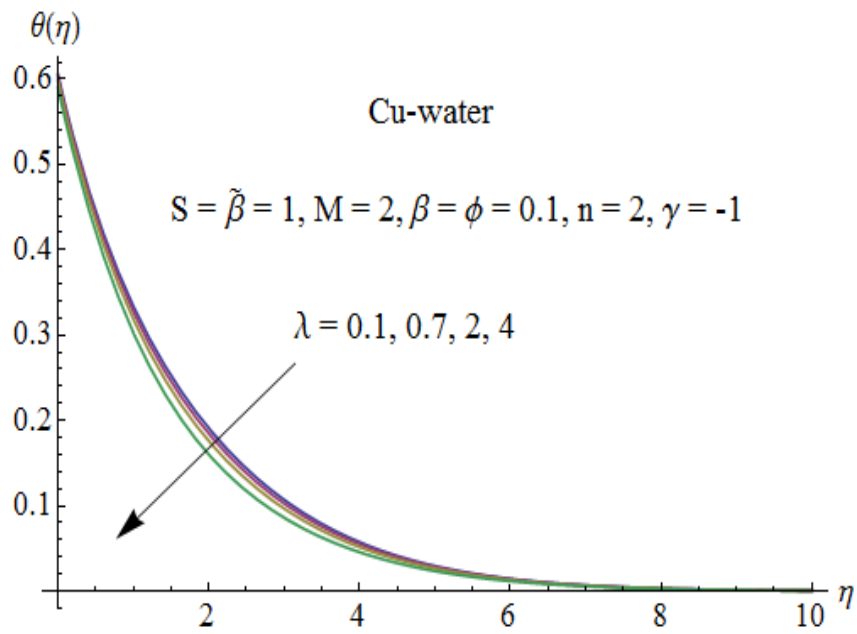


Fig. 11.10: Influence of λ on $\theta(\eta)$.

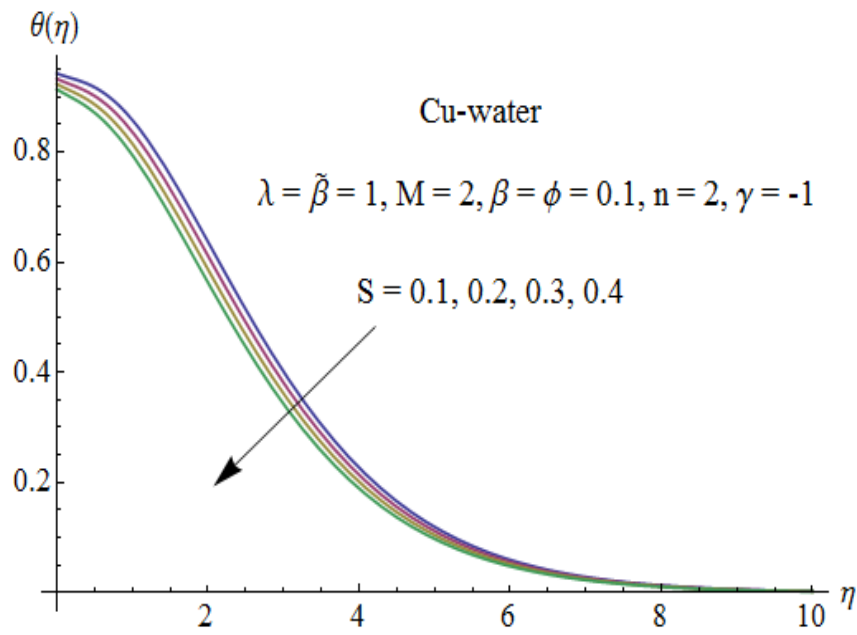


Fig. 11.11: Influence of S on $\theta(\eta)$.

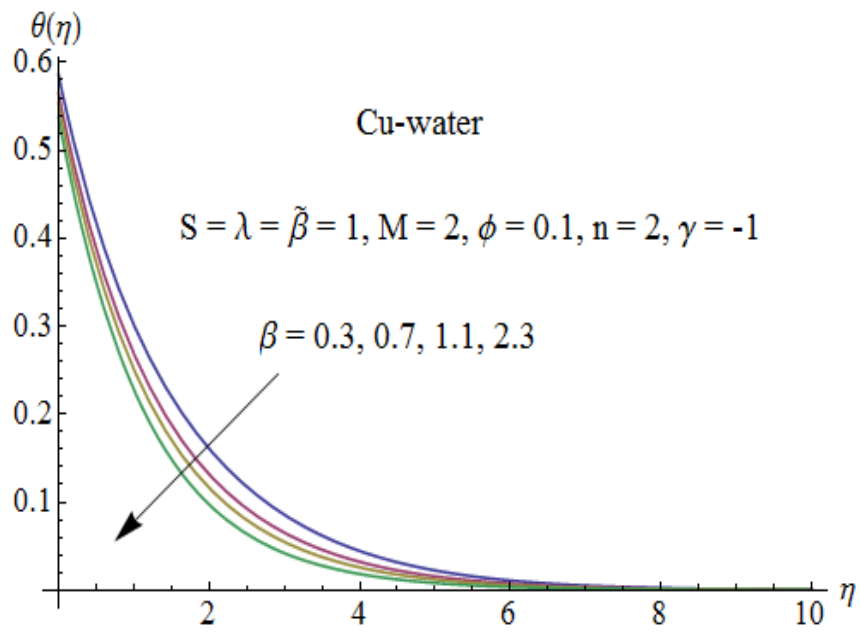


Fig. 11.12: Influence of β on $\theta(\eta)$.

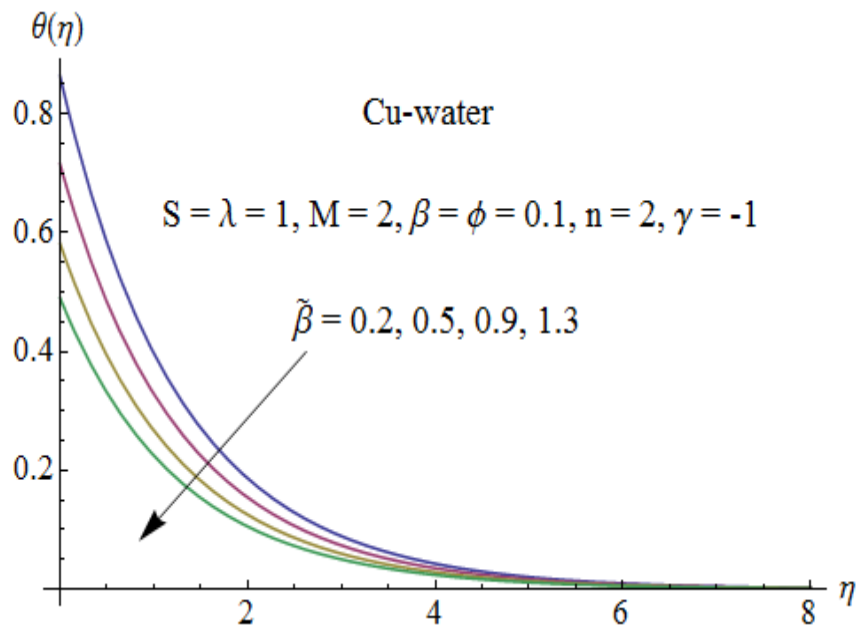


Fig. 11.13: Influence of $\tilde{\beta}$ on $\theta(\eta)$.

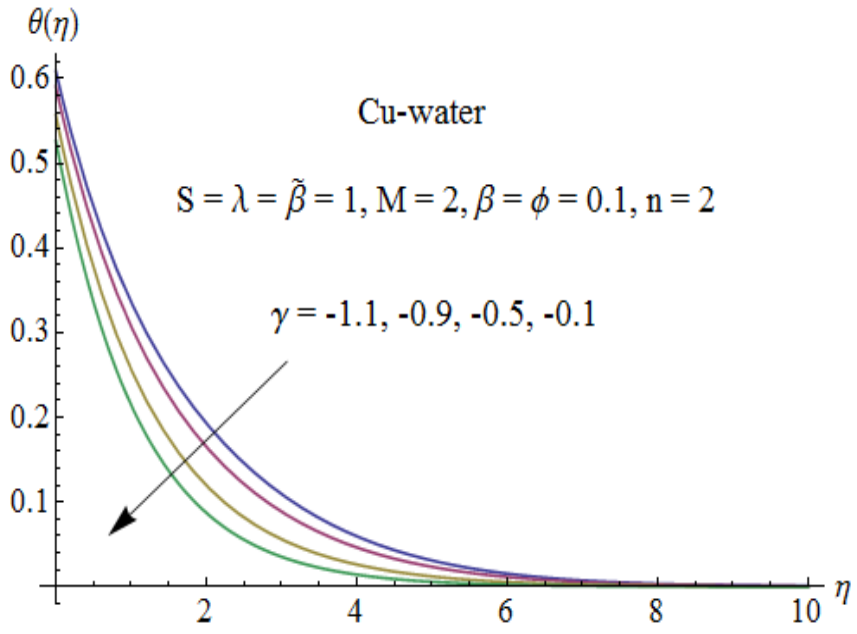


Fig. 11.14: Influence of γ on $\theta(\eta)$.

Table 11.2: Comparison of values of $f''(0)$ when $\lambda = 0$, $\beta = 0$, $\gamma = -1$ and $\phi = 0$.

n	M	S	Zheng et al. [36]	Present results
2	2	1.8	4.21671330	4.20406130
2	2	1	2.89187352	2.89160464
2	2	0.2	1.84296593	1.84287335
2	$\sqrt{5}$	2	4.75696326	4.74614023
2	$\sqrt{5}$	3	6.54909894	6.53871573
1	2	1.8	2.85192213	2.85192199
1	2	1	2.30277564	2.30277376
1	2	0.2	1.83493516	1.83493413

Table 11.3: Numerical values of Nusselt number Nu for different values of ϕ , γ , S , β and $\tilde{\beta}$.

ϕ	γ	S	β	$\tilde{\beta}$	$-\frac{k_{nf}}{k_f}\theta'(0)$
0.25	-0.1	0.5	1	1	1.97478
0.3					2.35243
0.4					3.43831
0.3	-0.4				2.30085
	-0.3				2.31914
	-0.2				2.33626
	-0.1	0.3			1.82586
		0.4			2.12684
		0.7			2.66889
		0.5	0.5		2.34389
			0.7		2.34821
			0.9		2.35123
			1	0.3	4.02267
				0.5	3.34427
				0.7	2.86169

11.5 Concluding remarks

Three-dimensional flow of viscous nanofluid due to porous shrinking surface is discussed. Attention is focused to the development of series solutions. The following observations are important.

- The velocity has similar pattern with respect to Hartman number, porosity parameter, mass suction parameter and velocity slip parameter.
- The shrinking parameter has reverse effect on the velocity and temperature profiles.
- Role of velocity slip, temperature jump and suction parameters on the temperature are similar in a qualitative sense.

- There is an increase in the temperature and thermal boundary layer when Hartman number increases.

Chapter 12

MHD three-dimensional flow of nanofluid in presence of convective conditions

This chapter deals with the boundary layer magnetohydrodynamic (MHD) flow of viscous nanofluid saturating porous medium. The flow is induced by a convectively heated permeable shrinking surface. Appropriate transformations reduce the nonlinear partial differential system to ordinary differential system. Flow and heat transfer characteristics are computed by homotopic procedure. The results of velocity, temperature and Nusselt number are analyzed for various parameters of interest. It is noted that higher nanoparticle volume fraction decreases the velocity field. Also temperature and heat transfer rate are enhanced for larger values of Biot number.

12.1 Model development

Let us consider the steady three-dimensional flow of an incompressible nanofluid over a shrinking surface. The fluid fills the porous medium. A uniform transverse magnetic field of strength B_0 is applied parallel to the z -axis. It is assumed that the induced magnetic and electric field effects are negligible. The convective boundary conditions are employed in the heat transfer

process. The governing equations are given by

$$\frac{\partial u}{\partial x} + \frac{\partial v}{\partial y} + \frac{\partial w}{\partial z} = 0, \quad (12.1)$$

$$u \frac{\partial u}{\partial x} + v \frac{\partial u}{\partial y} + w \frac{\partial u}{\partial z} = \nu_{nf} \frac{\partial^2 u}{\partial z^2} - \frac{\sigma_{nf} B_0^2 u}{\rho_{nf}} - \frac{\nu_{nf}}{K} u, \quad (12.2)$$

$$u \frac{\partial v}{\partial x} + v \frac{\partial v}{\partial y} + w \frac{\partial v}{\partial z} = \nu_{nf} \frac{\partial^2 v}{\partial z^2} - \frac{\sigma_{nf} B_0^2 v}{\rho_{nf}} - \frac{\nu_{nf}}{K} v, \quad (12.3)$$

$$u \frac{\partial T}{\partial x} + v \frac{\partial T}{\partial y} + w \frac{\partial T}{\partial z} = \alpha_{nf} \frac{\partial^2 T}{\partial y^2}, \quad (12.4)$$

where (u, v, w) are the velocity components along the (x, y, z) directions respectively and K the permeability of porous medium. The effective density ρ_{nf} , the effective dynamic viscosity μ_{nf} , the effective thermal diffusivity α_{nf} , the heat capacitance $(\rho c_p)_{nf}$, the thermal conductivity k_{nf} and the electrical conductivity σ_{nf} of the nanofluid are given by

$$\rho_{nf} = \rho_f(1 - \phi) + \rho_s \phi, \quad (12.5)$$

$$\mu_{nf} = \frac{\mu_f}{(1 - \phi)^{2.5}}, \quad (12.6)$$

$$\alpha_{nf} = \frac{k_{nf}}{(\rho c_p)_{nf}}, \quad (12.7)$$

$$(\rho c_p)_{nf} = (\rho c_p)_f(1 - \phi) + (\rho c_p)_s \phi, \quad (12.8)$$

$$\frac{k_{nf}}{k_f} = \frac{k_s + 2k_f - 2\phi(k_f - k_s)}{k_s + 2k_f + \phi(k_f - k_s)}, \quad (12.9)$$

$$\frac{\sigma_{nf}}{\sigma_f} = 1 + \frac{3 \left(\frac{\sigma_s}{\sigma_f} - 1 \right) \phi}{\left(\frac{\sigma_s}{\sigma_f} + 2 \right) - \left(\frac{\sigma_s}{\sigma_f} - 1 \right) \phi}. \quad (12.10)$$

Here ϕ is the solid volume fraction, s in subscript is for nano-solid-particles and f in subscript is for base fluid. The boundary conditions are

$$\begin{aligned} u &= dx, \quad v = d(n-1)y, \quad w = -W, \quad -k_f \frac{\partial T}{\partial z} = h(T_f - T) \quad \text{at } z = 0, \\ u &\rightarrow 0, \quad v \rightarrow 0, \quad T \rightarrow T_\infty, \quad \text{as } z \rightarrow \infty, \end{aligned} \quad (12.11)$$

where $d < 0$ is the shrinking constant, W is the suction velocity and h is the convective heat transfer coefficient. We observe that when $n = 1$, the sheet shrinks in x -direction only and the sheet shrinks axisymmetrically for $n = 2$. Employing

$$u = cx f'(\eta), \quad v = c(n-1)y f'(\eta), \quad w = -\sqrt{cv_f n} f(\eta), \quad \eta = \sqrt{\frac{c}{\nu_f}} z, \quad \theta(\eta) = \frac{T - T_\infty}{T_f - T_\infty}, \quad (12.12)$$

equation (12.1) is satisfied automatically and Eqs. (12.2 – 12.4) are reduced as follows:

$$\varepsilon_1 f''' - f'^2 + n f f'' - M \varepsilon_1 (1 - \phi)^{2.5} \frac{\sigma n f}{\sigma_f} f' - \lambda \varepsilon_1 f' = 0, \quad (12.13)$$

$$\frac{\varepsilon_2 (1 - \phi)^{2.5} k_{nf}}{\text{Pr}} \theta'' + n f \theta' = 0, \quad (12.14)$$

$$\begin{aligned} f(0) &= S, \quad f'(0) = \gamma, \quad \theta'(0) = -\gamma_1 [1 - \theta(0)], \\ f'(\infty) &\rightarrow 0, \quad \theta(\infty) \rightarrow 0. \end{aligned} \quad (12.15)$$

Here $a > 0$ and the porosity parameter λ , the Hartman number M , the Prandtl number Pr , the mass transfer parameter $S > 0$ holds for suction and $S < 0$ for injection, the shrinking parameter γ and the thermal Biot number γ_1 are defined as follows:

$$\lambda = \frac{\nu_f}{cK}, \quad M = \frac{\sigma B_0^2}{\rho_f c}, \quad \text{Pr} = \frac{\nu_f (\rho c_p)_f}{k_f}, \quad S = \frac{W}{\sqrt{cv_f n}}, \quad \gamma = \frac{d}{c}, \quad \gamma_1 = \frac{h}{k_f} \sqrt{\frac{\nu_f}{c}}, \quad (12.16)$$

in which ε_1 and ε_2 are constants relating to the properties of nanofluid defined by

$$\varepsilon_1 = \frac{1}{(1 - \phi)^{2.5} [1 - \phi + \phi \frac{\rho_s}{\rho_f}]}, \quad (12.17)$$

$$\varepsilon_2 = \frac{1}{(1 - \phi)^{2.5} [1 - \phi + \phi \frac{(\rho C)_s}{(\rho C)_f}]}. \quad (12.18)$$

Local Nusselt number Nu is

$$Nu = \frac{x q_w}{k_f (T_f - T_\infty)}, \quad (12.19)$$

where the surface heat flux q_w satisfies

$$q_w = -k_{nf} \left. \frac{\partial T}{\partial z} \right|_{z=0}. \quad (12.20)$$

Using Eqs. (12.12) and (12.20), we obtain

$$Nu \operatorname{Re}_x^{-\frac{1}{2}} = -\frac{k_{nf}}{k_f} \theta'(0), \quad (12.21)$$

in which $\operatorname{Re}_x = u_w x / \nu_f$ denotes the local Reynolds number.

12.2 Homotopy analysis solutions

We choose initial guesses $f_0(\eta)$ and $\theta_0(\eta)$ and auxiliary linear operators \mathcal{L}_f and \mathcal{L}_θ of the forms

$$f_0(\eta) = S + \gamma[1 - \exp(-\eta)], \quad \theta_0(\eta) = \frac{\gamma_1}{1 + \gamma_1} \exp(-\eta), \quad (12.22)$$

$$\mathcal{L}_f(f) = f''' - f', \quad \mathcal{L}_\theta(\theta) = \theta'' - \theta, \quad (12.23)$$

with

$$\begin{aligned} \mathcal{L}_f [c_1 + c_2 \exp(\eta) + c_3 \exp(-\eta)] &= 0, \\ \mathcal{L}_\theta [c_4 \exp(\eta) + c_5 \exp(-\eta)] &= 0, \end{aligned} \quad (12.24)$$

in which $c_1 - c_5$ are the constants.

The zeroth and m^{th} order problems are

$$(1-p)\mathcal{L}_f [\hat{f}(\eta; p) - f_0(\eta)] = p\hbar_f \mathcal{N}_f[\hat{f}(\eta; p)], \quad (12.25)$$

$$(1-p)\mathcal{L}_\theta [\hat{\theta}(\eta; p) - \theta_0(\eta)] = p\hbar_\theta \mathcal{N}_\theta[\hat{\theta}(\eta; p), \hat{f}(\eta; p)], \quad (12.26)$$

$$\begin{aligned} \hat{f}(0; p) &= S, \quad \hat{f}'(0; p) = \gamma, \quad \hat{f}'(\infty; p) = 0, \\ \hat{\theta}'(0; p) &= -\gamma_1[1 - \hat{\theta}(0; p)], \quad \hat{\theta}(\infty; p) = 0, \end{aligned} \quad (12.27)$$

$$\begin{aligned} \mathcal{N}_f [\hat{f}(\eta; p)] &= \varepsilon_1 \frac{\partial^3 \hat{f}(\eta; p)}{\partial \eta^3} - \left(\frac{\partial \hat{f}(\eta; p)}{\partial \eta} \right)^2 + n \hat{f}(\eta; p) \frac{\partial^2 \hat{f}(\eta; p)}{\partial \eta^2} \\ &\quad - M \varepsilon_1 (1 - \phi)^{2.5} \frac{\sigma_{nf}}{\sigma_f} \frac{\partial \hat{f}(\eta; p)}{\partial \eta} - \lambda \varepsilon_1 \frac{\partial \hat{f}(\eta; p)}{\partial \eta}, \end{aligned} \quad (12.28)$$

$$\mathcal{N}_\theta [\hat{\theta}(\eta; p), \hat{f}(\eta; p)] = \frac{\varepsilon_2}{\text{Pr}} \frac{k_{nf}}{k_f} (1 - \phi)^{2.5} \frac{\partial^2 \hat{\theta}(\eta; p)}{\partial \eta^2} + n \hat{f}(\eta; p) \frac{\partial \hat{\theta}(\eta; p)}{\partial \eta}. \quad (12.29)$$

$$\mathcal{L}_f [f_m(\eta) - \chi_m f_{m-1}(\eta)] = \hbar_f \mathcal{R}_{f,m}(\eta), \quad (12.30)$$

$$\mathcal{L}_\theta [\theta_m(\eta) - \chi_m \theta_{m-1}(\eta)] = \hbar_\theta \mathcal{R}_{\theta,m}(\eta), \quad (12.31)$$

$$f_n(0) = f'_n(0) = f'_n(\infty) = \theta'_n(0) - \gamma_1 \theta_n(0) = \theta_n(\infty) = 0, \quad (12.32)$$

$$\chi_m = \begin{cases} 0, & m \leq 1 \\ 1, & m > 1 \end{cases}, \quad (12.33)$$

$$\mathcal{R}_{f,m}(\eta) = \varepsilon_1 f'''_{m-1} - \sum_{k=0}^{m-1} [f'_{m-1-k} f'_k - n f_{m-1-k} f''_k] - M \varepsilon_1 (1 - \phi)^{2.5} \frac{\sigma_{nf}}{\sigma_f} f'_{m-1} - \lambda \varepsilon_1 f'_{m-1}, \quad (12.34)$$

$$\mathcal{R}_{\theta,m}(\eta) = \frac{\varepsilon_2}{\text{Pr}} \frac{k_{nf}}{k_f} (1 - \phi)^{2.5} \theta''_{m-1} + n \sum_{k=0}^{m-1} \theta'_{m-1-k} f_k. \quad (12.35)$$

The general solutions (f_m, θ_m) in terms of the special solutions (f_m^*, θ_m^*) are

$$f_m(\eta) = f_m^*(\eta) + c_1 + c_2 e^\eta + c_3 e^{-\eta},$$

$$\theta_m(\eta) = \theta_m^*(\eta) + c_4 e^\eta + c_5 e^{-\eta}, \quad (12.36)$$

where the constants c_i ($i = 1 - 5$) through the boundary conditions (12.32) have the values

$$\begin{aligned} c_1 &= -c_3 - f_m^*(0), \quad c_2 = c_4 = 0, \quad c_3 = \left. \frac{\partial f_m^*(\eta)}{\partial \eta} \right|_{\eta=0}, \\ c_5 &= \frac{1}{1 + \gamma_1} \left[\left. \frac{\partial \theta_m^*(\eta)}{\partial \eta} \right|_{\eta=0} - \gamma_1 \theta_m^*(0) \right]. \end{aligned} \quad (12.37)$$

12.3 Convergence of the series solutions

The series solutions of Eqs. (12.30) and (12.31) contain the non-zero auxiliary parameters \hbar_f and \hbar_θ which can adjust and control the convergence of the series solutions. In order to see the range of admissible values of \hbar_f and \hbar_θ of the functions $f''(0)$ and $\theta'(0)$, the \hbar -curves for 14th-order of approximations are displayed. Figs. (12.1) and (12.2) show that the range for the admissible values of \hbar_f and \hbar_θ are $-1 \leq \hbar_f \leq -0.5$ and $-1 \leq \hbar_\theta \leq -0.1$. Further, the series solutions converge in the whole region of η ($0 < \eta < \infty$) when $\hbar_f = -0.6$ and $\hbar_\theta = -0.5$.

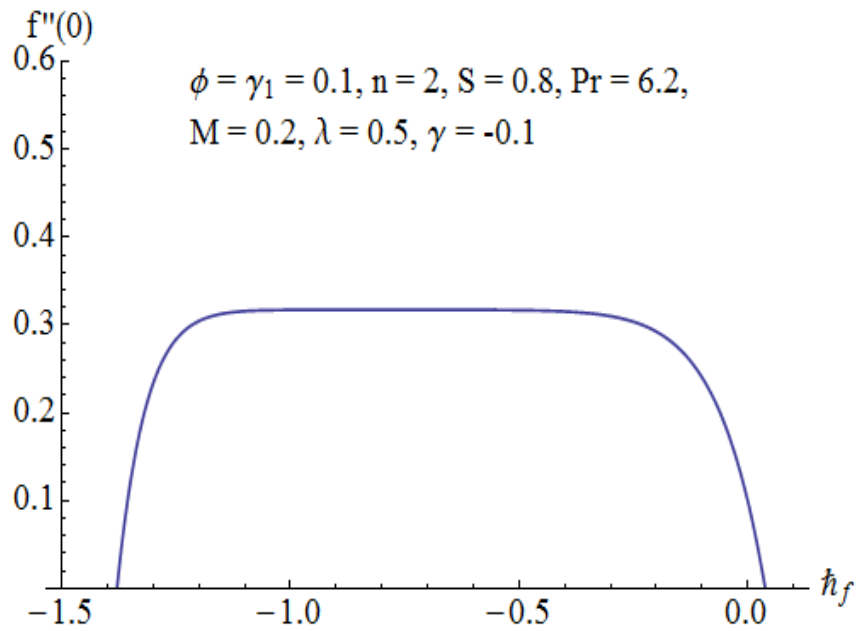


Fig. 12.1: \hbar - curve for the velocity field.

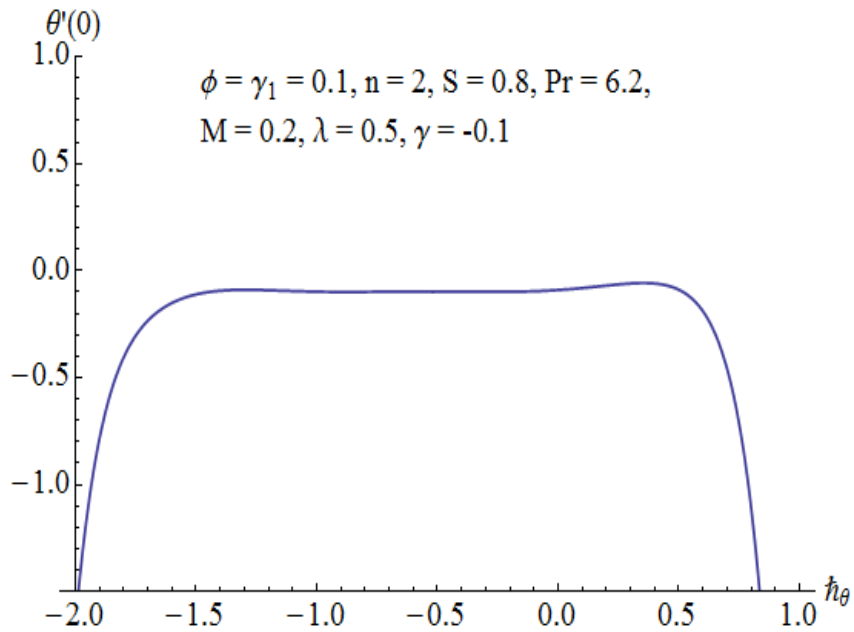


Fig. 12.2: h - curve for the temperature field.

Table 12.1: Convergence of HAM solutions for different order of approximations when $\phi = \gamma_1 = 0.1$, $n = 2$, $S = 0.8$, $\text{Pr} = 6.2$, $M = 0.2$, $\lambda = 5$ and $\gamma = -0.1$.

Order of approximations	$f''(0)$	$-\theta'(0)$
1	0.192992	0.0936255
5	0.304420	0.0996007
10	0.316424	0.0991102
15	0.317116	0.0990997
24	0.317159	0.0985958
30	0.317159	0.0982642
35	0.317159	0.0982642
40	0.317159	0.0982642
50	0.317159	0.0982642

12.4 Discussion

In this section, Figs. (12.3 – 12.13) are plotted to analyze the effects of mass transfer parameter S , Hartman number M , shrinking parameter γ , porosity parameter λ and nanoparticles volume

fraction ϕ on the velocity f' and temperature θ profiles. Effects of mass transfer parameter S on the velocity profile f' can be seen from Fig. 12.3. Here the magnitude of velocity profile f' decreases when mass transfer parameter S increases. Because applying suction leads to draw the amount of fluid particles into the wall and consequently the velocity boundary layer decreases. Fig. 12.4 displays the effect of Hartman number M on f' . The magnitude of velocity field f' is found to decrease when M increases. The application of an applied magnetic field has the tendency to slow down the movement of the fluid. It leads to a decrease in the velocity and momentum boundary layer thickness. Influence of shrinking parameter γ and porosity parameter λ on the velocity field f' is similar to that of M (see Figs. 12.5 and 12.6). The behavior of nanoparticle volume fraction ϕ on f' is shown in Fig. 12.7. This graph shows that magnitude of f' increases when nanoparticle volume fraction ϕ increases.

Fig. 12.8 illustrates the effects of mass transfer parameter S on temperature profile θ . Temperature θ decreases by increasing the mass transfer parameter S . Fig. 12.9 illustrates the effects of Hartman number M on temperature profile θ . The Lorentz force is a resistive force which opposes the fluid motion. As a sequence the heat is produced and thus thermal boundary layer thickness increases. Influence of shrinking parameter γ and porosity parameter λ on temperature profile θ can be seen in the Figs. (12.10–12.11). It is observed that the temperature profile θ decreases when the shrinking parameter γ and porosity parameter λ are increased. Fig. 12.12 represents the effect of nanoparticle volume fraction ϕ on temperature field θ . It is noted that the temperature profile θ increases for increasing values of nanoparticle volume fraction ϕ . It is because of the fact that by increasing the volume fraction of nanoparticles, the thermal conductivity increases. The behavior of thermal Biot number γ_1 on temperature profile θ is similar to that of nanoparticle volume fraction ϕ .

Table 12.1 shows the convergence of the series solutions. Some thermophysical properties of water and nanoparticles are given in Table 12.2. Numerical values of local Nusselt number for different emerging parameters are presented in Table 12.3. It is noticed that local Nusselt number $Nu(Re_x)^{-\frac{1}{2}}$ increases for larger values of Hartman number M , nanoparticle volume fraction ϕ and thermal Biot number γ_1 .

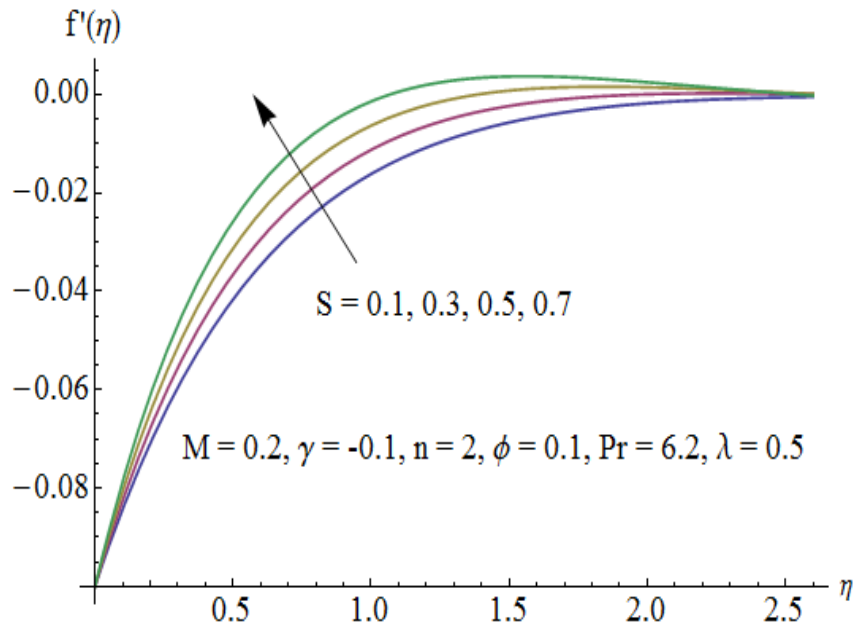


Fig. 12.3: Influence of S on $f'(\eta)$.

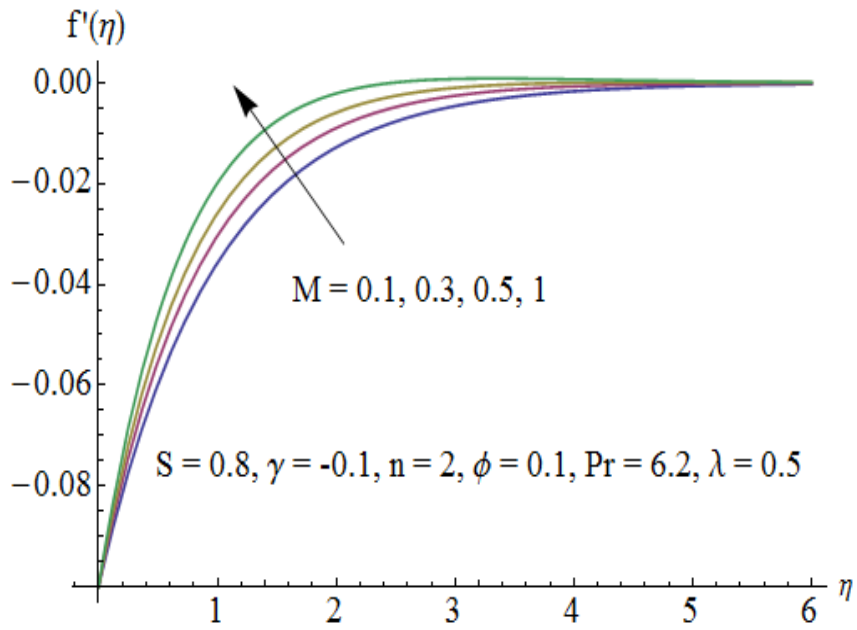


Fig. 12.4: Influence of M on $f'(\eta)$.

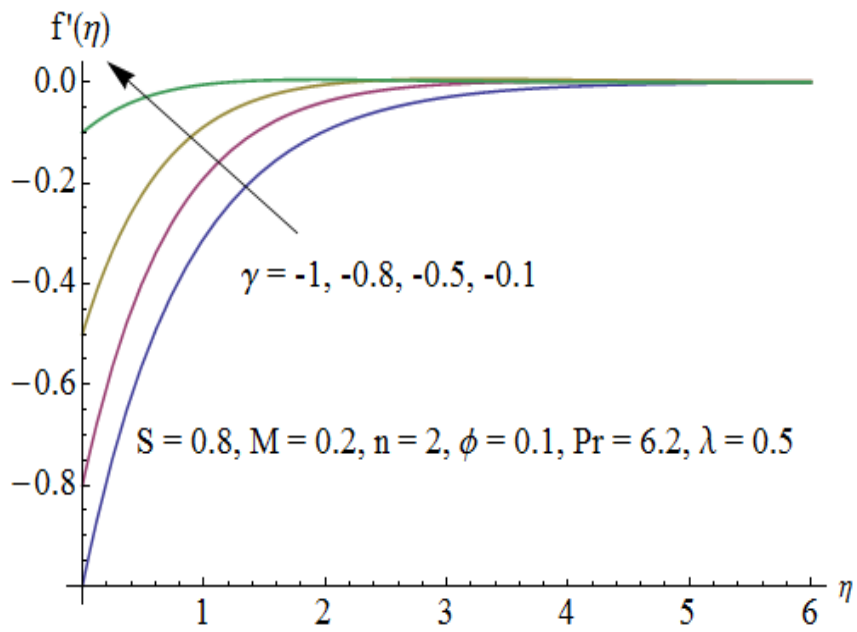


Fig. 12.5: Influence of γ on $f'(\eta)$.

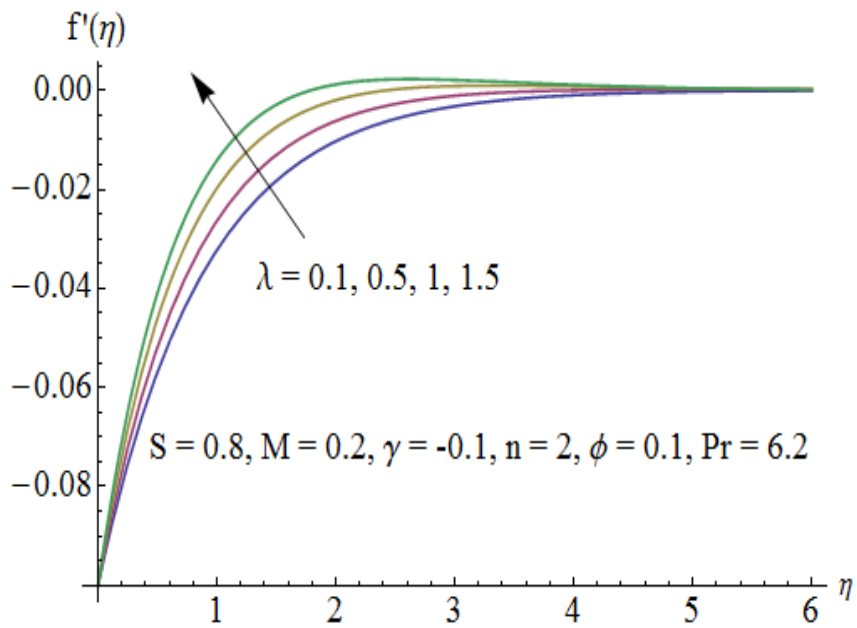


Fig. 12.6: Influence of λ on $f'(\eta)$.

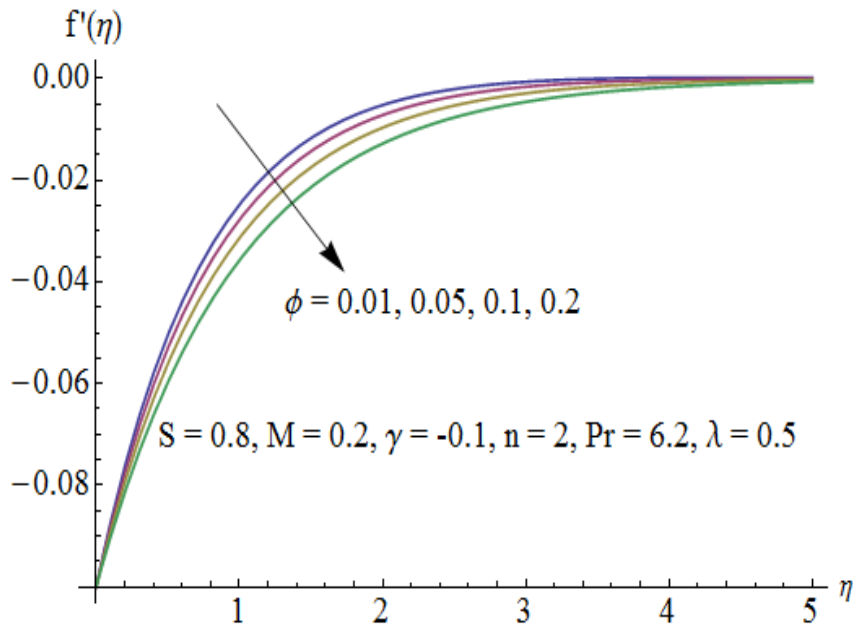


Fig. 12.7: Influence of ϕ on $f'(\eta)$.

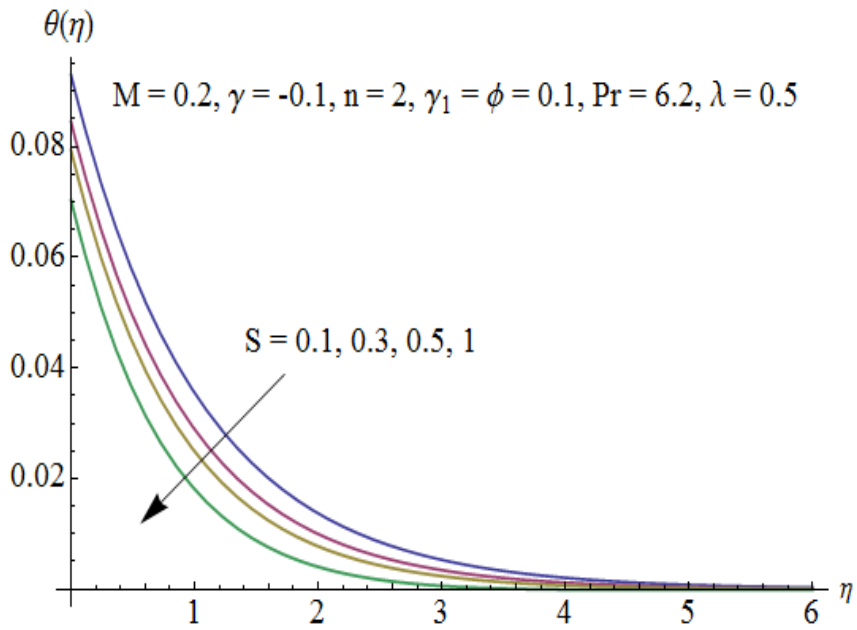


Fig. 12.8: Influence of S on $\theta(\eta)$.

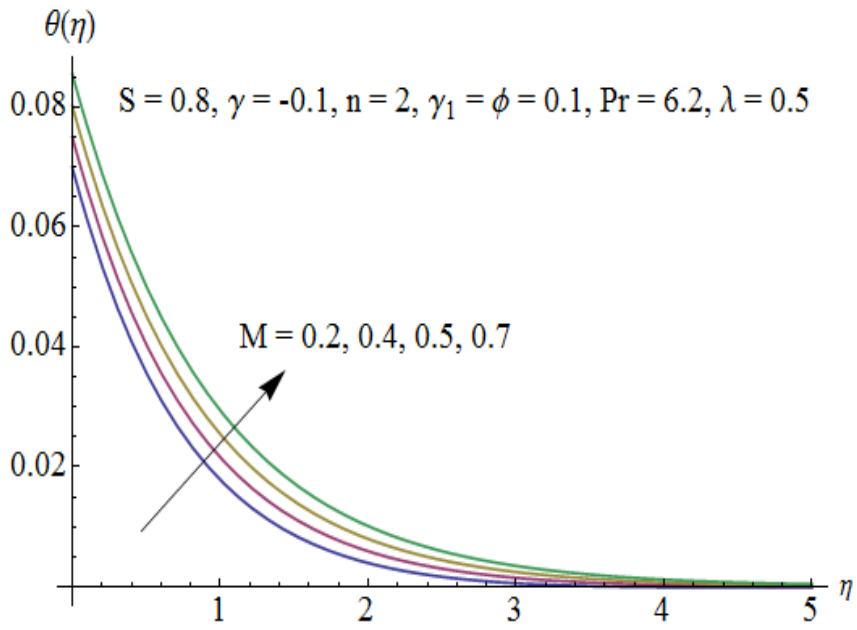


Fig. 12.9: Influence of M on $\theta(\eta)$.

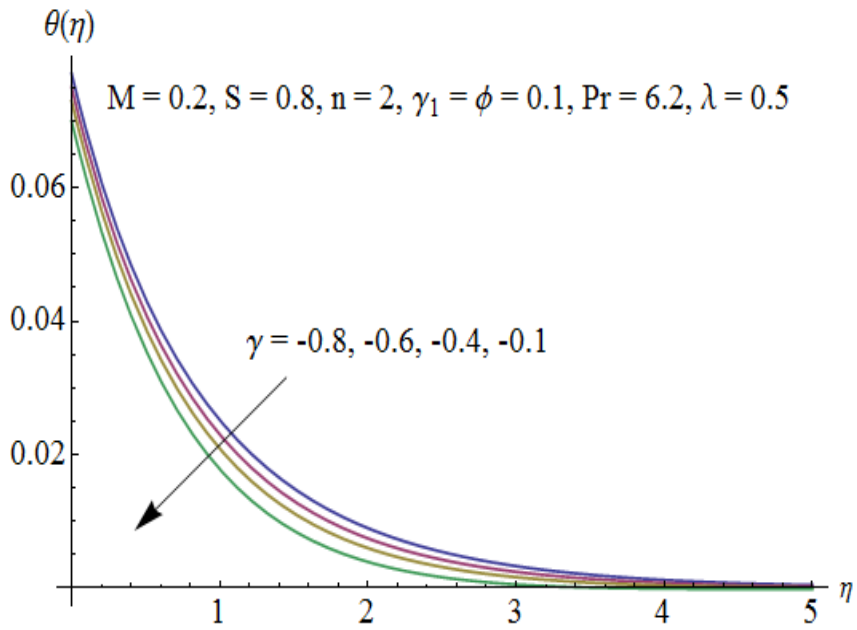


Fig. 12.10: Influence of γ on $\theta(\eta)$.

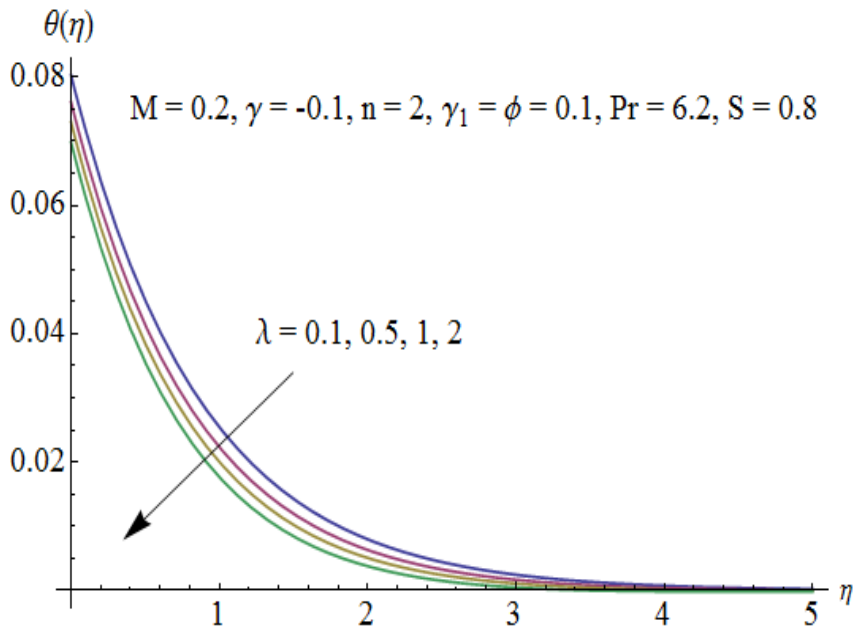


Fig. 12.11: Influence of λ on $\theta(\eta)$.

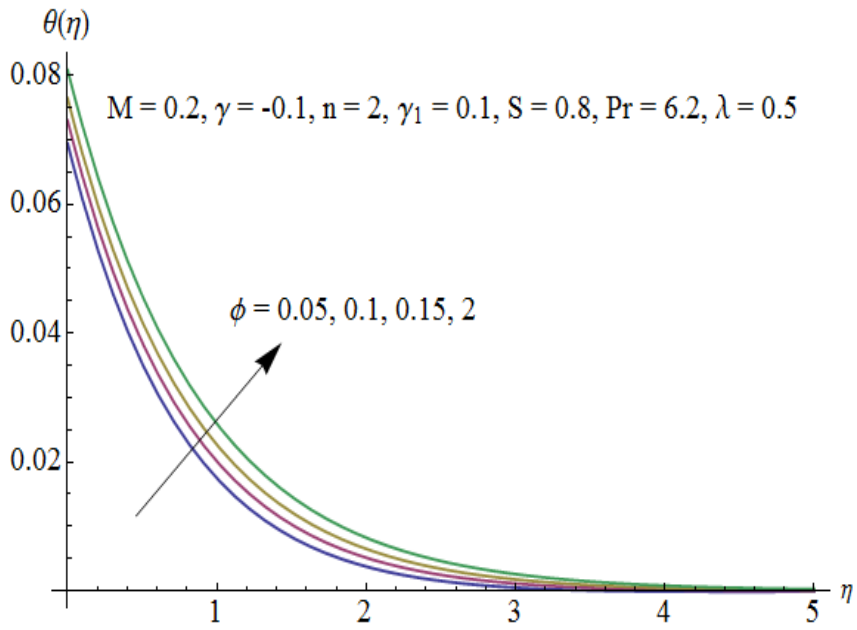


Fig. 12.12: Influence of ϕ on $\theta(\eta)$.

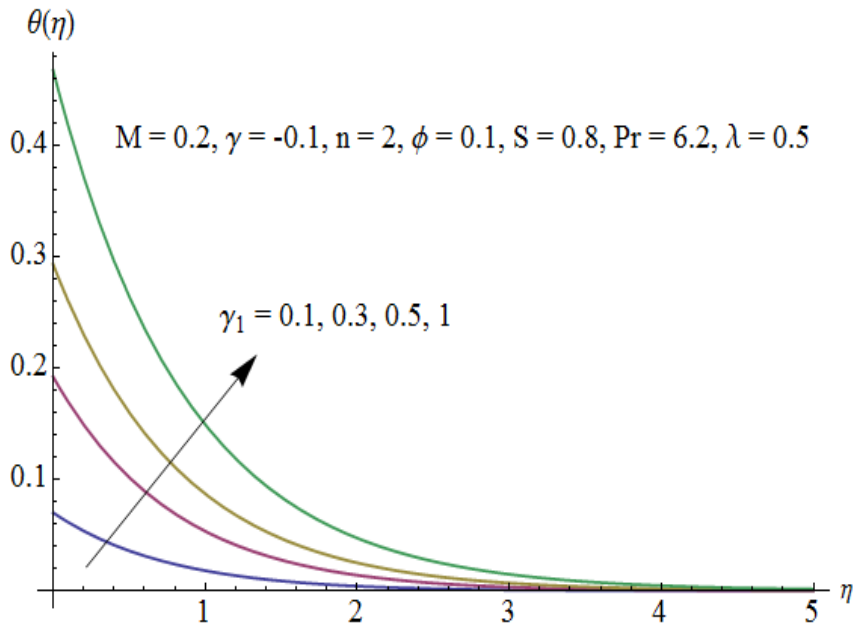


Fig. 12.13: Influence of γ_1 on $\theta(\eta)$.

Table 12.2: Thermo physical properties of water and nanoparticles[21].

	$\rho(kg/m^3)$	$c_p(j/kgk)$	$k(W/m.k)$	$\beta \times 10^5(K^{-1})$	$\sigma(\Omega m)^{-1}$
Pure water	997.1	4179	0.613	21	0.05
Copper(<i>Cu</i>)	8933	385	401	1.67	5.96×10^7
Silver(<i>Ag</i>)	10500	235	429	1.89	3.6×10^7
Alumina(Al_2O_3)	3970	765	40	0.85	1×10^{-10}
Titanium Oxide(TiO_2)	4250	686.2	8.9538	0.9	1×10^{-12}

Table 12.3: Values of $Nu(Re_x)^{-\frac{1}{2}}$ when $n = 2$, $Pr = 6.2$, $\lambda = 0.5$, $S = 0.8$ and $\gamma = -0.1$.

M	ϕ	γ_1	$-\frac{k_{nf}}{k_f}\theta'(0)$
0.5	0.05	0.3	0.336178
0.7			0.336187
1.0			0.336201
2.0			0.336996
0.2	0.01		0.301109
	0.05		0.334288
	0.07		0.355500
	0.1		0.379977
	0.05	0.1	0.113946
		0.3	0.332611
		0.5	0.537019
		0.7	0.767305

12.5 Final remarks

MHD flow of nanofluid over a permeable shrinking sheet with convective condition is studied.

The main results can be mentioned as follows:

- Effects of mass transfer parameter S , Hartman number M , shrinking parameter γ and porosity parameter λ are similar on the velocity profile f' .
- An increase in nanoparticle volume fraction ϕ reduces the velocity profile f' .
- There is a decrease in temperature profile θ for larger values of mass transfer parameter S , shrinking parameter γ and porosity parameter λ .
- An increase in nanoparticle volume fraction ϕ and thermal Biot number γ_1 enhances the temperature profile θ .

Bibliography

- [1] S. U. S. Choi, Enhancing thermal conductivity of fluids with nanoparticle, In proceedings of the ASME International Mechanical Engineering Congress and Exposition 66 (1995) 99 – 105.
- [2] J. A. Eastman, S. U. S. Choi, S. Li, W. Yu and L. J. Thompson, Anomalousy increased effective thermal conductivity of ethylene glycol-based nanofluids containing copper nanoparticles, Applied Physics Letters 78 (2001) 718 – 720.
- [3] S. U. S. Choi, Z. G. Zhang, W. Yu, F. E. Lockwoow and E. A. Grulke, Anomalous thermal conductivities enhancement on nanotube suspension, Applied Physics Letters 79 (2001) 2252 – 2254.
- [4] R. K. Tiwari and M. K. Das, Heat transfer augmentation in a two-sided lid-driven differentially heated square cavity utilizing nanofluids, International Journal of Heat and Mass Transfer 50 (2007) 2002 – 2018.
- [5] S. K. Das, S. U. S. Choi and W. Yu, Nanofluids, Science and Technology, Wiley New Jersey (2007).
- [6] W. Daungthongsuk and S. Wongwises, A critical review of convective heat transfer nanofluids, Renewable and Sustainable Energy Reviews 11 (5) (2007) 797 – 817.
- [7] V. Trisaksri and S. Wongwises, Critical review of heat transfer characteristics od nanofluids, Renewable and Sustainable Energy Reviews 11 (3) (2007) 512 – 523.
- [8] X. Q. Wang and A. S. Mujumdar, Heat transfer characteristics of nanofluids: A review, International Journal of Thermal Sciences 46 (1) (2007) 1 – 16.

- [9] X. Q. Wang and A. S. Mujumdar, A review on nanofluids-Part I: theoretical and numerical investigations, *Brazilian Journal of Chemical Engineering* 25 (4) (2008) 613 – 630.
- [10] X. Q. Wang and A. S. Mujumdar, A review on nanofluids-Part II: experiments and applications, *Brazilian Journal of Chemical Engineering* 25 (4) (2008) 631 – 648.
- [11] S. Kakac and A. Pramuanjaroenkij, Review of convective heat transfer enhancement with nanofluids, *International Journal of Heat and Mass Transfer* 52 (13 – 14) (2009) 3187 – 3196.
- [12] H. A. Mohammed, G. Bhaskaran, N. H. Shuaib and R. Saidur, Heat transfer and fluid flow characteristics in microchannels heat exchanger using nanofluids: A review, *Renewable and Sustainable Energy Reviews* 15 (3) (2011) 1502 – 1512.
- [13] A. S. Dalkilic, N. Kayaci, A. Celen, M. Tabatabaei, O. Yildiz, W. Daungthongsuk and S. Wongwises, Forced convective heat transfer of nanofluids: A review of the recent literature, *Current Nanoscience* 8 (6) (2012) 949 – 969.
- [14] J. Buongiorno, Convective transport in nanofluids, *ASME Journal of Heat Transfer* 128 (3) (2006) 240 – 250.
- [15] J. Buongiorno et al., A benchmark study on the thermal conductivity of nanofluids, *Journal of Applied Physics* 106 (2009) 094312.
- [16] J. Niu, C. Fu, and W. C. Tan, Slip flow and heat transfer of a non-Newtonian nanofluid in a microtube, *Plos One* 7 (5) (2012) e37274.
- [17] A. Alsaedi, M. Awais and T. Hayat, Effects of heat generation/absorption on stagnation point flow of nanofluid over a surface with convective boundary conditions, *Communications in Nonlinear Science and Numerical Simulation* 17 (11) (2012) 4210 – 4223.
- [18] H. Xu, I. Pop and X. C. You, Flow and heat transfer in a nano-liquid film over an unsteady stretching surface, *International Journal of Heat and Mass Transfer* 60 (2013) 646 – 652.
- [19] M. Imtiaz, T. Hayat, M. Hussain, S. A. Shehzad, G. Q. Chen and B. Ahmad, Mixed convection flow of nanofluid with Newtonian heating, *European Physical Journal Plus* 129 (2014) 97.

- [20] S. Khalili, H. Tamim, A. Khalili and M. M. Rashidi, Unsteady convective heat and mass transfer in pseudoplastic nanofluid over a stretching wall, *Advanced Powder Technology* 26 (5) (2015) 1319 – 1326.
- [21] M. M. Rashidi, S. Abelman and N. F. Mehr, Entropy generation in steady MHD flow due to a rotating porous disk in a nanofluid, *International Journal of Heat and Mass Transfer* 62 (2013) 515 – 525.
- [22] M. Sheikholeslami, M. Hatami and D. D. Ganji, Analytical investigation of MHD nanofluid flow in a semi-porous channel, *Powder Technology* 246 (2013) 327 – 336.
- [23] S. Khalili, S. Dinarvand, R. Hosseini, H. Tamim and I. Pop, Unsteady MHD flow and heat transfer near stagnation point over a stretching/shrinking sheet in porous medium filled with a nanofluid, *Chinese Physics B* 23 (4) (2014) 048203.
- [24] M. M. Rashidi, N. V. Ganesh, A. K. A. Hakeem and B. Ganga, Buoyancy effect on MHD flow of nanofluid over a stretching sheet in the presence of thermal radiation, *Journal of Molecular Liquids* 198 (2014) 234 – 238.
- [25] M. Sheikholeslami, D. D. Ganji, M. Y. Javed and R. Ellahi, Effect of thermal radiation on magnetohydrodynamics nanofluid flow and heat transfer by means of two phase model, *Journal of Magnetism and Magnetic Materials* 374 (2015) 36 – 43.
- [26] M. Sheikholeslami, M. Hatami and G. Domairry, Numerical simulation of two phase unsteady nanofluid flow and heat transfer between parallel plates in presence of time dependent magnetic field, *Journal of the Taiwan Institute of Chemical Engineers* 46 (2015) 43 – 50.
- [27] Y. Lin, L. Zheng, X. Zhang, L. Ma and G. Chen, MHD pseudoplastic nanofluid unsteady flow and heat transfer in a finite thin film over stretching surface with internal heat generation, *International Journal of Heat and Mass Transfer* 84 (2015) 903 – 911.
- [28] F. Mabood and A. Mastroberardino, Melting heat transfer on MHD convective flow of a nanofluid over a stretching sheet with viscous dissipation and second order slip, *Journal of the Taiwan Institute of Chemical Engineers* 57 (2015) 62 – 68.

- [29] T. Hayat, T. Muhammad, A. Alsaedi and M. S. Alhuthali, Magneto hydrodynamic three-dimensional flow of viscoelastic nanofluid in the presence of nonlinear thermal radiation, *Journal of Magnetism and Magnetic Materials* 385 (1) (2015) 222 – 229.
- [30] T. Hayat, T. Muhammad, S. A. Shehzad, G. Q. Chen and I. A. Abbas, Interaction of magnetic field in flow of Maxwell nanofluid with convective effect, *Journal of Magnetism and Magnetic Materials* 389 (1) (2015) 48 – 55.
- [31] L. J. Crane, Flow past a stretching plate, *Journal of Applied Mathematics and Physics (ZAMP)* 21 (1970) 645 – 647.
- [32] P. S. Gupta and A. S. Gupta, Heat and mass transfer on a stretching sheet with suction or blowing, *The Canadian Journal of Chemical Engineering* 55 (1977) 744 – 746.
- [33] N. Afzal, A. Baderuddin and A. A. Elgarvi, Momentum and heat transfer on a continuous flat surface moving in a parallel stream, *International Journal of Heat and Mass Transfer* 36 (1993) 3399 – 3403.
- [34] E. Magyari and B. Keller, Heat and mass transfer in the boundary layers on an exponentially stretching continuous surface, *Journal of Physics D: Applied Physics* 32 (1999) 577 – 585.
- [35] R. Cortell, Flow and heat transfer in a moving fluid over a moving flat surface, *Theoretical and Computational Fluid Dynamics* 21 (2007) 435 – 446.
- [36] L. Zheng, J. Niu, X. Zhang and Y. Gao, MHD flow and heat transfer over a porous shrinking surface with velocity slip and temperature jump, *Mathematical and Computer Modelling* 56 (2012) 133 – 144.
- [37] W. Ibrahim, B. Shankar and M. M. Nandeppanavar, MHD stagnation point flow and heat transfer due to nanofluid towards a stretching sheet, *International Journal of Heat and Mass Transfer* 56 (2013) 1 – 9.
- [38] S. Mukhopadhyay, Slip effects on MHD boundary layer flow over an exponentially stretching sheet with suction/blowing and thermal radiation, *Ain Shams Engineering Journal* 4 (2013) 485 – 491.

- [39] M. Turkyilmazoglu, Exact solutions for two-dimensional laminar flow over a continuously stretching or shrinking sheet in an electrically conducting quiescent couple stress fluid, *International Journal of Heat and Mass Transfer* 72 (2014) 1 – 8.
- [40] A. Malvandi, F. Hedayati and D. D. Ganji, Slip effects on unsteady stagnation point flow of a nanofluid over a stretching sheet, *Powder Technology* 253 (2014) 377 – 384.
- [41] S. Pramanik, Casson fluid flow and heat transfer past an exponentially porous stretching surface in presence of thermal radiation, *Ain Shams Engineering Journal* 5 (2014) 205 – 212.
- [42] M. S. Alhuthali, S. A. Shehzad, H. Malaikah and T. Hayat, Three dimensional flow of viscoelastic fluid by an exponentially stretching surface with mass transfer, *Journal of Petroleum Science Engineering* 119 (2014) 221 – 226.
- [43] A. V. Rosca and I. Pop, Flow and heat transfer of Powell–Eyring fluid over a shrinking surface in a parallel free stream, *International Journal of Heat and Mass Transfer* 71 (2014) 321 – 327.
- [44] S. K. Nandy and I. Pop, Effects of magnetic field and thermal radiation on stagnation flow and heat transfer of nanofluid over a shrinking surface, *International Communications in Heat and Mass Transfer* 53 (2014) 50 – 55.
- [45] S. K. Nandy, Unsteady flow of Maxwell fluid in the presence of nanoparticles toward a permeable shrinking surface with Navier slip, *Journal of the Taiwan Institute of Chemical Engineers* 52 (2015) 22 – 30.
- [46] P. D. Weidman and A. Ishak, Multiple solutions of two-dimensional and three-dimensional flows induced by a stretching flat surface, *Communications in Nonlinear Science and Numerical Simulation* 25 (2015) 1 – 9.
- [47] M. G. Reddy, P. Padma and B. Shankar, Effects of viscous dissipation and heat source on unsteady MHD flow over a stretching sheet, *Ain Shams Engineering Journal* 6 (4) (2015) 1195 – 1201.

- [48] S. Chen, L. Zheng, B. Shen and X. Chen, Time–space dependent fractional boundary layer flow of Maxwell fluid over an unsteady stretching surface, *Theoretical and Applied Mechanics Letters* 5 (6) (2015) 262 – 266.
- [49] M. Mustafa, A. Mushtaq, T. Hayat and A. Alsaedi, Radiation effects in three-dimensional flow over a bi-directional exponentially stretching sheet, *Journal of the Taiwan Institute of Chemical Engineers* 47 (2015) 43 – 49.
- [50] T. Hayat, Y. Saeed, A. Alsaedi and S. Asad, Effects of convective heat and mass transfer in flow of Powell-Eyring fluid past an exponentially stretching sheet, *Plos One* 10 (9) (2015) e0133831.
- [51] T. V. Karman, Uber laminare und turbulente reibung, *ZAMM* 1 (1921) 233 – 235.
- [52] M. E. Erdogan, Unsteady flow of a viscous fluid due to non-coaxial rotations of a disk and a fluid at infinity, *International Journal of Non-Linear Mechanics* 32 (1997) 285 – 290.
- [53] N. Kelson and A. Desseaux, Note on porous rotating disk flow, *ANZIAM Journal* 42 (2000) 837 – 855.
- [54] N. Bachok, A. Ishak and I. Pop, Flow and heat transfer over a rotating porous disk in a nanofluid, *Physica B* 406 (2011) 1767 – 1772.
- [55] M. M. Rashidi, S. A. M. Pour, T. Hayat and S. Obaidat, Analytic approximate solutions for steady flow over a rotating disk in porous medium with heat transfer by homotopy analysis method, *Computers & Fluids* 54 (2012) 1–9.
- [56] M. Turkyilmazoglu, Nanofluid flow and heat transfer due to a rotating disk, *Computers & Fluids* 94 (2014) 139 – 146.
- [57] T. Hayat, M. Rashid, M. Imtiaz and A. Alsaedi, Magnetohydrodynamic (MHD) flow of Cu-water nanofluid due to a rotating disk with partial slip, *AIP Advances* 5 (2015) 067169.
- [58] P. A. Thompson and S. M. Troian, A general boundary condition for liquid flow at solid surfaces, *Nature* (1997) 389.

- [59] R. Khare, P. Keblinski and A. Yethiraj, Molecular dynamics simulations of heat and momentum transfer at a solid-fluid interface: Relationship between thermal and velocity slip, *International Journal of Heat and Mass Transfer* 49 (2006) 3401 – 3407.
- [60] L. Wu, A slip model for rarefied gas flows at arbitrary Knudsen number, *Applied Physics Letters* 93 (2008) 253103.
- [61] T. Fang and A. Aziz, Viscous flow with second-order slip velocity over a stretching sheet, *Zeitschrift für Naturforschung A* 65a (2010) 1087 – 1092.
- [62] A. Akbarinia, M. Abdolzadeh and R. Laur, Critical investigation of heat transfer enhancement using nanofluids in microchannels with slip and non-slip flow regimes, *Applied Thermal Engineering* 31 (2011) 556 – 565.
- [63] M. A. A. Mahmoud and S. E. Waheed, MHD flow and heat transfer of a micropolar fluid over a stretching surface with heat generation (absorption) and slip velocity, *Journal of the Egyptian Mathematical Society* 20 (2012) 20 – 27.
- [64] W. Ibrahim and B. Shankar, MHD boundary layer flow and heat transfer of a nanofluid past a permeable stretching sheet with velocity, thermal and solutal slip boundary conditions, *Computers & Fluids* 75 (2013) 1 – 10.
- [65] W. A. Khan, M. J. Uddin and A. I. M. Ismail, Hydrodynamic and thermal slip effect on double-diffusive free convective boundary layer flow of a nanofluid past a flat vertical plate in the moving free stream, *Plos One* 8 (3) (2013) e54024.
- [66] S. A. Rooholghdos and E. Roohi, Extension of a second order velocity slip/temperature jump boundary condition to simulate high speed micro/nanoflows, *Computers & Mathematics with Applications* 67 (2014) 2029 – 2040.
- [67] A. Malvandi and D. D. Ganji, Brownian motion and thermophoresis effects on slip flow of alumina/water nanofluid inside a circular microchannel in the presence of a magnetic field, *International Journal of Thermal Sciences* 84 (2014) 196 – 206.
- [68] R. Sharma and A. Ishak, Second order slip flow of Cu-water nanofluid over a stretching sheet with heat transfer, *WSEAS Transactions on Fluid Mechanics* 9 (2014) 26 – 33.

- [69] M. M. Rashidi, N. Kavyani and S. Abelman, Investigation of entropy generation in MHD and slip flow over a rotating porous disk with variable properties, *International Journal of Heat and Mass Transfer* 70 (2014) 892 – 917.
- [70] A. Karimipour, A. H. Nezhad, A. D’Orazia, M. H. Esfe, M. R. Safaei, and E. Shiran, Simulation of copper-water nanofluid in a microchannel in slip flow regime using the lattice Boltzman method, *European Journal of Mechanics–B/Fluids* 49 (2015) 89 – 99.
- [71] A. M. Megahed, MHD viscous Casson fluid flow and heat transfer with second-order slip velocity and thermal slip over a permeable stretching sheet in the presence of internal heat generation/absorption and thermal radiation, *The European Physical Journal Plus* 130 (2015) 81.
- [72] A. K. A. Hakeem, N. V. Ganesh and B. Ganga, Magnetic field effect on second order slip flow of nanofluid over a stretching/shrinking sheet with thermal radiation effect, *Journal of Magnetism and Magnetic Materials* 381 (2015) 243 – 257.
- [73] J. H. Merkin, A model for isothermal homogeneous-heterogeneous reactions in boundary layer flow, *Mathematical and Computer Modelling* 24 (1996) 125 – 136.
- [74] M. A. Chaudhary and J. H. Merkin, A simple isothermal model for homogeneous-heterogeneous reactions in boundary layer flow: I. Equal diffusivities, *Fluid Dynamics Research* 16 (1995) 311 – 333.
- [75] W. A. Khan and I. Pop, Flow near the two-dimensional stagnation-point on an infinite permeable wall with a homogeneous–heterogeneous reaction, *Communications in Nonlinear Science and Numerical Simulation* 15 (2010) 3435 – 3443.
- [76] N. Bachok, A. Ishak and I. Pop, On the stagnation-point flow towards a stretching sheet with homogeneous–heterogeneous reactions effects, *Communications in Nonlinear Science and Numerical Simulation* 16 (2011) 4296 – 4302.
- [77] W. A. Khan and I. Pop, Effects of homogeneous-heterogeneous reactions on the viscoelastic fluid towards a stretching sheet, *ASME Journal of Heat Transfer* 134 (2012) 064506 1 – 5.

- [78] S. Shaw, P. K. Kameswaran and P. Sibanda, Homogeneous-heterogeneous reactions in micropolar fluid flow from a permeable stretching or shrinking sheet in a porous medium, *Boundary Value Problems* 2013 (2013) 77.
- [79] P. K. Kameswaran, S. Shaw, P. Sibanda and P. V. S. N. Murthy, Homogeneous-heterogeneous reactions in a nanofluid flow due to porous stretching sheet, *International Journal of Heat and Mass Transfer* 57 (2013) 465 – 472.
- [80] T. Hayat, M. Farooq and A. Alsaedi, Homogeneous-heterogeneous reactions in the stagnation point flow of carbon nanotubes with Newtonian heating, *AIP Advances* 5 (2015) 027130.
- [81] T. Hayat, M. Imtiaz and A. Alsaedi, Effects of homogeneous-heterogeneous reactions in flow of Powell-Eyring fluid, *Journal of Central South University* 22 (8) (2015) 3211 – 3216.
- [82] Z. Abbas, M. Sheikh and I. Pop, Stagnation-point flow of a hydromagnetic viscous fluid over stretching/shrinking sheet with generalized slip condition in the presence of homogeneous–heterogeneous reactions, *Journal of the Taiwan Institute of Chemical Engineers* 55 (2015) 69 – 75.
- [83] S. J. Liao and A. T. Chwang, Application of homotopy analysis method in nonlinear oscillations, *ASME Journal of Applied Mechanics* 65 (1998) 914 – 922.
- [84] S. J. Liao, Notes on the homotopy analysis method: Some definitions and theorems, *Communications in Nonlinear Science and Numerical Simulation* 14 (2009) 983 – 997.
- [85] S. Abbasbandy, E. Shivanian and K. Vajravelu, Mathematical properties of \hbar -curve in the frame work of the homotopy analysis method, *Communications in Nonlinear Science and Numerical Simulation* 16 (2011) 4268 – 4275.
- [86] M. Turkyilmazoglu and I. Pop, Exact analytical solutions for the flow and heat transfer near the stagnation point on a stretching/shrinking sheet in a Jeffrey fluid, *International Journal of Heat and Mass Transfer* 57 (2013) 82 – 88.
- [87] O. A. Arqub and A. El-Ajou, Solution of the fractional epidemic model by homotopy analysis method, *Journal of King Saud University–Science* 25 (1) (2013) 73 – 81.

- [88] M. Hatami, R. Nouri and D. D. Ganji, Forced convection analysis for MHD Al_2O_3 -water nanofluid flow over a horizontal plate, *Journal of Molecular Liquids* 187 (2013) 294 – 301.
- [89] M. M. Rashidi, M. Ali, N. Freidoonimehr, B. Rostami and A. Hossian, Mixed convective heat transfer for MHD viscoelastic fluid flow over a porous wedge with thermal radiation, *Advances in Mechanical Engineering* 204 (2014) 735939.
- [90] S. Abbasbandy, M. Yurusoy and H. Gulluce, Analytical solutions of non-linear equations of power-law fluids of second grade over an infinite porous plate, *Mathematical & Computational Applications* 19 (2) (2014) 124.
- [91] J. Sui, L. Zheng, X. Zhang and G. Chen, Mixed convection heat transfer in power law fluids over a moving conveyor along an inclined plate, *International Journal of Heat and Mass Transfer* 85 (2015) 1023 – 1033.
- [92] T. Hayat, S. A. Shehzad, A. Alsaedi and M. S. Alhothuali, Three-dimensional flow of Oldroyd-B fluid over surface with convective boundary conditions, *Applied Mathematics and Mechanics (English Edition)* 34 (4) (2015) 489 – 500.
- [93] U. Farooq, T. Hayat, A. Alsaedi and S. J. Liao, Heat and mass transfer of two-layer flows of third-grade nano-fluids in a vertical channel, *Applied Mathematics and Computations* 242 (2014) 528 – 540.
- [94] Y. Lin, L. Zheng and G. Chen, Unsteady flow and heat transfer of pseudoplastic nanofluid in a finite thin film on a stretching surface with variable thermal conductivity and viscous dissipation, *Powder Technology* 274 (2015) 324 – 332.
- [95] U. Farooq, Y. L. Zhao, T. Hayat, A. Alsaedi and S. J. Liao, Application of the HAM-based mathematica package BVPh 2.0 on MHD Falkner-Skan flow of nanofluid, *Computers & Fluids* 111 (2015) 69 – 75.
- [96] T. Hayat, A. Shafiq, A. Alsaedi and S. Asghar, Effect of inclined magnetic field in flow of third grade fluid with variable thermal conductivity, *AIP Advances* 5 (2015) 087108.
- [97] T. Hayat, S. Asad, M. Mustafa and A. Alsaedi, MHD stagnation-point flow of Jeffrey fluid over a convectively heated stretching sheet, *Computers & Fluids* 108 (2015) 179 – 185.

- [98] H. C. Brinkman, The viscosity of concentrated suspensions and solutions, *The Journal of Chemical Physics* 20 (1952) 571 – 581.
- [99] J. C. Maxwell, *A treatise on electricity and magnetism*, Cambridge Oxford University Press (1904).
- [100] T. Cebeci and P. Bradshaw, *Physical and computational aspects of convective heat transfer*, Springer-Verlag, New York (1988) (Chapter 13).

MHD flow of nanofluids over an exponentially stretching sheet in a porous medium with convective boundary conditions

T. Hayat^{a)b)†}, M. Imtiaz^{a)}, A. Alsaedi^{b)}, and R. Mansoor^{a)}

^{a)}Department of Mathematics, Quaid-I-Azam University, Islamabad 44000, Pakistan

^{b)}Department of Mathematics, Faculty of Science, King Abdulaziz University, Jeddah 21589, Saudi Arabia

(Received 29 April 2013; revised manuscript received 26 October 2013; published online 1 April 2014)

This article concentrates on the steady magnetohydrodynamic (MHD) flow of viscous nanofluid. The flow is caused by a permeable exponentially stretching surface. An incompressible fluid fills the porous space. A comparative study is made for the nanoparticles namely Copper (Cu), Silver (Ag), Alumina (Al_2O_3) and Titanium Oxide (TiO_2). Water is treated as a base fluid. Convective type boundary conditions are employed in modeling the heat transfer process. The non-linear partial differential equations governing the flow are reduced to an ordinary differential equation by similarity transformations. The obtained equations are then solved for the development of series solutions. Convergence of the obtained series solutions is explicitly discussed. The effects of different parameters on the velocity and temperature profiles are shown and analyzed through graphs.

Keywords: MHD nanofluid, exponentially stretching sheet, porous medium, convective boundary conditions

PACS: 47.15.-x, 47.65.-d

DOI: 10.1088/1674-1056/23/5/054701

1. Introduction

The boundary layer flow and heat transfer over a stretching sheet have momentous aspects not only from a theoretical point of view but also regarding their practical applications in the polymer industry, paper production, food processing, crystal growing etc. The rate of heat transfer between the stretching surface and fluid flow is important for the end product's desired quality. The boundary layer flow generated by a stretching sheet was first studied by Crane.^[1] He constructed an exact solution for the arising problem. Afterwards, the boundary layer flows by linear and nonlinear stretching surfaces have attracted a great deal of attention of the researchers.^[2-5] Some investigations in the past dealt with the flow induced by an exponentially stretching surface. Magyari and Keller^[6] discussed the steady boundary layer flow by an exponentially stretching surface with an exponential temperature distribution. The effect of viscous dissipation in the mixed convection flow due to an exponentially stretching sheet has been examined by Partha *et al.*^[7] Sajid and Hayat^[8] studied the thermal radiation effects on the flow due to an exponentially stretching sheet. They developed the analytic solution for the resulting problem. A numerical solution for the same problem was given by Bidin and Nazar.^[9] MHD boundary layer flow due to an exponentially stretching sheet with a radiation effect has been obtained by Anuar Ishak.^[10] Bachok *et al.*^[11] studied the boundary layer stagnation-point flow and heat transfer over an exponentially stretching/shrinking sheet. The boundary layer flow over an exponentially stretching porous sheet with heat flux in a porous medium has been obtained by Man-

dal and Mukhopadhyay.^[12] Bhattacharyya^[13] discussed the steady boundary layer flow and reactive mass transfer past an exponentially stretching surface in an exponentially moving free stream. Elbashbeshy^[14] studied the effects of thermal radiation and magnetic field on unsteady mixed convection flow and heat transfer over an exponentially stretching surface with suction in the presence of internal heat generation/absorption. Boundary layer flow and heat transfer over an exponentially shrinking vertical sheet with suction was analyzed by Azizah Mohd Rohni.^[15] Mukhopadhyay^[16] studied the MHD boundary layer flow and heat transfer over an exponentially stretching sheet embedded in a thermally stratified medium.

As oil, water and ethylene glycol mixtures are poor heat transfer fluids, they therefore have low thermal conductivities. Since the thermal conductivity of fluids plays an important role in the heat transfer coefficient, so many methods have been used to enhance the thermal conductivity of fluids. However, it is observed that enhancement of the thermal conductivity of poor heat transfer fluids is possible in view of the addition of nanoparticles in the base fluids. The nano particles can be found in metals such as (Cu, Ag), oxides (Al_2O_3), carbides (SiC), nitrides (AlN, SiN) or nonmetals (graphite, carbon nanotubes). Nanofluids have novel properties that make them potentially useful in many applications in heat transfer including microelectronics, fuel cells, pharmaceutical processes and hybrid-powered engines. Nanoparticles provide a bridge between bulk materials and molecular structure. The term "nanofluid" was first introduced by Choi.^[17] Recently many investigations regarding nanofluids have been reported^[18-21] Narayana and Sibanda^[22] studied the effects of laminar flow

[†]Corresponding author. E-mail: pensy_t@yahoo.com

of a nanoliquid film over an unsteady stretching sheet. Thermophysical properties of nanofluids such as thermal conductivity, diffusivity and viscosity have been studied by Kang *et al.*,^[23] Velagapudi *et al.*^[24] and Rudyak *et al.*^[25] Boundary layer flow of nanofluid past a stretching sheet with convective boundary condition was studied by Makinde and Aziz.^[26] Alsaedi *et al.*^[27] studied the effects of heat generation/absorption in stagnation point flow of a nanofluid over a linearly stretching surface with convective boundary conditions. Recently, Kandasamy^[28] investigated the unsteady Hiemenz flow of Cu-nanofluid over a porous wedge in the presence of thermal stratification. Kameswaran *et al.*^[29] examined the homogeneous-heterogeneous reactions in a nanofluid flow due to a porous stretching sheet. Mustafa *et al.*^[30] addressed the stagnation point flow of a viscous nanofluid towards a linear stretching sheet. Nandy and Mahapatra^[31] studied the effects of slip and heat generation/absorption in MHD stagnation point flow of a nanofluid past a stretching/shrinking surface with convective boundary conditions. Ibrahim^[32] analyzed the MHD stagnation point flow and heat transfer in a nanofluid towards a stretching sheet. Makinde^[33] examined the buoyancy effects on MHD stagnation point flow and heat transfer of a nanofluid past a convectively heated stretching/shrinking sheet. MHD boundary layer flow and heat transfer of a nanofluid past a permeable stretching sheet with velocity, thermal and solutal slip boundary conditions has been analyzed by Ibrahim.^[34] Zheng *et al.*^[35] studied the flow and radiation heat transfer of a nanofluid over a stretching sheet with velocity slip and temperature jump in a porous medium. The effects of a magnetic field on the radiative flow of a nanofluid past a stretching sheet have been examined by Khan.^[36]

The magnetic nanofluids are important to guide the particles up the bloodstream to a tumor with magnets. In fact, magnetic nanoparticles are more adhesive to tumor cells than nano-malignant cells and therefore absorb much more power than microparticles in alternating current magnetic fields tolerable in humans. No doubt, the magnetic nanoparticles have broad interest in medicine, in sink float separation and the construction of loudspeakers. Besides this, the heat transfer in a porous medium is significant in geothermal reservoirs, thermal insulation, nuclear reactors, underground energy transport etc. Hence, the present article is arranged to investigate the boundary layer flow of a magneto nanofluid in a porous medium. Exponentially permeable stretched surfaces possess the convective type boundary conditions. In fact, the nanoparticles are used to enhance the thermal conductivity of the fluid. On the other hand, the convective boundary condition in dimensionless form appears as a Biot number. An increase in the Biot number raises the temperature. An increase in temperature corresponds to an enhancement in the thermal conductivity. So the nanofluid with a convective boundary condition is a

more appropriate model in comparison to the constant surface temperature conditions. This article is structured as follows.

Section 2 consists of the problem formulation. Sections 3 and 4 develop the analysis for the series solutions by the homotopy analysis method (HAM)^[37–40] and related convergence domains. Discussion to various influential parameters is also made in Section 4. The conclusions are given in Section 5.

2. Model development

Let us consider the steady and two-dimensional flow of an incompressible nanofluid induced by an exponentially stretching surface in a porous medium with permeability K (Fig. 1). The x axis is taken along the stretching surface in the direction of motion and the y axis is perpendicular to it.

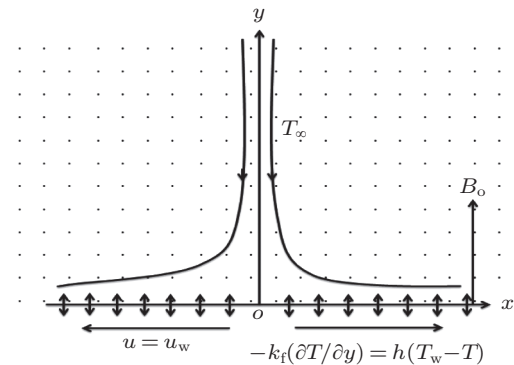


Fig. 1. Geometry of the problem.

A uniform transverse magnetic field of strength B_0 is applied parallel to the y axis. It is assumed that the induced magnetic field and the electric field effects are negligible. Further, the surface exhibits convective type boundary conditions. The boundary layer flow in the present analysis is governed by the following equations:

$$\frac{\partial u}{\partial x} + \frac{\partial v}{\partial y} = 0, \tag{1}$$

$$\rho_{nf} \left(u \frac{\partial u}{\partial x} + v \frac{\partial u}{\partial y} \right) = \mu_{nf} \frac{\partial^2 u}{\partial y^2} - \frac{\mu_{nf}}{K} u - \sigma B_0^2 u, \tag{2}$$

$$u \frac{\partial T}{\partial x} + v \frac{\partial T}{\partial y} = \frac{k_{nf}}{(\rho C_p)_{nf}} \frac{\partial^2 T}{\partial y^2}, \tag{3}$$

where u and v are the velocity components along the x and y directions respectively, and σ is the electrical conductivity of the fluid. The effective density ρ_{nf} , the effective dynamic viscosity μ_{nf} , the heat capacitance $(\rho C_p)_{nf}$ and the thermal conductivity k_{nf} of the nanofluid are given by

$$\rho_{nf} = \rho_f(1 - \phi) + \rho_s \phi, \tag{4}$$

$$\mu_{nf} = \frac{\mu_f}{(1 - \phi)^{2.5}}, \tag{5}$$

$$(\rho C_p)_{nf} = (\rho C_p)_f(1 - \phi) + (\rho C_p)_s \phi, \tag{6}$$

$$\frac{k_{nf}}{k_f} = \frac{k_s + 2k_f - 2\phi(k_f - k_s)}{k_s + 2k_f + 2\phi(k_f - k_s)}. \tag{7}$$

Here ϕ is the solid volume fraction, subscript s is for nano-solid-particles, and subscript f is for base fluid. Graphically, the present consideration of nanofluid model is significant for a comparative study of different nanoparticles. The present model is useful for a comparative study of different nanoparticles. In the present model, the preference can be tackled through Eqs. (4)–(7). The nanoparticles are assumed to have uniform shape and size. The subjected boundary conditions are

$$\begin{aligned} u &= u_w = U_o e^{x/L}, \quad v = v_w, \\ -k_f \frac{\partial T}{\partial y} &= h(T_w - T), \quad \text{as } y = 0, \\ u \rightarrow 0, \quad T &\rightarrow T_\infty, \quad \text{as } y \rightarrow \infty. \end{aligned} \quad (8)$$

Introducing

$$\begin{aligned} \eta &= y \sqrt{\frac{U_o}{2v_f L}} e^{x/2L}, \quad u = U_o e^{x/L} f'(\eta), \\ v &= -\sqrt{\frac{v_f U_o}{2L}} e^{x/2L} [f(\eta) + \eta f'(\eta)], \\ \theta(\eta) &= \frac{T - T_\infty}{T_f - T_\infty}. \end{aligned} \quad (9)$$

Equation (1) is satisfied automatically and equations (2) and (3) after using Eqs. (4)–(7) can be reduced as follows:

$$\begin{aligned} f''' + A_1(1 - \phi)^{2.5}(f f'' - 2f'^2) \\ - \lambda f' - (1 - \phi)^{2.5} M f' &= 0, \end{aligned} \quad (10)$$

$$\frac{1}{Pr} \theta'' + \frac{A_2}{A_3} f \theta' = 0, \quad (11)$$

$$\begin{aligned} f'(0) = 1, \quad f(0) = \alpha, \quad \theta'(0) = -\gamma[1 - \theta(0)], \\ f'(\infty) = 0, \quad \theta(\infty) = 0, \end{aligned} \quad (12)$$

in which prime indicates the differentiation with respect to η and the values of A_i ($i = 1, 2, 3$) are

$$A_1 = \frac{\rho_{nf}}{\rho_f} = (1 - \phi) + \frac{\rho_s}{\rho_f} \phi, \quad (13)$$

$$A_2 = \frac{(\rho C_p)_{nf}}{(\rho C_p)_f} = (1 - \phi) + \frac{(\rho C_p)_s}{(\rho C_p)_f} \phi, \quad (14)$$

$$A_3 = \frac{k_{nf}}{k_f} = \frac{k_s + 2k_f - 2\phi(k_f - k_s)}{k_s + 2k_f + 2\phi(k_f - k_s)}. \quad (15)$$

Moreover the porosity parameter λ , the Hartman number M , the Prandtl number Pr , the mass transfer parameter with $\alpha > 0$ for suction on and $\alpha < 0$ for injection and the Biot number γ are defined as follows:

$$\begin{aligned} \lambda &= \frac{v_f L}{KU_o} e^{-x/L}, \quad M = \frac{2\sigma B_o^2 L}{\rho_f U_o} e^{-x/L}, \quad Pr = \frac{v_f (\rho C_p)_f}{k_f}, \\ \alpha &= -\sqrt{\frac{2L}{v U_o}} e^{-x/2L} v_w, \quad \gamma = \frac{h}{k_f} \sqrt{\frac{v_f}{a}}. \end{aligned} \quad (16)$$

Local skin-friction coefficient C_f and local Nusselt number Nu are given by

$$C_f = \frac{2\tau_w|_{y=0}}{\rho U_o^2 e^{\frac{2x}{L}}}, \quad Nu = -\frac{x}{(T_w - T_\infty)} \frac{\partial T}{\partial y} \Big|_{y=0}, \quad (17)$$

$$C_f \sqrt{\frac{Re_x}{2}} = f''(0), \quad Nu Re_x^{-1/2} \sqrt{\frac{2L}{x}} = -\theta'(0), \quad (18)$$

in which $Re_x = U_o e^{x/L} x / \nu$ denotes the local Reynolds number.

3. Solutions derivation

3.1. Zeroth-order deformation problems

We choose the initial guesses $f_o(\eta)$ and $\theta_o(\eta)$ and the linear operators \mathcal{L}_1 and \mathcal{L}_2 in the forms

$$\begin{aligned} f_o(\eta) &= 1 + \alpha - \exp(-\eta), \\ \theta_o(\eta) &= \frac{\gamma}{1 + \gamma} \exp(-\eta), \end{aligned} \quad (19)$$

$$\mathcal{L}_1(f) = f''' - f', \quad \mathcal{L}_2(\theta) = \theta'' - \theta, \quad (20)$$

together with the properties

$$\begin{aligned} \mathcal{L}_1 [C_1 + C_2 \exp(\eta) + C_3 \exp(-\eta)] &= 0, \\ \mathcal{L}_2 [C_4 \exp(\eta) + C_5 \exp(-\eta)] &= 0, \end{aligned} \quad (21)$$

where $C_1 - C_5$ are the constants. With Eqs. (10) and (11), the definitions of operators \mathcal{N}_f and \mathcal{N}_θ can be written as

$$\begin{aligned} \mathcal{N}_f [\hat{f}(\eta; p), \hat{\theta}(\eta; p)] \\ = \frac{\partial^3 \hat{f}(\eta, p)}{\partial \eta^3} + A_1(1 - \phi)^{2.5} \\ \times \left(\hat{f}(\eta, p) \frac{\partial^2 \hat{f}(\eta, p)}{\partial \eta^2} - 2 \left(\frac{\partial \hat{f}(\eta, p)}{\partial \eta} \right)^2 \right) \\ - \lambda \frac{\partial \hat{f}(\eta, p)}{\partial \eta} - (1 - \phi)^{2.5} M \frac{\partial \hat{f}(\eta, p)}{\partial \eta}, \end{aligned} \quad (22)$$

$$\begin{aligned} \mathcal{N}_\theta [\hat{\theta}(\eta, p), \hat{f}(\eta, p)] \\ = \frac{1}{Pr} \frac{\partial^2 \hat{\theta}(\eta, p)}{\partial \eta^2} + \frac{A_2}{A_3} \hat{f}(\eta, p) \frac{\partial \hat{\theta}(\eta, p)}{\partial \eta}. \end{aligned} \quad (23)$$

We construct the zeroth order problems as follows:

$$(1 - p) \mathcal{L}_1 [\hat{f}(\eta, p) - f_o(\eta)] = p h_f \mathcal{N}_f [\hat{f}(\eta, p)], \quad (24)$$

$$(1 - p) \mathcal{L}_2 [\hat{\theta}(\eta, p) - \theta_o(\eta)] = p h_\theta \mathcal{N}_\theta [\hat{\theta}(\eta, p)], \quad (25)$$

$$\begin{aligned} \hat{f}'(0, p) = 1, \quad \hat{f}(0, p) = \alpha, \quad \hat{f}'(\infty, p) = 0, \\ \hat{\theta}'(0, p) = -\gamma[1 - \hat{\theta}(0, p)], \quad \hat{\theta}(\infty, p) = 0, \end{aligned} \quad (26)$$

where h_f and h_θ are the nonzero auxiliary parameters and for $p = 0$ and $p = 1$ we have

$$\begin{aligned} \hat{f}(\eta, 0) &= f_o(\eta), \quad \hat{f}(\eta, 1) = f(\eta), \\ \hat{\theta}(\eta, 0) &= \theta_o(\eta), \quad \hat{\theta}(\eta, 1) = \theta(\eta). \end{aligned} \quad (27)$$

Note that $f_o(\eta)$ and $\theta_o(\eta)$ approach $f(\eta)$ and $\theta(\eta)$ respectively, when p has variation from 0 to 1. According to the Taylor series we have

$$\begin{aligned} \hat{f}(\eta, p) &= f_o(\eta) + \sum_{m=1}^{\infty} f_m(\eta) p^m, \\ f_m(\eta) &= \frac{1}{m!} \left. \frac{\partial^m \hat{f}(\eta, p)}{\partial p^m} \right|_{p=0}, \\ \hat{\theta}(\eta, p) &= \theta_o(\eta) + \sum_{m=1}^{\infty} \theta_m(\eta) p^m, \\ \theta_m(\eta) &= \frac{1}{m!} \left. \frac{\partial^m \hat{\theta}(\eta, p)}{\partial p^m} \right|_{p=0}, \end{aligned} \quad (28)$$

where the convergence depends upon h_f and h_θ . By proper choice of h_f and h_θ , the series (28) converge for $p = 1$ and so

$$\begin{aligned} f(\eta) &= f_o(\eta) + \sum_{m=1}^{\infty} f_m(\eta), \\ \theta(\eta) &= \theta_o(\eta) + \sum_{m=1}^{\infty} \theta_m(\eta). \end{aligned} \quad (29)$$

3.2. m -th order deformation problems

The resulting problems at this order are given by

$$\mathcal{L}_1[f_m(\eta, p) - \chi_m f_{m-1}(\eta)] = h_f \mathcal{R}_{f,m}(\eta), \quad (30)$$

$$\mathcal{L}_2[\theta_m(\eta, p) - \chi_m \theta_{m-1}(\eta)] = h_\theta \mathcal{R}_{\theta,m}(\eta), \quad (31)$$

$$f_m(0) = f'_m(0) = f'_m(\infty) = \theta'_m(0) - \gamma \theta_m(0) = \theta_m(\infty) = 0, \quad (32)$$

$$\chi_m = \begin{cases} 0, & m \leq 1, \\ 1, & m > 1, \end{cases} \quad (33)$$

$$\begin{aligned} \mathcal{R}_{f,m}(\eta) &= f'''_{m-1} + A_1(1-\phi)^{2.5} \sum_{k=0}^{m-1} [2f'_{m-1-k} f'_k - f_{m-1-k} f''_k] \\ &\quad - \lambda f'_{m-1} - (1-\phi)^{2.5} M f'_{m-1}, \end{aligned} \quad (34)$$

$$\mathcal{R}_{\theta,m}(\eta) = \frac{1}{Pr} \theta''_{m-1} + \frac{A_2}{A_3} \sum_{k=0}^{m-1} \theta'_{m-1-k} f_k, \quad (35)$$

where the general solutions are

$$f_m(\eta) = f_m^*(\eta) + C_1 + C_2 e^\eta + C_3 e^{-\eta}, \quad (36)$$

$$\theta_m(\eta) = \theta_m^*(\eta) + C_4 e^\eta + C_5 e^{-\eta}, \quad (37)$$

in which f_m^* and θ_m^* denote the special solutions.

4. Analysis of the results

4.1. Convergence of the derived series solutions

Now the solutions of Eqs. (10) and (11) subject to the boundary conditions (12) are computed by means of a homotopy analysis method. We choose auxiliary parameters h_f and h_θ for the functions f and θ respectively. The convergence of the obtained series and the rate of the approximation for HAM strongly depend upon the values of the auxiliary parameters. For ranges of admissible values of h_f and h_θ , the h

curves for 12th-order of approximations are plotted in Figs. 2 and 3. We can see that the permissible values for h_f and h_θ are $-0.7 \leq h_f \leq -0.4$ and $-0.85 \leq h_\theta \leq -0.3$. Further, the series solutions converge in the whole region of η ($0 < \eta < \infty$) when $h_f = h_\theta = -0.6$.

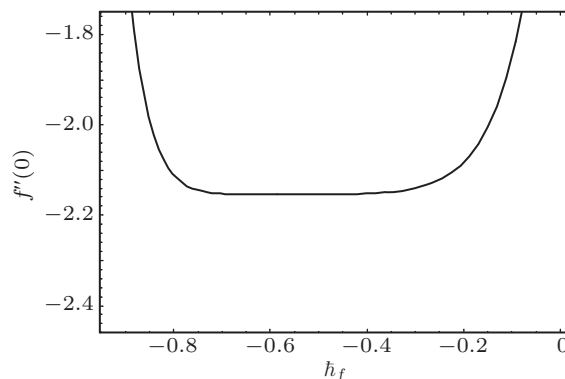


Fig. 2. The h curve for f . $M = 0.1$, $Pr = 1$, $\phi = 0.03$, $\gamma = 0.7$, $\alpha = 0.9$, and $\lambda = 0.5$.

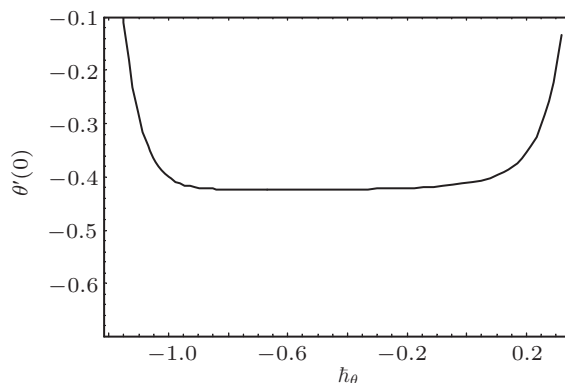


Fig. 3. The h curve for θ . $M = 0.1$, $Pr = 1$, $\phi = 0.03$, $\gamma = 0.7$, $\alpha = 0.9$, and $\lambda = 0.5$.

4.2. Results and discussion

In this section, we discuss the influence of various parameters on the velocity $f'(\eta)$ and temperature fields $\theta(\eta)$. Figures 4–7 are plotted to analyze the effects of volume fraction of nanoparticles (Cu), mass transfer parameter α , Hartman number M and porosity parameter λ on the velocity field f' . Effects of volume fraction of nanoparticles (Cu) on the velocity profile f' can be seen from Fig. 3. Here the values of f' and the boundary layer thickness decrease when the volume fraction for the nanoparticles increases. This is because of the fact that by increasing the volume of copper nanoparticles, the thermal conductivity increases and the boundary layer thickness decreases. The effects of the mass transfer parameter α on the velocity function f' are depicted in Fig. 4. This graph shows that the value of velocity function f' and the boundary layer thickness decrease by increasing α . Because applying suction leads to draw the amount of fluid particles into the wall and consequently the velocity boundary layer decreases.

Also suction is an agent which causes a reduction in the fluid velocity. Figure 5 shows the influence of Hartman number M on the velocity. Here we analyzed that the velocity is reduced when we increase the values of Hartman number. The application of an applied magnetic field has the tendency to slow down the movement of the fluid, which leads to a decrease in the velocity and momentum boundary layer thickness. From Fig. 6, we can see that higher values of porosity parameter λ correspond to the lower velocity. The porosity parameter depends on the permeability parameter K . An increase in the porosity parameter leads to the lower permeability parameter. This lower permeability parameter causes a reduction in the fluid velocity.

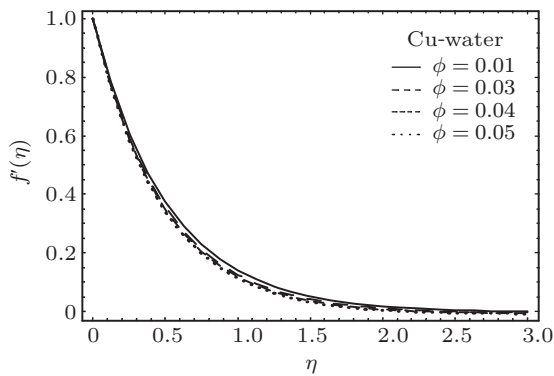


Fig. 4. Effects of ϕ on f' . $\lambda = 0.5, Pr = 1, M = 0.1, \alpha = 0.9, h = -0.6$.

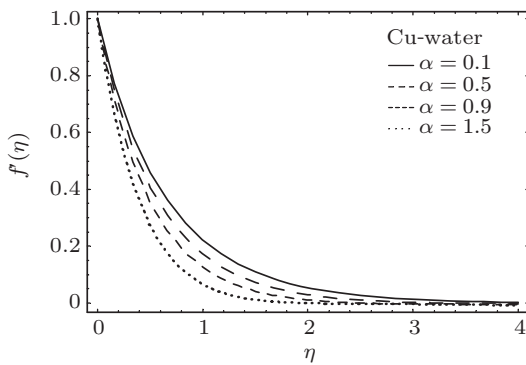


Fig. 5. Effects of α on f' . $\lambda = 0.5, Pr = 1, M = 0.1, \phi = 0.03$, and $h = -0.6$.

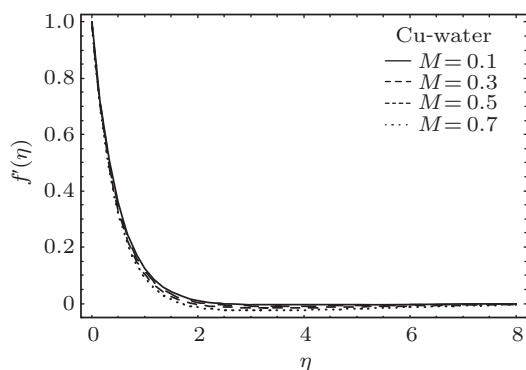


Fig. 6. Effects of M on f' . $\lambda = 0.5, Pr = 1, \alpha = 0.9, \phi = 0.03$, and $h = -0.6$.

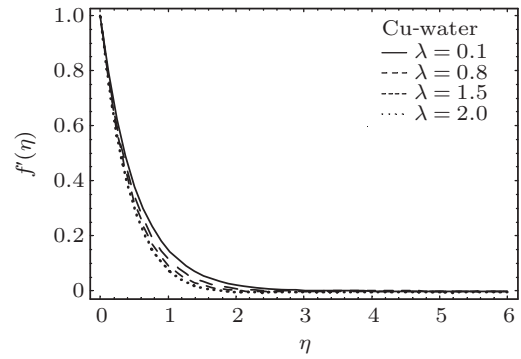


Fig. 7. Effects of λ on f' . $\alpha = 0.9, Pr = 1, M = 0.1, \phi = 0.03$, and $\lambda = 0.5$.

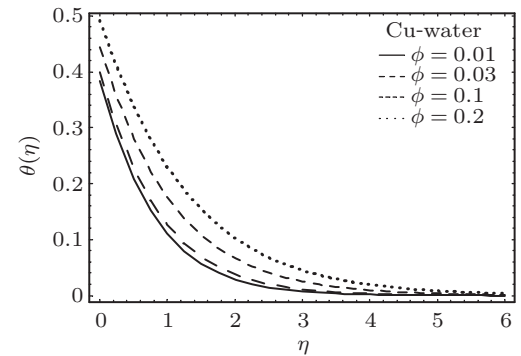


Fig. 8. Effects of ϕ on θ . $\lambda = 0.5, Pr = 1, \gamma = 0.7, \alpha = 0.9, M = 0.1, h = -0.6$.

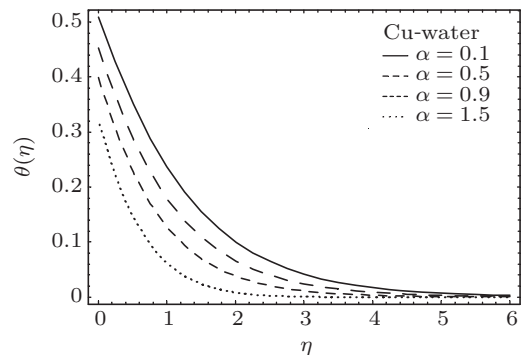


Fig. 9. Effects of α on θ . $\lambda = 0.5, Pr = 1, \gamma = 0.7, M = 0.1, \phi = 0.03$, and $h = -0.6$.

The effects of volume fraction of nanoparticles (Cu), mass transfer parameter α , Hartman number M , porosity parameter λ , Prandtl number Pr and Biot number γ on the temperature profile θ are shown in Figs. 8–13. Effect of ϕ on the temperature is analyzed in Fig. 7. It is observed that increasing the volume fraction of nanoparticles ϕ , increases the thermal conductivity of nanofluids and consequently the thermal boundary layer thickness increases. The behavior of α on the temperature profile is similar to that of the velocity profile (see Fig. 9). Figure 10 illustrates the effects of M on temperature profile θ . As the Lorentz force is a resistive force which opposes the fluid motion, so heat is produced and as a result, the thermal boundary layer thickness increases. Variations of

λ and Pr on temperature profile θ can be seen in Figs. 11–12. There is a decrease in temperature θ when porosity parameter λ and Prandtl number Pr are increased. In fact, the thermal diffusivity decreases by increasing Pr and thus the heat diffuses away slowly from the heated surface. Figure 13 represents the effect of Biot number γ on temperature profile θ . Temperature profile θ increases for an increase in γ . The Biot number involves the heat transfer coefficient. Higher values of the Biot number implies an enhancement in the heat transfer coefficient. This enhancement in the heat transfer coefficient give rise to the temperature and thermal boundary layer thickness.

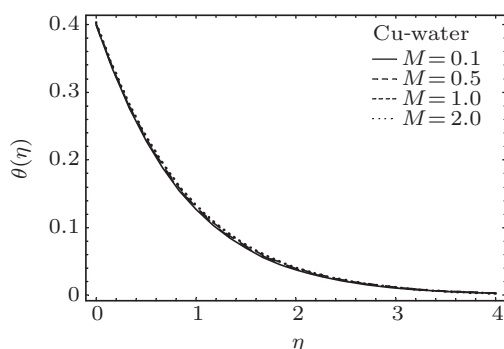


Fig. 10. Effects of M on θ . $\lambda = 0.5$, $Pr = 1$, $\gamma = 0.7$, $\alpha = 0.9$, $\phi = 0.03$, and $h = -0.6$.

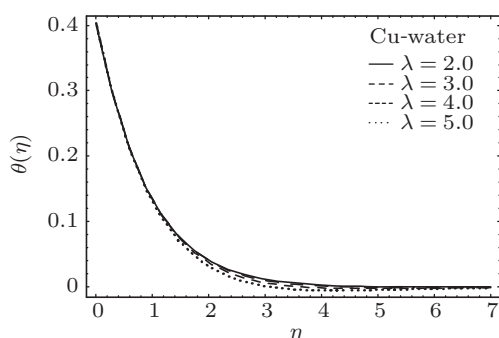


Fig. 11. Effects of λ on θ . $\phi = 0.03$, $Pr = 1$, $\gamma = 0.7$, $\alpha = 0.9$, $M = 0.1$, and $h = -0.6$.

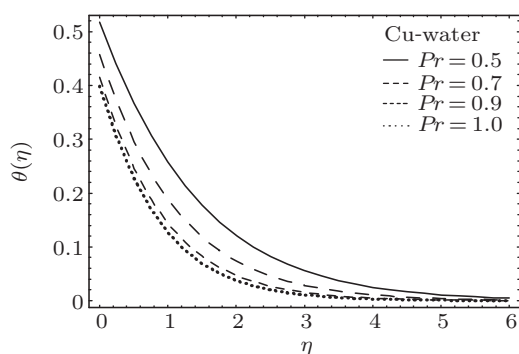


Fig. 12. Effects of Pr on θ . $\phi = 0.03$, $\lambda = 0.5$, $\gamma = 0.7$, $\alpha = 0.9$, $M = 0.1$, and $h = -0.6$.

In Figs. 14(a) and 14(b) we observe that boundary layer thickness is maximum when Alumina is chosen as the

nanoparticle. Figures 15(a) and 15(b) show the effects of nanoparticle volume fraction ϕ , mass transfer parameter α and porosity parameter λ on the skin friction coefficient in the case of Cu-water. It is noticed that the skin friction coefficient decreases when we increase ϕ for both α and λ . Figures 16(a) and 16(b) describe the variation of the Nusselt number for nanoparticle volume fraction ϕ , mass transfer parameter α and porosity parameter λ . In this figure, heat transfer rates decrease as ϕ increases for both α and λ .

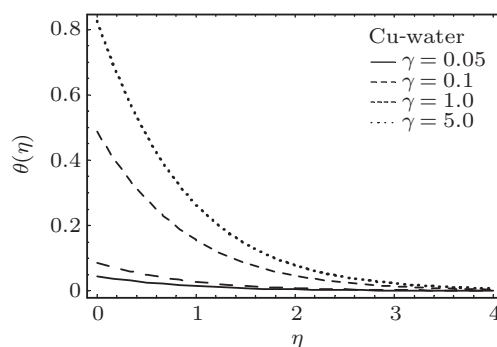


Fig. 13. Effects of γ on θ . $\phi = 0.03$, $\lambda = 0.5$, $Pr = 1$, $\alpha = 0.9$, $M = 0.1$, and $h = -0.6$.

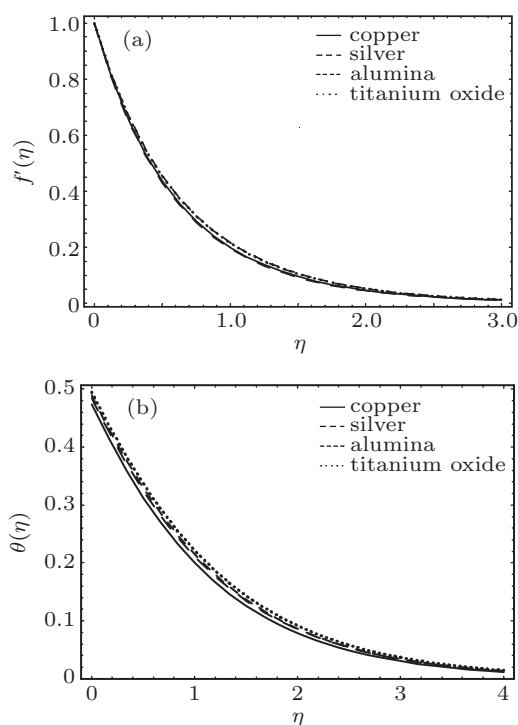


Fig. 14. (a) Velocity and (b) temperature profiles for different types of nanofluids.

Table 1 shows the convergence of the series solutions. It is observed that convergence is achieved at the 17-th order of approximations. In Table 2, some thermophysical properties of water and nanoparticles are given. Table 3 shows the effects of the nanoparticle volume fraction ϕ for different types of nanofluids on the skin friction coefficient when $\lambda = 0.5$, $M = 0.1$, and $\alpha = 0.9$. Table 4 shows the effects of the

nanoparticle volume fraction ϕ for different types of nanofluids on the Nusselt number when $\lambda = 0.5$, $Pr = 1$, $\gamma = 0.7$, $M = 0.1$, and $\alpha = 0.9$. These tables show that the shear stress and heat transfer rate change when we use different types of nanoparticles.

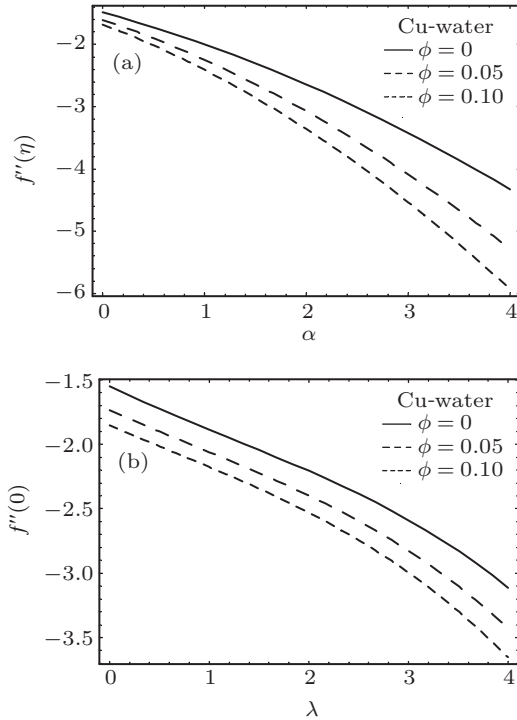


Fig. 15. (a) Effect of nanoparticle volume fraction ϕ , mass transfer parameter α and (b) porosity parameter λ on the skin friction coefficient when $M = 0.1$.

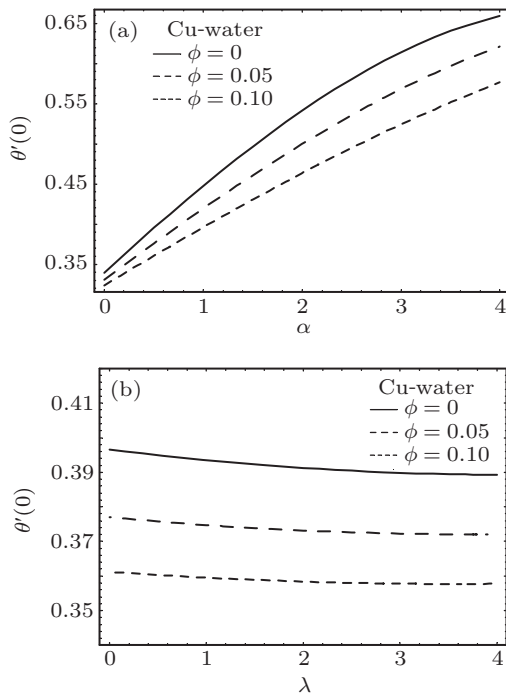


Fig. 16. Effect of nanoparticle volume fraction ϕ , (a) mass transfer parameter α and (b) porosity parameter λ on the Nusselt number when $M = 0.1$, $Pr = 1$, and $\gamma = 0.7$.

Table 1. Convergence of HAM solutions for different order of approximations when $Pr = 1$, $\phi = 0.03$, $\lambda = 0.5$, $\gamma = 0.7$, $M = 0.1$, and $\alpha = 0.9$.

Order	$-f''(0)$	$-\theta'(0)$
1	1.76172	0.416270
5	2.14446	0.422428
10	2.15409	0.423256
17	2.15426	0.423311
20	2.15426	0.423311
25	2.15426	0.423311
30	2.15426	0.423311
35	2.15426	0.423311
40	2.15426	0.423311

Table 2. Thermophysical properties of water and nanoparticles.

	$\rho/\text{kg}\cdot\text{m}^{-3}$	$C_p/\text{J}\cdot\text{kg}^{-1}\cdot\text{K}^{-1}$	$k/\text{W}\cdot\text{m}^{-1}\cdot\text{K}^{-1}$	$\beta \times 10^5/\text{K}^{-1}$
Pure water	997.1	4179	0.613	21
Copper (Cu)	8933	385	401	1.67
Silver (Ag)	10500	235	429	1.89
Alumina (Al_2O_3)	3970	765	40	0.85
Titanium Oxide (TiO_2)	4250	686.2	8.9538	0.9

Table 3. Effect of ϕ for different types of nanofluids on the skin friction coefficient when $\lambda = 0.5$, $M = 0.1$, and $\alpha = 0.9$.

ϕ	Cu	Ag	Al_2O_3	TiO_2
0.01	-2.05387	-2.07036	-2.00143	-2.00439
0.03	-2.15426	-2.20071	-2.00558	-2.01404
0.05	-2.23960	-2.31255	-2.00535	-2.01873

Table 4. Effect of ϕ for different types of nanofluids on the Nusselt number when $\lambda = 0.5$, $Pr = 1$, $\gamma = 0.7$, $M = 0.1$, and $\alpha = 0.9$.

ϕ	Cu	Ag	Al_2O_3	TiO_2
0.01	0.436981	0.436452	0.437649	0.438380
0.03	0.423311	0.421702	0.425326	0.427566
0.05	0.409403	0.406691	0.412767	0.416582

5. Concluding remarks

Here MHD flow of nanofluid by an exponentially permeable stretching sheet is studied. The effects of different parameters on the velocity and temperature profiles are shown. A convergent approximate solution is constructed. The following observations are made.

- (i) An increase in the values of ϕ , α , M and λ have similar effects on the velocity $f'(\eta)$ in a qualitative sense.
- (ii) The temperature profile increases by increasing ϕ , M and γ while it decreases when α and λ are increased.
- (iii) An increase in Prandtl number Pr reduces the temperature and the thermal boundary layer thickness.
- (iv) The values of the skin friction coefficient are higher for increasing values of ϕ .
- (v) Higher values of ϕ correspond to smaller values of the Nusselt number.

Acknowledgment

The research of Dr. Alsaedi was partially supported by the Deanship of Scientific Research (DSR), King Abdulaziz University, Jeddah, Saudi Arabia.

References

- [1] Crane L J 1970 *Zeitschrift Fur Angewandte Mathematik Und Physik* **21** 645
- [2] Cortell R 2006 *Phys. Lett. A* **357** 298
- [3] Bhattacharyya K, Hayat T and Alsaedi A 2013 *Chin. Phys. B* **22** 024702
- [4] Mukhopadhyay S 2013 *Chin. Phys. B* **22** 074701
- [5] Rashidi M M and Mohimani Pour S A 2010 *Nonlinear Analysis: Modelling and Control* **15** 83
- [6] Magyari E and Keller B 1999 *J. Phys. D: Appl. Phys.* **32** 577
- [7] Partha M K, Murthy P V S N and Rajasekhar G P 2005 *Heat Mass Transfer* **41** 360
- [8] Sajid M and Hayat T 2008 *Int. Comm. Heat Mass Transfer* **35** 347
- [9] Bidin B and Nazar R 2009 *Euro. J. Sci. Research* **33** 710
- [10] Ishak A 2011 *Sains Malaysiana* **40** 391
- [11] Bachok N, Ishak A and Pop I 2012 *Int. J. Heat Mass Transfer* **55** 8122
- [12] Mandal I C and Mukhopadhyay S 2013 *Ain Shams Eng. J.* **4** 103
- [13] Bhattacharyya K 2012 *J. Egy. Math. Society* **20** 223
- [14] Elbashareshy E M A, Emam T G and Abdelgaber K M 2012 *J. Egy. Math. Society* **20** 215
- [15] Rohni A M, Ahmad S, Ismail A I M and Pop I 2013 *I. J. Ther. Sci.* **64** 264
- [16] Mukhopadhyay S 2013 *Alexandria Eng. J.* **52** 259
- [17] Choi S U S 1995 *ASME FED* **231** 99
- [18] Buongiorno J 2006 *ASME J. Heat Transfer* **128** 240
- [19] Kuznetsov A V and Nield D A 2010 *Int. J. Therm. Sci.* **49** 243
- [20] Nield D A and Kuznetsov A V 2009 *Int. J. Heat Mass Transfer* **52** 5792
- [21] Cheng P and Minkowycz W 1977 *J. Geophys. Res.* **82** 2040
- [22] Narayana M and Sibanda P 2012 *Int. J. Heat and Mass Transfer* **55** 7552
- [23] Kang H U, Kim S H and Oh J M 2006 *Exp. Heat Transfer* **19** 181
- [24] Velagapudi V, Konijeti R K and Aduru C S K 2008 *Thermal Sci.* **12** 27
- [25] Rudyak V Y, Belkin A A and Tomilina E A 2010 *Tech. Phys. Lett.* **36** 660
- [26] Makinde O D and Aziz A 2011 *Int. J. Thermal Sci.* **50** 1326
- [27] Alsaedi A, Awais M and Hayat T 2012 *Comm. Nonlinear Sci Num. Simu.* **17** 4210
- [28] Kandasamy R, Muhaimin I, Khamis A B and Roslan R bin 2013 *Int. J. Thermal Sci.* **65** 196
- [29] Kameswaran P K, Shaw S, Sibanda P and Murthy P V S N 2013 *Int. J. Heat Mass Transfer* **57** 465
- [30] Mustafa M, Hayat T, Pop I, Asghar S and Obaidat S 2011 *Int. J. Heat Mass Transfer* **54** 5588
- [31] Nandy S K and Mahapatra T R 2013 *Int. J. Heat Mass Transfer* **64** 1091
- [32] Ibrahim W, Shankar B and Nandeppanavar M M 2013 *Int. J. Heat Mass Transfer* **56** 1
- [33] Makinde O D, Khan W A and Khan Z H 2013 *Int. J. Heat Mass Transfer* **62** 526
- [34] Ibrahim W and Shankar B 2013 *Computers and Fluids* **75** 1
- [35] Zheng L, Zhang C, Zhang X and Zhang J 2013 *J. Franklin Institute* **350** 990
- [36] Khan M S, Alam M M and Ferdows M 2013 *Procedia Engineering* **56** 316
- [37] Liao S J 2003 (Boca Raton: Chapman and Hall/CRC Press)
- [38] Abbasbandy S and Shirzadi A 2011 *Comm. Non-linear Sci. Num. Simul.* **16** 112
- [39] Rashidi M M and Erfani E 2009 *Comp. Phy. Comm.* **180** 1539
- [40] Hayat T, Shehzad S A, Alsaedi A and Alhothulai M S 2012 *Chin. Phys. Lett.* **29** 114704

Thesis

by Maria Imtiaz

FILE	THESIS.PDF (3.34M)	WORD COUNT	33251
TIME SUBMITTED	15-DEC-2015 02:37PM	CHARACTER COUNT	174081
SUBMISSION ID	615365006		

Contents

1 Literature review and governing equations	5
1.1 Background	5
1.2 Fundamental laws for Buongiorno's model	11
1.2.1 Law of conservation of mass	11
1.2.2 Law of conservation of linear momentum	11
1.2.3 Law of conservation of energy	12
1.2.4 Law of conservation of concentration	12
1.3 Basic laws for phase flow model	13
1.3.1 Law of conservation of linear Momentum	13
1.3.2 Law of conservation of Energy	13
1.4 Solution procedure	14
2 MHD flow of nanofluid over permeable stretching sheet with convective boundary conditions	15
2.1 Problem formulation	15
2.2 Homotopic solutions	18
2.2.1 Zeroth-order deformation problems	18
2.2.2 m^{th} order deformation problems	20
2.3 Analysis of series solutions	21
2.4 Results and discussion	23
2.5 Main points	36

3	MHD flow of nanofluids over an exponentially stretching sheet in a porous medium with convective boundary conditions	37
3.1	Mathematical formulation	38
3.2	Homotopy analysis solutions	41
1	3.3 Convergence of the homotopy solutions	43
3.4	Discussion	44
3.5	Concluding remarks	54
4	MHD flow of nanofluid with homogeneous-heterogeneous reactions and velocity slip	56
4.1	Mathematical formulation	56
4.2	Solutions derivation	60
4.3	Convergence of the homotopy solutions	62
4.4	Results and discussion	64
4.4.1	Dimensionless velocity profiles	64
4.4.2	Dimensionless concentration profiles	67
4.4.3	Skin friction coefficient and surface concentration	69
4.5	Final remarks	72
5	Impact of magnetohydrodynamics in bidirectional flow of nanofluid subject to second order slip velocity and homogeneous-heterogeneous reactions	74
5.1	Model development	75
5.2	Homotopic solutions	79
5.3	Convergence analysis	81
5.4	Results and discussion	83
5.4.1	Dimensionless velocity profiles	83
5.4.2	Dimensionless concentration profiles	89
5.4.3	Surface concentration and skin friction coefficient	91
5.5	Conclusions	94

6	Effects of homogeneous-heterogeneous reactions in flow of magnetite-Fe₃O₄ nanoparticles by a rotating disk	96
6.1	Model development	97
6.2	Solutions procedure	100
6.3	Convergence of series solutions	104
6.4	Discussion	105
6.5	Main points	114
7	Melting heat transfer in the MHD flow of Cu-water nanofluid with viscous dissipation and Joule heating	116
7.1	Model development	117
7.2	HAM Solution	120
7.3	Convergence of HAM solution	121
7.4	Results and discussion	124
7.4.1	Dimensionless velocity field	124
7.4.2	Dimensionless temperature field	125
7.4.3	Skin friction coefficient and Nusselt number	125
7.5	Concluding remarks	135
8	Unsteady flow of nanofluid with double stratification and magnetohydrodynamics	136
8.1	Flow equations	136
8.2	Homotopy analysis solutions	140
8.3	Convergence of the homotopy solutions	142
8.4	Interpretation of results	146
8.5	Concluding remarks	159
9	Magnetohydrodynamic stagnation point flow of a Jeffrey nanofluid with Newtonian heating	161
9.1	Flow equations	161
9.2	Problem formulation	162

9.3	Series solutions	164
9.4	Convergence analysis	166
9.5	Results and discussion	169
9.6	Conclusions	183
10	MHD three-dimensional flow of nanofluid with velocity slip and nonlinear thermal radiation	185
10.1	Flow description	185
10.2	Heat transfer analysis	187
10.3	Analytical solutions	189
10.4	Convergence of the developed solutions	192
10.5	Discussion	194
10.5.1	Dimensionless velocity profiles	194
10.5.2	Dimensionless temperature profiles	194
10.5.3	Skin friction coefficient and Nusselt number	195
10.6	Concluding remarks	201
11	Magnetohydrodynamic three-dimensional flow of nanofluid by a porous shrinking surface	203
11.1	Problem formulation	204
11.2	Homotopy analysis solutions	207
11.3	Convergence analysis	209
11.4	Results and discussion	211
11.5	Concluding remarks	219
12	MHD 3D flow of nanofluid in presence of convective conditions	221
12.1	Model development	221
12.2	Homotopy analysis solutions	224
12.3	Convergence of the series solutions	226
12.4	Results and discussion	227
12.5	Final remarks	235

Chapter 1

Literature review and governing equations

This chapter contains the literature review related to the nanofluid, magnetohydrodynamic, stretching surface, rotating disk, slip flows and homogeneous-heterogeneous reactions. Equations governing nanofluids flow for Buongiorno and phase flow model are presented. The basic idea of homotopy analysis method (HAM) is also included.

1.1 Background

Convective heat transfer through nanoparticles is a popular area of research at present. The nanoparticles (nanometer sized particles) are made up of metals, carbides, oxides or carbon nanotubes. The nanofluids are formed by adding nanoparticles into many conventional fluids like water, ethylene glycol and engine oil. The use of additive is a process which enhances the heat transfer performance of base fluids. Choi [1] experimentally found that addition of nanoparticles in conventional/base fluid appreciably enhances the thermal conductivity of the fluid. Eastman et al. [2] and Choi et al. [3] pointed out that a small amount ($< 1\%$ volume fraction) of Cu nanoparticles or carbon nanotubes dispersed in ethylene glycol or oil remarkably enhanced the thermal conductivity of a fluid by 40% and 50% respectively. Thus the nanomaterials are recognized more effective in micro/nano electromechanical devices, advanced cooling systems, large scale thermal management systems via evaporators, heat exchangers and

industrial cooling applications. Use of nanofluids as coolants allow for smaller size and better positioning of the radiators which eventually consumes less energy for overcoming resistance on the road. Nanoparticles in refrigerant/lubricant mixtures could enable a cost effective technology for improving the efficiency of chillers that cool buildings. Tiwari and Das [4] studied **heat transfer augmentation in a two-sided lid-driven differentially heated square cavity utilizing nanofluids.** At present, the literature on theoretical and experimental attempts about nanofluids is quite extensive. The comprehensive review on nanofluids can be found in the book [5] and refs. [6 – 11]. Detailed review on this topic up to 2012 has been made by Mohammed et al.[12] and Dalkilic et al. [13]. Besides these, a comprehensive survey of convective transport in nanofluids is presented by Buongiorno [14]. He developed a non-homogeneous equilibrium model for convective transport to describe the heat transfer enhancement of nanofluids. He concluded that abnormal increase **in thermal conductivity** occurs due to the presence of two main velocity-slip effects, namely, the Brownian diffusion and the thermophoretic diffusion of the nanoparticles. Later Buongiorno et al. [15] conducted novel investigations which show no anomalous thermal conductivity enhancement in the considered fluids. **Niu et al. [16] studied slip flow of a non-Newtonian nanofluid in a microtube.** **Effects of heat generation/absorption on stagnation point flow of nanofluid over a surface with convective boundary conditions** have been analyzed by **Alsaedi et al. [17].** Xu et al. [18] examined unsteady flow in a nano-liquid film over a stretching surface. Imtiaz et al. [19] presented mixed convection flow of nanofluid with Newtonian heating. Khalili et al. [20] considered unsteady convective heat and mass transfer in pseudoplastic nanofluid.

Magnetic nanofluids are more useful in the sense that their physical properties are tunable through the external magnetic field. **Many equipments such as MHD generators, pumps, bearings and boundary layer control are affected by the interaction between the electrically conducting fluid and a magnetic field.** The behavior of flow strongly depends on the orientation and intensity of the applied magnetic field. The exerted magnetic field manipulates the suspended particles and rearranges their concentration in the fluid which strongly changes heat transfer characteristics of the flow. A magnetic nanofluid has both the liquid and magnetic characteristics. Such materials have fascinating applications in optical modulators, magneto-optical wavelength filters, nonlinear optical materials, optical switches, optical gratings etc.

Magnetic particles have pivotal role in the construction of loud speakers as sealing materials and in sink float separation. Magneto nanofluids are useful to guide the particles up the blood stream to a tumor with magnets. This is due to the fact that the magnetic nanoparticles are regarded more adhesive to tumor cells than non-malignant cells. Such particles absorb more power than microparticles in alternating current magnetic fields tolerable in humans i.e. for cancer therapy. Numerous applications involving magnetic nanofluids include drug delivery, hyperthermia, contrast enhancement in magnetic resonance imaging and magnetic cell separation. Motivated by all the aforementioned facts, various scientists and engineers are engaged in the discussion of flows of nanofluids via different aspects. Rashidi et al. [21] analyzed entropy generation in MHD flow due to a rotating porous disk in a nanofluid. Sheikholeslami et al. [22] investigated MHD nanofluid flow in a semi-porous channel. Khalili et al. [23] discussed unsteady MHD nanofluid flow over a stretching/shrinking sheet in porous medium filled with a nanofluid. Rashidi et al. [24] reported buoyancy effect on MHD stretched flow of nanofluid with thermal radiation. Effect of thermal radiation on magnetohydrodynamics nanofluid flow and heat transfer by means of two phase model has been studied by Sheikholeslami et al. [25]. Numerical simulation of two phase unsteady nanofluid flow between parallel plates in presence of time dependent magnetic field has been investigated by Sheikholeslami et al. [26]. Lin et al. [27] analyzed MHD pseudo-plastic nanofluid flow in a finite thin film over stretching surface. They also considered heat transfer analysis with internal heat generation. Melting heat transfer on MHD convective flow of a nanofluid with viscous dissipation and second order slip has been presented by Mabood and Mastroberardino [28]. Hayat et al. [29] explored 3D MHD flow of viscoelastic nanofluid with nonlinear thermal radiation. Hayat et al. [30] also examined interaction of magnetic field in flow of Maxwell nanofluid with convective effect.

The fluid flow over stretching surface has gained the attention of researchers due to its important applications in engineering processes namely polymer extrusion, drawing of plastic films and wires, glass fiber and paper production, manufacture of foods, crystal growing, liquid films in condensation process, etc. Crane [31] investigated the flow caused by the stretching of a sheet. Most of the available literature deals with the study of boundary layer flow over a stretching surface where the velocity of the stretching sheet is assumed linearly proportional to the distance from the fixed origin. However, realistically stretching of plastic sheet may not

necessarily be linear. Flow and heat transfer characteristics past an exponentially stretching sheet has a wider applications in technology. For example, in case of annealing and thinning of copper wires, the final product depends on the rate of heat transfer at the surface with exponential variations of stretching velocity. During such processes, both the kinematics of stretching and the simultaneous heating or cooling have a decisive influence on the quality of the final product. Specific example in this direction can be mentioned through process in plastic industry. Gupta and Gupta [32] discussed Heat and mass transfer on a stretching sheet with suction or blowing. Afzal et al. [33] studied momentum and heat transfer on a continuous flat surface moving in a parallel stream. Magyari and Keller [34] focused on heat and mass transfer on boundary layer flow due to an exponentially continuous stretching sheet. Cortell [35] found the solutions for moving fluid over a moving flat surface. Zheng et al. [36] reported MHD flow and heat transfer over a porous shrinking surface with velocity slip and temperature jump. MHD stagnation point flow and heat transfer due to nanofluid towards a stretching sheet have been addressed by Ibrahim et al. [37]. Mukhopadhyay [38] investigated slip effects on MHD boundary layer flow by an exponentially stretching sheet with suction/blowing and thermal radiation. Exact solutions over stretching or shrinking sheet in an electrically conducting quiescent couple stress fluid have been computed by Turkyilmazoglu [39]. Malvandi et al. [40] presented slip effects on unsteady stagnation point flow of a nanofluid over a stretching sheet. Casson fluid flow and heat transfer past an exponentially porous stretching surface in presence of thermal radiation have been provided by Pramanik [41]. Three dimensional flow of viscoelastic fluid by an exponentially stretching surface with mass transfer has been obtained by Alhuthali et al. [42]. Rosca and Pop [43] studied Powell–Eyring fluid flow over a shrinking surface in a parallel free stream. Nandy and Pop [44] explored effects of magnetic field and thermal radiation on stagnation flow and heat transfer of nanofluid over a shrinking surface. Nandy [45] considered unsteady flow of Maxwell fluid in the presence of nanoparticles toward a permeable shrinking surface with Navier slip. Weidman and Ishak [46] computed multiple solutions of two-dimensional and three-dimensional flows induced by a stretching flat surface. Effects of viscous dissipation and heat source on unsteady MHD flow over a stretching sheet have been examined by Reddy et al. [47]. Chen et al. [48] discussed boundary layer flow of Maxwell fluid over an unsteady stretching surface. Mustafa et al. [49] analyzed radiation effects over

a bi-directional exponentially stretching sheet. Effects of convective heat and mass transfer in flow of Powell-Eyring fluid past an exponentially stretching sheet have been presented by Hayat et al. [50].

Fluid flow by a rotating disk is important in engineering and geophysical applications such as flows in spin coating, manufacturing and use of computer disks, rotational viscometer, centrifugal machinery, pumping of liquid metals at high melting point, crystal growth from molten silicon, turbo-machinery etc. Karman [51] investigated the classical problem of a rotating disk. Erdogan [52] analyzed unsteady viscous fluid flow by non-coaxial rotations of disk and a fluid at infinity. A note on porous rotating disk is presented by Kelson and Desseaux [53]. Flow due to a rotating porous disk in presence of nanoparticles is analyzed by Bachok et al. [54]. Rashidi et al. [55] developed approximate solutions for steady flow due to a rotating disk through porous medium and heat transfer. Turkyilmazoglu [56] studied nanofluid flow and heat transfer due to a rotating disk. Hayat et al. [57] analyzed MHD flow of Cu-water nanofluid due to a rotating disk with partial slip.

The formation and use of micro devices have attracted the attention of recent scientists. The small size as well as high efficiency of micro-devices-such as microsensors, microvalves and micropumps are some of the advantages of using MEMS and NEMS (Micro and Nano Electro Mechanical Systems). Many attempts addressing the flow and heat transfer have been presented to guarantee the performance of such devices. The surface effects at micro scale level lead to change in the classical conditions. Thus no-slip condition is inadequate for the fluid flows in MEMS and NEMS. No slip conditions show unrealistic behavior for the cases like the extrusion of polymer melts from a capillary tube, corner flow and spreading of liquid on a solid substrate [58]. The flow analysis with heat transfer at micro-scale is encountered in micro-electro-mechanical systems (MEMS). Such systems have association with consideration of velocity slip and temperature jump. Khare et al. [59] presented relationship between velocity and thermal slip. Wu [60] derived a slip model for rarefied gas flows at arbitrary Knudsen number. Fang and Aziz [61] considered viscous flow with second-order slip velocity over a stretching sheet. Heat transfer enhancement using nanofluids in microchannels with slip and non-slip flow regimes has been investigated by Akbarinia et al. [62]. Mahmoud and Waheed [63] examined stretched flow of a micropolar fluid with heat generation (absorption) and slip velocity. Ibrahim

and Shankar [64] presented MHD boundary layer flow and heat transfer of a nanofluid past a permeable stretching sheet with velocity, thermal and solutal slip boundary condition. Khan et al. [65] analyzed hydrodynamic and thermal slip effect on double-diffusive free convective boundary layer flow of a nanofluid. Extension of a second order velocity slip/temperature jump boundary condition to simulate high speed micro/nanoflows has been given by Rooholghdos and Roohi [66]. Malvandi and Ganji [67] considered Brownian motion and thermophoresis - effects on slip flow of alumina/water nanofluid inside a circular microchannel. Second order slip flow of Cu-water nanofluid over a stretching sheet with heat transfer has been investigated by Sharma and Ishak [68]. Rashidi et al. [69] investigated entropy generation in MHD and slip flow over a rotating porous disk with variable properties. Karimipour et al. [70] analyzed the simulation of copper-water nanofluid in a microchannel with slip flow effect. Here the lattice Boltzman method is used for the simulation. Megahed [71] studied MHD Casson fluid flow and heat transfer with second-order slip velocity and thermal slip over a permeable stretching sheet. Hakeem et al. [72] presented magnetic field effect on second order slip flow of nanofluid over a radiative stretching/shrinking sheet.

Homogeneous-heterogeneous reactions occur in many chemically reacting systems such as in combustion, catalysis and biochemical systems. Some of the reactions have the ability to proceed very slowly or not at all, except in the presence of a catalyst. The interaction between the homogeneous and heterogeneous reactions is very complex. It is involved in the production and consumption of reactant species at different rates both within the fluid and on the catalytic surfaces. Especially chemical reaction effects are quite significant in food processing, hydrometallurgical industry, manufacturing of ceramics and polymer production, fog formation and dispersion, chemical processing equipment design, crops damage via freezing, cooling towers and temperature distribution and moisture over agricultural fields and groves of fruit trees. A model for isothermal homogeneous-heterogeneous reactions in boundary layer flow of viscous fluid past a flat plate is studied by Merkin [73]. He presented the homogeneous reaction by cubic autocatalysis and the heterogeneous reaction with a first order process. It is shown that the surface reaction is the dominant mechanism near the leading edge of the plate. Chaudhary and Merkin [74] studied the homogenous-heterogeneous reactions in boundary layer flow of viscous fluid. They found the numerical solution near the leading edge of a flat plate. Khan and

Pop [75] studied two-dimensional stagnation-point flow with homogeneous–heterogeneous reaction. Bachok et al. [76] focused on the stagnation-point flow towards a stretching sheet with homogeneous–heterogeneous reaction effects. Effects of homogeneous-heterogeneous reactions in the flow of viscoelastic fluid towards a stretching sheet are investigated by Khan and Pop [77]. Homogeneous-heterogeneous reactions in micropolar fluid flow from a permeable stretching or shrinking sheet in a porous medium have been studied by Shaw et al. [78]. Kameswaran et al. [79] extended the work of Khan and Pop [77] for nanofluid over a porous stretching sheet. Hayat et al. [80] analyzed homogeneous-heterogeneous reactions in the stagnation point flow of carbon nanotubes with Newtonian heating. Effect of homogeneous-heterogeneous reactions in flow of Powell-Eyring fluid is examined by Hayat et al. [81]. Abbasi et al. [82] investigated stagnation-point flow of viscous fluid over stretching/shrinking sheet in the presence of homogeneous–heterogeneous reactions.

1.2 Fundamental laws for Buongiorno’s model

1.2.1 Law of conservation of mass

In absence of sources or sinks we can write equation of continuity as

$$\frac{\partial \rho}{\partial t} + \nabla \cdot (\rho \mathbf{V}) = 0. \quad (1.1)$$

in which ρ is fluid density, t is time and \mathbf{V} is fluid velocity. The above equation for an incompressible fluid takes the form

$$\nabla \cdot \mathbf{V} = 0. \quad (1.2)$$

1.2.2 Law of conservation of linear momentum

Generalized equation of motion can be expressed as

$$\rho \frac{d\mathbf{V}}{dt} = -\nabla \cdot \boldsymbol{\tau} + \rho \mathbf{b}, \quad (1.3)$$

which the left hand side represents an inertial force, the first term on right hand side is the surface force and the second term on right hand side is body force. For an incompressible

viscous fluid $\boldsymbol{\tau} = -P\mathbf{I} + \mathbf{A}_1$ is the Cauchy stress tensor, P the pressure, \mathbf{I} the identity tensor, $\mathbf{A}_1 = \nabla\mathbf{V} + (\nabla\mathbf{V})^t$ the first Rivlin-Erickson tensor, \mathbf{b} the body force and d/dt the material time derivative.

1.2.3 Law of conservation of energy

The energy equation for a nanofluid can be written as

$$\rho c_p \frac{dT}{dt} = -\text{div} \bar{\mathbf{q}} + h_p \nabla \cdot \vec{\mathbf{j}}_p, \quad (1.4)$$

where c_p is specific heat of nanofluid, T is the temperature, h_p is the specific enthalpy for nanoparticles, $\bar{\mathbf{q}}$ is the energy flux and $\vec{\mathbf{j}}_p$ is the nanoparticles diffusion mass flux. Energy flux $\bar{\mathbf{q}}$ and nanoparticles diffusion mass flux $\vec{\mathbf{j}}_p$ are given by

$$\bar{\mathbf{q}} = -k\nabla T + h_p \vec{\mathbf{j}}_p, \quad (1.5)$$

$$\vec{\mathbf{j}}_p = -\rho_p D_B \nabla C - \rho_p D_T \frac{\nabla T}{T_\infty}, \quad (1.6)$$

in which k the thermal conductivity, ρ_p is the nanoparticle mass density, D_B the Brownian motion parameter, D_T the thermophoretic diffusion coefficient and C the nanoparticles volume fraction. So Eq. (1.4) takes the form

$$\rho c_p \frac{dT}{dt} = k\nabla^2 T + \rho_p c_p \left[D_B \nabla C \cdot \nabla T + D_T \frac{\nabla T \cdot \nabla T}{T_\infty} \right], \quad (1.7)$$

which is the energy equation for nanofluids.

1.2.4 Law of conservation of concentration

The concentration equation for nanofluids is

$$\frac{\partial C}{\partial t} + \mathbf{V} \cdot \nabla C = -\frac{1}{\rho_p} \nabla \cdot \vec{\mathbf{j}}_p, \quad (1.8)$$

After utilizing Eq. (1.6), we get

$$\frac{\partial C}{\partial t} + \mathbf{V} \cdot \nabla C = D_B \nabla^2 C + D_T \frac{\nabla^2 T}{T_\infty}, \quad (1.9)$$

which is the concentration equation for nanofluids.

1.3 Basic laws for phase flow model

1.3.1 Law of conservation of linear Momentum

Generalized equation of motion can be expressed as

$$\rho_{nf} \frac{d\mathbf{V}}{dt} = -\nabla \cdot \boldsymbol{\tau} + \rho_{nf} \mathbf{b}, \quad (1.10)$$

where the effective nanofluid density ρ_{nf} and the heat capacity $(\rho c_p)_{nf}$ is taken as follows [4]:

$$\rho_{nf} = \rho_f(1 - \phi) + \rho_s \phi, \quad (1.11)$$

$$(\rho c_p)_{nf} = (\rho c_p)_f(1 - \phi) + (\rho c_p)_s \phi. \quad (1.12)$$

The dynamic viscosity of nanofluid μ_{nf} given by Brinkmann is [98]:

$$\mu_{nf} = \frac{\mu_f}{(1 - \phi)^{2.5}}, \quad (1.13)$$

The effective thermal conductivity of nanofluid k_{nf} by Maxwell-Garnett model is given by [99]:

$$\frac{k_{nf}}{k_f} = \frac{k_s + 2k_f - 2\phi(k_f - k_s)}{k_s + 2k_f + \phi(k_f - k_s)}. \quad (1.14)$$

1.3.2 Law of conservation of Energy

The energy equation for a nanofluid can be written as

$$\rho c_p \frac{dT}{dt} = -\text{div} \bar{\mathbf{q}} + h_p \nabla \cdot \vec{\mathbf{j}}_p, \quad (1.15)$$

Here ϕ is the solid volume fraction, s in subscript is for nano-solid-particles and f in subscript is for base fluid.

1.4 Solution procedure

Flow equations occurring in the field of science and engineering are highly nonlinear in general. Therefore it is very difficult to find the exact solution of such equations. Usually perturbation, Adomian decomposition and homotopy perturbation methods are used to find the solution of nonlinear equations. But these methods have some drawback through involvement of large/small parameters in the equations and convergence. Homotopy analysis method (HAM) [83 – 97] is one while is independent of small/large parameters. This method also gives us a way to adjust and control the convergence region (i.e. by plotting h-curve). It also provides exemption to choose different sets of base functions. We have used this technique in the subsequent chapters to get the analytical solutions.

Chapter 2

MHD ⁵ flow of nanofluid over permeable ² stretching sheet with convective boundary conditions

This chapter addresses the magnetohydrodynamic (MHD) boundary layer ² flow of nanofluid. Flow is induced by a permeable stretching sheet. Convective type boundary conditions are employed in modeling the heat and mass transfer process. ² Appropriate transformations reduce the nonlinear partial differential equations to ordinary differential equations. The convergent series solutions are constructed. Graphical results of different parameters are discussed. ² The behaviors of Brownian motion and thermophoretic diffusion of nanoparticles have been examined. The dimensionless expressions of ¹¹ local Nusselt and local Sherwood numbers have been evaluated and discussed.

2.1 ¹ Problem formulation

We consider the two-dimensional flow of nanofluid bounded by a permeable stretching sheet. The x -axis is taken along the stretching surface in the direction of motion and y -axis is perpendicular to it. A uniform transverse magnetic field of strength B_0 is applied parallel to the y -axis. It is assumed that the effects of induced magnetic and electric fields are negligible. ⁵⁶ Salient features of Brownian motion and thermophoresis are present. The temperature T and

the nanoparticle fraction C at the surface have constant values T_w and C_w respectively. The ambient values of T and C attained as y tends to infinity are denoted by T_∞ and C_∞ respectively. The conservation of mass, momentum, energy and nanoparticles equations for nanofluids are:

$$\frac{\partial u}{\partial x} + \frac{\partial v}{\partial y} = 0, \quad (2.1)$$

$$u \frac{\partial u}{\partial x} + v \frac{\partial u}{\partial y} = \nu \frac{\partial^2 u}{\partial y^2} - \frac{\sigma B_0^2 u}{\rho}, \quad (2.2)$$

$$u \frac{\partial T}{\partial x} + v \frac{\partial T}{\partial y} = \alpha \frac{\partial^2 T}{\partial y^2} + \tau \left[D_B \frac{\partial C}{\partial y} \frac{\partial T}{\partial y} + \frac{D_T}{T_\infty} \left(\frac{\partial T}{\partial y} \right)^2 \right], \quad (2.3)$$

$$u \frac{\partial C}{\partial x} + v \frac{\partial C}{\partial y} = D_B \frac{\partial^2 C}{\partial y^2} + \frac{D_T}{T_\infty} \frac{\partial^2 T}{\partial y^2}, \quad (2.4)$$

where u and v are the velocity components along x and y - directions respectively, ν the kinematic viscosity, ρ the fluid density, σ the electrical conductivity of the base fluid, α the thermal diffusivity, $\tau = (\rho c)_p / (\rho c)_f$ is the ratio between the effective heat capacity of the nanoparticle material and heat capacity of the fluid, D_B is the Brownian diffusion coefficient and D_T is the thermophoretic diffusion coefficient.

The boundary conditions are prescribed as follows:

$$\begin{aligned} u = u_w(x) = cx, \quad v = V_w, \quad -k \frac{\partial T}{\partial y} = h(T_f - T), \quad -D_m \frac{\partial C}{\partial y} = k_m(C_f - C) \quad \text{at } y = 0, \\ u = 0, \quad T \rightarrow T_\infty, \quad C \rightarrow C_\infty \quad \text{as } y \rightarrow \infty, \end{aligned} \quad (2.5)$$

in which V_w is the wall mass transfer velocity, k is the thermal conductivity of fluid, h is the convective heat transfer coefficient, T_f is the heated fluid temperature, D_m is the molecular diffusivity of the species concentration, k_m is the wall mass transfer coefficient and C_f is the heated fluid concentration. Using the transformations

$$\eta = \sqrt{\frac{a}{\nu}} y, \quad u = ax f'(\eta), \quad v = -\sqrt{\nu a} f(\eta), \quad \theta(\eta) = \frac{T - T_\infty}{T_f - T_\infty}, \quad \Phi(\eta) = \frac{C - C_\infty}{C_f - C_\infty}, \quad (2.6)$$

equation (2.1) is satisfied automatically and Eqs. (2.2 – 2.5) take the following forms

$$f''' - f'^2 + f f'' - M f' = 0, \quad (2.7)$$

$$\frac{1}{\text{Pr}}\theta'' + f\theta' + N_b\Phi'\theta' + N_t\theta'^2 = 0, \quad (2.8)$$

$$\Phi'' + Scf\Phi' + \frac{N_t}{N_b}\theta'' = 0, \quad (2.9)$$

$$\begin{aligned} f(0) = S, \quad f'(0) = 1, \quad \theta'(0) = -\gamma_1[1 - \theta(0)], \quad \Phi'(0) = -\gamma_2[1 - \Phi(0)], \\ f'(\infty) = 0, \quad \theta(\infty) = 0, \quad \Phi(\infty) = 0, \end{aligned} \quad (2.10)$$

where prime indicates the differentiation with respect to η . Moreover the Hartman number M , the Prandtl number Pr , the Brownian motion parameter N_b , the thermophoresis parameter N_t , the Schmidt number Sc , the mass transfer parameter S with $S > 0$ for suction and $S < 0$ for injection, the thermal Biot number γ_1 and the concentration Biot number γ_2 are defined by the following definitions:

$$\begin{aligned} M &= \frac{\sigma B_0^2}{\rho c}, \quad \text{Pr} = \frac{\nu}{\alpha}, \quad N_b = \frac{(\rho c)_p D_B (C_f - C_\infty)}{(\rho c)_f \nu}, \quad N_t = \frac{(\rho c)_p D_T (T_f - T_\infty)}{(\rho c)_f T_\infty \nu}, \\ Sc &= \frac{\nu}{D_B}, \quad S = -\frac{V_w}{\sqrt{\nu c}}, \quad \gamma_1 = \frac{h}{k} \sqrt{\frac{\nu}{c}}, \quad \gamma_2 = \frac{k_m}{D_m} \sqrt{\frac{\nu}{c}}. \end{aligned} \quad (2.11)$$

The local Nusselt number Nu and Sherwood number Sh are

$$Nu = \frac{xq_w}{k(T_f - T_\infty)}; \quad q_w = -k \frac{\partial T}{\partial y} \Big|_{y=0}, \quad (2.12)$$

$$Sh = \frac{xq_m}{D_B(C_f - C_\infty)}; \quad q_m = -D \frac{\partial C}{\partial y} \Big|_{y=0}, \quad (2.13)$$

in which q_w and q_m denote the wall heat and mass fluxes respectively. In dimensionless form

$$Nu \text{Re}_x^{-1/2} = -\theta'(0), \quad Sh \text{Re}_x^{-1/2} = -\Phi'(0), \quad (2.14)$$

where $\text{Re}_x = u_w(x)x/\nu$ is the local Reynolds number.

2.2 Homotopic solutions

2.2.1 Zeroth-order deformation problems

We choose initial guesses $f_0(\eta)$, $\theta_0(\eta)$ and $\Phi_0(\eta)$ and linear operators \mathcal{L}_f , \mathcal{L}_θ and \mathcal{L}_Φ in the form

$$f_0(\eta) = S + 1 - \exp(-\eta), \quad (2.15)$$

$$\theta_0(\eta) = \frac{\gamma_1}{1 + \gamma_1} \exp(-\eta), \quad (2.16)$$

$$\Phi_0(\eta) = \frac{\gamma_2}{1 + \gamma_2} \exp(-\eta), \quad (2.17)$$

$$\mathcal{L}_f(f) = f''' - f', \quad (2.18)$$

$$\mathcal{L}_\theta(\theta) = \theta'' - \theta, \quad (2.19)$$

$$\mathcal{L}_\Phi(\Phi) = \Phi'' - \Phi, \quad (2.20)$$

together with the properties

$$\mathcal{L}_f [c_1 + c_2 \exp(\eta) + c_3 \exp(-\eta)] = 0, \quad (2.21)$$

$$\mathcal{L}_\theta [c_4 \exp(\eta) + c_5 \exp(-\eta)] = 0, \quad (2.22)$$

$$\mathcal{L}_\Phi [c_6 \exp(\eta) + c_7 \exp(-\eta)] = 0, \quad (2.23)$$

where $c_1 - c_7$ are the constants. If $p \in [0, 1]$ denotes an embedding parameter and \hbar_f , \hbar_θ and \hbar_Φ represent the non-zero auxiliary parameters then the zeroth order deformation problems are defined as follows:

$$(1 - p)\mathcal{L}_f [\hat{f}(\eta; p) - f_0(\eta)] = p\hbar_f \mathcal{N}_f[\hat{f}(\eta; p)], \quad (2.24)$$

$$(1 - p)\mathcal{L}_\theta [\hat{\theta}(\eta; p) - \theta_0(\eta)] = p\hbar_\theta \mathcal{N}_\theta[\hat{\theta}(\eta; p), \hat{f}(\eta; p), \hat{\Phi}(\eta; p)], \quad (2.25)$$

$$(1 - p)\mathcal{L}_\Phi [\hat{\Phi}(\eta; p) - \Phi_0(\eta)] = p\hbar_\Phi \mathcal{N}_\Phi[\hat{\Phi}(\eta; p), \hat{f}(\eta; p), \hat{\theta}(\eta; p)], \quad (2.26)$$

$$\hat{f}(0; p) = S, \quad \hat{f}'(0; p) = 1, \quad \hat{f}'(\infty; p) = 0,$$

$$\hat{\theta}'(0; p) = -\gamma_1[1 - \hat{\theta}(0; p)], \quad \hat{\theta}(\infty; p) = 0,$$

$$\hat{\Phi}'(0; p) = -\gamma_2[1 - \hat{\Phi}(0; p)], \quad \hat{\Phi}(\infty; p) = 0, \quad (2.27)$$

where \mathcal{N}_f , \mathcal{N}_θ and \mathcal{N}_Φ are the nonlinear operators defined in the forms:

$$\mathcal{N}_f[\hat{f}(\eta; p)] = \frac{\partial^3 \hat{f}(\eta; p)}{\partial \eta^3} + \hat{f}(\eta; p) \frac{\partial^2 \hat{f}(\eta; p)}{\partial \eta^2} - \left(\frac{\partial \hat{f}(\eta; p)}{\partial \eta} \right)^2 - M \frac{\partial \hat{f}(\eta; p)}{\partial \eta}, \quad (2.28)$$

$$\begin{aligned} \mathcal{N}_\theta[\hat{\theta}(\eta; p), \hat{f}(\eta; p), \hat{\Phi}(\eta; p)] &= \frac{1}{\text{Pr}} \frac{\partial^2 \hat{\theta}(\eta; p)}{\partial \eta^2} + \hat{f}(\eta; p) \frac{\partial \hat{\theta}(\eta; p)}{\partial \eta} + N_t \left(\frac{\partial \hat{\theta}(\eta; p)}{\partial \eta} \right)^2 \\ &\quad + N_b \frac{\partial \hat{\Phi}(\eta; p)}{\partial \eta} \frac{\partial \hat{\theta}(\eta; p)}{\partial \eta}, \end{aligned} \quad (2.29)$$

$$\mathcal{N}_\Phi[\hat{\Phi}(\eta; p), \hat{f}(\eta; p), \hat{\theta}(\eta; p)] = \frac{\partial^2 \hat{\Phi}(\eta; p)}{\partial \eta^2} + S_c \hat{f}(\eta; p) \frac{\partial \hat{\Phi}(\eta; p)}{\partial \eta} + \frac{N_t}{N_b} \frac{\partial^2 \hat{\theta}(\eta; p)}{\partial \eta^2}. \quad (2.30)$$

For $p = 0$ and $p = 1$ we have

$$\begin{aligned} \hat{f}(\eta; 0) &= f_0(\eta), \quad \hat{f}(\eta; 1) = f(\eta), \\ \hat{\theta}(\eta; 0) &= \theta_0(\eta), \quad \hat{\theta}(\eta; 1) = \theta(\eta), \\ \hat{\Phi}(\eta; 0) &= \Phi_0(\eta), \quad \hat{\Phi}(\eta; 1) = \Phi(\eta). \end{aligned} \quad (2.31)$$

Note that $f_0(\eta)$, $\theta_0(\eta)$ and $\Phi_0(\eta)$ approach $f(\eta)$, $\theta(\eta)$ and $\Phi(\eta)$ respectively, when p has variation from 0 to 1. According to Taylor series we have

$$\begin{aligned} \hat{f}(\eta; p) &= f_0(\eta) + \sum_{m=1}^{\infty} f_m(\eta) p^m, \quad f_m(\eta) = \frac{1}{m!} \left. \frac{\partial^m \hat{f}(\eta; p)}{\partial p^m} \right|_{p=0}, \\ \hat{\theta}(\eta; p) &= \theta_0(\eta) + \sum_{m=1}^{\infty} \theta_m(\eta) p^m, \quad \theta_m(\eta) = \frac{1}{m!} \left. \frac{\partial^m \hat{\theta}(\eta; p)}{\partial p^m} \right|_{p=0}, \\ \hat{\Phi}(\eta; p) &= \Phi_0(\eta) + \sum_{m=1}^{\infty} \Phi_m(\eta) p^m, \quad \Phi_m(\eta) = \frac{1}{m!} \left. \frac{\partial^m \hat{\Phi}(\eta; p)}{\partial p^m} \right|_{p=0}, \end{aligned} \quad (2.32)$$

where the convergence depends upon \hbar_f , \hbar_θ and \hbar_Φ . By proper choice of \hbar_f , \hbar_θ and \hbar_Φ the series (2.32) converge for $p = 1$ and so

$$\begin{aligned} f(\eta) &= f_0(\eta) + \sum_{m=1}^{\infty} f_m(\eta), \\ \theta(\eta) &= \theta_0(\eta) + \sum_{m=1}^{\infty} \theta_m(\eta), \\ \Phi(\eta) &= \Phi_0(\eta) + \sum_{m=1}^{\infty} \Phi_m(\eta). \end{aligned} \quad (2.33)$$

2.2.2 m^{th} order deformation problems

m^{th} order deformation problems are given by

$$\mathcal{L}_f [f_m(\eta) - \chi_m f_{m-1}(\eta)] = \hbar_f \mathcal{R}_{f,m}(\eta), \quad (2.34)$$

$$\mathcal{L}_\theta [\theta_m(\eta) - \chi_m \theta_{m-1}(\eta)] = \hbar_\theta \mathcal{R}_{\theta,m}(\eta), \quad (2.35)$$

$$\mathcal{L}_\Phi [\Phi_m(\eta) - \chi_m \Phi_{m-1}(\eta)] = \hbar_\Phi \mathcal{R}_{\Phi,m}(\eta), \quad (2.36)$$

$$f_m(0) = f'_m(0) = f'_m(\infty) = \theta'_m(0) - \gamma_1 \theta_m(0) = \theta_m(\infty) = \Phi'_m(0) - \gamma_2 \Phi_m(0) = \Phi_m(\infty) = 0, \quad (2.37)$$

$$\chi_m = \begin{cases} 0, & m \leq 1 \\ 1, & m > 1 \end{cases}, \quad (2.38)$$

$$\mathcal{R}_{f,m}(\eta) = f'''_{m-1} + \sum_{k=0}^{m-1} (f_{m-1-k} f''_k - f'_{m-1-k} f'_k) - M f'_{m-1}, \quad (2.39)$$

$$\mathcal{R}_{\theta,m}(\eta) = \frac{1}{\Gamma} \theta''_{m-1} + \sum_{k=0}^{m-1} (\theta'_{m-1-k} f_k + N_b \Phi_{m-1-k} \theta'_k + N_t \theta'_{m-1-k} \theta'_k), \quad (2.40)$$

$$\mathcal{R}_{\Phi,m}(\eta) = \Phi''_{m-1} + S c \sum_{k=0}^{m-1} \Phi'_{m-1-k} f_k + \frac{N_t}{N_b} \theta''_{m-1}, \quad (2.41)$$

The general solutions can be expressed as follows:

$$f_m(\eta) = f_m^*(\eta) + c_1 + c_2 e^\eta + c_3 e^{-\eta}, \quad (2.42)$$

$$\theta_m(\eta) = \theta_m^*(\eta) + c_4 e^\eta + c_5 e^{-\eta}, \quad (2.43)$$

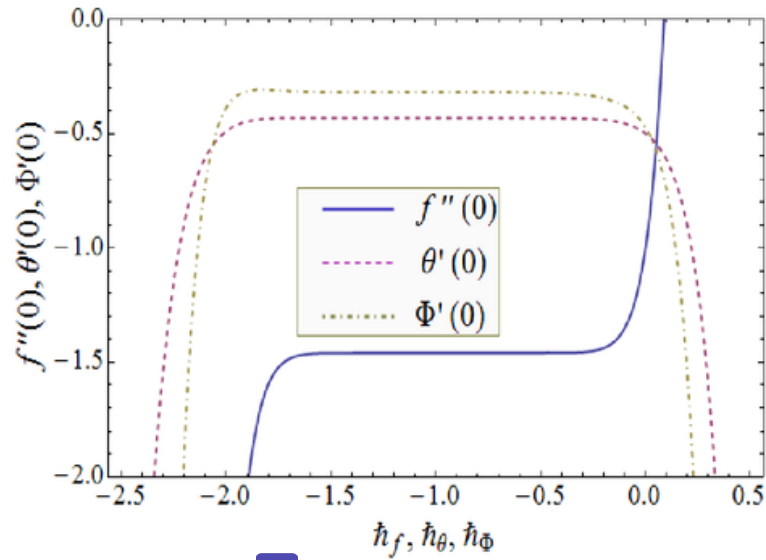
$$\Phi_m(\eta) = \Phi_m^*(\eta) + c_6 e^\eta + c_7 e^{-\eta}, \quad (2.44)$$

in which f_m^* , θ_m^* and Φ_m^* denote the particular solutions and constants c_i ($i = 1 - 7$) can be determined by the boundary conditions (2.37). They are given by

$$\begin{aligned} c_3 &= \left. \frac{\partial f^*(\eta)}{\partial \eta} \right|_{\eta=0}, \quad c_1 = -c_3 - f^*(0), \quad c_5 = \frac{1}{1 + \gamma_1} \left[\left. \frac{\partial \theta^*(\eta)}{\partial \eta} \right|_{\eta=0} - \gamma_1 \theta^*(0) \right], \\ c_2 &= c_4 = c_6 = 0, \quad c_7 = \frac{1}{1 + \gamma_2} \left[\left. \frac{\partial \Phi^*(\eta)}{\partial \eta} \right|_{\eta=0} - \gamma_2 \Phi^*(0) \right]. \end{aligned} \quad (2.45)$$

2.3 Analysis of series solutions

The solution of problems consisting of Eqs. (2.7) – (2.10) is computed employing homotopy analysis method. The convergence region and rate of approximations for the functions f , θ and Φ can be controlled and adjusted through the auxiliary parameters \hbar_f , \hbar_θ and \hbar_Φ . The \hbar -curves are sketched at 14th-order of approximations to obtain valid ranges of these parameters (see Fig. 2.1). Permissible values of the auxiliary parameters are $-1.5 \leq \hbar_f \leq -0.4$, $-1.5 \leq \hbar_\theta \leq -0.5$ and $-1.4 \leq \hbar_\Phi \leq -0.7$. Further, the series solutions converge in the whole region of η ($0 < \eta < \infty$) when $\hbar_f = \hbar_\theta = \hbar_\Phi = -1.2$. Table 2.1 displays the convergence of homotopy solutions for different orders of approximations.



11

Fig. 2.1: h -curves for velocity, temperature and concentration fields.

Table 2.1: Convergence of HAM solutions for different order of approximations when $M = N_b = 0.4$, $N_t = 0.3$, $Sc = Pr = \gamma_1 = 1$, $S = 0.5$ and $\gamma_2 = 0.9$.

Order of approximations	$-f''(0)$	$-\theta'(0)$	$-\Phi'(0)$
1	1.54000	0.441053	0.344668
5	1.45883	0.431349	0.319776
10	1.45934	0.430920	0.318765
15	1.45934	0.430912	0.318750
20	1.45934	0.430912	0.318750
25	1.45934	0.430912	0.318750
30	1.45934	0.430912	0.318750
35	1.45934	0.430912	0.318750
40	1.45934	0.430912	0.318750
50	1.45934	0.430912	0.318750
60	1.45934	0.430912	0.318750

2.4 Results and discussion

In this section, the effects of various involved parameters on the velocity, temperature and concentration profiles are discussed. Figs. (2.2 – 2.3) are plotted to show the effects of Hartman number M and mass transfer parameter S on the velocity profile f' . Fig. 2.2 shows the effects of M on f' . Application of magnetic field has the tendency to slow down the movement of the fluid particles and consequently the velocity decreases. Fig. 2.3 displays the effect of S on f' . In this Fig. the velocity field f' decreases when S increases. In fact applying suction leads to draw the amount of fluid particles into the wall and hence the velocity boundary layer decreases.

Effects of the Brownian motion parameter N_b , thermophoresis parameter N_t , Schmidt number Sc , Prandtl number Pr , Hartman number M , mass transfer parameter S , thermal Biot number γ_1 and concentration Biot number γ_2 on the temperature profile θ and the concentration profile ϕ are shown in the Figs. (2.4 – 2.18). It is noted that an increase in the Brownian motion parameter N_b , thermophoresis parameter N_t and Schmidt number Sc increase the temperature profile θ as shown in Figs. (2.4 – 2.6). The effects of Prandtl number Pr on the temperature profile are depicted in Fig. 2.7. This graph shows that the temperature profile θ decreases when Pr increases. In fact the thermal diffusivity decreases by increasing Pr and thus the heat diffused away slowly from the heated surface. Fig. 2.8 illustrates the effects of Hartman number M on temperature profile θ . The Lorentz force is a resistive force which opposes the fluid motion. As a sequence the heat is produced and thus thermal boundary layer thickness increases. Further, the temperature profile θ decreases when S is increased (see Fig. 2.9). Also the temperature profile θ increases when the thermal Biot number γ_1 increases (see Fig. 2.10). Fig. 2.11 illustrates the effects of N_b on Φ . The concentration profile Φ decreases by increasing the Brownian motion parameter N_b . Influence of N_t on Φ can be seen in Fig. 2.12. There is an increase in Φ when N_t is increased. Figs. (2.13 – 2.16) display the effects of Sc , Pr , M and S on the concentration profile Φ . It is observed that concentration profile Φ decreases by increasing these parameters. It is observed from Fig. 2.17 that the mass fraction field increases when thermal Biot number γ_1 is increased. Also the concentration profile increases by increasing concentration Biot number γ_2 as depicted in Fig. 2.18.

Numerical values of local Nusselt number and local Sherwood number for different emerging parameters are presented in Table 2. It is noticed that local Nusselt number $Nu(Re_x)^{-\frac{1}{2}}$

decreases for larger values of D_f , N_b and N_t . However it increases for larger values of S_r and Pr . The magnitude of local Sherwood number $Sh(Re_x)^{-1/2}$ decreases for larger values of S_r , Pr and N_t however it increases for larger values of D_f and N_b .

Figs. 2.19 and 2.20 describe the variations of the Nusselt number $Nu(Re_x)^{-1/2}$ for Brownian motion parameter N_b , thermophoresis parameter N_t and Schmidt number Sc . It is noticed that heat transfer rate decreases as N_b and N_t increase for Sc . Fig. 2.21 shows the effects of thermal Biot number γ_1 and mass transfer parameter S on the Nusselt number $Nu(Re_x)^{-1/2}$. In this figure, heat transfer rate increases as γ_1 increases for S . Figs. 2.22 and 2.23 illustrate the variation in dimensionless mass transfer rate $Sh(Re_x)^{-1/2}$ vs Brownian motion parameter N_b and thermophoresis parameter N_t . Here the mass transfer rate increases with an increase in N_b and decreases with an increase in N_t . Effects of concentration Biot number γ_2 and mass transfer parameter S on the Sherwood number $Sh(Re_x)^{-1/2}$ are displayed in Fig. 2.24. It is noted that mass transfer rate increases for higher γ_2 .

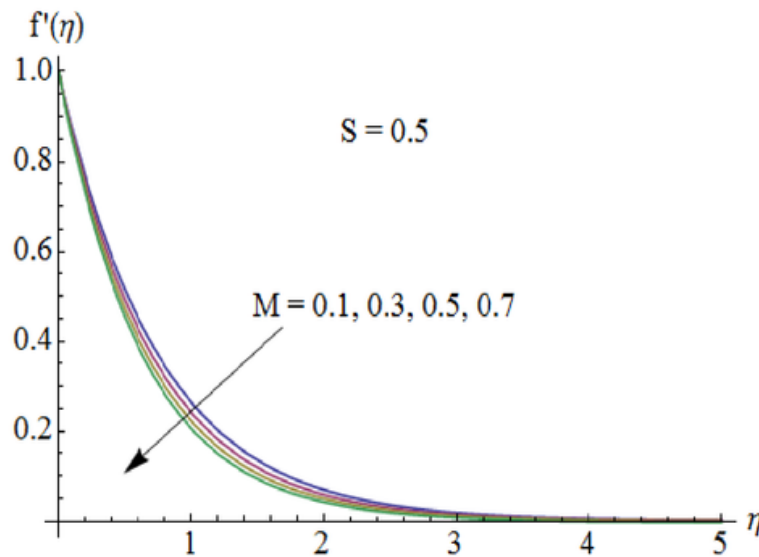
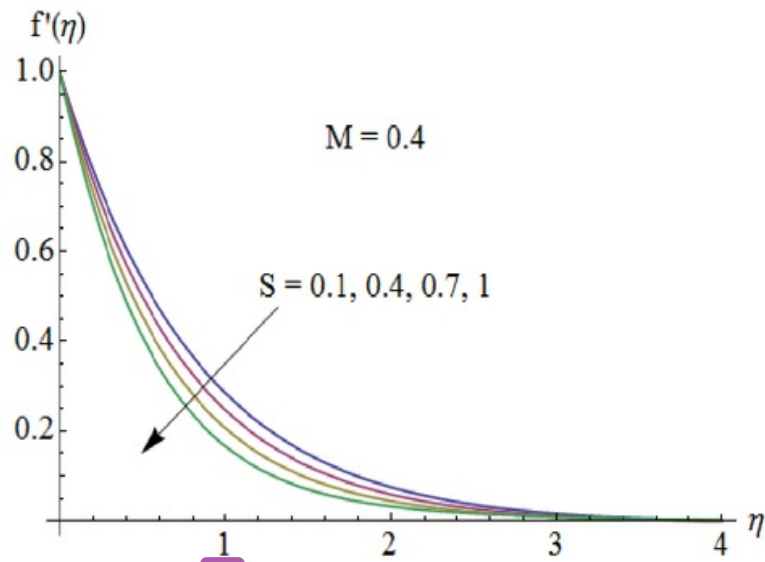


Fig. 2.2: Influence of M on $f'(\eta)$.



45

Fig. 2.3: Influence of S on $f'(\eta)$.

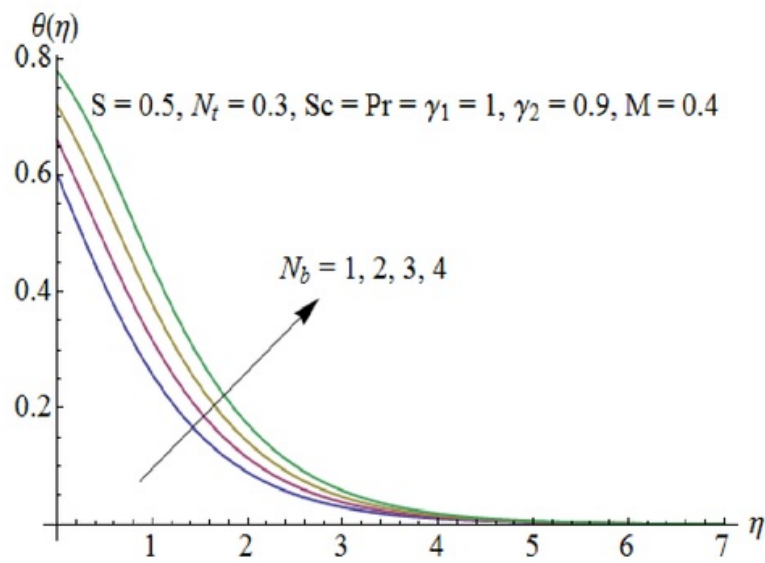
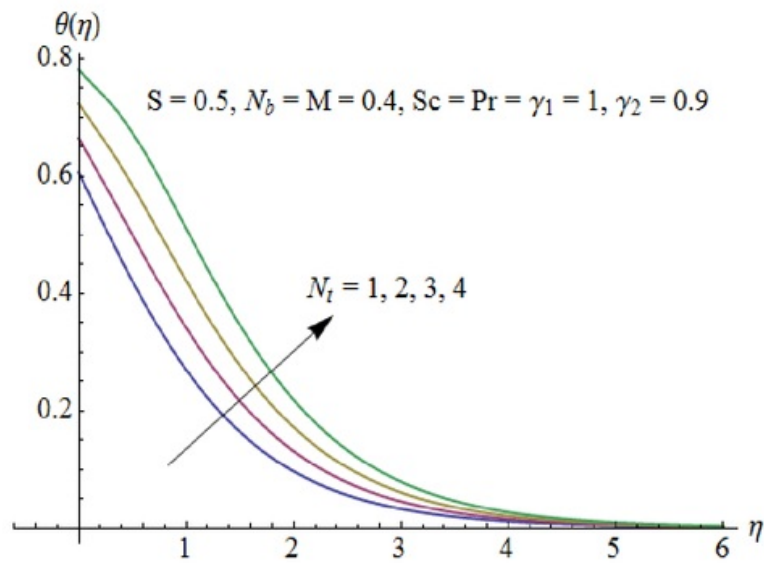


Fig. 2.4: Influence of N_b on $\theta(\eta)$.



23
 Fig. 2.5: Influence of N_t on $\theta(\eta)$.

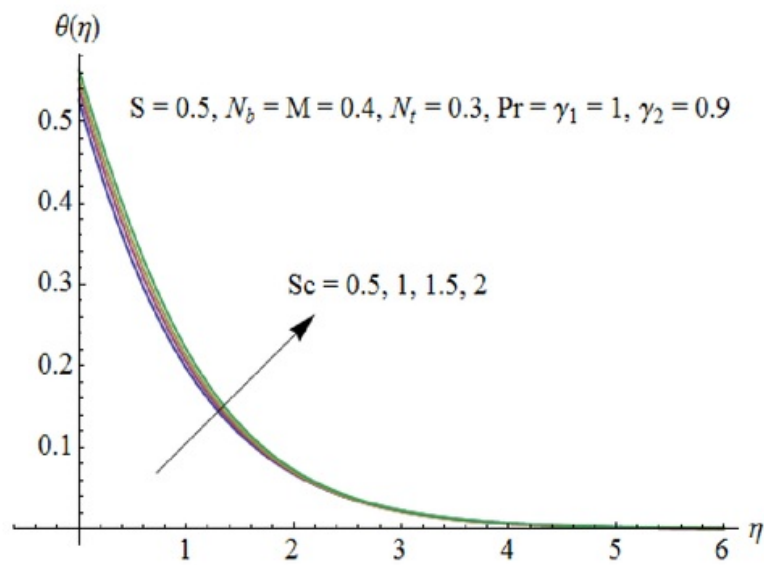


Fig. 2.6: Influence of Sc on $\theta(\eta)$.

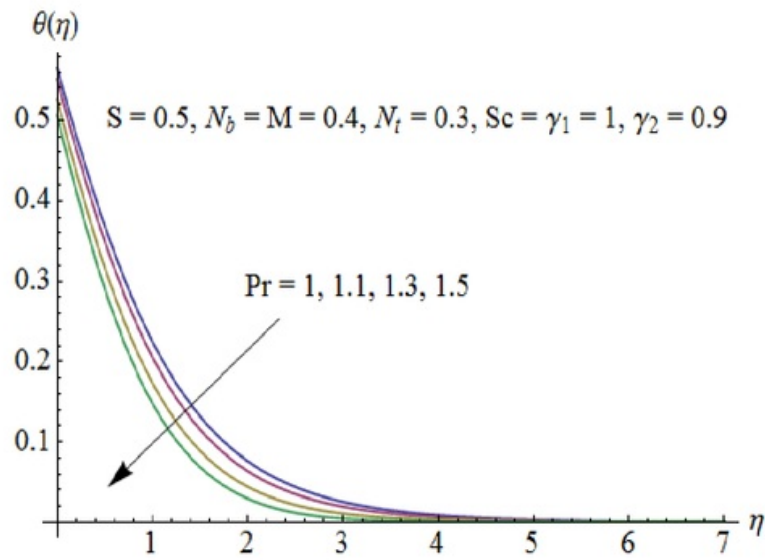


Fig. 2.7: Influence of Pr on $\theta(\eta)$.

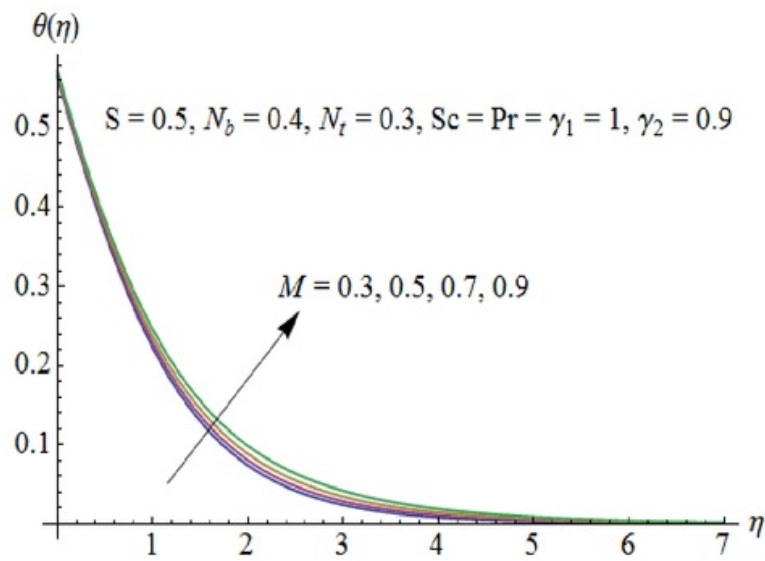


Fig. 2.8: Influence of M on $\theta(\eta)$.

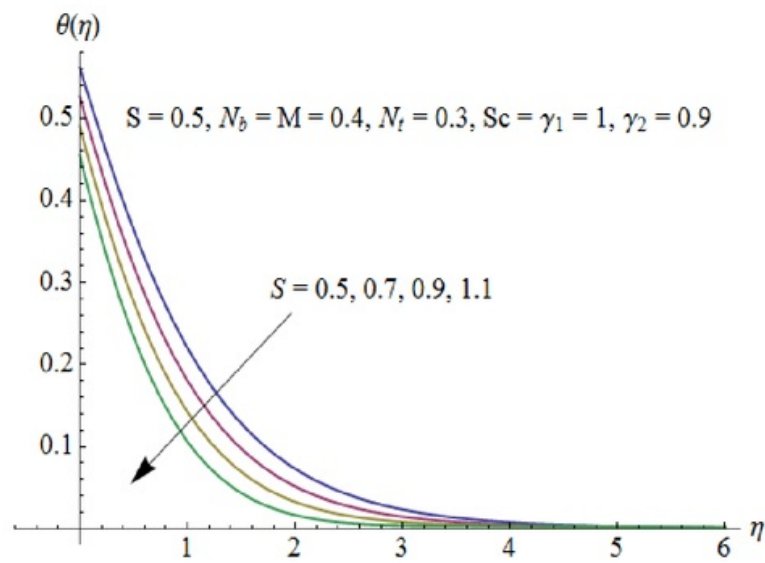


Fig. 2.9: Influence of S on $\theta(\eta)$.

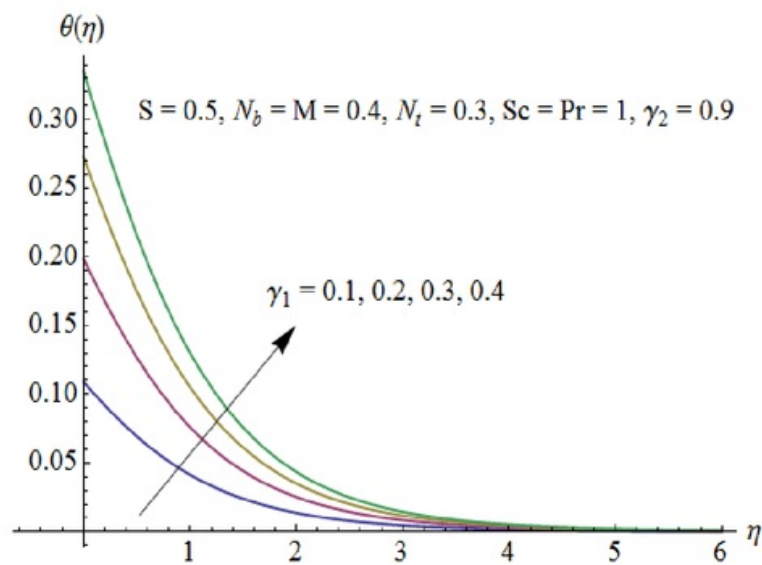


Fig. 2.10: Influence of γ_1 on $\theta(\eta)$.

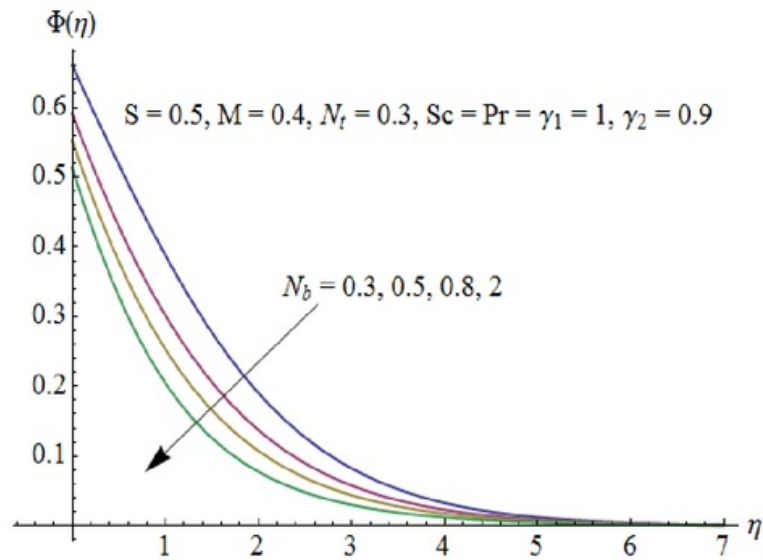


Fig. 2.11: Influence of N_b on $\Phi(\eta)$.

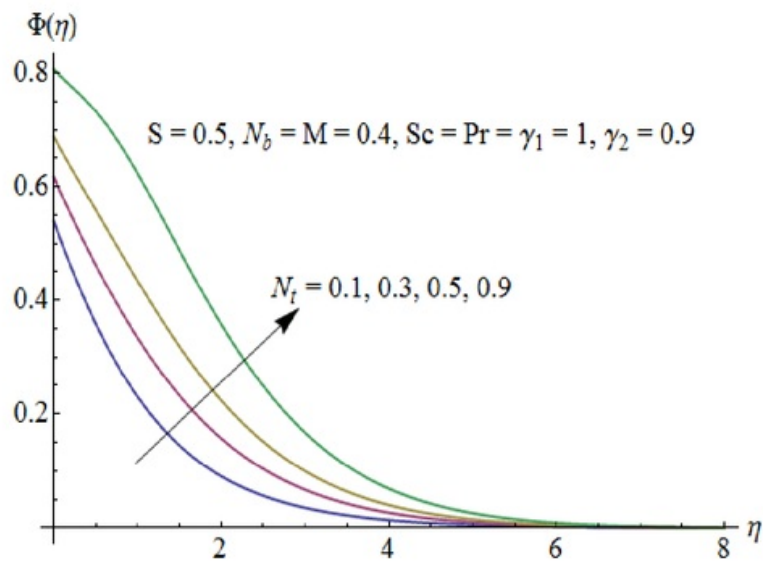
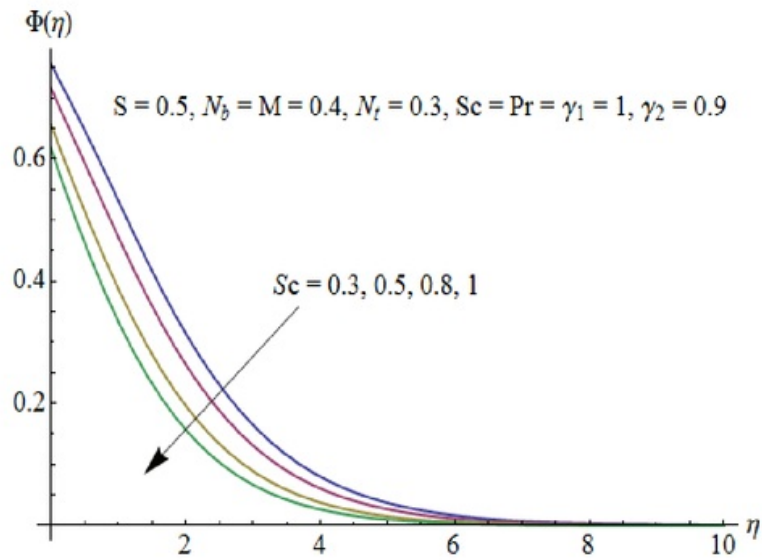


Fig. 2.12: Influence of N_t on $\Phi(\eta)$.



6
 Fig. 2.13: Influence of Sc on $\Phi(\eta)$.

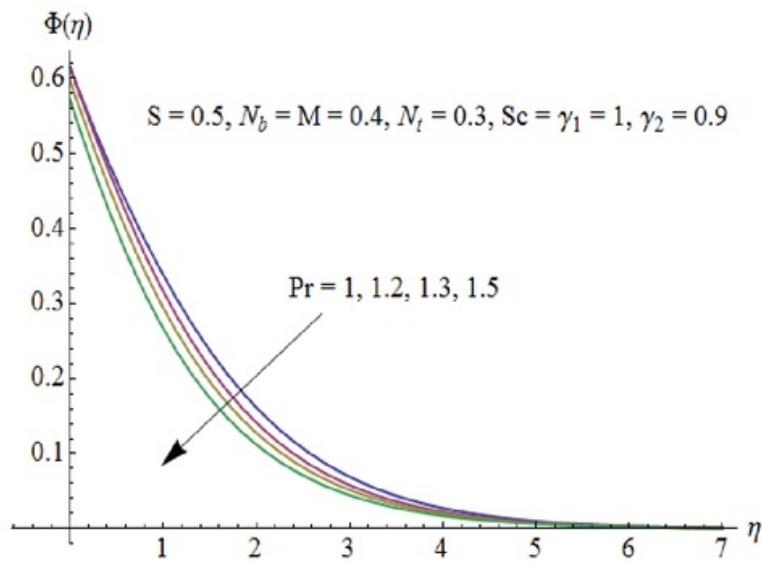


Fig. 2.14: Influence of Pr on $\Phi(\eta)$.

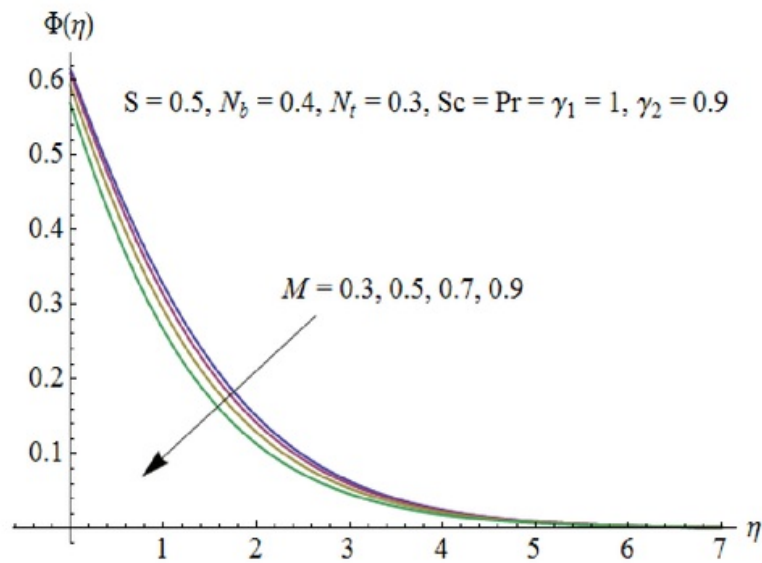


Fig. 2.15: Influence of M on $\Phi(\eta)$.

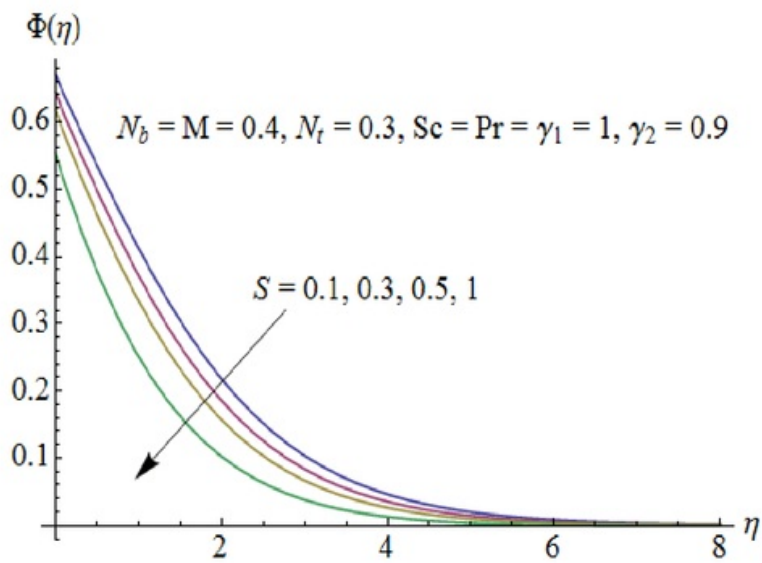


Fig. 2.16: Influence of S on $\Phi(\eta)$.

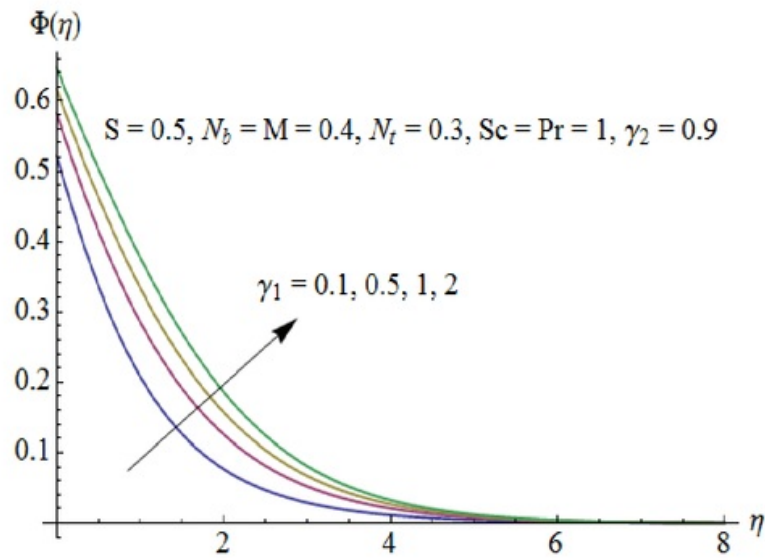


Fig. 2.17: Influence of γ_1 on $\Phi(\eta)$.

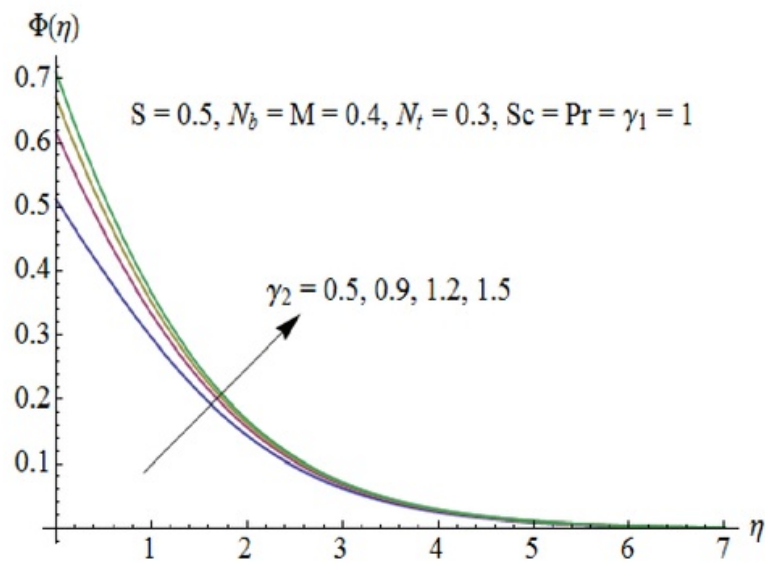


Fig. 2.18: Influence of γ_2 on $\Phi(\eta)$.

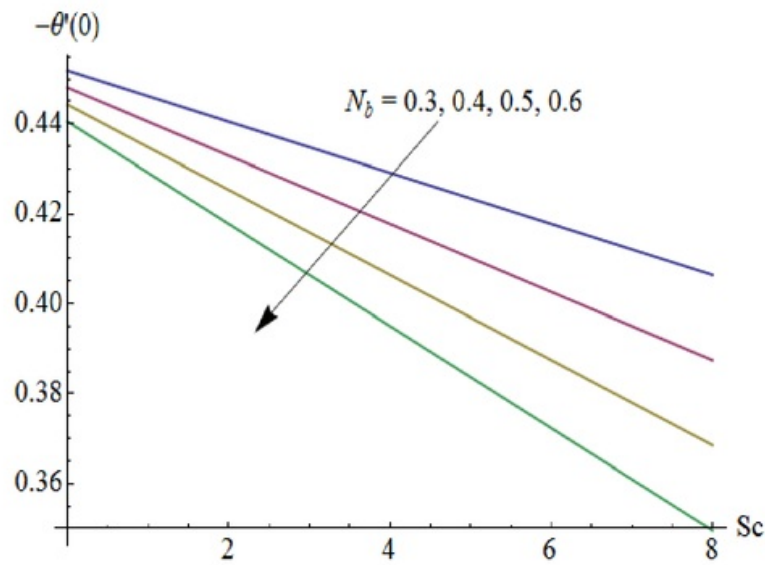


Fig. 2.19: Influence of N_b and Sc on $-\theta'(0)$.

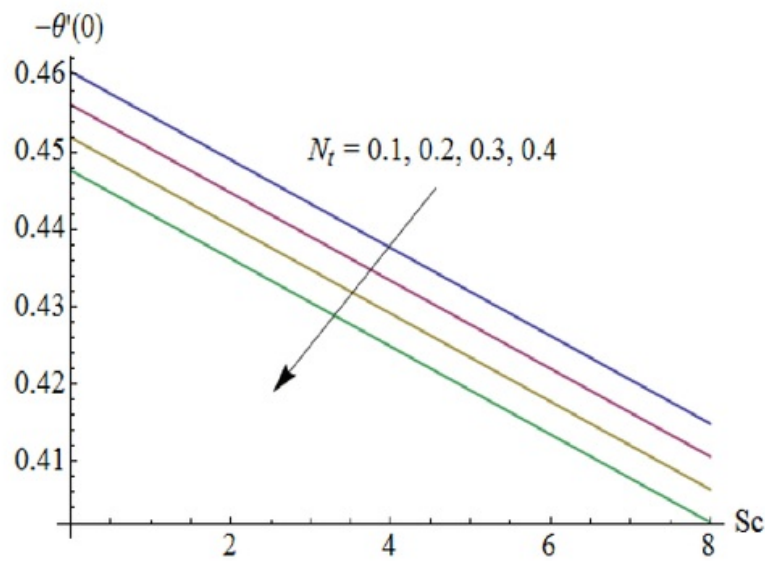


Fig. 2.20: Influence of N_t and Sc on $-\theta'(0)$.

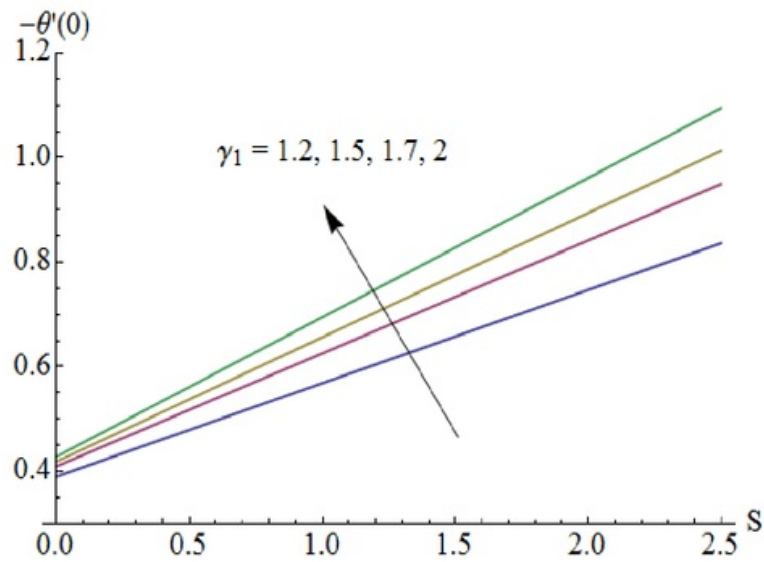


Fig. 2.21: Influence of γ_1 and S on $-\theta'(0)$.

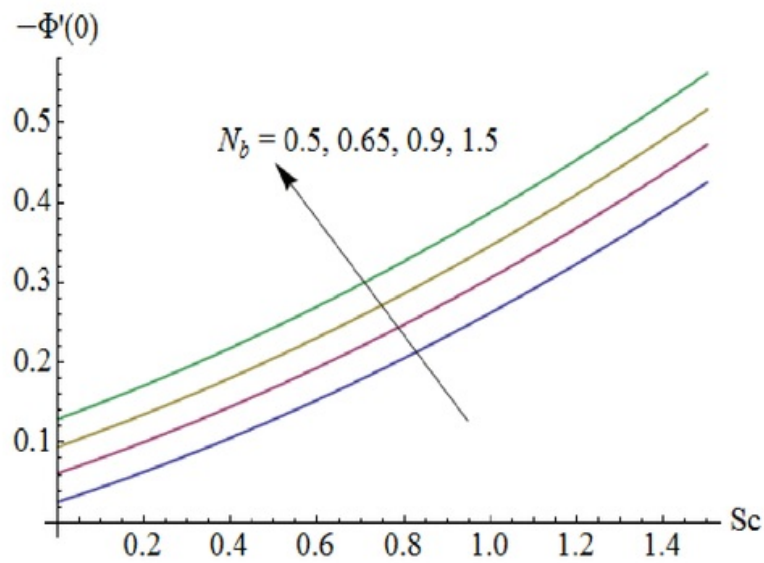


Fig. 2.22: Influence of N_b and Sc on $-\Phi'(0)$.

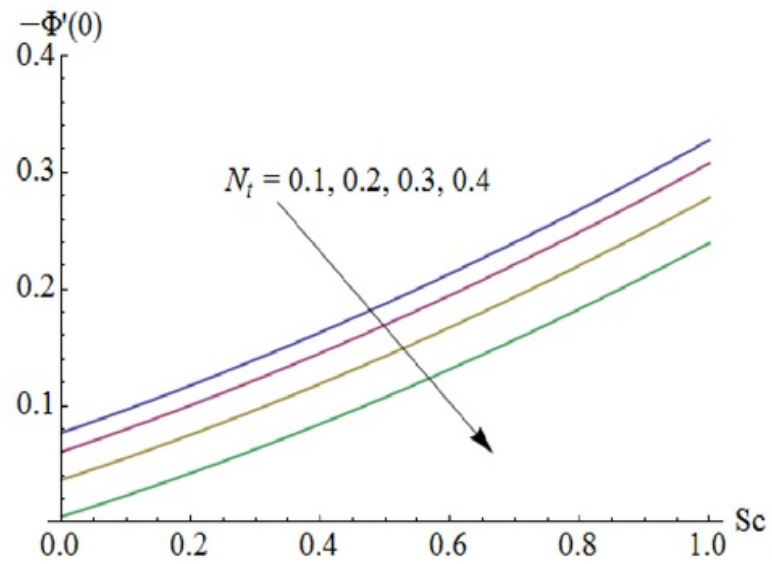


Fig. 2.23: Influence of N_t and Sc on $-\Phi'(0)$.

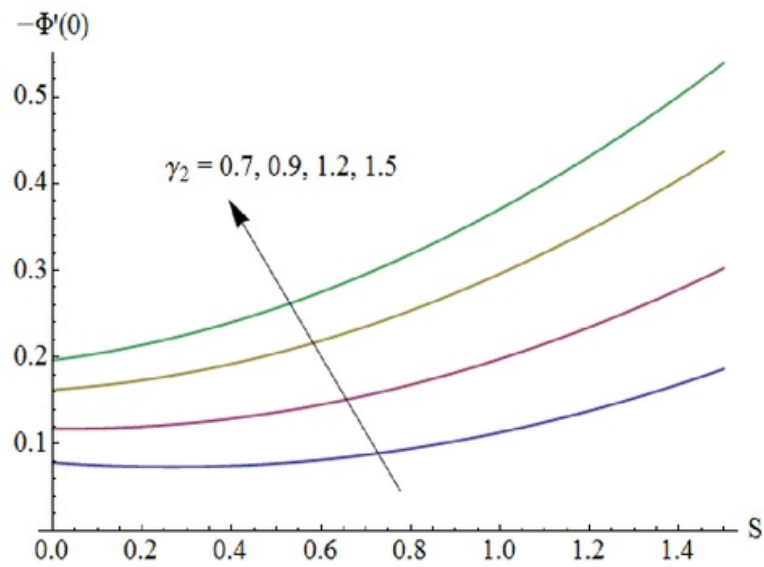


Fig. 2.24: Influence of γ_2 and S on $-\Phi'(0)$.

2.5 Main points

The flow of nanofluid generated by a permeable stretching sheet is studied. Effects of different parameters on the velocity, temperature and concentration distributions are explored. The following observations are worth mentioning.

- The effects of Hartman number and mass transfer parameter are similar on the velocity profile.
- Increase in Brownian motion parameter, thermophoresis parameter, Schmidt number, Hartman number and thermal Biot number enhances the temperature profile.
- There is enhancement of concentration for increasing thermophoresis parameter, thermal and concentration Biot numbers.
- Local Nusselt number increases by larger thermal Biot number.
- Local Sherwood number increases by increasing Brownian motion parameter and concentration Biot number.

Chapter 3

4 MHD flow of nanofluids over an exponentially stretching sheet in a porous medium with convective boundary conditions

This chapter ⁴ concentrates on the steady magnetohydrodynamic (MHD) flow of viscous nanofluid. The flow is caused by a permeable exponentially stretching surface. An incompressible fluid fills the porous space. A comparative study is made for the nanoparticles namely Copper (Cu), Silver (Ag), Alumina (Al_2O_3) and Titanium Oxide (TiO_2). Water is treated as a base fluid. Convective type boundary conditions are employed in modeling the heat transfer process. The non-linear partial differential equations governing the flow are reduced to an ordinary differential equation by similarity transformations. The obtained equations are then solved for the development of series solutions. Convergence of the obtained series solutions is explicitly discussed. Effects of different parameters on the velocity and temperature profiles are shown and analyzed through graphs.

3.1 Mathematical formulation

Here we investigate the steady two-dimensional flow of an incompressible nanofluid induced by an exponentially stretching surface in a porous medium with permeability K . The x -axis is taken along the stretching surface in the direction of motion and y -axis is perpendicular to it.

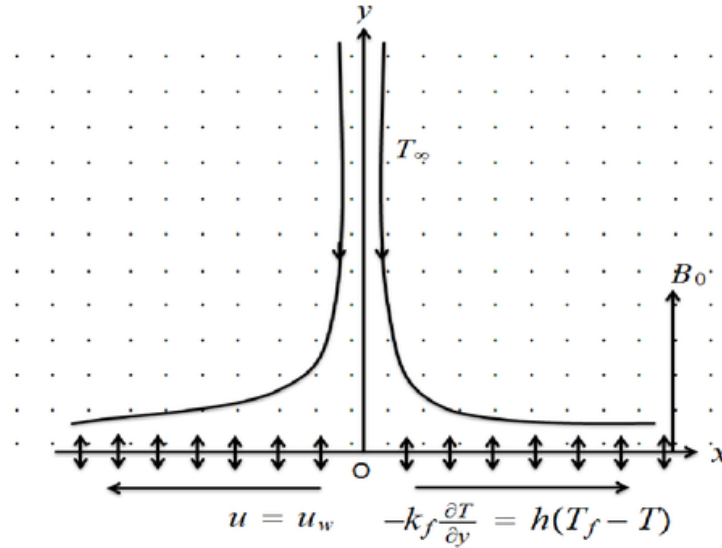


Fig. 3.1: Geometry of the problem.

A uniform transverse magnetic field of strength B_0 is applied parallel to the y -axis. It is assumed that the induced magnetic field and the electric field effects are negligible. Further, the surface exhibits convective type boundary conditions (see Fig. 3.1). The boundary layer flow in the present analysis is governed by the following equations:

$$\frac{\partial u}{\partial x} + \frac{\partial v}{\partial y} = 0, \quad (3.1)$$

$$\rho_{nf} \left(u \frac{\partial u}{\partial x} + v \frac{\partial u}{\partial y} \right) = \mu_{nf} \frac{\partial^2 u}{\partial y^2} - \frac{\mu_{nf}}{K} u - \sigma_{nf} B_0^2 u, \quad (3.2)$$

$$u \frac{\partial T}{\partial x} + v \frac{\partial T}{\partial y} = \frac{k_{nf}}{(\rho c_p)_{nf}} \frac{\partial^2 T}{\partial y^2}, \quad (3.3)$$

5

where u and v are the velocity components along the x - and y - directions respectively. The effective nanofluid density ρ_{nf} and heat capacity $(\rho c_p)_{nf}$ are taken as follows [4]:

$$\rho_{nf} = \rho_f(1 - \phi) + \rho_s\phi, \quad (3.4)$$

$$(\rho c_p)_{nf} = (\rho c_p)_f(1 - \phi) + (\rho c_p)_s\phi. \quad (3.5)$$

7

The dynamic viscosity of nanofluid μ_{nf} given by Brinkmann is [98]:

$$\mu_{nf} = \frac{\mu_f}{(1 - \phi)^{2.5}}, \quad (3.6)$$

The effective thermal conductivity of nanofluid k_{nf} by Maxwell-Garnett model is given by [99]:

$$\frac{k_{nf}}{k_f} = \frac{k_s + 2k_f - 2\phi(k_f - k_s)}{k_s + 2k_f + \phi(k_f - k_s)}. \quad (3.7)$$

and the electric conductivity σ_{nf} of nanofluid is [100]:

$$\frac{\sigma_{nf}}{\sigma_f} = 1 + \frac{3 \left(\frac{\sigma_s}{\sigma_f} - 1 \right) \phi}{\left(\frac{\sigma_s}{\sigma_f} + 2 \right) - \left(\frac{\sigma_s}{\sigma_f} - 1 \right) \phi}. \quad (3.8)$$

Here ϕ is the solid volume fraction, s in subscript is for nano-solid-particles and f in subscript is for base fluid. The subjected boundary conditions are

$$\begin{aligned} u &= u_w = U_0 e^{\frac{x}{L}}, \quad v = V_w, \quad -k_f \frac{\partial T}{\partial y} = h(T_f - T) \quad \text{at } y = 0, \\ u &\rightarrow 0, \quad T \rightarrow T_\infty, \quad \text{as } y \rightarrow \infty. \end{aligned} \quad (3.9)$$

Introducing

$$\eta = y \sqrt{\frac{U_0}{2\nu_f L}} e^{\frac{x}{2L}}, \quad u = U_0 e^{\frac{x}{L}} f'(\eta), \quad v = -\sqrt{\frac{\nu_f U_0}{2L}} e^{\frac{x}{2L}} [f(\eta) + \eta f'(\eta)], \quad \theta(\eta) = \frac{T - T_\infty}{T_f - T_\infty}. \quad (3.10)$$

Eq. (3.1) is satisfied automatically and Eqs. (3.2), (3.3) and (3.9) after using Eq. (3.10) can be reduced as follows:

$$\varepsilon_1 f''' + f f'' - 2f'^2 - \lambda \varepsilon_1 f' - (1 - \phi)^{2.5} M \varepsilon_1 \frac{\sigma_{nf}}{\sigma_f} f' = 0, \quad (3.11)$$

$$\frac{1}{\text{Pr}} \frac{k_{nf}}{k_f} \theta'' + \left((1 - \phi) + \frac{(\rho c_p)_s}{(\rho c_p)_f} \phi \right) f \theta' = 0, \quad (3.12)$$

$$\begin{aligned} f'(0) &= 1, \quad f(0) = S, \quad \theta'(0) = -\gamma_1 [1 - \theta(0)], \\ f'(\infty) &= 0, \quad \theta(\infty) = 0, \end{aligned} \quad (3.13)$$

in which ε_1 indicates the differentiation with respect to η and the value of ε_1 is

$$\varepsilon_1 = \frac{1}{\left((1 - \phi) + \frac{\rho_s}{\rho_f} \phi \right) (1 - \phi)^{2.5}}. \quad (3.14)$$

Moreover the porosity parameter λ , the Hartman number M , the Prandtl number Pr , the mass transfer parameter S with $S > 0$ for suction and $S < 0$ for injection and the thermal Biot number γ_1 are defined as follows:

$$\lambda = \frac{2\nu_f L}{KU_0} e^{-\frac{x}{L}}, \quad M = \frac{2\sigma_f B_0^2 L}{\rho_f U_0} e^{-\frac{x}{L}}, \quad \text{Pr} = \frac{\nu_f (\rho c_p)_f}{k_f}, \quad S = -\sqrt{\frac{2L}{\nu U_0}} e^{-\frac{x}{2L}} V_w, \quad \gamma_1 = \frac{h}{k_f} \sqrt{\frac{\nu_f}{\nu}} \quad (3.15)$$

Local skin-friction coefficient C_{sf} and local Nusselt number Nu are given by

$$C_{sf} = \frac{\tau_w}{\frac{1}{2} \rho U_0^2 e^{\frac{2x}{L}}}, \quad Nu = \frac{x q_w}{k_f (T_w - T_\infty)}, \quad (3.16)$$

where the surface shear stress τ_w and wall heat flux q_w are given by

$$\tau_w = \mu_{nf} \left. \frac{\partial u}{\partial y} \right|_{y=0}, \quad q_w = -k_{nf} \left. \frac{\partial T}{\partial y} \right|_{y=0}. \quad (3.17)$$

Dimensionless forms of skin friction coefficient C_{sf} and local Nusselt number Nu can be represented by the relations

$$C_{sf} \sqrt{\frac{Re_x}{2}} = \frac{1}{(1-\phi)^{2.5}} f''(0), \quad Nu Re_x^{-1/2} \sqrt{\frac{2L}{x}} = -\frac{k_{nf}}{k_f} \theta'(0), \quad (3.18)$$

in which $Re_x = U_0 e^{\frac{x}{L}} x / \nu$ denotes the local Reynolds number.

3.2 Homotopy analysis solutions

Employing the methodology of homotopy analysis solutions the initial approximations $f_0(\eta)$ and $\theta_0(\eta)$ and auxiliary linear operators \mathcal{L}_f and \mathcal{L}_θ are given by

$$f_0(\eta) = 1 + S - \exp(-\eta), \quad \theta_0(\eta) = \frac{\gamma_1}{1 + \gamma_1} \exp(-\eta), \quad (3.19)$$

$$\mathcal{L}_f(f) = f''' - f', \quad \mathcal{L}_\theta(\theta) = \theta'' - \theta, \quad (3.20)$$

together with the properties

$$\begin{aligned} \mathcal{L}_f [c_1 + c_2 \exp(\eta) + c_3 \exp(-\eta)] &= 0, \\ \mathcal{L}_\theta [c_4 \exp(\eta) + c_5 \exp(-\eta)] &= 0, \end{aligned} \quad (3.21)$$

where $c_1 - c_5$ are the constants. If $p \in [0, 1]$ indicates the embedding parameter then the zeroth order deformation problems are constructed as follows:

$$(1-p)\mathcal{L}_f [\hat{f}(\eta; p) - f_0(\eta)] = p\mathcal{H}_f \mathcal{N}_f[\hat{f}(\eta; p)], \quad (3.22)$$

$$(1-p)\mathcal{L}_\theta [\hat{\theta}(\eta; p) - \theta_0(\eta)] = p\mathcal{H}_\theta \mathcal{N}_\theta[\hat{\theta}(\eta; p), \hat{f}(\eta; p)], \quad (3.23)$$

$$\begin{aligned} \hat{f}'(0; p) &= 1, \quad \hat{f}(0; p) = S, \quad \hat{f}'(\infty; p) = 0, \\ \hat{\theta}'(0; p) &= -\gamma_1 [1 - \hat{\theta}(0; p)], \quad \hat{\theta}(\infty; p) = 0, \end{aligned} \quad (3.24)$$

where \hbar_f and \hbar_θ are the nonzero auxiliary parameters. With Eqs. (3.11) and (3.12), the definitions of operators \mathcal{N}_f and \mathcal{N}_θ can be written as

$$\begin{aligned} \mathcal{N}_f [\hat{f}(\eta; p)] &= \varepsilon_1 \frac{\partial^3 \hat{f}(\eta; p)}{\partial \eta^3} + \hat{f}(\eta; p) \frac{\partial^2 \hat{f}(\eta; p)}{\partial \eta^2} - 2 \left(\frac{\partial \hat{f}(\eta; p)}{\partial \eta} \right)^2 \\ &\quad - \lambda \varepsilon_1 \frac{\partial \hat{f}(\eta; p)}{\partial \eta} - (1 - \phi)^{2.5} M \varepsilon_1 \frac{\sigma_{nf}}{\sigma_f} \frac{\partial \hat{f}(\eta; p)}{\partial \eta}, \end{aligned} \quad (3.25)$$

$$\mathcal{N}_\theta [\hat{\theta}(\eta; p), \hat{f}(\eta; p)] = \frac{1}{\text{Pr}} \frac{k_{nf}}{k_f} \frac{\partial^2 \hat{\theta}(\eta; p)}{\partial \eta^2} + \left((1 - \phi) + \frac{(\rho c_p)_s}{(\rho c_p)_f} \phi \right) \hat{f}(\eta; p) \frac{\partial \hat{\theta}(\eta; p)}{\partial \eta}. \quad (3.26)$$

The resulting problems at m^{th} order are given by

$$\mathcal{L}_f [f_m(\eta) - \chi_m f_{m-1}(\eta)] = \hbar_f \mathcal{R}_{f,m}(\eta), \quad (3.27)$$

$$\mathcal{L}_\theta [\theta_m(\eta) - \chi_m \theta_{m-1}(\eta)] = \hbar_\theta \mathcal{R}_{\theta,m}(\eta), \quad (3.28)$$

$$f_m(0) = f'_m(0) = f'_m(\infty) = \theta'_m(0) - \gamma_1 \theta_m(0) = \theta_m(\infty) = 0, \quad (3.29)$$

$$\chi_m = \begin{cases} 0, & m \leq 1 \\ 1, & m > 1 \end{cases}, \quad (3.30)$$

$$\mathcal{R}_{f,m}(\eta) = \varepsilon_1 f'''_{m-1} + \sum_{k=0}^{m-1} [f_{m-1-k} f''_k - 2 f'_{m-1-k} f'_k] - \lambda \varepsilon_1 f'_{m-1} - (1 - \phi)^{2.5} M \varepsilon_1 \frac{\sigma_{nf}}{\sigma_f} f'_{m-1}, \quad (3.31)$$

$$\mathcal{R}_{\theta,m}(\eta) = \frac{1}{\text{Pr}} \frac{k_{nf}}{k_f} \theta''_{m-1} + \left((1 - \phi) + \frac{(\rho c_p)_s}{(\rho c_p)_f} \phi \right) \sum_{k=0}^{m-1} \theta'_{m-1-k} f_k, \quad (3.32)$$

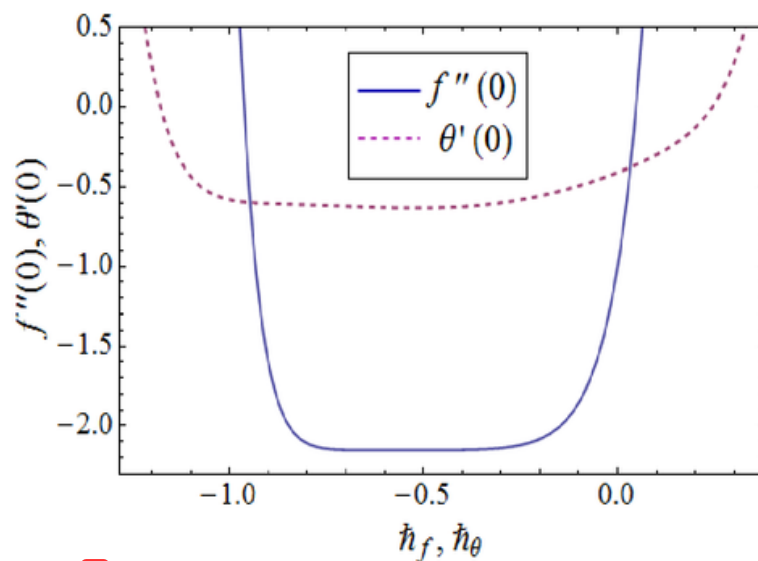
where the general solutions are

$$\begin{aligned} f_m(\eta) &= f_m^*(\eta) + c_1 + c_2 e^\eta + c_3 e^{-\eta}, \\ \theta_m(\eta) &= \theta_m^*(\eta) + c_4 e^\eta + c_5 e^{-\eta}, \end{aligned} \quad (3.33)$$

in which f_m^* and θ_m^* denote the special solutions.

3.3 ² Convergence of the homotopy solutions

Now the solutions of Eqs. (3.11) and (3.12) subject to the ¹ boundary conditions (3.13) is computed by means of homotopy analysis method. We choose auxiliary parameters \hbar_f and \hbar_θ for the functions f and θ respectively. The convergence of obtained series and rate of the ¹ approximation for HAM strongly depend upon the values of the auxiliary parameters. For ranges of ¹ admissible values of \hbar_f and \hbar_θ , the \hbar -curves for 12^{th} -order of approximations are plotted in the Fig. 3.2. We can see that ⁶ the permissible values for \hbar_f and \hbar_θ are $-0.7 \leq \hbar_f \leq -0.4$ and $-0.6 \leq \hbar_\theta \leq -0.45$. Further, the series solutions converge in the whole region of η ($0 < \eta < \infty$) when $\hbar_f = \hbar_\theta = -0.6$.



¹ Fig. 3.2: \hbar -curves for velocity and temperature fields.

Table 3.1: Convergence of HAM solutions for different order of approximations when $Pr = 6.2$, $\phi = 0.03$, $\lambda = 0.5$, $\gamma_1 = 0.7$, $M = 0.1$ and $S = 0.9$.

Order of approximations	$-f''(0)$	$-\theta'(0)$
1	1.761	0.4432
5	2.144	0.5421
10	2.154	0.6139
16	2.154	0.6336
20	2.154	0.6271
30	2.154	0.6184
35	2.154	0.6241
40	2.154	0.6241

3.4 Discussion

In this section we discuss the influence of various parameters on the velocity $f'(\eta)$ and temperature fields $\theta(\eta)$. Figs. (3.3 – 3.6) are plotted to analyze the effects of volume fraction of nanoparticles ϕ , mass transfer parameter S , Hartman number M and porosity parameter λ on the velocity field f' . Effects of volume fraction of nanoparticles ϕ on the velocity profile f' can be seen from Fig. 3.3. Here the values of f' and boundary layer thickness decrease when volume fraction for the nanoparticles increases. The effects of mass transfer parameter S on the velocity function f' are depicted in Fig. 3.4. This graph shows that the value of velocity function f' and the boundary layer thickness decrease by increasing S . Because applying suction leads to draw the amount of fluid particles into the wall and consequently the velocity boundary layer decreases. Influence of Hartman number M and parameter λ on the velocity field f' is similar to that of S . As application of a magnetic field has the tendency to slow down the movement of the fluid, causing its velocity to decrease. Also by increasing porosity parameter λ , the resistance to the fluid motion also increases. This causes the fluid velocity to decrease.

Effects of volume fraction of nanoparticles ϕ , mass transfer parameter S , Hartman number M , porosity parameter λ and Biot number γ_1 on the temperature profile θ are shown in the Figs. (3.7 – 3.11). Effect of ϕ on the temperature is analyzed in Fig. 3.7. It is observed

that increasing the volume fraction of nanoparticles ϕ , increases the thermal conductivity of nanofluid and consequently the thermal boundary layer thickness increases. The behavior of S on the temperature profile is similar to that of velocity profile (see Fig. 3.8). Fig. 3.9 illustrates the effects of M on temperature profile θ . As Lorentz force is a resistive force which opposes the fluid motion. So heat is produced and as a result thermal boundary layer thickness increases. Variations of λ on temperature profile θ can be seen in the Fig. 3.10. There is a decrease in temperature θ when porosity parameter λ is increased. Fig. 3.11 represents the effect of Biot number γ_1 on temperature profile θ . Temperature profile θ increases for an increase in γ_1 .

In Fig. 3.12 we observe that boundary layer thickness is maximum when Titanium oxide is chosen as nanoparticle. Fig. 3.13 shows the effects of nanoparticle volume fraction ϕ , mass transfer parameter S and porosity parameter λ on skin friction coefficient in the case of Cu-water. It is noticed that skin friction coefficient decreases when we increase ϕ for both S and λ . Fig. 3.14 describes the variation of Nusselt number for nanoparticle volume fraction ϕ , mass transfer parameter S and porosity parameter λ . In this Fig. heat transfer rates increase as ϕ increases for both S and λ .

Table 3.1 shows the convergence of the series solutions. In Table 3.2 some thermo physical properties of water and nanoparticles are given. Table 3.3 shows the effects of the nanoparticle volume fraction ϕ for different types of nanofluids on skin friction coefficient when $\lambda = 0.5$, $M = 0.1$ and $S = 0.9$. Table 3.4 shows the effects of the nanoparticle volume fraction ϕ for different types of nanofluids on Nusselt number when $\lambda = 0.5$, $Pr = 6.2$, $\gamma_1 = 0.7$, $M = 0.1$ and $S = 0.9$. These tables show that the shear stress and heat transfer rate change when we use different types of nanoparticles.

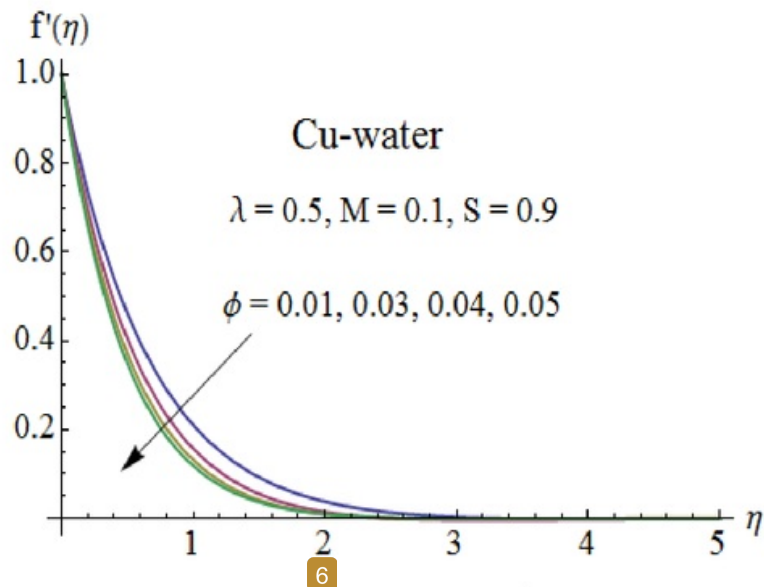


Fig. 3.3: Influence of ϕ on $f'(\eta)$.

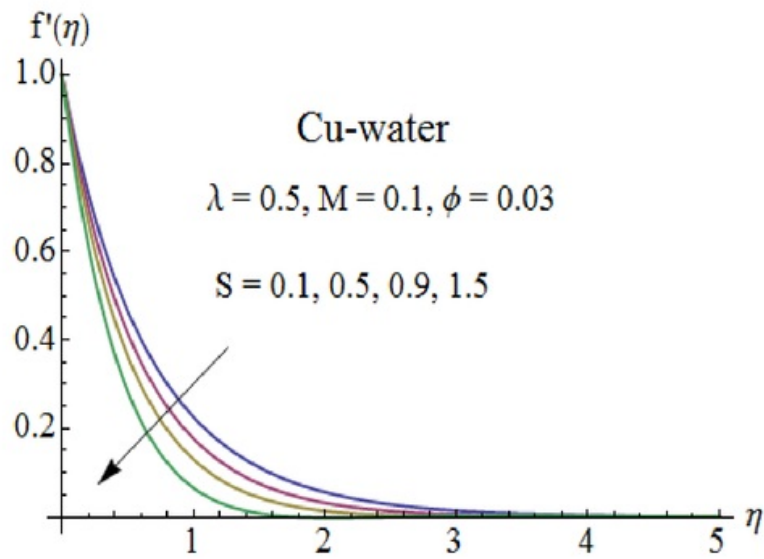
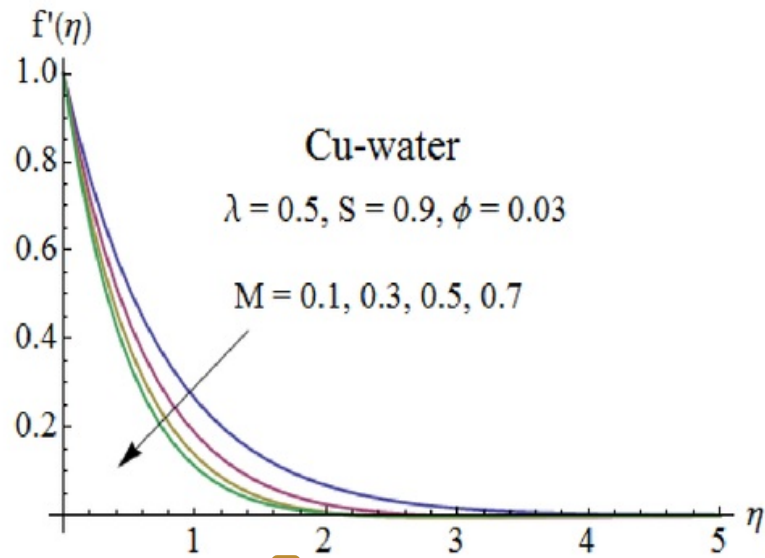


Fig. 3.4: Influence of S on $f'(\eta)$.



6
 Fig. 3.5: Influence of M on $f'(\eta)$.

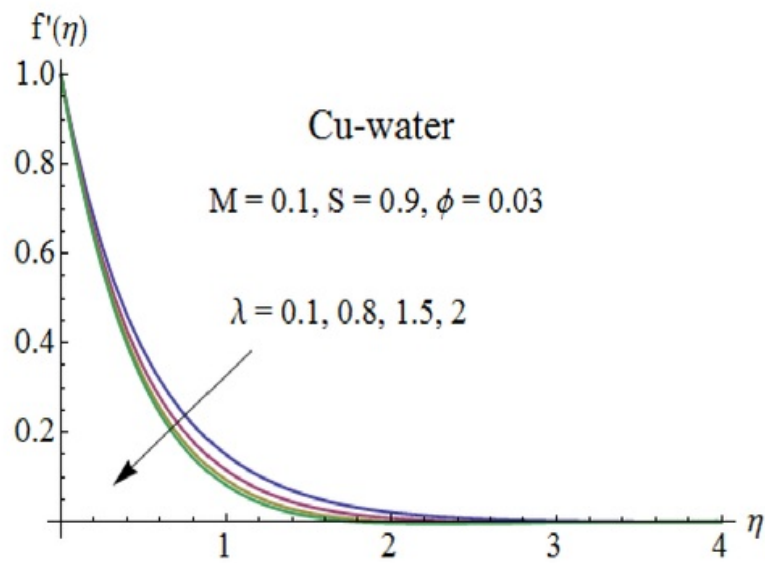


Fig. 3.6: Influence of λ on $f'(\eta)$.

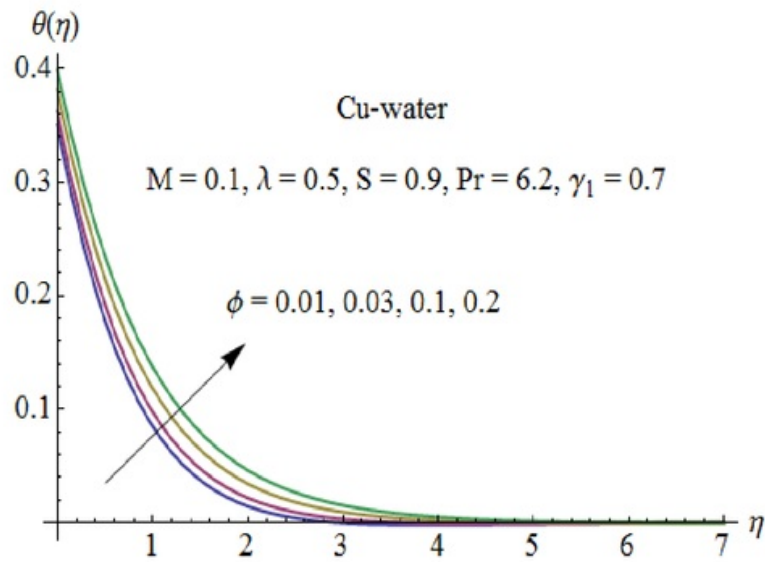


Fig. 3.7: Influence of ϕ on $\theta(\eta)$.

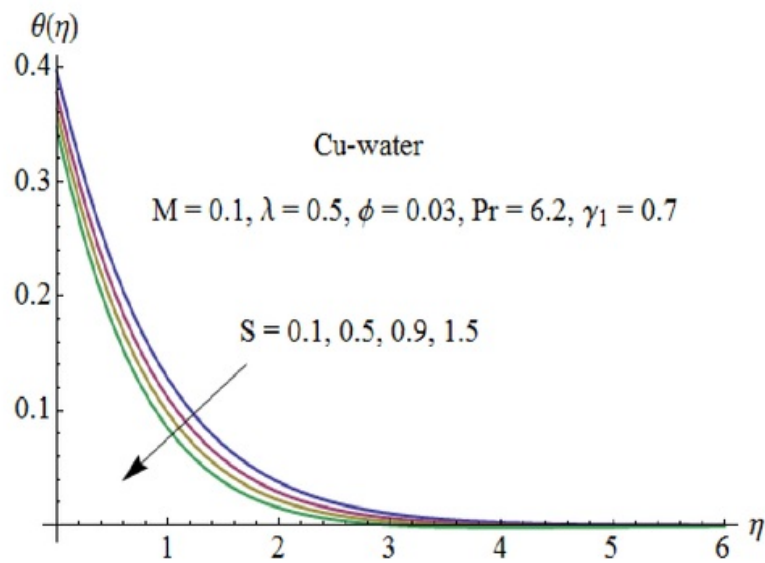


Fig. 3.8: Influence of S on $\theta(\eta)$.

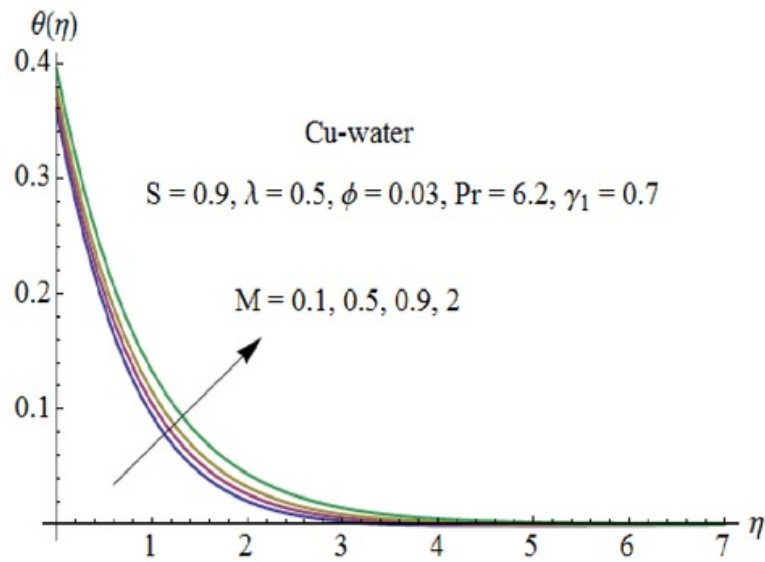


Fig. 3.9: Influence of M on $\theta(\eta)$.

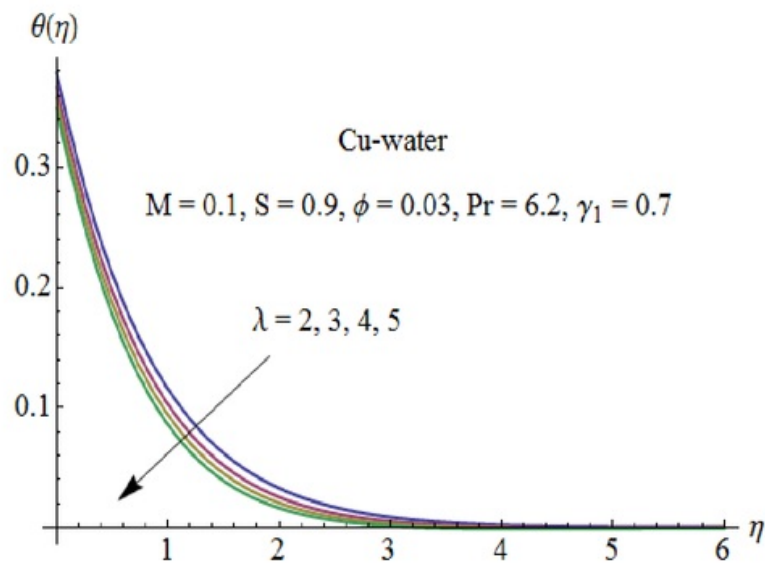


Fig. 3.10: Influence of λ on $\theta(\eta)$.

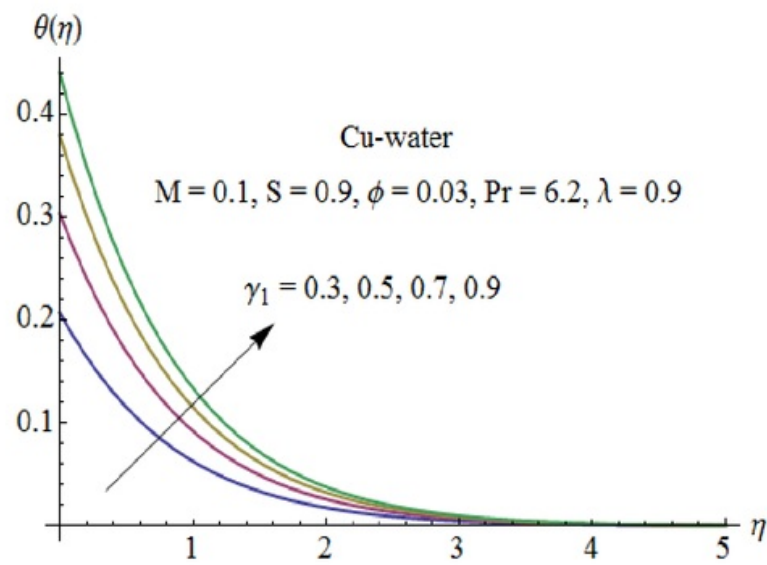
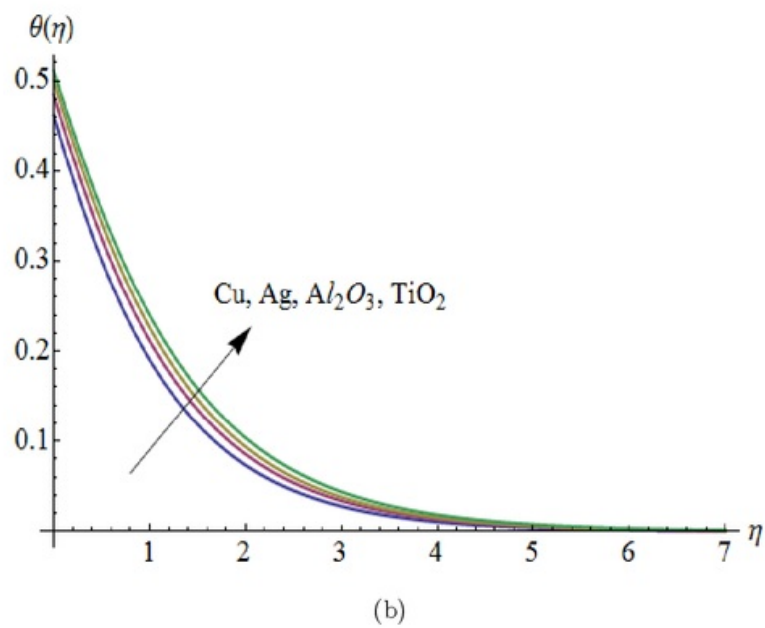
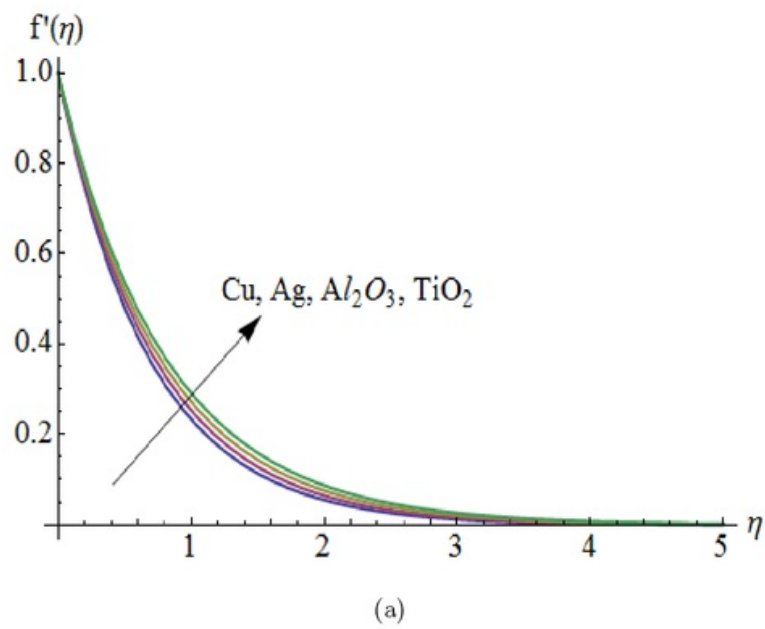


Fig. 3.11: Influence of γ_1 on $\theta(\eta)$.



8
 Fig. 3.12: (a) Velocity and (b) temperature profiles for different types of nanoparticles.

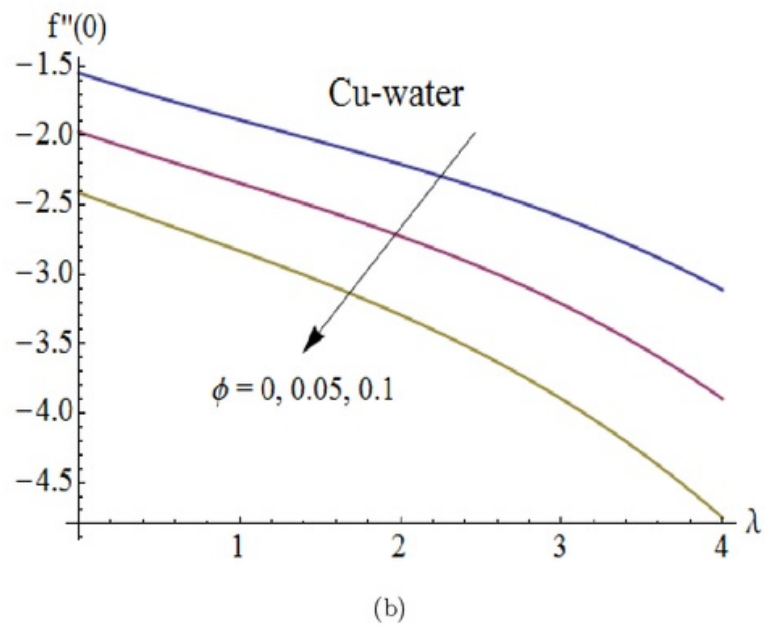
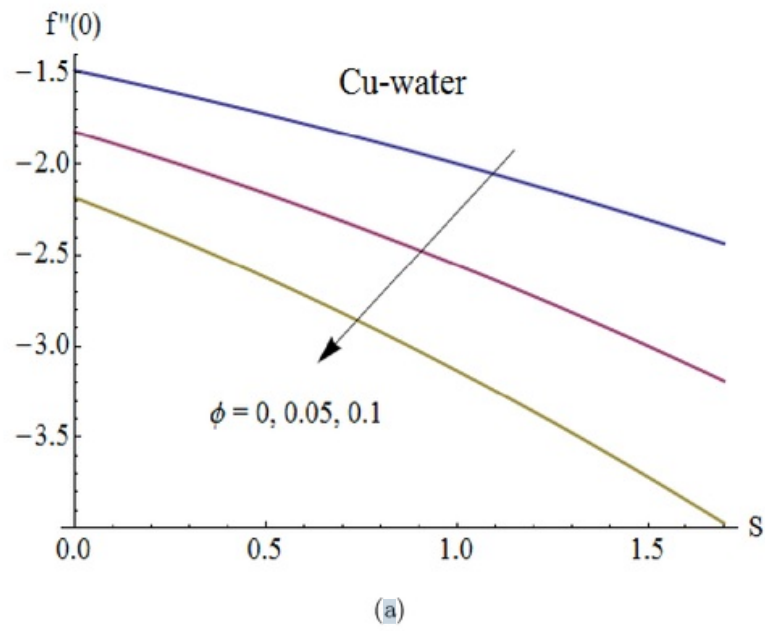


Fig. 3.13: Effects of nanoparticle volume fraction ϕ , (a) mass transfer parameter S and (b) porosity parameter λ on the skin friction coefficient when $M = 0.1$.

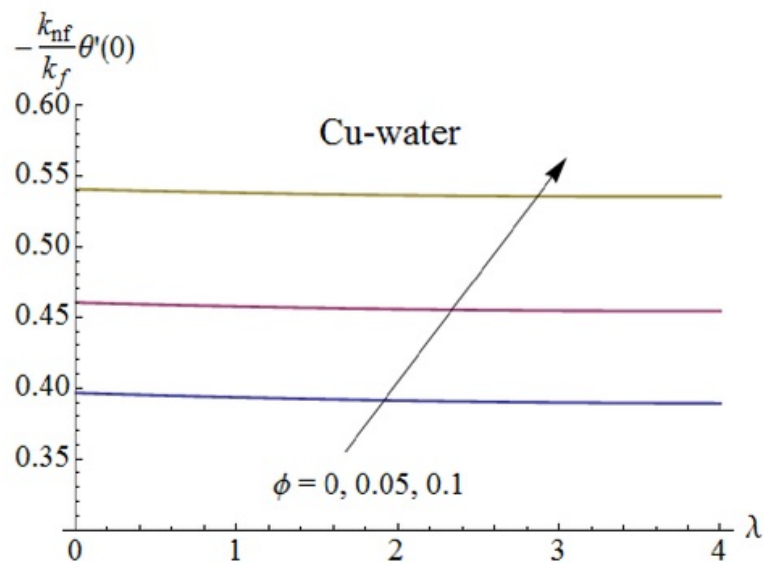
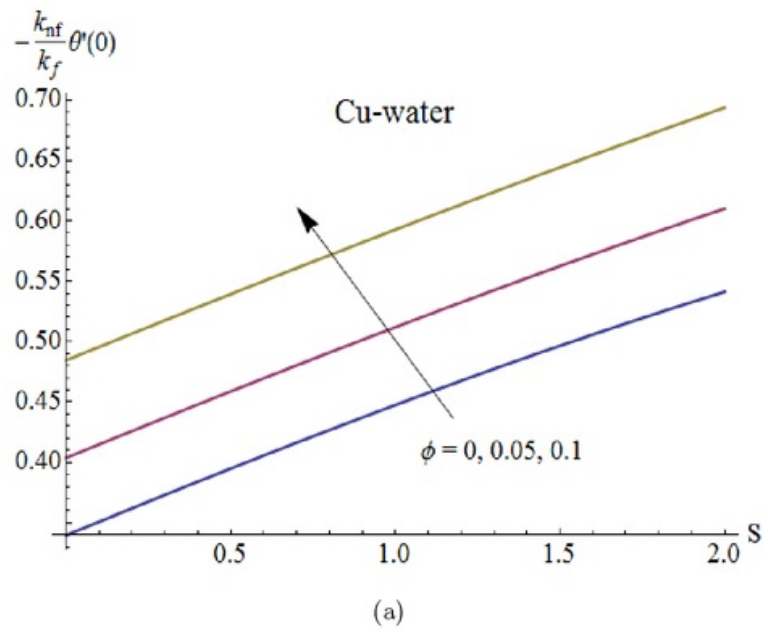


Fig. 3.14: Effects of nanoparticle volume fraction ϕ , (a) mass transfer parameter S and (b) porosity parameter λ on the Nusselt number when $M = 0.1$, $Pr = 6.2$ and $\gamma_1 = 0.7$.

13

Table 3.2: Thermo physical properties of water and nanoparticles.

	$\rho(kg/m^3)$	$c_p(j/kgk)$	$k(W/m.k)$	$\beta \times 10^5(K^{-1})$	$\sigma(\Omega m)^{-1}$
Pure water	997.1	4179	0.613	21	0.05
Copper(<i>Cu</i>)	8933	385	401	1.67	5.96×10^7
Silver(<i>Ag</i>)	10500	235	429	1.89	3.6×10^7
Alumina(Al_2O_3)	3970	765	40	0.85	1×10^{-10}
Titanium Oxide(TiO_2)	4250	686.2	8.9538	0.9	1×10^{-12}

13

Table 3.3: Effect of ϕ for different types of nanofluids on skin friction coefficient when $\lambda = 0.5$, $M = 0.1$ and $S = 0.9$.

ϕ	<i>Cu</i>	<i>Ag</i>	Al_2O_3	TiO_2
0.01	-2.05387	-2.07036	-2.00143	-2.00439
0.03	-2.15426	-2.20071	-2.00558	-2.01404
0.05	-2.23960	-2.31255	-2.00535	-2.01873

Table 3.4: Effect of ϕ for different types of nanofluids on Nusselt number when $\lambda = 0.5$, $Pr = 6.2$, $\gamma_1 = 0.7$, $M = 0.1$ and $S = 0.9$.

ϕ	<i>Cu</i>	<i>Ag</i>	Al_2O_3	TiO_2
0.01	0.436981	0.436452	0.437649	0.438380
0.03	0.423311	0.421702	0.425326	0.427566
0.05	0.409403	0.406691	0.412767	0.416582

1

3.5 Concluding remarks

Here MHD flow of nanofluid by an exponentially permeable stretching sheet is studied. Effects of different parameters on the velocity and temperature profiles are shown. Convergent approximate solution is constructed. The following observations are made

4

- An increase in the values of ϕ , S , M and λ have similar effects on the velocity profile in a qualitative sense.
- Temperature profile increases by increasing ϕ , M and γ_1 while it decreases when S and λ are increased.

- 9
- The values of skin friction coefficient are higher for increasing values of ϕ .
 - Higher values of ϕ correspond to smaller values of Nusselt number.

Chapter 4

MHD flow of nanofluid with homogeneous-heterogeneous reactions and velocity slip

Present chapter focuses ⁴ on the steady magnetohydrodynamic (MHD) flow of viscous nanofluid. The flow is caused by a stretching surface with homogeneous-heterogeneous reactions. An incompressible fluid fills the porous space. Copper-water and silver-water nanofluids are investigated in this study. Transformation method reduces the nonlinear partial differential equations governing the flow into the ⁴ ordinary differential equation by similarity transformations. The obtained equations are then solved for the development of series solutions. Convergence of the obtained series solutions is explicitly discussed. Effects of different parameters on the velocity, concentration and skin friction coefficient are shown and analyzed through graphs.

⁷ 4.1 Mathematical formulation

We consider the steady two-dimensional flow of an incompressible nanofluid over a stretching surface in porous medium with permeability K . The ¹ x -axis is taken along the stretching surface in the direction of motion and y -axis is perpendicular to it. A uniform transverse magnetic field of strength B_0 is applied parallel to the y -axis. It is assumed that the induced magnetic and electric fields effects are negligible (see Fig. 4.1). Nanoparticles such as copper

(Cu) and silver (Ag) are considered. Water is treated as a base fluid.

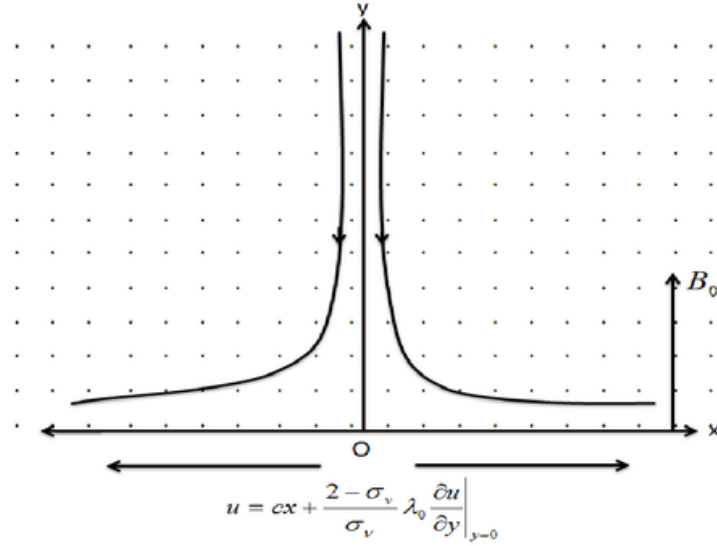
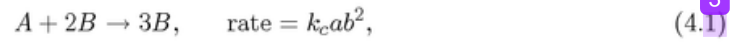


Fig. 4.1: Geometry of the problem.

We have taken a simple homogeneous-heterogeneous reaction model in the following form [73]:



while on the catalyst surface we have the single, isothermal, first order reaction



where a and b are the concentrations of the chemical species A and B and k_c and k_s denote the rate constants. We assume that both reaction processes are isothermal. Under these assumptions, the relevant boundary layer equations are

$$\frac{\partial u}{\partial x} + \frac{\partial v}{\partial y} = 0, \quad (4.3)$$

$$\rho_{nf} \left(u \frac{\partial u}{\partial x} + v \frac{\partial u}{\partial y} \right) = \mu_{nf} \frac{\partial^2 u}{\partial y^2} - \frac{\mu_{nf}}{K} u - \sigma_{nf} B_0^2 u, \quad (4.4)$$

$$u \frac{\partial a}{\partial x} + v \frac{\partial a}{\partial y} = D_A \frac{\partial^2 a}{\partial y^2} - k_c a b^2, \quad (4.5)$$

$$u \frac{\partial b}{\partial x} + v \frac{\partial b}{\partial y} = D_B \frac{\partial^2 b}{\partial y^2} + k_c a b^2. \quad (4.6)$$

The subjected boundary conditions are

$$u = cx + \frac{2 - \sigma_v}{\sigma_v} \lambda_0 \left. \frac{\partial u}{\partial y} \right|_{y=0}, \quad v = 0, \quad D_A \frac{\partial a}{\partial y} = k_s a, \quad D_B \frac{\partial b}{\partial y} = -k_s a \quad \text{at } y = 0, \\ u \rightarrow 0, \quad a \rightarrow a_0, \quad b \rightarrow 0 \quad \text{as } y \rightarrow \infty, \quad (4.7)$$

where u and v are the velocity components along the x - and y - directions respectively, D_A and D_B are the respective diffusion species coefficients of A and B , σ_v the tangential momentum accommodation coefficient and λ_0 the molecular mean free path. The effective density ρ_{nf} , the dynamic viscosity μ_{nf} , the electrical conductivity σ_{nf} , the heat capacitance $(\rho C_p)_{nf}$ and the thermal conductivity k_{nf} of the nanofluid are given by

$$\rho_{nf} = \rho_f(1 - \phi) + \rho_s \phi, \quad (4.8)$$

$$\mu_{nf} = \frac{\mu_f}{(1 - \phi)^{2.5}}, \quad (4.9)$$

$$\frac{\sigma_{nf}}{\sigma_f} = 1 + \frac{3 \left(\frac{\sigma_s}{\sigma_f} - 1 \right) \phi}{\left(\frac{\sigma_s}{\sigma_f} + 2 \right) - \left(\frac{\sigma_s}{\sigma_f} - 1 \right) \phi}, \quad (4.10)$$

Here ϕ is the nanoparticle volume fraction, s in subscript is for nano-solid-particles and f in subscript is for base fluid. Denoting a_0 (a constant) and $\xi(\eta)$ and $h(\eta)$ the dimensionless concentration and defining

$$\eta = \sqrt{\frac{c}{\nu_f}} y, \quad u = cx f'(\eta), \quad v = -\sqrt{c\nu_f} f(\eta), \quad a = a_0 \xi(\eta), \quad b = a_0 h(\eta), \quad (4.11)$$

equation (4.3) is satisfied automatically and Eqs. (4.4 – 4.7) reduce to

$$\varepsilon_1 f''' + f f'' - f'^2 - \lambda \varepsilon_1 f' - (1 - \phi)^{2.5} M \varepsilon_1 \frac{\sigma_{nf}}{\sigma_f} f' = 0, \quad (4.12)$$

$$\frac{1}{Sc} \xi'' + f \xi' - k_1 \xi h^2 = 0, \quad (4.13)$$

$$\frac{\delta}{Sc} h'' + f h' + k_1 \xi h^2 = 0, \quad (4.14)$$

$$f'(0) = 1 + \beta f''(0), \quad f(0) = 0, \quad f'(\infty) \rightarrow 0,$$

$$\xi'(0) = k_2 \xi(0), \quad \xi(\infty) \rightarrow 1,$$

$$\delta h'(0) = -k_2 \xi(0), \quad h(\infty) \rightarrow 0, \quad (4.15)$$

1 in which prime indicates the differentiation with respect to η . Moreover the non-dimensional constants in Eqs. (4.12 – 4.17) are the porosity parameter λ , the Hartman number M , the Schmidt number Sc , the measure of the strength of the homogeneous reaction k_1 , the measure of the strength of the heterogeneous reaction k_2 , the ratio of the diffusion coefficient δ and the velocity slip parameter β . These are defined as follows:

$$\lambda = \frac{\nu_f}{cK}, \quad M = \frac{\sigma_f B_0^2}{c\rho_f}, \quad Sc = \frac{\nu_f}{D_A}, \quad k_1 = \frac{k_c a_0^2}{c}, \quad k_2 = \frac{k_s}{D_A} \sqrt{\frac{\nu_f}{c}}, \quad \delta = \frac{D_B}{D_A}, \quad \beta = \frac{2 - \sigma_v}{\sigma_v} \lambda_0 \sqrt{\frac{c}{\nu_f}}, \quad (4.16)$$

where

$$\varepsilon_1 = \frac{1}{(1 - \phi)^{2.5} (1 - \phi + \phi \frac{\rho_s}{\rho_f})}. \quad (4.17)$$

3 The diffusion coefficients of chemical species A and B are expected to be of a comparable size. This leads to make a further assumption that the diffusion coefficients D_A and D_B are equal, i.e. to take $\delta = 1$ [73]. In this case we have from Eqs. (4.15)

$$\xi(\eta) + h(\eta) = 1 \quad (4.18)$$

Thus Eqs. (4.13) and (4.14) become

$$\frac{1}{Sc} \xi'' + f \xi' - k_1 \xi (1 - \xi)^2 = 0, \quad (4.19)$$

subject to the boundary conditions

$$\xi'(0) = k_2 \xi(0), \quad \xi(\infty) \rightarrow 1. \quad (4.20)$$

3

The physical quantity of interest is the skin-friction coefficient C_{sf} . It characterizes the surface drag. The shearing stress at the surface of the wall τ_w is given by

7

$$\tau_w = -\mu_{nf} \left. \frac{\partial u}{\partial y} \right|_{y=0} = -\frac{1}{(1-\phi)^{2.5}} \sqrt{\mu_f \rho_f c^3 x} f''(0). \quad (4.21)$$

The skin friction coefficient is defined as

$$C_{sf} = \frac{\tau_w}{\frac{1}{2} \rho_f u_w^2}, \quad (4.22)$$

$$C_{sf} \sqrt{\text{Re}_x} = -\frac{2}{(1-\phi)^{2.5}} f''(0), \quad (4.23)$$

in which $\text{Re}_x = u_w x / \nu_f$ denotes the local Reynolds number.

4.2 Solutions derivation

1

We choose the initial guesses $f_0(\eta)$ and $\xi_0(\eta)$ and the linear operators \mathcal{L}_f and \mathcal{L}_ξ in the forms

$$f_0(\eta) = \frac{1}{1+\beta} (1 - e^{-\eta}), \quad \xi_0(\eta) = 1 - \frac{1}{2} e^{-k_2 \eta}, \quad (4.24)$$

$$\mathcal{L}_f(f) = f''' - f', \quad \mathcal{L}_\xi(\xi) = \xi'' - \xi, \quad (4.25)$$

together with the properties

$$\begin{aligned} \mathcal{L}_f [c_1 + c_2 e^\eta + c_3 e^{-\eta}] &= 0, \\ \mathcal{L}_\xi [c_4 e^\eta + c_5 e^{-\eta}] &= 0, \end{aligned} \quad (4.26)$$

where $c_1 - c_5$ are the constants.

We construct the zeroth order problems as follows:

1

$$(1-p) \mathcal{L}_f [\hat{f}(\eta; p) - f_0(\eta)] = p \hbar_f \mathcal{N}_f[\hat{f}(\eta; p)], \quad (4.27)$$

$$(1-p) \mathcal{L}_\xi [\hat{\xi}(\eta; p) - \xi_0(\eta)] = p \hbar_\xi \mathcal{N}_\xi[\hat{\xi}(\eta; p), \hat{f}(\eta; p)], \quad (4.28)$$

$$\begin{aligned}
\hat{f}'(0; p) &= 1 + \beta \hat{f}''(0; p), \quad \hat{f}(0; p) = 0, \quad \hat{f}'(\infty; p) = 0, \\
\hat{\xi}'(0; p) &= k_2 \hat{\xi}(0; p), \quad \hat{\xi}(\infty; p) = 1,
\end{aligned} \tag{4.29}$$

where $p \in [0, 1]$ denotes an embedding parameter and h_f and h_ξ are the nonzero auxiliary parameters. With Eqs. (4.12) and (4.19), the definitions of operators \mathcal{N}_f and \mathcal{N}_ξ are

$$\begin{aligned}
\mathcal{N}_f [\hat{f}(\eta; p)] &= \varepsilon_1 \frac{\partial^3 \hat{f}(\eta; p)}{\partial \eta^3} + \hat{f}(\eta; p) \frac{\partial^2 \hat{f}(\eta; p)}{\partial \eta^2} - \left(\frac{\partial \hat{f}(\eta; p)}{\partial \eta} \right)^2 \\
&\quad - \lambda \varepsilon_1 \frac{\partial \hat{f}(\eta; p)}{\partial \eta} - (1 - \phi)^{2.5} M \varepsilon_1 \frac{\sigma_{nf}}{\sigma_f} \frac{\partial \hat{f}(\eta; p)}{\partial \eta},
\end{aligned} \tag{4.30}$$

$$\begin{aligned}
\mathcal{N}_\xi [\hat{\xi}(\eta; p), \hat{f}(\eta; p)] &= \frac{1}{Sc} \frac{\partial^2 \hat{\xi}(\eta; p)}{\partial \eta^2} + \hat{f}(\eta; p) \frac{\partial \hat{\xi}(\eta; p)}{\partial \eta} - k_1 (\hat{\xi}(\eta; p))^3 \\
&\quad - k_1 \hat{\xi}(\eta; p) + 2k_1 (\hat{\xi}(\eta; p))^2.
\end{aligned} \tag{4.31}$$

The resulting problems at m^{th} order are given by

$$\mathcal{L}_f [f_m(\eta) - \chi_m f_{m-1}(\eta)] = h_f \mathcal{R}_{f,m}(\eta), \tag{4.32}$$

$$\mathcal{L}_\xi [\xi_m(\eta) - \chi_m \xi_{m-1}(\eta)] = h_\xi \mathcal{R}_{\xi,m}(\eta), \tag{4.33}$$

$$f_m(0) = f'_m(0) - \beta f''_m(0) = f'_m(\infty) = \xi'_m(0) - k_2 \xi_m(0) = \xi_m(\infty) = 0, \tag{4.34}$$

$$\chi_m = \begin{cases} 0, & m \leq 1 \\ 1, & m > 1 \end{cases}, \tag{4.35}$$

$$\mathcal{R}_{f,m}(\eta) = \varepsilon_1 f'''_{m-1} + \sum_{l=0}^{m-1} [f_{m-1-l} f''_l - f'_{m-1-l} f'_l] - \lambda \varepsilon_1 f'_{m-1} - (1 - \phi)^{2.5} M \varepsilon_1 \frac{\sigma_{nf}}{\sigma_f} f'_{m-1}, \tag{4.36}$$

$$\mathcal{R}_{\xi,m}(\eta) = \frac{1}{Sc} \xi'''_{m-1} + \sum_{l=0}^{m-1} \left[\xi'_{m-1-l} f_l - k_1 \xi_{m-1-l} \sum_{j=0}^l \xi_{l-j} \xi_j + 2k_1 \xi_{m-1-l} \xi_l \right] - k_1 \xi_{m-1}, \tag{4.37}$$

where the general solutions are

$$\begin{aligned} f_m(\eta) &= f_m^*(\eta) + c_1 + c_2 e^\eta + c_3 e^{-\eta}, \\ \xi_m(\eta) &= \xi_m^*(\eta) + c_4 e^\eta + c_5 e^{-\eta}, \end{aligned} \quad (4.38)$$

in which f_m^* and ξ_m^* denote the special solutions. constants c_i ($i = 1 - 5$) can be determined by the boundary conditions (4.34). They are given by

$$\begin{aligned} c_3 &= \frac{1}{1 + \beta} \left[\frac{\partial f^*(\eta)}{\partial \eta} - \beta \frac{\partial^2 f^*(\eta)}{\partial \eta^2} \right]_{\eta=0}, \quad c_1 = -c_3 - f^*(0), \\ c_2 &= c_4 = 0, \quad c_5 = \frac{1}{1 + k_2} \left[\frac{\partial \xi^*(\eta)}{\partial \eta} \Big|_{\eta=0} - k_2^* \xi(0) \right]. \end{aligned} \quad (4.39)$$

4.3 Convergence of the homotopy solutions

Now the solutions of Eqs. (4.12) and (4.19) subject to the boundary conditions (4.15) and (4.20) are computed by means of homotopy analysis method. We choose auxiliary parameters \hbar_f and \hbar_ξ for the functions f and ξ respectively. The convergence of obtained series and rate of the approximation for HAM strongly depend upon the values of the auxiliary parameters. For ranges of admissible values of \hbar_f and \hbar_ξ , the \hbar -curves for 13th-order of approximations are plotted in the Figs. (4.2 and 4.3). We can see that the permissible values for \hbar_f and \hbar_ξ for *Cu*-water are $-1.6 \leq \hbar_f \leq -0.5$ and $-1.2 \leq \hbar_\xi \leq -0.3$ and for *Ag*-water are $-1.6 \leq \hbar_f \leq -0.6$ and $-1 \leq \hbar_\xi \leq -0.1$. Further, the series solutions converge in the whole region of η ($0 < \eta < \infty$) when $\hbar_f = \hbar_\xi = -1$.

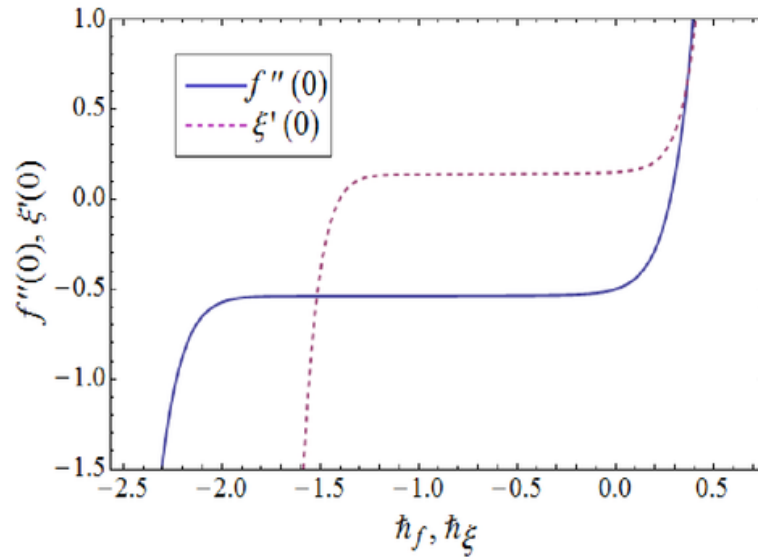


Fig. 4.2: h -curves of $f''(0)$ and $\xi'(0)$ for Cu-water when $\phi = 0.2$, $\lambda = 0.4$, $k_1 = k_2 = 0.3$, $M = Sc = 0.5$ and $\beta = 1$.

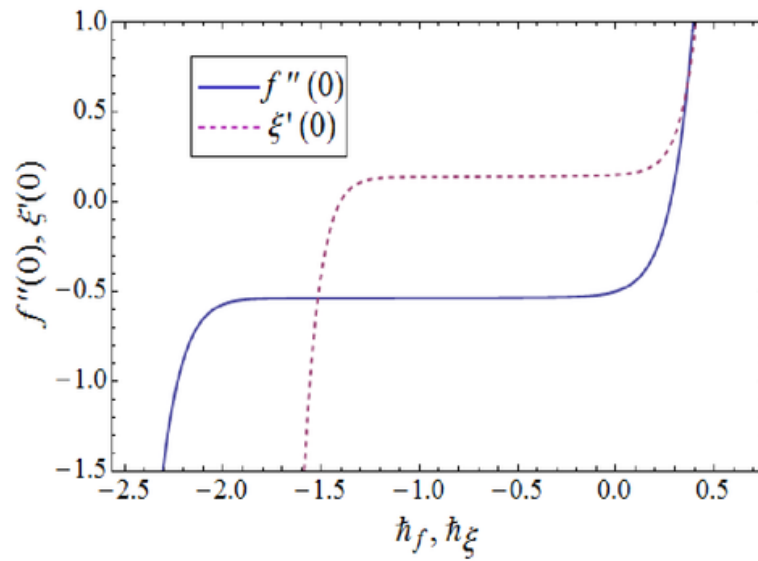


Fig. 4.3: h -curves of $f''(0)$ and $\xi'(0)$ for Ag-water when $\phi = 0.2$, $\lambda = 0.4$, $k_1 = k_2 = 0.3$, $M = Sc = 0.5$ and $\beta = 1$.

Table 4.1: Convergence of HAM solutions for different order of approximations when $\phi = 0.2$, $\lambda = 0.4$, $k_1 = k_2 = 0.3$, $M = Sc = 0.5$ and $\beta = 1$.

Order of approximations	$-f''(0)$	$g'(0)$
1	0.5455	0.04916
5	0.5564	0.04835
10	0.5588	0.04788
15	0.5596	0.04755
17	0.5594	0.04736
20	0.5594	0.04736
25	0.5594	0.04736

4.4 Results and discussion

The effects of different parameters on the dimensionless flow and concentration profiles are investigated and presented graphically in this section.

4.4.1 Dimensionless velocity profiles

Figs. (4.4 – 4.7) exhibit the dimensionless velocity profiles for different values of nanoparticle volume fraction ϕ , Hartman number M , velocity slip parameter β and porosity parameter λ . Effects of volume fraction of nanoparticles (Cu and Ag) on the velocity profile f' can be seen from Fig. 4.4. Here the velocity profile and boundary layer thickness decrease when volume fraction for the nanoparticles increases. The effects of Hartman number M on the velocity f' are depicted in Fig. 4.5. We analyzed that the velocity is reduced when we increase the values of Hartman number. In fact applied magnetic field has the tendency to slow down the movement of the fluid which leads to a decrease in the velocity and momentum boundary layer thickness. Variations of velocity slip parameter β on velocity profile f' can be seen in the Fig. 4.6. There is a decrease in velocity when velocity slip parameter β is increased. From Fig. 4.7, we have seen that larger values of porosity parameter λ correspond to the less velocity. Porosity parameter depends on the permeability parameter K . Increase in porosity parameter leads to the lower permeability parameter. This lower permeability parameter causes a reduction in the fluid velocity.

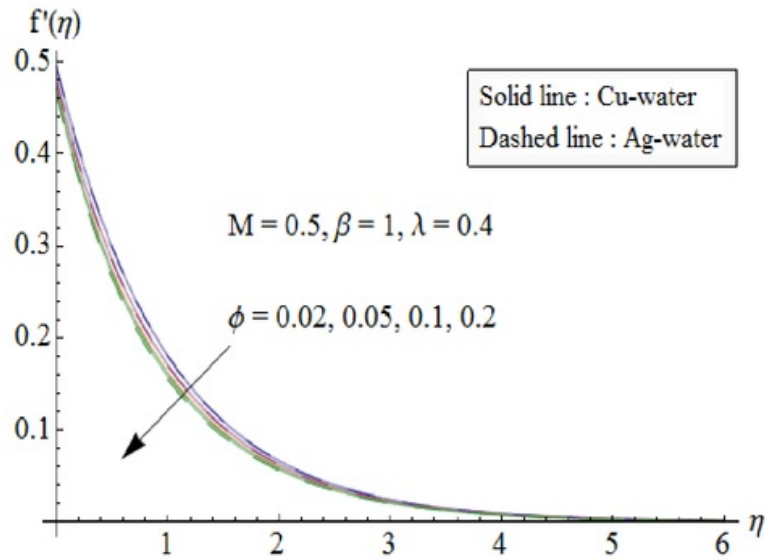


Fig. 4.4. Influence of ϕ on velocity field.

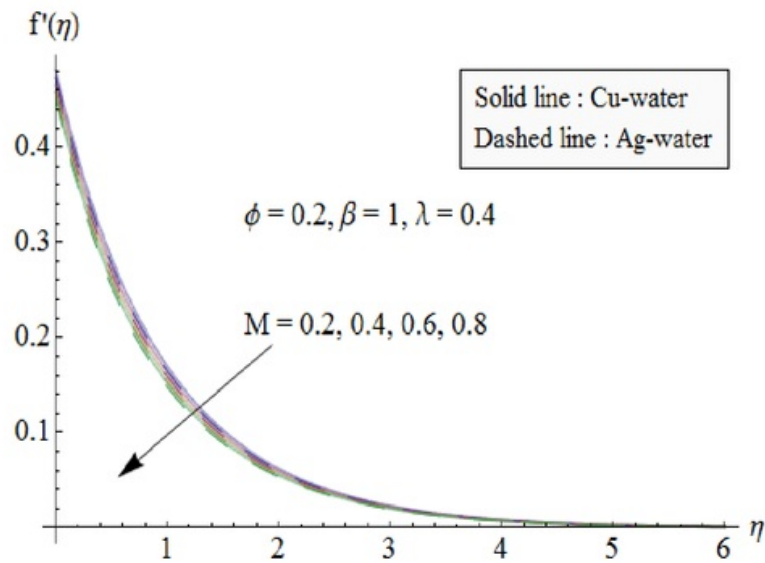


Fig. 4.5. Influence of M on velocity field.

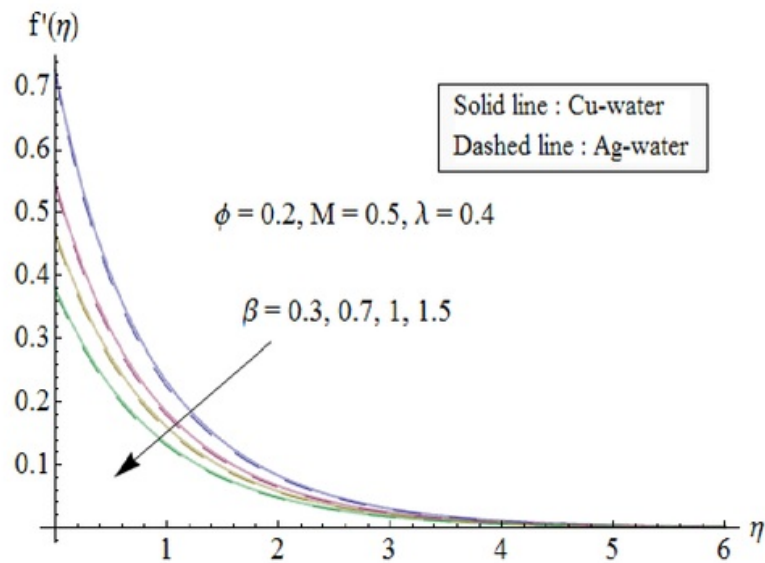


Fig. 4.6. Influence of β on velocity field.

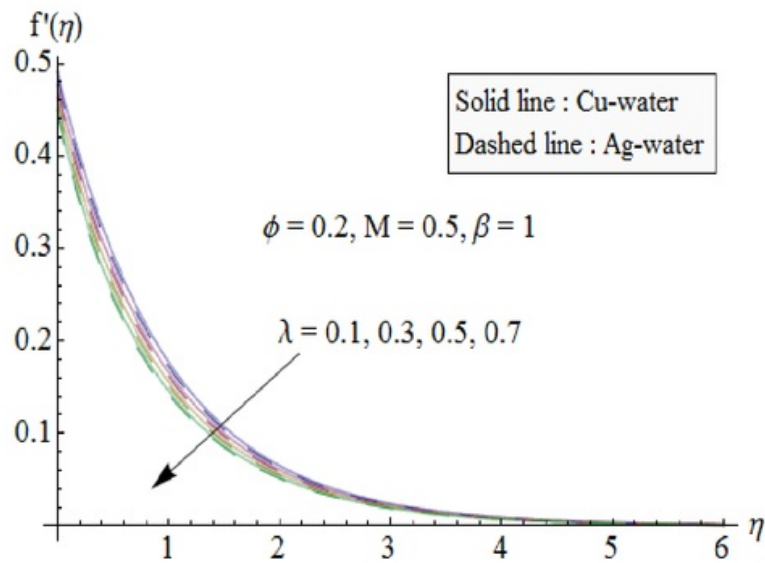


Fig. 4.7. Influence of λ on velocity field.

4.4.2 Dimensionless concentration profiles

Effects of the measure of the strength of the homogeneous reaction k_1 , the measure of the strength of the heterogeneous reaction k_2 and the Schmidt number Sc on the concentration profile ξ are shown in the Figs. (4.8 – 4.10). Effects of k_1 on the concentration is analyzed in Fig. 4.8. It is observed that increasing the measure of the strength of the homogeneous reaction k_1 decreases the thermal boundary layer thickness. Fig. 4.9 illustrates the effects of k_2 on concentration profile ξ . There is an increase in concentration ξ when the measure of the strength of the heterogeneous reaction k_2 is increased. The behavior of Schmidt number Sc on the concentration profile is similar to that of k_2 (see Fig. 4.10).

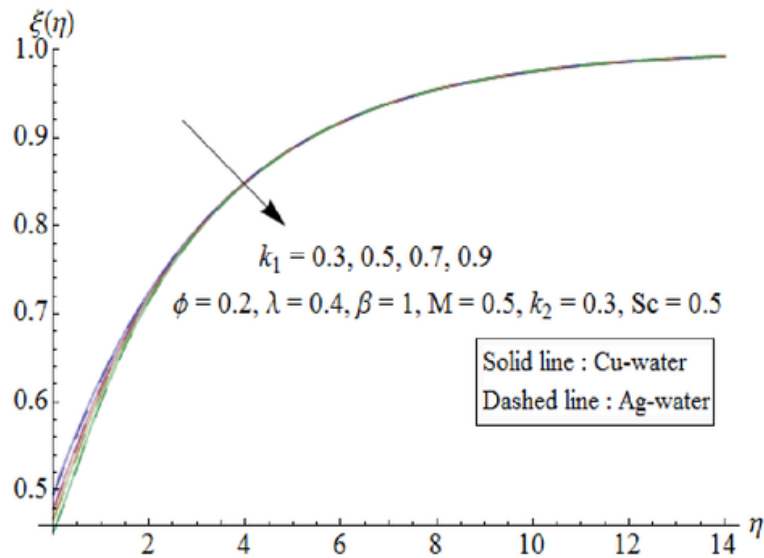


Fig. 4.8. Influence of k_1 on concentration field.

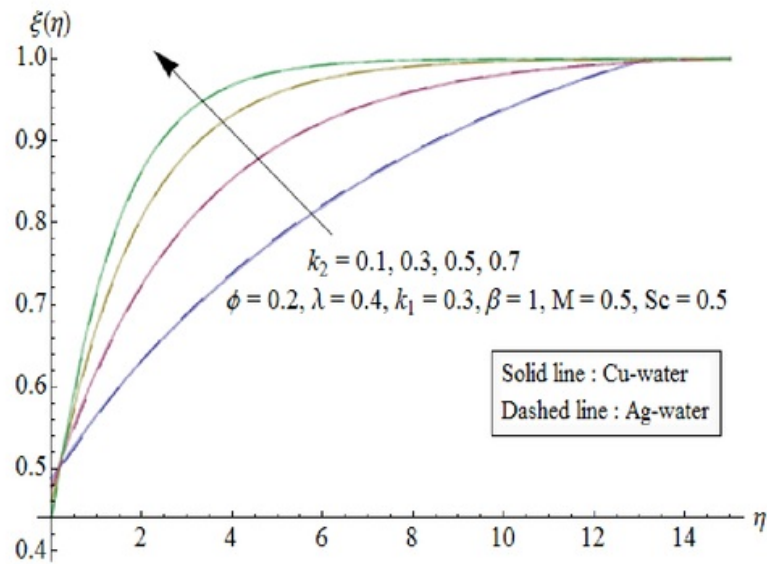


Fig. 4.9. Influence of k_2 on concentration field.

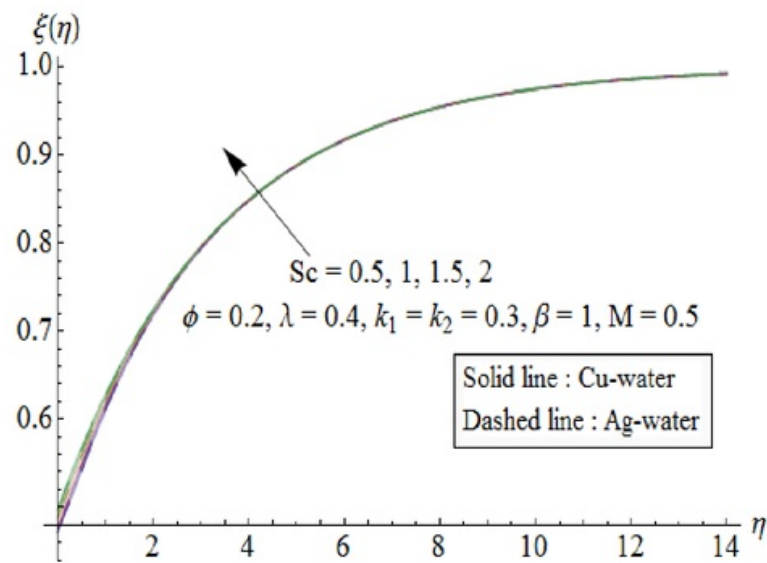


Fig. 4.10. Influence of Sc on concentration field.

4.4.3 Skin friction coefficient and surface concentration

Fig. 4.11 shows the skin friction coefficient $f''(0)$ as a function of nanoparticle volume fraction ϕ . The skin friction coefficient enhances with increasing values of ϕ . The results of the skin friction coefficient are examined for both types of nanofluids. We observe that the *Ag*-water nanofluid gives a higher drag force opposite to the flow when compared with the *Cu*-water nanofluid.

The variation of dimensionless concentration for different values of k_1 and k_2 are shown in Figs. 4.12 and 4.13 respectively. From Fig. 4.12 it is observed that concentration at the surface decreases as the strength of the heterogeneous reaction increases for different types of nanofluids. One can see from Fig. 4.13 that $\xi(0)$ decreases with the increase of homogeneous reaction strength k_1 . Influence of Sc on $\xi(0)$ for two different types of nanoparticles is shown in Fig. 4.14. It is clear that the concentration decreases with an increase of Schmidt number.

In Table 4.3 some numerical values of skin friction coefficient are given for copper and silver nanoparticles. Tabular values show that skin friction coefficient increases by increasing ϕ and M while it decreases for larger β . Table 4.4 shows that surface concentration decreases by increasing k_1 , k_2 , Sc and β .

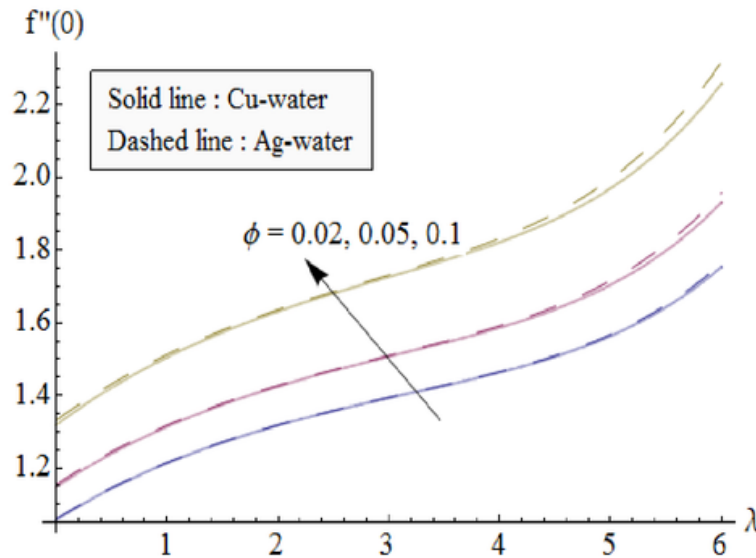


Fig. 4.11. Influence of ϕ on skin friction coefficient.

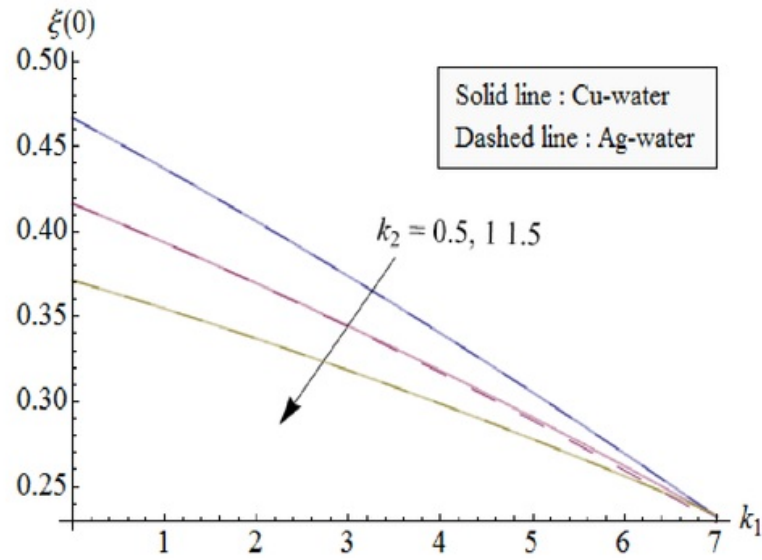


Fig. 4.12: Influence of k_2 on surface concentration.

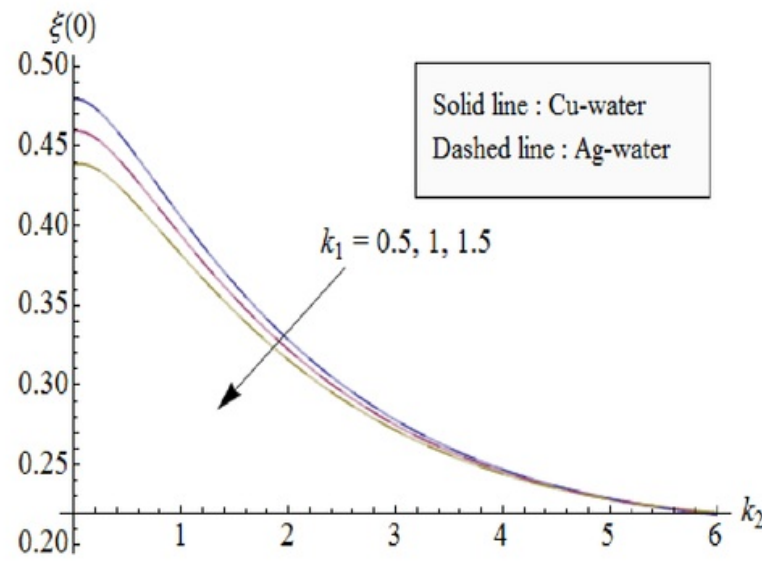


Fig. 4.13: Influence of k_1 on surface concentration.

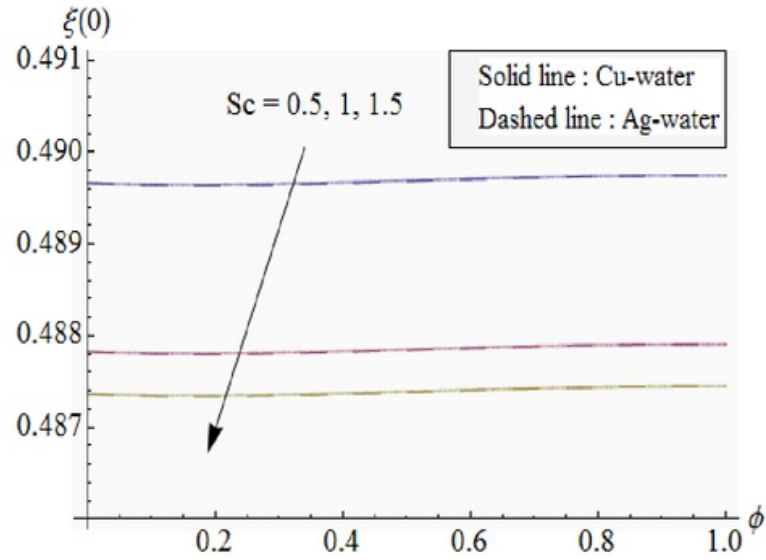


Fig. 4.14: Influence of Sc on surface concentration.

Table 4.2: Thermophysical properties of water and nanoparticles.

	$\rho(kg/m^3)$	$c_p(j/kgk)$	$k(W/m.k)$	$\beta \times 10^5(K^{-1})$	$\sigma(\Omega m)^{-1}$
Pure water	997.1	4179	0.613	21	0.05
Copper(Cu)	8933	385	401	1.67	5.96×10^7
Silver(Ag)	10500	235	429	1.89	3.6×10^7
Alumina(Al_2O_3)	3970	765	40	0.85	1×10^{-10}
Titanium Oxide(TiO_2)	4250	686.2	8.9538	0.9	1×10^{-12}

Table 4.3: Numerical values of skin friction coefficient for copper and silver when $\lambda = 0.4$.

ϕ	M	β	$C_{sf}\sqrt{\text{Re}_x}$ for <i>Cu</i>	$C_{sf}\sqrt{\text{Re}_x}$ for <i>Ag</i>
0.05	0.5		1.278	1.284
0.1			1.465	1.475
0.2			1.955	1.973
0.2	0.1		1.897	1.917
	0.3		1.928	1.945
	0.7		1.981	1.996
	0.5	0.1	4.542	4.672
		0.5	2.827	2.865
		0.9	2.079	2.098

Table 4.4: Numerical values of surface concentration for copper and silver when $\phi = 0.2$, $\lambda = 0.4$ and $M = 0.5$.

k_1	k_2	Sc	β	$\xi(0)$ for <i>Cu</i>	$\xi(0)$ for <i>Ag</i>
0.5				0.4407	0.4413
1				0.4087	0.3997
1.5				0.3645	0.3761
0.3	0.5			0.4169	0.4173
	1			0.3274	0.3321
	1.5			0.2856	0.2741
	0.5	0.4		0.4726	0.4675
		0.7		0.4703	0.4561
		1		0.4675	0.4532
		0.5	0.1	0.4618	0.4619
			0.5	0.4583	0.4537
			0.9	0.4565	0.4502

4.5 Final remarks

This chapter investigates the MHD flow of nanofluid by a stretching sheet in presence of homogeneous-heterogeneous reactions. Convergent approximate solution is constructed. The

following observations are made:

- An increase in the values of ϕ , M , β and λ has similar effects on the velocity in a qualitative sense.
- Concentration profile increases by increasing k_2 and Sc while it decreases when k_1 is increased.
- The values of skin friction coefficient are higher for Ag -water when ϕ enhances.
- Higher values of k_1 , k_2 and Sc correspond to smaller values of dimensionless surface concentration.

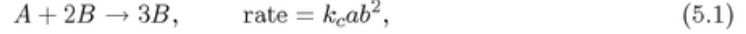
Chapter 5

Impact of magnetohydrodynamics in bidirectional flow of nanofluid subject to second order slip velocity and homogeneous-heterogeneous reactions

This chapter addresses the steady three-dimensional boundary layer flow of viscous nanofluid. The flow is caused by a permeable stretching surface with second order velocity slip and homogeneous-heterogeneous reactions. Water is treated as base fluid and copper as nanoparticle. An incompressible fluid fills the porous space. The fluid is electrically conducting in the presence of an applied magnetic field. A system of ordinary differential equations is obtained by using suitable transformations. Convergent series solutions are derived. Impact of various pertinent parameters on the velocity, concentration and skin friction coefficient is discussed. Analysis of the obtained results shows that the flow field is influenced appreciably by the presence of velocity slip parameters. Also concentration distribution decreases for larger values of strength of homogeneous reaction parameter while it increases for strength of heterogeneous reaction parameter.

5.1 Model development

We consider the steady three-dimensional incompressible flow of nanofluid saturating porous medium with permeability K . The porous medium features have been characterized by using Darcy's law. Material is water based nanofluid consisting of copper (Cu) as nanoparticle. Flow is induced by a permeable stretching sheet at $z = 0$. An incompressible fluid occupies $z > 0$. It is assumed that the sheet is stretched with velocities $u_w = cx$ and $v_w = dy$, where $c, d > 0$ are the stretching rates. A uniform magnetic field of strength B_0 is applied in the z -direction. Electric and induced magnetic fields are neglected. Flow analysis is carried out with homogeneous-heterogeneous reactions. The homogeneous reaction for cubic autocatalysis can be expressed as follows [73]:



while first-order isothermal reaction on the catalyst surface is presented in the form



where a and b are the concentrations of the chemical species A and B and k_c and k_s are the rate constants. We assume that both reaction processes are isothermal. Using the nanofluid model as proposed by Tiwari and Das [4], the boundary layer equations governing the flow can be written as follows:

$$\frac{\partial u}{\partial x} + \frac{\partial v}{\partial y} + \frac{\partial w}{\partial z} = 0, \quad (5.3)$$

$$\rho_{nf} \left(u \frac{\partial u}{\partial x} + v \frac{\partial u}{\partial y} + w \frac{\partial u}{\partial z} \right) = \mu_{nf} \frac{\partial^2 u}{\partial z^2} - \frac{\mu_{nf}}{K} u - \sigma_{nf} B_0^2 u, \quad (5.4)$$

$$\rho_{nf} \left(u \frac{\partial v}{\partial x} + v \frac{\partial v}{\partial y} + w \frac{\partial v}{\partial z} \right) = \mu_{nf} \frac{\partial^2 v}{\partial z^2} - \frac{\mu_{nf}}{K} v - \sigma_{nf} B_0^2 v, \quad (5.5)$$

$$u \frac{\partial a}{\partial x} + v \frac{\partial a}{\partial y} + w \frac{\partial a}{\partial z} = D_A \frac{\partial^2 a}{\partial z^2} - k_c ab^2, \quad (5.6)$$

$$u \frac{\partial b}{\partial x} + v \frac{\partial b}{\partial y} + w \frac{\partial b}{\partial z} = D_B \frac{\partial^2 b}{\partial z^2} + k_c ab^2. \quad (5.7)$$

The subjected boundary conditions are put into the form

$$\begin{aligned}
 u &= u_w + u_{slip}, \quad v = v_w + v_{slip}, \quad w = w_0, \quad \text{at } z = 0, \\
 D_A \frac{\partial a}{\partial z} &= k_s a, \quad D_B \frac{\partial b}{\partial z} = -k_s a \quad \text{at } z = 0, \\
 u &\rightarrow 0, \quad v \rightarrow 0, \quad a \rightarrow a_0, \quad b \rightarrow 0 \quad \text{as } z \rightarrow \infty,
 \end{aligned} \tag{5.8}$$

in which u , v and w are velocity components along x -, y - and z - directions respectively, w_0 is suction ($w_0 < 0$) or injection ($w_0 > 0$) velocity, D_A and D_B are diffusion species coefficients of A and B and a_0 is positive dimensional constant. Effective density ρ_{nf} , dynamic viscosity μ_{nf} and electrical conductivity σ_{nf} of nanofluid are given by

$$\rho_{nf} = \rho_f(1 - \phi) + \rho_s\phi, \tag{5.9}$$

$$\mu_{nf} = \frac{\mu_f}{(1 - \phi)^{2.5}}, \tag{5.10}$$

$$\frac{\sigma_{nf}}{\sigma_f} = 1 + \frac{3 \left(\frac{\sigma_s}{\sigma_f} - 1 \right) \phi}{\left(\frac{\sigma_s}{\sigma_f} + 2 \right) - \left(\frac{\sigma_s}{\sigma_f} - 1 \right) \phi}. \tag{5.11}$$

Here ϕ is the solid volume fraction, s in subscript is for nano-solid-particles and f in subscript is for base fluid. Also u_{slip} is the slip velocity at the wall. The Wu's slip velocity model (valid for arbitrary Knudsen number, Kn) is employed here as follows [60]:

$$\begin{aligned}
 u_{slip} &= \frac{2}{3} \left(\frac{3 - \kappa I^3}{\kappa} - \frac{3(1 - I^2)}{2Kn} \right) \Lambda \frac{\partial u}{\partial z} - \frac{1}{4} \left(I^4 + \frac{2}{Kn^2}(1 - I^2) \right) \Lambda^2 \frac{\partial^2 u}{\partial z^2}, \\
 &= N_1 \frac{\partial u}{\partial z} + N_2 \frac{\partial^2 u}{\partial z^2}, \\
 v_{slip} &= \frac{2}{3} \left(\frac{3 - \kappa I^3}{\kappa} - \frac{3(1 - I^2)}{2Kn} \right) \Lambda \frac{\partial v}{\partial z} - \frac{1}{4} \left(I^4 + \frac{2}{Kn^2}(1 - I^2) \right) \Lambda^2 \frac{\partial^2 v}{\partial z^2}, \\
 &= N_3 \frac{\partial v}{\partial z} + N_4 \frac{\partial^2 v}{\partial z^2},
 \end{aligned} \tag{5.12}$$

where $I = \min \left[\frac{1}{Kn}, 1 \right]$, κ is momentum accommodation coefficient with $0 \leq \kappa \leq 1$, Λ is molecular mean free path and Kn is Knudsen number defined as mean free path Λ divided by a characteristic length for the flow. Based on the definition of I , it is seen that for any given

value of Kn we have $0 \leq I \leq 1$. The molecular mean free path is always positive. Thus we know that $N_2, N_4 < 0$ and N_1, N_3 are positive numbers.

Making use of the following similarity transformations

$$\begin{aligned} u &= cx f'(\eta), \quad v = cy g'(\eta), \quad w = -\sqrt{c\nu} [f(\eta) + g(\eta)], \\ \eta &= \sqrt{\frac{c}{\nu}} z, \quad a = a_0 \xi(\eta), \quad b = a_0 h(\eta), \end{aligned} \quad (5.13)$$

the continuity equation is satisfied automatically and Eqs. (5.4 – 5.8) are reduced to

$$\varepsilon_1 f''' - f'^2 + (f + g) f'' - \lambda f' - \varepsilon_1 (1 - \phi)^{2.5} M \frac{\sigma_{nf}}{\sigma_f} f' = 0, \quad (5.14)$$

$$\varepsilon_1 g''' - g'^2 + (f + g) g'' - \lambda g' - \varepsilon_1 (1 - \phi)^{2.5} M \frac{\sigma_{ng}}{\sigma_g} g' = 0, \quad (5.15)$$

$$\frac{1}{Sc} \xi'' + (f + g) \xi' - k_1 \xi h^2 = 0, \quad (5.16)$$

$$\frac{\delta}{Sc} h'' + (f + g) h' + k_1 \xi h^2 = 0, \quad (5.17)$$

$$f'(0) = 1 + \beta_1 f''(0) + \beta_2 f'''(0), \quad g'(0) = \gamma + \beta_3 g''(0) + \beta_4 g'''(0),$$

$$f(0) + g(0) = S, \quad f'(\infty) \rightarrow 0, \quad g'(\infty) \rightarrow 0,$$

$$\xi'(0) = k_2 \xi(0), \quad \delta h'(0) = -k_2 \xi(0), \quad \xi(\infty) \rightarrow 1, \quad h(\infty) \rightarrow 0, \quad (5.18)$$

where λ is the porosity parameter, M is the Hartman number, γ is the ratio of the stretching rate along the y - direction to the stretching rate along the x - direction, β_1 and β_3 are the first order slip velocity parameters, β_2 and β_4 (< 0) are the second order slip velocity parameters, S is the suction/injection velocity parameter, Sc is the Schmidt number, k_1 is the measure of the strength of homogeneous reaction, δ is the ratio of diffusion coefficient and k_2 is the measure of

the strength of the heterogeneous reaction. These quantities are defined as follows:

$$\begin{aligned}
\varepsilon_1 &= \frac{1}{(1-\phi)^{2.5}(1-\phi+\frac{\rho_s}{\rho_f}\phi)}, \quad \lambda = \frac{\nu_f}{cK}, \quad M = \frac{\sigma_f B_0^2}{c\rho_f}, \quad \gamma = \frac{d}{c}, \\
\beta_1 &= N_1 \sqrt{\frac{c}{\nu_f}}, \quad \beta_2 = N_2 \sqrt{\frac{c}{\nu_f}}, \quad \beta_3 = N_3 \sqrt{\frac{c}{\nu_f}}, \quad \beta_4 = N_4 \sqrt{\frac{c}{\nu_f}}, \\
S &= -\frac{w_0}{\sqrt{c\nu_f}}, \quad Sc = \frac{\nu_f}{D_A}, \quad k_1 = \frac{k_c a_0^2}{c}, \quad \delta = \frac{D_B}{D_A}, \quad k_2 = \frac{k_s}{D_A} \sqrt{\frac{\nu_f}{c}}.
\end{aligned} \tag{5.19}$$

It is noticed that for $\beta = 0$ and $\beta = 1$ the two-dimensional and axisymmetric flows are respectively noticed. Here it is assumed that diffusion coefficients of chemical species A and B to be of a comparable size. This leads to make a further assumption that the diffusion coefficients D_A and D_B are equal, i.e. $\delta = 1$ [73] and thus

$$\xi(\eta) + h(\eta) = 1. \tag{5.20}$$

Now Eqs. (5.16) and (5.17) yield

$$\frac{1}{Sc} \xi'' + (f+g)\xi' - k_1 \xi(1-\xi)^2 = 0, \tag{5.21}$$

with the boundary conditions

$$\xi'(0) = k_2 \xi(0), \quad \xi(\infty) \rightarrow 1. \tag{5.22}$$

Skin friction coefficients along the x - and y - directions are defined as follows:

$$C_{fx} = \frac{\tau_{wx}}{\rho_f u_w^2}, \quad C_{fy} = \frac{\tau_{wy}}{\rho_f v_w^2}, \tag{5.23}$$

where the surface shear stresses τ_{wx} and τ_{wy} along the x - and y - directions are given by

$$\tau_{wx} = \mu_{nf} \left. \frac{\partial u}{\partial z} \right|_{z=0}, \quad \tau_{wy} = \mu_{nf} \left. \frac{\partial v}{\partial z} \right|_{z=0}. \tag{5.24}$$

Dimensionless skin friction coefficients are

$$C_{fx}(\text{Re}_x)^{1/2} = \frac{1}{(1-\phi)^{2.5}} f''(0), \quad C_{fy}(\text{Re}_y)^{1/2} = \frac{1}{\gamma^{3/2}(1-\phi)^{2.5}} g''(0), \quad (5.25)$$

where $(\text{Re}_x)^{1/2} = x\sqrt{c/\nu_f}$ and $(\text{Re}_y)^{1/2} = y\sqrt{c/\nu_f}$ denotes the local Reynolds number.

5.2 Homotopic solutions

The initial approximations $f_0(\eta)$, $g_0(\eta)$ and $\xi_0(\eta)$ and auxiliary linear operators \mathcal{L}_f , \mathcal{L}_g and \mathcal{L}_ξ are taken as follows:

$$f_0(\eta) = S + \frac{1}{1+\beta_1-\beta_2} (1-e^{-\eta}), \quad g_0(\eta) = \frac{\gamma}{1+\beta_3-\beta_4} (1-e^{-\eta}), \quad \xi_0(\eta) = 1 - \frac{1}{2} e^{-k_2\eta}, \quad (5.26)$$

$$\mathcal{L}_f = f''' - f', \quad \mathcal{L}_g = g''' - g', \quad \mathcal{L}_\xi = \xi'' - \xi, \quad (5.27)$$

$$\mathcal{L}_f [c_1 + c_2 e^\eta + c_3 e^{-\eta}] = 0,$$

$$\mathcal{L}_g [c_4 + c_5 e^\eta + c_6 e^{-\eta}] = 0,$$

$$\mathcal{L}_\xi [c_7 e^\eta + c_8 e^{-\eta}] = 0, \quad (5.28)$$

in which c_i ($i = 1 - 8$) are the constants.

If $p \in [0, 1]$ indicates the embedding parameter and \hbar_f , \hbar_g and \hbar_ξ the non-zero auxiliary parameters then the zeroth order deformation problems are constructed as follows:

$$(1-p)\mathcal{L}_f [\hat{f}(\eta; p) - f_0(\eta)] = p\hbar_f \mathcal{N}_f[\hat{f}(\eta; p), \hat{g}(\eta; p)], \quad (5.29)$$

$$(1-p)\mathcal{L}_g [\hat{g}(\eta; p) - g_0(\eta)] = p\hbar_g \mathcal{N}_g[\hat{g}(\eta; p), \hat{f}(\eta; p)], \quad (5.30)$$

$$(1-p)\mathcal{L}_\xi [\hat{\xi}(\eta; p) - \xi_0(\eta)] = p\hbar_\xi \mathcal{N}_\xi[\hat{\xi}(\eta; p), \hat{f}(\eta; p), \hat{g}(\eta; p)], \quad (5.31)$$

$$\hat{f}'(0; p) = 1 + \beta_1 \hat{f}''(0; p) + \beta_2 \hat{f}'''(0; p), \quad \hat{f}(0; p) = S, \quad \hat{f}'(\infty; p) = 0, \quad (5.32)$$

$$\hat{g}'(0; p) = \gamma + \beta_3 \hat{g}''(0; p) + \beta_4 \hat{g}'''(0; p), \quad \hat{g}(0; p) = 0, \quad \hat{g}'(\infty; p) = 0, \quad (5.33)$$

$$\hat{\xi}'(0; p) = k_2 \hat{\xi}(0; p), \quad \hat{\xi}(\infty; p) = 1, \quad (5.34)$$

where the nonlinear differential operators \mathcal{N}_f , \mathcal{N}_g and \mathcal{N}_ξ are given by

$$\begin{aligned} \mathcal{N}_f \left[\hat{f}(\eta; p), \hat{g}(\eta; p) \right] &= \varepsilon_1 \frac{\partial^3 \hat{f}(\eta; p)}{\partial \eta^3} - \left(\frac{\partial \hat{f}(\eta; p)}{\partial \eta} \right)^2 + \hat{f}(\eta; p) \frac{\partial^2 \hat{f}(\eta; p)}{\partial \eta^2} + \hat{g}(\eta; p) \frac{\partial^2 \hat{f}(\eta; p)}{\partial \eta^2} \\ &\quad - \left(\lambda + \varepsilon_1 (1 - \phi)^{2.5} M \frac{\sigma_{nf}}{\sigma_f} \right) \frac{\partial \hat{f}(\eta; p)}{\partial \eta}, \end{aligned} \quad (5.35)$$

$$\begin{aligned} \mathcal{N}_g \left[\hat{g}(\eta; p), \hat{f}(\eta; p) \right] &= \varepsilon_1 \frac{\partial^3 \hat{g}(\eta; p)}{\partial \eta^3} - \left(\frac{\partial \hat{g}(\eta; p)}{\partial \eta} \right)^2 + \hat{f}(\eta; p) \frac{\partial^2 \hat{g}(\eta; p)}{\partial \eta^2} + \hat{g}(\eta; p) \frac{\partial^2 \hat{g}(\eta; p)}{\partial \eta^2} \\ &\quad - \left(\lambda + \varepsilon_1 (1 - \phi)^{2.5} M \frac{\sigma_{nf}}{\sigma_f} \right) \frac{\partial \hat{g}(\eta; p)}{\partial \eta}, \end{aligned} \quad (5.36)$$

$$\begin{aligned} \mathcal{N}_\xi \left[\hat{\xi}(\eta; p), \hat{f}(\eta; p), \hat{g}(\eta; p) \right] &= \frac{1}{Sc} \frac{\partial^2 \hat{\xi}(\eta; p)}{\partial \eta^2} + \hat{f}(\eta; p) \frac{\partial \hat{\xi}(\eta; p)}{\partial \eta} + \hat{g}(\eta; p) \frac{\partial \hat{\xi}(\eta; p)}{\partial \eta} \\ &\quad - k_1 \left(\hat{\xi}(\eta; p) - 2 \left(\hat{\xi}(\eta; p) \right)^2 + \left(\hat{\xi}(\eta; p) \right)^3 \right). \end{aligned} \quad (5.37)$$

m^{th} order deformation equations can be written in the forms

$$\mathcal{L}_f [f_m(\eta) - \chi_m f_{m-1}(\eta)] = \hbar_f \mathcal{R}_{f,m}(\eta), \quad (5.38)$$

$$\mathcal{L}_g [g_m(\eta) - \chi_m g_{m-1}(\eta)] = \hbar_g \mathcal{R}_{g,m}(\eta), \quad (5.39)$$

$$\mathcal{L}_\xi [\xi_m(\eta) - \chi_m \xi_{m-1}(\eta)] = \hbar_\xi \mathcal{R}_{\xi,m}(\eta), \quad (5.40)$$

with

$$\begin{aligned} f'_m(0) - \beta_1 f''_m(0) - \beta_2 f'''_m(0) &= f_m(0) = f'_m(\infty) = 0 \\ g'_m(0) - \beta_3 g''_m(0) - \beta_4 g'''_m(0) &= g_m(0) = g'_m(\infty) = 0 \\ \xi'_m(0) - k_2 \xi_m(0) &= \xi_m(\infty) = 0, \end{aligned} \quad (5.41)$$

$$\mathcal{R}_{f,m}(\eta) = \varepsilon_1 f'''_{m-1} + \sum_{k=0}^{m-1} [f_{m-1-k} f''_k - f'_{m-1-k} f'_k + g_{m-1-k} f''_k] - \left(\lambda + \varepsilon_1 (1 - \phi)^{2.5} M \frac{\sigma_{nf}}{\sigma_f} \right) f'_{m-1}, \quad (5.42)$$

$$\mathcal{R}_{g,m}(\eta) = \varepsilon_1 g'''_{m-1} + \sum_{k=0}^{m-1} [f_{m-1-k} g''_k - g'_{m-1-k} g'_k + g_{m-1-k} g''_k] - \left(\lambda + \varepsilon_1 (1 - \phi)^{2.5} M \frac{\sigma_{nf}}{\sigma_f} \right) g'_{m-1}, \quad (5.43)$$

$$\begin{aligned} \mathcal{R}_{\xi,m}(\eta) = & \frac{1}{Sc} \xi''_{m-1} - k_1 \xi_{m-1} + \sum_{l=0}^{m-1} \left[\xi'_{m-1-l} f_l + \xi'_{m-1-l} g_l \right. \\ & \left. - k_1 \left(\xi_{m-1-l} \sum_{j=0}^l \xi_{l-j} \xi_j + 2 \xi_{m-1-l} \xi_l \right) \right], \end{aligned} \quad (5.44)$$

$$\chi_m = \begin{cases} 0, & m \leq 1 \\ 1, & m > 1 \end{cases}. \quad (5.45)$$

The general solutions (f_m, g_m, ξ_m) comprising the special solutions (f_m^*, g_m^*, ξ_m^*) are given by

$$\begin{aligned} f_m(\eta) &= f_m^*(\eta) + c_1 + c_2 e^\eta + c_3 e^{-\eta}, \\ g_m(\eta) &= g_m^*(\eta) + c_4 + c_5 e^\eta + c_6 e^{-\eta}, \\ \xi_m(\eta) &= \xi_m^*(\eta) + c_7 e^\eta + c_8 e^{-\eta}, \end{aligned} \quad (5.46)$$

where the constants c_i ($i = 1, 2, \dots, 8$) through the boundary conditions (5.41) have the values

$$\begin{aligned} c_2 &= c_5 = c_7 = 0, \quad c_1 = -c_3 - f_m^*(0), \quad c_4 = -c_6 - g_m^*(0), \\ c_3 &= \frac{1}{1 + \beta_1 - \beta_2} \left(\frac{\partial f_m^*(\eta)}{\partial \eta} - \beta_1 \frac{\partial^2 f_m^*(\eta)}{\partial \eta^2} - \beta_2 \frac{\partial^3 f_m^*(\eta)}{\partial \eta^3} \right) \Big|_{\eta=0}, \\ c_6 &= \frac{1}{1 + \beta_3 - \beta_4} \left(\frac{\partial g_m^*(\eta)}{\partial \eta} - \beta_3 \frac{\partial^2 g_m^*(\eta)}{\partial \eta^2} - \beta_4 \frac{\partial^3 g_m^*(\eta)}{\partial \eta^3} \right) \Big|_{\eta=0}, \\ c_8 &= \frac{1}{1 + k_2} \left(\frac{\partial \xi_m^*(\eta)}{\partial \eta} \Big|_{\eta=0} - k_2 \xi_m^*(0) \right). \end{aligned} \quad (5.47)$$

5.3 Convergence analysis

Homotopy analysis technique provides us great freedom and an easy way to adjust and control the convergence region of the series solutions. The auxiliary parameters \hbar_f , \hbar_g and \hbar_ξ play an important role for the convergence of the series solutions. Therefore, we have sketched the \hbar -curves at 10^{th} -order of approximations (see Fig. 5.1). The admissible ranges of the auxiliary parameters are $-1.4 \leq \hbar_f \leq -0.2$, $-1.5 \leq \hbar_g \leq -0.2$ and $-1.9 \leq \hbar_\xi \leq -0.8$. Also the HAM

solutions converge in the whole region of η ($0 < \eta < \infty$) when $\hbar_f = \hbar_g = -1$ and $\hbar_\xi = -1.2$. Table 5.1 shows the convergence of series solutions of momentum and concentration equations. It is noted that 14th order of approximations are sufficient for the convergence of functions $f''(0)$, $g''(0)$ and $\theta'(0)$.

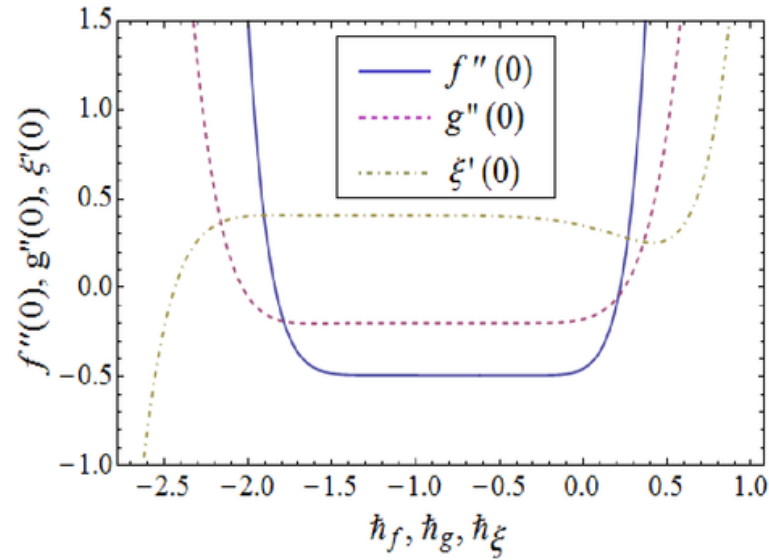


Fig. 5.1: \hbar -curves for $f''(0)$, $g''(0)$ and $\theta'(0)$ when $\phi = M = 0.5$, $\lambda = \beta_2 = \gamma = 0.3$, $S = \beta_1 = Sc = 0.9$, $k_1 = k_2 = 0.7$, $\beta_3 = -0.3$ and $\beta_4 = -0.2$.

Table 5.1: Convergence of HAM solutions for different order of approximations when $\phi = M = 0.5$, $\lambda = \beta_2 = \gamma = 0.3$, $S = \beta_1 = Sc = 0.9$, $k_1 = k_2 = 0.7$, $\beta_3 = -0.3$ and $\beta_4 = -0.2$.

Order of approximations	$-f''(0)$	$-g''(0)$	$\xi'(0)$
1	0.507202	0.200061	0.364126
5	0.491527	0.198039	0.395551
10	0.491387	0.197965	0.396517
14	0.491389	0.197965	0.396476
20	0.491389	0.197965	0.396476
26	0.491389	0.197965	0.396476
30	0.491389	0.197965	0.396476
35	0.491389	0.197965	0.396476
40	0.491389	0.197965	0.396476
45	0.491389	0.197965	0.396476

5.4 Results and discussion

This section presents the behavior of various involved parameters on the velocities along x - and y - directions and concentration in the form of graphical and tabulated results (see Figs. (5.2 – 5.15) and Tables (5.2 – 5.5)).

5.4.1 Dimensionless velocity profiles

The effects of nanoparticle volume fraction ϕ on both the x - and y - components of velocity f' and g' are depicted in Fig. 5.2. It is observed that velocity profiles decrease when ϕ is increased. Behaviors of porosity parameter λ on velocity profiles f' and g' are displayed in Fig. 5.3. An increase in the porosity parameter leads to the lower permeability parameter which decreases the fluid motion. Hence velocity profiles decreases. Fig. 5.4 displays the velocity profiles for different values of M . The applied magnetic field has the tendency to slow down the movement of the fluid which decreases the velocities and momentum boundary layer thickness. The influence of suction/injection velocity parameter S on f' and g' can be visualized in the Fig. 5.5. It is obvious that an increase in S reduces the velocity fields. Here applying suction leads to draw the amount of the fluid particles into the wall and consequently the velocity

fields decrease. From Figs. (5.6 – 5.9), we have seen that larger values of first order slip velocity parameters and magnitude of second order slip velocity parameters correspond to lower velocity. With an increase in slip velocity parameters, stretching velocity is partially transferred to the fluid so velocity profiles decrease. Fig. 5.10 illustrates the impact of stretching rates ratio γ on the velocity fields. Increasing values of γ indicates higher rate of stretching along the y -direction in comparison to x -direction. Therefore the velocity along x -direction f' decreases and velocity along y -direction g' increases when stretching rates ratio is increased.

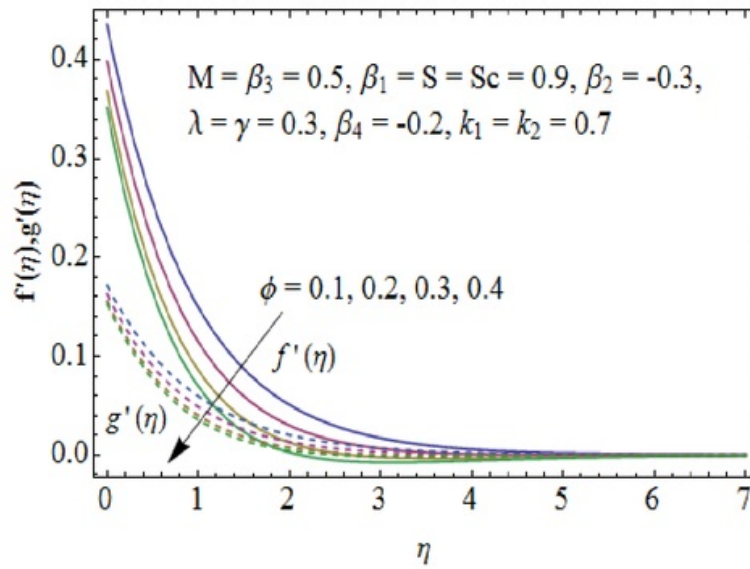


Fig. 5.2: Variation of ϕ on $f'(\eta)$ and $g'(\eta)$.

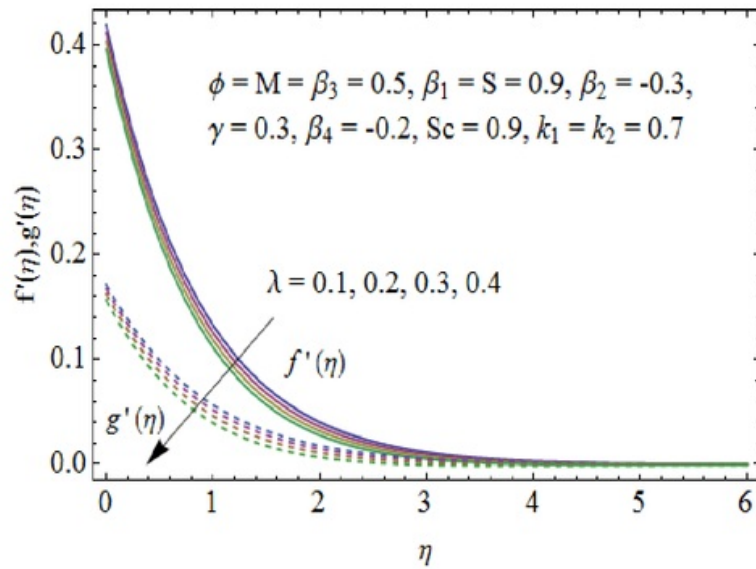


Fig. 5.3: Variation of λ on $f'(\eta)$ and $g'(\eta)$.

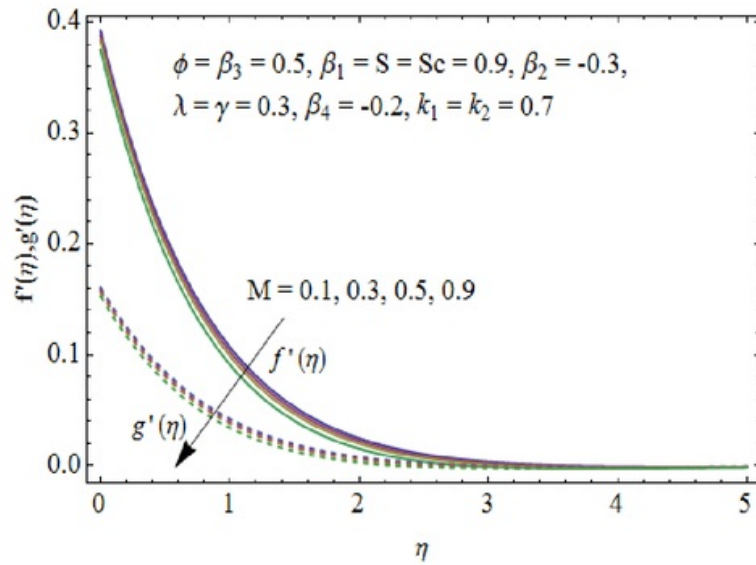


Fig. 5.4: Variation of M on $f'(\eta)$ and $g'(\eta)$.

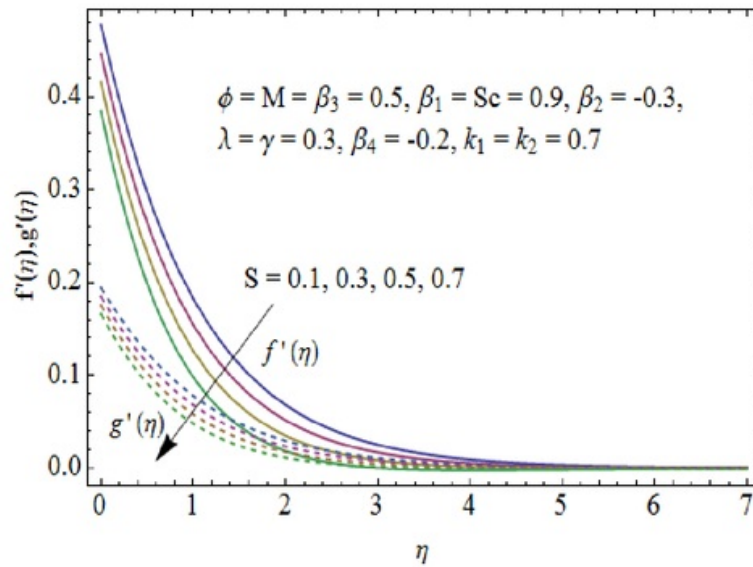


Fig. 5.5: Variation of S on $f'(\eta)$ and $g'(\eta)$.

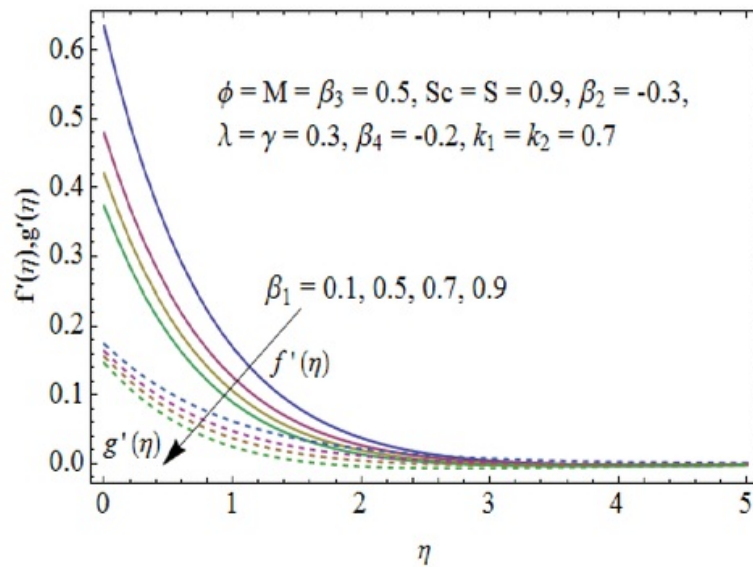


Fig. 5.6: Variation of β_1 on $f'(\eta)$ and $g'(\eta)$.

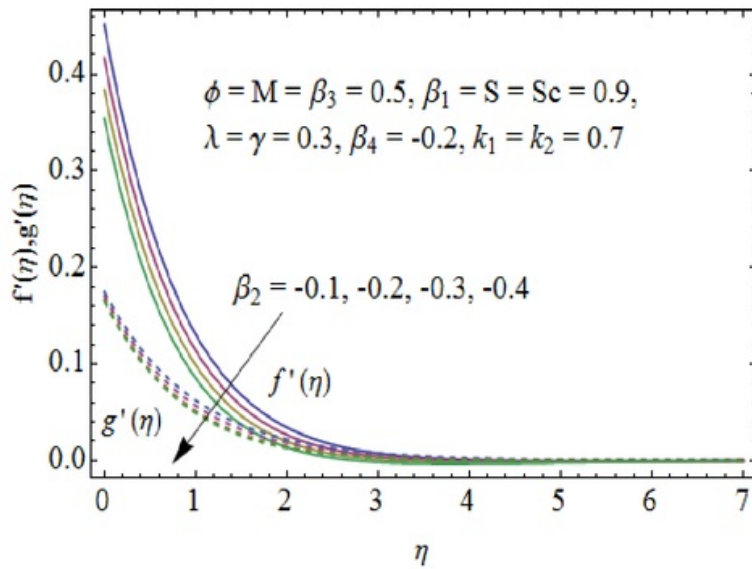


Fig. 5.7: Variation of β_2 on $f'(\eta)$ and $g'(\eta)$.

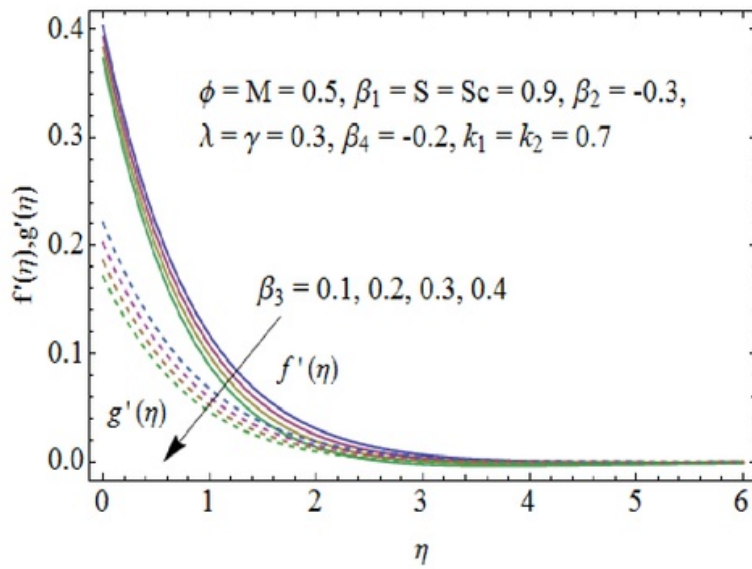


Fig. 5.8: Variation of β_3 on $f'(\eta)$ and $g'(\eta)$.

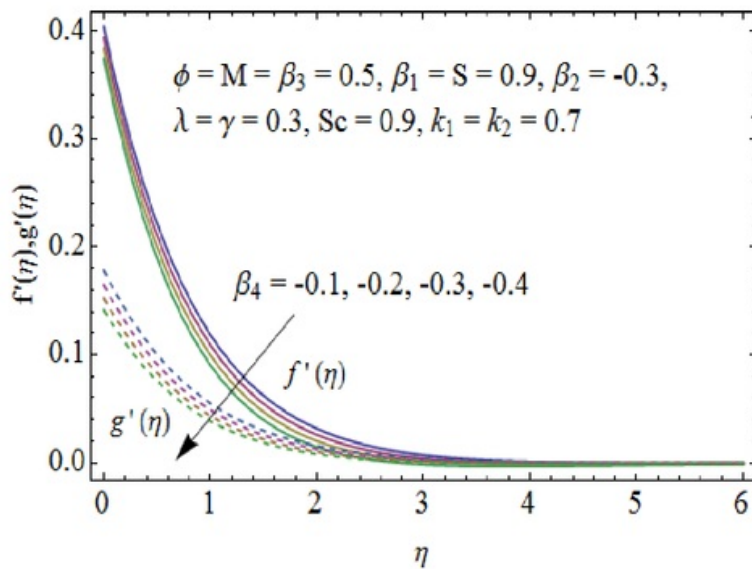


Fig. 5.9: Variation of β_4 on $f'(\eta)$ and $g'(\eta)$.

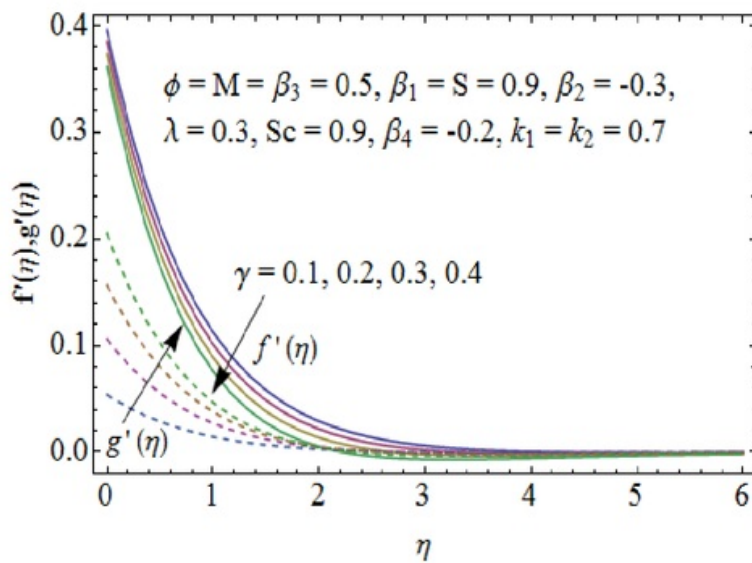


Fig. 5.10: Variation of γ on $f'(\eta)$ and $g'(\eta)$.

5.4.2 Dimensionless concentration profiles

Figs. (5.11–5.13) exhibit the dimensionless concentration profile for different values of measure of the strength of the homogeneous reaction k_1 , measure of the strength of the heterogeneous reaction k_2 and Schmidt number Sc . Effect of the strength of the homogeneous reaction k_1 on the concentration is analyzed in Fig. 5.11. There is a decrease in concentration when k_1 is increased. Fig. 5.12 illustrates the variation of measure of the strength of the heterogeneous reaction k_2 on concentration field ξ . Here concentration profile enhances with an increase in k_2 . Effect of Schmidt number Sc on concentration profile is shown in Fig. 5.13. Increasing behavior of concentration profile is noted for larger Schmidt number. In fact Schmidt number is the ratio of momentum diffusivity to mass diffusivity, so higher values of Schmidt number correspond to small mass diffusivity. Therefore concentration profile increases.

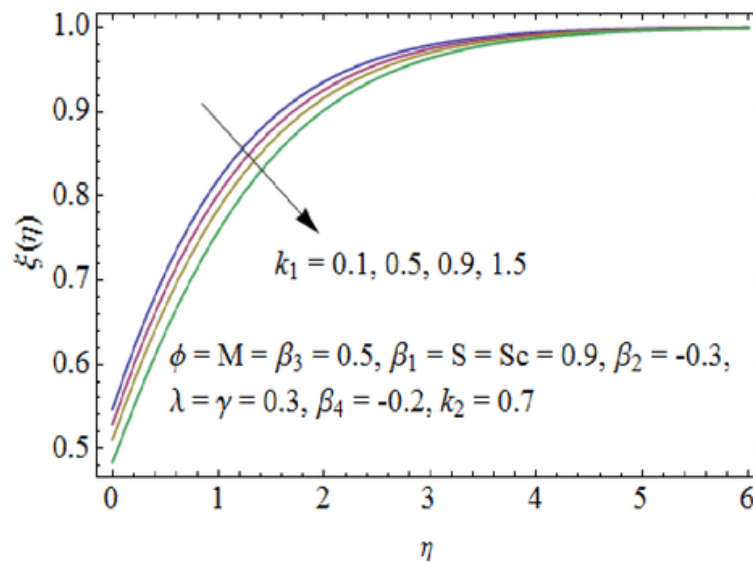


Fig. 5.11: Variation of k_1 on $\xi(\eta)$.

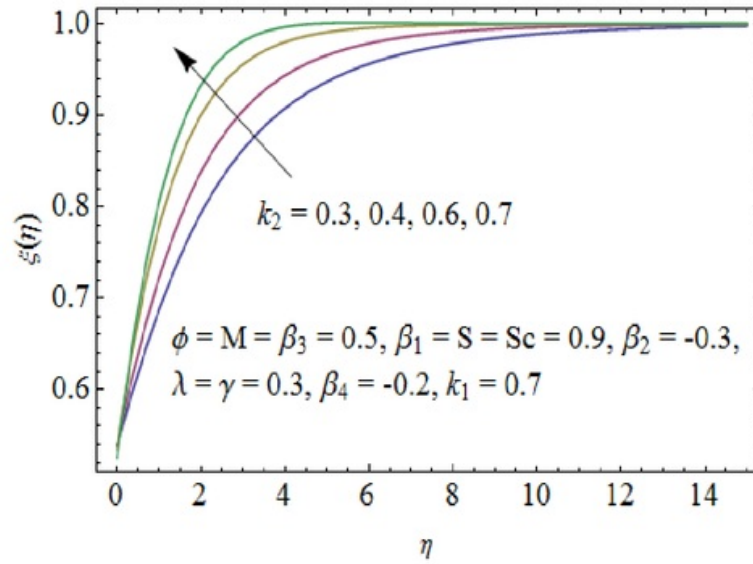


Fig. 5.12: Variation of k_2 on $\xi(\eta)$.

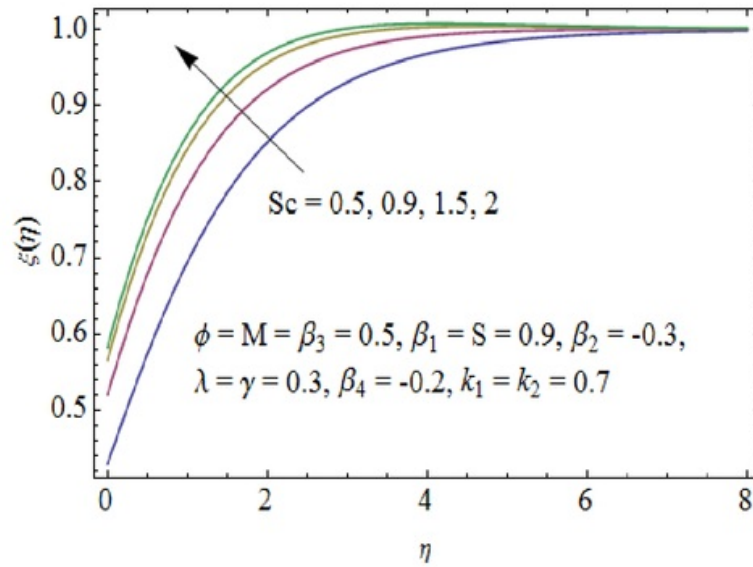


Fig. 5.13: Variation of Sc on $\xi(\eta)$.

5.4.3 Surface concentration and skin friction coefficient

The variation of dimensionless wall concentration $\xi(0)$ for different values of the strength of heterogeneous reaction parameter k_2 , strength of homogeneous reaction parameter k_1 and Schmidt number Sc are shown in Figs. 5.14 and 5.15 respectively. One can see from these Figs. that $\xi(0)$ decreases with the increase of the parameters k_1 and k_2 . Some thermo physical properties of water and nanoparticles are given in Table 5.2. Effects of the nanoparticle volume fraction for different types of nanofluids on skin friction coefficient along x - and y - directions are presented in Tables 5.3 and 5.4. Here we see that magnitude of skin friction coefficient increases with the increase in ϕ . Numerical values of skin friction coefficient for different values of first and second order slip velocity parameters, porosity parameter, Hartman number and suction/injection parameter are presented in Table 5.5. It is noted that the skin friction coefficients decrease for increasing values of first order slip velocity parameters and magnitude of second order slip velocity parameters while it increases for larger porosity parameter, Hartman number and suction/injection parameter.

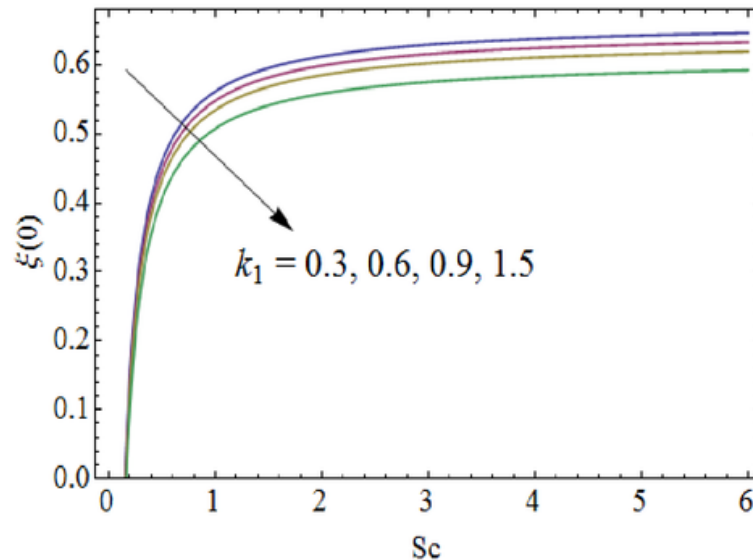


Fig. 5.14: Variation of k_1 and Sc on $\xi(0)$.

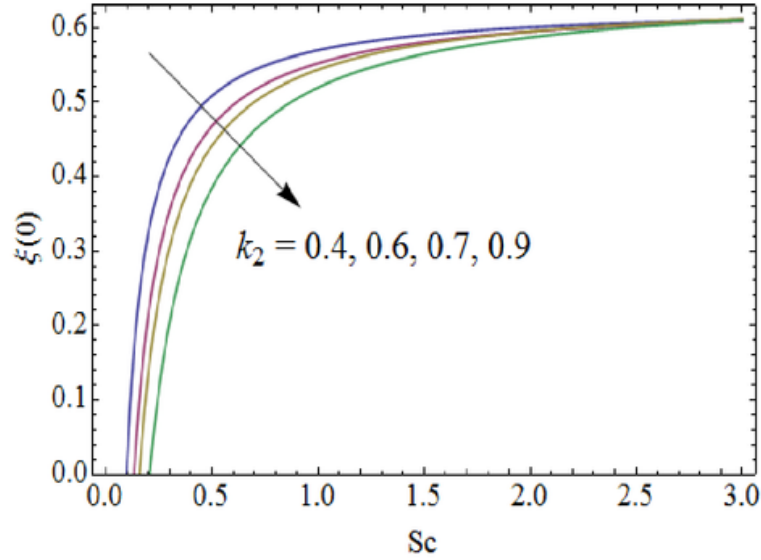


Fig. 5.15: Variation of k_2 and Sc on $\xi(0)$.

Table 5.2: Thermo physical properties of water and nanoparticles [].

	$\rho(kg/m^3)$	$c_p(j/kgk)$	$k(W/m.k)$	$\beta \times 10^5(K^{-1})$	$\sigma(\Omega m)^{-1}$
Pure water	997.1	4179	0.613	21	0.05
Copper(<i>Cu</i>)	8933	385	401	1.67	5.96×10^7
Silver(<i>Ag</i>)	10500	235	429	1.89	3.6×10^7
Alumina(Al_2O_3)	3970	765	40	0.85	1×10^{-10}
Titanium Oxide(TiO_2)	4250	686.2	8.9538	0.9	1×10^{-12}

Table 5.3: Effects of the nanoparticle volume fraction for different types of nanofluids on skin friction coefficient along x -direction when $M = \beta_3 = 0.5$, $\lambda = \gamma = 0.3$, $S = \beta_1 = Sc = 0.9$, $k_1 = k_2 = 0.7$, $\beta_2 = -0.3$ and $\beta_4 = -0.2$.

ϕ	<i>Cu</i>	<i>Ag</i>	Al_2O_3	TiO_2
0.1	-0.6555	-0.6543	-0.6516	-0.6521
0.2	-0.8795	-0.8757	-0.8684	-0.8703
0.3	-1.229	-1.226	-1.191	-1.195

Table 5.4: Effects of the nanoparticle volume fraction for different types of nanofluids on skin friction coefficient along y -direction when $M = \beta_3 = 0.5$, $\lambda = \gamma = 0.3$, $S = \beta_1 = Sc = 0.9$, $k_1 = k_2 = 0.7$, $\beta_2 = -0.3$ and $\beta_4 = -0.2$.

ϕ	Cu	Ag	Al_2O_3	TiO_2
0.1	-1.704	-1.714	-1.645	-1.650
0.2	-2.296	-2.310	-2.164	-2.176
0.3	-3.184	-3.215	-2.906	-2.931

Table 5.5: Numerical values of skin friction coefficient for different values of $\beta_1, \beta_2, \beta_3, \beta_4, \lambda, M$ and S .

β_1	β_2	β_3	β_4	λ	M	S	$-C_{fx}(Re_x)^{1/2}$	$-C_{fy}(Re_y)^{1/2}$
0.3	-0.3	0.5	-0.2	0.3	0.5	0.9	3.979	6.896
0.5							3.477	6.863
0.7							3.089	6.837
0.9	-0.1						3.203	6.844
	-0.2						2.974	6.829
	-0.3						2.779	6.815
	-0.3	0.1					2.789	9.314
		0.4					2.781	7.306
		0.7					2.776	6.008
		0.5	-0.1				2.781	7.403
			-0.3				2.777	6.19
			-0.5				2.774	5.526
			-0.2	0.1			2.748	6.641
				0.4			2.791	6.887
				0.5			2.802	6.949
				0.3	0.3		2.774	6.784
					0.7		2.784	6.845
					0.9		2.789	6.871
					0.5	0.2	2.592	5.906
						0.4	2.656	6.199
						0.7	2.737	6.691

5.5 Conclusions

Here flow of Cu-water nanofluid induced by bidirectional stretching surface is investigated. The effects of homogeneous-heterogeneous reactions and second order velocity slip are also taken into account. The key points are summarized as follows:

- Velocity profiles f' and g' are decreasing functions of velocity slip parameters and nanoparticle volume fraction.
- The velocity component f' decreases while g' increases for larger stretching rates ratio.
- Concentration of the reactants decreases for higher values of strength of homogeneous reaction parameter.
- Strength of heterogeneous reaction parameter results in the enhancement of concentration profile.
- There is an enhancement in concentration profile when Schmidt number increases.
- Concentration at the surface decreases for increasing values of the strengths of homogeneous and heterogeneous reaction parameters.
- Skin friction coefficients decrease for increasing values of first and second order velocity slip parameters.

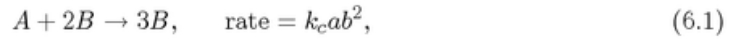
Chapter 6

Effects of homogeneous-heterogeneous reactions in flow of magnetite- Fe_3O_4 nanoparticles by a rotating disk

This chapter investigates the flow of ferrofluid due to a rotating disk in the presence of homogeneous-heterogeneous reactions. Water is used as base fluid while magnetite- Fe_3O_4 as nanoparticle. Fluid is electrically conducting in the presence of applied magnetic field. Effects of viscous dissipation are also considered. Appropriate transformations reduce the nonlinear partial differential system to ordinary differential system. Convergent series solutions are computed for the resulting nonlinear problems. Effects of different parameters on the velocity, temperature and concentration profiles are shown and analyzed. Computations for skin friction coefficient and Nusselt number are presented and examined for the influences of pertinent parameters. It is noted that concentration distribution decreases for larger values of strength of homogeneous reaction parameter while it increases for strength of heterogeneous reaction parameter. Skin friction coefficient and rate of heat transfer are enhanced when the strength of magnetic field is increased.

6.1 Model development

Here we consider an incompressible flow of ferrofluid induced by a rotating disk at $z = 0$. Magnetite- Fe_3O_4 nanoparticles in water are known as ferrofluid. The disk rotates with constant angular velocity Ω about the z -axis. Components of flow velocity are (u, v, w) in the direction of increasing (r, Θ, z) , respectively. A uniform magnetic field of strength B_0 is applied parallel to the z -axis. It is assumed that the induced magnetic field and the electric field effects are negligible. Effects of viscous dissipation are taken into account. The disk is kept at uniform temperature T_w while temperature far away from the disk is T_∞ . In view of the rotational symmetry, the derivatives in the azimuthal direction are neglected. Flow analysis is carried out with homogeneous-heterogeneous reactions of two chemical species A and B . The homogeneous reaction for cubic autocatalysis can be expressed as follows [73]:



while first-order isothermal reaction on the catalyst surface is presented in the form



where a and b are the concentrations of the chemical species A and B and k_c and k_s are the rate constants. We assume that both reaction processes are isothermal. Under these assumptions the relevant mass, momentum, energy and concentration equations are

$$\frac{\partial u}{\partial r} + \frac{u}{r} + \frac{\partial w}{\partial z} = 0, \quad (6.3)$$

$$\rho_{nf} \left(u \frac{\partial u}{\partial r} - \frac{v^2}{r} + w \frac{\partial u}{\partial z} \right) = -\frac{\partial P}{\partial r} + \mu_{nf} \left(\frac{\partial^2 u}{\partial r^2} + \frac{1}{r} \frac{\partial u}{\partial r} - \frac{u}{r^2} + \frac{\partial^2 u}{\partial z^2} \right) - \sigma_{nf} B_0^2 u, \quad (6.4)$$

$$\rho_{nf} \left(u \frac{\partial v}{\partial r} + \frac{uv}{r} + w \frac{\partial v}{\partial z} \right) = \mu_{nf} \left(\frac{\partial^2 v}{\partial r^2} + \frac{1}{r} \frac{\partial v}{\partial r} - \frac{v}{r^2} + \frac{\partial^2 v}{\partial z^2} \right) - \sigma_{nf} B_0^2 v, \quad (6.5)$$

$$\rho_{nf} \left(u \frac{\partial w}{\partial r} + w \frac{\partial w}{\partial z} \right) = -\frac{\partial P}{\partial z} + \mu_{nf} \left(\frac{\partial^2 w}{\partial r^2} + \frac{1}{r} \frac{\partial w}{\partial r} + \frac{\partial^2 w}{\partial z^2} \right), \quad (6.6)$$

$$u \frac{\partial T}{\partial r} + w \frac{\partial T}{\partial z} = \alpha_{nf} \left(\frac{\partial^2 T}{\partial r^2} + \frac{1}{r} \frac{\partial T}{\partial r} + \frac{\partial^2 T}{\partial z^2} \right) + \frac{\mu_{nf}}{(\rho c_p)_{nf}} \left[2 \left\{ \left(\frac{\partial u}{\partial r} \right)^2 + \left(\frac{u}{r} \right)^2 + \left(\frac{\partial w}{\partial z} \right)^2 \right\} + \left(r \frac{\partial}{\partial r} \left(\frac{v}{r} \right) \right)^2 + \left(\frac{\partial v}{\partial z} \right)^2 + \left(\frac{\partial u}{\partial z} + \frac{\partial w}{\partial r} \right)^2 \right], \quad (6.7)$$

$$u \frac{\partial a}{\partial r} + w \frac{\partial a}{\partial z} = D_A \left(\frac{\partial^2 a}{\partial r^2} + \frac{1}{r} \frac{\partial a}{\partial r} + \frac{\partial^2 a}{\partial z^2} \right) - k_c a b^2, \quad (6.8)$$

$$u \frac{\partial b}{\partial r} + w \frac{\partial b}{\partial z} = D_B \left(\frac{\partial^2 b}{\partial r^2} + \frac{1}{r} \frac{\partial b}{\partial r} + \frac{\partial^2 b}{\partial z^2} \right) + k_c a b^2, \quad (6.9)$$

with boundary conditions

$$\begin{aligned} u = 0, \quad v = r\Omega, \quad w = 0, \quad T = T_w, \quad D_A \frac{\partial a}{\partial z} = k_s a, \quad D_B \frac{\partial b}{\partial z} = -k_s b \quad \text{at } z = 0, \\ u \rightarrow 0, \quad v \rightarrow 0, \quad T \rightarrow T_\infty, \quad a \rightarrow a_0, \quad b \rightarrow 0 \quad \text{as } z \rightarrow \infty, \end{aligned} \quad (6.10)$$

where P is the pressure, T is the temperature, $\alpha_{nf} = k_{nf}/(\rho c)_{nf}$ is the thermal diffusivity and a_0 is the positive dimensional constant. The effective nanofluid dynamic viscosity μ_{nf} , density ρ_{nf} , heat capacity $(\rho c_p)_{nf}$, thermal conductivity k_{nf} and electric conductivity σ_{nf} are taken as follows:

$$\mu_{nf} = \frac{\mu_f}{(1 - \phi)^{2.5}}, \quad (6.11)$$

$$\rho_{nf} = (1 - \phi)\rho_f + \phi\rho_s, \quad (6.12)$$

$$(\rho c_p)_{nf} = (1 - \phi)(\rho c_p)_f + \phi(\rho c_p)_s, \quad (6.13)$$

$$\frac{k_{nf}}{k_f} = \frac{(k_s + 2k_f) - 2\phi(k_f - k_s)}{(k_s + 2k_f) + \phi(k_f - k_s)}, \quad (6.14)$$

$$\frac{\sigma_{nf}}{\sigma_f} = 1 + \frac{3 \left(\frac{\sigma_s}{\sigma_f} - 1 \right) \phi}{\left(\frac{\sigma_s}{\sigma_f} + 2 \right) - \left(\frac{\sigma_s}{\sigma_f} - 1 \right) \phi}, \quad (6.15)$$

where ϕ denotes the solid volume fraction of nanoparticles, s in subscript is for nano-solid-particles and f in subscript is for base fluid. We now consider transformations

$$\begin{aligned} u &= r\Omega f(\eta), \quad v = r\Omega g(\eta), \quad w = \sqrt{\nu_f \Omega} H(\eta), \quad \eta = \sqrt{\frac{\Omega}{\nu_f}} z, \quad P - P_\infty = \rho_f \nu_f \Omega \tilde{P}(\eta), \\ \theta(\eta) &= \frac{T - T_\infty}{T_w - T_\infty}, \quad a = a_0 \xi(\eta), \quad b = a_0 h(\eta). \end{aligned} \quad (6.16)$$

Eqs. (6.3) – (6.10) after using Eq. (6.16) can be reduced as follows:

$$H' + 2f = 0, \quad (6.17)$$

$$\frac{1}{(1 - \phi)^{2.5} \left(1 - \phi + \phi \frac{\rho_s}{\rho_f}\right)} f'' - H f' - f^2 + g^2 - \left(\frac{\frac{\sigma_{nf}}{\sigma_f}}{1 - \phi + \phi \frac{\rho_s}{\rho_f}}\right) M f = 0, \quad (6.18)$$

$$\frac{1}{(1 - \phi)^{2.5} \left(1 - \phi + \phi \frac{\rho_s}{\rho_f}\right)} g'' - H g' - 2fg - \left(\frac{\frac{\sigma_{nf}}{\sigma_f}}{1 - \phi + \phi \frac{\rho_s}{\rho_f}}\right) M g = 0, \quad (6.19)$$

$$\frac{1}{\text{Pr}} \frac{k_{nf}}{k_f} \theta'' - \left(1 - \phi + \phi \frac{(\rho c_p)_s}{(\rho c_p)_f}\right) H \theta' + \frac{Ec}{(1 - \phi)^{2.5}} \left(f'^2 + g'^2 + \frac{1}{\text{Re}} (4f^2 + 2H'^2)\right) = 0, \quad (6.20)$$

$$\frac{1}{Sc} \xi'' - H \xi' - k_1 \xi h^2 = 0, \quad (6.21)$$

$$\frac{\delta}{Sc} h'' - H h' + k_1 \xi h^2 = 0, \quad (6.22)$$

$$\begin{aligned} H(0) &= 0, \quad f(0) = 0, \quad g(0) = 1, \quad \theta(0) = 1, \quad \xi'(0) = k_2 \xi(0), \quad \delta h'(0) = -k_2 h(0), \\ f(\infty) &\rightarrow 0, \quad g(\infty) \rightarrow 0, \quad \theta(\infty) \rightarrow 0, \quad \xi(\infty) \rightarrow 1, \quad h(\infty) \rightarrow 0, \end{aligned} \quad (6.23)$$

where $M = \sigma_f B_0^2 / \rho_f \Omega$ is the Hartman number, $\text{Pr} = \nu_f / \alpha_f$ is the Prandtl number, $Ec = (r\Omega)^2 / (T_w - T_\infty)(c_p)_f$ is the local Eckert number, $\text{Re}_r = r^2 \Omega / \nu_f$ is the local Reynolds number, $Sc = \nu_f / D_A$ is the Schmidt number, $k_1 = a_0^2 k_c / \Omega$ is the measure of strength of homogeneous reaction, $\delta = D_B / D_A$ is the ratio of diffusion coefficient and $k_2 = k_s \sqrt{\nu_f} / D_A \sqrt{\Omega}$ is the measure of strength of the heterogeneous reaction.

Here it is assumed that diffusion coefficients of chemical species A and B to be of a comparable size. This leads to make a further assumption that the diffusion coefficients D_A and D_B

are equal, i.e. $\delta = 1$ and thus

$$\xi(\eta) + h(\eta) = 1. \quad (6.24)$$

Now Eqs. (6.21) and (6.22) yield

$$\frac{1}{Sc} \xi'' - H \xi' - k_1 \xi (1 - \xi)^2 = 0, \quad (6.25)$$

with the boundary conditions

$$\xi'(0) = k_2 \xi(0), \quad \xi(\infty) \rightarrow 1. \quad (6.26)$$

The important physical quantities of interest in this problem are the local skin-friction coefficient C_{sf} and Nusselt number Nu which are given by

$$C_{sf} = \frac{\sqrt{\tau_r^2 + \tau_\theta^2}}{\rho(r\Omega)^2}, \quad Nu = \frac{rq_w}{k_f(T_w - T_\infty)}, \quad (6.27)$$

where the surface radial stress τ_r , tangential stress τ_θ and heat flux q_w are given by

$$\tau_r = \mu_{nf} \left. \frac{\partial u}{\partial z} \right|_{z=0}, \quad \tau_\theta = \mu_{nf} \left. \frac{\partial v}{\partial z} \right|_{z=0}, \quad q_w = -k_{nf} \left. \frac{\partial T}{\partial z} \right|_{z=0}. \quad (6.28)$$

In dimensionless form the local skin friction coefficient C_{sf} and Nusselt number Nu can be written as follows:

$$C_{sf}(\text{Re}_r)^{1/2} = \frac{1}{(1 - \phi)^{2.5}} \sqrt{[f'(0)]^2 + [g'(0)]^2}, \quad Nu(\text{Re}_r)^{-1/2} = -\frac{k_{nf}}{k_f} \theta'(0). \quad (6.29)$$

6.2 Solutions procedure

Initial approximations $H_0(\eta)$, $f_0(\eta)$, $g_0(\eta)$, $\theta_0(\eta)$ and $\xi_0(\eta)$ and auxiliary linear operators \mathcal{L}_H , \mathcal{L}_f , \mathcal{L}_g , \mathcal{L}_θ and \mathcal{L}_ξ are taken in the forms

$$H_0(\eta) = 0, \quad f_0(\eta) = \eta e^{-\eta}, \quad g_0(\eta) = e^{-\eta}, \quad \theta_0(\eta) = e^{-\eta}, \quad \xi_0(\eta) = 1 - \frac{1}{2} e^{-k_2 \eta}, \quad (6.30)$$

$$\mathcal{L}_H = H', \quad \mathcal{L}_f = f'' - f, \quad \mathcal{L}_g = g'' - g, \quad \mathcal{L}_\theta = \theta'' - \theta, \quad \mathcal{L}_\xi = \xi'' - \xi, \quad (6.31)$$

subject to the properties

$$\begin{aligned}
\mathcal{L}_H[c_1] &= 0 \\
\mathcal{L}_f[c_2e^\eta + c_3e^{-\eta}] &= 0, \\
\mathcal{L}_g[c_4e^\eta + c_5e^{-\eta}] &= 0, \\
\mathcal{L}_\theta[c_6e^\eta + c_7e^{-\eta}] &= 0, \\
\mathcal{L}_\xi[c_8e^\eta + c_9e^{-\eta}] &= 0,
\end{aligned} \tag{6.32}$$

in which c_i ($i = 1 - 9$) are the constants.

If $p \in [0, 1]$ indicates the embedding parameter then the zeroth order deformation problems are constructed as follows:

$$(1-p)\mathcal{L}_H[\hat{H}(\eta, p) - H_0(\eta)] = p\hbar_H\mathcal{N}_H[\hat{H}(\eta, p), \hat{f}(\eta, p), \hat{g}(\eta, p)], \tag{6.33}$$

$$(1-p)\mathcal{L}_f[\hat{f}(\eta, p) - f_0(\eta)] = p\hbar_f\mathcal{N}_f[\hat{f}(\eta, p), \hat{H}(\eta, p), \hat{g}(\eta, p)], \tag{6.34}$$

$$(1-p)\mathcal{L}_g[\hat{g}(\eta, p) - g_0(\eta)] = p\hbar_g\mathcal{N}_g[\hat{g}(\eta, p), \hat{f}(\eta, p), \hat{H}(\eta, p)], \tag{6.35}$$

$$(1-p)\mathcal{L}_\theta[\hat{\theta}(\eta, p) - \theta_0(\eta)] = p\hbar_\theta\mathcal{N}_\theta[\hat{\theta}(\eta, p), \hat{H}(\eta, p), \hat{f}(\eta, p), \hat{g}(\eta, p)], \tag{6.36}$$

$$(1-p)\mathcal{L}_\xi[\hat{\xi}(\eta, p) - \xi_0(\eta)] = p\hbar_\xi\mathcal{N}_\xi[\hat{\xi}(\eta, p), \hat{H}(\eta, p), \hat{f}(\eta, p), \hat{g}(\eta, p)], \tag{6.37}$$

$$\begin{aligned}
\hat{H}(0, p) &= 0, \hat{f}(0, p) = 0, \hat{g}(0, p) = 1, \hat{\theta}(0, p) = 1, \hat{\xi}'(0, p) = k_2\hat{\xi}(0, p), \\
\hat{f}(\infty, p) &= 0, \hat{g}(\infty, p) = 0, \hat{\theta}(\infty, p) = 0, \hat{\xi}(\infty, p) = 1,
\end{aligned} \tag{6.38}$$

where $\hbar_H, \hbar_f, \hbar_g, \hbar_\theta$ and \hbar_ξ are the nonzero auxiliary parameters and the nonlinear operators $\mathcal{N}_H, \mathcal{N}_f, \mathcal{N}_g, \mathcal{N}_\theta$ and \mathcal{N}_ξ are given by

$$\mathcal{N}_H = \frac{\partial \hat{H}(\eta, p)}{\partial \eta} + 2\hat{f}(\eta, p), \tag{6.39}$$

$$\begin{aligned} \mathcal{N}_f = & \frac{1}{(1-\phi)^{2.5} \left(1 - \phi + \phi \frac{\rho_s}{\rho_f}\right)} \frac{\partial^2 f(\eta, p)}{\partial \eta^2} - \hat{H}(\eta, p) \frac{\partial f(\eta, p)}{\partial \eta} - \left(\hat{f}(\eta, p)\right)^2 \\ & + \left(\hat{g}(\eta, p)\right)^2 - \left(\frac{\sigma_{nf}}{\sigma_f}\right) M \hat{f}(\eta, p), \end{aligned} \quad (6.40)$$

$$\begin{aligned} \mathcal{N}_g = & \frac{1}{(1-\phi)^{2.5} \left(1 - \phi + \phi \frac{\rho_s}{\rho_f}\right)} \frac{\partial^2 \hat{g}(\eta, p)}{\partial \eta^2} - \hat{H}(\eta, p) \frac{\partial \hat{g}(\eta, p)}{\partial \eta} - 2\hat{f}(\eta, p)\hat{g}(\eta, p) \\ & - \left(\frac{\sigma_{nf}}{\sigma_f}\right) M \hat{g}(\eta, p), \end{aligned} \quad (6.41)$$

$$\begin{aligned} \mathcal{N}_\theta = & \frac{1}{\text{Pr}} \frac{k_{nf}}{k_f} \frac{\partial^2 \hat{\theta}(\eta, p)}{\partial \eta^2} - \left(1 - \phi + \phi \frac{(\rho c_p)_s}{(\rho c_p)_f}\right) \hat{H}(\eta, p) \frac{\partial \hat{\theta}(\eta, p)}{\partial \eta} + \frac{Ec}{(1-\phi)^{2.5}} \left[\left(\frac{\partial \hat{f}(\eta, p)}{\partial \eta}\right)^2 \right. \\ & \left. + \left(\frac{\partial \hat{g}(\eta, p)}{\partial \eta}\right)^2 + \frac{1}{\text{Re}} \left(4 \left(\hat{f}(\eta, p)\right)^2 + 2 \left(\frac{\partial \hat{H}(\eta, p)}{\partial \eta}\right)^2 \right) \right], \end{aligned} \quad (6.42)$$

$$\mathcal{N}_\xi = \frac{1}{Sc} \frac{\partial^2 \hat{\xi}(\eta, p)}{\partial \eta^2} - \hat{H}(\eta, p) \frac{\partial \hat{\xi}(\eta, p)}{\partial \eta} - k_1 \hat{\xi}(\eta, p) \left(1 - \hat{\xi}(\eta, p)\right)^2. \quad (6.43)$$

The resulting problems at m^{th} order can be presented in the following forms

$$\mathcal{L}_H [H_m(\eta) - \chi_m H_{m-1}(\eta)] = \hbar_H \mathcal{R}_{H,m}(\eta), \quad (6.44)$$

$$\mathcal{L}_f [f_m(\eta) - \chi_m f_{m-1}(\eta)] = \hbar_f \mathcal{R}_{f,m}(\eta), \quad (6.45)$$

$$\mathcal{L}_g [g_m(\eta) - \chi_m g_{m-1}(\eta)] = \hbar_g \mathcal{R}_{g,m}(\eta), \quad (6.46)$$

$$\mathcal{L}_\theta [\theta_m(\eta) - \chi_m \theta_{m-1}(\eta)] = \hbar_\theta \mathcal{R}_{\theta,m}(\eta), \quad (6.47)$$

$$\mathcal{L}_\xi [\xi_m(\eta) - \chi_m \xi_{m-1}(\eta)] = \hbar_\xi \mathcal{R}_{\xi,m}(\eta), \quad (6.48)$$

$$H_m(0) = f_m(0) = f_m(\infty) = g_m(0) = g_m(\infty) = \theta_m(0) = \theta_m(\infty) = \xi'_m(0) - k_2 \xi_m(0) = \xi_m(\infty) = 0, \quad (6.49)$$

$$\mathcal{R}_{H,m}(\eta) = H'_{m-1} + 2f_{m-1}, \quad (6.50)$$

$$\begin{aligned} \mathcal{R}_{f,m}(\eta) &= \frac{1}{(1-\phi)^{2.5} \left(1 - \phi + \phi \frac{\rho_s}{\rho_f}\right)} f''_{m-1} - \sum_{k=0}^{m-1} [H_{m-1-k} f'_k + f_{m-1-k} f_k - g_{m-1-k} g_k] \\ &\quad - \left(\frac{\frac{\sigma_{nf}}{\sigma_f}}{1 - \phi + \phi \frac{\rho_s}{\rho_f}} \right) M f_{m-1}, \end{aligned} \quad (6.51)$$

$$\begin{aligned} \mathcal{R}_{g,m}(\eta) &= \frac{1}{(1-\phi)^{2.5} \left(1 - \phi + \phi \frac{\rho_s}{\rho_f}\right)} g''_{m-1} - \sum_{k=0}^{m-1} [H_{m-1-k} g'_k + 2f_{m-1-k} g_k] \\ &\quad - \left(\frac{\frac{\sigma_{nf}}{\sigma_f}}{1 - \phi + \phi \frac{\rho_s}{\rho_f}} \right) M g_{m-1}, \end{aligned} \quad (6.52)$$

$$\begin{aligned} \mathcal{R}_{\theta,m}(\eta) &= \frac{1}{\text{Pr}} \frac{k_{nf}}{k_f} \theta''_{m-1} - \left(1 - \phi + \phi \frac{(\rho c_p)_s}{(\rho c_p)_f}\right) \sum_{k=0}^{m-1} H_{m-1-k} \theta'_k + \frac{Ec}{(1-\phi)^{2.5}} \sum_{k=0}^{m-1} [f'_{m-1-k} f'_k \\ &\quad + g'_{m-1-k} g'_k + \frac{1}{\text{Re}} (4f_{m-1-k} f_k + 2H'_{m-1-k} H'_k)], \end{aligned} \quad (6.53)$$

$$\mathcal{R}_{\xi,m}(\eta) = \frac{1}{Sc} \xi''_{m-1} - \sum_{k=0}^{m-1} \left[H'_{m-1-k} \xi_k - k_1 \left(\xi_{m-1-l} \sum_{j=0}^l \xi_{l-j} \xi_j - 2\xi_{m-1-l} \xi_l \right) \right] - k_1 \xi_{m-1}, \quad (6.54)$$

$$\chi_m = \begin{cases} 0, & m \leq 1 \\ 1, & m > 1 \end{cases}. \quad (6.55)$$

The general solutions ($H_m, f_m, g_m, \theta_m, \xi_m$) comprising the special solutions ($H_m^*, f_m^*, g_m^*, \theta_m^*, \xi_m^*$) are

$$\begin{aligned} H_m(\eta) &= H_m^*(\eta) + c_1, \\ f_m(\eta) &= f_m^*(\eta) + c_2 e^\eta + c_3 e^{-\eta}, \\ g_m(\eta) &= g_m^*(\eta) + c_4 e^\eta + c_5 e^{-\eta}, \\ \theta_m(\eta) &= \theta_m^*(\eta) + c_6 e^\eta + c_7 e^{-\eta}, \\ \xi_m(\eta) &= \xi_m^*(\eta) + c_8 e^\eta + c_9 e^{-\eta}, \end{aligned} \quad (6.56)$$

where the constants c_i ($i = 1 - 9$) through the boundary conditions (6.49) have the values

$$\begin{aligned} c_1 &= -H_m^*(0), \quad c_2 = c_4 = c_6 = c_8 = 0, \quad c_3 = -f_m^*(0), \quad c_5 = -g_m^*(0), \\ c_7 &= \theta_m^*(0), \quad c_9 = \frac{1}{1+k_2} \left[\frac{\partial \xi_m^*(\eta)}{\partial \eta} \Big|_{\eta=0} - k_2 \xi_m^*(0) \right]. \end{aligned} \quad (6.57)$$

6.3 Convergence of series solutions

The auxiliary parameters \hbar_H , \hbar_f , \hbar_g , \hbar_θ and \hbar_ξ play an important role for convergence of series solutions. The \hbar -curves are sketched at 10th-order of approximations to obtain valid ranges of these parameters (see Fig. 6.1). Permissible values of the auxiliary parameters are $-1.1 \leq \hbar_H \leq -0.7$, $-1.1 \leq \hbar_f \leq -0.6$, $-1.2 \leq \hbar_g \leq -0.6$, $-1.1 \leq \hbar_\theta \leq -1$ and $-1.5 \leq \hbar_\xi \leq -0.5$. Further the series solutions converge in the whole region of η ($0 < \eta < \infty$) when $\hbar_H = \hbar_g = -0.7$ and $\hbar_f = \hbar_\theta = \hbar_\xi = -1$. Also Table 6.1 ensures that the series solutions are convergent up to four decimal places.

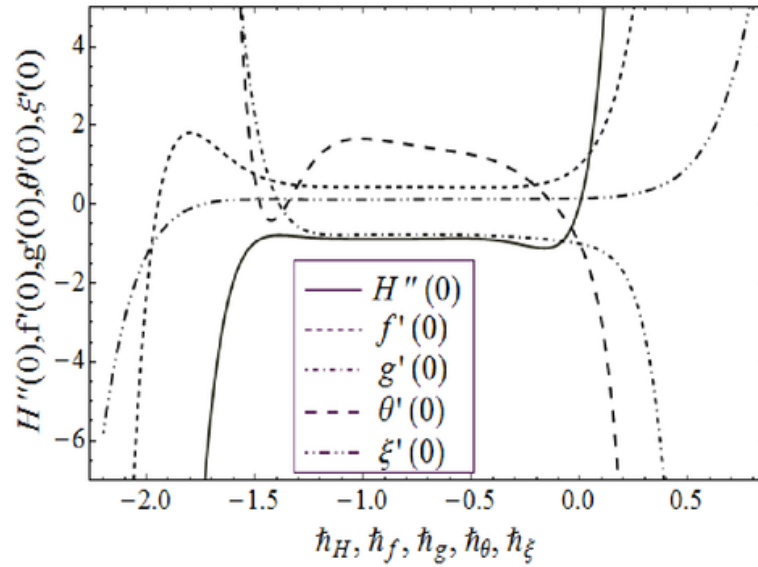


Fig. 6.1: The \hbar -curves for $H''(0)$, $f'(0)$, $g'(0)$, $\theta'(0)$ and $\xi'(0)$ when $M = k_1 = k_2 = 0.3$, $\phi = 0.2$, $Pr = 6.2$, $Ec = 0.7$ and $Re_r = Sc = 0.9$.

Table 6.1: Convergence of HAM solutions for different order of approximations when $M = k_1 = k_2 = 0.3$, $\phi = 0.2$, $Pr = 6.2$, $Ec = 0.7$ and $Re_r = Sc = 0.9$.

Order of approximations	$-H''(0)$	$f'(0)$	$-g'(0)$	$\theta'(0)$	$\xi'(0)$
1	1.400	0.4754	0.9230	0.1656	0.1349
5	0.8466	0.4276	0.7790	1.343	0.1260
10	0.8832	0.4420	0.7672	1.660	0.1208
15	0.8863	0.4434	0.7680	1.797	0.1194
20	0.8858	0.4429	0.7683	1.830	0.1190
26	0.8858	0.4429	0.7683	1.839	0.1193
30	0.8858	0.4429	0.7683	1.839	0.1193
35	0.8858	0.4429	0.7683	1.839	0.1193

6.4 Discussion

The effects of different parameters on the dimensionless velocity, temperature and concentration are examined graphically in this section. Effects of Hartman number M on the axial velocity profile $H(\eta)$ can be seen from Fig. 6.2. Here negative values of $H(\eta)$ indicate downward flow in the vertical direction. As the magnetic field has the tendency to slow down the movement of the fluid which leads to a decrease in the velocity and momentum boundary layer thickness. Fig. 6.3 illustrates the behavior of M on the radial component of velocity $f(\eta)$. There is a decrease in velocity and associated boundary layer thickness when M is increased. Also flow distribution is parabolic and positive values of $f(\eta)$ indicate radially outward flow. Fig. 6.4 depicts the distribution of azimuthal velocity $g(\eta)$ at various values of M . It is observed that $g(\eta)$ is decreasing function of Hartman number M .

Influence of Hartman number M on the temperature profile $\theta(\eta)$ is analyzed in Fig. 6.5. Since Lorentz force is a resistive force which opposes the fluid motion therefore heat is produced and consequently thermal boundary layer thickness increases. Fig. 6.6 shows that temperature is an increasing function of nanoparticle volume fraction ϕ . This is because of the fact that when the volume fraction of nanoparticles increases, the thermal conductivity enhances and consequently thermal boundary layer thickness increases. Variations of Eckert number Ec on temperature profile $\theta(\eta)$ can be seen in Fig. 6.7. When Ec is increased the temperature profile

first rises to a maximum value and then it asymptotically approaches to zero. It reveals that "Sparrow-Gregg type Hill" phenomenon exists in the presence of viscous dissipation. Fig. 6.8 represents the effect of rotational Reynolds number Re_r on temperature profile $\theta(\eta)$. Here the temperature profile and thermal boundary layer thickness decrease when Re_r is increased.

Fig. 6.9 shows the impact of strength of homogeneous reaction parameter k_1 on the concentration profile $\xi(\eta)$. Concentration decreases since the reactants are consumed during homogeneous reaction. Influence of strength of heterogeneous reaction parameter k_2 on the concentration distribution is analyzed in Fig. 6.10. It is noted that for higher values of k_2 the diffusion reduces and less diffused particles enhance the concentration. Influence of Schmidt number Sc on concentration profile $\xi(\eta)$ is shown in Fig. 6.11. Increasing behavior of concentration profile is noted for larger Schmidt number. In fact Schmidt number is the ratio of viscous diffusion rate to molecular diffusion rate. Therefore higher values of Schmidt number correspond to higher viscous diffusion rate which in turn increases the fluid concentration.

Fig. 6.12 presents the skin friction coefficient $C_{sf}(Re_r)^{1/2}$ as a function of nanoparticles volume fraction ϕ for different values of Hartman number M . When ϕ increases the magnitude of $C_{sf}(Re_r)^{1/2}$ grows in nonlinear way. Also magnitude of $C_{sf}(Re_r)^{1/2}$ is directly proportional to M . Fig. 6.13 shows local Nusselt number $Nu(Re_r)^{-1/2}$ as a function of ϕ at different values of Re_r . There is an increase in the magnitude of $Nu(Re_r)^{-1/2}$ when ϕ is increased. While magnitude of $Nu(Re_r)^{-1/2}$ has inverse relationship with Re_r .

Variations of surface concentration $\xi(0)$ via nanoparticles volume fraction ϕ for different values of the strength of homogeneous reaction parameter k_1 and strength of heterogeneous reaction parameter k_2 are shown in the Figs. 6.14 and 6.15. One can see from these Figs. that $\xi(0)$ decreases with the increase of k_1 and k_2 . It is in view of the fact that surface concentration reduces due to the consumption of reactants during homogeneous-heterogeneous reactions.

Some thermo-physical properties of water and magnetite Fe_3O_4 are given in Table 6.2. In Table 6.3 we compared the results of $f'(0)$, $g'(0)$, $H(\infty)$ and $\theta'(0)$ with existing literature in limiting sense. Obtained results are in good agreement. Table 6.4 includes the values of local Nusselt number $Nu(Re_r)^{-1/2}$ for different values of ϕ , M and Ec . It is noted that heat transfer rate enhances by increasing $Nu(Re_r)^{-1/2}$ for different values of ϕ , M and Ec .

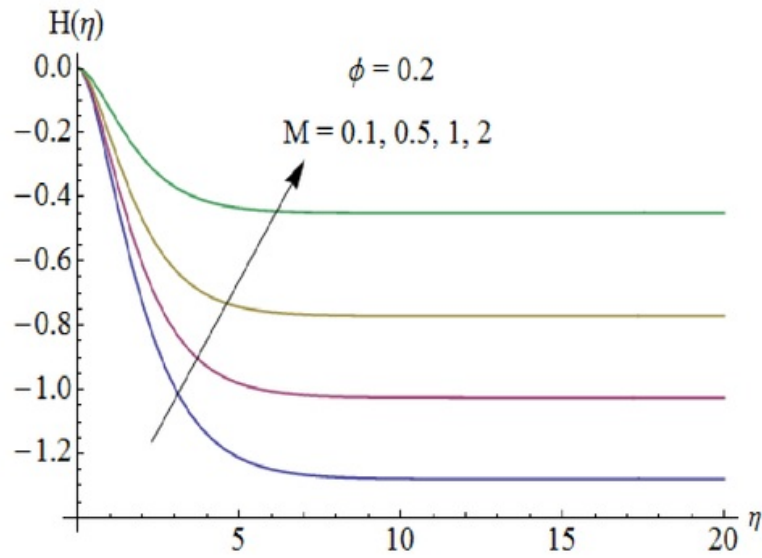
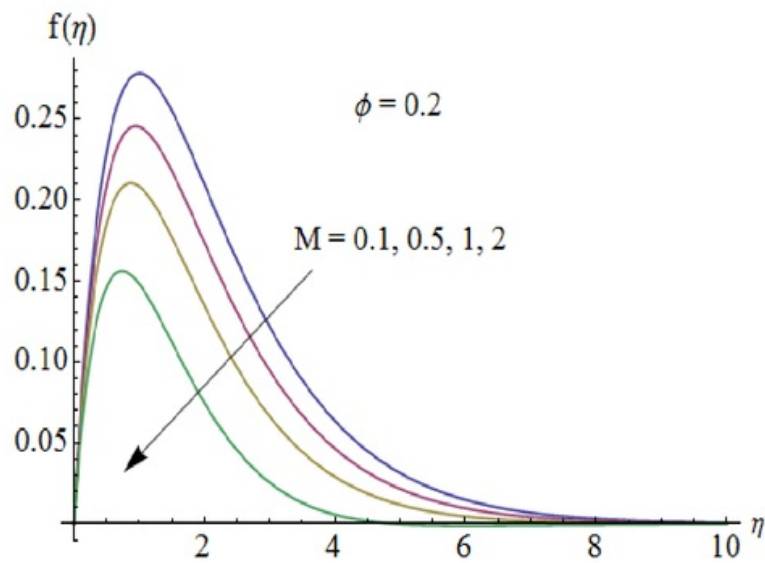


Fig. 6.2: Influence of M on $H(\eta)$.



23
Fig. 6.3: Influence of M on $f(\eta)$.

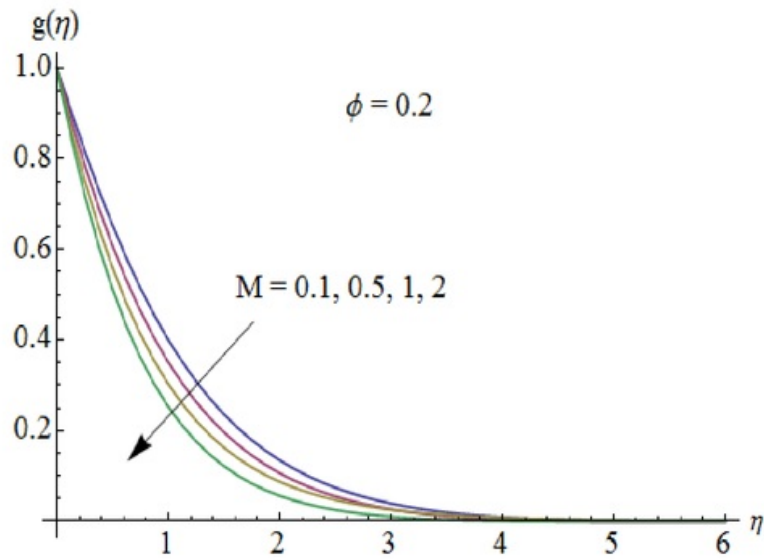
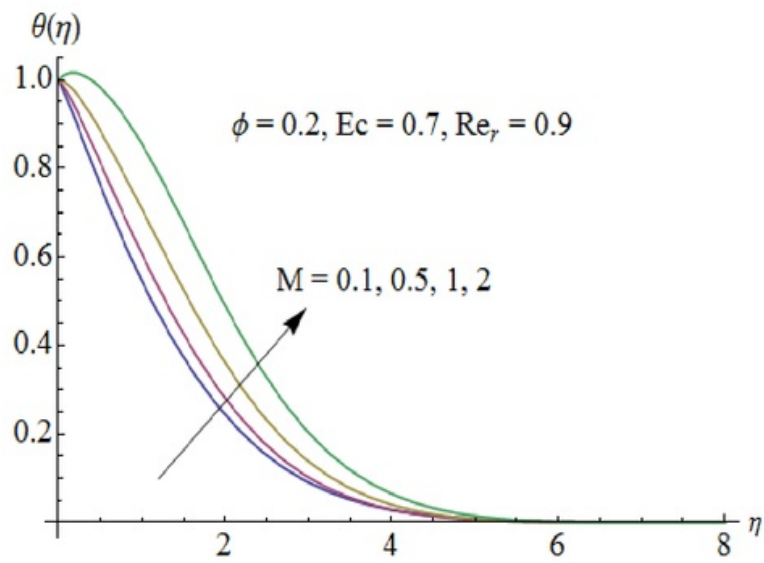


Fig. 6.4: Influence of M on $g(\eta)$.



6
 Fig. 6.5: Influence of M on $\theta(\eta)$.

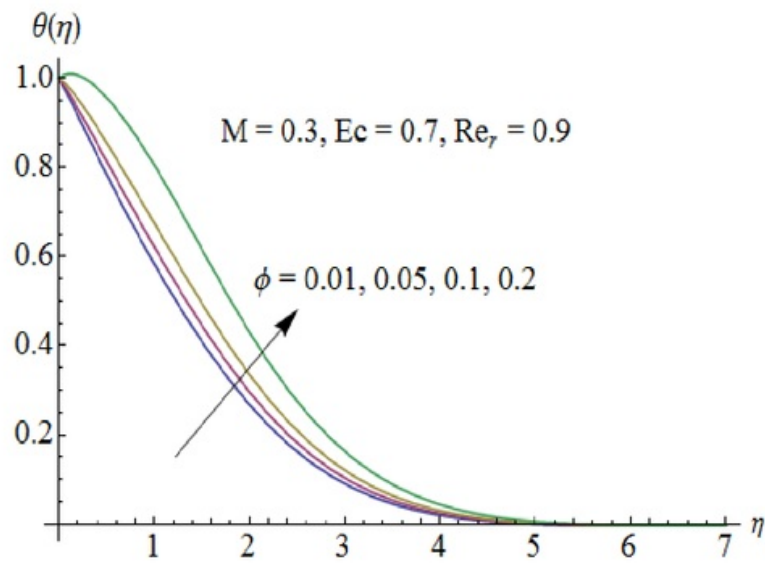
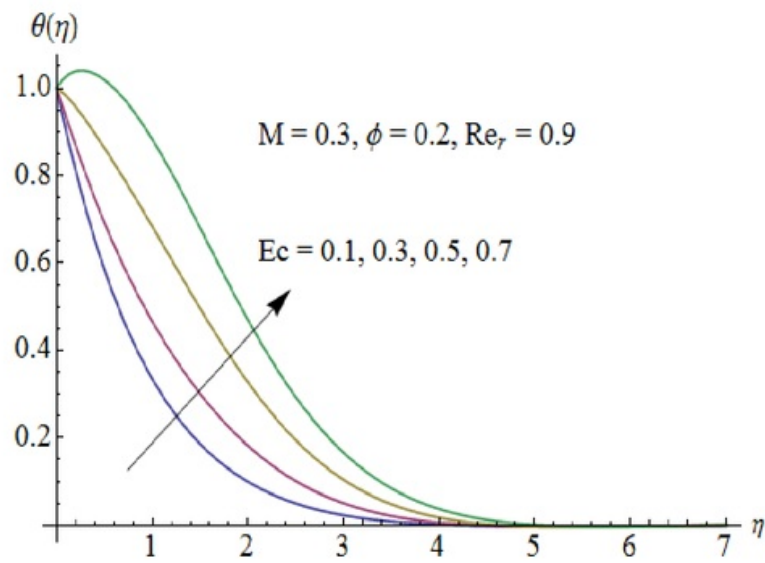


Fig. 6.6: Influence of ϕ on $\theta(\eta)$.



23
Fig. 6.7: Influence of Ec on $\theta(\eta)$.

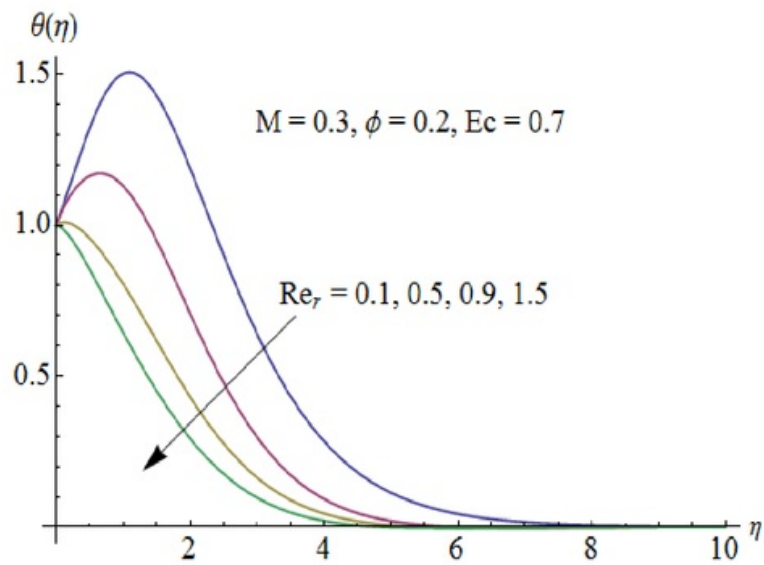


Fig. 6.8: Influence of Re_r on $\theta(\eta)$.

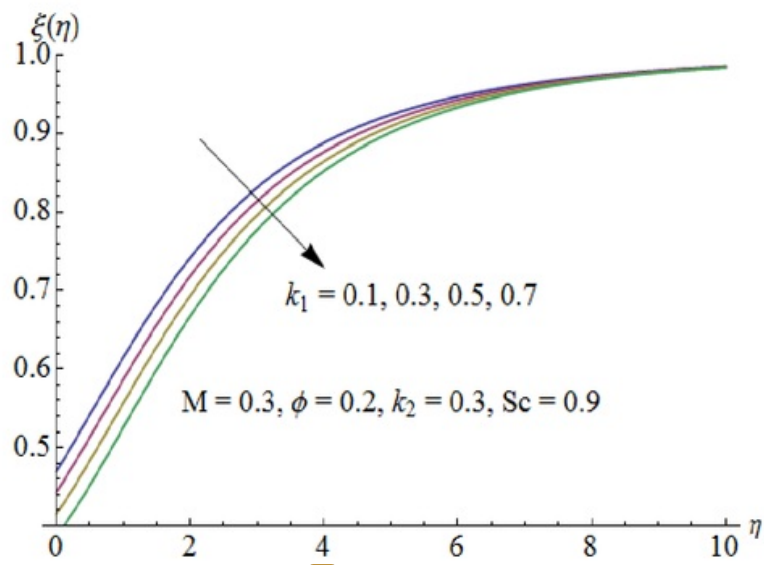


Fig. 6.9: Influence of k_1 on $\xi(\eta)$.

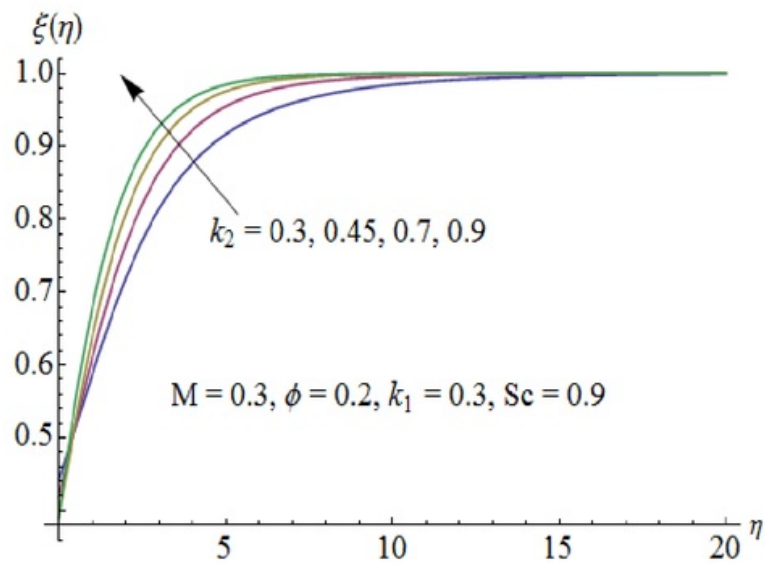


Fig. 6.10: Influence of k_2 on $\xi(\eta)$.

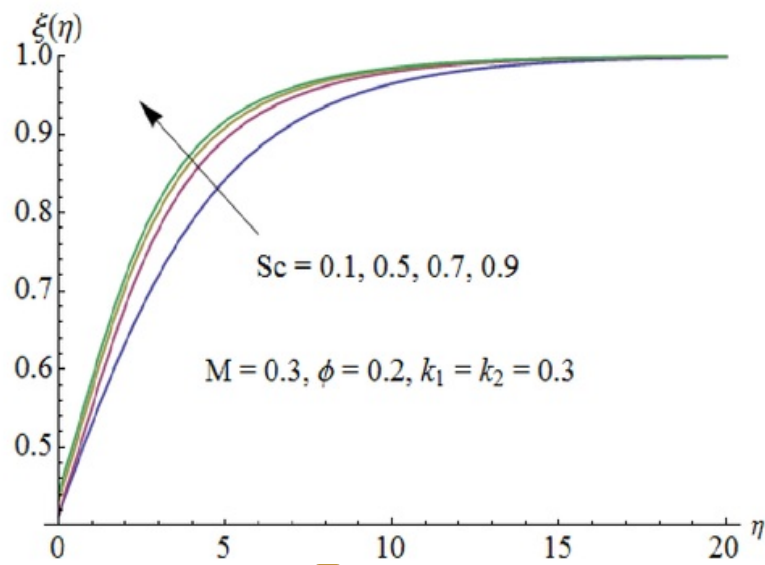


Fig. 6.11: Influence of Sc on $\xi(\eta)$.

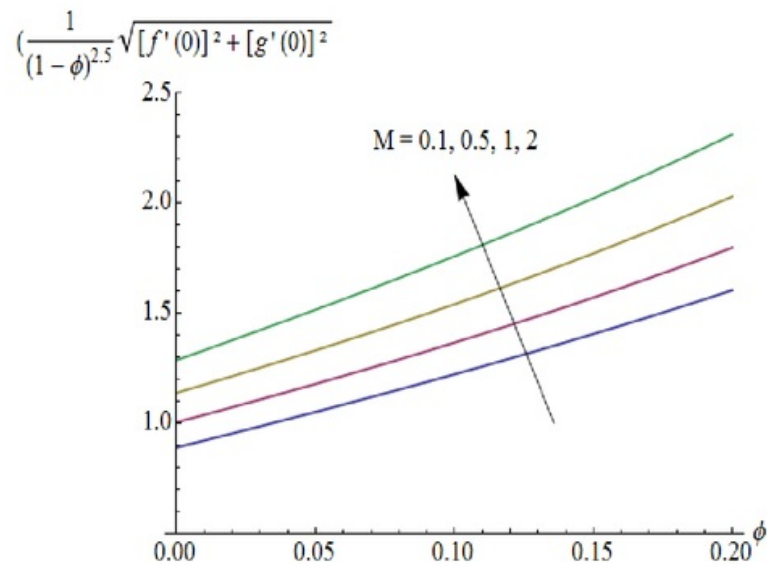


Fig. 6.12. Influence of M on $C_{sf}(\text{Re}_r)^{1/2}$.

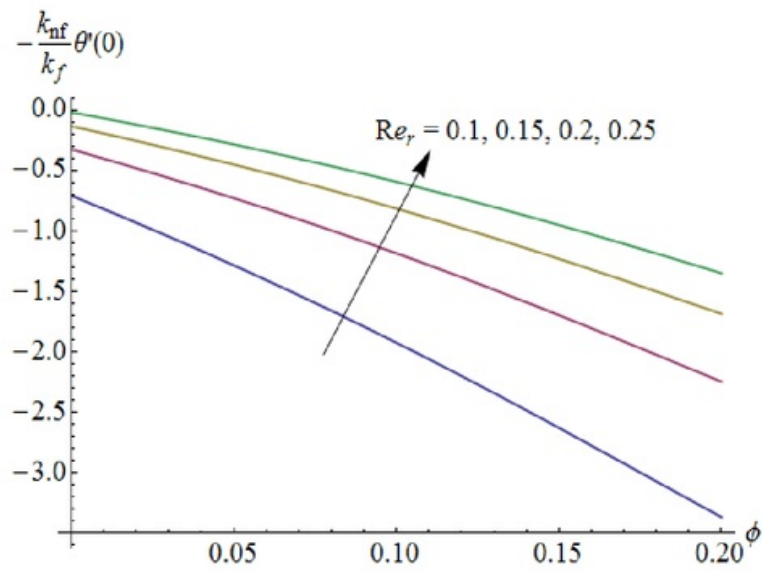


Fig. 6.13: Influence of Re_r on $Nu(\text{Re}_r)^{-1/2}$

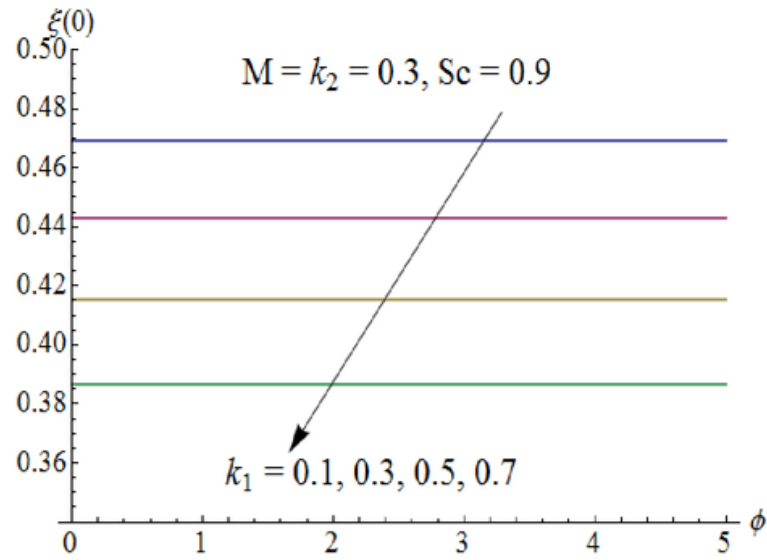


Fig. 6.14: Influence of k_1 on $\xi(0)$.

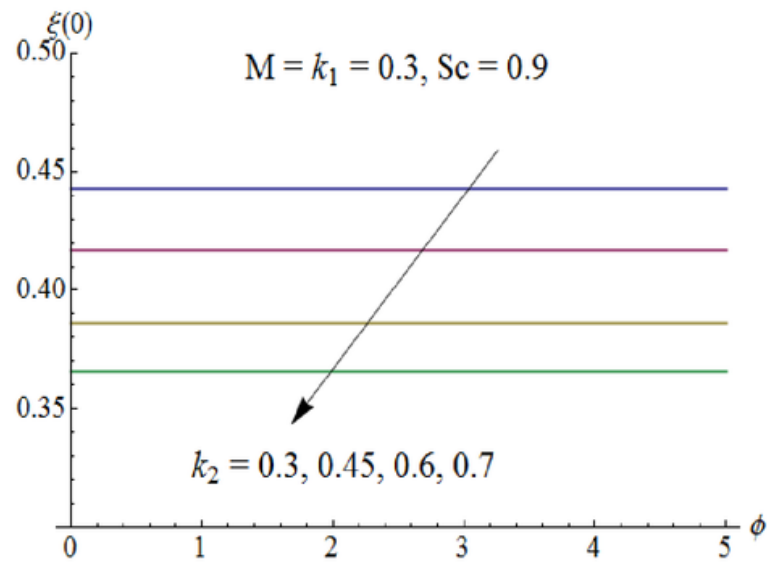


Fig. 6.15: Influence of k_2 on $\xi(0)$.

Table 6.2: Thermo-physical properties of water and magnetite Fe_3O_4 .

	$\rho(\text{kg}/\text{m}^3)$	$c_p(\text{J}/\text{kgK})$	$k(\text{W}/\text{mK})$	$\sigma(\Omega\text{m})^{-1}$
Water	997.1	4179	0.613	0.05
Fe_3O_4	5180	670	9.7	25000

Table 6.3: Comparison of present results with previously published work when $M = \phi = Ec = 0$.

	Kelson and Desseaux [53]	Bachok et al. [54]	Turkyilmazoglu [56]	Present
$f'(0)$	0.510233	0.5101	0.51023262	0.5102
$-g'(0)$	0.615922	0.6158	0.61592201	0.6160
$-H(\infty)$	0.884474	—	0.88447411	0.8843
$-\theta'(0)$	—	0.9337	0.93387794	0.9335

Table 6.4: Numerical values of Nusselt number $Nu(\text{Re}_r)^{-1/2}$ for different values of ϕ , M and Ec when $\text{Pr} = 6.2$ and $\text{Re}_r = 0.9$.

ϕ	M	Ec	$-\frac{k_{mf}\theta'(0)}{k_f}$
0	0.3	0.7	-1.189
0.05			-1.532
0.1			-1.847
0.2	0.5		-2.853
	0.7		-3.065
	1		-3.391
	0.3	0.4	-1.229
		0.6	-2.327
		0.8	-3.549

6.5 Main points

Here flow of ferrofluid induced by a rotating disk is investigated. Effects of homogeneous-heterogeneous reactions and viscous dissipation are also taken into account. The following observations are made.

- The axial, radial and azimuthal velocity profiles are decreasing function of Hartman number.
- Opposite behavior of homogeneous and heterogeneous reaction parameters are seen on the concentration profiles.
- Surface drag force has direct relationship with the strength of magnetic field.
- Heat transfer rate rises for increasing values of nanoparticles volume fraction, Hartman number and Eckert number.
- Surface concentration decreases for both the strength of homogeneous reaction parameter and the strength of heterogeneous reaction parameter.
- There is an excellent agreement between present and previously published results in limiting case when $M = \phi = Ec = 0$.

¹Chapter 7

Melting heat transfer in the MHD flow of Cu-water nanofluid with viscous dissipation and Joule heating

⁹An analysis has been carried out in this chapter for the characteristics of non-uniform melting heat transfer in the boundary layer flow of nanofluid past a stretching sheet. Water is treated as a base fluid and copper as a nanoparticle. An incompressible fluid fills the porous space. ⁵Effects of viscous dissipation and Joule heating are also examined. ¹²Fluid is electrically conducting in the presence of applied magnetic field. ⁵Appropriate transformations reduce the nonlinear partial differential system to ordinary differential system. Convergent series solutions are computed for the velocity and temperature. Effects of different parameters on the velocity and temperature profiles are shown and analyzed. ¹It is revealed that an increase in the melting parameter increases the velocity and decreases the temperature. ⁵Impact of different parameters on skin friction coefficient and Nusselt number are computed through numerical values. It is concluded that temperature gradient at the surface increases for higher Hartman number and nanoparticle volume fraction.

7.1 Model development

11 We consider the steady two-dimensional incompressible flow of nanofluid past a stretching sheet situated at $y = 0$. We have taken x - and y - axes along and perpendicular to the sheet, respectively, and the flow is confined to $y \geq 0$. It is assumed that the velocity of the stretching sheet is $u_w(x) = cx$, where c is a positive constant. We have chosen $T_\infty > T_m$ where $T_m = T_\infty - \tilde{a}x^2$ is the non-uniform temperature of the melting surface and T_∞ is the ambient temperature. Also a uniform magnetic field of intensity B_0 acts in the y -direction. The magnetic Reynolds number is assumed to be small so that the induced magnetic field is negligible in comparison with the applied magnetic field. We incorporate the Joule heating and viscous dissipation effects in the energy equation. The continuity, momentum and energy equations which govern such type of flow are written as:

$$\frac{\partial u}{\partial x} + \frac{\partial v}{\partial y} = 0, \quad (7.1)$$

$$u \frac{\partial u}{\partial x} + v \frac{\partial u}{\partial y} = \nu_{nf} \frac{\partial^2 u}{\partial y^2} - \frac{\nu_{nf}}{K} u - \frac{\sigma_{nf} B_0^2}{\rho_{nf}} u, \quad (7.2)$$

$$u \frac{\partial T}{\partial x} + v \frac{\partial T}{\partial y} = \alpha_{nf} \frac{\partial^2 T}{\partial y^2} + \frac{\mu_{nf}}{(\rho c_p)_{nf}} \left(\frac{\partial u}{\partial y} \right)^2 + \frac{\sigma_{nf} B_0^2}{(\rho c_p)_{nf}} u^2. \quad (7.3)$$

The subjected boundary conditions are

$$\begin{aligned} u &= u_w = cx, \quad v = 0, \quad T = T_m \quad \text{at } y = 0, \\ u &\rightarrow 0, \quad T \rightarrow T_\infty \quad \text{as } y \rightarrow \infty, \end{aligned} \quad (7.4)$$

and

$$k_{nf} \left(\frac{\partial T}{\partial y} \right)_{y=0} = \rho_{nf} [\Gamma + c_s(T_m - T_0)v(x, 0)], \quad (7.5)$$

7 where u and v are the velocity components along the x - and y - directions respectively, K is the permeability of porous medium, c is the stretching constant, $\Gamma = \Gamma_0 x^2$ is the non-uniform latent heat of the fluid and c_s is the heat capacity of the solid surface. The boundary condition (7.5) shows that the heat conducted to the melting surface is equal to the heat of melting plus the sensible heat required to raise the solid temperature $T_0 = T_m - \tilde{b}x^2$ to its melting temperature

T_m .

The effective nanofluid dynamic viscosity μ_{nf} , density ρ_{nf} , thermal diffusivity α_{nf} , heat capacitance $(\rho c_p)_{nf}$, thermal conductivity k_{nf} and electrical conductivity σ_{nf} are

$$\mu_{nf} = \frac{\mu_f}{(1 - \phi)^{2.5}}, \quad (7.6)$$

$$\rho_{nf} = \rho_f(1 - \phi) + \rho_s\phi, \quad (7.7)$$

$$\alpha_{nf} = \frac{k_{nf}}{(\rho c_p)_{nf}}, \quad (7.8)$$

$$(\rho c_p)_{nf} = (\rho c_p)_f(1 - \phi) + (\rho c_p)_s\phi, \quad (7.9)$$

$$\frac{k_{nf}}{k_f} = \frac{k_s + 2k_f - 2\phi(k_f - k_s)}{k_s + 2k_f + 2\phi(k_f - k_s)}, \quad (7.10)$$

$$\frac{\sigma_{nf}}{\sigma_f} = 1 + \frac{3 \left(\frac{\sigma_s}{\sigma_f} - 1 \right) \phi}{\left(\frac{\sigma_s}{\sigma_f} + 2 \right) - \left(\frac{\sigma_s}{\sigma_f} - 1 \right) \phi}, \quad (7.11)$$

where ϕ denotes the solid volume fraction of nanoparticles. Here the subscripts nf represents the thermophysical properties of the nanofluid, f explains base fluid and s is defined as nano solid particles. We now introduce the following similarity transformations

$$u = cx f'(\eta), \quad v = -\sqrt{\nu_f c} f(\eta), \quad \eta = \sqrt{\frac{c}{\nu_f}} y, \quad \theta(\eta) = \frac{T - T_m}{T_\infty - T_m}, \quad (7.12)$$

Now eq. (7.1) is satisfied automatically and substituting Eq. (7.12) into Eqs. (7.2) and (7.3), we get the following ordinary differential equations:

$$\varepsilon_1 (f''' - \lambda f') - f'^2 + f f'' - M \varepsilon_1 (1 - \phi)^{2.5} \frac{\sigma_{nf}}{\sigma_f} f' = 0, \quad (7.13)$$

$$\frac{1}{Pr} \frac{k_{nf}}{k_f} \varepsilon_2 (1 - \phi)^{2.5} \theta'' + f \theta' - 2 f' \theta + 2 f' + \varepsilon_2 Ec M (1 - \phi)^{2.5} \frac{\sigma_{nf}}{\sigma_f} f'^2 + \varepsilon_2 Ec f''^2 = 0, \quad (7.14)$$

where prime indicates the differentiation with respect to η , λ is the porosity parameter, M is the Hartman number, Pr is the Prandtl number and Ec is the Eckert number. These quantities

are defined as

$$\lambda = \frac{\nu_f}{cK}, \quad M = \frac{\sigma_f B_0^2}{c\rho_f}, \quad \text{Pr} = \frac{\nu_f}{\alpha_f}, \quad Ec = \frac{\rho_f u_w^2}{(\rho c_p)_f (T_\infty - T_m)} = \frac{\rho_f c^2}{(\rho c_p)_f \bar{a}}, \quad (7.15)$$

The boundary conditions (7.4) and (7.5) become

$$\begin{aligned} f'(0) &= 1, \quad \epsilon_3 \text{Pr} f(0) + \frac{k_{nf}}{k_f} \epsilon \theta'(0) = 0, \quad \theta(0) = 0, \\ f'(\infty) &\rightarrow 0, \quad \theta(\infty) \rightarrow 1, \end{aligned} \quad (7.16)$$

where ϵ is the dimensionless melting parameter

$$\epsilon = \frac{c_f(T_\infty - T_m)}{\Gamma + c_s(T_m - T_0)} = \frac{c_f \bar{a}}{\Gamma_0 + c_s \bar{b}}, \quad (7.17)$$

which is a combination of the Stefan numbers $c_f(T_\infty - T_m)/\Gamma$ and $c_s(T_m - T_0)/\Gamma$ for the liquid and solid phases, respectively. When $\phi = 0$ we obtain the governing equations for a viscous fluid. Also

$$\epsilon_1 = \frac{1}{(1 - \phi)^{2.5} \left(1 - \phi + \frac{\rho_s}{\rho_f} \phi\right)}, \quad \epsilon_2 = \frac{1}{(1 - \phi)^{2.5} \left(1 - \phi + \frac{(\rho c_p)_s}{(\rho c_p)_f} \phi\right)}, \quad \epsilon_3 = 1 - \phi + \frac{\rho_s}{\rho_f} \phi, \quad (7.18)$$

Local skin friction coefficient C_{sf} and Nusselt number Nu are given by

$$C_{sf} = \frac{\tau_w}{\rho u_w^2}, \quad Nu = \frac{x q_w}{k_{nf} (T_\infty - T_m)}, \quad (7.19)$$

where the surface shear stress τ_w and wall heat flux q_w are given by

$$\tau_w = \mu_{nf} \frac{\partial u}{\partial y} \Big|_{y=0}, \quad q_w = -k_{nf} \frac{\partial T}{\partial y} \Big|_{y=0}. \quad (7.20)$$

By using the above equations we get

$$C_{sf}(\text{Re}_x)^{1/2} = \frac{1}{(1 - \phi)^{2.5}} f''(0), \quad Nu(\text{Re}_x)^{-1/2} = -\frac{k_{nf}}{k_f} \theta'(0), \quad (7.21)$$

where $\text{Re}_x = x\sqrt{a/\nu_f}$ is the local Reynolds number.

7.2 HAM Solution

The initial approximations $f_0(\eta)$ and $\theta_0(\eta)$ and auxiliary linear operators \mathcal{L}_f and \mathcal{L}_θ are taken as follows:

$$f_0(\eta) = 1 - e^{-\eta} - \frac{k_{nf}\delta}{k_f \varepsilon_3 \text{Pr}}, \quad \theta_0(\eta) = 1 - e^{-\eta}, \quad (7.22)$$

$$\mathcal{L}_f = f''' - f', \quad \mathcal{L}_\theta = \theta'' - \theta, \quad (7.23)$$

with

$$\begin{aligned} \mathcal{L}_f [c_1 + c_2 e^\eta + c_3 e^{-\eta}] &= 0, \\ \mathcal{L}_\theta [c_4 e^\eta + c_5 e^{-\eta}] &= 0, \end{aligned} \quad (7.24)$$

in which c_i ($i = 1 - 5$) are the constants.

If $p \in [0, 1]$ indicates the embedding parameter then the zeroth order deformation problems are established as follows:

$$(1 - p)\mathcal{L}_f [\hat{f}(\eta; p) - f_0(\eta)] = p\hbar_f \mathcal{N}_f[\hat{f}(\eta; p)], \quad (7.25)$$

$$(1 - p)\mathcal{L}_\theta [\hat{\theta}(\eta; p) - \theta_0(\eta)] = p\hbar_\theta \mathcal{N}_\theta[\hat{\theta}(\eta; p), \hat{f}(\eta; p)], \quad (7.26)$$

$$\hat{f}'(0; p) = 1, \quad \varepsilon_3 \text{Pr} \hat{f}(0; p) + \frac{k_{nf}}{k_f} \varepsilon \hat{\theta}'(0; p) = 0, \quad \hat{f}'(\infty; p) = 0, \quad (7.27)$$

$$\hat{\theta}(0; p) = 0, \quad \hat{\theta}(\infty; p) = 1, \quad (7.28)$$

where nonzero auxiliary parameters are represented as \hbar_f and \hbar_θ and \mathcal{N}_f and \mathcal{N}_θ are the nonlinear operators given as

$$\begin{aligned} \mathcal{N}_f [\hat{f}(\eta; p)] &= \varepsilon_1 \left(\frac{\partial^3 \hat{f}(\eta; p)}{\partial \eta^3} - \lambda \frac{\partial \hat{f}(\eta; p)}{\partial \eta} \right) - \left(\frac{\partial \hat{f}(\eta; p)}{\partial \eta} \right)^2 + \hat{f}(\eta; p) \frac{\partial^2 \hat{f}(\eta; p)}{\partial \eta^2} \\ &\quad - M \varepsilon_1 (1 - \phi)^{2.5} \frac{\sigma_{nf}}{\sigma_f} \frac{\partial \hat{f}(\eta; p)}{\partial \eta}, \end{aligned} \quad (7.29)$$

$$\mathcal{N}_\theta \left[\theta(\eta; p), \hat{f}(\eta; p) \right] = \frac{1}{\text{Pr}} \frac{k_{nf}}{k_f} \varepsilon_2 (1 - \phi)^{2.5} \frac{\partial^2 \hat{\theta}(\eta; p)}{\partial \eta^2} + \hat{f}(\eta; p) \frac{\partial \hat{\theta}(\eta; p)}{\partial \eta} + \varepsilon_2 Ec \left(\frac{\partial^2 \hat{f}(\eta; p)}{\partial \eta^2} \right)^2 - 2 \frac{\partial \hat{f}(\eta; p)}{\partial \eta} \hat{\theta}(\eta; p) + 2 \frac{\partial \hat{f}(\eta; p)}{\partial \eta} + \varepsilon_2 EcM (1 - \phi)^{2.5} \frac{\sigma_{nf}}{\sigma_f} \left(\frac{\partial \hat{f}(\eta; p)}{\partial \eta} \right)^2 \quad (7.30)$$

The m^{th} order deformation problems can be written as

$$\mathcal{L}_f [f_m(\eta) - \chi_m f_{m-1}(\eta)] = \hbar_f \mathcal{R}_{f,m}(\eta), \quad (7.31)$$

$$\mathcal{L}_\theta [\theta_m(\eta) - \chi_m \theta_{m-1}(\eta)] = \hbar_\theta \mathcal{R}_{\theta,m}(\eta), \quad (7.32)$$

$$f'_m(0) = \varepsilon_3 \text{Pr} f_m(0) + \frac{k_{nf}}{k_f} \varepsilon \theta'_m(0) = f'_m(\infty) = \theta_m(0) = \theta_m(\infty) = 0, \quad (7.33)$$

$$\mathcal{R}_{f,m}(\eta) = \varepsilon_1 (f'''_{m-1} - \lambda f'_{m-1}) + \sum_{k=0}^{m-1} [f_{m-1-k} f''_k - f'_{m-1-k} f'_k] - M \varepsilon_1 (1 - \phi)^{2.5} \frac{\sigma_{nf}}{\sigma_f} f'_{m-1}, \quad (7.34)$$

$$\begin{aligned} \mathcal{R}_{\theta,m}(\eta) &= \frac{1}{\text{Pr}} \frac{k_{nf}}{k_f} \varepsilon_2 (1 - \phi)^{2.5} \theta''_{m-1} + \sum_{k=0}^{m-1} f_{m-1-k} \theta'_k + \varepsilon_2 Ec \sum_{k=0}^{m-1} f''_{m-1-k} f''_k \\ &+ \varepsilon_2 EcM (1 - \phi)^{2.5} \frac{\sigma_{nf}}{\sigma_f} \sum_{k=0}^{m-1} f'_{m-1-k} f'_k, \end{aligned} \quad (7.35)$$

$$\chi_m = \begin{cases} 0, & m \leq 1 \\ 1, & m > 1 \end{cases}. \quad (7.36)$$

The general solutions (f_m, θ_m) comprising the special solutions (f_m^*, θ_m^*) are

$$\begin{aligned} f_m(\eta) &= f_m^*(\eta) + c_1 + c_2 e^\eta + c_3 e^{-\eta}, \\ \theta_m(\eta) &= \theta_m^*(\eta) + c_4 e^\eta + c_5 e^{-\eta}. \end{aligned} \quad (7.37)$$

7.3 Convergence of HAM solution

Homotopy analysis method is employed to obtain the solutions of Eqs. (7.13) and (7.14) along with the boundary conditions (7.16). The auxiliary parameters \hbar_f and \hbar_θ play an important role for the convergence of the series solutions. \hbar -curves are sketched at 14th-order of ap

proximations to get valid ranges of these parameters (see Fig. 7.1). The permissible values of auxiliary parameters are $-1.5 \leq \hbar_f \leq -0.85$ and $-1.2 \leq \hbar_\theta \leq -1$. The residual errors are calculated for momentum and energy equations by the expressions

$$\begin{aligned}\Delta_m^f &= \int_0^1 [R_m^f(\eta, \hbar_f)]^2 d\eta, \\ \Delta_m^\theta &= \int_0^1 [R_m^\theta(\eta, \hbar_\theta)]^2 d\eta.\end{aligned}\tag{7.38}$$

In Figs. (7.2 – 7.3), the \hbar -curves for residual error of f and θ are sketched in order to get the admissible range for \hbar . It is noted that correct result up to 4th decimal place is obtained by choosing the values of \hbar from this range. Also, the HAM solutions converge in the whole region of η ($0 < \eta < \infty$) when $\hbar_f = -1.5$ and $\hbar_\theta = -1$. Table 7.1 is prepared to check the convergence of obtained HAM solutions. This table shows that convergence is attained for the functions $f''(0)$ and $\theta'(0)$ at 24th and 40th order of approximations respectively.

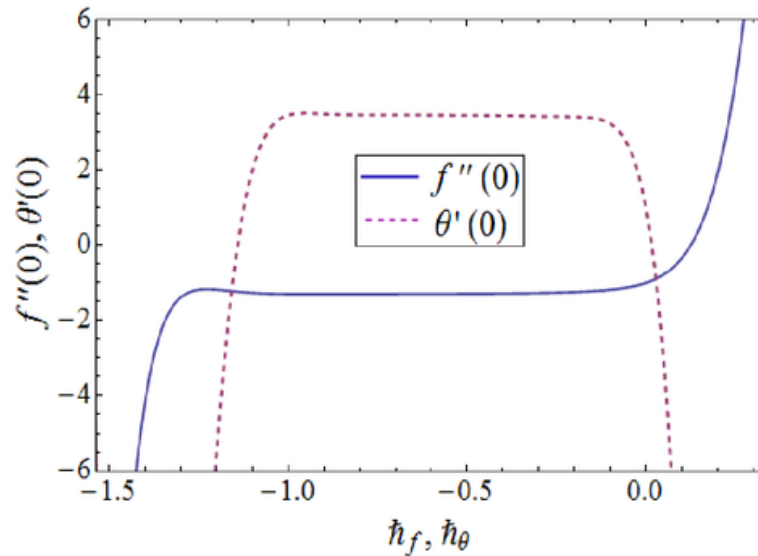


Fig. 7.1: Combined \hbar -curves for velocity and temperature when $M = 0.7$, $\lambda = 0.3$, $Ec = \epsilon = 0.5$ and $\phi = 0.1$.

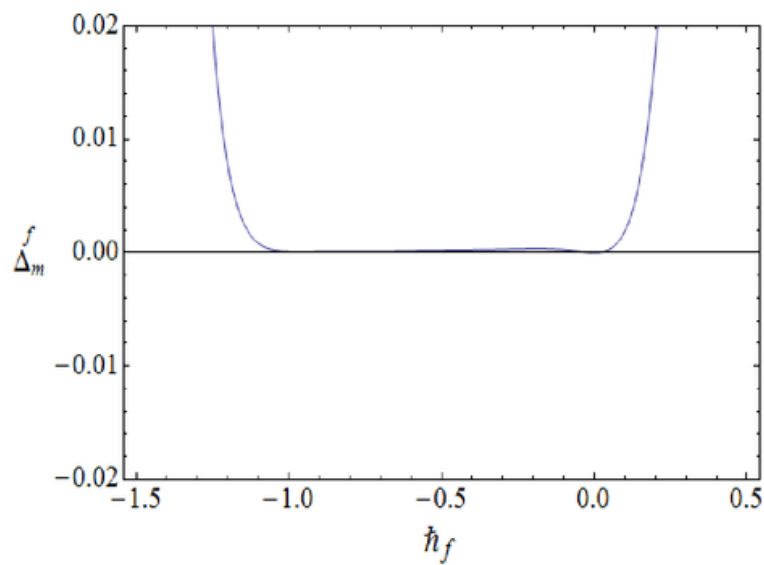


Fig. 7.2: \hbar_f -curve for the residual error Δ_m^f .

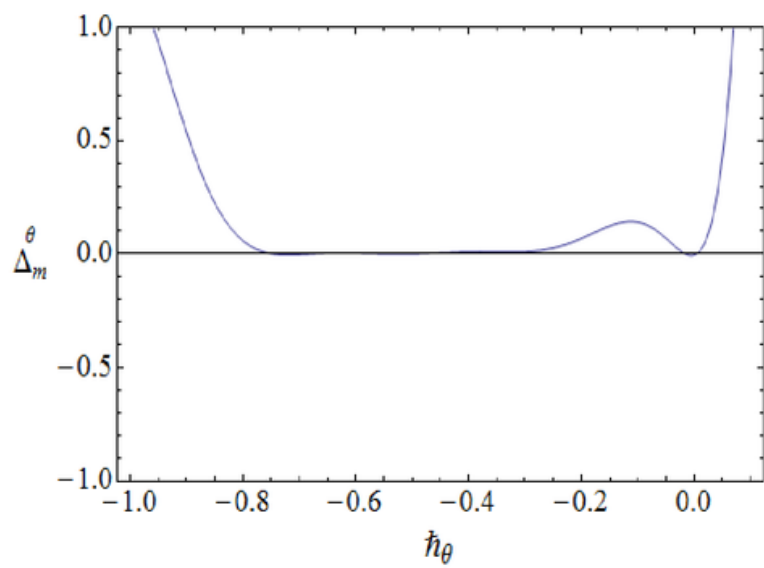


Fig. 7.3: \hbar_θ -curve for the residual error Δ_m^θ .

Table 7.1: Convergence of HAM solutions for different order of approximations when $M = 0.7$, $\lambda = 0.3$, $Ec = \epsilon = 0.5$ and $\phi = 0.1$.

Order of approximations	$-f''(0)$	$\theta'(0)$
1	1.225	3.215
5	1.286	3.433
10	1.296	3.467
15	1.300	3.475
20	1.302	3.479
25	1.303	3.481
32	1.304	3.483
40	1.309	3.484
50	1.309	3.484

7.4 Results and discussion

This section presents the effects of various parameters on the velocity, temperature, skin friction coefficient and Nusselt number in the form of graphical and tabulated results (see Figs. (7.4 – 7.17) and Table 7.2).

7.4.1 Dimensionless velocity field

Fig. (7.4 – 7.7) exhibit the dimensionless velocity profiles for different values of porosity parameter λ , Hartman number M , nanoparticle volume fraction ϕ and melting parameter ϵ . Fig. 7.4 displays the velocity profiles for different values of porosity parameter λ . The porosity parameter depends on the permeability parameter K . An increase in the porosity parameter leads to the lower permeability parameter. This lower permeability parameter causes a reduction in the fluid velocity. Fig. 7.5 illustrates the influence of Hartman number M on the velocity $f'(\eta)$. As the applied magnetic field is a resistive force which reduces the fluid motion, so the velocity field decreases. The effects of nanoparticle volume fraction ϕ on the velocity field $f'(\eta)$ are depicted in the Fig. 7.6. It is evident that an increase in the values of nanoparticle volume fraction corresponds to a decrease in the velocity profile $f'(\eta)$. The effect of Melting parameter ϵ is seen in Fig. 7.7. It is quite obvious from the Fig. that larger values of ϵ increase the velocity

profile. It is because of the fact that an increase in melting causes an increase in the molecular motion which enhances the flow.

7.4.2 Dimensionless temperature field

Effects of Eckert number Ec , Hartman number M , nanoparticle volume fraction ϕ and melting parameter ϵ on the temperature profile θ are shown in the Figs. (7.8 – 7.11). Fig. 7.8 depicts that temperature is an increasing function of the Eckert number Ec . Eckert number is defined as the ratio of kinetic energy to enthalpy. With the increase in Ec , kinetic energy increases which consequently enhances temperature. Effect of Hartman number M on the temperature is analyzed in Fig. 7.9. As the Lorentz force opposes the fluid motion, so heat is produced and as a result, the thermal boundary layer thickness increases. Fig. 7.10 illustrates the variation of nanoparticle volume fraction ϕ on temperature field θ . Here temperature profile θ increases for an increase in ϕ . Because there is enhancement in thermal conductivity by increasing the volume fraction of nanoparticles, so thermal boundary layer thickness enhances. Fig. 7.11 shows the variations of melting parameter ϵ on temperature profile. It is noted that temperature profile decreases for larger values of melting parameter due to the fact that temperature difference increases between ambient and melting surface which reduces the temperature of the fluid. Further the thermal boundary layer thickness increases when melting parameter is increased.

7.4.3 Skin friction coefficient and Nusselt number

Figs. (7.12 – 7.14) represent variation of skin friction coefficient for larger values of porosity parameter, nanoparticles volume fraction and melting parameter. It is observed that λ and ϕ are increasing functions of $f''(0)$ whereas with the increase of ϵ it decreases. The variation of heat transfer rate for Ec , ϵ and ϕ is shown in Figs. (7.15 – 7.17). It is found that the Nusselt number decreases with the increase of ϵ , while it increases by increasing Ec and ϕ .

Some thermo physical properties of water and copper are given in Table 7.2. CPU time in seconds is given for different order of approximations in Table 7.3. Table 7.4 presents some numerical values of $-C_{sf}(Re_x)^{1/2}$ and $-Nu(Re_x)^{-1/2}$ for different parameters. It is noted here that magnitude of skin friction coefficient increases for higher Cu -nanoparticles volume fraction ϕ , Hartman number M and porosity parameter λ . However it decreases when Eckert number Ec

and melting parameter ϵ are increased. The increase in the values of Cu -nanoparticles volume fraction ϕ , Hartman number M , porosity parameter λ and Eckert number Ec enhances the magnitude of local Nusselt number. Furthermore rate of heat transfer decreases when melting parameter ϵ is increased.

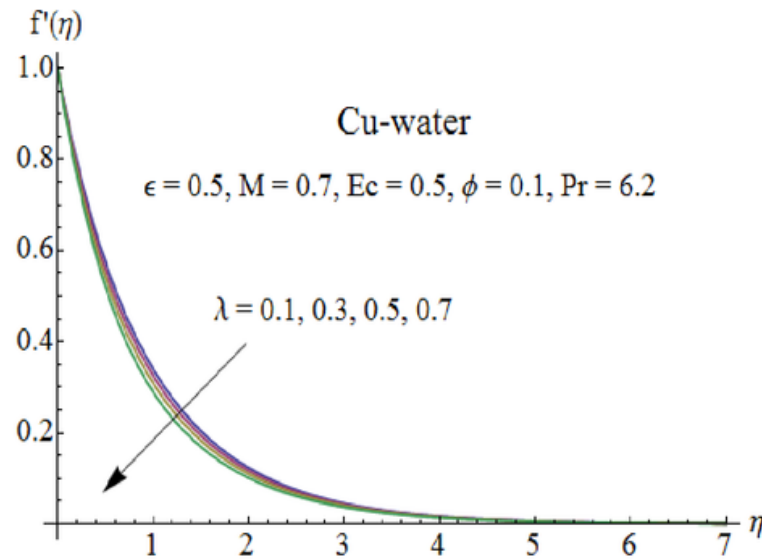


Fig. 7.4: Influence of λ on velocity field.

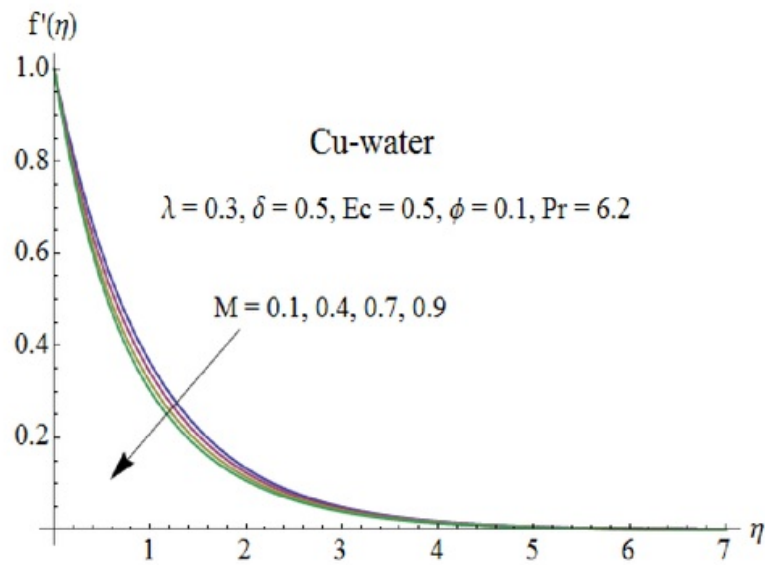


Fig. 7.5: Influence of M on velocity field.

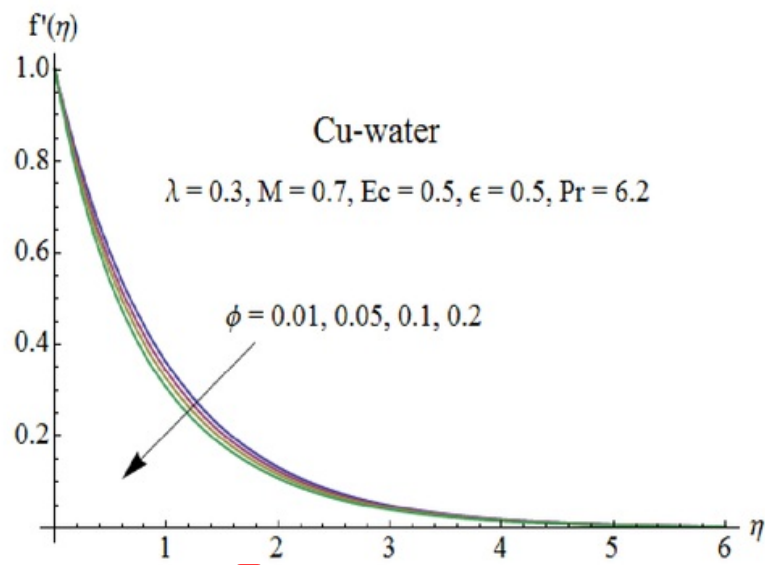


Fig. 7.6: Influence of ϕ on velocity field.

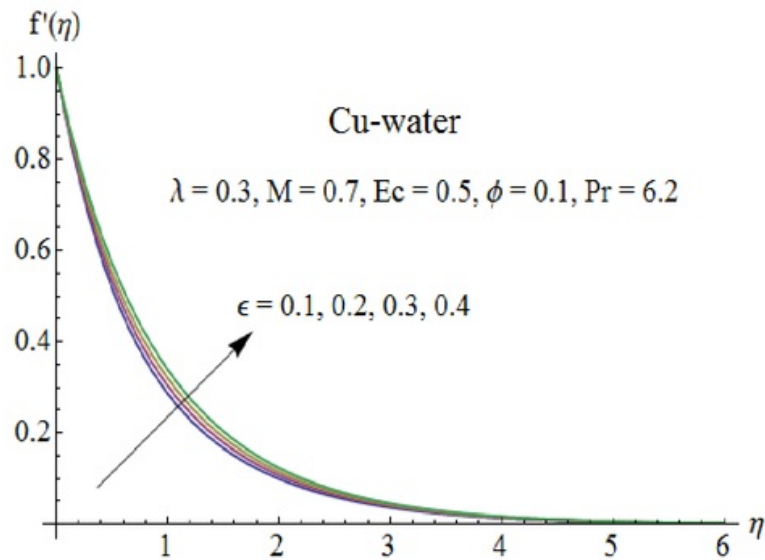


Fig. 7.7: Influence of ϵ on velocity field.

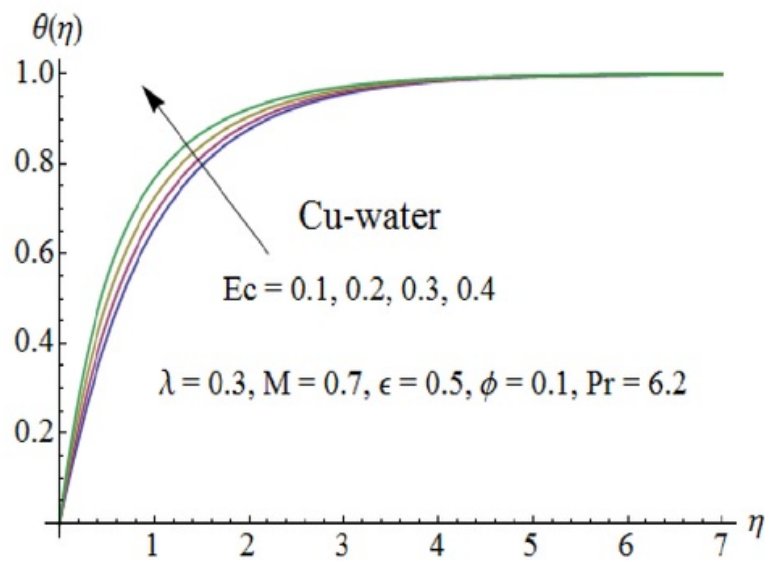


Fig. 7.8: Influence of Ec on temperature field.

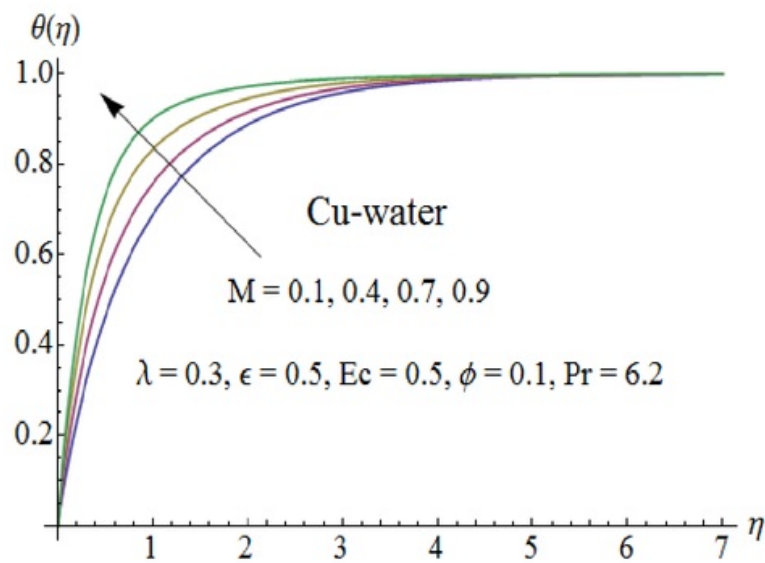


Fig. 7.9: Influence of M on temperature field.

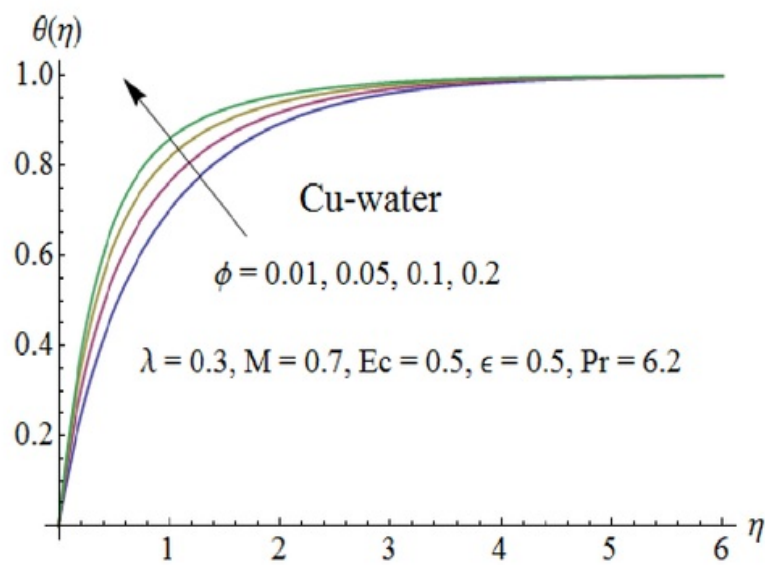


Fig. 7.10: Influence of ϕ on temperature field.

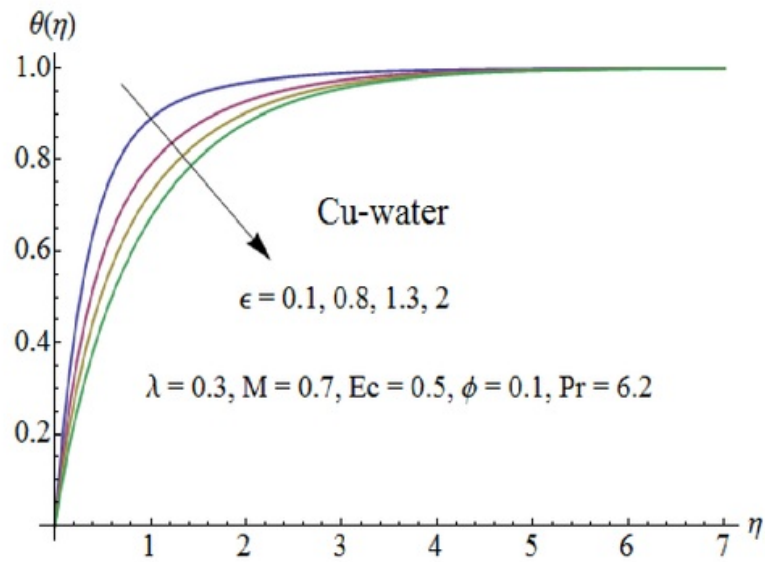


Fig. 7.11: Influence of ϵ on temperature field.

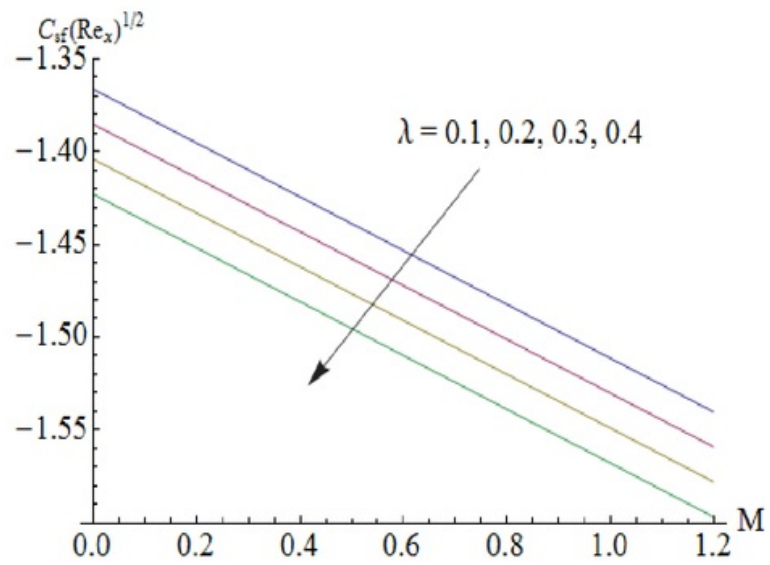


Fig. 7.12: Influence of λ and M on skin friction coefficient.

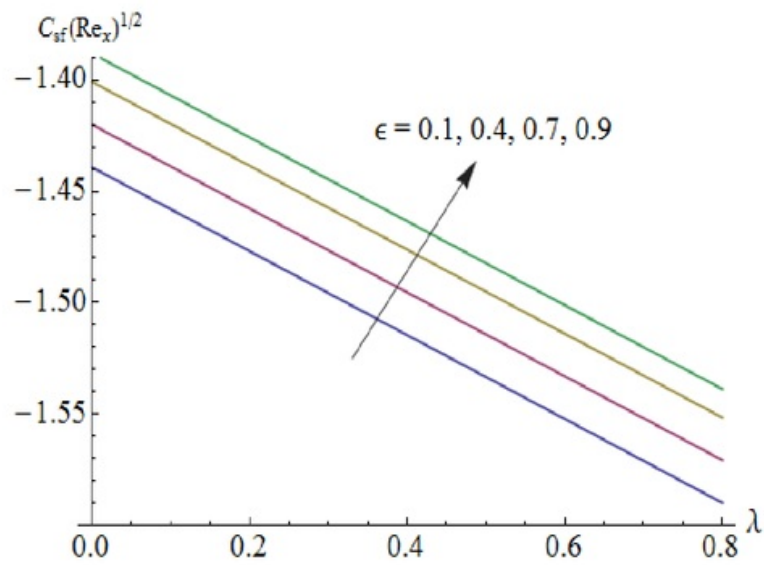


Fig. 7.13: Influence of ϵ and λ on skin friction coefficient.

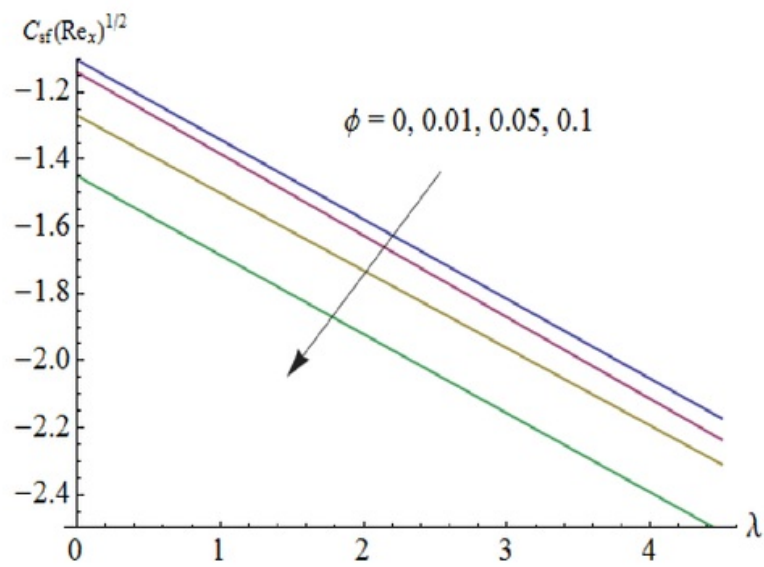


Fig. 7.14: Influence of ϕ and λ on skin friction coefficient.

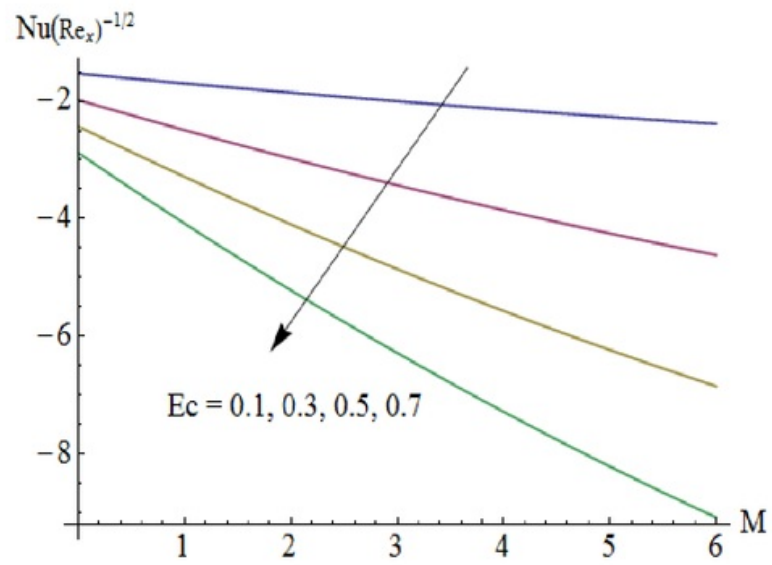


Fig. 7.15: Influence of Ec and M on Nusselt number.

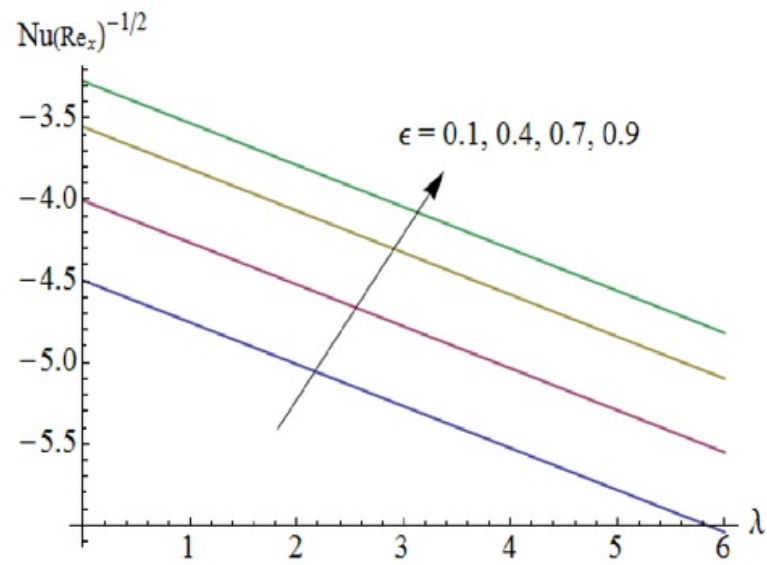


Fig. 7.16: Influence of ϵ and λ on Nusselt number.

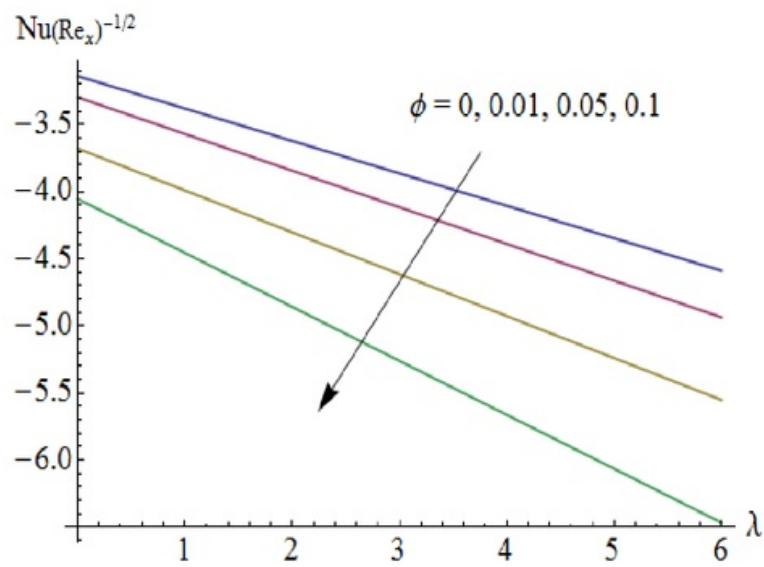


Fig. 7.17: Influence of ϕ and λ on Nusselt number.

13

Table 7.2: Thermo physical properties of water and copper.

	$\rho(\text{kg}/\text{m}^3)$	$c_p(\text{j}/\text{kgk})$	$k(\text{W}/\text{m.k})$	$\beta \times 10^5(\text{K}^{-1})$	$\sigma(\Omega\text{m})^{-1}$
Pure water	997.1	4179	0.613	21	0.05
Copper(Cu)	8933	385	401	1.67	5.96×10^7

13

Table 7.3: CPU time (seconds) used by HAM for different order of approximations.

Order of approximations	CPU time (sec)
2	0.387022
4	0.932053
6	1.99511
8	3.84522
10	6.46637
12	10.3336
14	15.6849
16	20.6332
18	27.0535
20	35.221

Table 7.4: Numerical values of skin friction coefficient and Nusselt number for different parameters.

ϕ	M	λ	Ec	ϵ	$-C_{sf}(Re_x)^{1/2}$	$-Nu(Re_x)^{-1/2}$
0.01	0.7	0.3	0.5	0.5	1.3065	3.9187
0.05					1.4749	4.2285
0.1					1.6971	4.6398
0.1	0.1				1.4543	4.1486
	0.4				1.5798	4.4009
	0.9				1.7713	4.7915
	0.7	0.1			1.6151	4.5939
		0.2			1.6565	4.6167
		0.4			1.7369	4.6615
		0.3	0.1		1.7645	3.5463
			0.2		1.7459	3.8347
			0.3		1.7292	4.1119
			0.5	0.1	1.9215	5.8563
				0.4	1.7420	4.8745
				0.7	1.6204	4.2512

7.5 Concluding remarks

Influence of MHD flow of Cu -water nanofluid over a stretching sheet is presented in this article. Melting heat transfer and effects of viscous dissipation are also considered. HAM is used to obtain analytic solutions. It is observed that velocity profile is decreasing function of Eckert number, Hartman number and nanoparticle volume fraction. Melting parameter enhances the velocity and reduces the temperature field. Temperature profile increases when volume fraction of copper nanoparticles is increased. Higher values of Cu -nanoparticles volume fraction, Hartman number and porosity parameter correspond to larger values of skin friction coefficient and local Nusselt number. Temperature gradient at the surface decreases for larger values of melting parameter.

Chapter 8

Unsteady flow of nanofluid with double stratification and magnetohydrodynamics

This chapter addresses the unsteady flow of viscous nanofluid caused by an inclined stretching sheet. Effects of thermal radiation, viscous dissipation and stratification process due to temperature and concentration are analyzed. Fluid is electrically conducting in the presence of applied magnetic field. The flow consideration is subjected to small magnetic Reynolds number. Induced magnetic field is absent. Appropriate transformations reduce the nonlinear partial differential system to ordinary differential system. Convergent solutions are computed. Interval of convergence is determined. Effects of different parameters on the velocity, temperature and concentration profiles are shown and analyzed. It is concluded that thermal and solutal stratification parameters reduce the velocity distribution. It is also observed that velocity is decreasing function of Hartman number.

8.1 Flow equations

Consider an unsteady two-dimensional incompressible flow of nanofluid past a stretching sheet. The sheet makes an angle Ψ with the horizontal direction. The x -axis is taken along the stretching surface in the direction of motion and y -axis is perpendicular to it. Thermal and

concentration buoyancy forces are applied to the fluid with double stratified phenomena due to temperature and concentration. The sheet is maintained at temperature $T_w = T_0 + A^*x/(1 - a^*t)$ and concentration $C_w = C_0 + D^*x/(1 - a^*t)$. The temperature and mass concentration of the ambient fluid are assumed to be stratified in the form $T_\infty = T_0 + B^*x/(1 - a^*t)$ and $C_\infty = C_0 + E^*x/(1 - a^*t)$ respectively (see Fig. 8.1).

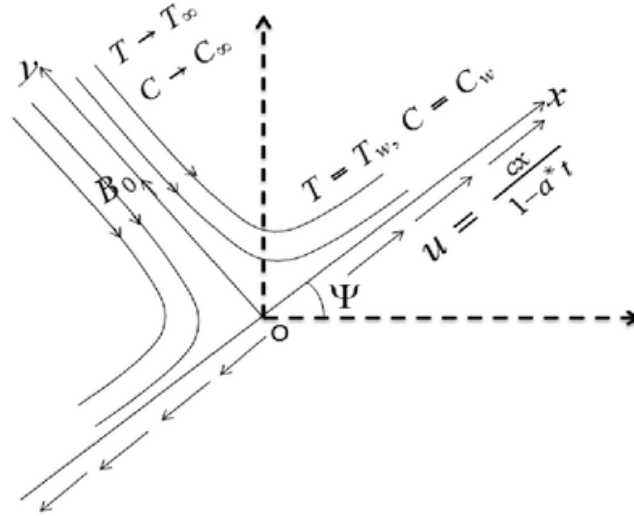


Fig. 8.1: Geometry of the problem.

2

It is assumed that a uniform magnetic field of intensity B_0 acts in the y -direction. The magnetic Reynolds number is assumed to be small so that the induced magnetic field is negligible in comparison with the applied magnetic field. In addition the effects of thermal radiation and viscous dissipation are considered. The continuity, momentum, energy and concentration equations which govern such type of flow are written as:

$$\frac{\partial u}{\partial x} + \frac{\partial v}{\partial y} = 0, \quad (8.1)$$

$$\frac{\partial u}{\partial t} + u \frac{\partial u}{\partial x} + v \frac{\partial u}{\partial y} = \nu \frac{\partial^2 u}{\partial y^2} + g \sin \Psi \left[\beta_T (T - T_\infty) (1 - C_\infty) + \frac{(\rho^* - \rho)}{\rho} (C - C_\infty) \right] - \frac{\sigma B_0^2 u}{\rho}, \quad (8.2)$$

$$\begin{aligned} \frac{\partial T}{\partial t} + u \frac{\partial T}{\partial x} + v \frac{\partial T}{\partial y} = & \alpha \frac{\partial^2 T}{\partial y^2} + \tau \left[D_B \frac{\partial T}{\partial y} \frac{\partial C}{\partial y} + \frac{D_T}{T_\infty} \left(\frac{\partial T}{\partial y} \right)^2 \right] + \frac{\mu}{(\rho c_p)_f} \left(\frac{\partial u}{\partial y} \right)^2 \\ & + \frac{16\sigma^* T_\infty^3}{3k^*(\rho c_p)_f} \frac{\partial^2 T}{\partial y^2}, \end{aligned} \quad (8.3)$$

$$\frac{\partial C}{\partial t} + u \frac{\partial C}{\partial x} + v \frac{\partial C}{\partial y} = D_B \frac{\partial^2 C}{\partial y^2} + \frac{D_T}{T_\infty} \frac{\partial^2 T}{\partial y^2}. \quad (8.4)$$

The subjected boundary conditions are

$$\begin{aligned} u &= U = \frac{cx}{1-a^*t}, \quad v = 0, \quad T = T_w = T_0 + \frac{A^*x}{1-a^*t}, \quad C = C_w = C_0 + \frac{D^*x}{1-a^*t} \quad \text{at } y = 0, \\ u &\rightarrow 0, \quad T \rightarrow T_\infty = T_0 + \frac{B^*x}{1-a^*t}, \quad C \rightarrow C_\infty = C_0 + \frac{E^*x}{1-a^*t} \quad \text{as } y \rightarrow \infty, \end{aligned} \quad (8.5)$$

where u and v are the velocity components along the x - and y - directions respectively, ν , ρ and σ are the kinematic viscosity, density and electrical conductivity of the fluid, g is the gravitational acceleration, β_T is the coefficient of thermal expansion, T , T_∞ , C and C_∞ are the fluid temperature, ambient fluid temperature, fluid concentration and ambient fluid concentration, $\alpha = k/(\rho c_p)_f$ is the thermal diffusivity, $\tau = (\rho c)_p/(\rho c)_f$ is the ratio between the effective heat capacity of the nanoparticle material and heat capacity of the fluid, D_B is the Brownian diffusion coefficient, D_T is the thermophoretic diffusion coefficient, k^* is the mean absorption coefficient, σ^* is the Stefan-Boltzmann constant, k is the thermal conductivity, c and a^* are positive constants having dimension T^{-1} , A^* , B^* , D^* and E^* are the dimensional constants having dimension L^{-1} and T_0 and C_0 are the reference temperature and concentration.

We now introduce the following similarity transformations

$$\begin{aligned} u &= \frac{cx}{1-a^*t} f'(\eta), \quad v = -\sqrt{\frac{\nu c}{1-a^*t}} f(\eta), \quad \eta = \sqrt{\frac{c}{\nu(1-a^*t)}} y, \\ \theta(\eta) &= \frac{T - T_\infty}{T_w - T_0}, \quad \Phi(\eta) = \frac{C - C_\infty}{C_w - C_0}. \end{aligned} \quad (8.6)$$

Now eq. (8.1) is satisfied automatically and Eqs. (8.2) – (8.5) after using Eq. (8.6) can be reduced as follows:

$$f''' - f'^2 + f f'' - \delta^* \left(f' + \frac{1}{2} \eta f'' \right) + N_c \sin \Psi[\theta + N_r \Phi] - M f' = 0, \quad (8.7)$$

$$\frac{1}{\text{Pr}} \left(1 + \frac{4}{3} R_d \right) \theta'' + f\theta' - f'\theta - S_t f' - \delta^* \left(S_t + \theta + \frac{1}{2} \eta \theta' \right) + N_b \theta' \Phi' + N_t \theta'^2 + Ec f''^2 = 0, \quad (8.8)$$

$$\Phi'' + Sc(f\Phi' - f'\Phi) - S_m Sc f' - \delta^* Sc \left(S_m + \Phi + \frac{1}{2} \eta \Phi' \right) + \frac{N_t}{N_b} \theta'' = 0, \quad (8.9)$$

$$f'(0) = 1, f(0) = 0, \theta(0) = 1 - S_t, \Phi(0) = 1 - S_m,$$

$$f'(\infty) = 0, \theta(\infty) = 0, \Phi(\infty) = 0, \quad (8.10)$$

where prime indicates the differentiation with respect to η . Moreover the unsteady parameter δ^* , mixed convection parameter N_c , Buoyancy ratio N_r , Hartman number M , Prandtl number Pr , Radiation parameter R_d , thermal stratification parameter S_t , Brownian motion parameter N_b , thermophoresis parameter N_t , Eckert number Ec , Schmidt number Sc and solutal stratification parameter S_m are defined by the following definitions:

$$\begin{aligned} \delta^* &= \frac{a^*}{c}, N_c = \frac{g(1-a^*t)^2 \beta_T}{c^2 x} (1 - C_\infty)(T_w - T_0), N_r = \frac{(\rho^* - \rho)(C_w - C_0)}{\rho \beta_T (T_w - T_0)(1 - C_\infty)}, \\ M &= \frac{\sigma B_0^2 (1 - a^*t)}{\rho c}, \text{Pr} = \frac{\nu}{\alpha}, R_d = \frac{4\sigma^* T_\infty^3}{3kk^*}, S_t = \frac{B^*}{A^*}, N_b = \frac{\tau D_B (C_w - C_0)}{\nu}, \\ N_t &= \frac{\tau D_T (T_w - T_0)}{\nu T_\infty}, Ec = \frac{\rho U^2}{(\rho c_p)_f (T_w - T_0)}, Sc = \frac{\nu}{D_B}, S_m = \frac{E^*}{D^*}. \end{aligned} \quad (8.11)$$

The important physical quantities of interest in this problem are the local skin friction coefficient C_{sf} , Nusselt number Nu and Sherwood number Sh which are given by

$$C_{sf} = \frac{\tau_w}{\frac{1}{2} \rho U^2}, Nu = \frac{x q_w}{k(T_w - T_\infty)}, Sh = \frac{x q_m}{D_B (C_w - C_\infty)}, \quad (8.12)$$

where the surface shear stress τ_w , wall heat flux q_w and wall mass flux q_m are given by

$$\tau_w = \mu \frac{\partial u}{\partial y} \Big|_{y=0}, q_w = - \left(k + \frac{16\sigma^* T_\infty^3}{3k^*} \right) \frac{\partial T}{\partial y} \Big|_{y=0}, q_m = - D_B \frac{\partial C}{\partial y} \Big|_{y=0}. \quad (8.13)$$

By using the above equations we get

$$\begin{aligned} C_{sf} \left(\frac{\text{Re}_x}{2} \right)^{1/2} &= f''(0), \quad Nu(\text{Re}_x)^{-1/2} = - \left(1 + \frac{4}{3} R_d \right) \left(\frac{1}{1 - S_t} \right) \theta'(0), \\ Sh(\text{Re}_x)^{-1/2} &= - \left(\frac{1}{1 - S_m} \right) \Phi'(0), \end{aligned} \quad (8.14)$$

where $\text{Re}_x = Ux/\nu$ is the local Reynolds number.

8.2 Homotopy analysis solutions

Initial approximations $f_0(\eta)$, $\theta_0(\eta)$ and $\Phi_0(\eta)$, auxiliary linear operators \mathcal{L}_f , \mathcal{L}_θ and \mathcal{L}_Φ and auxiliary functions \mathcal{H}_f , \mathcal{H}_θ and \mathcal{H}_Φ are taken in the forms

$$f_0(\eta) = 1 - e^{-\eta}, \quad \theta_0(\eta) = (1 - S_t)e^{-\eta}, \quad \Phi_0(\eta) = (1 - S_m)e^{-\eta}, \quad (8.15)$$

$$\mathcal{L}_f = f''' - f', \quad \mathcal{L}_\theta = \theta'' - \theta, \quad \mathcal{L}_\Phi = \Phi'' - \Phi, \quad (8.16)$$

$$\mathcal{H}_f = e^{-\eta}, \quad \mathcal{H}_\theta = e^{-\eta}, \quad \mathcal{H}_\Phi = e^{-\eta}, \quad (8.17)$$

with

$$\begin{aligned} \mathcal{L}_f [c_1 + c_2 e^\eta + c_3 e^{-\eta}] &= 0, \\ \mathcal{L}_\theta [c_4 e^\eta + c_5 e^{-\eta}] &= 0, \\ \mathcal{L}_\Phi [c_6 e^\eta + c_7 e^{-\eta}] &= 0, \end{aligned} \quad (8.18)$$

in which c_i ($i = 1 - 7$) are the constants.

If $p \in [0, 1]$ indicates the embedding parameter then the zeroth order deformation problems are constructed as follows:

$$(1 - p)\mathcal{L}_f [\hat{f}(\eta; p) - f_0(\eta)] = p\hbar_f \mathcal{H}_f \mathcal{N}_f [\hat{f}(\eta; p), \hat{\theta}(\eta; p), \hat{\Phi}(\eta; p)], \quad (8.19)$$

$$(1 - p)\mathcal{L}_\theta [\hat{\theta}(\eta; p) - \theta_0(\eta)] = p\hbar_\theta \mathcal{H}_\theta \mathcal{N}_\theta [\hat{\theta}(\eta; p), \hat{f}(\eta; p), \hat{\Phi}(\eta; p)], \quad (8.20)$$

$$(1 - p)\mathcal{L}_\Phi [\hat{\Phi}(\eta; p) - \Phi_0(\eta)] = p\hbar_\Phi \mathcal{H}_\Phi \mathcal{N}_\Phi [\hat{\Phi}(\eta; p), \hat{f}(\eta; p), \hat{\theta}(\eta; p)], \quad (8.21)$$

$$\begin{aligned}
\hat{f}'(0; p) &= 1, \quad \hat{f}(0; p) = 0, \quad \hat{f}'(\infty; p) = 0, \\
\hat{\theta}(0; p) &= 1 - S_t, \quad \hat{\theta}(\infty; p) = 0, \\
\hat{\Phi}(0; p) &= 1 - S_m, \quad \hat{\Phi}(\infty; p) = 0,
\end{aligned} \tag{8.22}$$

where \hbar_f , \hbar_θ and \hbar_ϕ are the nonzero auxiliary parameters and the nonlinear operators \mathcal{N}_f , \mathcal{N}_θ and \mathcal{N}_ϕ are given by

$$\begin{aligned}
\mathcal{N}_f [\hat{f}(\eta; p), \hat{\theta}(\eta; p), \hat{\Phi}(\eta; p)] &= \frac{\partial^3 \hat{f}(\eta; p)}{\partial \eta^3} - \left(\frac{\partial \hat{f}(\eta; p)}{\partial \eta} \right)^2 + \hat{f}(\eta; p) \frac{\partial^2 \hat{f}(\eta; p)}{\partial \eta^2} \\
&\quad - \delta^* \left(\frac{\partial \hat{f}(\eta; p)}{\partial \eta} + \frac{1}{2} \eta \frac{\partial^2 \hat{f}(\eta; p)}{\partial \eta^2} \right) + N_c \sin \Psi[\hat{\theta}(\eta; p) \\
&\quad + N_r \hat{\Phi}(\eta; p)] - M \frac{\partial \hat{f}(\eta; p)}{\partial \eta},
\end{aligned} \tag{8.23}$$

$$\begin{aligned}
\mathcal{N}_\theta [\hat{\theta}(\eta; p), \hat{f}(\eta; p), \hat{\Phi}(\eta; p)] &= \frac{1}{\text{Pr}} \left(1 + \frac{4}{3} R_d \right) \frac{\partial^2 \hat{\theta}(\eta; p)}{\partial \eta^2} + \hat{f}(\eta; p) \frac{\partial \hat{\theta}(\eta; p)}{\partial \eta} - \hat{\theta}(\eta; p) \frac{\partial \hat{f}(\eta; p)}{\partial \eta} \\
&\quad - S_t \frac{\partial \hat{f}(\eta; p)}{\partial \eta} - \delta^* \left(S_t + \hat{\theta}(\eta; p) + \frac{1}{2} \eta \frac{\partial \hat{\theta}(\eta; p)}{\partial \eta} \right) + N_t \left(\frac{\partial \hat{\theta}(\eta; p)}{\partial \eta} \right)^2 \\
&\quad + N_b \frac{\partial \hat{\theta}(\eta; p)}{\partial \eta} \frac{\partial \hat{\Phi}(\eta; p)}{\partial \eta} + E_c \left(\frac{\partial^2 \hat{\theta}(\eta; p)}{\partial \eta^2} \right)^2,
\end{aligned} \tag{8.24}$$

$$\begin{aligned}
\mathcal{N}_\phi [\hat{\Phi}(\eta; p), \hat{f}(\eta; p), \hat{\theta}(\eta; p)] &= \frac{\partial^2 \hat{\Phi}(\eta; p)}{\partial \eta^2} + S_c \left(\hat{f}(\eta; p) \frac{\partial \hat{\Phi}(\eta; p)}{\partial \eta} - \hat{\Phi}(\eta; p) \frac{\partial \hat{f}(\eta; p)}{\partial \eta} \right) \\
&\quad - S_m S_c \frac{\partial \hat{f}(\eta; p)}{\partial \eta} - \delta^* S_c \left(S_m + \hat{\Phi}(\eta; p) + \frac{1}{2} \eta \frac{\partial \hat{\Phi}(\eta; p)}{\partial \eta} \right) \\
&\quad + \frac{N_t}{N_b} \frac{\partial^2 \hat{\theta}(\eta; p)}{\partial \eta^2}.
\end{aligned} \tag{8.25}$$

The resulting problems at m^{th} order can be presented in the following forms

$$\mathcal{L}_f [f_m(\eta) - \chi_m f_{m-1}(\eta)] = \hbar_f \mathcal{R}_{f,m}(\eta), \tag{8.26}$$

$$\mathcal{L}_\theta [\theta_m(\eta) - \chi_m \theta_{m-1}(\eta)] = \hbar_\theta \mathcal{R}_{\theta,m}(\eta), \quad (8.27)$$

$$\mathcal{L}_\Phi [\Phi_m(\eta) - \chi_m \Phi_{m-1}(\eta)] = \hbar_\Phi \mathcal{R}_{\Phi,m}(\eta), \quad (8.28)$$

$$f'_m(0) = f_m(0) = f'_m(\infty) = \theta_m(0) = \theta_m(\infty) = \Phi_m(0) = \Phi_m(\infty) = 0, \quad (8.29)$$

$$\mathcal{R}_{f,m}(\eta) = f'''_{m-1} + \sum_{k=0}^{m-1} [f_{m-1-k} f''_k - f'_{m-1-k} f'_k] - \delta^* \left(f'_{m-1} + \frac{1}{2} \eta f''_{m-1} \right) + N_c \sin \Psi [\theta_{m-1} + N_r \Phi_{m-1}] - M f'_{m-1}, \quad (8.30)$$

$$\begin{aligned} \mathcal{R}_{\theta,m}(\eta) = & \frac{1}{\text{Pr}} \left(1 + \frac{4}{3} R_d \right) \theta''_{m-1} + \sum_{k=0}^{m-1} (f_{m-1-k} \theta'_k - \theta_{m-1-k} f'_k) - S_t f'_{m-1} - \delta^* \left(S_t + \theta_{m-1} + \frac{1}{2} \eta \theta'_{m-1} \right) \\ & + \sum_{k=0}^{m-1} (N_b \theta'_{m-1-k} \Phi'_k + N_t \theta'_{m-1-k} \theta'_k + E c f''_{m-1-k} f'_k), \end{aligned} \quad (8.31)$$

$$\mathcal{R}_{\Phi,m}(\eta) = \Phi''_{m-1} + S c \sum_{k=0}^{m-1} (f_{m-1-k} \Phi'_k - \Phi_{m-1-k} f'_k) - S_m S c f'_{m-1} - \delta^* S c \left(S_m + \Phi_{m-1} + \frac{1}{2} \eta \Phi'_{m-1} \right) + \frac{N_t}{N_b} \theta''_{m-1}, \quad (8.32)$$

$$\chi_m = \begin{cases} 0, & m \leq 1 \\ 1, & m > 1 \end{cases}. \quad (8.33)$$

The general solutions (f_m, θ_m, Φ_m) comprising the special solutions $(f_m^*, \theta_m^*, \Phi_m^*)$ are

$$\begin{aligned} f_m(\eta) &= f_m^*(\eta) + c_1 + c_2 e^\eta + c_3 e^{-\eta}, \\ \theta_m(\eta) &= \theta_m^*(\eta) + c_4 e^\eta + c_5 e^{-\eta}, \\ \Phi_m(\eta) &= \Phi_m^*(\eta) + c_6 e^\eta + c_7 e^{-\eta}, \end{aligned} \quad (8.34)$$

where the constants c_i ($i = 1, 2, \dots, 7$) through the boundary conditions (8.29) have the values

$$\begin{aligned} c_2 &= c_4 = c_6 = 0, \quad c_1 = -c_3 - f_m^*(0), \quad c_3 = \left. \frac{\partial f_m^*(\eta)}{\partial \eta} \right|_{\eta=0}, \\ c_5 &= -\theta_m^*(0), \quad c_7 = -\Phi_m^*(0). \end{aligned} \quad (8.35)$$

8.3 Convergence of the homotopy solutions

Now the solutions of Eqs. (8.7 – 8.9) subject to the boundary conditions (8.10) are computed by means of homotopy analysis method. The convergence of the series solutions is highly

dependent upon the auxiliary parameters \hbar_f , \hbar_θ and \hbar_Φ . For valid ranges of these parameters, we have sketched the \hbar -curves at 15th-order of approximations (see Fig. 8.2). We can see that the admissible values of \hbar_f , \hbar_θ and \hbar_Φ are $-1.5 \leq \hbar_f \leq -0.7$, $-1.3 \leq \hbar_\theta \leq -0.4$ and $-1.2 \leq \hbar_\Phi \leq -0.4$. The residual errors are calculated for momentum, energy and concentration equations by the expressions

$$\begin{aligned}\Delta_m^f &= \int_0^1 [R_m^f(\eta, \hbar_f)]^2 d\eta, \\ \Delta_m^\theta &= \int_0^1 [R_m^\theta(\eta, \hbar_\theta)]^2 d\eta, \\ \Delta_m^\Phi &= \int_0^1 [R_m^\Phi(\eta, \hbar_\Phi)]^2 d\eta.\end{aligned}\tag{8.36}$$

In Figs. (8.3 – 8.5), the \hbar -curves for residual error of f , θ and Φ are sketched in order to get the admissible range for \hbar . It is noted that correct result up to 4th decimal place is obtained by choosing the values of \hbar from this range. Further the series solutions converge in the whole region of η ($0 < \eta < \infty$) when $\hbar_f = -1.2$, $\hbar_\theta = -1.1$ and $\hbar_\Phi = -0.9$.

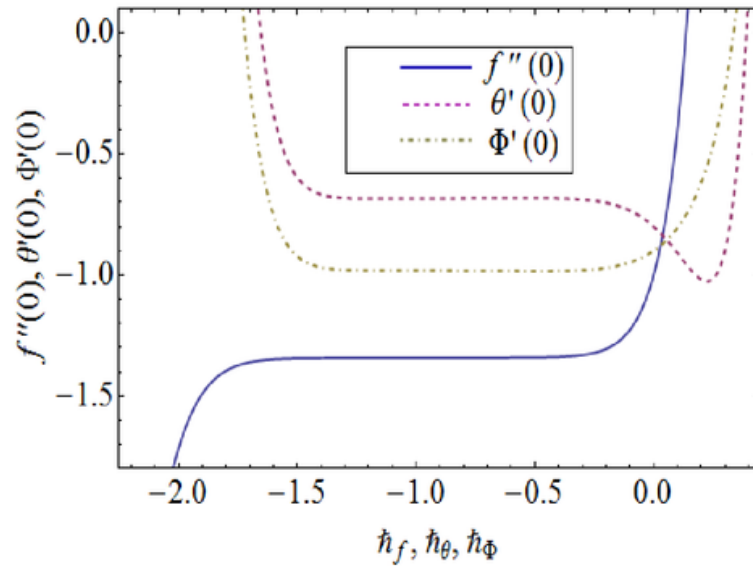


Fig. 8.2. \hbar - curves for $f''(0)$, $\theta'(0)$ and $\Phi'(0)$.

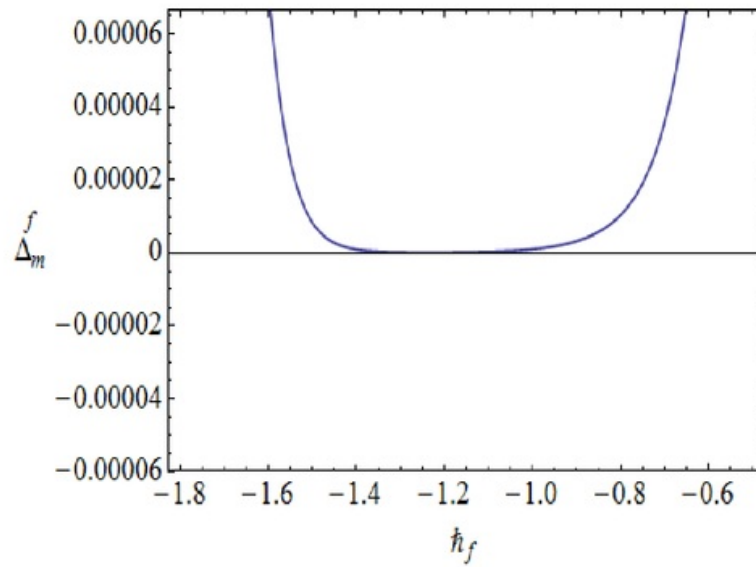


Fig. 8.3: h_f -curve for the residual error Δ_m^f .

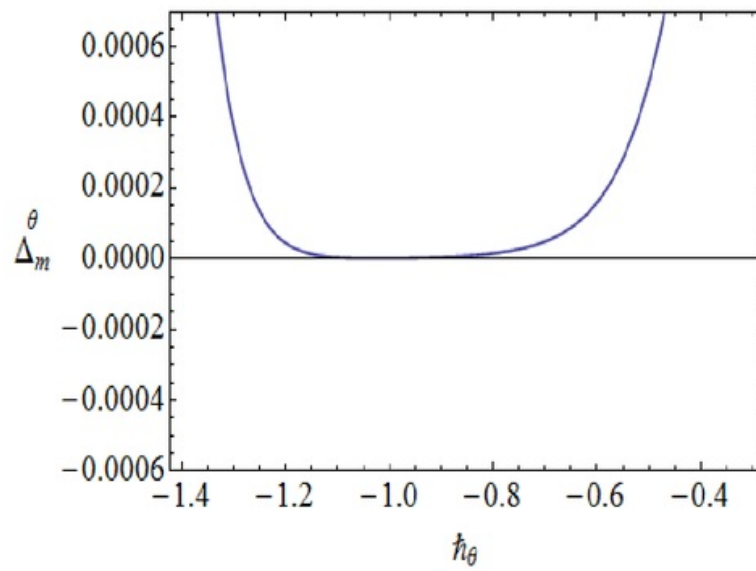


Fig. 8.4: h_θ -curve for the residual error Δ_m^θ .

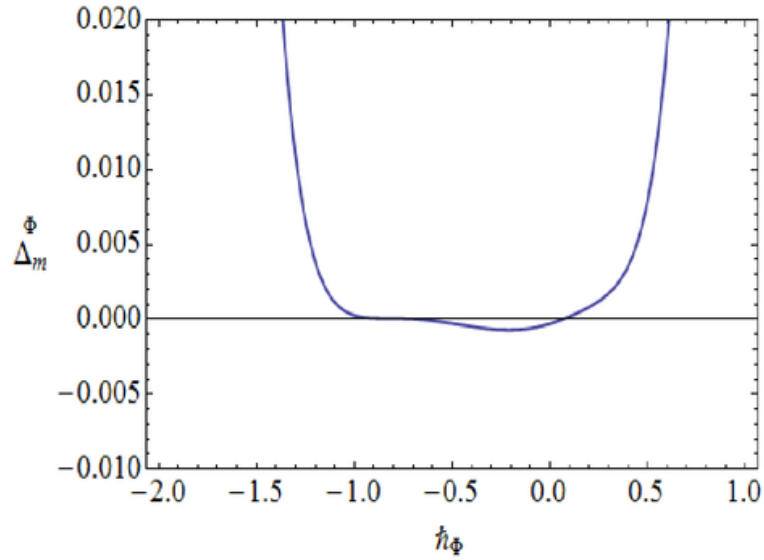


Fig. 8.5: h_Φ -curve for the residual error Δ_m^Φ .

Table 8.1: Convergence of HAM solutions for different order of approximations when $M = 0.7$, $N_c = R_d = 0.4$, $N_r = 0.3$, $\Psi = \pi/4$, $\text{Pr} = 1.2$, $S_\ell = 0.2$, $\delta^* = N_b = 0.5$, $N_\ell = 0.1$, $Sc = 0.9$, $Ec = 0.6$ and $S_m = 0.1$.

Order of approximations	$-f''(0)$	$-\theta'(0)$	$-\phi'(0)$
1	1.358	0.7193	0.9608
5	1.341	0.6832	0.9856
10	1.342	0.6839	0.9815
14	1.343	0.6855	0.9810
20	1.343	0.6868	0.9808
25	1.343	0.6876	0.9809
29	1.343	0.6880	0.9810
35	1.343	0.6887	0.9810
40	1.343	0.6887	0.9810
45	1.343	0.6887	0.9810

8.4 Interpretation of results

The effects of different parameters on the velocity, temperature and concentration fields are investigated through plots in this section. Figs. (8.6 – 8.12) exhibit the dimensionless velocity profiles for different values of inclination angle Ψ , unsteady parameter δ^* , Hartman number M , mixed convection parameter N_c , Buoyancy ratio N_r , thermal stratification parameter S_t and solutal stratification parameter S_m . Variation in velocity with an increase in angle of inclination Ψ can be seen from Fig. 8.6. It is noticed that with an increase in Ψ i.e. when the sheet moves from horizontal to vertical direction, the strength of buoyancy force increases and consequently the velocity and boundary layer thickness increase. Influence of unsteady parameter δ^* on the velocity profile f' can be seen in Fig. 8.7. Increasing values of δ^* indicates smaller stretching rate in the x - direction which eventually decrease the velocity and boundary layer thickness. The effects of Hartman number M are displayed in Fig. 8.8, which shows that an increase in M reduces the velocity profile. This is because of the reason that Lorentz force acts as a retarding force. Such retarding force enhances the frictional resistance opposing the fluid motion in the momentum boundary layer thickness. Fig. 8.9 elucidates the behavior of mixed convection parameter N_c on the velocity profile. This Fig. shows that the values of velocity function f' and the boundary layer thickness increase by increasing N_c . This is because a larger value of N_c accompanies a stronger buoyancy force which leads to an increase in velocity. The effects of Buoyancy ratio N_r on the velocity profile are depicted in Fig. 8.10. This Fig. shows that velocity profile increases when N_r increases. N_r is the ratio of concentration to thermal buoyancy forces. With an increase in buoyancy ratio parameter, concentration buoyancy force increases which results in higher velocity profile. Fig. 8.11 is plotted to show the influence of thermal stratification parameter S_t on the velocity profile $f'(\eta)$. With an increase in thermal stratification parameter the density of the fluid in the lower region is high than the upper region. So thermal stratification reduces the convective flow between the sheet and ambient fluid. Therefore velocity profile decreases. Behavior of solutal stratification parameter S_m on velocity profile is sketched in Fig. 8.12. It is depicted that velocity and boundary layer thickness decrease with an increase in solutal stratification parameter.

Effects of Prandtl number Pr , unsteady parameter δ^* , Brownian motion parameter N_b , thermophoresis parameter N_t , thermal stratification parameter S_t , radiation parameter R_d and

Eckert number Ec on the temperature profile θ are shown in the Figs. (8.13 – 8.19). Fig. 8.13 indicates that temperature profile θ is a decreasing function of Pr . In fact thermal diffusivity decreases by increasing Pr and thus the heat diffuses away slowly from the heated surface. Effect of unsteady parameter δ^* on the temperature is analyzed in Fig. 8.14. It is observed that the temperature and thermal boundary layer thickness are decreasing function of δ^* . Fig. 8.15 illustrates the effects of Brownian motion parameter N_b on temperature profile θ . When N_b increases, random motion of nanoparticles increases. Therefore collision of particles increases and kinetic energy converted to heat energy. Hence temperature profile θ increases for an increase in N_b . The behavior of N_t on the temperature profile is similar to that of N_b (see Fig. 8.16). Also the temperature profile θ and thermal boundary layer thickness decrease when the thermal stratification parameter S_t increases (see Fig. 8.17). Because temperature difference gradually decreases between the sheet and ambient fluid which causes a reduction in the temperature profile. Radiation effects on the temperature profile are displayed in Fig. 8.18. An increase in R_d enhances the heat flux from the sheet which gives rise to the fluid's temperature. Therefore the temperature profile and thermal boundary layer increase with an increase in R_d . Fig. 8.19 depicts that temperature is an increasing function of the Eckert number Ec . Eckert number is defined as the ratio of kinetic energy to enthalpy. With the increase in Ec , kinetic energy increases which consequently enhances temperature.

Figs. (8.20 – 8.24) illustrate the effects of Schmidt number Sc , unsteady parameter δ^* , Brownian motion parameter N_b , thermophoresis parameter N_t and concentration stratification number S_m on the dimensionless nanoparticle volume fraction profile Φ . It is observed that the mass fraction Φ and the associated boundary layer decrease for an increase in Schmidt number Sc (see Fig. 8.20). This is due to the fact that an increase in Sc reduces the molecular diffusivity. Fig. 8.21 indicates that an increase in the unsteady parameter δ^* decreases the concentration profile. The effects of Brownian motion parameter N_b on the concentration profile are depicted in Fig. 8.22. This Fig. shows that Φ decreases when N_b increases. Also the concentration profile Φ increases when thermophoresis parameter N_t is increased as shown in Fig. 8.23. Variations of solutal stratification parameter S_m on the dimensionless nanoparticle volume fraction profile Φ can be seen in Fig. 8.24. It is noted that there is a decrease in concentration profile when S_m is increased. Because increase in S_m decreases the concentration difference between the sheet

and ambient fluid.

Table 8.1 shows the convergence of the series solutions. It is observed that convergence for velocity, temperature and concentration is achieved at 14th, 35th and 29th order of approximations respectively. Table 8.2 shows the comparison of the present results with the numerical solution of Ibrahim and Shankar [64] in limiting case. It is found that our solution has good agreement with the limiting numerical solution. In Table 8.3 some numerical values of skin friction coefficient are given. Tabular values shows that skin friction coefficient decreases by increasing Ψ , N_c and N_r while it increases for larger values of M , δ^* , S_t and S_m . Numerical values of local Nusselt and Sherwood numbers for different emerging parameters are presented in Table 8.4. It is noted that local Nusselt number increases for larger values of S_t , S_m and Pr . However it decreases for larger values of N_b , N_t and Sc . It is noted that local Sherwood number decreases by increasing N_t , S_t and Pr and it increases for larger values of N_b , S_m and Sc .

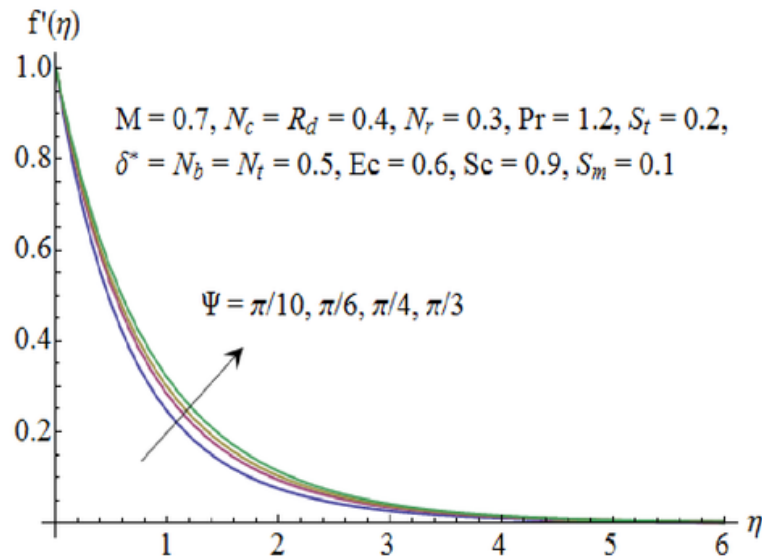


Fig. 8.6: Influence of Ψ on $f'(\eta)$.

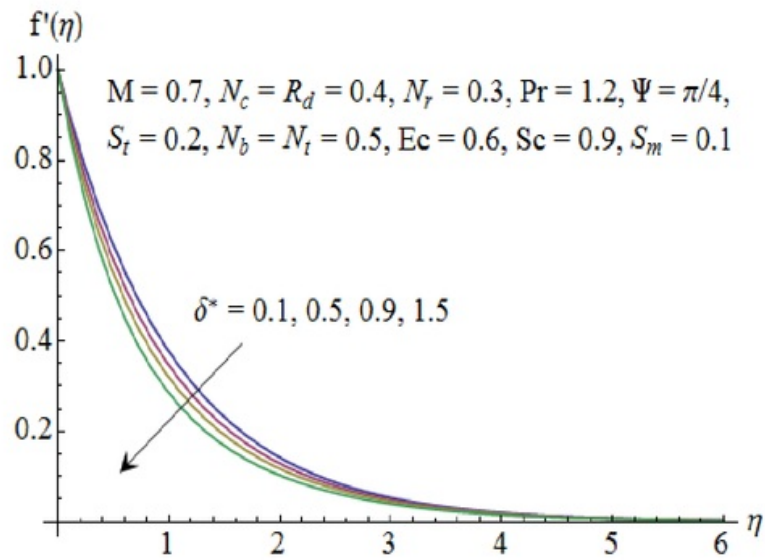


Fig. 8.7: Influence of δ^* on $f'(\eta)$.

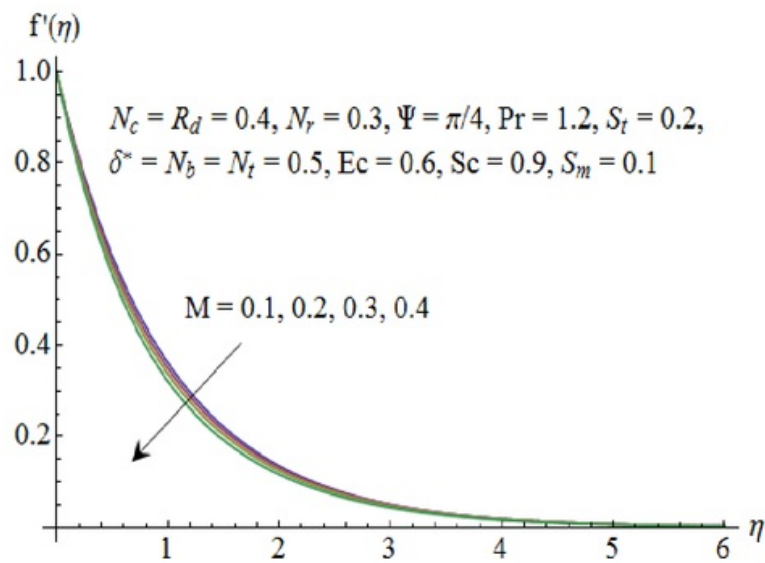


Fig. 8.8: Influence of M on $f'(\eta)$.

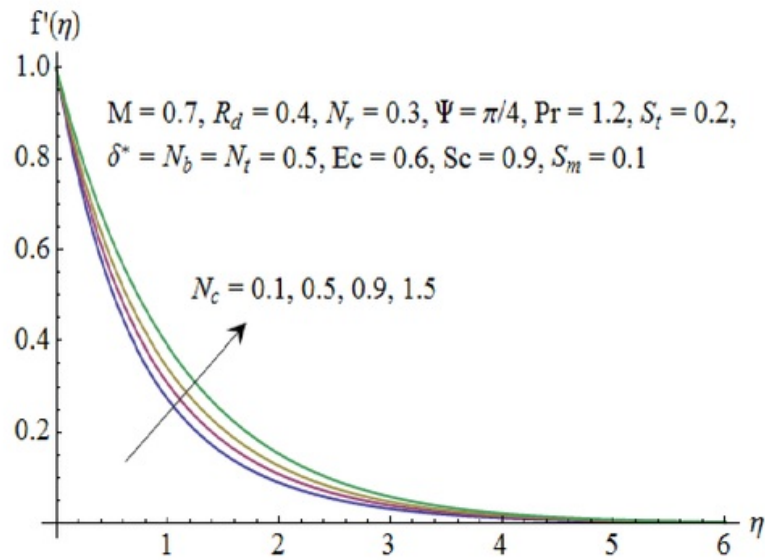


Fig. 8.9: Influence of N_c on $f'(\eta)$.

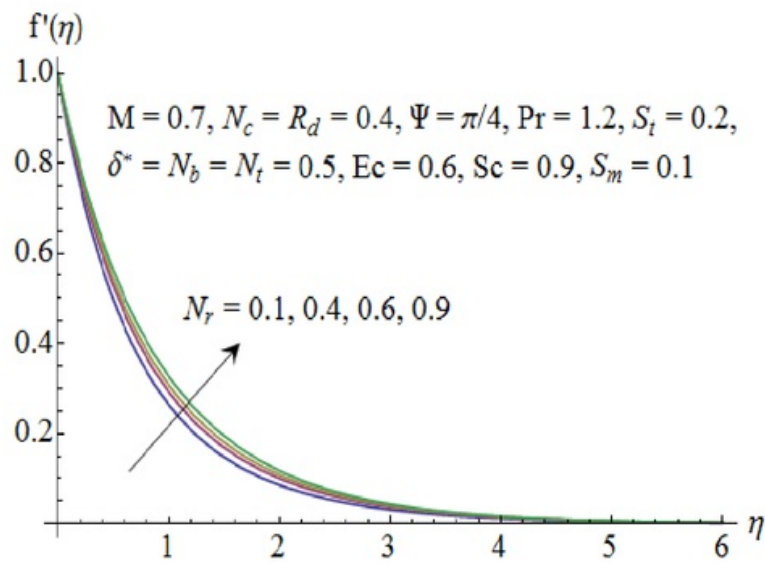


Fig. 8.10: Influence of N_r on $f'(\eta)$.

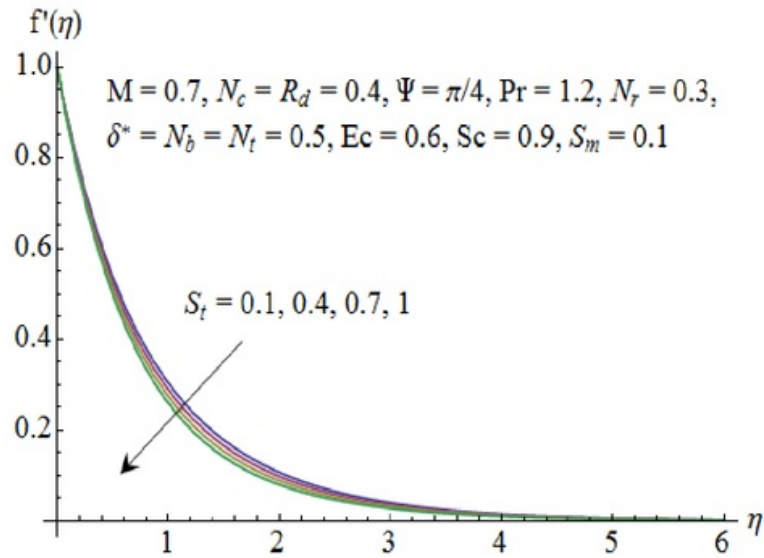


Fig. 8.11: Influence of S_t on $f'(\eta)$.

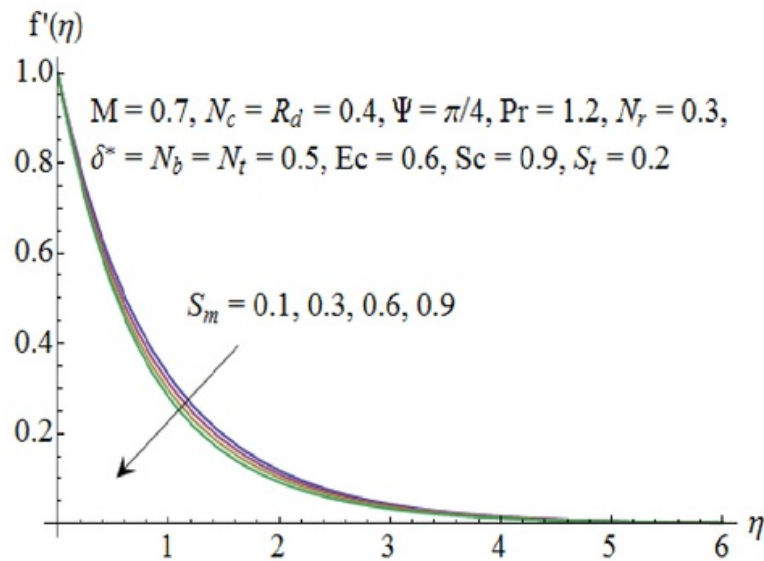


Fig. 8.12: Influence of S_m on $f'(\eta)$.

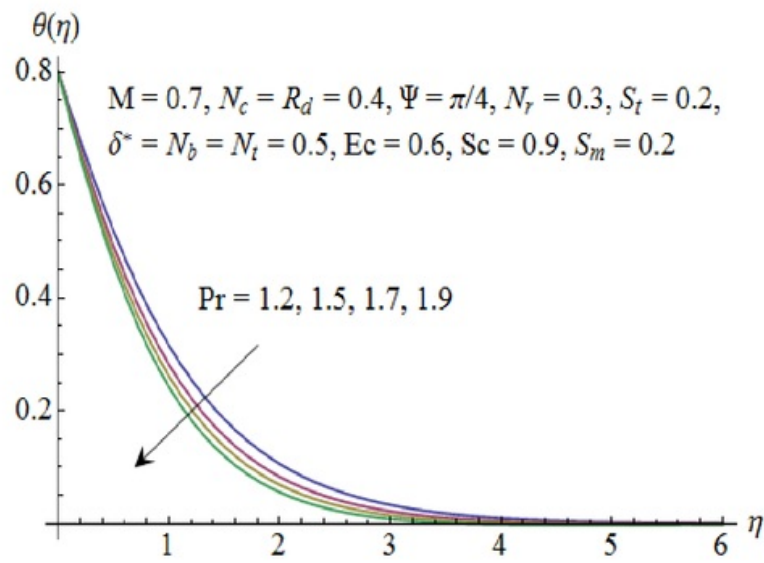


Fig. 8.13: Influence of Pr on $\theta(\eta)$.

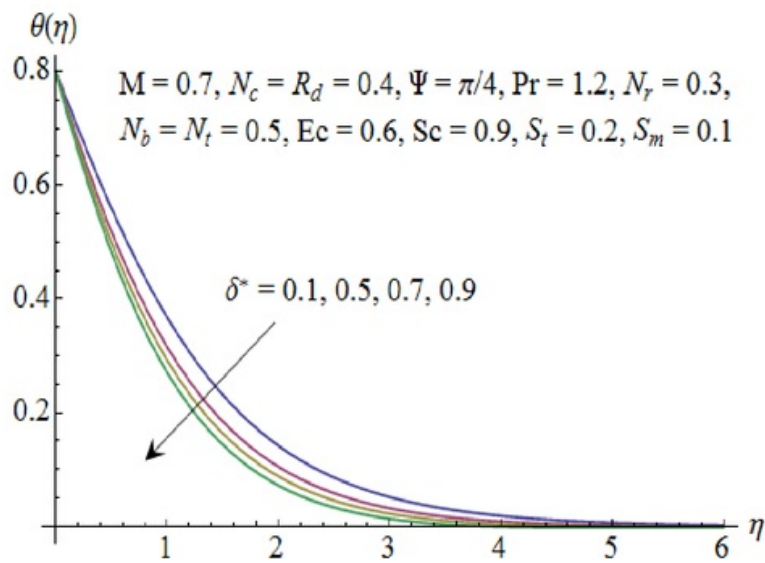


Fig. 8.14: Influence of δ^* on $\theta(\eta)$.

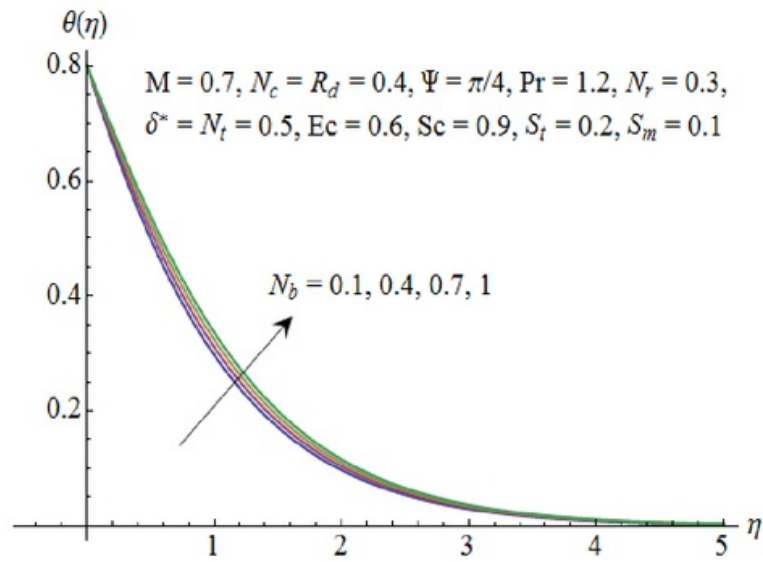


Fig. 8.15: Influence of N_b on $\theta(\eta)$.

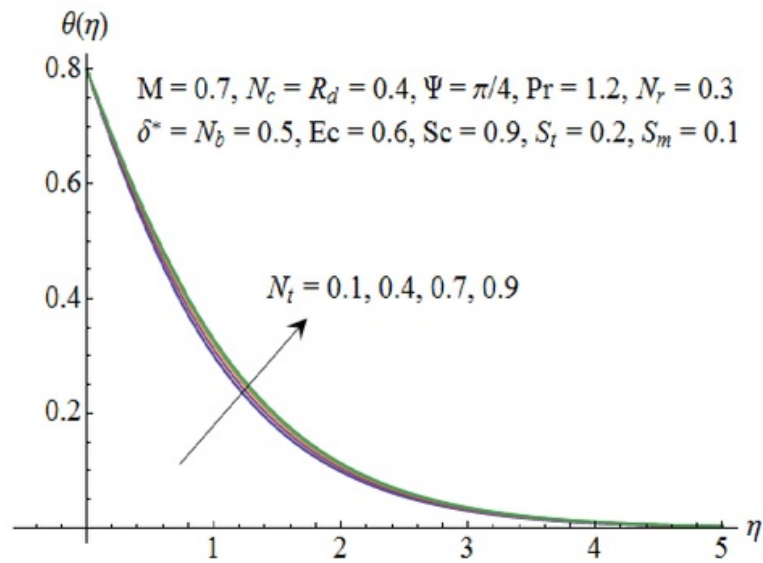


Fig. 8.16: Influence of N_t on $\theta(\eta)$.

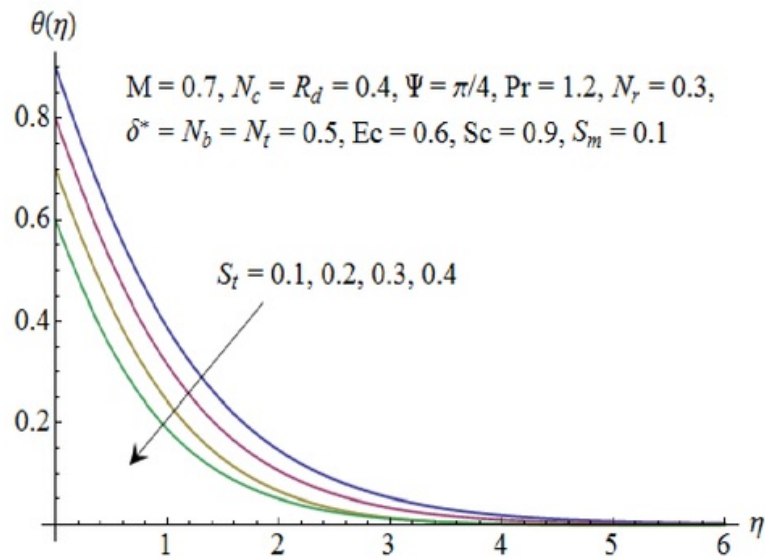


Fig. 8.17: Influence of S_t on $\theta(\eta)$.

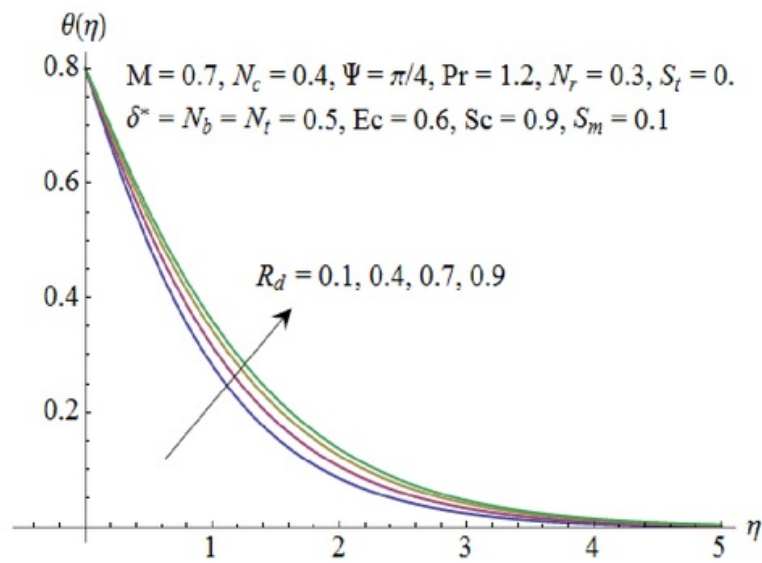


Fig. 8.18: Influence of R_d on $\theta(\eta)$.

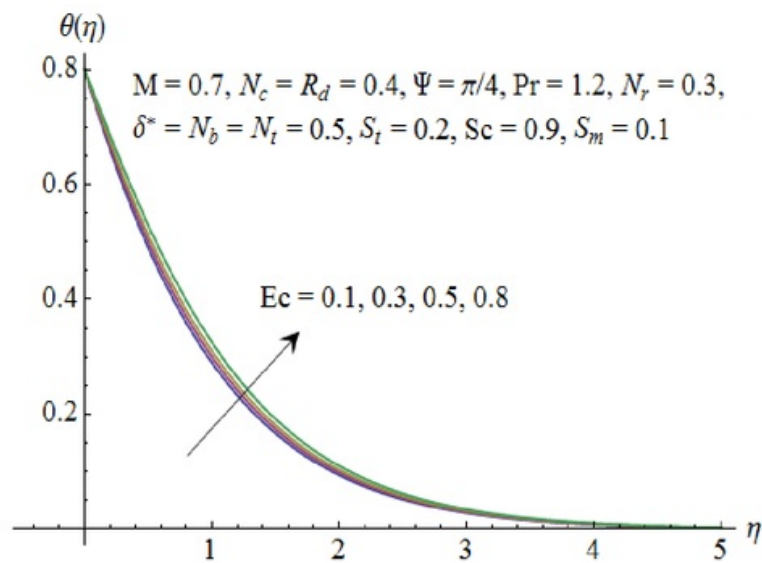


Fig. 8.19: Influence of Ec on $\theta(\eta)$.

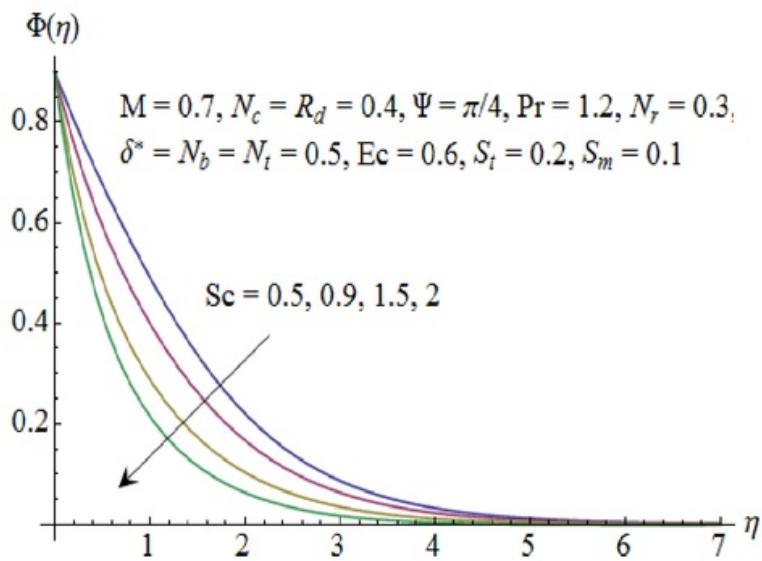


Fig. 8.20: Influence of Sc on $\Phi(\eta)$.

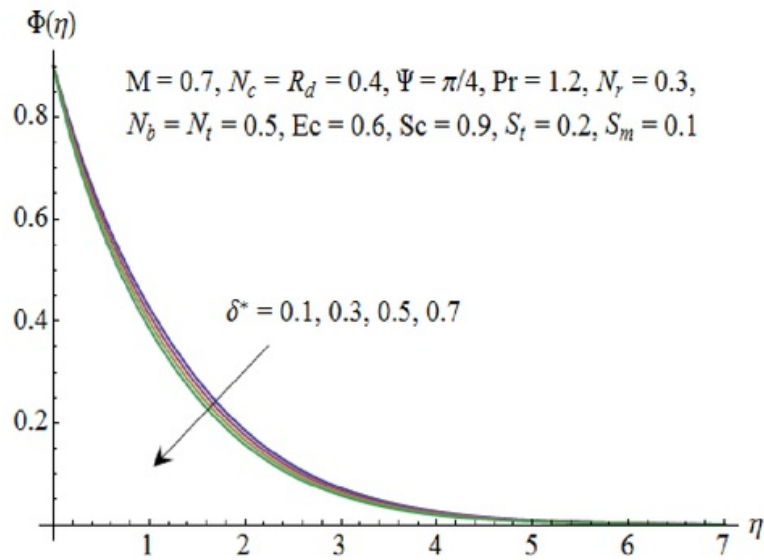


Fig. 8.21: Influence of δ^* on $\Phi(\eta)$.

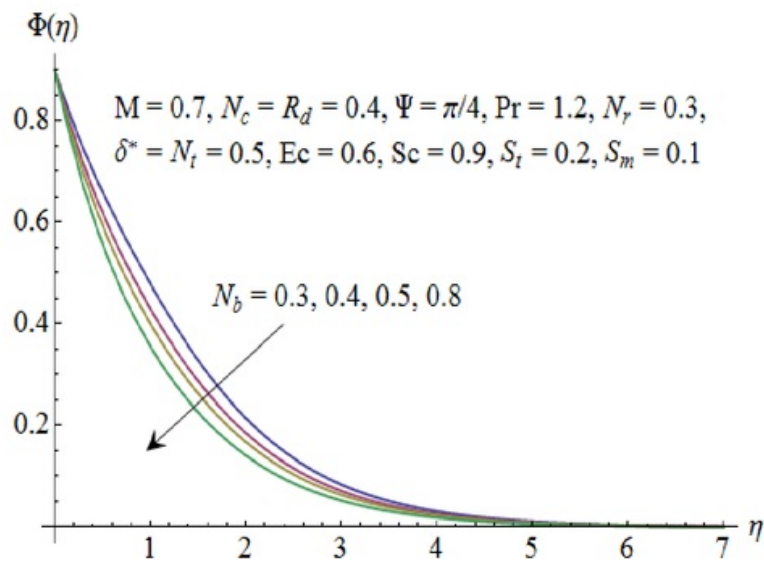


Fig. 8.22: Influence of N_b on $\Phi(\eta)$.

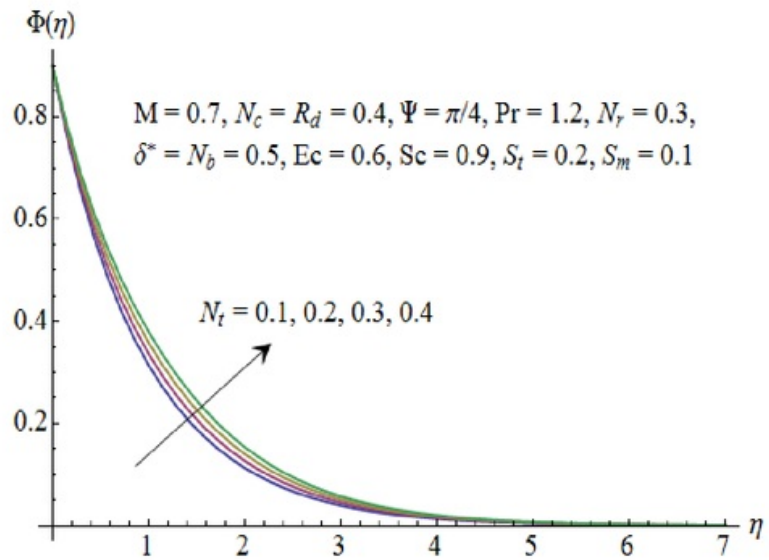


Fig. 8.23: Influence of N_t on $\Phi(\eta)$.

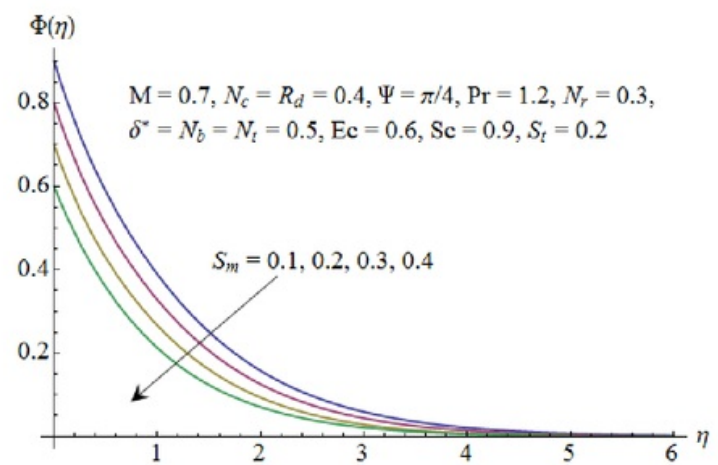


Fig. 8.24: Influence of S_m on $\Phi(\eta)$.

Table 8.2: Comparison of skin friction coefficient with Ibrahim and Shankar [64] when $N_c = R_d = N_r = \Psi = Pr = S_t = \delta^* = N_b = N_t = Sc = Ec = S_m = 0$.

M	Ibrahim and Shankar [64]	Present results
0	1.2808	1.2808
1	1.4142	1.4142
5	2.4494	2.4494

Table 8.3: Numerical values of skin friction coefficient for different parameters when $N_b = 0.9, N_t = 0.2, Pr = 1.2, Sc = 0.9, R_d = 0.4$ and $Ec = 0.6$.

Ψ	M	λ	N_r	δ	S_t	S_m	$-f''(0)$
$\pi/6$	0.7	0.4	0.3	0.6	0.1	0.1	1.365
$\pi/3$							1.294
$\pi/2$							1.269
$\pi/4$	0.5						1.252
	0.6						1.289
	0.8						1.360
	0.7	0.1					1.428
		0.3					1.359
		0.5					1.291
		0.4	0.5				1.306
			0.6				1.297
			0.7				1.287
			0.3	0.1			1.169
				0.2			1.203
				0.3			1.235
				0.6	0.1		1.325
					0.2		1.342
					0.3		1.359
					0.1	0.2	1.330
						0.3	1.336
						0.4	1.341

Table 8.4: Numerical values of Nusselt and Sherwood numbers for different parameters when $M = 0.7$, $N_c = 0.4$, $N_r = 0.3$, $\Psi = \pi/4$, $R_d = 0.4$, $\delta^* = 0.6$ and $Ec = 0.6$.

S_t	S_m	N_b	N_t	Pr	Sc	$-\left(1 + \frac{4}{3}R_d\right)\left(\frac{1}{1-S_t}\right)\theta'(0)$	$-\left(\frac{1}{1-S_m}\right)\phi'(0)$
0.1	0.1	0.9	0.2	1.2	0.9	1.078	1.197
	0.2					1.190	1.193
	0.3					1.334	1.189
0.1	0.2					1.080	1.333
	0.3					1.082	1.511
	0.4					1.083	1.746
	0.1	0.5				1.209	1.157
		0.7				1.142	1.183
		1.0				1.047	1.201
		0.9	0.1			1.078	1.197
			0.3			1.047	1.142
			0.5			1.017	1.093
			0.2	1.5		1.215	1.187
				1.7		1.294	1.183
				2.0		1.398	1.177
				1.2	0.5	1.141	0.8375
					0.7	1.105	1.028
					1.0	1.066	1.275

8.5 Concluding remarks

MHD unsteady flow of viscous nanofluid over an inclined stretching sheet has been studied. Effects of different parameters on the velocity, temperature and concentration profiles are analyzed. The following observations are worth mentioning.

- Angle of inclination enhances the velocity.
- Velocity profile decreases with an increase in thermal and solutal stratification parameters.

- Increase in the mixed convection parameter enhances the velocity profile.
- Thermal stratification parameter reduces the temperature field.
- Concentration profile decreases with the increase in solutal stratification parameter.
- The impact of thermophoresis parameter and Schmidt number on the concentration profile is opposite.
- Higher values of solutal stratification parameter correspond to larger values of local Nusselt and Sherwood numbers.

Chapter 9

Magneto hydrodynamic stagnation point flow of a Jeffrey nanofluid with Newtonian heating

The purpose of present chapter is to examine the stagnation point flow of a Jeffrey nanofluid towards a stretching surface in the presence of Newtonian heating. Fluid is electrically conducting in the presence of applied magnetic field. Appropriate transformations reduce the non-linear partial differential system to ordinary differential system. Governing nonlinear system is computed for the convergent solutions. Results of velocity, temperature and concentration fields are calculated in series forms. Effects of different parameters on the velocity, temperature and concentration profiles are shown and analyzed. Skin friction coefficient, Nusselt and Sherwood numbers are also computed and examined.

9.1 Flow equations

The extra stress tensor for Jeffrey fluid is

$$\mathbf{S} = \frac{\mu}{1 + \lambda_1} \left[\mathbf{A}_1 + \lambda_2 \frac{d\mathbf{A}_1}{dt} \right]. \quad (9.1)$$

In above expressions μ is the dynamic viscosity, λ_1 is the ratio of relaxation to retardation times, λ_2 is the retardation time, \mathbf{A}_1 is the first Rivlin-Erickson tensor, d/dt is the material derivative define as

$$\frac{d}{dt} = \frac{\partial}{\partial t} + (\mathbf{V} \cdot \nabla). \quad (9.2)$$

Eq. (9.1) reduces to a Newtonian fluid when $\lambda_1 = \lambda_2 = 0$.

9.2 Problem formulation

Let us consider the steady two-dimensional stagnation point flow of a Jeffrey nanofluid towards a stretching surface-. The x -axis is taken along the stretching surface in the direction of motion and y -axis is perpendicular to it. A uniform transverse magnetic field of strength B_0 is applied parallel to the y -axis. It is assumed that the induced magnetic field and the electric field effects are negligible. Effects of Brownian motion and thermophoresis are presented. Further, the surface exhibits Newtonian heating boundary condition. The boundary layer flow in the present analysis is governed by the following equations:

$$\frac{\partial u}{\partial x} + \frac{\partial v}{\partial y} = 0, \quad (9.3)$$

$$\begin{aligned} u \frac{\partial u}{\partial x} + v \frac{\partial u}{\partial y} = & \frac{\mu}{1 + \lambda_1} \left[\frac{\partial^2 u}{\partial y^2} + \lambda_2 \left(\frac{\partial u}{\partial y} \frac{\partial^2 u}{\partial x \partial y} + u \frac{\partial^3 u}{\partial x \partial y^2} - \frac{\partial u}{\partial x} \frac{\partial^2 u}{\partial y^2} + v \frac{\partial^3 u}{\partial y^3} \right) \right] \\ & + U_\infty \frac{\partial U_\infty}{\partial x} + \frac{\sigma B_0^2}{\rho} (U_\infty - u), \end{aligned} \quad (9.4)$$

$$u \frac{\partial T}{\partial x} + v \frac{\partial T}{\partial y} = \alpha \frac{\partial^2 T}{\partial y^2} + \tau \left[D_B \frac{\partial T}{\partial y} \frac{\partial C}{\partial y} + \frac{D_T}{T_\infty} \left(\frac{\partial T}{\partial y} \right)^2 \right], \quad (9.5)$$

$$u \frac{\partial C}{\partial x} + v \frac{\partial C}{\partial y} = D_B \frac{\partial^2 C}{\partial y^2} + \frac{D_T}{T_\infty} \frac{\partial^2 T}{\partial y^2}. \quad (9.6)$$

The subjected boundary conditions are

$$\begin{aligned} u &= u_w(x) = cx, \quad v = 0, \quad \frac{\partial T}{\partial y} = -h_s T, \quad C = C_w \quad \text{at } y = 0, \\ u &\rightarrow dx, \quad T \rightarrow T_\infty, \quad C \rightarrow C_\infty \quad \text{as } y \rightarrow \infty. \end{aligned} \quad (9.7)$$

where u and v are the velocity components along the x - and y - directions respectively, μ , ρ and σ are the dynamic viscosity, density and electrical conductivity of the fluid, λ_1 is the ratio of relaxation to retardation times, λ_2 is the retardation time, U_∞ is the free stream velocity, T , T_∞ , C_w and C_∞ are the fluid temperature, ambient fluid temperature, constant wall concentration and ambient fluid concentration, $\tau = (\rho c)_p/(\rho c)_f$ is the ratio between the effective heat capacity of the nanoparticle material and heat capacity of the fluid, D_B is the Brownian diffusion coefficient, D_T is the thermophoretic diffusion coefficient, $\alpha = k/(\rho c)_f$ is the thermal diffusivity and h_s is the heat transfer parameter.

We now introduce the following similarity transformations

$$u = cx f'(\eta), \quad v = -\sqrt{\nu c} f(\eta), \quad \eta = \sqrt{\frac{c}{\nu}} y, \quad \theta(\eta) = \frac{T - T_\infty}{T_\infty}, \quad \Phi(\eta) = \frac{C - C_\infty}{C_w - C_\infty}. \quad (9.8)$$

Eq. (9.3) is satisfied automatically and Eqs. (9.4 – 9.7) after using Eq. (9.8) can be reduced as follows:

$$f''' + (1 + \lambda_1)(f f'' - f'^2) + \beta^*(f''^2 - f f^{iv}) + (1 + \lambda_1)(\gamma^2 + M(\gamma - f')) = 0, \quad (9.9)$$

$$\frac{1}{\text{Pr}} \theta'' + f \theta' + N_b \theta' \Phi' + N_t \theta'^2 = 0, \quad (9.10)$$

$$\Phi'' + Sc f \Phi' + \frac{N_t}{N_b} \theta'' = 0, \quad (9.11)$$

$$\begin{aligned} f'(0) &= 1, \quad f(0) = 0, \quad \theta'(0) = -\gamma^*[1 + \theta(0)], \quad \Phi(0) = 1 \\ f'(\infty) &\rightarrow \frac{d}{c} = \gamma, \quad \theta(\infty) \rightarrow 0, \quad \Phi(\infty) \rightarrow 0, \end{aligned} \quad (9.12)$$

where $\beta^* = c\lambda_2$ is the Deborah number, $M = \sigma B_0^2/\rho c$ is the Hartman number, $\text{Pr} = \nu/\alpha$ is the Prandtl number, $N_b = \tau D_B(C_w - C_\infty)/\nu$ is the Brownian motion parameter, $N_t = \tau D_T/\nu$ is the thermophoresis parameter, $\gamma^* = h_s \sqrt{\nu/c}$ is the conjugate parameter for Newtonian heating, γ is the ratio of rates and $Sc = \nu/D_B$ is the Schmidt number.

The important physical quantities of interest in this problem are the local skin-friction coefficient $C_{s,f}$, local Nusselt number Nu and the local Sherwood number Sh which are given

by

$$C_{sf} = \frac{\tau_w}{\frac{1}{2}\rho u_w^2}, \quad Nu = \frac{xq_w}{k(T - T_\infty)}, \quad Sh = \frac{xq_m}{D_B(C_w - C_\infty)}, \quad (9.13)$$

where the surface shear stress τ_w , wall heat flux q_w and wall mass flux q_m are given by

$$\tau_w = \mu \frac{\partial u}{\partial y} \Big|_{y=0}, \quad q_w = -k \frac{\partial T}{\partial y} \Big|_{y=0}, \quad q_m = -D_B \frac{\partial C}{\partial y} \Big|_{y=0}. \quad (9.14)$$

By using the above equations, we get

$$C_{sf}(\text{Re}_x)^{1/2} = f''(0), \quad Nu(\text{Re}_x)^{-1/2} = \gamma^* \left[1 + \frac{1}{\theta(0)} \right], \quad Sh(\text{Re}_x)^{-1/2} = -\Phi'(0), \quad (9.15)$$

where $\text{Re}_x = cx^2/\nu$ is the local Reynolds number.

9.3 Series solutions

Initial approximations $f_0(\eta)$, $\theta_0(\eta)$ and $\Phi_0(\eta)$ and auxiliary linear operators \mathcal{L}_f , \mathcal{L}_θ and \mathcal{L}_Φ are taken in the forms

$$f_0(\eta) = (\gamma - 1)(e^{-\eta} - 1), \quad \theta_0(\eta) = \frac{\gamma^*}{1 - \gamma^*} e^{-\eta}, \quad \Phi_0(\eta) = e^{-\eta}, \quad (9.16)$$

$$\mathcal{L}_f = f''' + f'', \quad \mathcal{L}_\theta = \theta'' - \theta, \quad \mathcal{L}_\Phi = \Phi'' - \Phi, \quad (9.17)$$

subject to the properties

$$\begin{aligned} \mathcal{L}_f[c_1 + c_2\eta + c_3e^{-\eta}] &= 0, \\ \mathcal{L}_\theta[c_4e^\eta + c_5e^{-\eta}] &= 0, \\ \mathcal{L}_\Phi[c_6e^\eta + c_7e^{-\eta}] &= 0, \end{aligned} \quad (9.18)$$

in which c_i ($i = 1 - 7$) are the constants.

If $p \in [0, 1]$ indicates the embedding parameter then the zeroth order deformation problems are constructed as follows:

$$(1 - p)\mathcal{L}_f[\hat{f}(\eta; p) - f_0(\eta)] = p\mathcal{H}_f\mathcal{N}_f[\hat{f}(\eta; p)], \quad (9.19)$$

$$(1-p)\mathcal{L}_\theta[\hat{\theta}(\eta;p) - \theta_0(\eta)] = p\hbar_\theta\mathcal{N}_\theta[\hat{\theta}(\eta;p), \hat{f}(\eta;p), \hat{\Phi}(\eta;p)], \quad (9.20)$$

$$(1-p)\mathcal{L}_\Phi[\hat{\Phi}(\eta;p) - \Phi_0(\eta)] = p\hbar_\Phi\mathcal{N}_\Phi[\hat{\Phi}(\eta;p), \hat{f}(\eta;p), \hat{\theta}(\eta;p)], \quad (9.21)$$

$$\begin{aligned} \hat{f}'(0;p) &= 1, \quad \hat{f}(0;p) = 0, \quad \hat{f}'(\infty;p) = \gamma, \\ \hat{\theta}'(0;p) &= -\gamma^*[1 + \hat{\theta}(0;p)], \quad \hat{\theta}(\infty;p) = 0, \\ \hat{\Phi}(0;p) &= 1, \quad \hat{\Phi}(\infty;p) = 0, \end{aligned} \quad (9.22)$$

where \hbar_f , \hbar_θ and \hbar_Φ are the nonzero auxiliary parameters and the nonlinear operators \mathcal{N}_f , \mathcal{N}_θ and \mathcal{N}_Φ are given by

$$\begin{aligned} \mathcal{N}_f[\hat{f}(\eta;p)] &= \frac{\partial^3 \hat{f}(\eta;p)}{\partial \eta^3} + (1 + \lambda_1) \left[\hat{f}(\eta;p) \frac{\partial^2 \hat{f}(\eta;p)}{\partial \eta^2} - \left(\frac{\partial \hat{f}(\eta;p)}{\partial \eta} \right)^2 \right] \\ &+ \beta^* \left[\left(\frac{\partial^2 \hat{f}(\eta;p)}{\partial \eta^2} \right)^2 - \hat{f}(\eta;p) \frac{\partial^4 \hat{f}(\eta;p)}{\partial \eta^4} \right] + (1 + \lambda_1) [\gamma^2 \\ &+ M \left(\gamma - \frac{\partial \hat{f}(\eta;p)}{\partial \eta} \right)], \end{aligned} \quad (9.23)$$

$$\begin{aligned} \mathcal{N}_\theta[\hat{\theta}(\eta;p), \hat{f}(\eta;p), \hat{\Phi}(\eta;p)] &= \frac{1}{\text{Pr}} \frac{\partial^2 \hat{\theta}(\eta;p)}{\partial \eta^2} + \hat{f}(\eta;p) \frac{\partial \hat{\theta}(\eta;p)}{\partial \eta} + N_b \frac{\partial \hat{\theta}(\eta;p)}{\partial \eta} \frac{\partial \hat{\Phi}(\eta;p)}{\partial \eta} \\ &+ N_t \left(\frac{\partial \hat{\theta}(\eta;p)}{\partial \eta} \right)^2, \end{aligned} \quad (9.24)$$

$$\mathcal{N}_\Phi[\hat{\Phi}(\eta;p), \hat{f}(\eta;p), \hat{\theta}(\eta;p)] = \frac{\partial^2 \hat{\Phi}(\eta;p)}{\partial \eta^2} + Sc \hat{f}(\eta;p) \frac{\partial \hat{\Phi}(\eta;p)}{\partial \eta} + \frac{N_t}{N_b} \frac{\partial^2 \hat{\theta}(\eta;p)}{\partial \eta^2}. \quad (9.25)$$

The m^{th} order deformation equations can be presented in the following forms

$$\mathcal{L}_f[f_m(\eta) - \chi_m f_{m-1}(\eta)] = \hbar_f \mathcal{R}_{f,m}(\eta), \quad (9.26)$$

$$\mathcal{L}_\theta[\theta_m(\eta) - \chi_m \theta_{m-1}(\eta)] = \hbar_\theta \mathcal{R}_{\theta,m}(\eta), \quad (9.27)$$

$$\mathcal{L}_\Phi[\Phi_m(\eta) - \chi_m \Phi_{m-1}(\eta)] = \hbar_\Phi \mathcal{R}_{\Phi,m}(\eta), \quad (9.28)$$

$$f_m(0) = f'_m(0) = f'_m(\infty) = \theta'_m(0) + \gamma^* \theta_m(0) = \theta_m(\infty) = \Phi_m(0) = \Phi_m(\infty) = 0, \quad (9.29)$$

$$\begin{aligned} \mathcal{R}_{f,m}(\eta) = & f'''_{m-1} + (1 + \lambda_1) \sum_{k=0}^{m-1} [f_{m-1-k} f''_k - f'_{m-1-k} f'_k] + \beta^* [f''_{m-1-k} f''_k - f_{m-1-k} f''_k] \\ & + (1 + \lambda_1) [\gamma^2 + M(\gamma - f'_{m-1})], \end{aligned} \quad (9.30)$$

$$\mathcal{R}_{\theta,m}(\eta) = \frac{1}{\text{Pr}} \theta''_{m-1} + \sum_{k=0}^{m-1} [f_{m-1-k} \theta'_k + N_b \theta'_{m-1-k} \Phi'_k + N_t \theta'_{m-1-k} \theta'_k], \quad (9.31)$$

$$\mathcal{R}_{\Phi,m}(\eta) = \Phi''_{m-1} + Sc \sum_{k=0}^{m-1} f_{m-1-k} \Phi'_k + \frac{N_t}{N_b} \theta''_{m-1}, \quad (9.32)$$

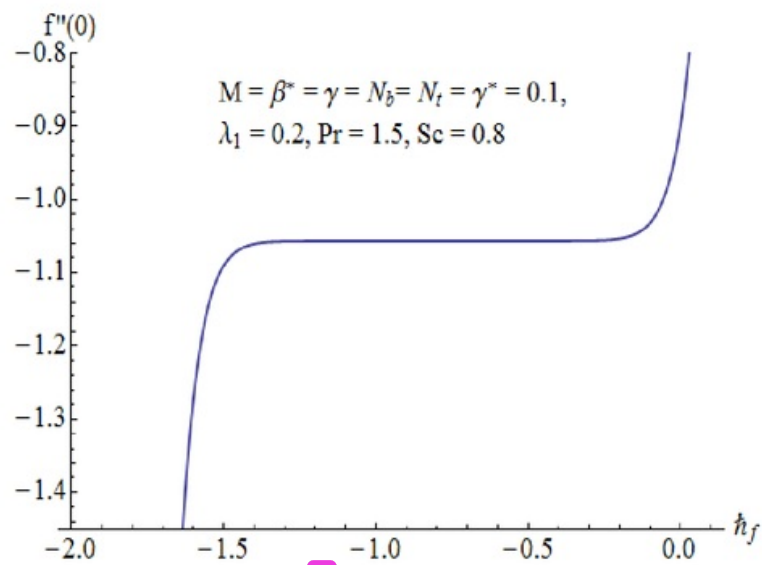
$$\chi_m = \begin{cases} 0, & m \leq 1 \\ 1, & m > 1 \end{cases}. \quad (9.33)$$

The general solutions (f_m, θ_m, Φ_m) comprising the special solutions $(f_m^*, \theta_m^*, \Phi_m^*)$ are

$$\begin{aligned} f_m(\eta) &= f_m^*(\eta) + c_1 + c_2 \eta + c_3 e^{-\eta}, \\ \theta_m(\eta) &= \theta_m^*(\eta) + c_4 e^\eta + c_5 e^{-\eta}, \\ \Phi_m(\eta) &= \Phi_m^*(\eta) + c_6 e^\eta + c_7 e^{-\eta}. \end{aligned} \quad (9.34)$$

9.4 Convergence analysis

2 Now the solutions of Eqs. (9.9 – 9.11) subject to the boundary conditions (9.12) is computed by means of homotopy analysis method. The convergence of the series solutions is highly dependent upon the auxiliary parameters \hbar_f , \hbar_θ and \hbar_Φ . For valid ranges of these parameters, we have sketched the \hbar -curves at 15th-order of approximations (see Figs. 9.1 – 9.3). We can see that the admissible values of \hbar_f , \hbar_θ and \hbar_Φ are $-1.3 \leq \hbar_f \leq -0.2$, $-1.3 \leq \hbar_\theta \leq -0.2$ and $-1.5 \leq \hbar_\Phi \leq -0.7$. Further, the series solutions converge in the whole region of η ($0 < \eta < \infty$) when $\hbar_f = -1$, $\hbar_\theta = -1.1$ and $\hbar_\Phi = -1.3$.



2
 Fig. 9.1: h - curve for the velocity field.

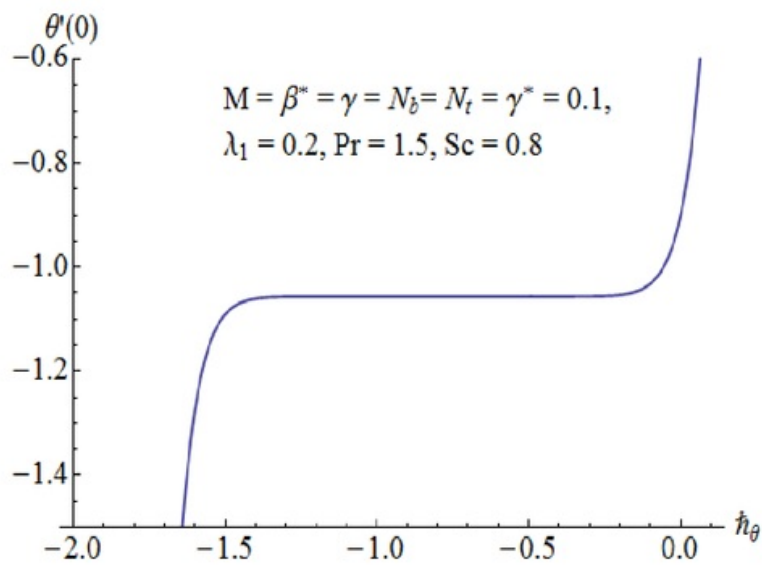


Fig. 9.2: h - curve for the temperature field.

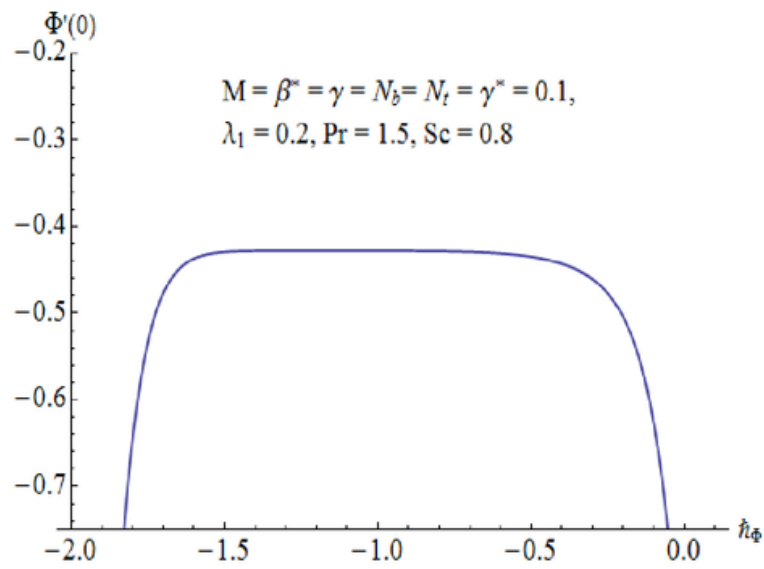


Fig. 9.3: $h-$ curve for the concentration field.

Table 9.1: Convergence of HAM solutions for different order of approximations when $\lambda_1 = 0.2$, $Pr = 1.5$, $\beta^* = \gamma = M = N_b = N_t = \gamma^* = 0.1$ and $Sc = 0.8$.

Order of approximations	$-f''(0)$	$-\theta'(0)$	$-\Phi'(0)$
1	1.08225	0.113764	0.459778
5	1.05658	0.116260	0.433609
8	1.05648	0.116289	0.428189
15	1.05648	0.116273	0.427542
18	1.05648	0.116273	0.427544
20	1.05648	0.116273	0.427544
25	1.05648	0.116273	0.427544
30	1.05648	0.116273	0.427544
35	1.05648	0.116273	0.427544

9.5 Results and discussion

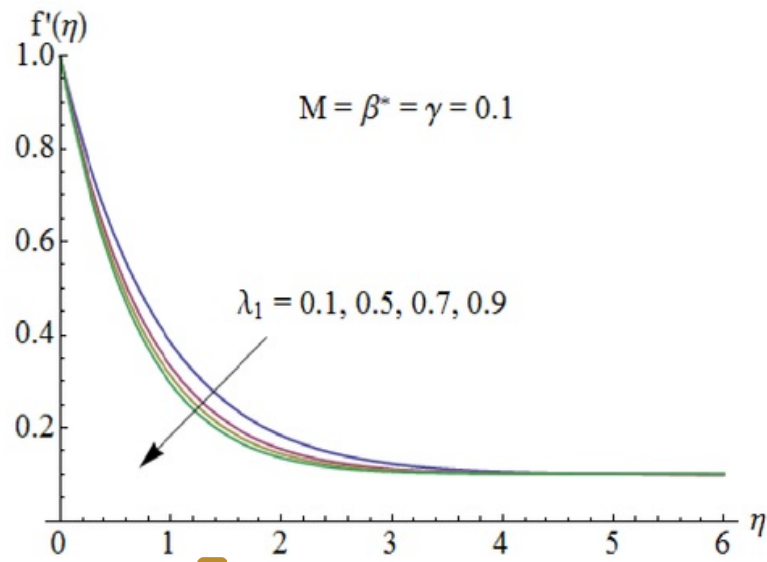
The effects of different parameters on the dimensionless flow, heat and mass transfer rates are investigated and presented graphically in this section. Figs. (9.4 – 9.7) exhibit the dimensionless velocity profiles for different values of ratio of relaxation to retardation times λ_1 , Hartman number M , Deborah number β^* and ratio parameter γ . Effects of λ_1 on the velocity profile f' can be seen from Fig. 9.4. Here the values of f' and boundary layer thickness decrease when λ_1 increases. Effects of Hartman number M on the velocity f' are depicted in Fig. 9.5. The graph shows that the values of velocity function f' and the boundary layer thickness decrease by increasing M . As the magnetic field has the tendency to slow down the movement of the fluid which leads to a decrease in the velocity and momentum boundary layer thickness. Fig. 9.6 shows that larger values of Deborah number β^* correspond to higher velocity. Fig. 9.7 illustrates the influence of ratio parameter γ on the velocity profile f' . There is an increase in velocity field f' and boundary layer thickness when the velocity of the stretching sheet exceeds the free stream velocity ($\gamma < 1$).

Effects of ratio of relaxation to retardation times λ_1 , Hartman number M , Deborah number β^* , ratio parameter γ , Prandtl number Pr , Brownian motion parameter N_b , thermophoresis parameter N_t , Schmidt number Sc and Newtonian heating parameter γ^* on the temperature

profile θ are shown in the Figs. (9.8 – 9.16). Effect of λ_1 on the temperature is analyzed in Fig. 9.8. It is observed that the temperature and the thermal boundary layer thickness are increasing function of λ_1 . Fig. 9.9 illustrates the effects of M on temperature profile θ . As Lorentz force is a resistive force that opposes the fluid motion. So heat is produced and as a result thermal boundary layer thickness increases. Variations of β^* , γ and Pr on temperature profile θ can be seen in the Figs. (9.10 – 9.12). There is a decrease in temperature θ when Deborah number β^* , ratio parameter γ and Prandtl number Pr are increased. In fact the thermal diffusivity decreases by increasing Pr and thus the heat diffused away slowly from the heated surface. Fig. 9.13 represents the effect of Brownian motion parameter N_b on temperature profile θ . Temperature profile θ increases for an increase in N_b . The behavior of N_t on the temperature profile is similar to that of N_b (see Fig. 9.14). Also the temperature profile θ and thermal boundary layer thickness decrease when the Schmidt number Sc increases. This is due to the fact that an increase in Sc reduces the molecular diffusivity. Fig. 9.16 displays the effect of Newtonian heating parameter γ on temperature field θ . The temperature field θ is found to increase when γ increases.

Figs. (9.17 – 9.25) illustrate the effects of ratio of relaxation to retardation times λ_1 , Hartman number M , Deborah number β^* , ratio parameter γ , Brownian motion parameter N_b , Schmidt number Sc , Prandtl number Pr , thermophoresis parameter N_t and Newtonian heating parameter γ^* on the dimensionless nanoparticle volume fraction profile Φ . It is observed that the mass fraction Φ and the associated boundary layer decrease when the values of λ_1 , M , β^* , γ , N_b and Sc are increased and these quantities increase for higher Pr , N_t and γ^* .

Table 9.1 shows the convergence of the series solutions. It is observed that convergence is achieved at 18th order of approximations. In Table 9.2 some numerical values of skin friction coefficient are given. This Table depicts that skin friction coefficient decreases by increasing λ_1 and M while it increases for larger values of β^* and γ . Table 9.3 includes the values of local Nusselt and Sherwood numbers. It is noted that Nusselt number decreases by increasing N_b , N_t , M and γ^* while Sherwood number increases for higher N_b and it decreases for larger vales of N_t , M and γ^* .



6
Fig. 9.4: Influence of λ_1 on $f'(\eta)$.

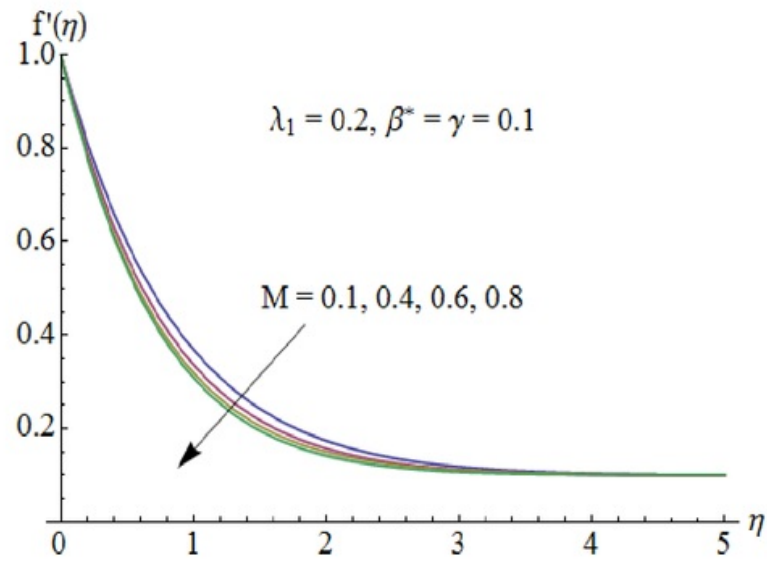
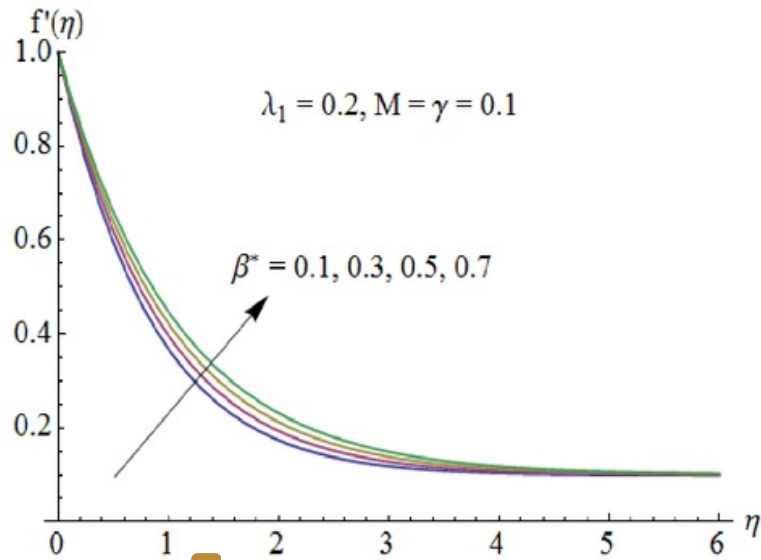


Fig. 9.5: Influence of M on $f'(\eta)$.



6

Fig. 9.6: Influence of β^* on $f'(\eta)$.

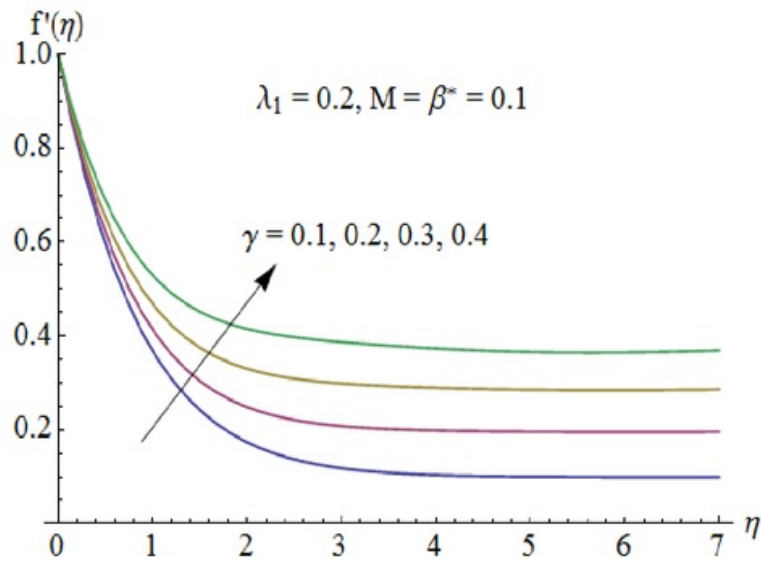


Fig. 9.7: Influence of γ on $f'(\eta)$.

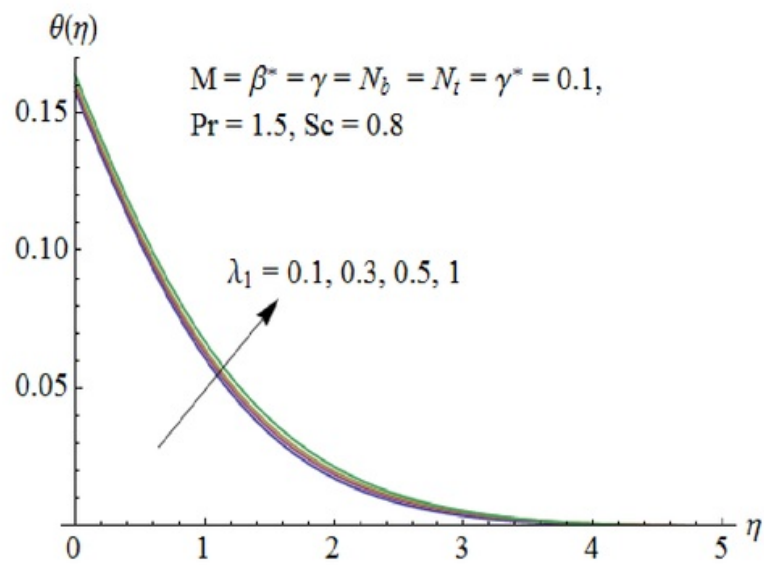


Fig. 9.8: Influence of λ_1 on $\theta(\eta)$.

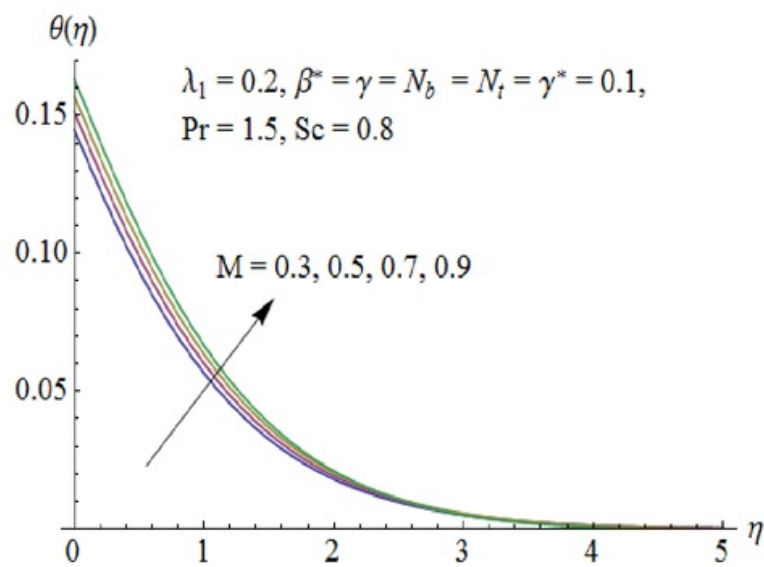


Fig. 9.9: Influence of M on $\theta(\eta)$.

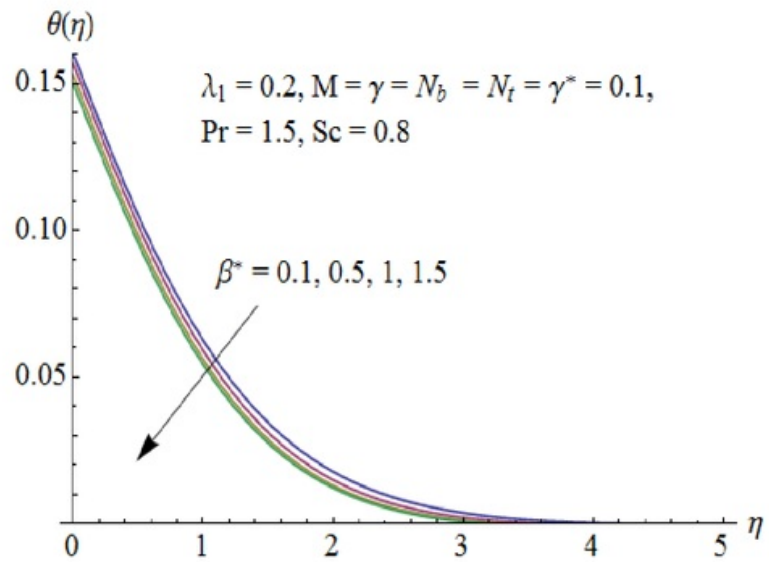


Fig. 9.10: Influence of β^* on $\theta(\eta)$.

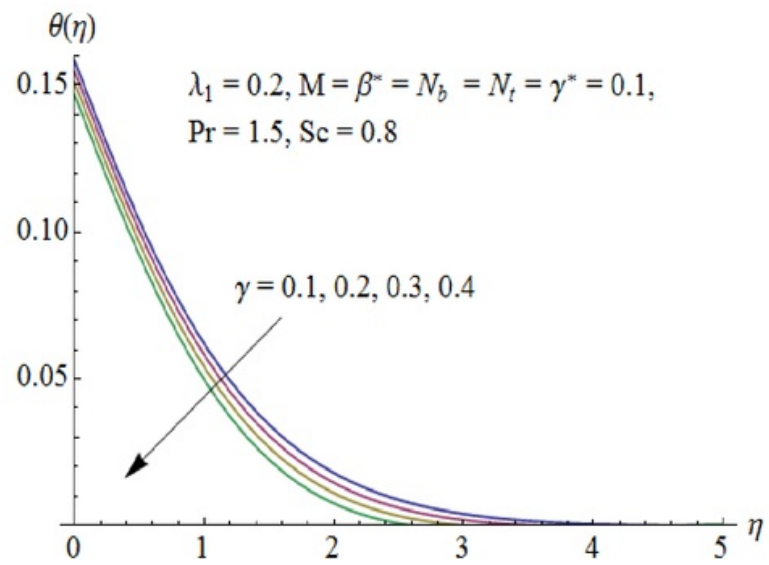


Fig. 9.11: Influence of γ on $\theta(\eta)$.

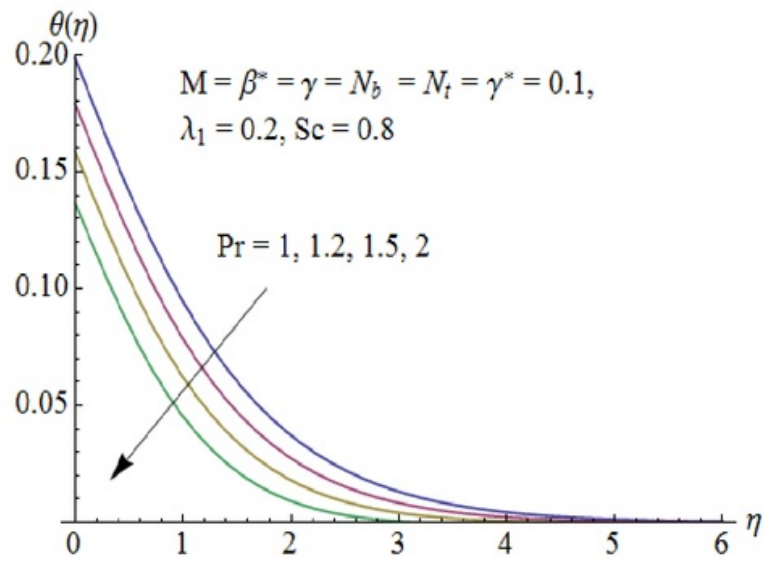
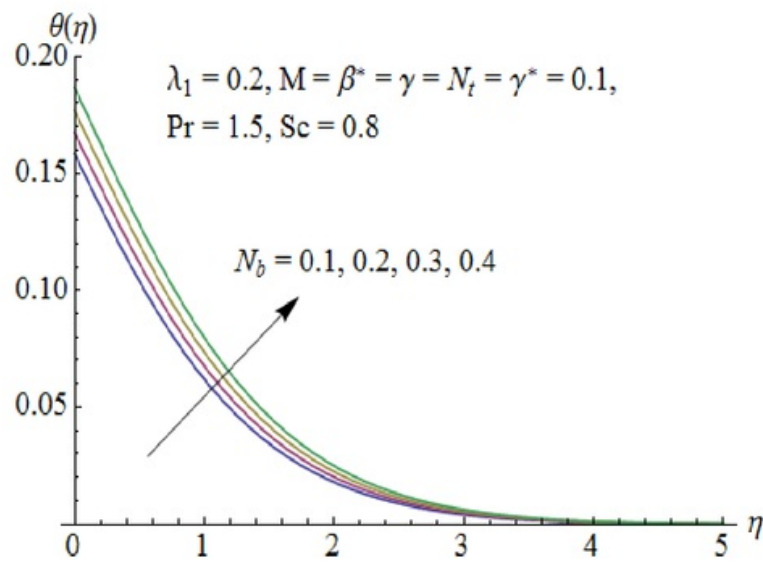


Fig. 9.12: Influence of Pr on $\theta(\eta)$.



6
Fig. 9.13: Influence of N_b on $\theta(\eta)$.

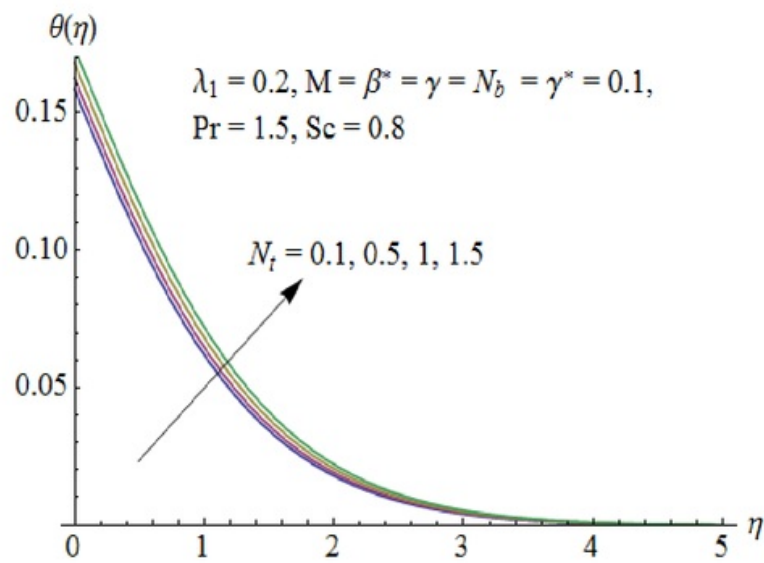
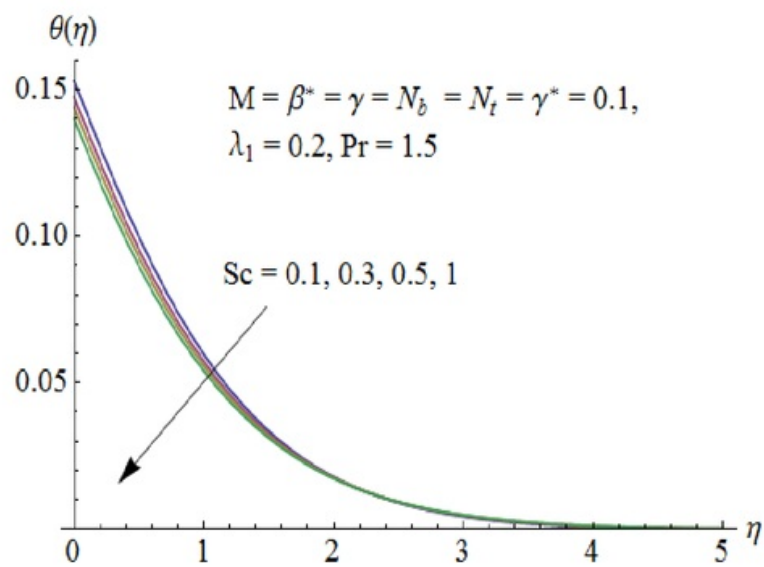


Fig. 9.14: Influence of N_t on $\theta(\eta)$.



6
Fig. 9.15: Influence of Sc on $\theta(\eta)$.

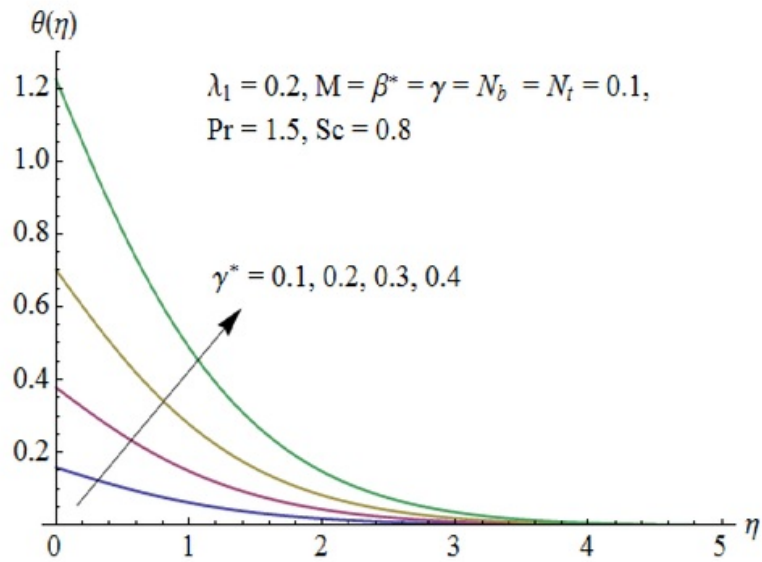


Fig. 9.16: Influence of γ^* on $\theta(\eta)$.

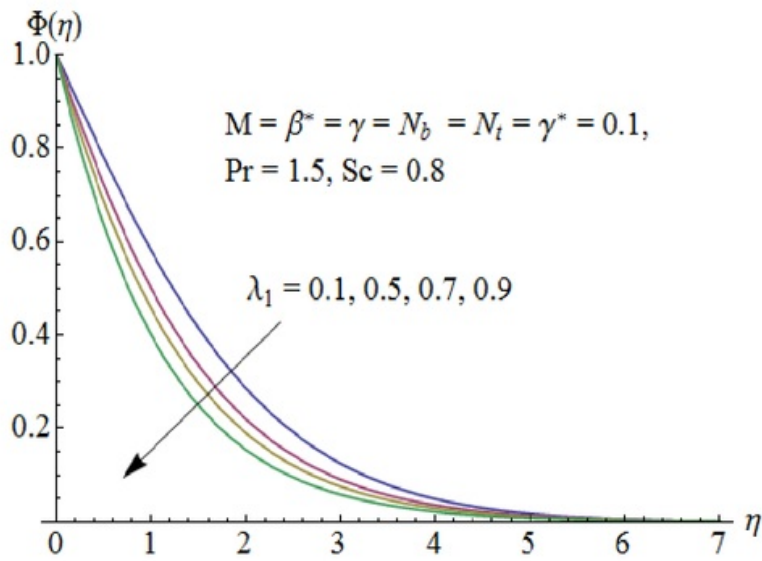
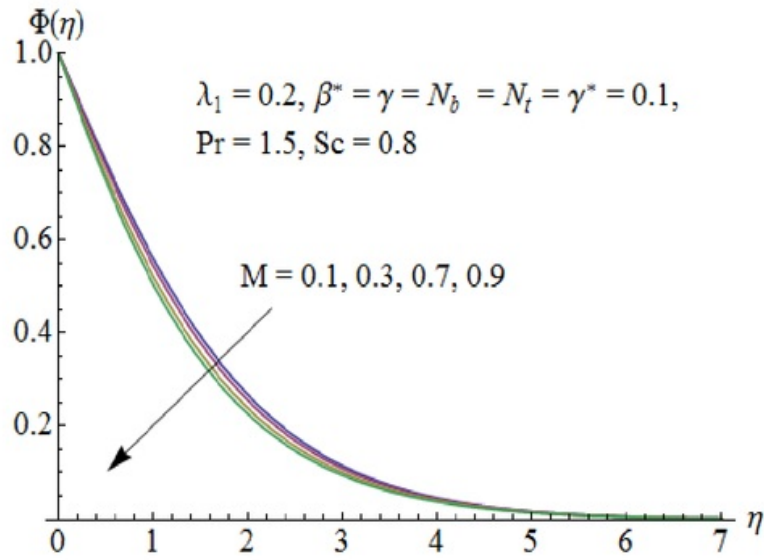


Fig. 9.17: Influence of λ_1 on $\Phi(\eta)$.



6
 Fig. 9.18: Influence of M on $\Phi(\eta)$.

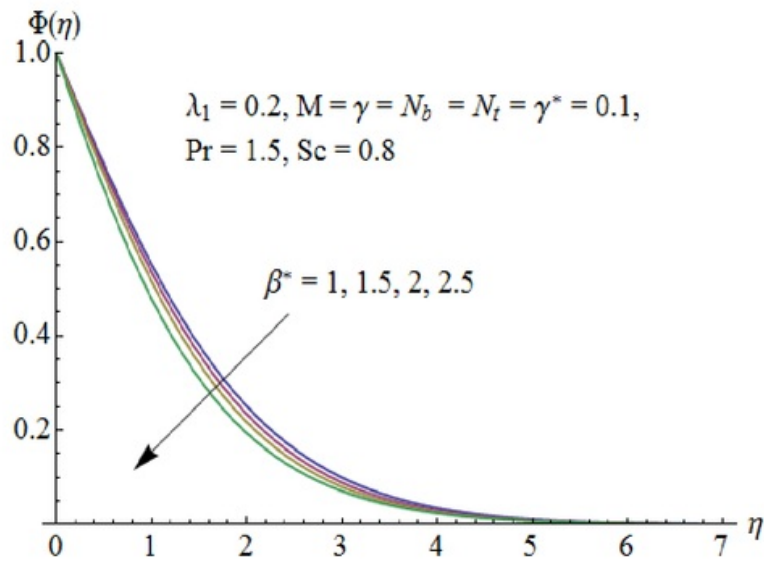
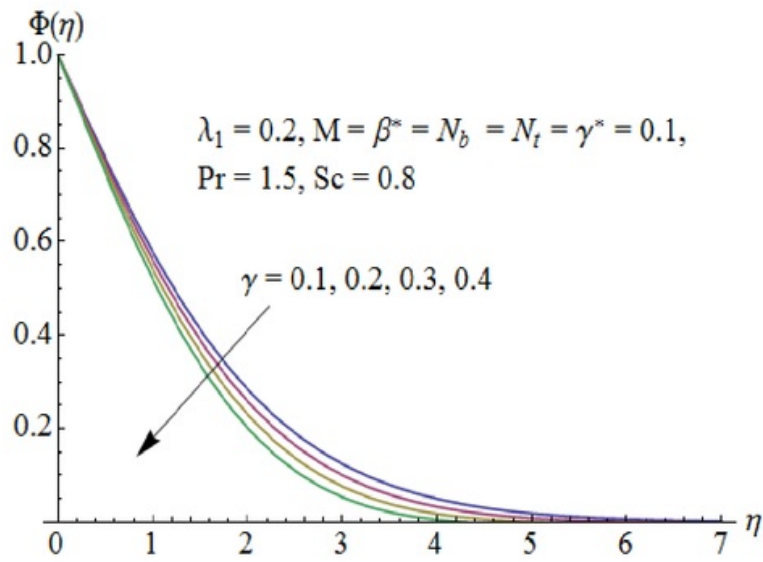


Fig. 9.19: Influence of β^* on $\Phi(\eta)$.



6
 Fig. 9.20: Influence of γ on $\Phi(\eta)$.

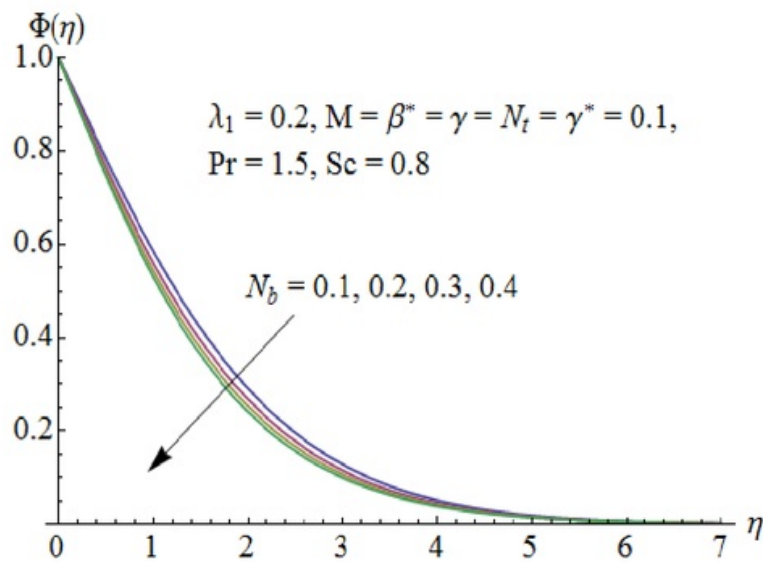
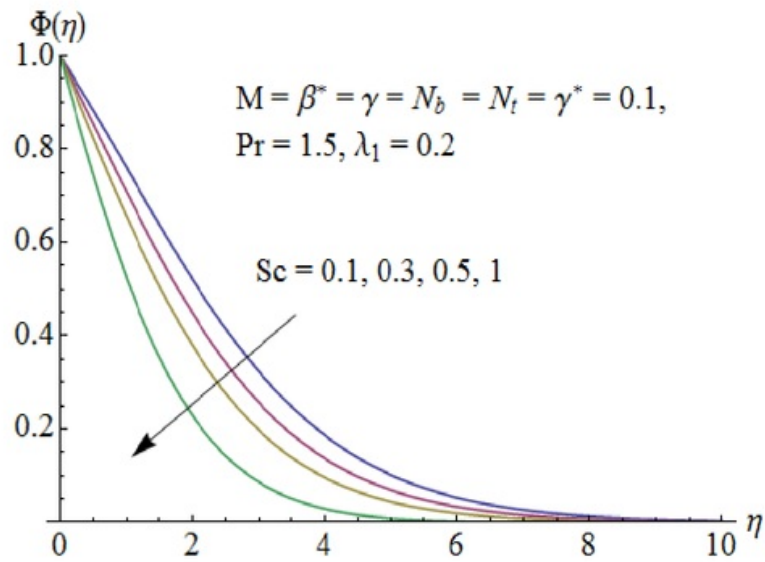


Fig. 9.21: Influence of N_b on $\Phi(\eta)$.



6
 Fig. 9.22: Influence of Sc on $\Phi(\eta)$.

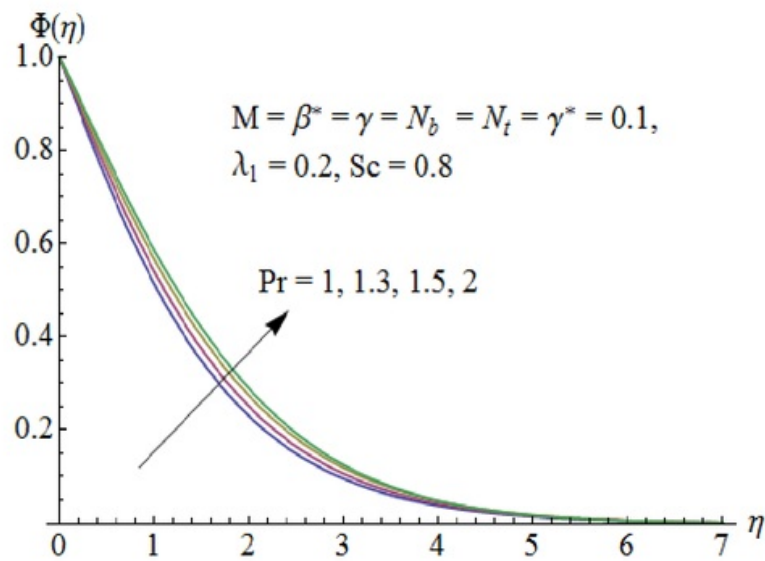
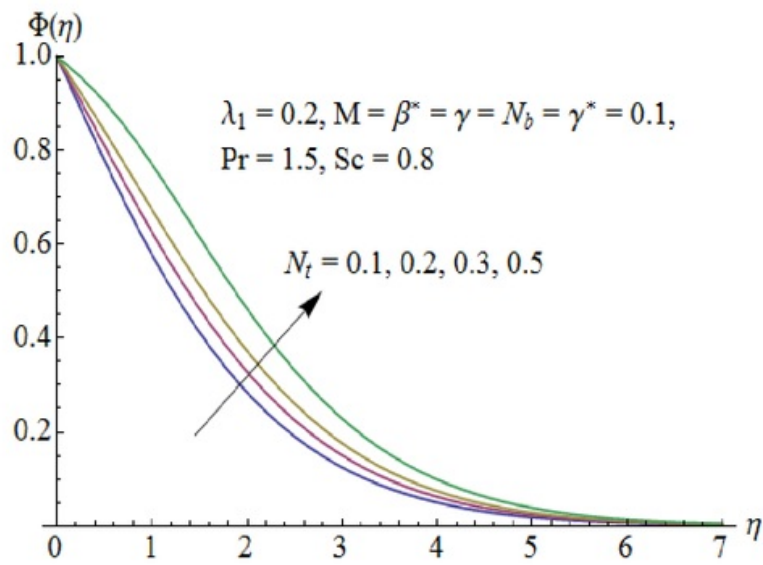


Fig. 9.23: Influence of Pr on $\Phi(\eta)$.



6

Fig. 9.24: Influence of N_t on $\Phi(\eta)$.

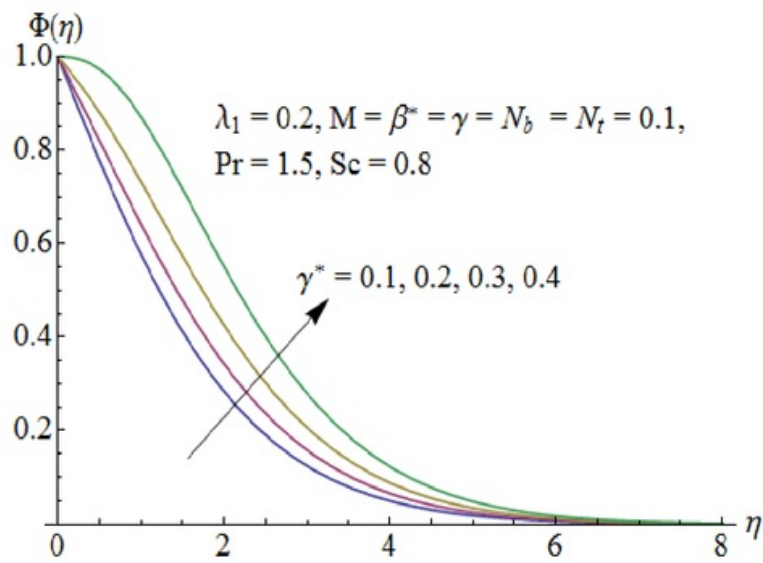


Fig. 9.25: Influence of γ^* on $\Phi(\eta)$.

1

Table 9.2: Numerical values of skin friction coefficient for different values of λ_1 , M , β^* and γ .

λ_1	M	β^*	γ	$C_{sf}(\text{Re}_x)^{1/2}$
0.1	0.1	0.1	0.1	-1.05648
			0.3	-1.09962
			0.4	-1.14114
			0.5	-1.18116
0.2	0.15			-1.03400
			0.2	-1.09737
			0.3	-1.13684
			0.4	-1.17502
	0.1	0.15		-1.03399
			0.2	-1.01290
			0.25	-0.993061
			0.3	-0.974349
		0.1	0.01	-1.09255
			0.03	-1.08605
			0.05	-1.07866
			0.07	-1.07040

Table 9.3: Numerical values of local Nusselt and Sherwood numbers when $\lambda_1 = 0.2$, $\beta^* = \gamma = 0.1$, $Pr = 1.5$ and $Sc = 0.8$.

N_b	N_t	M	γ^*	$\gamma^* \left(1 + \frac{1}{\theta(0)}\right)$	$-\Phi'(0)$	
0.1	0.1	0.1	0.1	0.714516	0.427544	
	0.2			0.673145	0.468469	
	0.3			0.633230	0.482122	
	0.5			0.557819	0.493069	
	0.1	0.2		0.710164	0.346337	
		0.3		0.705776	0.265221	
		0.4		0.701351	0.184186	
		0.5		0.696886	0.103238	
		0.1	0.2	0.708029	0.421407	
			0.25	0.704905	0.418477	
			0.3	0.701856	0.415635	
			0.4	0.695969	0.410193	
			0.1	0.15	0.711763	0.376091
				0.2	0.708442	0.314421
				0.25	0.704340	0.238845
				0.3	0.699108	0.143430

9.6 Conclusions

Here MHD stagnation point flow of Jeffrey nanofluid over a stretching sheet is studied. Effects of different parameters on the velocity, temperature and concentration profiles are analyzed. The following observations are made.

- Velocity profile decreases by increasing λ_1 and M while it increases when β^* and γ are increased.
- An increase in the values of λ_1 , M , N_b , N_t and γ^* have similar effects on the temperature $\theta(\eta)$ in a qualitative sense.

- Temperature profile decreases by increasing β^* , γ and Sc .
- ¹ An increase in Prandtl number Pr reduces the temperature and thermal boundary layer thickness.
- Concentration profile $\Phi(\eta)$ decreases by increasing λ_1 , M , β^* , γ , N_b and Sc .
- ⁹ The values of skin friction coefficient are higher for increasing values of β^* and γ .
- ² Higher values of N_t , M and γ^* correspond to smaller values of local Nusselt and Sherwood numbers.

Chapter 10

5 MHD three-dimensional flow of nanofluid with velocity slip and nonlinear thermal radiation

5 An analysis has been carried out in this chapter to investigate three-dimensional flow of viscous nanofluid in the presence of partial slip and thermal radiation effects. The flow is induced by a permeable stretching surface. Water is treated as a base fluid and alumina as a nanoparticle. Fluid is electrically conducting in the presence of applied magnetic field. Entire different concept of nonlinear thermal radiation is utilized in the heat transfer process. Different from the previous literature, the nonlinear system for temperature distribution is solved and analyzed. Appropriate transformations reduce the nonlinear partial differential system to ordinary differential system. Convergent series solutions are computed for the velocity and temperature. Effects of different parameters on the velocity, temperature, skin friction coefficient and Nusselt number are computed and examined. It is concluded that heat transfer rate increases when temperature and radiation parameters are increased.

10.1 Flow description

7 Consider the steady three-dimensional nanofluid flow over a stretching sheet situated at $z = 0$. Let (u, v, w) be the velocity components along the (x, y, z) directions, respectively. A constant

5

magnetic field of strength B_0 is applied in the z -direction. The governing boundary layer equations can be written as

$$\frac{\partial u}{\partial x} + \frac{\partial v}{\partial y} = 0, \quad (10.1)$$

$$u \frac{\partial u}{\partial x} + v \frac{\partial u}{\partial y} + w \frac{\partial u}{\partial z} = \nu_{nf} \frac{\partial^2 u}{\partial z^2} - \frac{\sigma_{nf} B_0^2 u}{\rho_{nf}}, \quad (10.2)$$

$$u \frac{\partial v}{\partial x} + v \frac{\partial v}{\partial y} + w \frac{\partial v}{\partial z} = \nu_{nf} \frac{\partial^2 v}{\partial z^2} - \frac{\sigma_{nf} B_0^2 v}{\rho_{nf}}, \quad (10.3)$$

with the boundary conditions given by

$$\begin{aligned} u &= cx + \frac{2 - \sigma_\nu}{\sigma_\nu} \lambda_0 \frac{\partial u}{\partial z}, \quad v = dy + \frac{2 - \sigma_\nu}{\sigma_\nu} \lambda_0 \frac{\partial v}{\partial z}, \quad w = -W \quad \text{at } z = 0, \\ u &\rightarrow 0, \quad v \rightarrow 0 \quad \text{as } z \rightarrow \infty, \end{aligned} \quad (10.4)$$

where c and d are stretching rate constants, $W (> 0)$ is the suction velocity, σ_ν is the tangential momentum accommodation coefficient and λ_0 is the molecular mean free path. The effective nanofluid dynamic viscosity μ_{nf} , density ρ_{nf} , thermal diffusivity α_{nf} , heat capacitance $(\rho c_p)_{nf}$, thermal conductivity k_{nf} and electrical conductivity σ_{nf} are given by

$$\rho_{nf} = \rho_f(1 - \phi) + \rho_s \phi, \quad (10.5)$$

$$\mu_{nf} = \frac{\mu_f}{(1 - \phi)^{2.5}}, \quad (10.6)$$

$$(\rho c_p)_{nf} = (\rho c_p)_f(1 - \phi) + (\rho c_p)_s \phi, \quad (10.7)$$

$$\frac{k_{nf}}{k_f} = \frac{k_s + 2k_f - 2\phi(k_f - k_s)}{k_s + 2k_f + 2\phi(k_f - k_s)}, \quad (10.8)$$

$$\frac{\sigma_{nf}}{\sigma_f} = 1 + \frac{3 \left(\frac{\sigma_s}{\sigma_f} - 1 \right) \phi}{\left(\frac{\sigma_s}{\sigma_f} + 2 \right) - \left(\frac{\sigma_s}{\sigma_f} - 1 \right) \phi}. \quad (10.9)$$

26

Here ϕ is the nanoparticle volume fraction, ρ_f and ρ_s are the densities of the fluid and of the solid fractions, respectively, k_f and k_s are the thermal conductivities of the fluid and of the solid fractions, respectively, and σ_f and σ_s are the electrical conductivity of the fluid and of the solid fractions, respectively.

3

Making use of the following transformations

$$u = cx f'(\eta), \quad v = cy g'(\eta), \quad w = -\sqrt{\nu_f c}(f + g), \quad \eta = \sqrt{\frac{c}{\nu_f}} z, \quad (10.10)$$

equation (10.1) is identically satisfied and Eqs. (10.2 – 10.4) become

$$\frac{1}{(1 - \phi)^{2.5} [1 - \phi + \frac{\rho_s \phi}{\rho_f}]} f''' - f'^2 + (f + g) f'' - \frac{M}{1 - \phi + \frac{\rho_s \phi}{\rho_f}} \frac{\sigma_{nf}}{\sigma_f} f' = 0, \quad (10.11)$$

$$\frac{1}{(1 - \phi)^{2.5} [1 - \phi + \frac{\rho_s \phi}{\rho_f}]} g''' - g'^2 + (f + g) g'' - \frac{M}{1 - \phi + \frac{\rho_s \phi}{\rho_f}} \frac{\sigma_{nf}}{\sigma_f} g' = 0, \quad (10.12)$$

$$\begin{aligned} f'(0) &= 1 + \beta f''(0), \quad g'(0) = \gamma + \beta g''(0), \quad f(0) + g(0) = S, \\ f'(\infty) &\rightarrow 0, \quad g'(\infty) \rightarrow 0, \end{aligned} \quad (10.13)$$

where prime denotes the differentiation with respect to η , M is the Hartman number, β is the velocity slip parameter, γ is the ratio of stretching rates and S is the suction/injection parameter. These quantities are defined by

$$M = \frac{\sigma_f B_0^2}{\rho_f c}, \quad \beta = \frac{2 - \sigma_\nu}{\sigma_\nu} \sqrt{\frac{c}{\nu_f}} \lambda_0, \quad \gamma = \frac{d}{c}, \quad S = \frac{W}{\sqrt{\nu_f c}}. \quad (10.14)$$

10.2 Heat transfer analysis

The boundary layer energy equation in the presence of thermal radiation effects is given by

$$u \frac{\partial T}{\partial x} + v \frac{\partial T}{\partial y} + w \frac{\partial T}{\partial z} = \alpha_{nf} \frac{\partial^2 T}{\partial z^2} - \frac{1}{(\rho c_p)_{nf}} \frac{\partial q_r}{\partial z}, \quad (10.15)$$

where T is the temperature, α_{nf} is the nanofluid thermal diffusivity, c_p is the specific heat at constant pressure and q_r is the radiative heat flux. Using Rosseland approximation for thermal radiation, the radiative heat flux is simplified as follows:

$$q_r = -\frac{4\sigma^*}{3k^*} \frac{\partial T^4}{\partial z} = -\frac{16\sigma^*}{3k^*} T^3 \frac{\partial T}{\partial z}, \quad (10.16)$$

in which σ^* and k^* are the Stefan-Boltzmann constant and the mean absorption coefficient, respectively. Now Eq. (10.15) can be written in the form

$$u \frac{\partial T}{\partial x} + v \frac{\partial T}{\partial y} + w \frac{\partial T}{\partial z} = \alpha_{nf} \frac{\partial^2 T}{\partial z^2} + \frac{16\sigma^*}{3k^*(\rho c_p)_{nf}} \frac{\partial}{\partial z} \left(T^3 \frac{\partial T}{\partial z} \right). \quad (10.17)$$

It is worth mentioning to note that for thermal radiation effect in the existing literature, T^4 in Eq. (10.16) was expanded about the ambient temperature T_∞ . However in the present case this has been avoided to get more meaningful results. Therefore in present analysis the energy equation is nonlinear.

The boundary conditions are

$$T = T_w \text{ at } z = 0, \quad T \rightarrow T_\infty \text{ as } z \rightarrow \infty, \quad (10.18)$$

where T_w and T_∞ are the sheet and ambient fluid temperatures respectively. We define the non-dimensional temperature by

$$\theta(\eta) = \frac{T - T_\infty}{T_w - T_\infty}, \quad (10.19)$$

or

$$T = T_\infty(1 + (\theta_w - 1)\theta), \quad (10.20)$$

where $\theta_w = T_w/T_\infty$ is the temperature parameter. Using Eq. (10.20), Eq. (10.17) takes the form

$$\begin{aligned} \frac{1}{\text{Pr}} \left(\frac{k_{nf}}{k_f} + R_d \right) \theta'' + \frac{R_d}{\text{Pr}} \left[(\theta_w - 1)^3 (3\theta^2 \theta'^2 + \theta^3 \theta'') + 3(\theta_w - 1)^2 (2\theta \theta'^2 + \theta^2 \theta'') \right. \\ \left. + 3(\theta_w - 1)(\theta'^2 + \theta \theta'') \right] + \left(1 - \phi + \frac{(\rho c_p)_s}{(\rho c_p)_f} \phi \right) \theta' (f + g) = 0 \end{aligned} \quad (10.21)$$

where Prandtl number Pr and radiation parameter R_d are defined by

$$\text{Pr} = \frac{\nu_f (\rho c_p)_f}{k_f}, \quad R_d = \frac{16\sigma^* T_\infty^3}{3kk^*}, \quad (10.22)$$

with the boundary conditions

$$\theta(0) = 1, \quad \theta(\infty) \rightarrow 0. \quad (10.23)$$

Surface shear stresses τ_{wx} and τ_{wy} along the x and y directions are given by

$$\tau_{wx} = \mu_{nf} \left. \frac{\partial u}{\partial z} \right|_{z=0}, \quad \tau_{wy} = \mu_{nf} \left. \frac{\partial v}{\partial z} \right|_{z=0}, \quad (10.24)$$

The heat transfer rate at the sheet is defined as follows:

$$q_w = -k_{nf} \left(\frac{\partial T}{\partial z} \right)_{z=0} + (q_r)_w = -(T_w - T_\infty) \sqrt{\frac{c}{\nu_f}} (1 + R_d \theta_w^3) \theta'(0). \quad (10.25)$$

Local skin friction coefficients along the x and y directions and Nusselt number for the problem are given by

$$\begin{aligned} (\text{Re}_x)^{\frac{1}{2}} C_{fx} &= \frac{1}{(1-\phi)^{2.5}} f''(0), \quad (\text{Re}_y)^{\frac{1}{2}} C_{fy} = \frac{1}{\gamma^{\frac{3}{2}} (1-\phi)^{2.5}} g''(0), \\ \frac{Nu}{\sqrt{\text{Re}_x}} &= -(1 + R_d \theta_w^3) \theta'(0), \end{aligned} \quad (10.26)$$

in which $(\text{Re}_x)^{\frac{1}{2}} = x \sqrt{c/\nu_f}$ and $(\text{Re}_y)^{\frac{1}{2}} = y \sqrt{c/\nu_f}$ denotes the local Reynolds number.

10.3 Analytical solutions

Employing the homotopy analysis method the initial approximations and auxiliary linear operators are given by

$$f_0(\eta) = S + \frac{1}{1+\beta}(1 - e^{-\eta}), \quad g_0(\eta) = \frac{\gamma}{1+\beta}(1 - e^{-\eta}), \quad \theta_0(\eta) = e^{-\eta}, \quad (10.27)$$

$$\mathcal{L}_f(f) = \frac{d^3 f}{d\eta^3} - \frac{df}{d\eta}, \quad \mathcal{L}_g(g) = \frac{d^3 g}{d\eta^3} - \frac{dg}{d\eta}, \quad \mathcal{L}_\theta(\theta) = \frac{d^2 \theta}{d\eta^2} - \theta, \quad (10.28)$$

with

$$\mathcal{L}_f [c_1 + c_2 \exp(\eta) + c_3 \exp(-\eta)] = 0, \quad (10.29)$$

$$\mathcal{L}_g [c_4 + c_5 \exp(\eta) + c_6 \exp(-\eta)] = 0, \quad (10.30)$$

$$\mathcal{L}_\theta [c_7 \exp(\eta) + c_8 \exp(-\eta)] = 0, \quad (10.31)$$

in which c_i ($i = 1 - 8$) are the arbitrary constants. If $p \in [0, 1]$ indicates the embedding parameter then the zeroth order deformation problems are constructed as follows:

$$(1-p) \mathcal{L}_f [\hat{f}(\eta; p) - f_0(\eta)] = p \hbar_f \mathcal{N}_f [\hat{f}(\eta; p), \hat{g}(\eta; p)], \quad (10.32)$$

$$(1-p) \mathcal{L}_g [\hat{g}(\eta; p) - g_0(\eta)] = p \hbar_g \mathcal{N}_g [\hat{g}(\eta; p), \hat{f}(\eta; p)], \quad (10.33)$$

$$(1-p) \mathcal{L}_\theta [\hat{\theta}(\eta; p) - \theta_0(\eta)] = p \hbar_\theta \mathcal{N}_\theta [\hat{\theta}(\eta; p), \hat{f}(\eta; p), \hat{g}(\eta; p)], \quad (10.34)$$

$$\hat{f}(0; p) = S, \hat{f}'(0; p) = 1 + \beta \hat{f}''(0; p), \hat{f}'(\infty; p) = 0, \quad (10.35)$$

$$\hat{g}(0; p) = 0, \hat{g}'(0; p) = \gamma + \beta \hat{g}''(0; p), \hat{g}'(\infty; p) = 0, \quad (10.36)$$

$$\hat{\theta}(0; p) = 1, \hat{\theta}(\infty; p) = 0, \quad (10.37)$$

where \hbar_f , \hbar_g and \hbar_θ are the nonzero auxiliary parameters and the nonlinear operators \mathcal{N}_f , \mathcal{N}_g and \mathcal{N}_θ are given by

$$\begin{aligned} \mathcal{N}_f [\hat{f}(\eta; p), \hat{g}(\eta; p)] &= \frac{1}{(1-\phi)^{2.5} [1-\phi + \frac{\rho_s}{\rho_f} \phi]} \frac{\partial^3 \hat{f}(\eta; p)}{\partial \eta^3} - \left(\frac{\partial \hat{f}(\eta; p)}{\partial \eta} \right)^2 \\ &+ \left(\hat{f}(\eta; p) + \hat{g}(\eta; p) \right) \frac{\partial^2 \hat{f}(\eta; p)}{\partial \eta^2} - \frac{M}{1-\phi + \frac{\rho_s}{\rho_f} \phi} \frac{\sigma_{nf}}{\sigma_f} \frac{\partial \hat{f}(\eta; p)}{\partial \eta} \end{aligned} \quad (10.38)$$

$$\begin{aligned} \mathcal{N}_g [\hat{g}(\eta; p), \hat{f}(\eta; p)] &= \frac{1}{(1-\phi)^{2.5} [1-\phi + \frac{\rho_s}{\rho_f} \phi]} \frac{\partial^3 \hat{g}(\eta; p)}{\partial \eta^3} - \left(\frac{\partial \hat{g}(\eta; p)}{\partial \eta} \right)^2 \\ &+ \left(\hat{f}(\eta; p) + \hat{g}(\eta; p) \right) \frac{\partial^2 \hat{g}(\eta; p)}{\partial \eta^2} - \frac{M}{1-\phi + \frac{\rho_s}{\rho_f} \phi} \frac{\sigma_{ng}}{\sigma_g} \frac{\partial \hat{g}(\eta; p)}{\partial \eta} \end{aligned} \quad (10.39)$$

$$\begin{aligned}
\mathcal{N}_\theta [\hat{\theta}(\eta; p), \hat{f}(\eta; p), \hat{g}(\eta; p)] &= \frac{1}{\text{Pr}} \left(\frac{k_{nf}}{k_f} + R_d \right) \frac{\partial^2 \hat{\theta}(\eta; p)}{\partial \eta^2} + \frac{R_d}{\text{Pr}} [(\theta_w - 1)^3 \\
&\quad \left(3 (\hat{\theta}(\eta; p))^2 \left(\frac{\partial \hat{\theta}(\eta; p)}{\partial \eta} \right)^2 + (\hat{\theta}(\eta; p))^3 \frac{\partial^2 \hat{\theta}(\eta; p)}{\partial \eta^2} \right) \\
&\quad + 3(\theta_w - 1)^2 \left(2\hat{\theta}(\eta; p) \left(\frac{\partial \hat{\theta}(\eta; p)}{\partial \eta} \right)^2 + (\hat{\theta}(\eta; p))^2 \frac{\partial^2 \hat{\theta}(\eta; p)}{\partial \eta^2} \right) \\
&\quad + 3(\theta_w - 1) \left(\left(\frac{\partial \hat{\theta}(\eta; p)}{\partial \eta} \right)^2 + \hat{\theta}(\eta; p) \frac{\partial^2 \hat{\theta}(\eta; p)}{\partial \eta^2} \right) \right] \\
&\quad + \left(1 - \phi + \frac{(\rho c_p)_s}{(\rho c_p)_f} \phi \right) (\hat{f}(\eta; p) + \hat{g}(\eta; p)) \frac{\partial \hat{\theta}(\eta; p)}{\partial \eta}. \quad (10.40)
\end{aligned}$$

The m^{th} order deformation equations are

$$\mathcal{L}_f [f_m(\eta) - \chi_m f_{m-1}(\eta)] = \hbar_f \mathcal{R}_{f,m}(\eta), \quad (10.41)$$

$$\mathcal{L}_g [g_m(\eta) - \chi_m g_{m-1}(\eta)] = \hbar_g \mathcal{R}_{g,m}(\eta), \quad (10.42)$$

$$\mathcal{L}_\theta [\theta_m(\eta) - \chi_m \theta_{m-1}(\eta)] = \hbar_\theta \mathcal{R}_{\theta,m}(\eta), \quad (10.43)$$

$$f_m(0) = f'_m(0) - \beta f''_m(0) = f'_m(\infty) = 0, \quad (10.44)$$

$$g_m(0) = g'_m(0) - \beta g''_m(0) = g'_m(\infty) = 0, \quad (10.45)$$

$$\theta_m(0) = \theta_m(\infty) = 0, \quad (10.46)$$

$$\begin{aligned}
\mathcal{R}_{f,m}(\eta) &= \frac{1}{(1-\phi)^{2.5} [1 - \phi + \frac{\rho_s}{\rho_f} \phi]} f'''_{m-1}(\eta) + \sum_{k=0}^{m-1} (f_{m-1-k} f''_k + g_{m-1-k} f''_k - f'_{m-1-k} f'_k) \\
&\quad - \frac{\sigma_{nf}}{\sigma_f} \frac{M}{1 - \phi + \frac{\rho_s}{\rho_f} \phi} f'_{m-1}, \quad (10.47)
\end{aligned}$$

$$\begin{aligned}
\mathcal{R}_{g,m}(\eta) &= \frac{1}{(1-\phi)^{2.5} [1 - \phi + \frac{\rho_s}{\rho_f} \phi]} g'''_{m-1}(\eta) + \sum_{k=0}^{m-1} (f_{m-1-k} g''_k + g_{m-1-k} g''_k - g'_{m-1-k} g'_k) \\
&\quad - \frac{\sigma_{ng}}{\sigma_g} \frac{M}{1 - \phi + \frac{\rho_s}{\rho_f} \phi} g'_{m-1}, \quad (10.48)
\end{aligned}$$

$$\begin{aligned}
\mathcal{R}_{\theta,m}(\eta) &= \frac{1}{\text{Pr}} \left(\frac{k_{nf}}{k_f} + R_d \right) \theta''_{m-1} + \frac{R_d}{\text{Pr}} \sum_{k=0}^{m-1} \left[(\theta_w - 1)^3 \theta_{m-1-k} \sum_{l=0}^k \theta_{k-l} \sum_{s=0}^l (3\theta'_{l-s} \theta'_s + \theta_{l-s} \theta''_s) \right. \\
&\quad \left. + 3(\theta_w - 1)^2 \theta_{m-1-k} \sum_{l=0}^k (2\theta'_{k-l} \theta'_l + \theta_{k-l} \theta''_l) + 3(\theta_w - 1) (\theta'_{m-1-k} \theta'_k + \theta_{m-1-k} \theta''_k) \right] \\
&\quad + \left(1 - \phi + \frac{(\rho c_p)_s}{(\rho c_p)_f} \phi \right) \sum_{k=0}^{m-1} (\theta'_{m-1-k} f_k + \theta'_{m-1-k} g_k), \tag{10.49}
\end{aligned}$$

$$\chi_m = \begin{cases} 0, & m \leq 1 \\ 1, & m > 1 \end{cases}. \tag{10.50}$$

The general solutions in terms of particular solutions f_m^* , g_m^* and θ_m^* are

$$f_m(\eta) = f_m^*(\eta) + c_1 + c_2 e^\eta + c_3 e^{-\eta}, \tag{10.51}$$

$$g_m(\eta) = g_m^*(\eta) + c_4 + c_5 e^\eta + c_6 e^{-\eta}, \tag{10.52}$$

$$\theta_m(\eta) = \theta_m^*(\eta) + c_7 e^\eta + c_8 e^{-\eta}, \tag{10.53}$$

10.4 Convergence of the developed solutions

The convergence of the series solutions is highly dependent upon auxiliary parameters \hbar_f , \hbar_g and \hbar_θ . For valid ranges of these parameters, we have sketched the \hbar -curves at 10th-order of approximations (see Fig. 10.1). This Fig. shows that the admissible values of \hbar_f , \hbar_g and \hbar_θ are $-2 \leq \hbar_f \leq -0.2$, $-2 \leq \hbar_g \leq -0.2$ and $-1.6 \leq \hbar_\theta \leq -1.3$. Further Table 10.1 ensures that when $\hbar_f = \hbar_g = -1.1$ and $\hbar_\theta = -1.3$ the series solutions are convergent up to six decimal places.

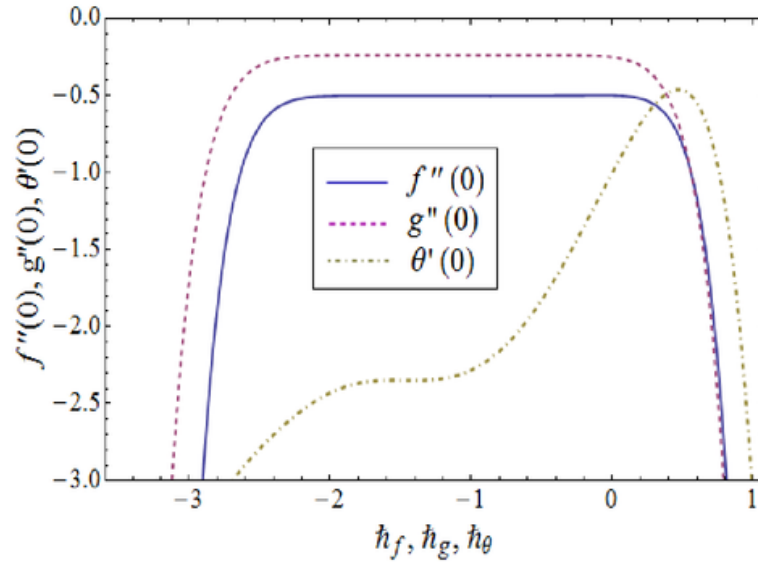


Fig. 10.1: Combined h -curves for $f''(0)$, $g''(0)$ and $\theta'(0)$ when $Pr = 6.2$, $\gamma = 0.5$, $\phi = 0.03$, $\beta = 1$, $R_d = M = 0.1$, $\theta_w = 1.1$ and $S = 0.3$.

Table 10.1: Convergence of HAM solutions for different order of approximations when $Pr = 6.2$, $\gamma = 0.5$, $\phi = 0.03$, $\beta = 1$, $R_d = M = 0.1$, $\theta_w = 1.1$ and $S = 0.3$ and $h_f = h_g = -1.1$ and $h_\theta = -1.3$.

Order of approximation	$-f''(0)$	$-g''(0)$	$-\theta'(0)$
5	0.501136	0.238561	2.18655
9	0.501129	0.238543	2.34913
15	0.501129	0.238543	2.41402
20	0.501129	0.238543	2.40545
25	0.501129	0.238543	2.39321
30	0.501129	0.238543	2.39321
35	0.501129	0.238543	2.39321
40	0.501129	0.238543	2.39321

10.5 Discussion

This section presents the effects of various parameters on the velocity, temperature, skin friction coefficient and Nusselt number in the form of graphical and tabulated results.

10.5.1 Dimensionless velocity profiles

Figs. (10.2 – 10.6) exhibit the dimensionless velocity profiles for different values of Hartman number M , velocity slip parameter β , nanoparticle volume fraction ϕ , suction/injection velocity parameter S and stretching parameter γ . Fig. 10.2 plots the velocity profiles f' and g' for various values of Hartman number M . It is observed that velocity fields f' and g' decrease when M increases. The application of an applied magnetic field has the tendency to slow down the movement of the fluid, which leads to a decrease in the velocity and momentum boundary layer thickness. Fig. 10.3 shows the effects of velocity slip parameter β . This Fig. shows that by increasing the values of velocity slip parameter β , there is a gradual decrease in the velocity profiles. The effects of nanoparticle volume fraction ϕ on velocity profile are presented in the Fig. 10.4. It is noted that an increase in the values of ϕ decreases the velocity profiles f' and g' . The effect of suction/injection velocity parameter S on f' and g' can be visualized in the Fig. 10.5. It is obvious that an increase in S reduces the velocity fields f' and g' . Because applying suction leads to draw the amount of fluid particles into the wall and consequently the velocity boundary layer decreases. Also suction is an agent which causes a reduction in the fluid velocity. Influence of stretching parameter γ on the velocity profiles is displayed in the Fig. 10.6. It is observed that velocity field f' decreases with an increase in γ while g' increases when γ is increased.

10.5.2 Dimensionless temperature profiles

Effects of Hartman number M , nanoparticle volume fraction ϕ , temperature parameter θ_w and radiation parameter R_d on the temperature profile θ are shown in the Figs. (10.7 – 10.10). To capture the effects of Hartman number M on the temperature θ , Fig. 10.7 is displayed. It is depicted that temperature is an increasing function of M . As the Lorentz force is a resistive force which opposes the fluid motion, so heat is produced and as a result, the thermal boundary

layer thickness increases. Fig. 10.8 portrays the influence of ϕ on θ . It is found that temperature increases when values of nanoparticle volume fraction ϕ are increased. This is because of the fact that by increasing the volume fraction of nanoparticles, the thermal conductivity increases and thermal boundary layer increases. Figs. 10.9 and 10.10 indicate that temperature increases by increasing values of temperature parameter θ_w and radiation parameter R_d . Physically this is due to the fact that with the increase in radiation parameter, the mean absorption coefficient decreases. Hence the rate of radiative heat transfer to the fluid increases.

10.5.3 Skin friction coefficient and Nusselt number

In Table 10.2 the thermophysical properties of water and nanoparticles are given. Tables 10.3 and 10.4 show the effects of nanoparticle volume fraction ϕ on skin friction coefficient for different types of nanofluids in the x and y -directions. Effects of the nanoparticle volume fraction ϕ on Nusselt number are presented in Table 10.5. These Tables show that the values of skin friction coefficient and Nusselt number change for different nanofluids. It means that by using different types of nanofluid, the shear stress and rate of heat transfer change. Numerical values of local Nusselt number for different emerging parameters are presented in Table 10.6. It is noticed that local Nusselt number $Nu(Re_x)^{-\frac{1}{2}}$ increases for larger values of θ_w and R_d . However it decreases by increasing M .

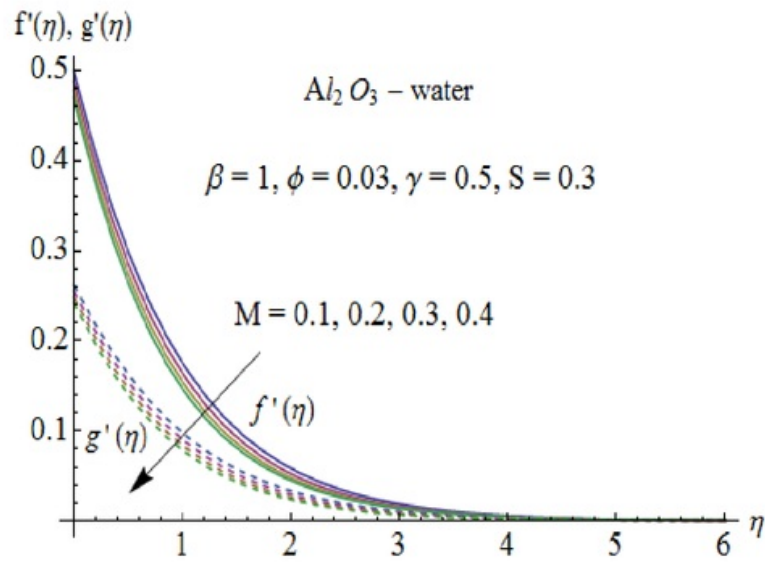


Fig. 10.2: Effect of M on f' and g' .

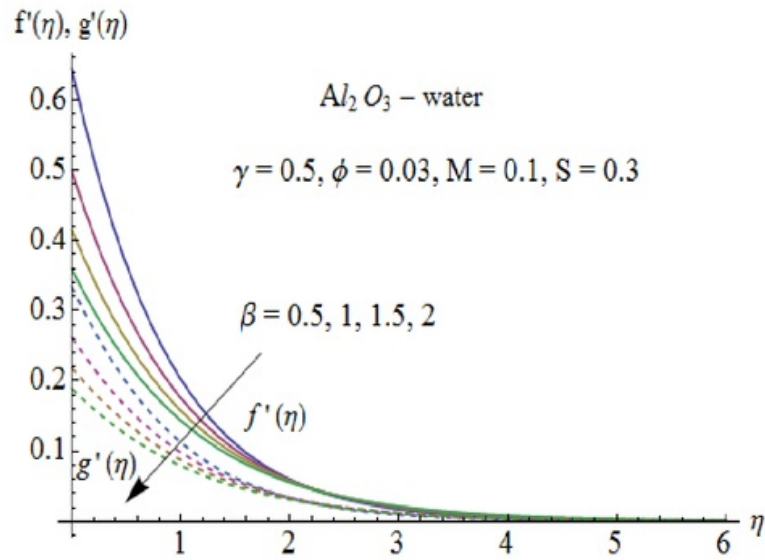


Fig. 10.3: Effect of β on f' and g' .

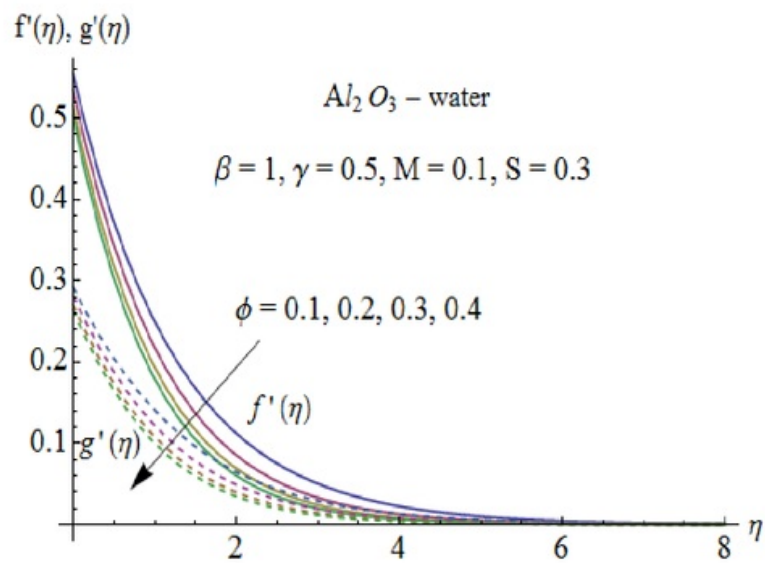


Fig. 10.4: Effect of ϕ on f' and g' .

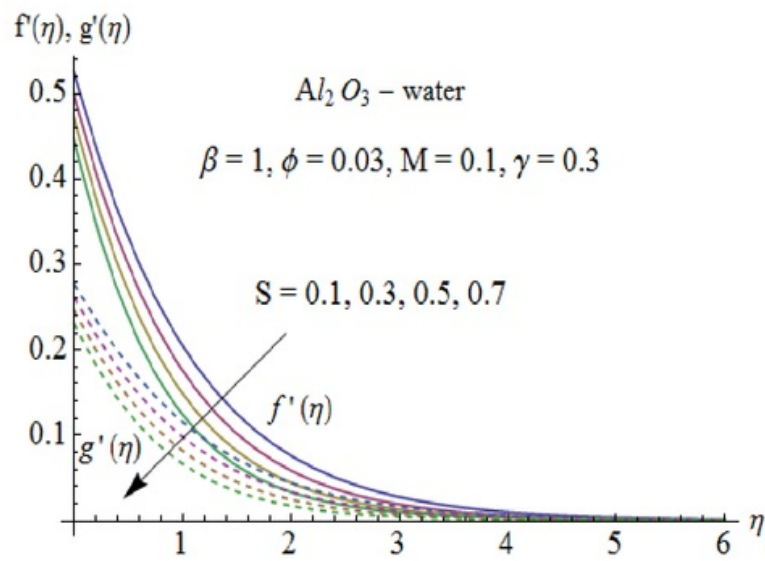


Fig. 10.5: Effect of S on f' and g' .

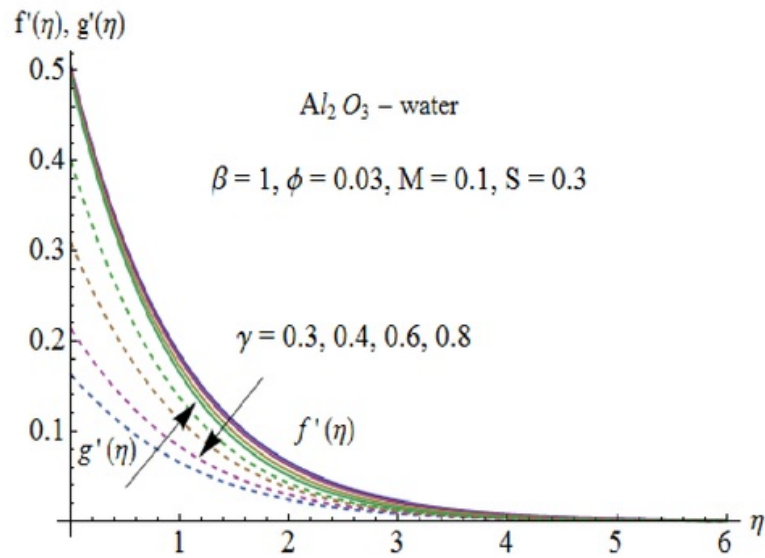


Fig. 10.6: Effect of γ on f' and g' .

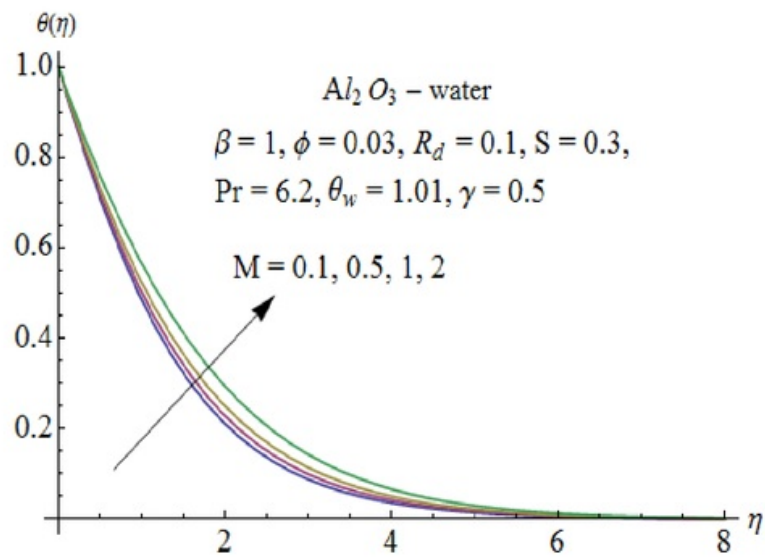


Fig. 10.7: Effect of M on $\theta(\eta)$.

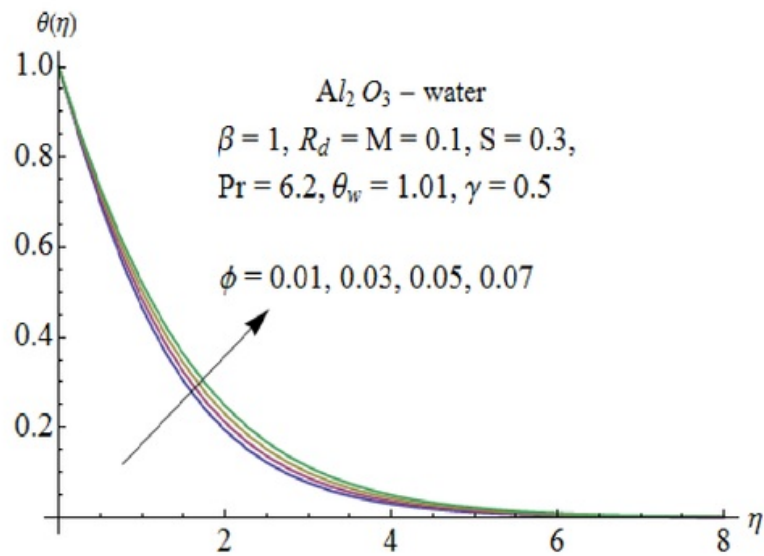


Fig. 10.8: Effect of ϕ on $\theta(\eta)$.

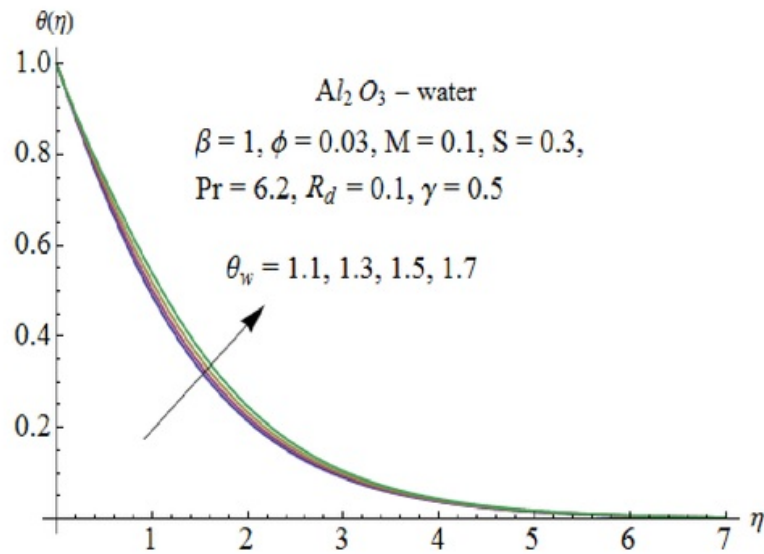


Fig. 10.9: Effect of θ_w on $\theta(\eta)$.

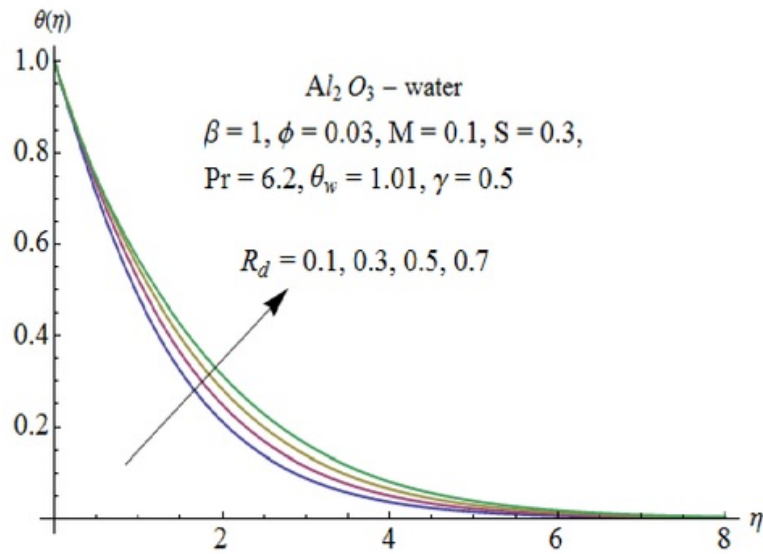


Fig. 10.10: Effect of R_d on $\theta(\eta)$.

Table 10.2: Thermo physical properties of water and nanoparticles.

	$\rho(kg/m^3)$	$c_p(j/kgk)$	$k(W/m.k)$	$\beta \times 10^5(K^{-1})$	$\sigma(\Omega m)^{-1}$
Pure water	997.1	4179	0.613	21	0.05
Copper(Cu)	8933	385	401	1.67	5.96×10^7
Silver(Ag)	10500	235	429	1.89	3.6×10^7
Alumina(Al_2O_3)	3970	765	40	0.85	1×10^{-10}
Titanium Oxide(TiO_2)	4250	686.2	8.9538	0.9	1×10^{-12}

Table 10.3: Effects of the nanoparticle volume fraction for different types of nanofluids on skin friction coefficient along x -direction when $M = 0.1, \beta = 1, Pr = 6.2, S = 0.3, \gamma = 0.5, R_d = 0.1$ and $\theta_w = 1.1$.

ϕ	Cu	Ag	Al_2O_3	TiO_2
0.01	-0.519383	-0.521081	-0.513864	-0.514181
0.03	-0.556763	-0.561468	-0.540779	-0.541729
0.05	-0.595136	-0.602496	-0.569204	-0.570789

Table 10.4: Effects of the nanoparticle volume fraction for different types of nanofluids on skin friction coefficient along y -direction when $M = 0.1$, $\beta = 1$, $Pr = 6.2$, $S = 0.3$, $\gamma = 0.5$, $R_d = 0.1$ and $\theta_w = 1.1$.

ϕ	Cu	Ag	Al_2O_3	TiO_2
0.01	-0.699999	-0.702450	-0.692049	-0.692506
0.03	-0.751194	-0.758029	-0.728085	-0.729453
0.05	-0.803691	-0.814440	-0.766089	-0.768375

Table 10.5: Effects of the nanoparticle volume fraction for different types of nanofluids on Nusselt number when $M = 0.1$, $\beta = 1$, $Pr = 6.2$, $S = 0.3$, $\gamma = 0.5$, $R_d = 0.1$ and $\theta_w = 1.1$.

ϕ	Cu	Ag	Al_2O_3	TiO_2
0.01	-0.726911	-0.723181	-0.733826	-0.732487
0.03	-0.720997	-0.710335	-0.740837	-0.736838
0.05	-0.716675	-0.699623	-0.748444	-0.741798

Table 10.6: Values of $Nu(Re_x)^{-\frac{1}{2}}$ when $\phi = 0.03$, $\beta = 1$, $S = 0.3$ and $\gamma = 0.5$.

M	θ_w	R_d	$-(1 + R_d\theta_w^3)\theta'(0)$
0.1	1.1	0.1	0.74084
			0.70977
			0.68279
0.1	1.2		0.74410
	1.3		0.74775
	1.4		0.75180
	1.1	0.05	0.73328
		0.15	0.74802
		0.2	0.75482

10.6 Concluding remarks

Three-dimensional flow of Al_2O_3 nanofluid over a permeable stretching surface with partial slip and nonlinear thermal radiation is studied. The outcomes are given as:

- Increasing values of Hartman number, velocity slip parameter and suction/injection velocity parameter decrease the velocity profiles.
- The velocity profiles f' and g' decrease by Increasing nanoparticle volume fraction.
- Effect of stretching parameter on the velocity profiles and momentum boundary layers are opposite.
- The temperature and thermal boundary layer thickness increases via larger nanoparticle volume fraction.
- Increasing values of temperature and radiation parameters show enhancement in the temperature and thermal boundary layer thickness.
- Temperature gradient at the surface increases for higher temperature and radiation parameters.
- The governing equations for a viscous fluid are obtained when $\phi = 0$.

Chapter 11

Magnetohydrodynamic three-dimensional flow of nanofluid by a porous shrinking surface

This chapter investigates the steady three-dimensional flow of viscous nanofluid past a permeable shrinking surface with velocity slip and temperature jump. An incompressible fluid fills the porous space. The fluid is electrically conducting in the presence of an applied magnetic field. The governing nonlinear partial differential equations are reduced to ordinary differential equations by similarity transformations. The analytic solutions are presented in series form by the homotopy analysis method. Convergence of the obtained series solutions is explicitly discussed. The velocity and temperature profiles are shown and analyzed for different emerging parameters of interest. It is observed that by increasing the volume of copper nanoparticles, the thermal conductivity increases and the boundary layer thickness decreases. The velocity profile increases and temperature profile decreases for the larger velocity slip parameter. The temperature is a decreasing function of the thermal slip parameter. Hence, less heat is transferred to the fluid from the sheet

11.1 Problem formulation

Let us consider steady three dimensional flow of viscous nanofluid over a shrinking surface. A cartesian coordinate system is used with (u, v, w) as the velocity components in the (x, y, z) directions. An incompressible nanofluid flows at $z = 0$, where z is the coordinate measured normal to the shrinking surface (see Fig. 11.1). The fluid is water based nanofluid consisting of nanoparticles like copper (Cu), silver (Ag), alumina (Al_2O_3), Titanium oxide (TiO_2) and copper oxide (CuO).

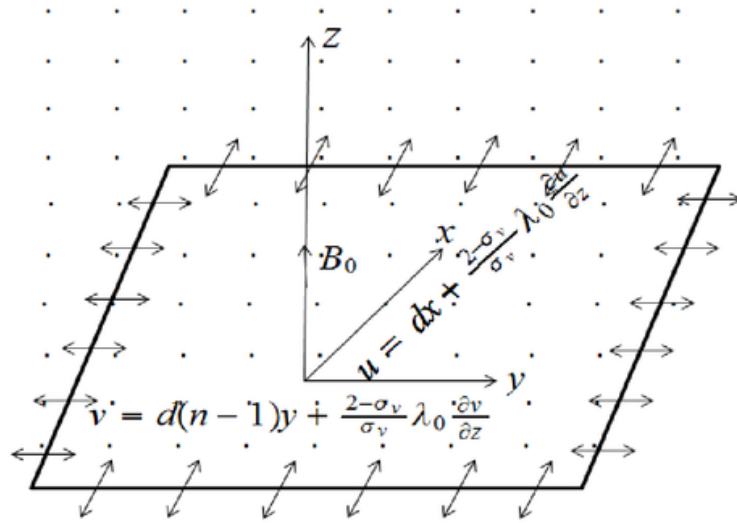


Fig. 11.1: Physical model of the problem.

Further, the fluid is subjected to a uniform magnetic field with strength B_0 in the transverse direction to flow. Here induced magnetic field is taken small in comparison to the applied magnetic field and thus neglected. Under the aforementioned assumptions the equations of continuity, momentum and thermal energy can be expressed in the forms

$$\frac{\partial u}{\partial x} + \frac{\partial v}{\partial y} + \frac{\partial w}{\partial z} = 0, \quad (11.1)$$

$$u \frac{\partial u}{\partial x} + v \frac{\partial u}{\partial y} + w \frac{\partial u}{\partial z} = \nu_{nf} \left(\frac{\partial^2 u}{\partial x^2} + \frac{\partial^2 u}{\partial y^2} + \frac{\partial^2 u}{\partial z^2} \right) - \frac{1}{\rho_{nf}} \frac{\partial P}{\partial x} - \frac{\sigma_{nf} B_0^2 u}{\rho_{nf}} - \frac{\nu_{nf} u}{K}, \quad (11.2)$$

$$u \frac{\partial v}{\partial x} + v \frac{\partial v}{\partial y} + w \frac{\partial v}{\partial z} = \nu_{nf} \left(\frac{\partial^2 v}{\partial x^2} + \frac{\partial^2 v}{\partial y^2} + \frac{\partial^2 v}{\partial z^2} \right) - \frac{1}{\rho_{nf}} \frac{\partial P}{\partial y} - \frac{\sigma_{nf} B_0^2 v}{\rho_{nf}} - \frac{\nu_{nf} v}{K}, \quad (11.3)$$

$$u \frac{\partial w}{\partial x} + v \frac{\partial w}{\partial y} + w \frac{\partial w}{\partial z} = \nu_{nf} \left(\frac{\partial^2 w}{\partial x^2} + \frac{\partial^2 w}{\partial y^2} + \frac{\partial^2 w}{\partial z^2} \right) - \frac{1}{\rho_{nf}} \frac{\partial P}{\partial z}, \quad (11.4)$$

$$u \frac{\partial T}{\partial x} + v \frac{\partial T}{\partial y} + w \frac{\partial T}{\partial z} = \alpha_{nf} \left(\frac{\partial^2 T}{\partial x^2} + \frac{\partial^2 T}{\partial y^2} + \frac{\partial^2 T}{\partial z^2} \right), \quad (11.5)$$

subject to the boundary conditions

$$u = dx + \frac{2 - \sigma_v}{\sigma_v} \lambda_0 \frac{\partial u}{\partial z}, \quad v = d(n-1)y + \frac{2 - \sigma_v}{\sigma_v} \lambda_0 \frac{\partial v}{\partial z}, \quad w = -W,$$

$$T = T_w + \frac{2 - \sigma_T}{\sigma_T} \left(\frac{2\tilde{r}}{\tilde{r} + 1} \right) \frac{\lambda_0}{Pr} \frac{\partial T}{\partial z} \quad \text{at } z = 0,$$

$$u \rightarrow 0, \quad v \rightarrow 0, \quad T \rightarrow T_\infty, \quad \text{as } z \rightarrow \infty. \quad (11.6)$$

In the above equations ρ_{nf} denotes the effective density of the nanofluid, ν_{nf} the effective kinematic viscosity of the nanofluid, μ_{nf} the effective dynamic viscosity, σ_{nf} the effective electrical conductivity, P the pressure, K the permeability of porous medium, $W > 0$ the suction velocity, $d < 0$ the shrinking rate, T the temperature of nanofluid, σ_v the tangential momentum accommodation coefficient, σ_T the thermal accommodation coefficient, λ_0 the molecular mean free path, \tilde{r} the specific heat ratio and sheet shrinks only in the x -direction when $n = 1$. The sheet shrinks asymmetrically for $n = 2$.

The effective dynamic viscosity of the nanofluid is

$$\mu_{nf} = \frac{\mu_f}{(1 - \phi)^{2.5}}, \quad (11.7)$$

where ϕ is the solid volume fraction of nanoparticles and the effective density of nanofluids is given by

$$\rho_{nf} = (1 - \phi)\rho_f + \phi\rho_s. \quad (11.8)$$

The thermal diffusivity of the nanofluid is

$$\alpha_{nf} = \frac{k_{nf}}{(\rho c_p)_{nf}}, \quad (11.9)$$

where the heat capacitance of nanofluid is given by

$$(\rho c_p)_{nf} = (1 - \phi)(\rho c_p) + \phi(\rho c_p). \quad (11.10)$$

For spherical nanoparticles, the thermal conductivity of the nanofluid is

$$\frac{k_{nf}}{k_f} = \frac{k_s + 2k_f - 2\phi(k_f - k_s)}{k_s + 2k_f + 2\phi(k_f - k_s)}. \quad (11.11)$$

The effective electrical conductivity is

$$\frac{\sigma_{nf}}{\sigma_f} = 1 + \frac{3 \left(\frac{\sigma_s}{\sigma_f} - 1 \right) \phi}{\left(\frac{\sigma_s}{\sigma_f} + 2 \right) - \left(\frac{\sigma_s}{\sigma_f} - 1 \right) \phi}. \quad (11.12)$$

Here the subscripts nf represents the thermophysical properties of the nanofluid, f explains base fluid and s is defined as nano solid particles.

In order to attain similarity solution, the following transformations can be posited:

$$u = cx f'(\eta), \quad v = c(n-1)y f'(\eta), \quad w = -\sqrt{cv_f} n f'(\eta), \quad \eta = \sqrt{\frac{c}{v_f}} z, \quad \theta(\eta) = \frac{T - T_\infty}{T_w - T_\infty}. \quad (11.13)$$

Continuity equation (11.1) is automatically satisfied and the other equations and conditions give

$$\varepsilon_1 f''' - \varepsilon_1 \left[M^2 (1 - \phi)^{2.5} \frac{\sigma_{nf}}{\sigma_f} + \lambda \right] f' - f'^2 + n f'' f = 0, \quad (11.14)$$

$$\frac{k_{nf}}{k_f} \frac{1}{\text{Pr}} \theta'' + \left(1 - \phi + \phi \frac{(\rho c)_s}{(\rho c)_f} \right) n f \theta' = 0, \quad (11.15)$$

$$\begin{aligned} f'(0) &= \gamma + \beta f''(0), \quad f(0) = S, \quad \theta(0) = 1 + \tilde{\beta} \theta'(0), \\ f'(\infty) &\rightarrow 0, \quad \theta(\infty) \rightarrow 0, \end{aligned} \quad (11.16)$$

where M^2 is the Hartman number, Pr the Prandtl number, S the mass suction parameter, $\gamma < 0$ the shrinking parameter, β the velocity slip parameter, λ the porosity parameter and $\tilde{\beta}$

the temperature jump parameter. These parameters are defined by

$$\begin{aligned} M^2 &= \frac{B_0^2 \sigma_f}{\rho_f c}, \quad \text{Pr} = \frac{\nu_f}{\alpha}, \quad S = \frac{W}{\sqrt{c\nu_f n}}, \quad \gamma = \frac{d}{c}, \quad \beta = \frac{2 - \sigma_v}{\sigma_v} \lambda_0 \sqrt{\frac{c}{\nu_f}}, \\ \lambda &= \frac{\nu_f}{cK}, \quad \tilde{\beta} = \frac{2 - \sigma_T}{\sigma_T} \left(\frac{2\tilde{r}}{\tilde{r} + 1} \right) \frac{\lambda_0}{\text{Pr}} \sqrt{\frac{c}{\nu_f}}, \end{aligned} \quad (11.17)$$

where ε_1 is defined as

$$\varepsilon_1 = \frac{1}{(1 - \phi)^{2.5} \left[1 - \phi + \phi \left(\frac{\rho_s}{\rho_f} \right) \right]}, \quad (11.18)$$

with ρ_s as nano solid particle density and ρ_f as base fluid density.

The important physical quantities of interest are local skin friction coefficient C_{sf} and Nusselt number Nu which are given by

$$C_{sf} = \frac{\tau_w|_{z=0}}{\frac{1}{2}\rho_w u_w^2}, \quad Nu = \frac{xq_w}{k_f(T_f - T_\infty)}, \quad (11.19)$$

where the surface shear stress τ_w and surface heat flux q_w satisfies

$$\tau_w = -\mu_{nf} \left. \frac{\partial u}{\partial z} \right|_{z=0}, \quad q_w = -k_{nf} \left. \frac{\partial T}{\partial z} \right|_{z=0}. \quad (11.20)$$

Dimensionless forms of local skin friction coefficient and Nusselt number are

$$C_{sf} \sqrt{\frac{\text{Re}_x}{2}} = \frac{1}{(1 - \phi)^{2.5}} f''(0), \quad Nu \text{Re}_x^{-\frac{1}{2}} = -\frac{k_{nf}}{k_f} \theta'(0), \quad (11.21)$$

in which $\text{Re}_x = u_w x / \nu_f$ denotes the local Reynolds number.

11.2 Homotopy analysis solutions

The initial guesses $f_0(\eta)$ and $\theta_0(\eta)$ and the linear operators \mathcal{L}_f and \mathcal{L}_θ are selected in the following forms

$$f_0(\xi) = S + \frac{\gamma}{1 + \beta} - \frac{\gamma}{1 + \beta} \exp(-\eta), \quad \theta_0(\eta) = \frac{1}{1 + \beta} \exp(-\eta), \quad (11.22)$$

$$\mathcal{L}_f(f) = \frac{\partial^3 f}{\partial \eta^3} - \frac{\partial f}{\partial \eta}, \quad \mathcal{L}_\theta(\theta) = \frac{\partial^2 \theta}{\partial \eta^2} - \theta, \quad (11.23)$$

with the properties mentioned below

$$\begin{aligned} \mathcal{L}_f [c_1 + c_2 \eta + c_3 e^{-\eta}] &= 0, \\ \mathcal{L}_\theta [c_4 + c_5 e^{-\eta}] &= 0, \end{aligned} \quad (11.24)$$

and $c_1 - c_5$ are the constants. With Eqs. (11.14) and (11.15), the definitions of operators \mathcal{N}_f and \mathcal{N}_θ can be introduced as follows

$$\begin{aligned} \mathcal{N}_f [\hat{f}(\eta; p)] &= \varepsilon_1 \frac{\partial^3 \hat{f}(\eta; p)}{\partial \eta^3} - \varepsilon_1 \left[M^2 (1 - \phi)^{2.5} \frac{\sigma_{nf}}{\sigma_f} + \lambda \right] \frac{\partial \hat{f}(\eta; p)}{\partial \eta} \\ &\quad - \left(\frac{\partial \hat{f}(\eta; p)}{\partial \eta} \right)^2 + n \frac{\partial \hat{f}(\eta; p)}{\partial \eta} \frac{\partial^2 \hat{f}(\eta; p)}{\partial \eta^2}, \end{aligned} \quad (11.25)$$

$$\mathcal{N}_\theta [\hat{\theta}(\eta; p), \hat{f}(\eta; p)] = \frac{k_{nf}}{k_f} \frac{1}{\text{Pr}} \frac{\partial^2 \hat{\theta}(\eta; p)}{\partial \eta^2} + \left(1 - \phi + \phi \frac{(\rho c)_s}{(\rho c)_f} \right) n \hat{f}(\eta; p) \frac{\partial \hat{\theta}(\eta; p)}{\partial \eta}. \quad (11.26)$$

The problems subjected to zeroth order deformation can be written as

$$(1 - p) \mathcal{L}_f [\hat{f}(\eta; p) - f_0(\eta)] = p \hbar_f \mathcal{N}_f [\hat{f}(\eta; p)], \quad (11.27)$$

$$(1 - p) \mathcal{L}_\theta [\hat{\theta}(\eta; p) - \theta_0(\eta)] = p \hbar_\theta \mathcal{N}_\theta [\hat{\theta}(\eta; p), \hat{f}(\eta; p)], \quad (11.28)$$

$$\begin{aligned} \hat{f}(0; p) &= S, \quad \frac{\partial \hat{f}(0; p)}{\partial \eta} = \gamma + \beta \frac{\partial^2 \hat{f}(0; p)}{\partial \eta^2}, \quad \frac{\partial \hat{f}(\infty; p)}{\partial \eta} = 0, \\ \hat{\theta}(0; p) &= 1 + \tilde{\beta} \frac{\partial \hat{\theta}(0; p)}{\partial \eta}, \quad \hat{\theta}(\infty; p) = 0, \end{aligned} \quad (11.29)$$

in which \hbar_f and \hbar_θ are the nonzero auxiliary parameters.

The corresponding problems at m^{th} order satisfy the following expressions

$$\mathcal{L}_f [f_m(\eta) - \chi_m f_{m-1}(\eta)] = \hbar_f \mathcal{R}_{f,m}(\eta), \quad (11.30)$$

$$\mathcal{L}_\theta [\theta_m(\eta) - \chi_m \theta_{m-1}(\eta)] = \hbar_\theta \mathcal{R}_{\theta,m}(\eta), \quad (11.31)$$

$$f_m(0) = f'_m(0) - \beta f''_m(0) = f'_m(\infty) = \theta_m(0) - \hat{\beta} \theta'_m(0) = \theta_m(\infty) = 0, \quad (11.32)$$

$$\mathcal{R}_{f,m}(\eta) = \varepsilon_1 f'''_{m-1}(\eta) - \varepsilon_1 \left[M^2(1-\phi)^{2.5} \frac{\sigma_{nf}}{\sigma_f} + \lambda \right] f'_{m-1}(\eta) + \sum_{k=0}^{m-1} [n f_{m-1-k} f''_k - f'_{m-1-k} f'_k], \quad (11.33)$$

$$\mathcal{R}_{\theta,m}(\eta) = \frac{k_{nf}}{k_f} \frac{1}{\text{Pr}} \theta''_{m-1}(\eta) + \left(1 - \phi + \phi \frac{(\rho c)_s}{(\rho c)_f} \right) n \sum_{k=0}^{m-1} f_{m-1-k} \theta'_k, \quad (11.34)$$

and

$$\chi_m = \begin{cases} 0, & m \leq 1 \\ 1, & m > 1 \end{cases}. \quad (11.35)$$

If f_m^* and θ_m^* denote the special solutions then the general solutions can be written as

$$f_m(\eta) = f_m^*(\eta) + c_1 + c_2 \eta + c_3 e^{-\eta},$$

$$\theta_m(\eta) = \theta_m^*(\eta) + c_4 + c_5 e^{-\eta}. \quad (11.36)$$

11.3 Convergence analysis

We note that the computed series solutions depend upon the auxiliary parameters. The convergence region and rate of approximations for the functions f and θ can be controlled and adjusted through the auxiliary parameters \hbar_f and \hbar_θ . For admissible values of \hbar_f and \hbar_θ , the \hbar -curves of $f''(0)$ and $\theta'(0)$ for 17th-order of approximations are displayed. Figs. 11.1 and 11.2 depict that the range of admissible values of \hbar_f and \hbar_θ are $-1.5 \leq \hbar_f \leq -0.1$ and $-1.4 \leq \hbar_\theta \leq -0.6$. It is found that the series solutions converge in the whole region of η ($0 < \eta < \infty$) when $\hbar_f = -0.7$ and $\hbar_\theta = -0.9$.

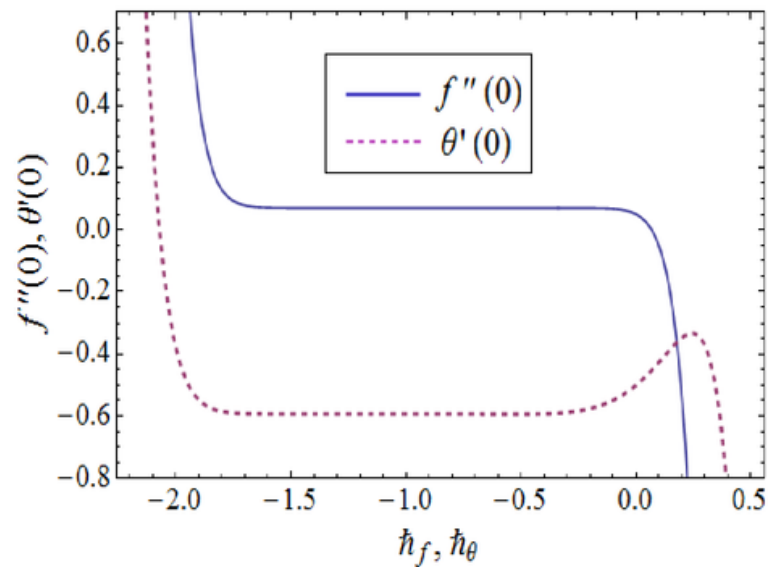


Fig. 11.2: h -curves of $f''(0)$ and $\theta'(0)$.

Table 11.1: Convergence of HAM solutions for different order of approximations when $\gamma = -0.1$, $\tilde{\beta} = \beta = M = 1$, $n = 2$, $\lambda = \phi = 0.3$ and $S = 0.5$.

Order of approximations	$f''(0)$	$-\theta'(0)$
1	0.0661678	0.532809
5	0.0700218	0.589974
10	0.0700198	0.594100
15	0.0700198	0.593038
20	0.0700198	0.593149
25	0.0700198	0.593162
28	0.0700198	0.593155
35	0.0700198	0.593155
40	0.0700198	0.593155
45	0.0700198	0.593155

11.4 Results and discussion

This section is prepared to examine the impact of pertinent parameters on the velocity and temperature. This objective has been achieved by plots of Figs. (11.3 – 11.14). Here Figs (11.3 – 11.8) have been plotted for the effects of M (Hartman number), λ (porosity parameter), S (mass suction parameter), β (velocity slip parameter), ϕ (nanoparticles volume fraction) on the velocity f' and γ (shrinking parameter). The behavior of Hartman number M for the boundary layer is shown in Fig. 11.3. There is decrease in thickness of boundary layer due to an increase in M . This is because of the reason that Lorentz force acts as a retarding force. Such retarding force enhances the frictional resistance opposing the fluid motion in the momentum boundary layer. Fig. 11.4 depicts that the velocity is increased when porosity parameter λ increases. As noted in Fig. 11.5 the associated boundary layer thickness decays when mass suction parameter S increases. Because applying suction leads to draw the amount of fluid particles into the wall and consequently the velocity boundary layer decreases. Also suction is an agent which cause a reduction in the fluid velocity. Fig. 11.6 shows that velocity rises when values of velocity slip parameter β are enhanced. However velocity is a decreasing function of ϕ (see Fig. 11.7). This is because of the fact that by increasing the volume of copper nanoparticles, the thermal conductivity increases and the boundary layer thickness decreases. Fig. 11.8 portrays the influence of γ on f' . It is found that velocity increases when values of γ are increased. Figs. 11.9 – 11.14 depict the effects of Hartman number M , porosity parameter λ , mass suction parameter S , velocity slip parameter β , temperature jump parameter $\tilde{\beta}$ and shrinking parameter γ on temperature profile θ . Effect of M on the temperature is analyzed in Fig. 11.9. As Lorentz force is a resistive force which opposes the fluid motion. So heat is produced and as a result thermal boundary layer thickness increases. It is observed that increasing the porosity parameter λ decreases the thermal boundary layer thickness. Variations of S and β on temperature profile θ can be seen in the Figs. (11.11 – 11.12). There is a decrease in temperature when mass suction parameter S and velocity slip parameter β are increased. Fig. 11.13 indicates that the surface temperature and thermal boundary layer decrease by increasing value of temperature jump $\tilde{\beta}$. With the increase of thermal slip parameter, less heat is transferred to the fluid from the sheet and so temperature is found to decrease. Fig. 11.14 represents the effect of shrinking parameter γ on temperature profile. It is observed that

temperature profile decreases for an increase in γ .

Table 11.1 is prepared for the convergence of series solutions. It is observed that convergence for velocity is achieved at 10^{th} order of approximation and for temperature convergence is achieved at 28^{th} order of approximation. The values of shear stress at the surface are compared with previous published results in Table 11.2. Here it is seen that the obtained solutions agree well with results of Zheng et al. [36]. Numerical values of the local Nusselt number for different emerging parameters are presented in Table 11.3. It is noted that the local Nusselt number increases for larger values of ϕ , γ , S and β . However, it decreases for larger values of $\tilde{\beta}$.

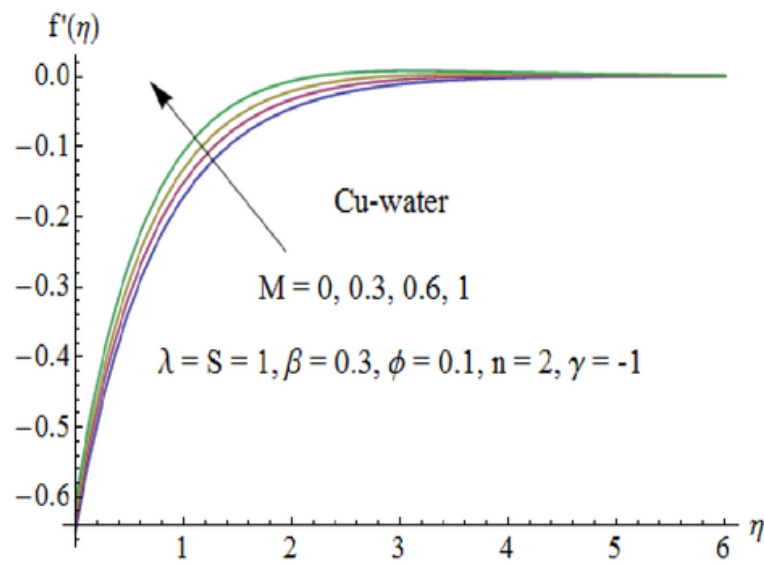


Fig. 11.3: Influence of M on $f'(\eta)$.

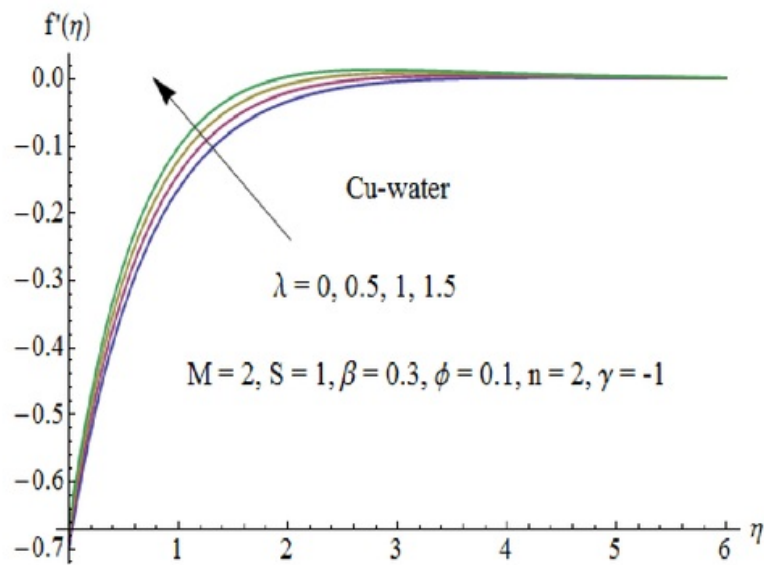


Fig. 11.4: Influence of λ on $f'(\eta)$.

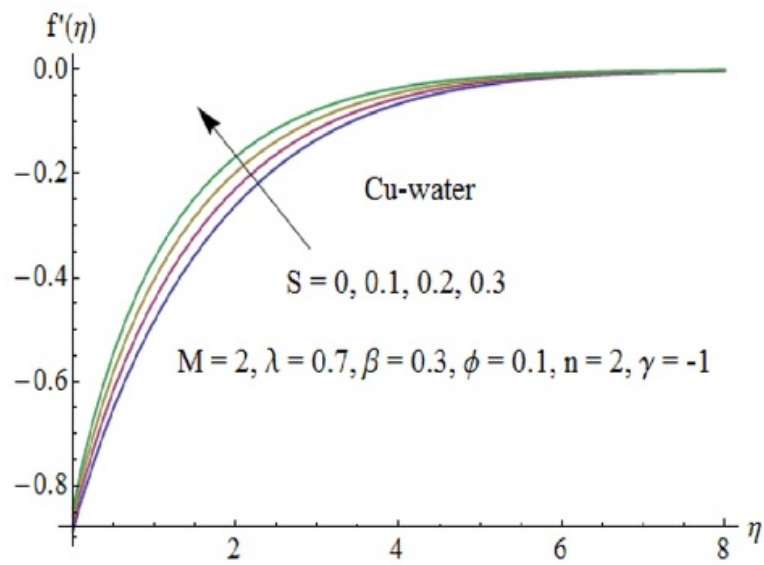


Fig. 11.5: Influence of S on $f'(\eta)$.

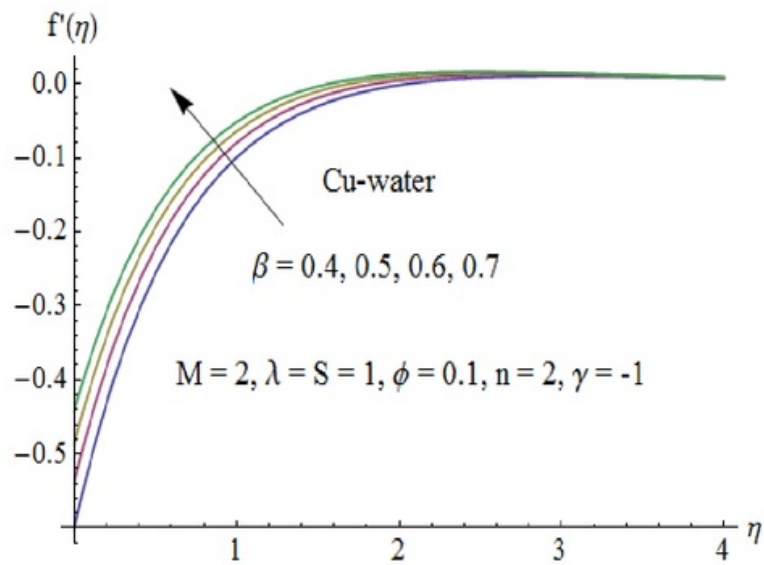


Fig. 11.6: Influence of β on $f'(\eta)$.

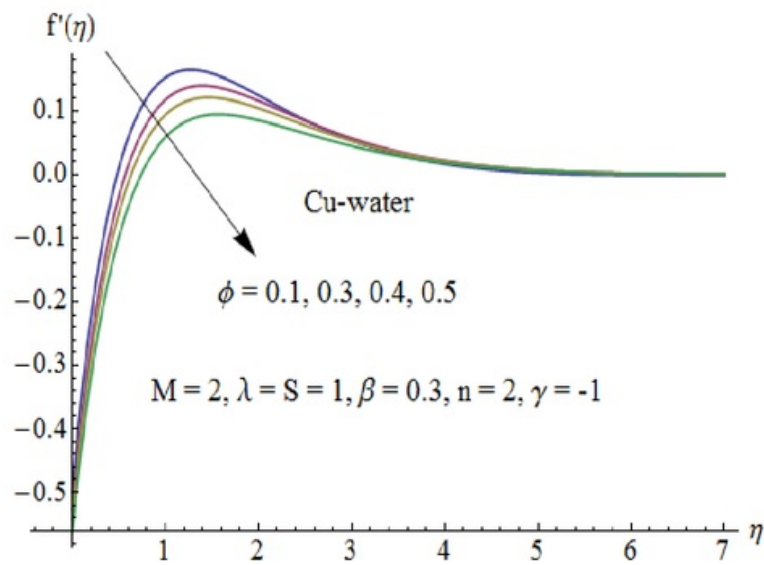


Fig. 11.7: Influence of ϕ on $f'(\eta)$.

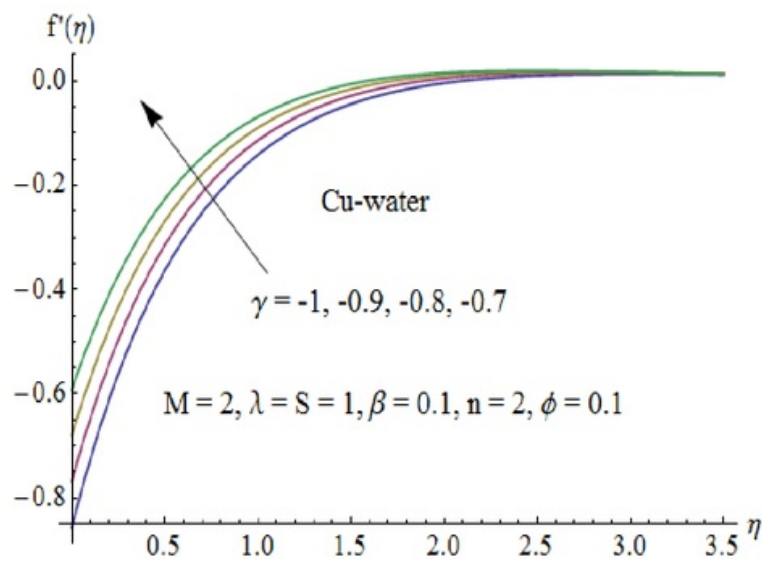


Fig. 11.8: Influence of γ on $f'(\eta)$.

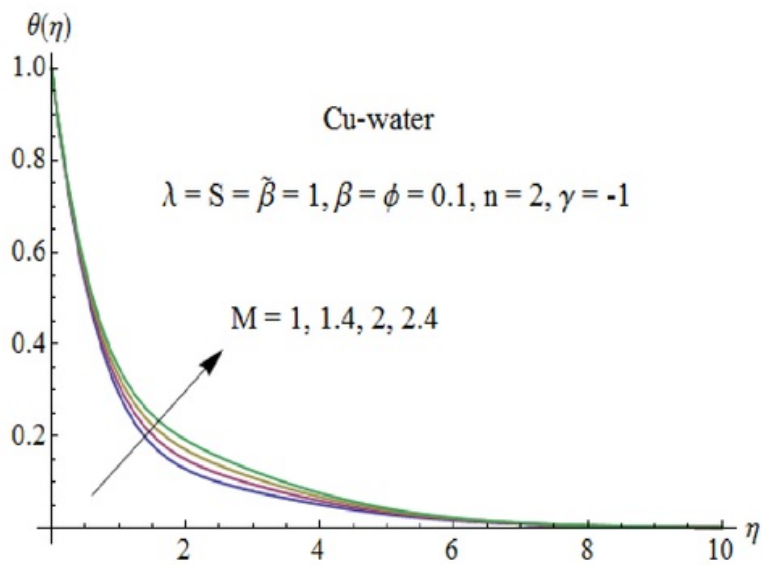


Fig. 11.9: Influence of M on $\theta(\eta)$.

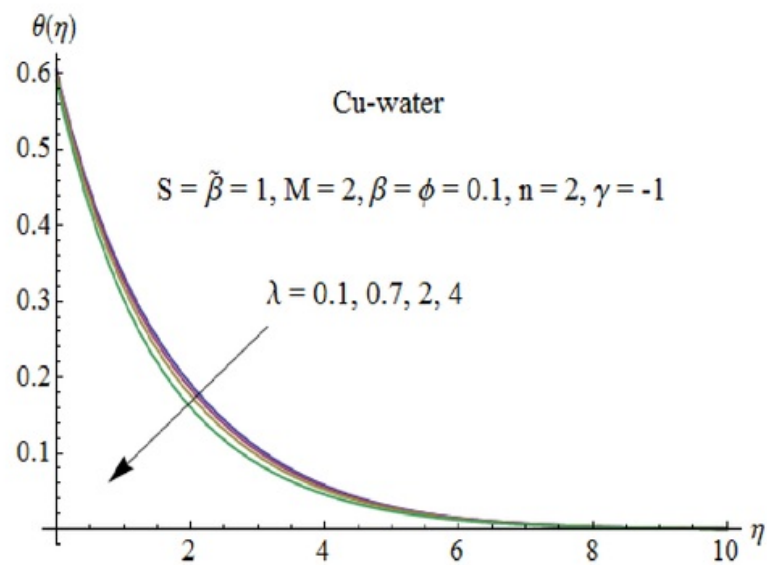


Fig. 11.10: Influence of λ on $\theta(\eta)$.

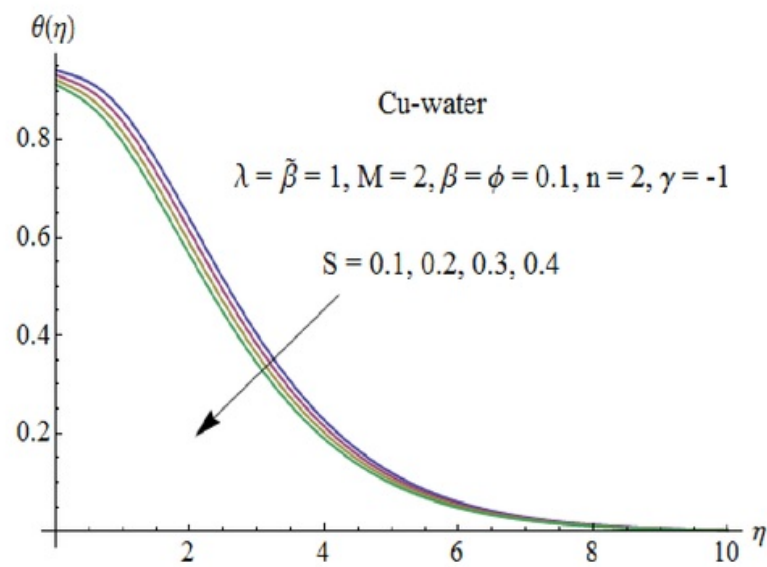


Fig. 11.11: Influence of S on $\theta(\eta)$.

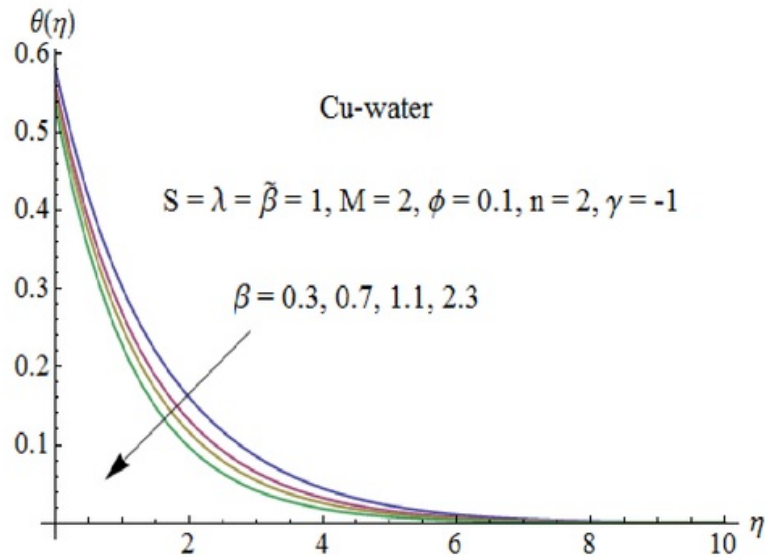


Fig. 11.12: Influence of β on $\theta(\eta)$.

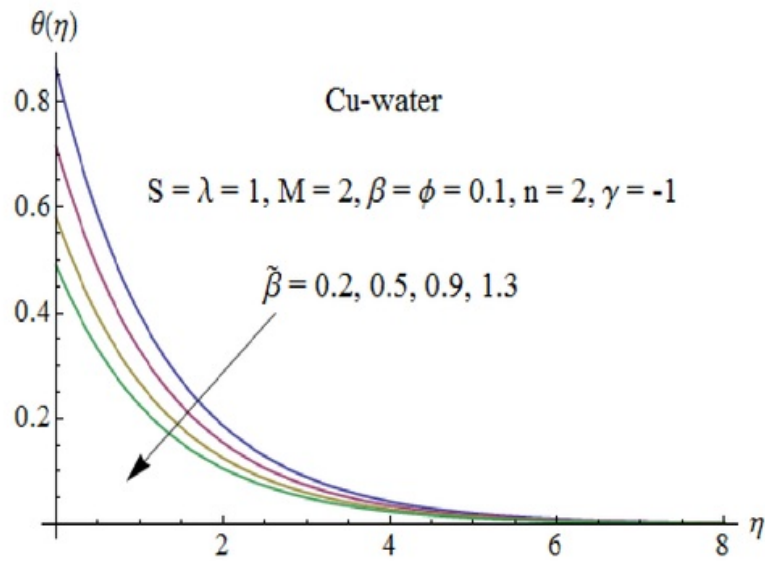


Fig. 11.13: Influence of $\tilde{\beta}$ on $\theta(\eta)$.

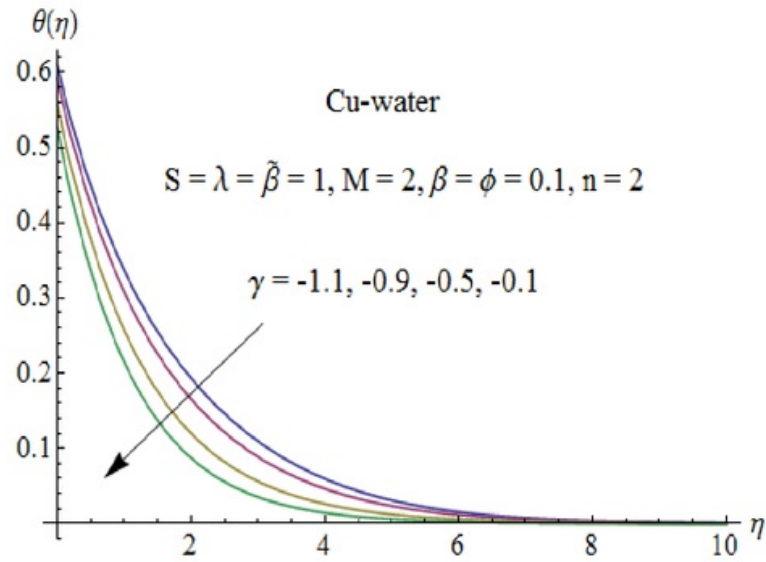


Fig. 11.14: Influence of γ on $\theta(\eta)$.

Table 11.2: Comparison of values of $f''(0)$ when $\lambda = 0$, $\beta = 0$, $\gamma = -1$ and $\phi = 0$.

n	M	S	Zheng et al. [36]	Present results
2	2	1.8	4.21671330	4.20406130
2	2	1	2.89187352	2.89160464
2	2	0.2	1.84296593	1.84287335
2	$\sqrt{5}$	2	4.75696326	4.74614023
2	$\sqrt{5}$	3	6.54909894	6.53871573
1	2	1.8	2.85192213	2.85192199
1	2	1	2.30277564	2.30277376
1	2	0.2	1.83493516	1.83493413

Table 11.3: Numerical values of Nusselt number Nu for different values of ϕ , γ , S , β and $\tilde{\beta}$.

ϕ	γ	S	β	$\tilde{\beta}$	$-\frac{k_n L}{k_f} \theta'(0)$
0.25	-0.1	0.5	1	1	1.97478
0.3					2.35243
0.4					3.43831
0.3	-0.4				2.30085
	-0.3				2.31914
	-0.2				2.33626
	-0.1	0.3			1.82586
		0.4			2.12684
		0.7			2.66889
		0.5	0.5		2.34389
			0.7		2.34821
			0.9		2.35123
			1	0.3	4.02267
				0.5	3.34427
				0.7	2.86169

11.5 Concluding remarks

Three dimensional flow of viscous nanofluid due to porous shrinking surface is discussed. Attention is focused to the development of series solutions. The following observations have been made:

- The velocity has similar pattern with respect to Hartman number, porosity parameter, mass suction parameter and velocity slip parameter.
- The Shrinking parameter has reverse effect on the velocity and temperature profiles.
- Role of velocity slip, temperature jump and suction parameters on the temperature are similar in a qualitative sense.

- There is an increase in the temperature and thermal boundary layer when Hartman number increases.

Chapter 12

MHD 3D flow of nanofluid in presence of convective conditions

This chapter deals with the boundary layer magnetohydrodynamic (MHD) flow of viscous nanofluid saturating porous medium. The flow is induced by a convectively heated permeable shrinking surface. Appropriate transformations reduce the nonlinear partial differential system to ordinary differential system. Flow and heat transfer characteristics are computed by HAM solutions. The results of velocity, temperature and Nusselt number are analyzed for various parameters of interest. It is noted that higher nanoparticle volume fraction decreases the velocity field. Also temperature and heat transfer rate enhance for larger values of Biot number.

12.1 Model development

Let us consider the steady three-dimensional flow of an incompressible nanofluid over a shrinking surface. The fluid fills the porous medium. A uniform transverse magnetic field of strength B_0 is applied parallel to the z -axis. It is assumed that the induced magnetic and electric field effects are negligible. The convective boundary conditions are employed in the heat transfer process. The governing equations are given by

$$\frac{\partial u}{\partial x} + \frac{\partial v}{\partial y} + \frac{\partial w}{\partial z} = 0, \quad (12.1)$$

$$u \frac{\partial u}{\partial x} + v \frac{\partial u}{\partial y} + w \frac{\partial u}{\partial z} = \nu_{nf} \frac{\partial^2 u}{\partial z^2} - \frac{\sigma_{nf} B_0^2 u}{\rho_{nf}} - \frac{\nu_{nf}}{K} u, \quad (12.2)$$

$$u \frac{\partial v}{\partial x} + v \frac{\partial v}{\partial y} + w \frac{\partial v}{\partial z} = \nu_{nf} \frac{\partial^2 v}{\partial z^2} - \frac{\sigma_{nf} B_0^2 v}{\rho_{nf}} - \frac{\nu_{nf}}{K} v, \quad (12.3)$$

$$u \frac{\partial T}{\partial x} + v \frac{\partial T}{\partial y} + w \frac{\partial T}{\partial z} = \alpha_{nf} \frac{\partial^2 T}{\partial y^2}, \quad (12.4)$$

where (u, v, w) are the velocity components along the (x, y, z) directions respectively and K the permeability of porous medium. The effective density ρ_{nf} , the effective dynamic viscosity μ_{nf} , the effective thermal diffusivity α_{nf} , the heat capacitance $(\rho c_p)_{nf}$, the thermal conductivity k_{nf} and the electrical conductivity σ_{nf} of the nanofluid are given by

$$\rho_{nf} = \rho_f(1 - \phi) + \rho_s \phi, \quad (12.5)$$

$$\mu_{nf} = \frac{\mu_f}{(1 - \phi)^{2.5}}, \quad (12.6)$$

$$\alpha_{nf} = \frac{k_{nf}}{(\rho c_p)_{nf}}, \quad (12.7)$$

$$(\rho c_p)_{nf} = (\rho c_p)_f(1 - \phi) + (\rho c_p)_s \phi, \quad (12.8)$$

$$\frac{k_{nf}}{k_f} = \frac{k_s + 2k_f - 2\phi(k_f - k_s)}{k_s + 2k_f + \phi(k_f - k_s)}, \quad (12.9)$$

$$\frac{\sigma_{nf}}{\sigma_f} = 1 + \frac{3 \left(\frac{\sigma_s}{\sigma_f} - 1 \right) \phi}{\left(\frac{\sigma_s}{\sigma_f} + 2 \right) - \left(\frac{\sigma_s}{\sigma_f} - 1 \right) \phi}. \quad (12.10)$$

Here ϕ is the solid volume fraction, s in subscript is for nano-solid-particles and f in subscript is for base fluid. The boundary conditions are

$$\begin{aligned} u &= dx, \quad v = d(n - 1)y, \quad w = -W, \quad -k_f \frac{\partial T}{\partial z} = h(T_f - T) \quad \text{at } z = 0, \\ u &\rightarrow 0, \quad v \rightarrow 0, \quad T \rightarrow T_\infty, \quad \text{as } z \rightarrow \infty, \end{aligned} \quad (12.11)$$

where $d < 0$ is the shrinking constant, W is the suction velocity and h is the convective heat transfer coefficient. We observe that when $n = 1$, the sheet shrinks in x -direction only and the

sheet shrinks axisymmetrically for $n = 2$. Introducing

$$u = cx f'(\eta), \quad v = c(n-1)y f'(\eta), \quad w = -\sqrt{c\nu_f n} f(\eta), \quad \eta = \sqrt{\frac{c}{\nu_f}} z, \quad \theta(\eta) = \frac{T - T_\infty}{T_f - T_\infty}, \quad (12.12)$$

equation (12.1) is satisfied automatically and Eqs. (??) are reduced as follows:

$$\varepsilon_1 f''' - f'^2 + n f f'' - M \varepsilon_1 (1 - \phi)^{2.5} \frac{\sigma n f}{\sigma_f} f' - \lambda \varepsilon_1 f' = 0, \quad (12.13)$$

$$\frac{\varepsilon_2 (1 - \phi)^{2.5} k_{nf} \theta''}{\text{Pr}} + n f \theta' = 0, \quad (12.14)$$

with the boundary conditions

$$\begin{aligned} f(0) &= S, \quad f'(0) = \gamma, \quad \theta'(0) = -\gamma_1 [1 - \theta(0)], \\ f'(\infty) &\rightarrow 0, \quad \theta(\infty) \rightarrow 0. \end{aligned} \quad (12.15)$$

Here $a > 0$ and the porosity parameter λ , the Hartman number M , the Prandtl number Pr , the mass transfer parameter $S > 0$ holds for suction and $S < 0$ for injection, the shrinking parameter γ and the thermal Biot number γ_1 are defined as follows:

$$\lambda = \frac{\nu_f}{cK}, \quad M = \frac{\sigma B_0^2}{\rho_f c}, \quad \text{Pr} = \frac{\nu_f (\rho c_p)_f}{k_f}, \quad S = \frac{W}{\sqrt{c\nu_f n}}, \quad \gamma = \frac{d}{c}, \quad \gamma_1 = \frac{h}{k_f} \sqrt{\frac{\nu_f}{c}}, \quad (12.16)$$

in which ε_1 and ε_2 are constants relating to the properties of nanofluid defined by

$$\varepsilon_1 = \frac{1}{(1 - \phi)^{2.5} [1 - \phi + \phi \frac{\rho_s}{\rho_f}]}, \quad (12.17)$$

$$\varepsilon_2 = \frac{1}{(1 - \phi)^{2.5} [1 - \phi + \phi \frac{(\rho C)_s}{(\rho C)_f}]}. \quad (12.18)$$

Local Nusselt number Nu is

$$Nu = \frac{x q_w}{k_f (T_f - T_\infty)}, \quad (12.19)$$

where the surface heat flux q_w satisfies

$$q_w = -k_{nf} \left. \frac{\partial T}{\partial z} \right|_{z=0}. \quad (12.20)$$

Using Eqs. (12.12) and (12.20), we obtain

$$Nu Re_x^{-\frac{1}{2}} = -\frac{k_{nf}}{k_f} \theta'(0), \quad (12.21)$$

in which $Re_x = u_w x / \nu_f$ denotes the local Reynolds number.

12.2 Homotopy analysis solutions

We choose initial guesses $f_0(\eta)$ and $\theta_0(\eta)$ and auxiliary linear operators \mathcal{L}_f and \mathcal{L}_θ of the forms

$$f_0(\eta) = S + \gamma[1 - \exp(-\eta)], \quad \theta_0(\eta) = \frac{\gamma_1}{1 + \gamma_1} \exp(-\eta), \quad (12.22)$$

$$\mathcal{L}_f(f) = f''' - f', \quad \mathcal{L}_\theta(\theta) = \theta'' - \theta, \quad (12.23)$$

with

$$\begin{aligned} \mathcal{L}_f [c_1 + c_2 \exp(\eta) + c_3 \exp(-\eta)] &= 0, \\ \mathcal{L}_\theta [c_4 \exp(\eta) + c_5 \exp(-\eta)] &= 0, \end{aligned} \quad (12.24)$$

in which $c_1 - c_5$ are the constants.

If $p \in [0, 1]$ indicates the embedding parameter then the zeroth order problems are constructed as follows:

$$(1 - p)\mathcal{L}_f [\hat{f}(\eta; p) - f_0(\eta)] = p\hbar_f \mathcal{N}_f[\hat{f}(\eta; p)], \quad (12.25)$$

$$(1 - p)\mathcal{L}_\theta [\hat{\theta}(\eta; p) - \theta_0(\eta)] = p\hbar_\theta \mathcal{N}_\theta[\hat{\theta}(\eta; p), \hat{f}(\eta; p)], \quad (12.26)$$

$$\begin{aligned} \hat{f}(0; p) &= S, \quad \hat{f}'(0; p) = \gamma, \quad \hat{f}'(\infty; p) = 0, \\ \hat{\theta}'(0; p) &= -\gamma_1[1 - \hat{\theta}(0; p)], \quad \hat{\theta}(\infty; p) = 0, \end{aligned} \quad (12.27)$$

where \hbar_f and \hbar_θ are the nonzero auxiliary parameters and the nonlinear operators \mathcal{N}_f and \mathcal{N}_θ are given by

$$\begin{aligned} \mathcal{N}_f [\hat{f}(\eta; p)] &= \varepsilon_1 \frac{\partial^3 \hat{f}(\eta; p)}{\partial \eta^3} - \left(\frac{\partial \hat{f}(\eta; p)}{\partial \eta} \right)^2 + n \hat{f}(\eta; p) \frac{\partial^2 \hat{f}(\eta; p)}{\partial \eta^2} \\ &\quad - M \varepsilon_1 (1 - \phi)^{2.5} \frac{\sigma_{nf}}{\sigma_f} \frac{\partial \hat{f}(\eta; p)}{\partial \eta} - \lambda \varepsilon_1 \frac{\partial \hat{f}(\eta; p)}{\partial \eta}, \end{aligned} \quad (12.28)$$

$$\mathcal{N}_\theta [\hat{\theta}(\eta; p), \hat{f}(\eta; p)] = \frac{\varepsilon_2}{\text{Pr}} \frac{k_{nf}}{k_f} (1 - \phi)^{2.5} \frac{\partial^2 \hat{\theta}(\eta; p)}{\partial \eta^2} + n \hat{f}(\eta; p) \frac{\partial \hat{\theta}(\eta; p)}{\partial \eta}. \quad (12.29)$$

The m^{th} order deformation problems are given by

$$\mathcal{L}_f [f_m(\eta) - \chi_m f_{m-1}(\eta)] = \hbar_f \mathcal{R}_{f,m}(\eta), \quad (12.30)$$

$$\mathcal{L}_\theta [\theta_m(\eta) - \chi_m \theta_{m-1}(\eta)] = \hbar_\theta \mathcal{R}_{\theta,m}(\eta), \quad (12.31)$$

$$f_n(0) = f'_n(0) = f'_n(\infty) = \theta'_n(0) - \gamma_1 \theta_n(0) = \theta_n(\infty) = 0, \quad (12.32)$$

$$\chi_m = \begin{cases} 0, & m \leq 1 \\ 1, & m > 1 \end{cases}, \quad (12.33)$$

$$\mathcal{R}_{f,m}(\eta) = \varepsilon_1 f'''_{m-1} - \sum_{k=0}^{m-1} [f'_{m-1-k} f'_k - n f_{m-1-k} f''_k] - M \varepsilon_1 (1 - \phi)^{2.5} \frac{\sigma_{nf}}{\sigma_f} f'_{m-1} - \lambda \varepsilon_1 f'_{m-1}, \quad (12.34)$$

$$\mathcal{R}_{\theta,m}(\eta) = \frac{\varepsilon_2}{\text{Pr}} \frac{k_{nf}}{k_f} (1 - \phi)^{2.5} \theta''_{m-1} + n \sum_{k=0}^{m-1} \theta'_{m-1-k} f_k. \quad (12.35)$$

The general solutions (f_m, θ_m) comprising the special solutions (f_m^*, θ_m^*) are

$$f_m(\eta) = f_m^*(\eta) + c_1 + c_2 e^\eta + c_3 e^{-\eta},$$

$$\theta_m(\eta) = \theta_m^*(\eta) + c_4 e^\eta + c_5 e^{-\eta}, \quad (12.36)$$

where the constants c_i ($i = 1 - 5$) through the boundary conditions (12.32) have the values

$$\begin{aligned} c_1 &= -c_3 - f_m^*(0), \quad c_2 = c_4 = 0, \quad c_3 = \left. \frac{\partial f_m^*(\eta)}{\partial \eta} \right|_{\eta=0}, \\ c_5 &= \frac{1}{1 + \gamma_1} \left[\left. \frac{\partial \theta_m^*(\eta)}{\partial \eta} \right|_{\eta=0} - \gamma_1 \theta_m^*(0) \right]. \end{aligned} \quad (12.37)$$

12.3 Convergence of the series solutions

The series solutions of Eqs. (12.30) and (12.31) contain the non-zero auxiliary parameters \hbar_f and \hbar_θ which can adjust and control the convergence of the series solutions. In order to see the range of admissible values of \hbar_f and \hbar_θ of the functions $f'''(0)$ and $\theta'(0)$, the \hbar -curves for 14th-order of approximations are displayed. Figs. (12.1) and (12.2) show that the range for the admissible values of \hbar_f and \hbar_θ are $-1 \leq \hbar_f \leq -0.5$ and $-1 \leq \hbar_\theta \leq -0.1$. Further, the series solutions converge in the whole region of η ($0 < \eta < \infty$) when $\hbar_f = -0.6$ and $\hbar_\theta = -0.5$.

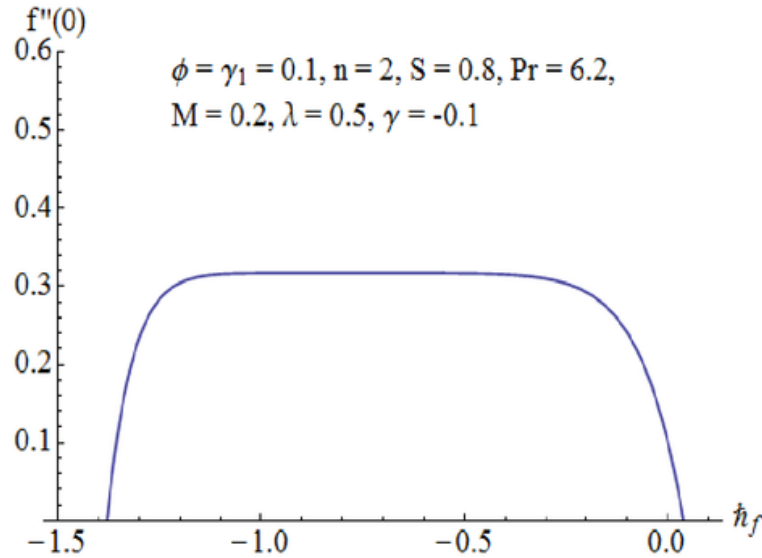


Fig. 12.1: \hbar - curve for the velocity field.

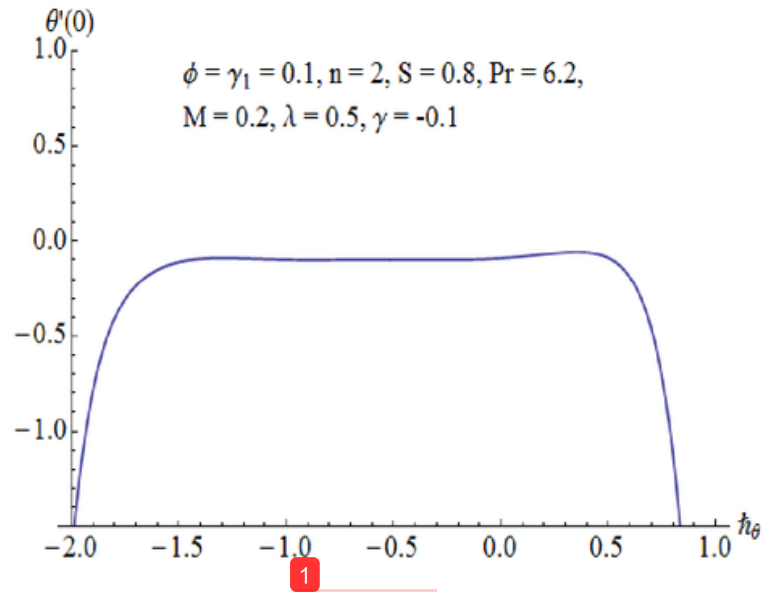


Fig. 12.2: h -curve for the temperature field.

Table 12.1: Convergence of HAM solutions for different order of approximations when

$\phi = \gamma_1 = 0.1, n = 2, S = 0.8, Pr = 6.2, M = 0.2, \lambda = 5$ and $\gamma = -0.1$.

Order of approximations	$f''(0)$	$-\theta'(0)$
1	0.192992	0.0936255
5	0.304420	0.0996007
10	0.316424	0.0991102
15	0.317116	0.0990997
24	0.317159	0.0985958
30	0.317159	0.0982642
35	0.317159	0.0982642
40	0.317159	0.0982642
50	0.317159	0.0982642

12.4 Results and discussion

In this section, Figs. (12.3 – 12.13) are plotted to analyze the effects of mass transfer parameter S , Hartman number M , shrinking parameter γ , porosity parameter λ and nanoparticles volume

fraction ϕ on the velocity f' and temperature θ profiles. Effects of mass transfer parameter S on the velocity profile f' can be seen from Fig. 12.3. Here the magnitude of velocity profile f' decreases when mass transfer parameter S increases. Because applying suction leads to draw the amount of fluid particles into the wall and consequently the velocity boundary layer decreases. Fig. 12.4 displays the effect of Hartman number M on f' . The magnitude of velocity field f' is found to decrease when M increases. The application of an applied magnetic field has the tendency to slow down the movement of the fluid, which leads to a decrease in the velocity and momentum boundary layer thickness. Influence of shrinking parameter γ and porosity parameter λ on the velocity field f' is similar to that of M (see Figs. 12.5 and 12.6). The behavior of nanoparticle volume fraction ϕ on f' is shown in Fig. 12.7. This graph shows that magnitude of f' increases when nanoparticle volume fraction ϕ increases.

Fig. 12.8 illustrates the effects of mass transfer parameter S on temperature profile θ . Temperature θ decreases by increasing the mass transfer parameter S . Fig. 12.9 illustrates the effects of Hartman number M on temperature profile θ . The Lorentz force is a resistive force which opposes the fluid motion. As a sequence the heat is produced and thus thermal boundary layer thickness increases. Influence of shrinking parameter γ and porosity parameter λ on temperature profile θ can be seen in the Figs. (12.10–12.11). It is observed that the temperature profile θ decreases when the shrinking parameter γ and porosity parameter λ are increased. Fig. 12.12 represents the effect of nanoparticle volume fraction ϕ on temperature field θ . It is noted that the temperature profile θ increases for increasing values of nanoparticle volume fraction ϕ . This is because of the fact that by increasing the volume fraction of nanoparticles, the thermal conductivity increases. The behavior of thermal Biot number γ_1 on temperature profile θ is similar to that of nanoparticle volume fraction ϕ .

Table 12.1 shows the convergence of the series solutions. Some thermo physical properties of water and nanoparticles are given in Table 12.2. Numerical values of local Nusselt number for different emerging parameters are presented in Table 12.3. It is noticed that local Nusselt number $Nu(Re_x)^{-\frac{1}{2}}$ increases for larger values of Hartman number M , nanoparticle volume fraction ϕ and thermal Biot number γ_1 .

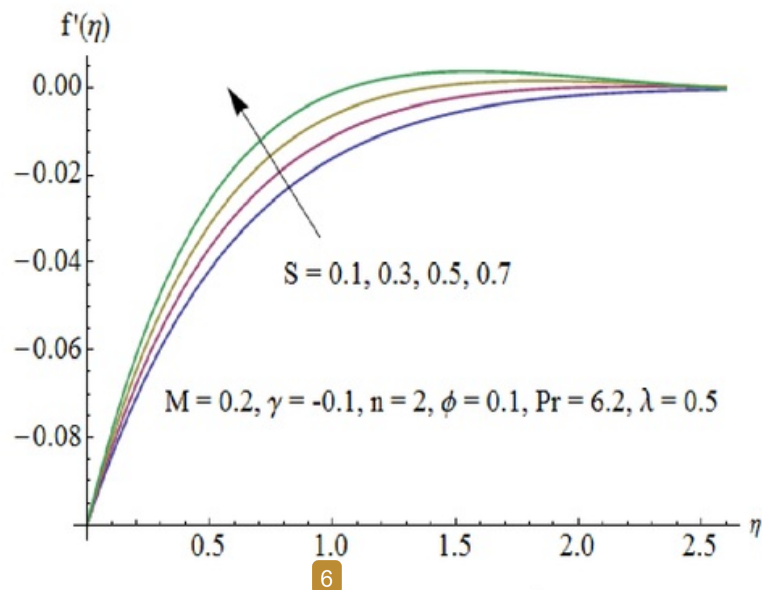


Fig. 12.3: Influence of S on $f'(\eta)$.

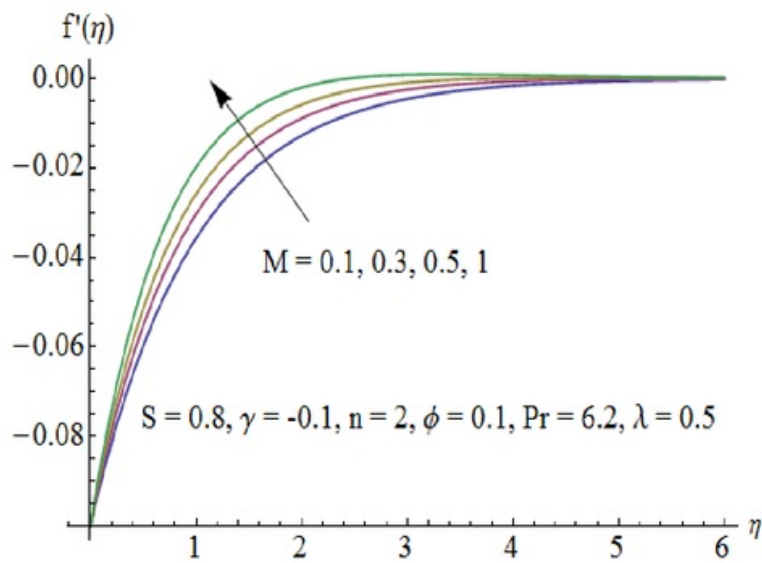
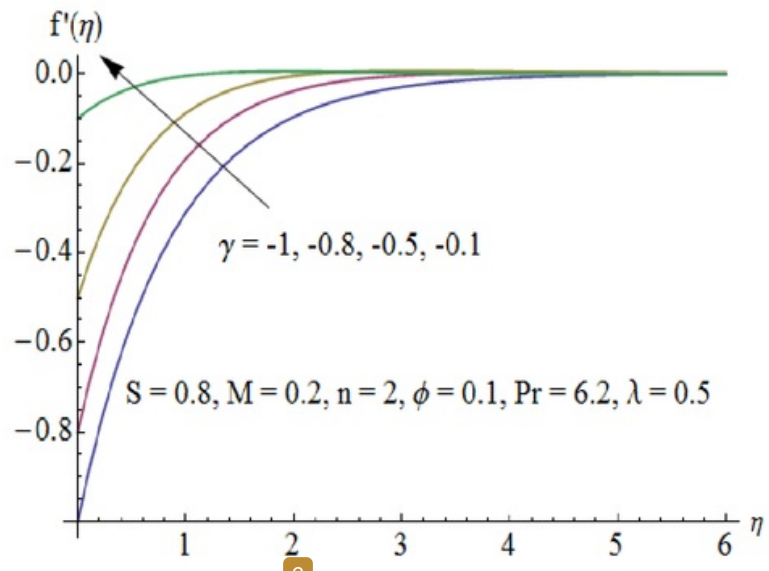


Fig. 12.4: Influence of M on $f'(\eta)$.



6
 Fig. 12.5: Influence of γ on $f'(\eta)$.

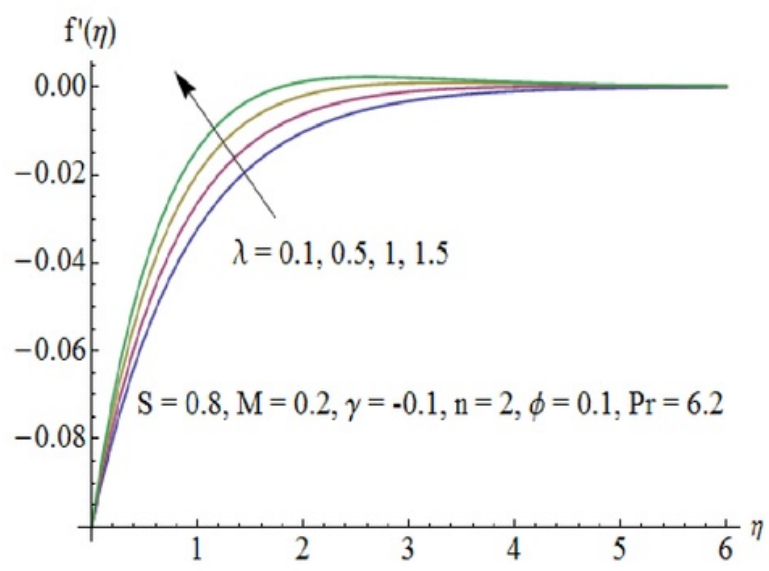


Fig. 12.6: Influence of λ on $f'(\eta)$.

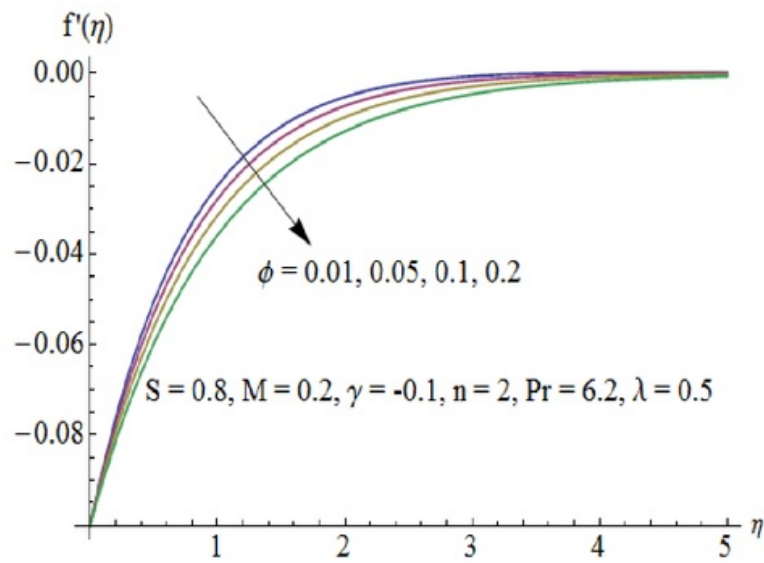


Fig. 12.7: Influence of ϕ on $f'(\eta)$.

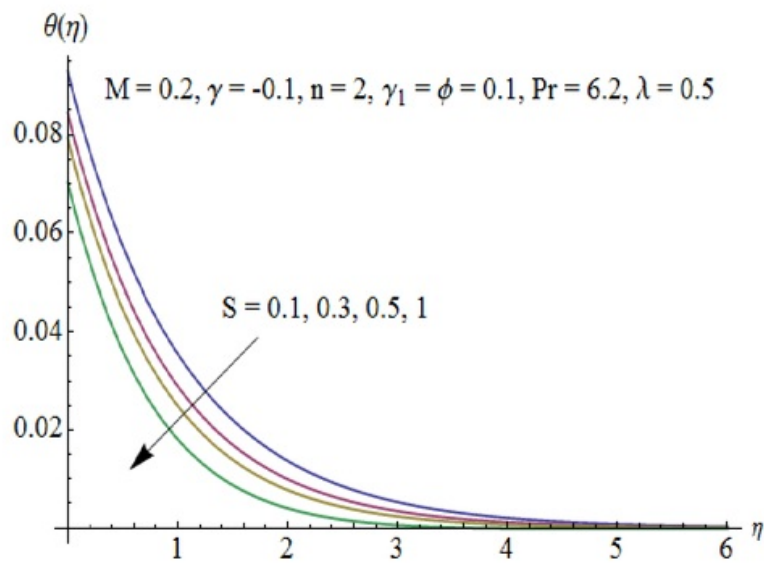


Fig. 12.8: Influence of S on $\theta(\eta)$.

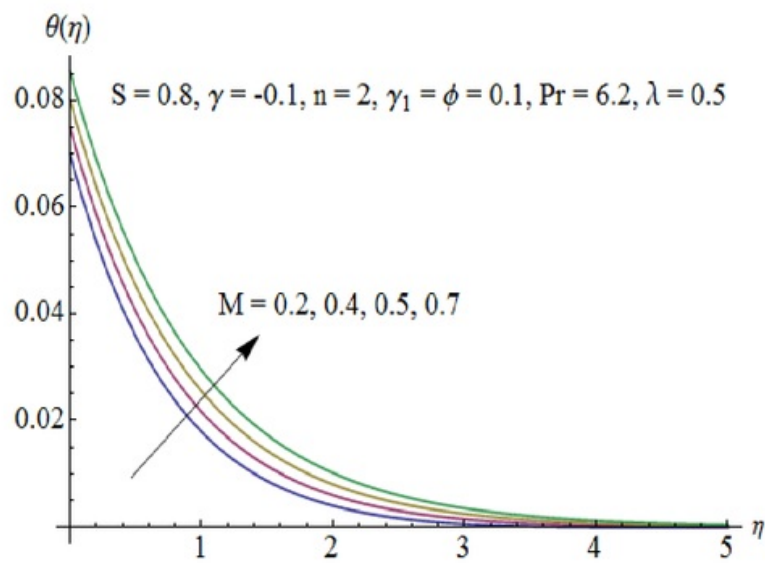


Fig. 12.9: Influence of M on $\theta(\eta)$.

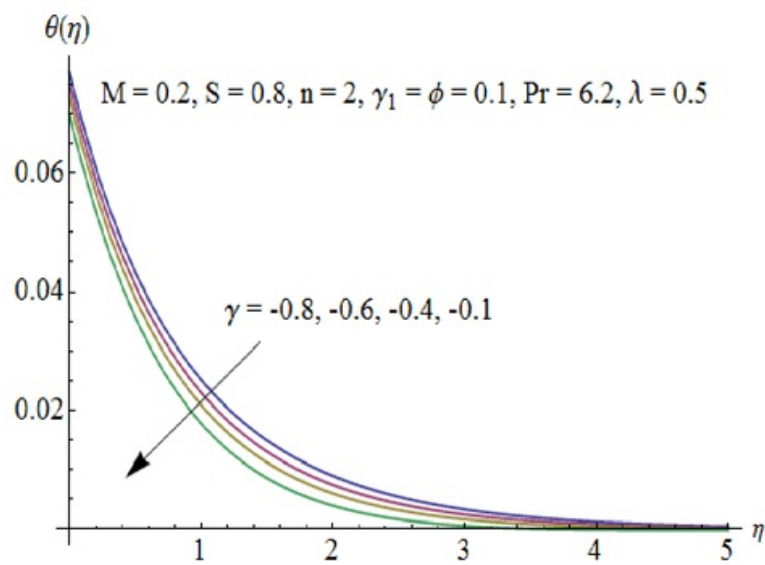


Fig. 12.10: Influence of γ on $\theta(\eta)$.

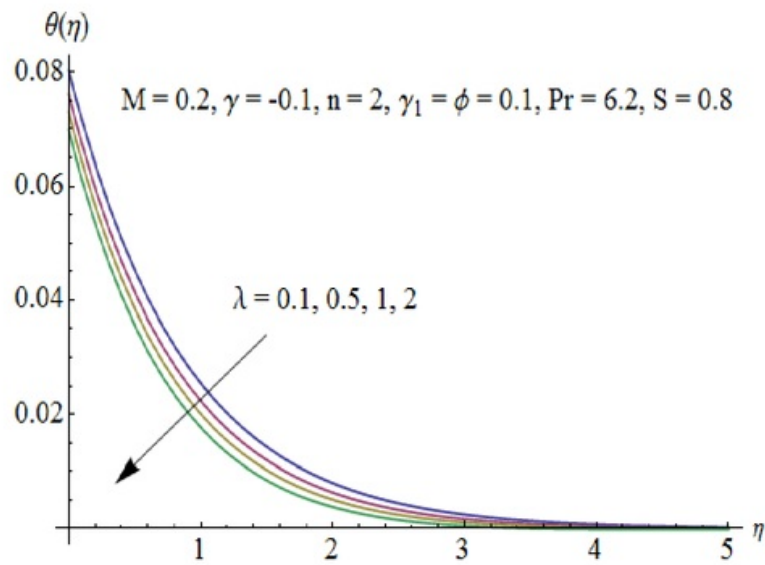


Fig. 12.11: Influence of λ on $\theta(\eta)$.

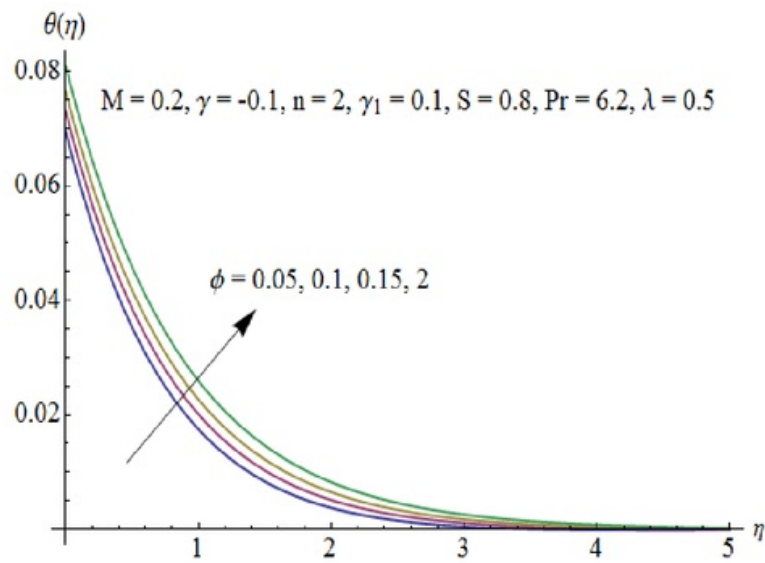


Fig. 12.12: Influence of ϕ on $\theta(\eta)$.

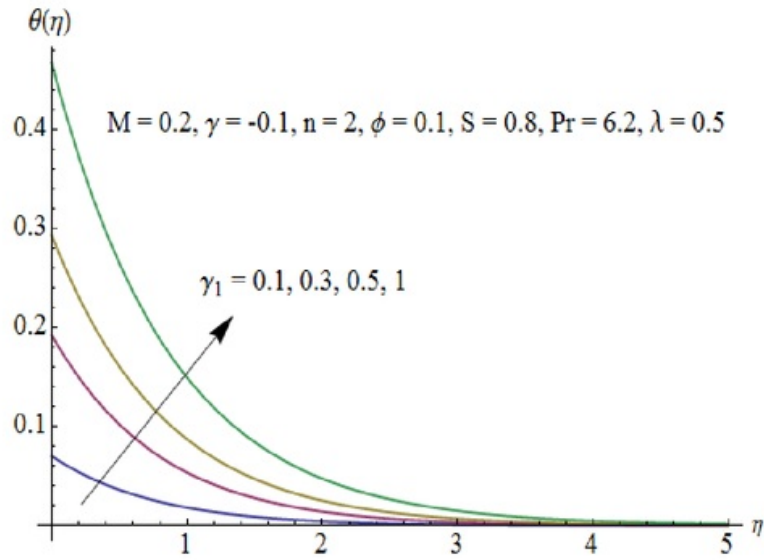


Fig. 12.13: Influence of γ_1 on $\theta(\eta)$.

Table 12.2: Thermo physical properties of water and nanoparticles.

	$\rho(\text{kg}/\text{m}^3)$	$c_p(\text{j}/\text{kgk})$	$k(\text{W}/\text{m.k})$	$\beta \times 10^5(\text{K}^{-1})$	$\sigma(\Omega\text{m})^{-1}$
Pure water	997.1	4179	0.613	21	0.05
Copper(<i>Cu</i>)	8933	385	401	1.67	5.96×10^7
Silver(<i>Ag</i>)	10500	235	429	1.89	3.6×10^7
Alumina(<i>Al₂O₃</i>)	3970	765	40	0.85	1×10^{-10}
Titanium Oxide(<i>TiO₂</i>)	4250	686.2	8.9538	0.9	1×10^{-12}

Table 12.3: Values of $Nu(Re_x)^{-\frac{1}{2}}$ when $n = 2$, $Pr = 6.2$, $\lambda = 0.5$, $S = 0.8$ and $\gamma = -0.1$.

M	ϕ	γ_1	$-\frac{k_n f}{k_f} \theta'(0)$
0.5	0.05	0.3	0.336178
0.7			0.336187
1.0			0.336201
2.0			0.336996
0.2	0.01		0.301109
	0.05		0.334288
	0.07		0.355500
	0.1		0.379977
	0.05	0.1	0.113946
		0.3	0.332611
		0.5	0.537019
		0.7	0.767305

12.5 Final remarks

MHD flow of nanofluid over a permeable shrinking sheet with convective condition is studied.

The main results can be mentioned as follows:

- Effects of mass transfer parameter S , Hartman number M , shrinking parameter γ and porosity parameter λ are similar on the velocity profile f' .
- An increase in nanoparticle volume fraction ϕ reduces the velocity profile f' .
- There is a decrease in temperature profile θ for larger values of mass transfer parameter S , shrinking parameter γ and porosity parameter λ .
- An increase in nanoparticle volume fraction ϕ and thermal Biot number γ_1 enhances the temperature profile θ .

Bibliography

- [1] S. U. S. Choi, Enhancing thermal conductivity of fluids with nanoparticle, In proceedings of the ASME International Mechanical Engineering Congress and Exposition 66 (1995) 99 – 105.
- [2] J. A. Eastman, S. U. S. Choi, S. Li, W. Yu and L. J. Thompson, Anomalous increased effective thermal conductivity of ethylene glycol-based nanofluids containing copper nanoparticles, *Applied Physics Letters* 78 (2001) 718 – 720.
- [3] S. U. S. Choi, Z. G. Zhang, W. Yu, F. E. Lockwoow and E. A. Grulke, Anomalous thermal conductivities enhancement on nanotube suspension, *Applied Physics Letters* 79 (2001) 2252 – 2254.
- [4] R. K. Tiwari and M. K. Das, Heat transfer augmentation in a two-sided lid-driven differentially heated square cavity utilizing nanofluids, *International Journal of Heat and Mass Transfer* 50 (2007) 2002 – 2018.
- [5] S. K. Das, S. U. S. Choi and W. Yu, *Nanofluids, Science and Technology*, Wiley New Jersey (2007).
- [6] W. Daungthongsuk and S. Wongwises, A critical review of convective heat transfer nanofluids, *Renewable and Sustainable Energy Reviews* 11 (5) (2007) 797 – 817.
- [7] V. Trisaksri and S. Wongwises, Critical review of heat transfer characteristics of nanofluids, *Renewable and Sustainable Energy Reviews* 11 (3) (2007) 512 – 523.
- [8] X. Q. Wang and A. S. Mujumdar, Heat transfer characteristics of nanofluids: a review, *Heat transfer characteristics of nanofluids: a review* 46 (1) (2007) 1 – 16.

- [9] X. Q. Wang and A. S. Mujumdar, A review on nanofluids-Part I: theoretical and numerical investigations, *Brazilian Journal of Chemical Engineering* 25 (4) (2008) 613 – 630.
- [10] X. Q. Wang and A. S. Mujumdar, A review on nanofluids-Part II: experiments and applications, *Brazilian Journal of Chemical Engineering* 25 (4) (2008) 631 – 648.
- [11] S. Kakac and A. Pramuanjaroenkij, Review of convective heat transfer enhancement with nanofluids, *International Journal of Heat and Mass Transfer* 52 (13 – 14) (2009) 3187 – 3196.
- [12] H. A. Mohammed, G. Bhaskaran, N. H. Shuaib and R. Saidur, Heat transfer and fluid flow characteristics in microchannels heat exchanger using nanofluids: A review, *Renewable and Sustainable Energy Reviews* 15 (3) (2011) 1502 – 1512.
- [13] A. S. Dalkilic, N. Kayaci, A. Celen, M. Tabatabaei, O. Yildiz, W. Daungthongsuk and S. Wongwises, Forced convective heat transfer of nanofluids: A review of the recent literature, *Current Nanoscience* 8 (6) (2012) 949 – 969.
- [14] J. Buongiorno, Convective transport in nanofluids, *ASME Journal of Heat Transfer* 128 (3) (2006) 240 – 250.
- [15] J. Buongiorno et al., A benchmark study on the thermal conductivity of nanofluids, *Journal of Applied Physics* 106 (2009) 094312.
- [16] J. Niu, C. Fu, and W. C. Tan, Slip flow and heat transfer of a non-Newtonian nanofluid in a microtube, *Plos One* 7 (5) (2012) e37274.
- [17] A. Alsaedi, M. Awais and T. Hayat, Effects of heat generation/absorption on stagnation point flow of nanofluid over a surface with convective boundary conditions, *Communications in Nonlinear Science and Numerical Simulation* 17 (11) (2012) 4210 – 4223.
- [18] H. Xu, I. Pop, X. C. You, Flow and heat transfer in a nano-liquid film over an unsteady stretching surface, *International Journal of Heat and Mass Transfer* 60 (2013) 646 – 652.
- [19] M. Imtiaz, T. Hayat, M. Hussain, S. A. Shehzad, G. Q. Chen and B. Ahmad, Mixed convection flow of nanofluid with Newtonian heating, *European Physical Journal Plus* 129 (2014) 97.

- [20] S. Khalili, H. Tamim, A. Khalili and M. M. Rashidi, Unsteady convective heat and mass transfer in pseudoplastic nanofluid over a stretching wall, *Advanced Powder Technology* 26 (5) (2015) 1319 – 1326.
- [21] M. M. Rashidi, S. Abelman and N. F. Mehr, Entropy generation in steady MHD flow due to a rotating porous disk in a nanofluid, *International Journal of Heat and Mass Transfer* 62 (2013) 515 – 525.
- [22] M. Sheikholeslami, M. Hatami and D. D. Ganji, Analytical investigation of MHD nanofluid flow in a semi-porous channel, *Powder Technology* 246 (2013) 327 – 336.
- [23] S. Khalili, S. Dinarvand, R. Hosseini, H. Tamim and I. Pop, Unsteady MHD flow and heat transfer near stagnation point over a stretching/shrinking sheet in porous medium filled with a nanofluid, *Chinese Physics B* 23 (4) (2014) 048203.
- [24] M. M. Rashidi, N. V. Ganesh, A. K. A. Hakeem and B. Ganga, Buoyancy effect on MHD flow of nanofluid over a stretching sheet in the presence of thermal radiation, *Journal of Molecular Liquids* 198 (2014) 234 – 238.
- [25] M. Sheikholeslami, D. D. Ganji, M. Y. Javed and R. Ellahi, Effect of thermal radiation on magnetohydrodynamics nanofluid flow and heat transfer by means of two phase model, *Journal of Magnetism and Magnetic Materials* 374 (2015) 36 – 43.
- [26] M. Sheikholeslami, M. Hatami and G. Domairry, Numerical simulation of two phase unsteady nanofluid flow and heat transfer between parallel plates in presence of time dependent magnetic field, *Journal of the Taiwan Institute of Chemical Engineers* 46 (2015) 43 – 50.
- [27] Y. Lin, L. Zheng, X. Zhang, L. Ma and G. Chen, MHD pseudo-plastic nanofluid unsteady flow and heat transfer in a finite thin film over stretching surface with internal heat generation, *International Journal of Heat and Mass Transfer* 84 (2015) 903 – 911.
- [28] F. Mabood and A. Mastroberardino, Melting heat transfer on MHD convective flow of a nanofluid over a stretching sheet with viscous dissipation and second order slip, *Journal of the Taiwan Institute of Chemical Engineers* 57 (2015) 62 – 68.

- [29] T. Hayat, T. Muhammad, A. Alsaedi and M. S. Alhuthali, Magneto hydrodynamic three-dimensional flow of viscoelastic nanofluid in the presence of nonlinear thermal radiation, *Journal of Magnetism and Magnetic Materials* 385 (1) (2015) 222 – 229.
- [30] T. Hayat, T. Muhammad, S. A. Shehzad, G. Q. Chen and I. A. Abbas, Interaction of magnetic field in flow of Maxwell nanofluid with convective effect, *Journal of Magnetism and Magnetic Materials* 389 (1) (2015) 48 – 55.
- [31] L. J. Crane, Flow past a stretching plate, *Journal of Applied Mathematics and Physics (ZAMP)* 21 (1970) 645 – 647.
- [32] P. S. Gupta and A. S. Gupta, Heat and mass transfer on a stretching sheet with suction or blowing, *The Canadian Journal of Chemical Engineering* 55 (1977) 744 – 746.
- [33] N. Afzal, A. Baderuddin and A. A. Elgarvi, Momentum and heat transfer on a continuous flat surface moving in a parallel stream, *International Journal of Heat and Mass Transfer* 36 (1993) 3399 – 3403.
- [34] E. Magyari and B. Keller, Heat and mass transfer in the boundary layers on an exponentially stretching continuous surface, *Journal of Physics D: Applied Physics* 32 (1999) 577 – 585.
- [35] R. Cortell, Flow and heat transfer in a moving fluid over a moving flat surface, *Theoretical and Computational Fluid Dynamics* 21 (2007) 435 – 446.
- [36] L. Zheng, J. Niu, X. Zhang and Y. Gao, MHD flow and heat transfer over a porous shrinking surface with velocity slip and temperature jump, *Mathematical and Computer Modelling* 56 (2012) 133 – 144.
- [37] W. Ibrahim, B. Shankar and M. M. Nandeppanavar, MHD stagnation point flow and heat transfer due to nanofluid towards a stretching sheet, *International Journal of Heat and Mass Transfer* 56 (2013) 1 – 9.
- [38] S. Mukhopadhyay, Slip effects on MHD boundary layer flow over an exponentially stretching sheet with suction/blowing and thermal radiation, *Ain Shams Engineering Journal* 4 (2013) 485 – 491.

- [39] M. Turkyilmazoglu, Exact solutions for two-dimensional laminar flow over a continuously stretching or shrinking sheet in an electrically conducting quiescent couple stress fluid, *International Journal of Heat and Mass Transfer* 72 (2014) 1 – 8.
- [40] A. Malvandi, F. Hedayati and D. D. Ganji, Slip effects on unsteady stagnation point flow of a nanofluid over a stretching sheet, *Powder Technology* 253 (2014) 377 – 384.
- [41] S. Pramanik, Casson fluid flow and heat transfer past an exponentially porous stretching surface in presence of thermal radiation, *Ain Shams Engineering Journal* 5 (2014) 205 – 212.
- [42] M. S. Alhuthali, S. A. Shehzad, H. Malaikah and T. Hayat, Three dimensional flow of viscoelastic fluid by an exponentially stretching surface with mass transfer, *Journal of Petroleum Science Engineering* 119 (2014) 221 – 226.
- [43] A. V. Rosca and I. Pop, Flow and heat transfer of Powell–Eyring fluid over a shrinking surface in a parallel free stream, *International Journal of Heat and Mass Transfer* 71 (2014) 321 – 327.
- [44] S. K. Nandy and I. Pop, Effects of magnetic field and thermal radiation on stagnation flow and heat transfer of nanofluid over a shrinking surface, *International Communications in Heat and Mass Transfer* 53 (2014) 50 – 55.
- [45] S. K. Nandy, Unsteady flow of Maxwell fluid in the presence of nanoparticles toward a permeable shrinking surface with Navier slip, *Journal of the Taiwan Institute of Chemical Engineers* 52 (2015) 22 – 30.
- [46] P. D. Weidman and A. Ishak, Multiple solutions of two-dimensional and three-dimensional flows induced by a stretching flat surface, *Communications in Nonlinear Science and Numerical Simulation* 25 (2015) 1 – 9.
- [47] M. G. Reddy, P. Padma and B. Shankar, Effects of viscous dissipation and heat source on unsteady MHD flow over a stretching sheet, *Ain Shams Engineering Journal* 6 (4) (2015) 1195 – 1201.

- [48] S. Chen, L. Zheng, B. Shen and X. Chen, Time-space dependent fractional boundary layer flow of Maxwell fluid over an unsteady stretching surface, *Theoretical and Applied Mechanics Letters*, 5 (6) (2015) 262 – 266.
- [49] M. Mustafa, A. Mushtaq, T. Hayat and A. Alsaedi, Radiation effects in three-dimensional flow over a bi-directional exponentially stretching sheet, *Journal of the Taiwan Institute of Chemical Engineers*, 47 (2015) 43 – 49.
- [50] T. Hayat, Y. Saeed, A. Alsaedi and S. Asad, Effects of convective heat and mass transfer in flow of Powell-Eyring fluid past an exponentially stretching sheet, *Plos One* 10 (9) (2015) e0133831.
- [51] T. V. Karman, Uber laminare und turbulente reibung, *ZAMM* 1 (1921) 233 – 235.
- [52] M. E. Erdogan, Unsteady flow of a viscous fluid due to non-coaxial rotations of a disk and a fluid at infinity, *International Journal of Non-Linear Mechanics* 32 (1997) 285 – 290.
- [53] N. Kelson and A. Desseaux, Note on porous rotating disk flow, *ANZIAM Journal* 42 (2000) 837 – 855.
- [54] N. Bachok, A. Ishak and I. Pop, Flow and heat transfer over a rotating porous disk in a nanofluid, *Physica B* 406 (2011) 1767 – 1772.
- [55] M. M. Rashidi, S. A. M. Pour, T. Hayat and S. Obaidat, Analytic approximate solutions for steady flow over a rotating disk in porous medium with heat transfer by homotopy analysis method, *Computers & Fluids* 54 (2012) 1–9.
- [56] M. Turkyilmazoglu, Nanofluid flow and heat transfer due to a rotating disk, *Computers & Fluids* 94 (2014) 139 – 146.
- [57] T. Hayat, M. Rashid, M. Imtiaz and A. Alsaedi, Magnetohydrodynamic (MHD) flow of Cu-water nanofluid due to a rotating disk with partial slip, *AIP Advances* 5 (2015) 067169.
- [58] P. A. Thompson and S. M. Troian, A general boundary condition for liquid flow at solid surfaces, *Nature* (1997) 389.

- [59] R. Khare, P. Keblinski and A. Yethiraj, Molecular dynamics simulations of heat and momentum transfer at a solid-fluid interface: Relationship between thermal and velocity slip, *International Journal of Heat and Mass Transfer* 49 (2006) 3401 – 3407.
- [60] L. Wu, A slip model for rarefied gas flows at arbitrary Knudsen number, *Applied Physics Letters* 93 (2008) 253103.
- [61] T. Fang and A. Aziz, Viscous flow with second-order slip velocity over a stretching sheet, *Zeitschrift für Naturforschung A* 65a (2010) 1087 – 1092.
- [62] A. Akbarinia, M. Abdolzadeh and R. Laur, Critical investigation of heat transfer enhancement using nanofluids in microchannels with slip and non-slip flow regimes, *Applied Thermal Engineering* 31 (2011) 556 – 565.
- [63] M. A. A. Mahmoud and S. E. Waheed, MHD flow and heat transfer of a micropolar fluid over a stretching surface with heat generation (absorption) and slip velocity, *Journal of the Egyptian Mathematical Society*, 20 (2012) 20 – 27.
- [64] W. Ibrahim and B. Shankar, MHD boundary layer flow and heat transfer of a nanofluid past a permeable stretching sheet with velocity, thermal and solutal slip boundary conditions, *Computers & Fluids* 75 (2013) 1 – 10.
- [65] W. A. Khan, M. J. Uddin and A. I. M. Ismail, Hydrodynamic and thermal slip effect on double-diffusive free convective boundary layer flow of a nanofluid past a flat vertical plate in the moving free stream, *Plos One*, 8, (3) (2013) e54024.
- [66] S. A. Rooholghdos and E. Roohi, Extension of a second order velocity slip/temperature jump boundary condition to simulate high speed micro/nanoflows, *Computers & Mathematics with Applications* 67 (2014) 2029 – 2040.
- [67] A. Malvandi and D. D. Ganji, Brownian motion and thermophoresis effects on slip flow of alumina/water nanofluid inside a circular microchannel in the presence of a magnetic field, *International Journal of Thermal Sciences* 84 (2014) 196 – 206.
- [68] R. Sharma and A. Ishak, Second order slip flow of Cu-water nanofluid over a stretching sheet with heat transfer, *WSEAS Transactions on Fluid Mechanics* 9 (2014) 26 – 33.

- [69] M. M. Rashidi, N. Kavyani and S. Abelman, Investigation of entropy generation in MHD and slip flow over a rotating porous disk with variable properties, *International Journal of Heat and Mass Transfer* 70 (2014) 892 – 917.
- [70] A. Karimipour, A. H. Nezhad, A. D’Orazia, M. H. Esfe, M. R. Safaei, and E. Shiran, Simulation of copper-water nanofluid in a microchannel in slip flow regime using the lattice Boltzman method, *European Journal of Mechanics–B/Fluids* 49 (2015) 89 – 99.
- [71] A. M. Megahed, MHD viscous Casson fluid flow and heat transfer with second-order slip velocity and thermal slip over a permeable stretching sheet in the presence of internal heat generation/absorption and thermal radiation, *The European Physical Journal Plus* 130 (2015) 81.
- [72] A. K. A. Hakeem, N. V. Ganesh and B. Ganga, Magnetic field effect on second order slip flow of nanofluid over a stretching/shrinking sheet with thermal radiation effect, *Journal of Magnetism and Magnetic Materials* 381 (2015) 243 – 257.
- [73] J. H. Merkin, A model for isothermal homogeneous-heterogeneous reactions in boundary layer flow, *Mathematical and Computer Modelling* 24 (1996) 125 – 136.
- [74] M. A. Chaudhary and J. H. Merkin, A simple isothermal model for homogeneous-heterogeneous reactions in boundary layer flow: I. Equal diffusivities, *Fluid Dynamics Research* 16 (1995) 311 – 333.
- [75] W. A. Khan and I. Pop, Flow near the two-dimensional stagnation-point on an infinite permeable wall with a homogeneous–heterogeneous reaction, *Communications in Nonlinear Science and Numerical Simulation* 15 (2010) 3435 – 3443.
- [76] N. Bachok, A. Ishak and I. Pop, On the stagnation-point flow towards a stretching sheet with homogeneous–heterogeneous reactions effects, *Communications in Nonlinear Science and Numerical Simulation* 16 (2011) 4296 – 4302.
- [77] W. A. Khan and I. Pop, Effects of homogeneous-heterogeneous reactions on the viscoelastic fluid towards a stretching sheet, *ASME Journal of Heat Transfer* 134 (2012) 064506 1 – 5.

- [78] S. Shaw, P. K. Kameswaran and P. Sibanda, Homogeneous-heterogeneous reactions in micropolar fluid flow from a permeable stretching or shrinking sheet in a porous medium, *Boundary Value Problems* 2013 (2013) 77.
- [79] P. K. Kameswaran, S. Shaw, P. Sibanda and P. V. S. N. Murthy, Homogeneous-heterogeneous reactions in a nanofluid flow due to porous stretching sheet, *International Journal of Heat and Mass Transfer* 57 (2013) 465 – 472.
- [80] T. Hayat, M. Farooq and A. Alsaedi, Homogeneous-heterogeneous reactions in the stagnation point flow of carbon nanotubes with Newtonian heating, *AIP Advances* 5 (2015) 027130.
- [81] T. Hayat, M. Imtiaz and A. Alsaedi, Effects of homogeneous-heterogeneous reactions in flow of Powell-Eyring fluid, *Journal of Central South University* 22 (8) (2015) 3211 – 3216.
- [82] Z. Abbas, M. Sheikh and I. Pop, Stagnation-point flow of a hydromagnetic viscous fluid over stretching/shrinking sheet with generalized slip condition in the presence of homogeneous-heterogeneous reactions, *Journal of the Taiwan Institute of Chemical Engineers* 55 (2015) 69 – 75.
- [83] S. J. Liao and A. T. Chwang, Application of homotopy analysis method in nonlinear oscillations, *ASME Journal of Applied Mechanics* 65 (1998) 914 – 922.
- [84] S. J. Liao, Notes on the homotopy analysis method: Some definitions and theorems, *Communications in Nonlinear Science and Numerical Simulation* 14 (2009) 983 – 997.
- [85] S. Abbasbandy, E. Shivanian and K. Vajravelu, Mathematical properties of h -curve in the frame work of the homotopy analysis method, *Communications in Nonlinear Science and Numerical Simulation*.16 (2011) 4268 – 4275.
- [86] M. Turkyilmazoglu and I. Pop, Exact analytical solutions for the flow and heat transfer near the stagnation point on a stretching/shrinking sheet in a Jeffrey fluid, *International Journal of Heat and Mass Transfer* 57 (2013) 82 – 88.
- [87] O. A. Arqub and A. El-Ajou, Solution of the fractional epidemic model by homotopy analysis method, *Journal of King Saud University–Science* 25 (1) (2013) 73 – 81.

- [88] M. Hatami, R. Nouri and D. D. Ganji, Forced convection analysis for MHD Al_2O_3 -water nanofluid flow over a horizontal plate, *Journal of Molecular Liquids* 187 (2013) 294 – 301.
- [89] M. M. Rashidi, S. Abelman and F. N. Mehr, Entropy generation in steady MHD flow due to a rotating disk in a nanofluid. *International Journal of Heat and Mass Transfer* 62 (2013) 515 – 525.
- [90] M. M. Rashidi, M. Ali, N. Freidoonimehr, B. Rostami and A. Hossian, Mixed convective heat transfer for MHD viscoelastic fluid flow over a porous wedge with thermal radiation, *Advances in Mechanical Engineering* 204 (2014) 735939.
- [91] S. Abbasbandy, M. Yurusoy and H. Gulluce, Analytical solutions of non-linear equations of power-law fluids of second grade over an infinite porous plate, *Mathematical & Computational Applications* 19 (2) (2014) 124.
- [92] J. Sui, L. Zheng, X. Zhang and G. Chen, Mixed convection heat transfer in power law fluids over a moving conveyor along an inclined plate, *International Journal of Heat and Mass Transfer* 85 (2015) 1023 – 1033.
- [93] T. Hayat, S. A. Shehzad, A. Alsaedi and M. S. Alhothuali, Three-dimensional flow of Oldroyd-B fluid over surface with convective boundary conditions, *Applied Mathematics and Mechanics (English Edition)* 34 (4) (2015) 489 – 500.
- [94] J. Sui, L. Zheng, X. Zhang and G. Chen, Mixed convection heat transfer in power law fluids over a moving conveyor along an inclined plate, *International Journal of Heat and Mass Transfer* 85 (2015) 1023 – 1033.
- [95] Y. Lin, L. Zheng and G. Chen, Unsteady flow and heat transfer of pseudoplastic nanofluid in a finite thin film on a stretching surface with variable thermal conductivity and viscous dissipation, *Powder Technology* 274 (2015) 324 – 332.
- [96] U. Farooq, Y. L. Zhao, T. Hayat, A. Alsaedi and S. J. Liao, Application of the HAM-based mathematica package BVPh 2.0 on MHD Falkner-Skan flow of nanofluid, *Computers & Fluids* 111 (2015) 69 – 75.

- [97] T. Hayat, S. Asad, M. Mustafa and A. Alsaedi, MHD stagnation-point flow of Jeffrey fluid over a convectively heated stretching sheet, *Computers & Fluids* 108 (2015) 179 – 185.
- [98] H. C. Brinkman, The viscosity of concentrated suspensions and solutions, *The Journal of Chemical Physics* 20 (1952) 571 – 581.
- [99] J. C. Maxwell, *A treatise on electricity and magnetism*, Cambridge Oxford University Press (1904).
- [100] T. Cebeci and P. Bradshaw, *Physical and computational aspects of convective heat transfer*, Springer-Verlag, New York (1988) (Chapter 13).

Thesis

ORIGINALITY REPORT

17 %	9 %	8 %	12 %
SIMILARITY INDEX	INTERNET SOURCES	PUBLICATIONS	STUDENT PAPERS

PRIMARY SOURCES

1	Submitted to Higher Education Commission Pakistan Student Paper	5 %
2	Submitted to National Tsing Hua University Student Paper	4 %
3	www.boundaryvalueproblems.com Internet Source	1 %
4	www.science.gov Internet Source	1 %
5	www.researchgate.net Internet Source	1 %
6	Submitted to National Chiao-Tung University Student Paper	1 %
7	International Journal of Numerical Methods for Heat & Fluid Flow, Volume 24, Issue 5 (2014- 09-16) Publication	<1 %
8	journals.plos.org Internet Source	<1 %

9

HAYAT, Tasawar; IQBAL, Zahid; MUSTAFA, Meraj and HENDI, Awatif A.. "MELTING HEAT TRANSFER IN THE STAGNATION-POINT FLOW OF THIRD GRADE FLUID PAST A STRETCHING SHEET WITH VISCOUS DISSIPATION", Thermal Science, 2013.

Publication

<1%

10

www.lukechueh.com

Internet Source

<1%

11

International Journal of Numerical Methods for Heat & Fluid Flow, Volume 24, Issue 2 (2014-03-28)

Publication

<1%

12

International Journal of Numerical Methods for Heat & Fluid Flow, Volume 25, Issue 3 (2015)

Publication

<1%

13

YAHYAZADEH, Hossein; GANJI, Davood Domairry; YAHYAZADEH, Arash; KHALILI, Mohammad Taghi; JALILI, Payam and Mohsen JOUYA. "EVALUATION OF NATURAL CONVECTION FLOW OF A NANOFUID OVER A LINEARLY STRETCHING SHEET IN THE PRESENCE OF MAGNETIC FIELD BY THE DIFFERENTIAL TRANSFORMATION METHOD", Thermal Science, 2012.

Publication

<1%

14

Internet Source

<1%

15

iisonline.org

Internet Source

<1%

16

www.digitalmindscape.net

Internet Source

<1%

17

www.legrand.fr

Internet Source

<1%

18

www.ssm.org.rs

Internet Source

<1%

19

ijsetr.org

Internet Source

<1%

20

deposit.e-mengine.com

Internet Source

<1%

21

scholar.google.com

Internet Source

<1%

22

hal.physast.uga.edu

Internet Source

<1%

23

Submitted to University of Bristol

Student Paper

<1%

24

www.ispacs.com

Internet Source

<1%

25

Singh, K. D. and Pathak, R.. "EFFECT OF SLIP

<1%

CONDITIONS AND HALL CURRENT ON AN OSCILLATORY CONVECTIVE MHD FLOW IN A ROTATING VERTICAL POROUS CHANNEL WITH THERMAL RADIATION", International Journal of Applied Mathematics & Mechanics, 2013.

Publication

26

Ahmad Fauzi, Ezzah Liana; Ahmad, Syakila and Pop, Ioan. "Mixed Convection Boundary Layer Flow from a Vertical Cone in a Porous Medium Filled with a Nanofluid", World Academy of Science, Engineering & Technology, 2012.

Publication

<1%

27

Chandrasekar, M. and Kasiviswanathan, M. S.. "MHD Mixed Convection CU-Water Nano Fluid Flow With Viscous Dissipation Effects In The Presence Of Suction And Injection", International Journal of Applied Engineering Research, 2015.

Publication

<1%

28

Abbas, Z. Sheikh, Mariam Sajid, M.. "Hydromagnetic stagnation point flow of a micropolar viscoelastic fluid towards a stretching/shrinkin", Canadian Journal of Physics, Oct 2014 Issue

Publication

<1%

29

journal-enertech.eu

Internet Source

<1%

30

Ali, M.M. Mamun, A.A. Maleque, M.A..
"Radiation and heat generation effects on
viscous Joule heating MHD-conjugate heat
transfer for a ver", Canadian Journal of
Physics, June 2014 Issue

Publication

<1%

31

Mohamed, Mona A. A.. "The Effects of
Radiation and Hall Current on The Unsteady
MHD Laminar Convective Fluid Flow Through
Porous Medium Due to A Porous Rotating
Disk", International Journal of Theoretical &
Applied Mechanics/09736085, 20090301

Publication

<1%

32

Bidin, Biliانا. "Numerical Solution of the
Boundary Layer Flow Over an Exponentially
Stretching Sheet with Thermal Radiation",
European Journal of Scientific
Research/1450216X, 20090715

Publication

<1%

33

Freidoonimehr, Navid Rostami, Behnam Ras.
"Analytical modelling of three-dimensional
squeezing nanofluid flow in a rotating channel
on a lower ", Mathematical Problems in
Engineering, Annual 2014 Issue

Publication

<1%

34

ns.snd.edu.gr

Internet Source

<1%

35

202.204.50.104

Internet Source

<1%

36

www.waset.org

Internet Source

<1%

37

Pullepu, Bapuji Sambath, P. Viswanathan,.
"Effects of chemical reactions on unsteady free
convective and mass transfer flow from a
vertical con", Mathematical Problems in
Engineering, Annual 2014 Issue

Publication

<1%

38

Mahmoud, Mostafa A.A.. "A note on variable
viscosity and chemical reaction effects on
mixed convection heat and mass transfe",
Mathematical Problems in Engineering, Annual
2007 Issue

Publication

<1%

39

Kumar Ch., Kishore Bandari, Shankar. "Melting
heat transfer in boundary layer stagnation-
point flow of a nanofluid towards a stretching-
sh", Canadian Journal of Physics, Dec 2014
Issue

Publication

<1%

40

www.lana.it

Internet Source

<1%

41	lambda.gsfc.nasa.gov Internet Source	<1%
42	Submitted to Loughborough University Student Paper	<1%
43	www.ijastnet.com Internet Source	<1%
44	www.scik.org Internet Source	<1%
45	CHOI, Sung-Min. "Fatigue Resistance of Angle Shape Shear Connector used in Steel-Concrete Composite Slab", NAGOYA Repository (New oai_dc setup Aug 2014), 2011. Publication	<1%
46	Rashidi, M.M. Momoniat, E. Ferdows, M. B. "Lie group solution for free convective flow of a nanofluid past a chemically reacting horizontal pla", Mathematical Problems in Engineering, Annual 2014 Issue Publication	<1%
47	www.zju.edu.cn Internet Source	<1%
48	www.ijame.uz.zgora.pl Internet Source	<1%
49	Mahmoud, Mostafa Waheed, Shimaa. "Effects of slip and heat generation/absorption on MHD	<1%

mixed convection flow of a micropolar fluid ov",
Mathematical Problems in Engineering, Annual
2010 Issue

Publication

50

www.sdss.org

Internet Source

<1%

51

Abbasbandy, S. Hayat, T.. "On series solutions for MHD plane and axisymmetric flow near a stagnation point.(Research Article)(m",
Mathematical Problems in Engineering, Annual
2009 Issue

Publication

<1%

52

icking-music-archive.org

Internet Source

<1%

53

Khan, Arshad Khan, Ilyas Ali, Farhad Sha.
"Effects of wall shear stress on MHD conjugate flow over an inclined plate in a porous medium with ra",
Mathematical Problems in
Engineering, Annual 2014 Issue

Publication

<1%

54

www.classicistranieri.it

Internet Source

<1%

55

paduaresearch.cab.unipd.it

Internet Source

<1%

56

Uddin, Mohammed Jashim Beg, Osman Anwar
. "Mathematical modelling of radiative

<1%

hydromagnetic thermosolutal nanofluid
convection slip flow in sa", Mathematical
Problems in Engineering, Annual 2014 Issue

Publication

57

Yazdi, M.H. Hashim, I. Fudholi, A. Oosha.
"Entropy generation analysis of power-law non-
Newtonian fluid flow caused by micropatterned
moving su", Mathematical Problems in
Engineering, Annual 2014 Issue

Publication

<1%

58

www.darmowe-ebooki.com

Internet Source

<1%

EXCLUDE QUOTES ON

EXCLUDE MATCHES < 3 WORDS

EXCLUDE
BIBLIOGRAPHY ON